frontiers | Research Topics

Metabolic regulation under oxidative stress in cancer

Edited by
Ali Vaziri-Gohar, Ilya R. Bederman and Elavarasan Subramani

Published in
Frontiers in Oncology

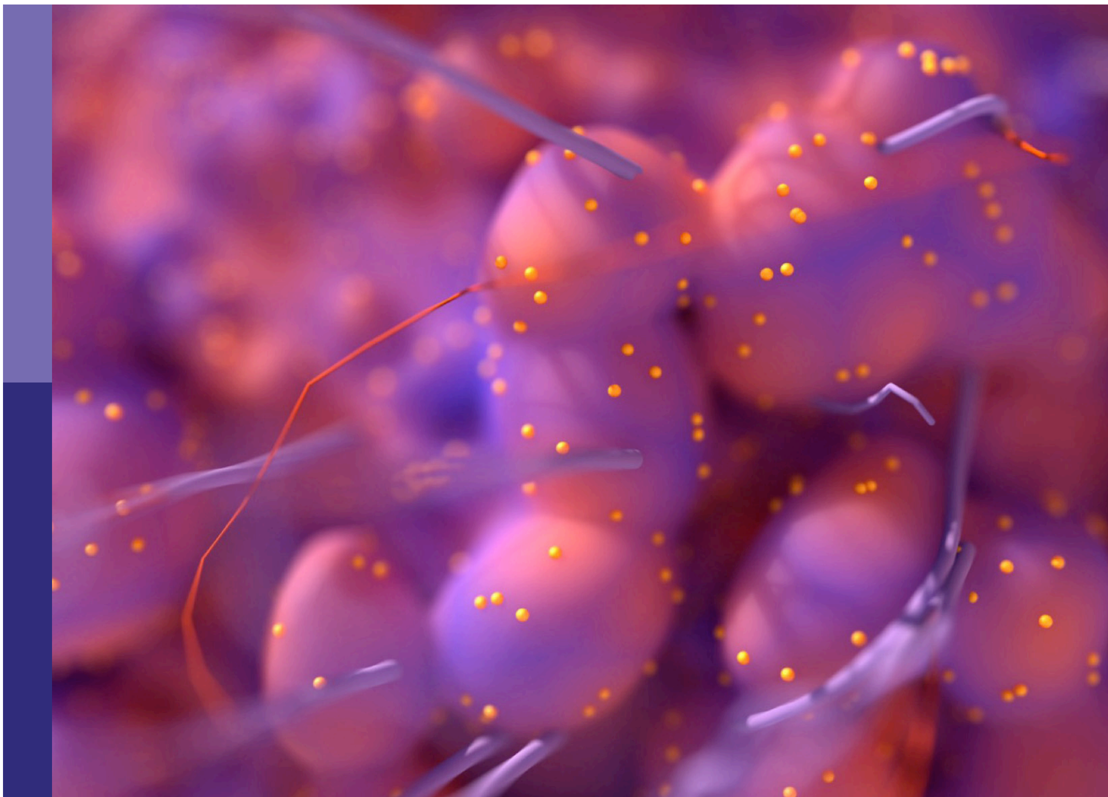

October 2023

ISSN 1664-8714
ISBN 978-2-8325-3569-1
DOI 10.3389/978-2-8325-3569-1

About Frontiers

Frontiers is more than just an open access publisher of scholarly articles: it is a pioneering approach to the world of academia, radically improving the way scholarly research is managed. The grand vision of Frontiers is a world where all people have an equal opportunity to seek, share and generate knowledge. Frontiers provides immediate and permanent online open access to all its publications, but this alone is not enough to realize our grand goals.

Frontiers journal series

The Frontiers journal series is a multi-tier and interdisciplinary set of open-access, online journals, promising a paradigm shift from the current review, selection and dissemination processes in academic publishing. All Frontiers journals are driven by researchers for researchers; therefore, they constitute a service to the scholarly community. At the same time, the *Frontiers journal series* operates on a revolutionary invention, the tiered publishing system, initially addressing specific communities of scholars, and gradually climbing up to broader public understanding, thus serving the interests of the lay society, too.

Dedication to quality

Each Frontiers article is a landmark of the highest quality, thanks to genuinely collaborative interactions between authors and review editors, who include some of the world's best academicians. Research must be certified by peers before entering a stream of knowledge that may eventually reach the public - and shape society; therefore, Frontiers only applies the most rigorous and unbiased reviews. Frontiers revolutionizes research publishing by freely delivering the most outstanding research, evaluated with no bias from both the academic and social point of view. By applying the most advanced information technologies, Frontiers is catapulting scholarly publishing into a new generation.

What are Frontiers Research Topics?

Frontiers Research Topics are very popular trademarks of the *Frontiers journals series*: they are collections of at least ten articles, all centered on a particular subject. With their unique mix of varied contributions from Original Research to Review Articles, Frontiers Research Topics unify the most influential researchers, the latest key findings and historical advances in a hot research area.

Find out more on how to host your own Frontiers Research Topic or contribute to one as an author by contacting the Frontiers editorial office: frontiersin.org/about/contact

Metabolic regulation under oxidative stress in cancer

Topic editors
Ali Vaziri-Gohar — Loyola University Chicago, United States
Ilya R. Bederman — Case Western Reserve University, United States
Elavarasan Subramani — University of Texas MD Anderson Cancer Center, United States

Citation
Vaziri-Gohar, A., Bederman, I. R., Subramani, E., eds. (2023). *Metabolic regulation under oxidative stress in cancer*. Lausanne: Frontiers Media SA. doi: 10.3389/978-2-8325-3569-1

Table of contents

frontiers | Frontiers in Oncology

TYPE Editorial
PUBLISHED 12 September 2023
DOI 10.3389/fonc.2023.1286086

EDITED AND REVIEWED BY
Michael P. Lisanti,
University of Salford, United Kingdom

*CORRESPONDENCE
Elavarasan Subramani
esubramani@mdanderson.org
Ilya Bederman
ilya@case.edu
Ali Vaziri-Gohar
avaziri1@luc.edu

RECEIVED 30 August 2023
ACCEPTED 05 September 2023
PUBLISHED 12 September 2023

CITATION
Subramani E, Dominic A, Bhattacharya PK, Frigo DE, Bederman I and Vaziri-Gohar A (2023) Editorial: Metabolic regulation under oxidative stress in cancer.
Front. Oncol. 13:1286086.
doi: 10.3389/fonc.2023.1286086

Editorial: Metabolic regulation under oxidative stress in cancer

Elavarasan Subramani[1]*, Abishai Dominic[1],
Pratip K. Bhattacharya[1], Daniel E. Frigo[1,2,3,4], Ilya Bederman[5]*
and Ali Vaziri-Gohar[6]*

[1]Department of Cancer Systems Imaging, The University of Texas MD Anderson Cancer Center, Houston, TX, United States, [2]Department of Genitourinary Medical Oncology, The University of Texas MD Anderson Cancer Center, Houston, TX, United States, [3]Center for Nuclear Receptors and Cell Signaling, University of Houston, Houston, TX, United States, [4]Department of Biology and Biochemistry, University of Houston, Houston, TX, United States, [5]Department of Genetics and Genome Sciences, Case Western Reserve University, Cleveland, OH, United States, [6]Department of Cancer Biology, Cardinal Bernardin Cancer Center, Stritch School of Medicine, Loyola University Chicago, Maywood, IL, United States

KEYWORDS

oxidative stress, metabolism, cancer, therapy, biomarker

Editorial on the Research Topic
Metabolic regulation under oxidative stress in cancer

Oxidative stress has emerged as a key component of cancer metabolism that impacts multiple facets of tumor biology (1). Recent studies have shed light on the complex interplay of cellular redox and its impact on molecular mechanisms that govern metabolic reprogramming under oxidative stress (2, 3). It is well established that altered glucose metabolism exhibited by tumor cells leads to an enormous oxidative burden through various metabolic routes (4, 5). What is less known but remains a great interest to the field is whether elevated oxidative stress has a causal role in the development of aggressive and resistant tumor phenotypes (6). To that end, this Research Topic explores various metabolic routes that protect tumor cells against oxidative stress in diverse cancer models. It is anticipated that the development of advanced therapeutic approaches requires an in-depth understanding of the oxidative stress-mediated metabolic processes in cancer, including its effects on aspects of the tumor milieu such as immune cells-related functions.

The study by Koc et al. in this Research Topic identified the role of oxidative phosphorylation (OXPHOS) in ovarian cancer through mitochondrial proteomic analysis. They found that increased levels of mitochondrial- and nuclear-encoded OXPHOS subunits correlated with the increased rates of mitochondrial biogenesis in ovarian cancer cell lines. Furthermore, they identified that reduced OXPHOS subunits expression and mitochondrial translation significantly increased mitochondrial reactive oxygen species (ROS) production while decreasing superoxide dismutase 2 (SOD2). This study makes an interesting case for including mitochondrial biogenesis- and redox state-targeted therapies, which may have significant therapeutic impact when combined with current treatment strategies. To explore insights into the mitochondrial nucleic acids sensing signaling pathways, Gong et al. described a specific role of Y-box binding protein (YB1) with mitochondria-derived RNAs in breast cancer cell apoptosis and ROS production. As such, it is of great importance in exploring the inter-linkage of cytoplasmic and mitochondrial factors facilitating metabolic regulation for understanding redox metabolism in cancer. In an interesting study by Yuan et al. in this Research Topic, the research team has developed a prognostic risk model based on oxygen metabolism for colorectal cancer. Although this study was only a proof of concept for future studies of similar prognostic models, development of these correlative biomarkers will be useful in clinical cancer progression monitoring and can change the current management of colorectal cancer.

Glutathione peroxidases (GPX) protect cells from oxidative insults and they have been implicated in cancer progression and metastasis (7). In this Research Topic, Hu et al. showed that GPX3 was downregulated in several tumor types and that the expression levels correlate with patient outcomes. This finding suggests that GPX3 has a specific role in regulating redox states in cancer and could regulate the progression and metastasis of the disease. In another study by Canevarolo et al., increased glutathione (GSH) levels and other cellular oxidative stress mechanisms were found to be a key resistance mechanism to the antifolate methotrexate, a drug used for acute lymphoblastic leukemia (ALL). These findings point to another critical metabolic feature that mediates drug resistance in ALL.

Another rapidly emerging field in metabolism is ferroptosis, an iron-dependent cell death mechanism characterized mainly by substantial lipid peroxidation (8). Anti-ferroptotic mechanisms have been implicated in cancer progression and accordingly, inducers of ferroptosis are being actively pursued as a novel class of cancer treatments (9). In this special edition, Yuan et al. identified that STEAP3 gene is a key regulator of ferroptosis by evaluating patient data and molecular validation. Further, Han et al. developed a prognostic model for hepatocellular carcinoma and discovered a set of genes regulating ferroptosis mediated inflammatory responses. Similarly, Zhu et al. developed a 10-gene ferroptosis prognostic model in acute myeloid leukemia which might be of interest in future therapeutic targets. A more focused study by Yi et al. described the specific role of CXCL2 gene in ferroptosis related mechanisms and its negative association with clinical malignancy features. In search of new biomarkers and drug targets of hepatocellular carcinoma, Wen et al. revealed the mechanistic role of oncoprotein-induced transcript 3 protein (OIT3) regulating ferroptosis via arachidonic metabolism. Thus, OIT3 is suggested to be a potential diagnostic marker and therapeutic target of hepatocellular carcinoma.

In the recent years, there is a considerable increase in investigations on cuproptosis, a new form of copper-dependent regulated cell death and highly regulated by cellular metabolism (10). Zhang et al. found that 14 cuproptosis and copper metabolism-related genes significantly correlated with the immune microenvironment, suggesting its involvement in cancer progression. Their investigation suggested the potential use of cuproptosis and copper metabolism–related gene signatures as prognostic biomarkers of head and neck squamous cell carcinoma for better patient outcomes. Further, Wang et al. discussed the insights into copper metabolism and cuproptosis in cancer progression and its potential as targeted therapy. Although future studies are required to validate these initial findings of biomarker-based monitoring strategies, the studies covered in this Research Topic highlight the significance and potential impact in clinical settings.

Future investigation into the foundational mechanisms underlying metabolic signatures of tumor cells under oxidative stress will provide the knowledge needed to develop novel therapeutic strategies. In many cancer types, oxidative stress is highly elevated. Strategies leveraging this increased oxidative burden can lead to novel treatments such as those augmenting ferroptosis or cuproptosis. While much work has been done in this regard, an increased understanding of the molecular mechanisms underlying aberrant cellular metabolism and, in particular, oxidative stress in cancer progression and treatment resistance will enable the inception of new treatment strategies that leverage these tumor characteristics, ultimately yielding improved patient outcomes.

Author contributions

ES: Writing – original draft, Writing – review & editing. AD: Writing – original draft, Writing – review & editing. PB: Writing – review & editing. DF: Writing – review & editing. IB: Writing – review & editing. AV-G: Writing – review & editing.

Acknowledgments

ES, IB and AV-G are deeply grateful to the Chief Editors and the editorial board for the opportunity to be the guest editors of this Research Topic.

Conflict of interest

DF has received research funding from GTx, Inc, and has a familial relationship with Biocity Biopharmaceuticals, Hummingbird Bioscience, Bellicum Pharmaceuticals, Maia Biotechnology, Alms Therapeutics, Hinova Pharmaceuticals, and Barricade Therapeutics.

The remaining authors declare that the research was conducted in the absence of any commercial or financial relationships that could be construed as a potential conflict of interest.

Publisher's note

References

1. Pavlova NN, Zhu J, Thompson CB. The hallmarks of cancer metabolism: still emerging. *Cell Metab* (2022) 34(3):355–77. doi: 10.1016/j.cmet.2022.01.007

2. Lennicke C, Cochemé HM. Redox metabolism: ros as specific molecular regulators of cell signaling and function. *Mol Cell* (2021) 81(18):3691–707. doi: 10.1016/j.molcel.2021.08.018

3. Wang K, Jiang J, Lei Y, Zhou S, Wei Y, Huang C. Targeting metabolic–redox circuits for cancer therapy. *Trends Biochem Sci* (2019) 44(5):401–14. doi: 10.1016/j.tibs.2019.01.001

4. Vaziri-Gohar A, Cassel J, Mohammed FS, Zarei M, Hue JJ, Hajihassani O, et al. Limited nutrient availability in the tumor microenvironment renders pancreatic tumors sensitive to allosteric IDH1 inhibitors. *Nat Cancer* (2022) 3(7):852–65. doi: 10.1038/s43018-022-00393-y

5. Ahmad IM, Aykin-Burns N, Sim JE, Walsh SA, Higashikubo R, Buettner GR, et al. Mitochondrial $O2\cdot^-$ and H2O2 mediate glucose deprivation-induced stress in human cancer cells. *J Biol Chem* (2005) 280(6):4254–63. doi: 10.1074/jbc.M411662200

6. Vaziri-Gohar A, Hue JJ, Abbas A, Graor HJ, Hajihassani O, Zarei M, et al. Increased glucose availability sensitizes pancreatic cancer to chemotherapy. *Nat Commun* (2023) 14(1):3823. doi: 10.1038/s41467-023-38921-8

7. Chang C, Worley BL, Phaëton R, Hempel N. Extracellular glutathione peroxidase GPx3 and its role in cancer. *Cancers* (2020) 12(8):2197. doi: 10.3390/cancers12082197

8. Dixon SJ, Lemberg KM, Lamprecht MR, Skouta R, Zaitsev EM, Gleason CE, et al. Ferroptosis: an iron-dependent form of nonapoptotic cell death. *cell* (2012) 149(5):1060–72. doi: 10.1016/j.cell.2012.03.042

9. Lei G, Zhuang L, Gan B. Targeting ferroptosis as a vulnerability in cancer. *Nat Rev Cancer* (2022) 22(7):381–96. doi: 10.1038/s41568-022-00459-0

10. Xie J, Yang Y, Gao Y, He J. Cuproptosis: mechanisms and links with cancers. *Mol Cancer* (2023) 22(1):46. doi: 10.1186/s12943-023-01732-y

Frontiers in Oncology

TYPE Original Research
PUBLISHED 22 August 2022
DOI 10.3389/fonc.2022.955336

OPEN ACCESS

EDITED BY
Jungsu S. Oh,
University of Ulsan, South Korea

REVIEWED BY
Haolong Li,
University of California, San Francisco, United States
Sunghoon Kwon,
Konkuk University, South Korea

*CORRESPONDENCE
Jingsong Hou
houjs@mail.sysu.edu.cn

†These authors have contributed equally to this work

SPECIALTY SECTION
This article was submitted to Head and Neck Cancer, a section of the journal Frontiers in Oncology

RECEIVED 28 May 2022
ACCEPTED 01 August 2022
PUBLISHED 22 August 2022

CITATION
Zhang S, Zhang L, Lu H, Yao Y, Liu X and Hou J (2022) A cuproptosis and copper metabolism–related gene prognostic index for head and neck squamous cell carcinoma.
Front. Oncol. 12:955336.
doi: 10.3389/fonc.2022.955336

A cuproptosis and copper metabolism–related gene prognostic index for head and neck squamous cell carcinoma

Shuaiyuan Zhang[1,2†], Lujin Zhang[1,2†], Huanzi Lu[1,2†], Yihuan Yao[1,2], Xiaoyong Liu[1,2] and Jingsong Hou[1,2*]

[1]Department of Oral and Maxillofacial Surgery, Guanghua School of Stomatology, Hospital of Stomatology, Sun Yat-sen University, Guangzhou, China, [2]Guangdong Provincial Key Laboratory of Stomatology, Sun Yat-sen University, Guangzhou, China

Background: The purpose of this study was to identify the prognostic value of cuproptosis and copper metabolism–related genes, to clarify their molecular and immunological characteristics, and to elucidate their benefits in head and neck squamous cell carcinoma (HNSCC).

Methods: The details of human cuproptosis and copper metabolism–related genes were searched and filtered from the msigdb database and the latest literature. To identify prognostic genes associated with cuproptosis and copper metabolism, we used least absolute shrinkage and selection operator regression, and this coefficient was used to set up a prognostic risk score model. HNSCC samples were divided into two groups according to the median risk. Afterwards, the function and immune characteristics of these genes in HNSCC were analyzed.

Results: The 14-gene signature was constructed to classify HNSCC patients into low-risk and high-risk groups according to the risk level. In the The Cancer Genome Atlas (TCGA) cohort, the overall survival (OS) rate of the high-risk group was lower than that of the low-risk group ($P < 0.0001$). The area under the curve of the time-dependent Receiver Operator Characteristic (ROC) curve assessed the good performance of the genetic signature in predicting OS and showed similar performance in the external validation cohort. Gene Ontology and Kyoto Encyclopedia of Genes and Genomes enrichment assays and Protein-Protein Interaction (PPI) protein networks have been used to explore signaling pathways and potential mechanisms that were markedly active in patients with HNSCC. Furthermore, the 14 cuproptosis and copper metabolism-related genes were significantly correlated with the immune microenvironment, suggesting that these genes may be linked with the immune regulation and development of HNSCC.

Conclusions: Our results emphasize the significance of cuproptosis and copper metabolism as a predictive biomarker for HNSCC, and its expression levels seem to be correlated with immune- related features; thus, they may be a possible biomarker for HNSCC prognosis.

KEYWORDS

cuproptosis, copper metabolism-related genes, gene signature, nomogram, prognosis, head and neck squamous cell carcinoma

Introduction

Head and neck squamous cell carcinoma (HNSCC) originates from the epithelial cells of the mouth, pharynx, and larynx, which is a kind of malignant tumor with high incidence (1, 2). Smoking, alcohol consumption, viral infection, environmental pollutants, and genetics are all risk factors for HNSCC (1). Since the beginning of this century, great progress has been made in the research of immunotherapy and other targeted drugs related to HNSCC, which have been applied in clinic. However, the five-year survival rate of HNSCC is only 50% (3, 4). In addition, due to the asymptomatic character of HNSCC and the lack of early detection, the risk of recurrence and metastasis of cancer patients is still high (5). Therefore, it is particularly critical to uncover new biomarkers for HNSCC patients and to better customize the prevention, screening, and treatment of HNSCC.

Copper is a trace element that has a significant impact on human health. It exists in organisms in the form of Cu (I) and Cu (II). Existing experimental results show that copper plays an important role in being an intracellular antioxidant, cellular respiration, nerve signal transduction, and the development of extracellular matrix (6). However, at high concentrations, copper can also cause the destruction of intracellular lipids, proteins, and nucleic acids (7). Unlike the known mechanisms of cell death, copper-dependent cell death depends on mitochondrial respiration, which occurs through the direct combination of copper with the fatty acylation component of the tricarboxylic acid (TCA) cycle (8). At present, some antitumor drugs can specifically induce cancer cell death, but how to overcome drug resistance is still an important problem to be solved. Platinum-based antitumor drugs (cisplatin and carboplatin) are commonly used to treat multiple types of solid tumors, including HNSCC. However, there is sufficient evidence to suggest that the long-term use of platinum-based antitumor agents in HNSCC patients can develop drug resistance (9–11). Cuproptosis and copper metabolism may be beneficial to the treatment of drug-resistant HNSCC. Copper homeostasis imbalance can be observed in the progression of HNSCC, and copper metabolism–related genes are related to the sensitivity of HNSCC to platinum compounds (9, 12). Copper can enhance the sensitivity of HNSCC patients to cisplatin by combining with copper ionophore disulfide (13). Therefore, it is very important to explore new forms of regulatory cell death, such as cuproptosis, and to find practical and effective prognostic markers for HNSCC. Thus, Tsvetkov et al. suggest that there may be a window that allows an increased concentration of copper in cells to be used to selectively kill cancer cells (14). The activation of the copper-induced cell death pathway may surpass the current drug resistance of chemotherapeutic drugs and open a new research field for new tumor therapies. At present, researchers have great interest in the relationship between cuproptosis and tumor, and its function in HNSCC needs to be further clarified (15–18). Therefore, the role of the entire cuproptosis and copper metabolism–related gene repertoire, in the prognosis of HNSCC, needs to be investigated.

In this study, HNSCC transcripts from several patient cohorts were downloaded from the public database, and 14 genetic signatures of cuproptosis and copper metabolism were identified by bioinformatics analysis. These markers related to cuproptosis and copper metabolism may become an effective index for predicting the prognosis of HNSCC patients

Method

Data collection

Through a comprehensive analysis of the source literature, we screened 139 genes related to cuproptosis and copper metabolism from the msigdb database and added recently reported genes to integrate them for the next step. The TCGA database was used to obtain patient clinicopathological data (https://portal.gdc.cancer.gov/). The data of 546 HNSCC samples were downloaded, including 502 cancer samples and

44 precancerous samples. All 44 adjacent normal tissue specimens belong to the normal group. The phenotype information, survival data (version: 12-06-2021), and RNA sequence data (version: 12-06-2021) of HNSCC patients, cervical cancer Cervical squamous cell carcinoma andendocervical adenocarcinoma (CESC) patients and esophageal cancer (ESCA) patients were acquired from the public database UCSC Xena (https://xenabrowser.net/datapages/). Those without RNA-seq data were excluded.

Construction and validation of the cuproptosis and copper metabolism–related gene prognostic index

Univariate Cox regression analysis (P<0.05) was applied to sift prognostic-related genes; 35 genes were identified, and 14 differentially related genes were identified by least absolute shrinkage and selection operator (LASSO) regression. Complete the above steps through the glmnet package. The coefficient (β) of LASSO regression corresponding to each gene was performed to construct the risk score for predicting the prognosis. Risk score = (coefficient Gene1 × expression of Gene1) + (coefficient Gene2 × expression of Gene2) +……+ (coefficient Gene n × expression Gene n), and the intermediate value of risk score is used to distinguish high-risk groups from low-risk groups. The prognostic power of the index was assessed by Kaplan-Meier (K-M) survival curves with log-rank tests. In order to test the independent prognostic accuracy of the index, we established 1-year, 3-year and 5-year time-dependent ROC charts, analyzed them with survival ROC software, and calculated the area under the curve (AUC).

Differentially expressed gene identification and bioinformatics analysis

The Wilcoxon function in R is used to calculate differentially expressed genes (DEGs) between clustering subgroups False discovery rate (FDR<0.05 and |log2FC|>1). According to all the data of DEGs, Gene Ontology (GO) and Kyoto Encyclopedia of Genes and Genomes (KEGG) analyses were studied. Then, the function enrichment analysis of DEGs protein–protein interaction network was fulfilled through the Search tool for the retrieval of interacting genes/proteins (STRING) database (https://string-db.org/), and the online calculation and prediction were carried out. On this basis, the visibility of PPI is analyzed by using Cytoscape. Principal component analysis (PCA) was used for realizing the dimensionality reduction and visualization of signature genes. In addition, the potential biological functions were studied by gene set enrichment analysis (GSEA 4.1.0), and $P < 0.05$ and $FDR < 0.05$ were considered statistically significant.

Tumor immune microenvironment analysis

In order to clarify the prognostic characteristics of the tumor immune microenvironment, the high-risk group and low-risk group were compared. We applied the CIBERSORTx website (https://cibersortx.stanford.edu/) to compare and reckon the abundance of 22 immune cells in the two populations. Platform xCell (xCell signature) (19) was used to calculate the proportion of immune cell infiltration in the tumor environment.

Construction of the predictive nomogram

Using the “rms” R package, a nomogram was established to predict the 1–5 year survival rate of HNSCC patients. The calibration curve is used to evaluate the prediction ability of nomogram. The closer to the 45° line, the better the prediction ability. Then, the independent prognostic factors were compared by decision curve analysis (DCA) to explore the difference of the combined nomogram in clinical benefit.

Genomic variance analysis

In order to identify the genomic variation, the distribution of all somatic mutant genes was compared. Somatic mutation data were downloaded from the Genomic data commons (GDC) database (https://portal.gdc.cancer.gov/). A comparison of tumor mutation burden (TMB) was conducted between the high-risk group and low-risk group.

Statistical analysis

All the statistical analyses of this study were performed using R software. The Wilcoxon test was used to selected DEGs of the two groups. Kaplan–Meier survival analysis and the Cox regression model were used for univariate survival analysis and multivariate survival analysis, respectively. Wilcoxon test was used to determine whether there was a difference in the proportion of somatic mutations. Bilateral $P < 0.05$ was considered significant.

Results

Construction the prognostic signature of cuproptosis and copper metabolism–related genes and validating its predictive performance

In this study, our bioinformatics analysis is based on the workflow shown in Figure 1. A total of 546 samples from the TCGA database were used; 44 normal samples, incomplete prognostic information, and OS less than 30 days were excluded; and 493 cancer samples were eventually included in the study. To establish a novel prognostic model, 35 genes related to prognosis were selected from 139 genes by univariate Cox analysis, and then, the appropriate genes related to cuproptosis and copper metabolism were selected by LASSO regression analysis (Figure 2A and Additional Figure 1). Finally, based on the optimal value of λ, a 14-gene signature was identified (Figures 2B, C). Figure 2D shows the K-M curve of each gene.

As mentioned above, 14 gene-based prognostic signatures were used to compute the risk score for each sample (Figures 3A, B). The formula is as follows: risk score = (-0.3847 × expression of *CYP2D6*) + (0.1679 × expression of *PRKN*) + (-0.2781 × expression of *ABCB1*) + (-0.0177 × expression of *CCL5*) + (-0.0066 × expression of *LOX*L1) + (0.0252 × expression of *MT1E*) + (-0.0554 × expression of *CDKN2A*) + (0.1500 × expression of *CXCL8*) + (0.3308 × expression of *COX11*) + (0.0942 × expression of *COX5A*) + (0.0945 × expression of *COX19*) + (0.0222 × expression of *ACLY*) + (-0.0005 × expression of *BCL2*) + (-0.0047 × expression of *DAPK2*). All patients were grouped into a high-risk group (n=246) or a low-risk group (n=247) according to the median risk score. Kaplan–Meier survival analysis indicated that the OS of high-risk groups was markedly lower than that of low-risk groups (Kaplan–Meier survival analysis P < 0.0001, Figure 3D). The ROC curve showed that the risk score development in our present study had a good predictive value of 0.70, 0.69, and 0.63 for 1-year AUC, 3-year AUC, and 5-year AUC, respectively (Figure 3C). Therefore, according to the survival curve, we finally determined that 14 genes related to cuproptosis and copper metabolism were significantly correlated with prognosis: *ACLY*, *COX5A*, *COX11*, *COX19*, *CXCL8*, *PRKN*, and *MTIE* were negatively correlated with OS, while *ABCB1*, *BCL2*, *CCL5*, *CDKN2A*, *CYP2D6*, *DAPK2*, and *LOXL1* were positively correlated with OS. Similarly, PCA confirmed that these 14 genes have implications for OS prediction (Additional Figure 1). In conclusion, the above results suggest that the model composed of cuproptosis and copper metabolism–related genes may be a credible and valuable indicator for predicting the prognosis of HNSCC.

We intended to select the available HNSCC sample cohort to verify the above results. However, the model genes were incomplete in any other HNSCC cohort of Gene expression omnibus (GEO) databases. Therefore, we selected other cohorts for validation. All three malignancies contain an epithelial origin (1, 20, 21). On one hand, ESCA and HNSCC have high homology; they have a similar metastatic behavior and have common internal resistance to conventional systemic therapy (22). On the other hand, esophagus is a high-risk site for HNSCC patients to develop

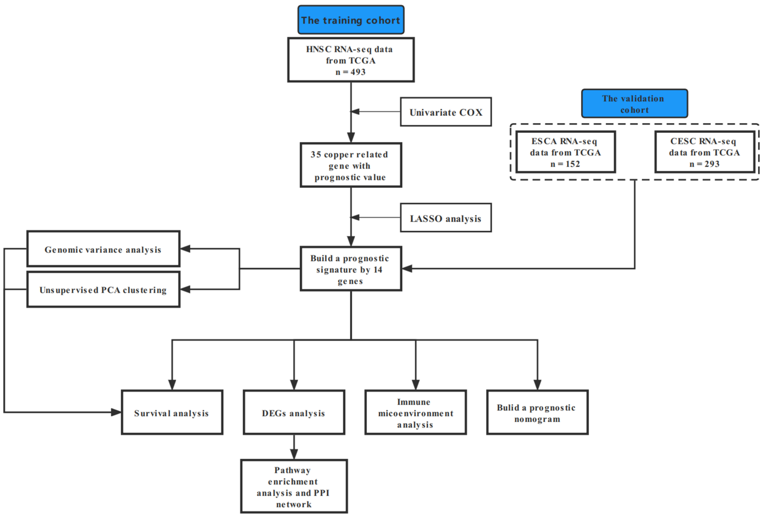

FIGURE 1
A flowchart outlining the schematic design of a study.

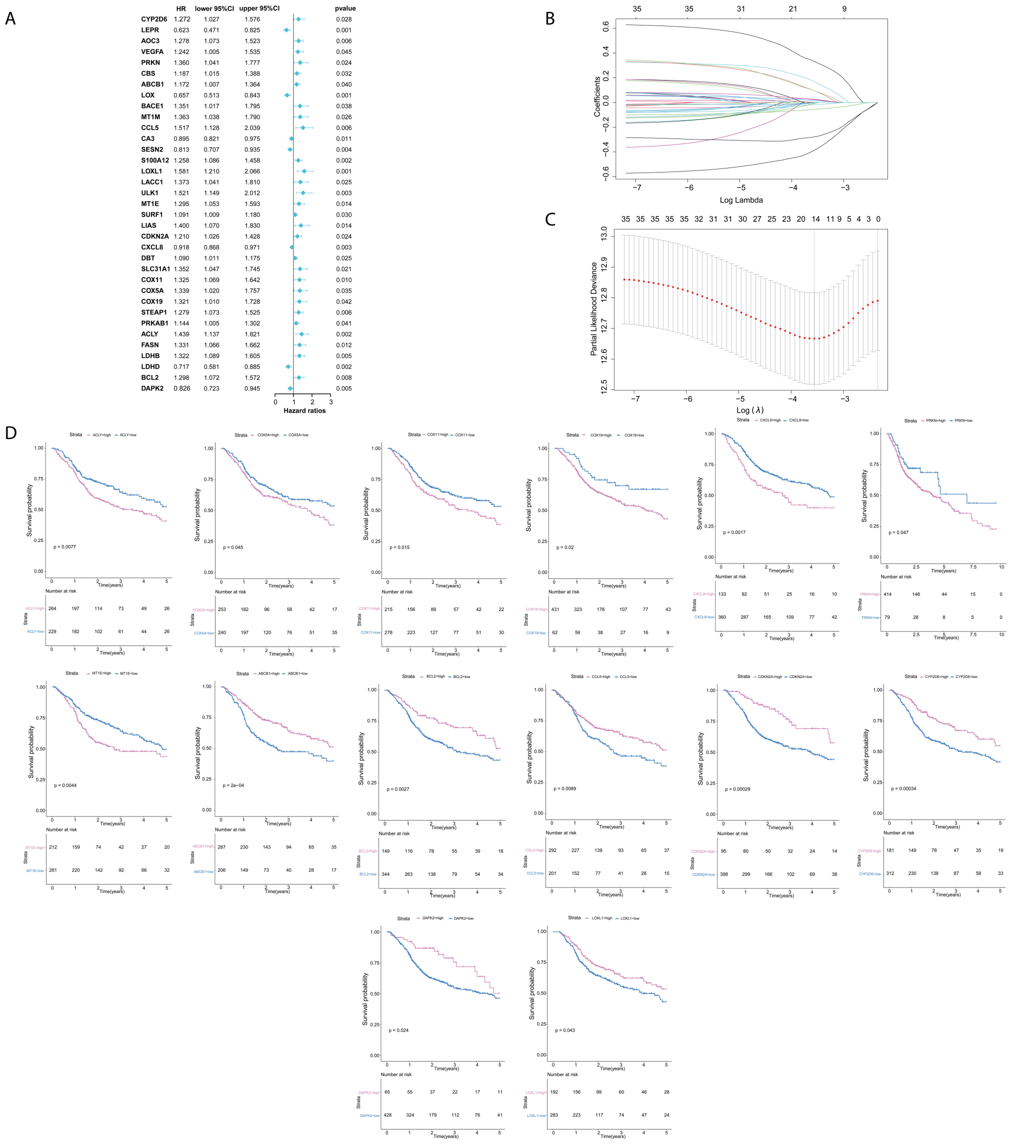

FIGURE 2
Construction of cuproptosis and copper metabolism–related gene prognostic signature. **(A)** Cuproptosis and copper metabolism–related genes of Cox analysis. **(B, C)** Least absolute shrinkage and selection operator analysis was performed to select the optimum genes to construct a 14-gene signature. **(D)** K-M curve of 14 genes.

secondary primary malignant tumors (23, 24). Based on these correlations, we selected the available cohorts of ESCA samples from the TCGA database for verification, including 152 patients with ESCA (Figures 3E–G). For HNSCC and CESC, studies have shown that their immune activation transcriptome has a certain correlation (25). Therefore, we also validated our model in the CESC cohort (Figures 3H–J). The results of this validation queue were consistent with the results we obtained before, which showed that it had excellent reliability and repeatability.

Differentially expressed gene identification and bioinformatics analysis

To further investigate the possible biological functions of 14 genes related to cuproptosis and copper metabolism, we used the "clusterProfiler" package for GO annotations and KEGG pathway enrichment analysis. Figure 2 lists the enriched GO terms and KEGG pathways. DEGs were significantly enriched in immunoglobulin production, the detection of chemicals, stimulus involved in sensory, olfactory pathways, T-cell

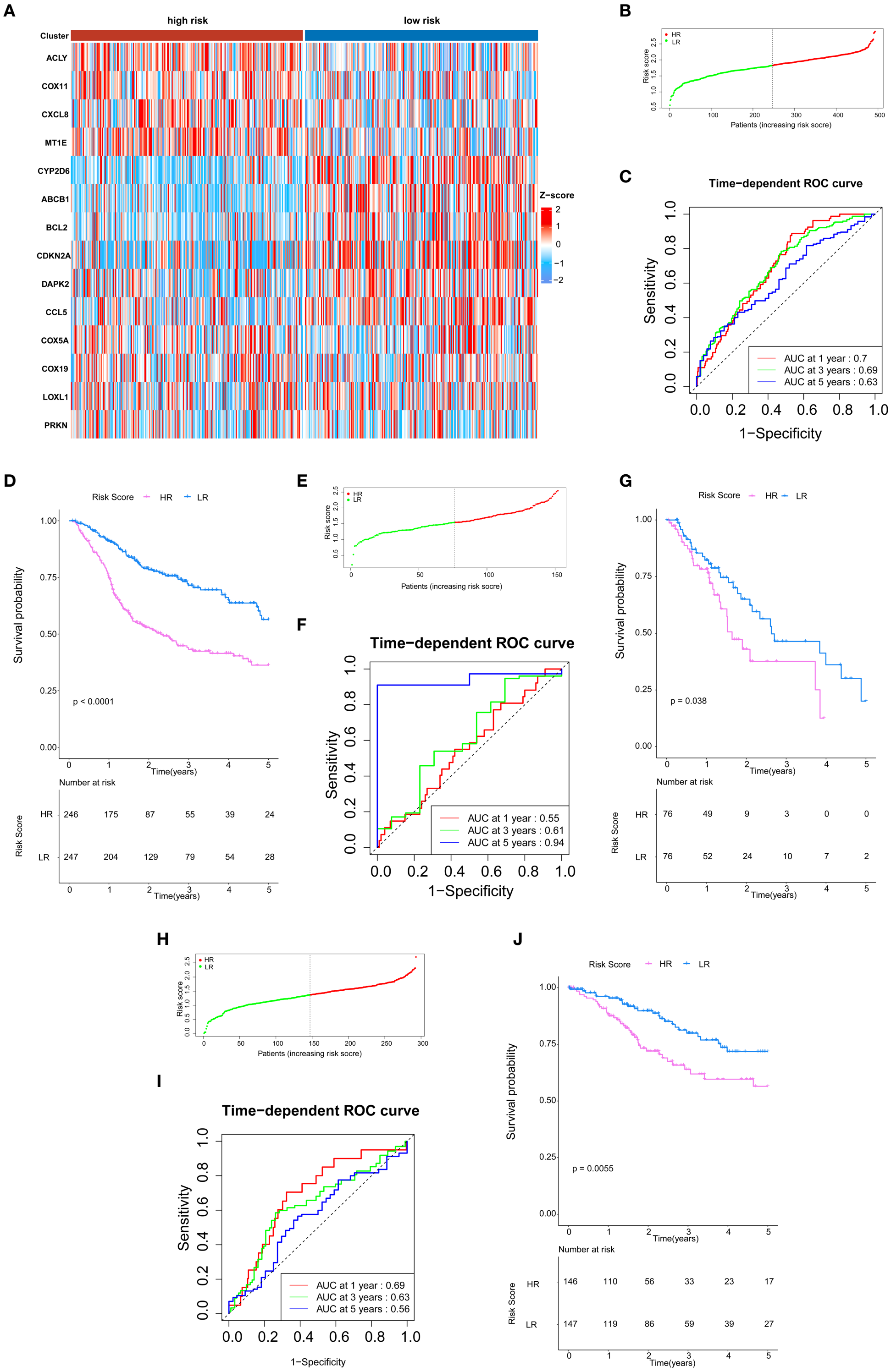

FIGURE 3

Validation of cuproptosis and copper metabolism−related gene prognostic signature. **(A)** Heat map representing the expression level of the prognostic genes based on the high-risk group and the low-risk group of head and neck squamous cell carcinoma (HNSCC) patients. **(B, E, H)** Association between the risk score and the distribution of high- (red) and low- (green) risk groups of HNSCC patients **(B)**, esophageal cancer (ESCA) patients **(E)**, and CESC patients **(H)**. **(C, F, I)** The ROC curves for evaluating the prognostic value by the 14-gene signature in the TCGA cohort of HNSCC patients **(C)**, ESCA patients **(F)**, and CESC patients **(I)**. **(D, G, J)** The overall survival (OS) rates of different groups of HNSCC patients **(D)**, ESCA patients **(G)**, and CESC patients **(J)**.

receptor complexes, and plasma membrane signals (Figures 4A, B). The top three significantly enriched molecular function terms include olfactory receptor activity, antigen binding, and neurotransmitter receptor activity (Figure 4C). In addition, KEGG analysis revealed that the significant enrichment pathway of these DEGs was the olfactory transduction pathway (Figure 4D). The PPI network of DEGs was acquired through the application of the online STRING tool. The results showed that the CD19 molecule (CD19) was the most important gene (Figure 4E). The gene coding protein is a member of immunoglobulin gene superfamily. Its coding protein is cell surface protein, and its expression is limited to B-cell lymphocytes. Moreover, we used GSEA to explore the potential biological functions of 14 genes involved in cuproptosis and copper metabolism. The results of GSEA confirm these findings (Figure 4F).

Analysis of tumor immune microenvironment

Through DEG analysis, we found that these genes play a role in immune-related pathways. As a result, we explored the connection between the cuproptosis and copper metabolism–related signature and the tumor immune microenvironment. We used the CIBERSORTx algorithm and xCell to compare the distribution of immune cells in different groups. It was observed that M2 macrophages, naïve CD4 T cells, resting memory CD4 T cells, resting NK cells, activated mast cells, eosinophils, M0 macrophages, cancer cells, and lymph vessels were more abundant in the high-risk group, while Th17 cells, DC, naïve B cells, plasma cells, CD8 T cells, follicular helper T cells, activated NK cells, activated memory CD4 T cells, M1 macrophages, and resting mast cells were more abounding in the low-risk group (Figure 5A, Additional Figure 2). We also displayed the characteristics related to the immune landscape of the two groups (Figure 5B, Additional Figure 2). Immune-related functions such as human leukocyte antigen, immune checkpoint, and inflammation-related promotion between the two groups were usually more significant in low-risk populations (Figure 5C).

Establishment and evaluation of the predictive nomogram

Multivariate Cox regression was used for determining whether the risk characteristics were independent prognostic

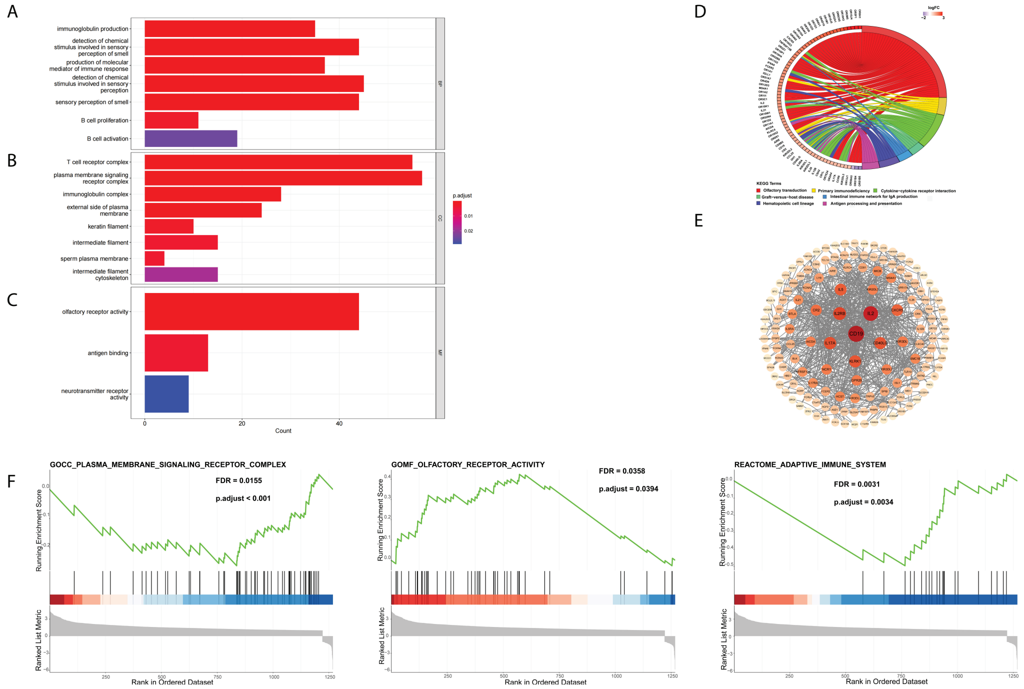

FIGURE 4
DEG Identification and bioinformatics analysis. **(A–D)** The enriched GO **(A)** BP, **(B)** CC, and **(C)** MF terms as well as **(D)** KEGG pathways. GO, gene ontology; KEGG, Kyoto Encyclopedia of Genes and Genomes; DEG, differentially expressed gene; BP, biological process; CC, cellular component; MF, molecular function. **(E)** The PPI network downloaded from the STRING database indicated the interactions among the candidate genes. **(F)** Gene set enrichment analysis.

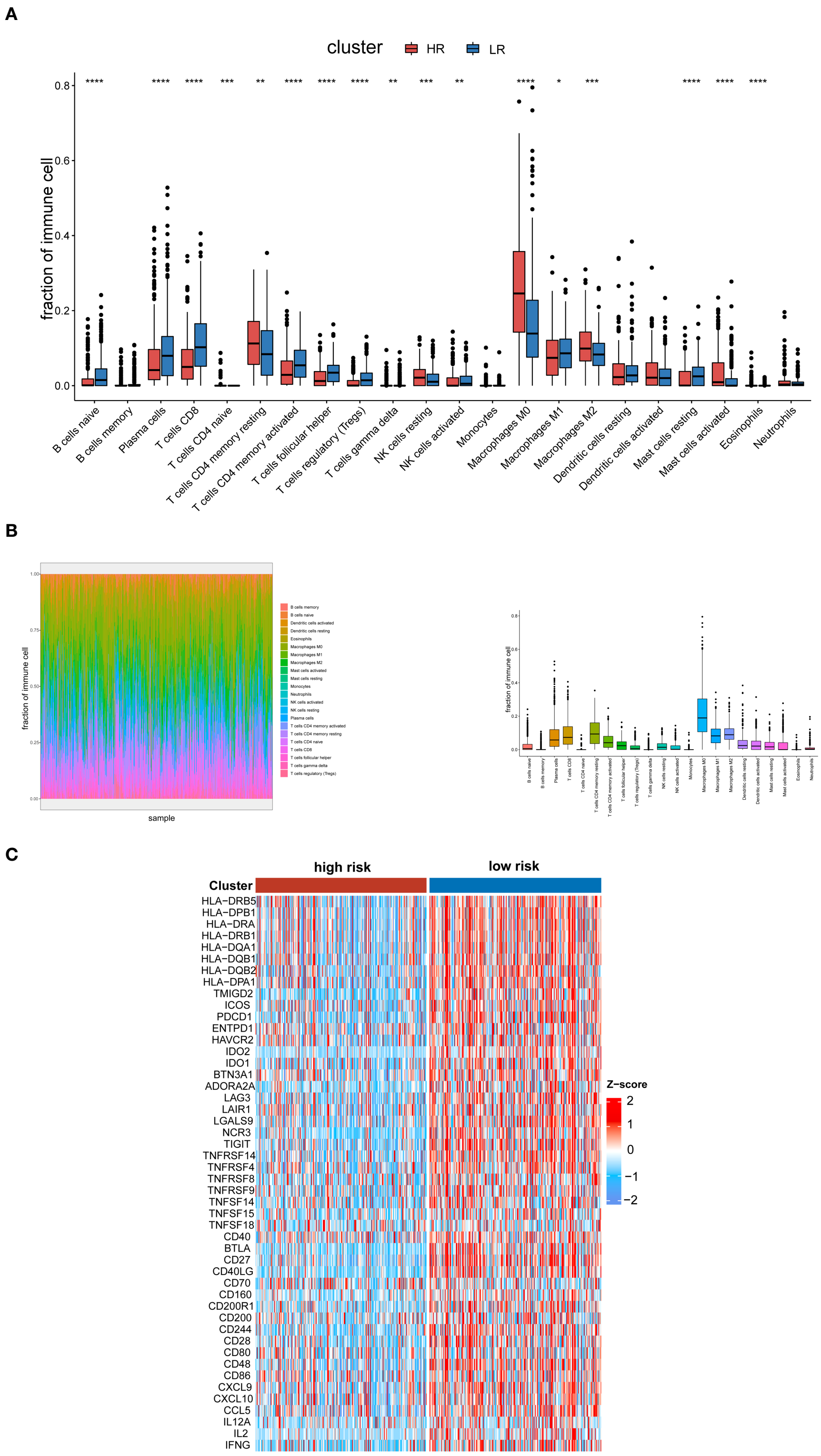

FIGURE 5

Analysis of the tumor immune microenvironment. **(A)** Analysis of the abundance of immune cells *via* the CIBERSORTx algorithm based on the TCGA cohort. **(B)** The characteristics related to the immune landscape of two groups *via* the CIBERSORTx algorithm. **(C)** Heat map of human leukocyte antigen, immune checkpoint, and inflammation-related promotion in the low- and high-risk groups in the TCGA databases. The p-values were shown as: *p < 0.05; **p < 0.01; ***p < 0.001. ****p < 0.0001.

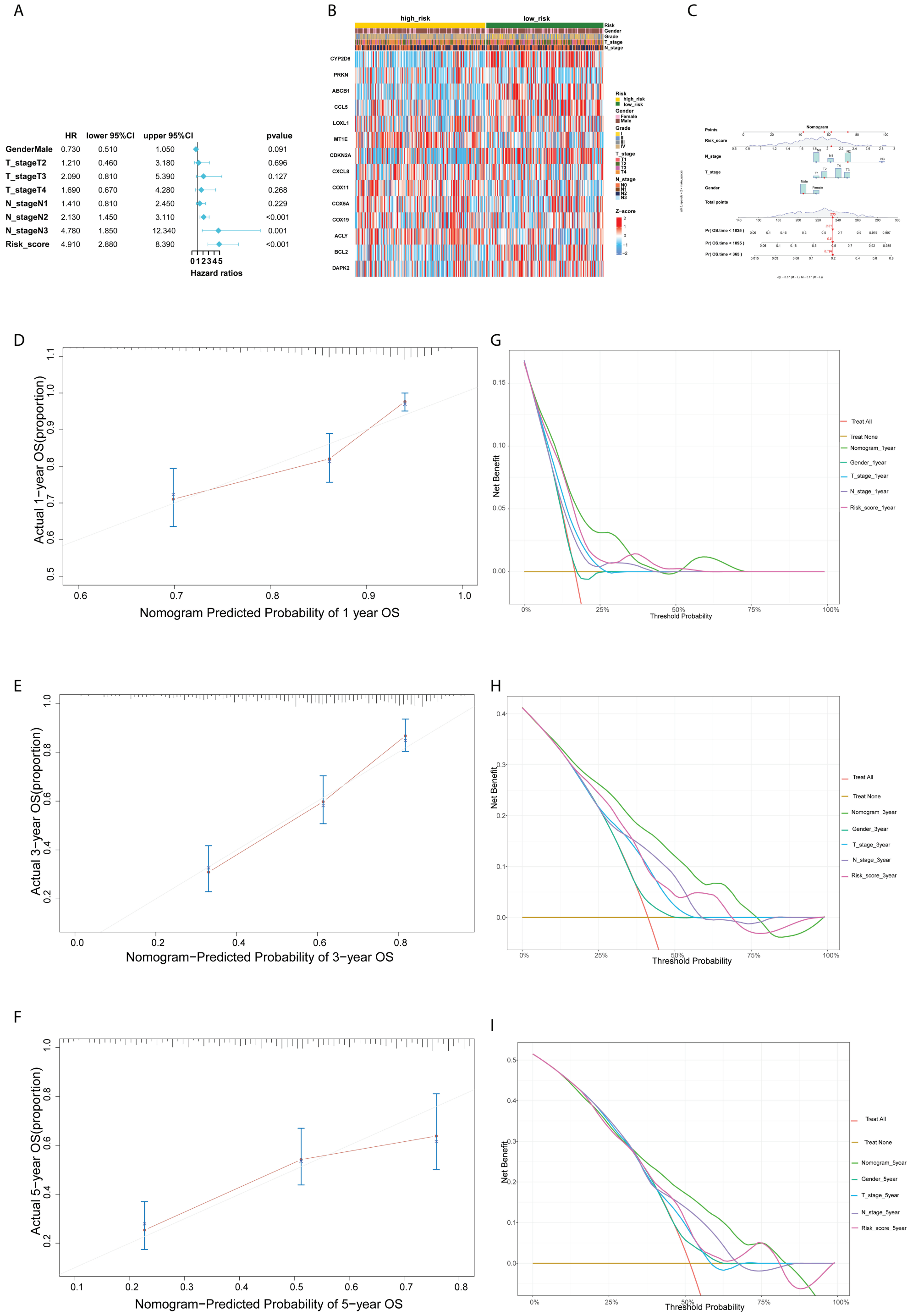

FIGURE 6
Establishment and evaluation of the predictive nomogram.**(A)** Multivariate Cox regression analysis of the clinicopathological features in the TCGA cohort. **(B)** Heat map for cuproptosis and copper metabolism−related gene prognostic signature and clinicopathological manifestations. **(C)** A nomogram for both clinic-pathological factors and prognostic cuproptosis and copper metabolism−related genes. **(D–F)** Plots depict the calibration of nomograms based on the risk score in terms of the agreement between predicted and observed 1-year **(D)**, 3-year **(E)**, and 5-year **(F)** outcomes in the TCGA cohort. **(G, H, I)** Decision curve analyses of the nomograms based on OS in two cohorts for 1 year **(G)**, 3 years **(H)**, and 5 years **(I)**.

factors (Figure 6A). We analyzed the heat map of the association between the prognostic characteristics of cuproptosis and copper metabolism related genes and clinicopathological manifestations, which can be used for the clinical management of HNSCC patients (Figure 6B). To further enhance the predictive ability, a predictive nomogram ground on the integration of the risk score and pathological stage was constructed in the TCGA cohort (Figure 6C). The calibration curve of the nomogram showed that the standard curves for predicting and observing 1-year, 3-year, and 5-year results in the cohort were fairly consistent (Figures 6D–F). In addition, we used DCA analysis to evaluate the predicted values of nomogram for the TCGA cohort 1, 3, and 5 years in clinical decision-making (Figures 6G–I).

Genomic variance analysis in the TCGA cohort

In order to explore whether the difference of the copper metabolism gene expression between the two groups is related to gene variation, we conducted genomic variance analysis. We found that *CDKN2A* and *ABCB1* had a high mutation probability in HNSCC (Figure 7A). The results showed that TMB in high-risk patients was higher than that in low-risk groups (P < 0.05, Figure 7B). The OS of patients with low risk and low TMB is higher than that of patients with high risk and high TMB (P < 0.0001, Figure 6C).

Discussion

In this study, we divided HNSCC into two risk subgroups with different TME characteristics based on 14 genes related to cuproptosis and copper metabolism. The characteristics of subgroup survival analysis were also well displayed according to clinical characteristics such as the tumor grade and stage. These results show the cuproptosis and copper metabolism-related genes signature can be considered as a validated dependable model for HNSCC.

All genes are involved in copper homeostasis and transport, oxidative stress, and the TCA cycle (26–34). *COX11* is a copper transfer factor, while *COX19* facilitates the transfer of copper (26). It was found that among multiple MT subtypes, *MT1E* was significantly upregulated in transcription after copper treatment, and its expression change can be used as an indicator of intracellular copper ion variation (6). The interaction between copper chelate and *ABCB1* inhibited its mediated transport and downregulated the expression of *ABCB1* (27). The genetic variation of *PRKN* is closely related to the pathogenesis of

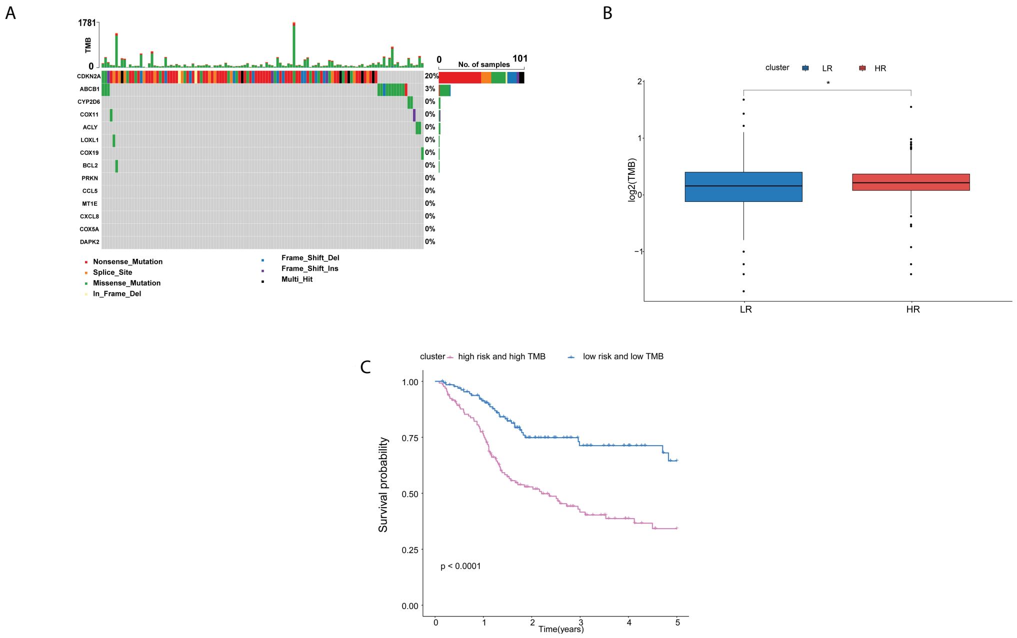

FIGURE 7
Analysis of the differences of genomics between high- and low-risk groups in the TCGA cohort.**(A)** Waterfall chart depicting the differential signature genes in somatic mutations of the HNSCC. **(B)** Boxplots displaying the TMB of the high-risk patients compared to low-risk patients. **(C)** OS rates in low-risk patients with low TMB were higher than those in high-risk patients with high TMB. Adjusted P-values were shown as: ns, not significant; *P < 0.05.

Parkinson's disease, mainly manifested in mitochondrial dysfunction (35–37). *CYP2D6*, *DAPK2*, *BCL2*, *RANTES*, and *IL-8* are all related to the redox characteristics of copper (29, 34, 38). *LOX* inactivation due to copper metabolism disorders or genetic mutations leads to the dysfunction of connective tissue (39). The enzymatic activity of *ACLY* has important functions in the TCA cycle (40). In addition, *CDKN2A* is a key gene regulating cuproptosis and has a high mutation probability in HNSCC (41).

The enrichment analysis of the two groups displayed that the 14 genes related to cuproptosis and copper metabolism were significantly enriched in immunocytes, tumorigenesis, such as immune response, intermediate filament, B-cell proliferation, and so on (42–46) The correlation analysis of the tumor immune microenvironment revealed that the activation of cells in the high-risk group had the characteristics of "cold tumor", such as naïve CD4 T cells, resting NK cells, and M0 macrophages. On the contrary, in the low-risk group, Th17 cells, DC, B cells, plasma cells, CD8 T cells, activated memory CD4 T cells, follicular helper T cells, activated NK cells, and M1 macrophage cells were more abundant and had a longer survival time. In addition, we investigated and studied the relevance between cuproptosis and copper metabolism–related genes, immune activity, and immune checkpoints. Our results show that there is a close interaction between copper metabolism and immunity. Immunity may play a crucial part in the occurrence of cuproptosis. Cuproptosis may affect the immune state of HNSCC, thus affecting the occurrence and development of tumor. Previous studies have shown that the imbalance of copper metabolism and the changes of copper protein levels are closely related to cancer (47). The dysfunction of copper metabolic proteins may be the initiation of processes such as the generation of pretransfer niche, immune defense escape, and angiogenesis. However, the potential mechanism of inducing the cuproptosis behavior of tumor cells and enhancing antitumor immune response needs to be further clarified, and our research will help to provide new ideas into the exploration of potential tumor-targeted therapies.

Interestingly, using GO, KEGG, and GSEA enrichment analyses, we found that 14 genes associated with cuproptosis and copper metabolism were significantly enriched in the olfactory transduction pathway. In mammals, copper is highly concentrated in brain regions, including the major organs of olfactory receptors (48). The destruction of copper homeostasis is the basis of neurodegenerative diseases, which can be manifested as olfactory dysfunction (49). Patients with Alzheimer's disease show serious olfactory defects in the early stage, and olfactory dysfunction may occur in patients with Wilson's disease with neurological symptoms (48, 50). Recent studies have shown that olfactory receptor–related genes not only act on proprioceptive nerves but also play a crucial role in promoting tissue inflammation and cancer metastasis (51). At the same time, combined with the correlation between copper metabolism and tumor in this study, we speculate that there may be a potential relationship between copper metabolism–related genes and olfactory receptors on tumors. This discovery may offer new ideas for the diagnosis and treatment of HNSCC.

In recent years, the establishment of prognostic models for HNSCC has developed rapidly. Some researchers have developed a prognostic signature of regulatory cell death–related genes in HNSCC (52–54). Compared with ferroptosis, pyroptosis, and apoptosis, cuproptosis is a new concept. In this paper, we preliminarily discussed the role of cuproptosis in HNSCC and constructed a robust correlation model to predict the prognosis of HNSCC patients. Some researchers have paid attention to the TMB, which is related to the immunotherapeutic response of HNSCC (55). Therefore, the prognostic value of TMB in HNSCC researchers has been studied (55, 56). Interestingly, we found that the difference of copper metabolism gene expression in HNSCC patients was related to TMB, and the internal relationship between them remains to be explored. As an immunogenic tumor, the establishment of immune checkpoint–related gene signature is helpful to determine which HNSCC patients can benefit from immunotherapy (57, 58). In this study, we explored the possible role of cuproptosis in the progression of HNSCC from the perspective of immunity. We found that cuproptosis may be connected with the immune status of HNSCC and may thus play a role in the occurrence and development of tumors. The in-depth study of their internal mechanism may help to provide new ideas for tumor immunotherapy.

As with all studies, our study also had limitations. Our bioinformatics analysis identified potential cancer diagnostic genes associated with cuproptosis and copper metabolism, but its accuracy remains to be verified for each HNSCC subtype. In addition, our current research results are obtained from databases, and a series of biological experiments should be conducted to further examine the molecular mechanisms involved in cuproptosis and copper metabolism–related genes that affect the prognosis of HNSCC patients.

Data availability statement

Publicly available datasets were analyzed in this study. This data can be found here: HNSCC, CESC, ESCA cohort from TCGA database, https://portal.gdc.cancer.gov/.

Author contributions

SZ and JH conceived and designed the study. HL, SZ, and XL performed the data analysis. SZ, LZ, HL, and YY analyzed and interpreted the results. LZ wrote the original manuscript. SZ and JH reviewed and revised the manuscript. All authors contributed to the article and approved the submitted version.

Funding

This research was supported by the National Natural Science Foundation of China (grant numbers 81874128 and 82072994); Sun Yat-Sen University Clinical Research 5010 Program (grant numbers 2015018).

Conflict of interest

The authors declare that the research was conducted in the absence of any commercial or financial relationships that could be construed as a potential conflict of interest.

Publisher's note

Supplementary material

The Supplementary Material for this article can be found online at: https://www.frontiersin.org/articles/10.3389/fonc.2022.955336/full#supplementary-material

References

1. Johnson DE, Burtness B, Leemans CR, Lui VWY, Bauman JE, Grandis JR. Head and neck squamous cell carcinoma. *Nat Rev Dis Primers* (2020) 6(1):92. doi: 10.1038/s41572-020-00224-3

2. von Witzleben A, Wang C, Laban S, Savelyeva N, Ottensmeier CH. Hnscc: Tumour antigens and their targeting by immunotherapy. *Cells* (2020) 9(9):2103. doi: 10.3390/cells9092103

3. Solomon B, Young RJ, Rischin D. Head and neck squamous cell carcinoma: Genomics and emerging biomarkers for immunomodulatory cancer treatments. *Semin Cancer Biol* (2018) 52(Pt 2):228–40. doi: 10.1016/j.semcancer.2018.01.008

4. Queiroz A, Albuquerque-Souza E, Gasparoni LM, de França BN, Pelissari C, Trierveiler M, et al. Therapeutic potential of periodontal ligament stem cells. *World J Stem Cells* (2021) 13(6):605–18. doi: 10.4252/wjsc.v13.i6.605

5. Kumpitsch C, Moissl-Eichinger C, Pock J, Thurnher D, Wolf A. Preliminary insights into the impact of primary radiochemotherapy on the salivary microbiome in head and neck squamous cell carcinoma. *Sci Rep* (2020) 10(1):16582. doi: 10.1038/s41598-020-73515-0

6. Ma M, Qiu B, Jin J, Wang J, Nie Y, Liang Y, et al. Establishment of a specific in vivo cu() reporting system based on metallothionein screening. *Metallomics* (2021) 13(7):mfab035. doi: 10.1093/mtomcs/mfab035

7. Bigagli E, Luceri C, Bernardini S, Dei A, Dolara P. Extremely low copper concentrations affect gene expression profiles of human prostate epithelial cell lines. *Chem Biol Interact* (2010) 188(1):214–9. doi: 10.1016/j.cbi.2010.06.009

8. Tsvetkov P, Coy S, Petrova B, Dreishpoon M, Verma A, Abdusamad M, et al. Copper induces cell death by targeting lipoylated tca cycle proteins. *Science* (2022) 375(6586):1254–61. doi: 10.1126/science.abf0529

9. Vyas A, Duvvuri U, Kiselyov K. Copper-dependent Atp7b up-regulation drives the resistance of Tmem16a-overexpressing head-and-Neck cancer models to platinum toxicity. *Biochem J* (2019) 476(24):3705–19. doi: 10.1042/BCJ20190591

10. Kitamura N, Sento S, Yoshizawa Y, Sasabe E, Kudo Y, Yamamoto T. Current trends and future prospects of molecular targeted therapy in head and neck squamous cell carcinoma. *Int J Mol Sci* (2020) 22(1):240. doi: 10.3390/ijms22010240

11. Atashi F, Vahed N, Emamverdizadeh P, Fattahi S, Paya L. Drug resistance against 5-fluorouracil and cisplatin in the treatment of head and neck squamous cell carcinoma: A systematic review. *J Dent Res Dent Clin Dent Prospects* (2021) 15 (3):219–25. doi: 10.34172/joddd.2021.036

12. Ressnerova A, Raudenska M, Holubova M, Svobodova M, Polanska H, Babula P, et al. Zinc and copper homeostasis in head and neck cancer: Review and meta-analysis. *Curr Med Chem* (2016) 23(13):1304–30. doi: 10.2174/0929867323666160405111543

13. Yao W, Qian X, Ochsenreither S, Soldano F, DeLeo AB, Sudhoff H, et al. Disulfiram acts as a potent radio-chemo sensitizer in head and neck squamous cell carcinoma cell lines and transplanted xenografts. *Cells* (2021) 10(3):517. doi: 10.3390/cells10030517

14. Kahlson MA, Dixon SJ. Copper-induced cell death. *Science* (2022) 375 (6586):1231–2. doi: 10.1126/science.abo3959

15. Bian Z, Fan R, Xie L. A novel cuproptosis-related prognostic gene signature and validation of differential expression in clear cell renal cell carcinoma. *Genes (Basel)* (2022) 13(5):851. doi: 10.3390/genes13050851

16. Zhang G, Sun J, Zhang X. A novel cuproptosis-related lncrna signature to predict prognosis in hepatocellular carcinoma. *Sci Rep* (2022) 12(1):11325. doi: 10.1038/s41598-022-15251-1

17. Han J, Hu Y, Liu S, Jiang J, Wang H. A newly established cuproptosis-associated long non-coding rna signature for predicting prognosis and indicating immune microenvironment features in soft tissue sarcoma. *J Oncol* (2022) 2022:8489387. doi: 10.1155/2022/8489387

18. Lv H, Liu X, Zeng X, Liu Y, Zhang C, Zhang Q, et al. Comprehensive analysis of cuproptosis-related genes in immune infiltration and prognosis in melanoma. *Front Pharmacol* (2022) 13:930041. doi: 10.3389/fphar.2022.930041

19. Aran D, Hu Z, Butte AJ. Xcell: Digitally portraying the tissue cellular heterogeneity landscape. *Genome Biol* (2017) 18(1):220. doi: 10.1186/s13059-017-1349-1

20. Domper Arnal MJ, Ferrandez Arenas A, Lanas Arbeloa A. Esophageal cancer: Risk factors, screening and endoscopic treatment in Western and Eastern countries. *World J Gastroenterol* (2015) 21(26):7933–43. doi: 10.3748/wjg.v21.i26.7933

21. Burd EM. Human papillomavirus and cervical cancer. *Clin Microbiol Rev* (2003) 16(1):1–17. doi: 10.1128/CMR.16.1.1-17.2003

22. Sproll C, Fluegen G, Stoecklein NH. Minimal residual disease in head and neck cancer and esophageal cancer. *Adv Exp Med Biol* (2018) 1100:55–82. doi: 10.1007/978-3-319-97746-1_4

23. Kim J, Bowlby R, Mungall AJ, Robertson AG, Odze RD, Cherniack AD, et al. Integrated genomic characterization of oesophageal carcinoma. *Nature* (2017) 541 (7636):169–75. doi: 10.1038/nature20805

24. Businello G, Fassan M, Degasperi S, Traverso G, Scarpa M, Angriman I, et al. Esophageal squamous cell carcinoma metachronous to head and neck cancers. *Pathol Res Pract* (2021) 219:153346. doi: 10.1016/j.prp.2021.153346

25. Saiz-Ladera C, Baliu-Pique M, Cimas FJ, Manzano A, Garcia-Barberan V, Camarero SC, et al. Transcriptomic correlates of immunologic activation in head and neck and cervical cancer. *Front Oncol* (2021) 11:714550. doi: 10.3389/fonc.2021.714550

26. Bode M, Woellhaf MW, Bohnert M, van der Laan M, Sommer F, Jung M, et al. Redox-regulated dynamic interplay between Cox19 and the copper-binding protein Cox11 in the intermembrane space of mitochondria facilitates biogenesis of cytochrome c oxidase. *Mol Biol Cell* (2015) 26(13):2385–401. doi: 10.1091/mbc.E14-11-1526

27. Ghosh RD, Chakraborty P, Banerjee K, Adhikary A, Sarkar A, Chatterjee M, et al. The molecular interaction of a copper chelate with human p-glycoprotein. *Mol Cell Biochem* (2012) 364(1-2):309–20. doi: 10.1007/s11010-012-1232-z

28. Pan M, Cheng ZW, Huang CG, Ye ZQ, Sun LJ, Chen H, et al. Long-term exposure to copper induces mitochondria-mediated apoptosis in mouse hearts. *Ecotoxicol Environ Saf* (2022) 234:113329. doi: 10.1016/j.ecoenv.2022.113329

29. Schlegel CR, Georgiou ML, Misterek MB, Stocker S, Chater ER, Munro CE, et al. Dapk2 regulates oxidative stress in cancer cells by preserving mitochondrial function. *Cell Death Dis* (2015) 6:e1671. doi: 10.1038/cddis.2015.31

30. Hartwig C, Zlatic SA, Wallin M, Vrailas-Mortimer A, Fahrni CJ, Faundez V. Trafficking mechanisms of p-type atpase copper transporters. *Curr Opin Cell Biol* (2019) 59:24–33. doi: 10.1016/j.ceb.2019.02.009

31. Xu M, Tang H, Zhou X, Chen H, Dong Q, Zhang Y, et al. Effects and mechanisms of Sub-chronic exposure to copper nanoparticles on renal cytochrome P450 enzymes in rats. *Environ Toxicol Pharmacol* (2018) 63:135–46. doi: 10.1016/j.etap.2018.08.004

32. Yang L, Xing S, Wang K, Yi H, Du B. Paeonol attenuates aging mrc-5 cells and inhibits epithelial-mesenchymal transition of premalignant hacat cells induced by aging mrc-5 cell-conditioned medium. *Mol Cell Biochem* (2018) 439(1-2):117–29. doi: 10.1007/s11010-017-3141-7

33. Kang Z, Qiao N, Liu G, Chen H, Tang Z, Li Y. Copper-induced apoptosis and autophagy through oxidative stress-mediated mitochondrial dysfunction in Male germ cells. *Toxicol In Vitro* (2019) 61:104639. doi: 10.1016/j.tiv.2019.104639

34. MacGregor HJ, Kato Y, Marshall LJ, Nevell TG, Shute JK. A copper-hydrogen peroxide redox system induces dityrosine cross-links and chemokine oligomerisation. *Cytokine* (2011) 56(3):669–75. doi: 10.1016/j.cyto.2011.08.025

35. Zhu YF, Aredo B, Chen B, Zhao CX, He YG, Ufret-Vincenty RL. Mice with a combined deficiency of superoxide dismutase 1 (Sod1), dj-1 (Park7), and parkin (Prkn) develop spontaneous retinal degeneration with aging. *Invest Ophth Vis Sci* (2019) 60(12):3740–51. doi: 10.1167/iovs.19-27212

36. Aboud AA, Tidball AM, Kumar KK, Neely MD, Han B, Ess KC, et al. Park2 patient neuroprogenitors show increased mitochondrial sensitivity to copper. *Neurobiol Dis* (2015) 73:204–12. doi: 10.1016/j.nbd.2014.10.002

37. Pickrell AM, Youle RJ. The roles of Pink1, parkin, and mitochondrial fidelity in parkinson's disease. *Neuron* (2015) 85(2):257–73. doi: 10.1016/j.neuron.2014.12.007

38. Yang F, Pei R, Zhang Z, Liao J, Yu W, Qiao N, et al. Copper induces oxidative stress and apoptosis through mitochondria-mediated pathway in chicken hepatocytes. *Toxicol In Vitro* (2019) 54:310–6. doi: 10.1016/j.tiv.2018.10.017

39. Lin W, Xu L, Li G. Molecular insights into lysyl oxidases in cartilage regeneration and rejuvenation. *Front Bioeng Biotechnol* (2020) 8:359. doi: 10.3389/fbioe.2020.00359

40. Noe JT, Rendon BE, Geller AE, Conroy LR, Morrissey SM, Young LEA, et al. Lactate supports a metabolic-epigenetic link in macrophage polarization. *Sci Adv* (2021) 7(46):eabi8602. doi: 10.1126/sciadv.abi8602

41. McBride S, Sherman E, Tsai CJ, Baxi S, Aghalar J, Eng J, et al. Randomized phase ii trial of nivolumab with stereotactic body radiotherapy versus nivolumab alone in metastatic head and neck squamous cell carcinoma. *J Clin Oncol Off J Am Soc Clin Oncol* (2021) 39(1):30–7. doi: 10.1200/jco.20.00290

42. Kim SS, Shen S, Miyauchi S, Sanders PD, Franiak-Pietryga I, Mell L, et al. B cells improve overall survival in hpv-associated squamous cell carcinomas and are activated by radiation and pd-1 blockade. *Clin Cancer Res* (2020) 26(13):3345–59. doi: 10.1158/1078-0432.CCR-19-3211

43. Spector ME, Bellile E, Amlani L, Zarins K, Smith J, Brenner JC, et al. Prognostic value of tumor-infiltrating lymphocytes in head and neck squamous cell carcinoma. *JAMA Otolaryngol Head Neck Surg* (2019) 145(11):1012–9. doi: 10.1001/jamaoto.2019.2427

44. Bisheshar SK, De Ruiter EJ, Devriese LA, Willems SM. The prognostic role of nk cells and their ligands in squamous cell carcinoma of the head and neck: A systematic review and meta-analysis. *Oncoimmunology* (2020) 9(1):1747345. doi: 10.1080/2162402X.2020.1747345

45. Cillo AR, Kurten CHL, Tabib T, Qi Z, Onkar S, Wang T, et al. Immune landscape of viral- and carcinogen-driven head and neck cancer. *Immunity* (2020) 52(1):183–99.e9. doi: 10.1016/j.immuni.2019.11.014

46. Komi DEA, Redegeld FA. Role of mast cells in shaping the tumor microenvironment. *Clin Rev Allergy Immunol* (2020) 58(3):313–25. doi: 10.1007/s12016-019-08753-w

47. Serra M, Columbano A, Ammarah U, Mazzone M, Menga A. Understanding metal dynamics between cancer cells and macrophages: Competition or synergism? *Front Oncol* (2020) 10:646. doi: 10.3389/fonc.2020.00646

48. Horning MS, Trombley PQ. Zinc and copper influence excitability of rat olfactory bulb neurons by multiple mechanisms. *J Neurophysiol* (2001) 86(4):1652–60. doi: 10.1152/jn.2001.86.4.1652

49. Adamson SX, Zheng W, Agim ZS, Du S, Fleming S, Shannahan J, et al. Systemic copper disorders influence the olfactory function in adult rats: Roles of altered adult neurogenesis and neurochemical imbalance. *Biomolecules* (2021) 11 (9):1315. doi: 10.3390/biom11091315

50. Mueller A, Reuner U, Landis B, Kitzler H, Reichmann H, Hummel T. Extrapyramidal symptoms in wilson's disease are associated with olfactory dysfunction. *Mov Disord* (2006) 21(9):1311–6. doi: 10.1002/mds.20989

51. Orecchioni M, Kobiyama K, Winkels H, Ghosheh Y, McArdle S, Mikulski Z, et al. Olfactory receptor 2 in vascular macrophages drives atherosclerosis by Nlrp3-dependent il-1 production. *Science* (2022) 375(6577):214–21. doi: 10.1126/science.abg3067

52. He F, Chen Z, Deng W, Zhan T, Huang X, Zheng Y, et al. Development and validation of a novel ferroptosis-related gene signature for predicting prognosis and immune microenvironment in head and neck squamous cell carcinoma. *Int Immunopharmacol* (2021) 98:107789. doi: 10.1016/j.intimp.2021.107789

53. Zhu W, Zhang J, Wang M, Zhai R, Xu Y, Wang J, et al. Development of a prognostic pyroptosis-related gene signature for head and neck squamous cell carcinoma patient. *Cancer Cell Int* (2022) 22(1):62. doi: 10.1186/s12935-022-02476-3

54. Huang J, Huo H, Lu R. A novel signature of necroptosis-associated genes as a potential prognostic tool for head and neck squamous cell carcinoma. *Front Genet* (2022) 13:907985. doi: 10.3389/fgene.2022.907985

55. Zhang L, Li B, Peng Y, Wu F, Li Q, Lin Z, et al. The prognostic value of tmb and the relationship between tmb and immune infiltration in head and neck squamous cell carcinoma: A gene expression-based study. *Oral Oncol* (2020) 110:104943. doi: 10.1016/j.oraloncology.2020.104943

56. Wu F, Du Y, Hou X, Cheng W. A prognostic model for oral squamous cell carcinoma using 7 genes related to tumor mutational burden. *BMC Oral Health* (2022) 22(1):152. doi: 10.1186/s12903-022-02193-3

57. Song D, Tian J, Han X, Li X. A model of seven immune checkpoint-related genes predicting overall survival for head and neck squamous cell carcinoma. *Eur Arch Otorhinolaryngol* (2021) 278(9):3467–77. doi: 10.1007/s00405-020-06540-4

58. Wang J, Tian Y, Zhu G, Li Z, Wu Z, Wei G, et al. Establishment and validation of immune microenvironmental gene signatures for predicting prognosis in patients with head and neck squamous cell carcinoma. *Int Immunopharmacol* (2021) 97:107817. doi: 10.1016/j.intimp.2021.107817

frontiers | Frontiers in Oncology

TYPE Original Research
PUBLISHED 05 October 2022
DOI 10.3389/fonc.2022.998736

Application of genomic selection and experimental techniques to predict cell death and immunotherapeutic efficacy of ferroptosis-related CXCL2 in hepatocellular carcinoma

Qiaoli Yi[1,2], Qiuju Liang[1], Yuanhong Liu[1], Zhicheng Gong[1]* and Yuanliang Yan[1,2]*

[1]Department of Pharmacy, Xiangya Hospital, Central South University, Changsha, China, [2]National Clinical Research Center for Geriatric Disorders, Xiangya Hospital, Central South University, Changsha, China

OPEN ACCESS

EDITED BY
Xiao Zhu,
Guangdong Medical University, China

REVIEWED BY
Xiaomeng Yin,
University of Massachusetts Medical School, United States
Yaying Sun,
Fudan University, China

*CORRESPONDENCE
Yuanliang Yan
yanyuanliang@csu.edu.cn
Zhicheng Gong
gongzhicheng@csu.edu.cn

SPECIALTY SECTION
This article was submitted to Cancer Genetics, a section of the journal Frontiers in Oncology

RECEIVED 03 August 2022
ACCEPTED 15 September 2022
PUBLISHED 05 October 2022

CITATION
Yi Q, Liang Q, Liu Y, Gong Z and Yan Y (2022) Application of genomic selection and experimental techniques to predict cell death and immunotherapeutic efficacy of ferroptosis-related CXCL2 in hepatocellular carcinoma. *Front. Oncol.* 12:998736. doi: 10.3389/fonc.2022.998736

Since most hepatocellular carcinoma (HCC) patients are diagnosed at advanced stages, there is no effective treatment to improve patient survival. Ferroptosis, a regulated cell death driven by iron accumulation and lipid peroxidation, has been reported to play an important role in tumorigenesis. However, the detailed mechanism and biological function of ferroptosis are still incompletely understood in HCC patients. In this study, we analyzed genomic profiles of three HCC datasets, GSE6764, GSE14520, and GSE14323. Venn diagrams were implemented to visualize the overlapping genes between differentially expressed genes and ferroptosis-related gene set. Then, one up-regulated gene, ACSL4, and five down-regulated genes, STEAP3, MT1G, GCH1, HAMP, and CXCL2, were screened. Based on the survival analysis performed by Kaplan-Meier plotter database, ferroptosis-related gene CXCL2 was demonstrated positively-correlated with the patients' prognosis. Moreover, CXCL2 overexpression significantly inhibited cell growth and improved cellular ROS, Fe^{2+} and MDA levels in HCC cells Huh7 and MHCC97H, suggesting the roles of CXCL2 in inducing ferroptotic cell death. In addition, aberrantly expressed CXCL2 was negatively associated with malignancy clinical features, such as nodal metastasis and higher grades. The ssGSEA enrichment analysis revealed that CXCL2 co-expressed molecules were mainly involved in inflammation and immune-related pathways, such as acute inflammatory response, humoral immune response, adaptive immune response. TISIDB algorithm indicated the positive correlation between CXCL2 expression and tumor-infiltrating immune cells, including neutrophils and macrophages. Additionally, we also found that CXCL2 was positively correlated with immune infiltration score, and HCC patients with higher score harbored better prognosis. Together, these findings suggested that CXCL2 may enhance ferroptosis sensitivity and regulate immune microenvironment in HCC, and serve as a promising prognosis biomarker for HCC patients.

KEYWORDS

ferroptosis, hepatocellular carcinoma, CXCL2, immune infiltration, prognosis

Introduction

Liver cancer is the third leading cause of cancer-related mortality worldwide after lung cancer and colorectal cancer, and hepatocellular carcinoma (HCC) accounts for approximately 90% of all cases (1, 2). The main risk factors for HCC include chronic viral infection by hepatitis B virus (HBV) or hepatitis C virus (HCV), habitual alcohol consumption, and non-alcoholic steatohepatitis (NASH) associated with metabolic syndrome, indicating that inflammation has an important function in the development of HCC (3, 4). Patients with HCC are often diagnosed at advanced stages, which contributes to its poor prognosis. Currently, surgical resection, liver transplantation, trans-arterial chemoembolization, local ablation, and systemic therapy are the major therapeutic modalities for HCC (5). Immunotherapy is emerging as a promising and effective therapeutic approach among systemic therapy after sorafenib. Nivolumab is the first anti-programmed death-1 (PD-1) antibody approved by the United States Food and Drug Administration (FDA) as a second-line treatment for patients with advanced HCC (6). Furthermore, clinical trials evaluating PD-1 blockade as first-line treatment strategy in HCC are underway (NCT02576509). However, it is only a small subset of patients treated with immune checkpoint inhibitors that benefit from these agents (7). Therefore, it is urgently necessary to identify novel potential biomarkers to improve patient response rates and survival.

Ferroptosis is a novel form of regulated cell death driven by iron-dependent lipid peroxidation (8, 9). Accumulating evidence suggests that ferroptosis has significant implications on tumorigenesis and cancer progression (10, 11). P53, one of the most extensively studied tumor suppressor genes, promotes ferroptosis pathway by repressing the expression of solute carrier family 7 member 11 (SLC7A11), a pivotal component of the cystine/glutamate antiporter. Moreover, SLC7A11 is up-regulated in human tumors, and its upregulation inhibits reactive oxygen species (ROS)–induced ferroptosis and abrogates $p53^{3KR}$ (an acetylation-defective mutant)-mediated tumor growth suppression (12, 13). Ferroptosis induction in combination of other cancer treatments might enhance the therapeutic response in patients by increasing drug sensitivity (14, 15). However, the possible roles and underlying mechanisms of ferroptosis in HCC remain incompletely characterized.

C-X-C motif chemokine ligand 2 (CXCL2) is a member of chemokine superfamily, which encodes secreted proteins participated in inflammatory processes and immunoregulatory (16, 17). Moreover, increasing evidence indicates that CXCL2 is also involved in tumor initiation and progression. A recent study reported that elevated CXCL2 in the tumor microenvironment promoted the recruitment of myeloid-derived suppressor cells and was correlated with poor prognosis in patients with bladder cancer (18). Intriguingly, Ding and the colleague revealed that CXCL2 expression was down-regulated in HCC and overexpression of CXCL2 inhibited tumor cell proliferation and promoted apoptosis (19). However, the underlying mechanisms of CXCL2 in inflammation and HCC progression remains to be further investigated.

In this study, we comprehensively analyzed the biological functions of CXCL2 in HCC. According to several genomic selection strategies, CXCL2, a ferroptosis-related gene, was found to be down-regulated in HCC and influence tumor progression and clinical prognosis of HCC patients. Furthermore, we explored the possible roles of CXCL2 in inducing ferroptotic cell death. These results indicated that CXCL2 harbored vast potential significance as a prognostic biomarker and therapeutic target for patients with HCC.

Materials and methods

Multi-omics data collection

Three HCC datasets, GSE6764 (20), GSE14520 (21), and GSE14323 (22), were screened according to the inclusion criteria detailed in a previous study by our research group (23). Detailed characteristics of the three GEO datasets were shown in Table 1. Differentially expressed genes (DEGs) between HCC tumor samples and normal tissues were identified based on the criteria: $P < 0.01$ and $|\text{Log2 FC (Fold Change)}| > 1$. Moreover, 259 ferroptosis-related genes were downloaded from FerrDb (http://www.zhounan.org/ferrdb/legacy/index.html) (24). Next, Venn diagrams (http://bioinformatics.psb.ugent.be/webtools/Venn/) were generated to identify the co-DEGs among three GEO datasets and ferroptosis-related gene dataset.

TABLE 1 Detailed characteristics of the three GEO datasets in our study.

GEO datasets	Platform	Sample type	Sample size (tumor/control)	References
GSE6764	GPL570	tissue	75 (35/40)	(20)
GSE14520	GPL571 GPL3921	tissue	43 (22/21) 445 (225/220)	(21)
GSE14323	GPL96 GPL571	tissue	9 (9/0) 115 (55/60)	(22)

Genomic selection analyses

The integrative bioinformatics analysis was performed using several online bioinformatics databases (Table 2).

We employed the Kaplan-Meier plotter (25) and GEPIA2 database (26) to assess the prognostic values of co-DEGs in HCC patients, including overall survival (OS), progression-free survival (PFS) and disease-specific survival (DSS). The expression levels of CXCL2 in GSE6764, GSE14520, and GSE14323 were analyzed by using the GEO2R algorithm (https://www.ncbi.nlm.nih.gov/geo/geo2r/). Furthermore, the expression pattern of CXCL2 between HCC tumor samples and normal tissues was cross-validated by the TNMplot (27), Xiantao tool (https://www.xiantao.love/products) and UALCAN (28). Xiantao tool is a comprehensive bioinformatics toolbox to perform differential expression analysis, functional enrichment analysis, interaction networks, and clinical prognosis across different cancer types from The Cancer Genome Atlas (TCGA) database. We used Xiantao toolbox and UALCAN to assess the association between CXCL2 and clinical pathological parameters in TCGA-LIHC cohort.

LinkedOmics could be used to analyze the multi-omics data across various cancer types, with three analytical algorithms: LinkFinder, LinkInterpreter, and LinkCompare (29). The heatmaps of the top 50 genes positively and negatively correlated with CXCL2 were analyzed with the LinkFinder module. Furthermore, Gene Ontology (GO) and Kyoto Encyclopedia of Genes and Genomes (KEGG) pathway analysis were implemented using the LinkInterpreter algorithm.

Next, we performed the single sample Gene set enrichment analysis (ssGSEA) (33) to assess the correlation between CXCL2 expression and 24 immune cell types in TCGA-LIHC. In addition, we used the TISIDB (30) to validate the roles of CXCL2 in immune-related responses, such as tumor-infiltrating immune cells, and immunomodulators. In addition, Tumor Immune Dysfunction and Exclusion (TIDE) (31, 32) was applied to predict the roles of CXCL2 in immunotherapy response of HCC patients.

TABLE 2 The bioinformatics databases analyzed in this study.

Database	URL	References
Kaplan-Meier Plotter	https://kmplot.com/analysis/	(25)
GEPIA2	http://gepia2.cancer-pku.cn/#index	(26)
TNMplot	https://tnmplot.com/	(27)
UALCAN	http://ualcan.path.uab.edu/	(28)
LinkedOmics	http://linkedomics.org/login.php	(29)
TISIDB	http://cis.hku.hk/TISIDB	(30)
TIDE	http://tide.dfci.harvard.edu/	(31, 32)

Cell cultures and reagents

Human HCC cells, Huh7 and MHCC97H, and human immortalized hepatocyte, HHL-5, were kindly provided from the Cancer Research Institute of the Central South University (Changsha, China) and cultured in DMEM (C11995500, HyClone, USA) supplemented with 10% fetal bovine serum (04-001-1A, BI, Israel) and 1% penicillin and streptomycin (10378016, Gibco, USA) at 37°C with 5% CO2. The overexpression plasmid HY21177 pcDNA3.1-CXCL2 (NM_002089)-3xFlag-C plasmid was purchased from Guangzhou Dahong Biological Technology Co., Ltd. (China). The CXCL2 overexpression plasmid was extracted with a SanPrep Column Plasmid Mini-Preps kit (Sangon Biotech, Shanghai, China), and then transfected into Huh7 and MHCC97H cell lines for 24 h using Lipofectamine 3000 (L300015, Thermo Fisher Scientific, USA) following the manufacturer's instructions.

RNA isolation and real-time PCR

Total RNA was extracted from cells with TRIzol reagent (Invitrogen, USA), and then reverse-transcribed into cDNA using a PrimeScriptTM RT reagent kit (RR047A, Takara, China) with gDNA Eraser (Perfect Real Time) according to the manufacturer's protocol. The qPCR reaction was performed with iTaqTM Universal SYBR green Supermix (1725121, Bio-Rad, USA). Relative RNA levels were calculated using the 2-ΔΔct method with RNA levels of GAPDH used as internal controls. The sequences of gene-specific primers are listed as follows: CXCL2 forward: 5'-GCTTGTC TCAACCCCGCATC-3' and reverse: 5'-TGGATTTGCCATTTTTCAGCATCTT-3'; GAPDH forward: 5'-ACAGCCTCAAGATCATCAGC-3' and reverse: 5'-GGTCATGAGTCCTTCCACGAT-3'.

Western Blot

The cultured cell lines were collected and then lysed with RIPA lysis buffer (20101ES60, Yeasen Biotech, China) supplemented with proteinase inhibitors (B14012, Bimake, USA). Equal amounts of total protein (50 μg) were loaded into each lane of 15% SDS–polyacrylamide gel electrophoresis (PAGE). Subsequently, proteins were transferred to PVDF membranes (0.22 μm: ISEQ00010; 0.45 μm: IPVH00010). Next, membranes were blocked in 5% skimmed milk at RT for 1 h, and then incubated overnight at 4 °C with primary antibodies in 5% Bovine Serum Albumin (D620272, Sangon Biotech, China), followed by HRP-conjugated secondary antibody (1:3000; SA00001-2, proteintech) at RT for 1 h. Primary antibodies are described as follows: CXCL2 (1:1000; bs-1162R, Bioss); Actin (1:2000; sc-58673, Santa Cruz Biotechnology). Finally, proteins were visualized using Immobilon Western Chemiluminescent HRP Substrate (WBKLS0500, Millipore, USA).

Tissue microarray and immunohistochemistry

Tissue microarrays (TMAs) containing 80 pairs of HCC and matched paracancerous tissues were purchased from shanghai Outdo biotechnology company Ltd. (HLivH160CS02, Shanghai, China). Immunohistochemistry (IHC) staining of CXCL2 was conducted using a Histomouse SP Kit (959551, Invitrogen, USA) according to the manufacturer's protocal. The concentration of antibody against CXCL2 was 1:100. The results of CXCL2 staining in tissues were independently evaluated by two pathologists. The evaluation of proportion score was on a scale of 1-4 (1, 0%-25%; 2, 25.1%-50%; 3, 50.1%-75%; 4, 75.1%-100%). The staining intensity score was graded as follows: 0, negative; 1, weak; 2, moderate; 3, strong. Then the histologic score for each tissue was calculated with the formula: histologic score = proportion score × intensity score.

Iron assay

The concentration of ferrous iron (Fe^{2+}) was measured using an iron colorimetric assay kit (ab83366, Abcam, USA) according to the manufacturer's instructions. After CXCL2 or control plasmids overexpression, Huh7 and MHCC97H cells were treated with erastin (10 μM) for 24 hours. Cells were harvested using trypsin without EDTA and homogenized in iron assay buffer on ice, then centrifuged at 4°C (14,000×g, 15 min) to remove insoluble material. Subsequently, collect the supernatant and add assay buffer, mix and incubate for 30 min at 25°C. Add 100ul iron probe into each sample and incubate at 25°C for 60 min protected from light. Detect the absorbance at 593 nm using the VICTOR X2 microplate reader (PerkinElmer, Waltham, USA).

Malondialdehyde assay

The relative MDA concentration was determined using a lipid peroxidation assay (MAK085, Sigma, USA) according to the manufacturer's protocol. Cells were processed with CXCL2 overexpression plasmids or erastin as described previously, then collected and homogenized in MDA lysis buffer with BHT on ice. Centrifuge the samples at 13,000 × g for 10 minutes to remove insoluble material. Collect the supernatant and add thiobarbituric acid (TBA) into each sample. Then incubate the samples at 95 °C for 60 min to form the MDA-TBA adduct. Measure the absorbance at 532 nm using the VICTOR X2 microplate reader (PerkinElmer, Waltham, USA).

ROS assay

Intracellular ROS level was evaluated by CytoFLEX flow cytometry (Beckman Coulter, USA). Briefly, about 10^5 cells were collected after CXCL2 overexpression plasmids or erastin treatment as described previously, and then stained with the oxidation-sensitive fluorescent probe dye 2′,7′-dichlorodihydrofluorescein diacetate (DCFDA; Abcam, ab113851) according to the manufacturer's instructions. Finally, flow cytometry analysis was performed using FlowJo software (v10.8.1, USA).

Cell counting kit 8

Huh7 and MHCC97H cells were transfected with pcDNA3.1-CXCL2 overexpression plasmid or empty pcDNA3.1 (+) plasmid as control for 24 h and then seeded in 96-well culture plates (2×10^3 cells/well). At 24h, 48h, 72h, 96h, and 120h, cell viability was assessed by performing CCK-8 assay (B34304, Bimake, USA) reading absorbance at 450 nm using a VICTOR X2 microplate reader (PerkinElmer, USA) according to the manufacturer's protocols.

Colony formation assay

Huh7 and MHCC97H cells were transfected as previously described and then seeded in 6-well plates (10^3 cells/well). After incubating at 37°C for about 14 days, the cells were washed twice with PBS and then stained with 0.3% w/v crystal violet/methanol for 15-20 min at room temperature (RT).

Statistical analysis

All experiments and assays were independently repeated by at least three times and results were reported as means ± standard deviations (SD). Statistically significant differences were performed using Student's t-test or ANOVA. Kaplan–Meier survival analysis was assessed by log-rank test. The immune score, stromal score, and ESTIMATE score of each tumor sample were estimated using the R package "ESTIMATE" based on expression data (34). Statistical analysis was carried out using GraphPad Prism 8 and $P < 0.05$ was considered as statistically significant difference.

RESULTS

Identification of differentially expressed genes

We analyzed the gene expression profiles of three HCC datasets (GSE6764, GSE14323, and GSE14520) and screened the DEGs between HCC and normal liver tissues according to the screening criteria: $P < 0.01$ and $|\log2\ FC| > 1$. We identified 826 up-regulated genes in GSE6764, 332 in GSE14323, and 505 in GSE14520, respectively. Meanwhile, 859 genes in GSE6764, 257 in GSE14323, and 583 in GSE14520 had been identified to be significantly down-regulated in HCC (Supplementary Table S1). And 259 ferroptosis-related genes were downloaded from the FerrDb database.

Recently, increasing evidence suggests that ferroptosis has significant implications on tumorigenesis and cancer progression, and ferroptosis induction might ameliorate antitumor efficacy by increasing drug sensitivity (35, 36). In order to explore the roles of ferroptosis in HCC, we employed Venn diagrams to identify co-DEGs between three GEO datasets and ferroptosis-related gene set. As shown in Figures 1A, B, one up-regulated gene, ACSL4, and five down-regulated genes, STEAP3, MT1G, GCH1, HAMP, and CXCL2, were preliminarily screened, and the gene expression heatmaps of these co-DEGs in each GEO dataset were presented in Figure 1C. These six selected genes were presumed to have potential roles in the occurrence and development of HCC.

CXCL2 shows the promising prognostic value in HCC

Using 60 ferroptosis-related genes dataset, previous study analyzed the diagnostic and prognostic roles of STEAP3, ACSL4 and MT1G in HCC (23). In this study, the correlations between the expression levels of GCH1 (RNAseq ID: 2643), HAMP (RNAseq ID: 57817), and CXCL2 (RNAseq ID: 2920) and prognosis in HCC patients were analyzed using the Kaplan–Meier plotter database. The expression of CXCL2 was significantly associated with favorable OS (HR = 0.61, 95% CI = 0.43–0.86, P = 0.0046), PFS (HR = 0.66, 95% CI = 0.48–0.90, P = 0.0083), and DSS (HR = 0.45, 95% CI = 0.29–0.71, P = 0.00045), which was consistent with low expression of CXCL2 in HCC tissues. However, there was no obvious relationship between the expression of GCH1 or HAMP and prognosis in HCC patients (P > 0.05) (Figures 2A–I). In addition, we employed the GEPIA2 database to cross-validate the prognostic value of CXCL2, GCH1, and HAMP, and drew consistent

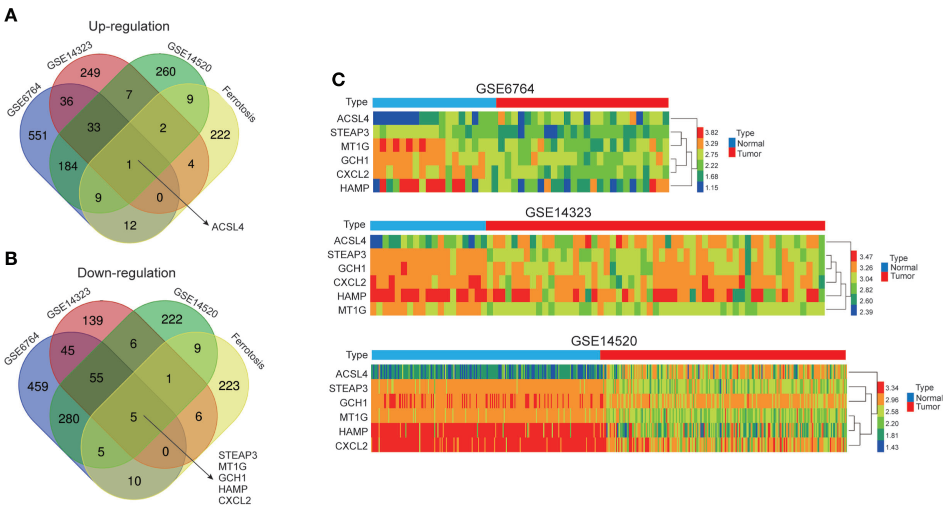

FIGURE 1
Identification of co-differentially expressed genes (co-DEG). **(A, B)** Venn diagrams exhibited one up-regulated gene, ACSL4, and five down-regulated genes, STEAP3, MT1G, GCH1, HAMP, and CXCL2, between three HCC GEO datasets and ferroptosis-related gene set. The number in overlapping area represents the number of genes. **(C)** The gene expression heatmaps of co-DEGs in GSE6764, GSE14323, GSE14520.

conclusions (Supplementary Figure S1). Therefore, these results revealed that CXCL2 expression might associated with clinical outcomes in HCC and warrants further investigation.

Low expression of CXCL2 in HCC and its correlation with clinicopathologic characteristics

The expression profiles of CXCL2 were further confirmed by several independent online bioinformatics databases, such as TNMplot, Xiantao tool, and UALCAN. Firstly, TNMplot revealed that CXCL2 mRNA expression levels were significantly down-regulated in HCC samples from gene chip data and RNA-seq data (Figures 3A, B). Next, Xiantao tool also exhibited the low expression of CXCL2 in HCC tissues compared to normal liver tissues including non-cancerous patients (Figure 3C) or matched adjacent para-tumor tissues (Figure 3D). We then analyzed the correlations between CXCL2 expression level and clinicopathological characteristics in HCC patients. As shown in Figures 3E, F, CXCL2 expression levels were significantly correlated with AFP (alpha-fetoprotein) ($P < 0.001$) and histologic grade ($P = 0.048$). Other clinicopathological features of CXCL2 expression in HCC were exhibited in Supplementary Table S2. In addition, we explored the diagnostic value of CXCL2 in HCC with receiver operation characteristic (ROC) curve, and the area under the ROC curve (AUC) was 0.903 (Figure 3G). This result indicated that CXCL2 might be a potential diagnostic biomarker in HCC patients. Then, we further validated the expression of CXCL2 and its correlation with clinicopathologic characteristics with UALCAN database. Figure 3H showed the expression pattern of CXCL2

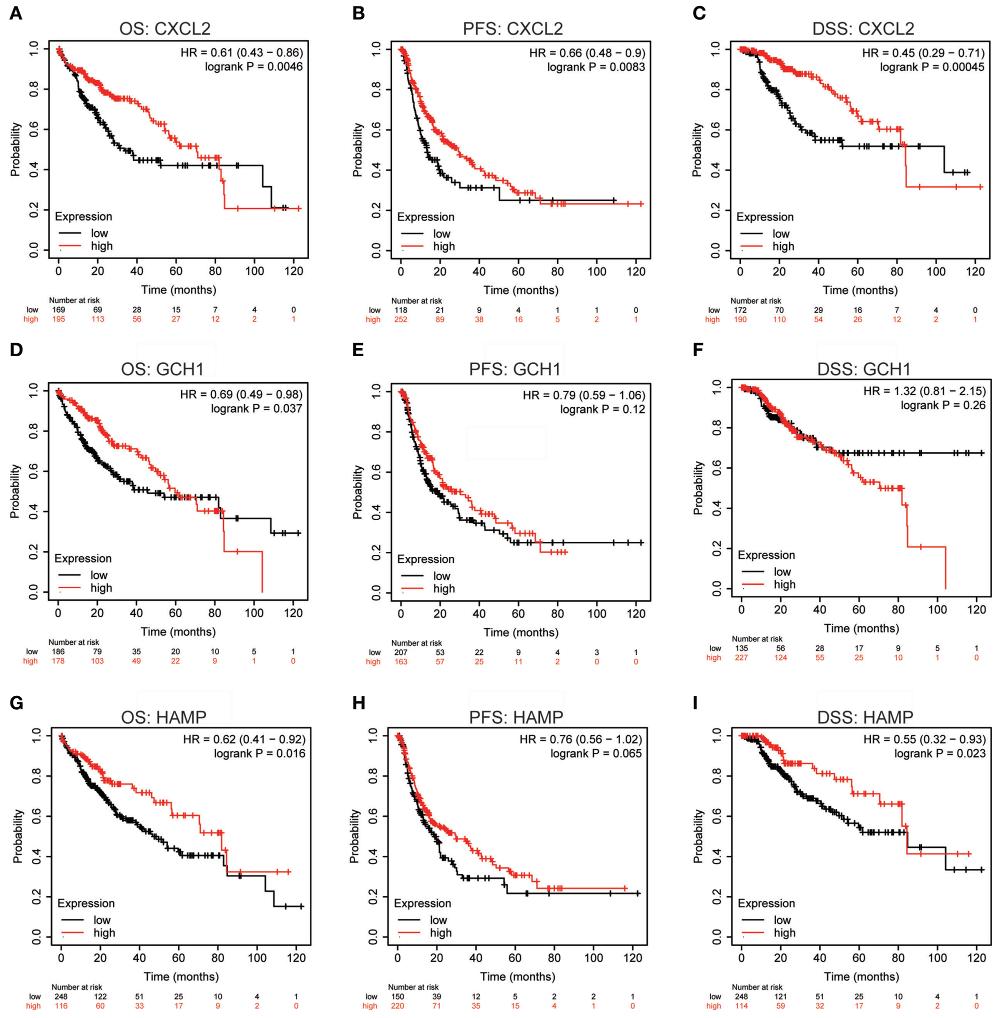

FIGURE 2
Prognostic values of CXCL2, GCH1, and HAMP in HCC. **(A-I)** Overall survival (OS), progression-free survival (PFS), and disease-specific survival (DSS) Kaplan-Meier curves of CXCL2, GCH1, and HAMP in patients with HCC by Kaplan–Meier plotter database.

across diverse TCGA cancer types, and low expression of CXCL2 was associated with malignancy clinical features, such as tumor grade, stage, and nodal metastasis (Figures 3I–K). Finally, the low expression of CXCL2 in two HCC cell lines, Huh7 and MHCC97H, was further confirmed by real-time PCR and western blotting, compared with the normal hepatocyte cell line HHL-5 (Figures 3L, M).

The expression of CXCL2 was then examined with IHC staining in tissue microarrays containing 80 pairs of HCC and matched paracancerous tissues, and the results confirmed that HCC tissues harbored significantly lower levels of CXCL2 than paracancer tissues (Figures 4A, B). To further explore the role of CXCL2 in HCC, we overexpressed CXCL2 with the overexpression plasmid in Huh7 and MHCC97H cell lines (Figure 4C). CCK-8 and colony formation assay indicated that CXCL2 overexpression significantly repressed cell growth and proliferation compared with control group (Figures 4D–F). Ferroptosis is a form of regulated cell death characterized by increased intracellular Fe^{2+} and lipid peroxidation, and the marker of lipid peroxidation is MDA (37). After CXCL2 overexpression, the levels of intracellular Fe^{2+} and MDA were significantly increased in Huh7 and MHCC97H cells compared with vectors (Figures 4G–J). Similarly, flow cytometry analysis indicated that CXCL2 overexpression elevated intracellular ROS levels with or without erastin (Figures 4K–N). CCK-8 assay suggested that the combination of CXCL2 overexpression and erastin significantly inhibited cell survival in Huh7 and MHCC97H cells (Figures 4O, P). These findings suggested that CXCL2 overexpression might suppress cell survival in HCC by promoting ferroptosis.

CXCL2 co-expression network in HCC

To explore the biological roles of CXCL2 in HCC, we performed the co-expression profile of CXCL2 in the TCGA-LIHC cohort by the LinkFinder module of LinkedOmics. As can be seen from Figure 5A, 4643 genes (red dots) were positively related with CXCL2, and 4232 genes (green dots) were negatively associated with CXCL2. Figures 5B, C exhibited the heatmaps of the top 50 genes positively and negatively correlated with CXCL2, respectively (Supplementary Tables S3, S4). Notably, the top 50 positively correlated genes owned a high probability of being low-risk markers in HCC, of which 9/50 genes harbored protective hazard ratio (HR). Contrarily, there were 33 of the top 50 negatively associated genes with unfavorable HR (Figures 5D, E).

In addition, we further conducted functional enrichment analysis by the LinkInterpreter module of the LinkedOmics database. GO-biological process showed that genes co-expressed with CXCL2 mainly participated in the inflammation and immune-related terms, such as acute inflammatory response, humoral immune response, adaptive immune response, response to molecule of bacterial origin (Figure 5F). KEGG pathway analysis showed that these co-expressed genes were mainly involved in complement and coagulation cascades, staphylococcus aureus infection, cell adhesion molecules, cytokine-cytokine receptor interaction, etc. (Figure 5G). In addition, we performed GO and KEGG enrichment analysis in the GSE14520, and the results were similar with the original results (Supplementary Figure S2). Taken together, these results suggested that CXCL2-associated network might have a significant impact on inflammation and immune regulation in HCC.

Role of CXCL2 in the immune microenvironment of HCC

Increasing evidence suggests that ferroptosis has great potential in regulating tumor immune microenvironment (38, 39). Hence, we explored the role of ferroptosis-related gene CXCL2 in HCC immune microenvironment through Xiantao tool. As presented in Figure 6A, CXCL2 expression was positively associated with the abundance of several tumor-infiltrating immune cells, including neutrophils, immature dendritic cell (iDC), macrophages, type 1 T helper cell (Th1), and natural killer (NK) cells. Similar lymphocyte infiltration profiles were attained by TISIDB database (Figure 6B). We continued to analyze the correlation between CXCL2 expression and immunostimulators. Figures 6C–F exhibited immunostimulators positively correlated with CXCL2, including interleukin 16 (IL-16), CD40 ligand (CD40LG), CD48, and TNF superfamily member 14 (TNFSF14). Given the clinical implications of checkpoint blockade-based immunotherapy in HCC (3), we further explored the associations between CXCL2 expression and several immune checkpoints. As shown in Figures 6G–J, CXCL2 expression was positively associated with programmed cell death ligand 1 (PD-L1), and negatively associated with indoleamine 2,3-dioxygenase 1 (IDO1), sialic acid binding Ig like lectin 15 (SIGLEC15), and B7-H3 (CD276). Additionally, Figures 6K, L exhibited positive correlations between CXCL2 and immune infiltration score in TCGA-LIHC cohort and GSE14520 dataset. Patients with high immune infiltration score had better 3-year OS in GSE14520 (Figure 6M). In addition, we employed the TIDE algorithm to predict the immunotherapy response of HCC patients based on pre-treatment expression profiles. As shown in Figure 6N, the response rate of CXCL2 high expression group predicted by the TIDE database was lower than that of CXCL2 low expression group. This inconsistency with the results of “ESTIMATE” algorithm may be that TIDE database focused on predicting the efficacy of anti-PD1 and anti-CTLA4 therapies. Together, these results suggested that ferroptosis-related gene CXCL2 might affect the prognosis of HCC patients by regulating the immune microenvironment.

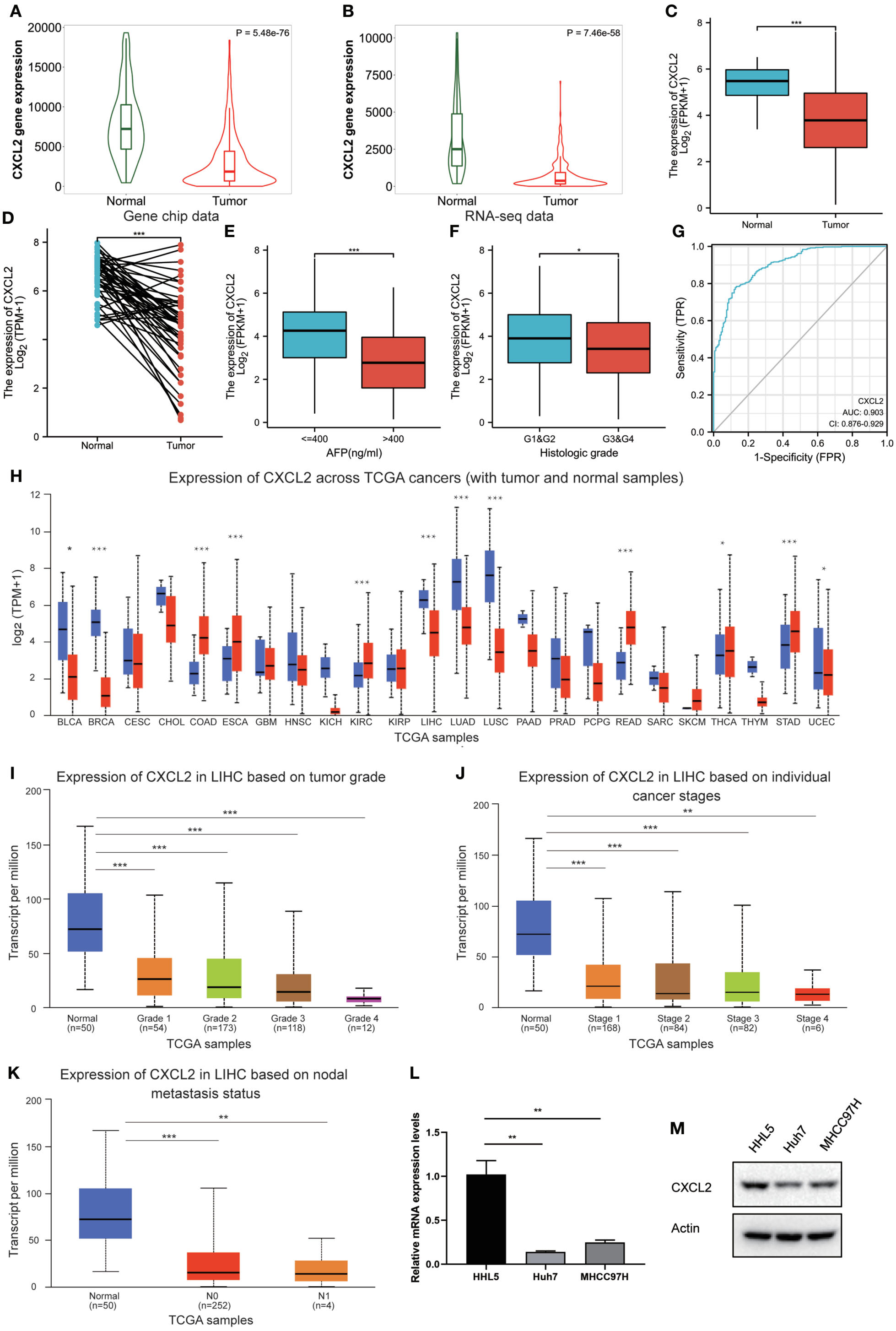

FIGURE 3
The expression level and clinicopathologic characteristics of CXCL2 in HCC. **(A, B)** Low expression of CXCL2 in HCC samples in gene chip data and RNA-seq data of TNMplot database. **(C, D)** The validation of low expression of CXCL2 in HCC samples in TCGA-LIHC cohort **(C)** or in comparison with matched adjacent para-tumor tissues **(D)** by Xiantao tool. **(E, F)** Correlation of CXCL2 expression with AFP **(E)** and histologic grade **(F)**. **(G)** Receiver operation characteristic (ROC) curve to evaluate the diagnostic value of CXCL2 in HCC. **(H)** Expression pattern of CXCL2 across diverse TCGA cancer types by UALCAN database. **(I-K)** Correlation of CXCL2 expression with tumor grade **(I)**, stage **(J)**, and nodal metastasis **(K)**. **(L, M)** Low expression of CXCL2 in two HCC cell lines, Huh7 and MHCC97H, was further confirmed by real-time PCR **(L)** and western blotting **(M)**, compared with the normal hepatocyte cell line HHL-5. * represents P < 0.05, ** represents P < 0.01, *** represents P < 0.001.

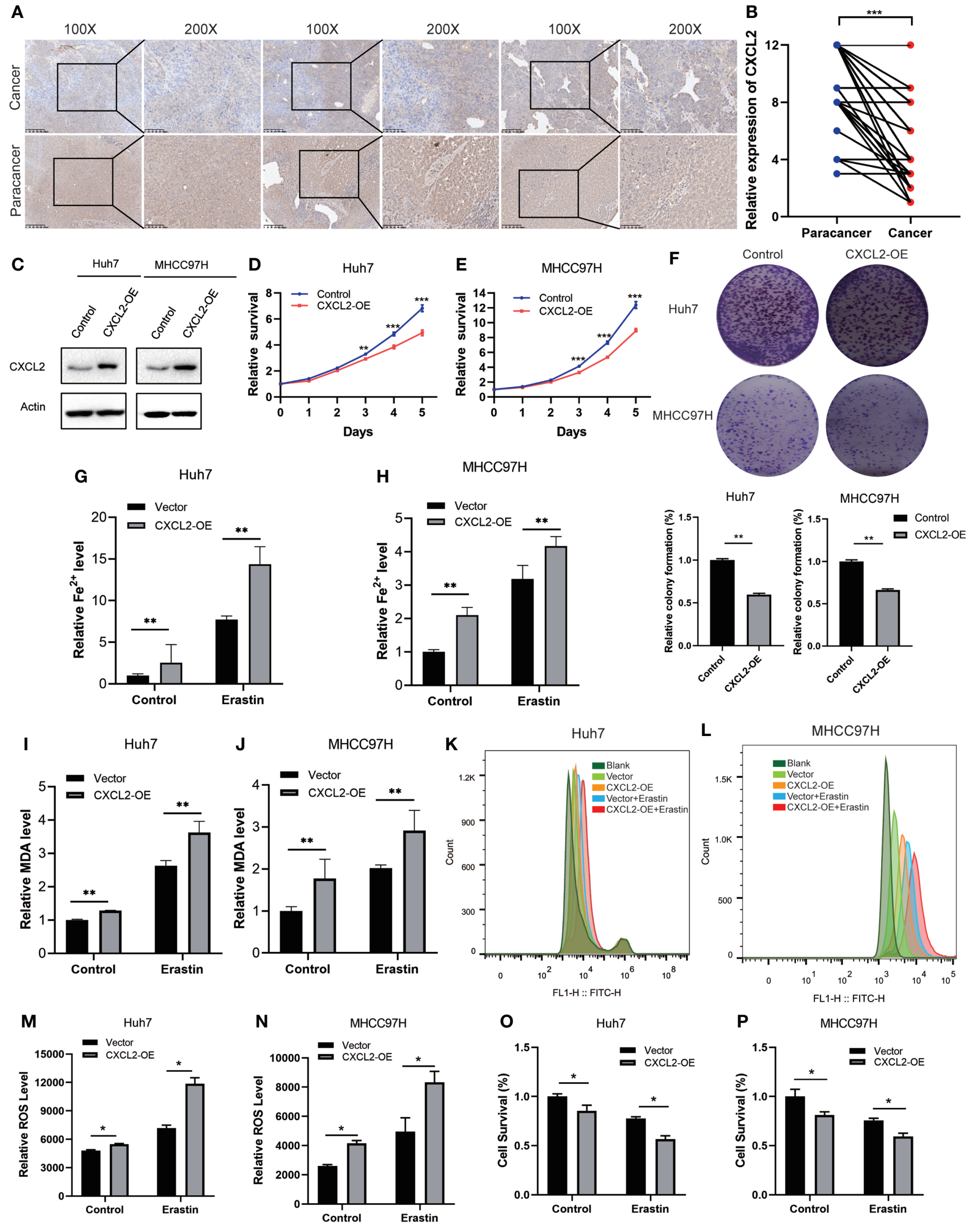

FIGURE 4
CXCL2 overexpression inhibited cell proliferation. **(A)** IHC images of CXCL2 in paired HCC and paracancerous tissues. **(B)**The histologic score of CXCL2 expression in paired HCC and paracancerous tissues. **(C)** Western blotting validated the overexpression of CXCL2 in two HCC cell lines, Huh7 and MHCC97H. **(D-F)** CCK-8 and colony formation assay revealed that CXCL2 overexpression inhibited cell growth and proliferation. **(G-J)** Fe^{2+} and MDA levels were detected in Huh7 and MHCC97H cells transfected with CXCL2 overexpression plasmids. **(K-N)** Intracellular ROS levels were elevated in Huh7 and MHCC97H cells with CXCL2 overexpression. **(O, P)** CCK-8 assay suggested that the combination of CXCL2 overexpression and erastin significantly inhibited cell survival in Huh7 and MHCC97H cells. * represents P < 0.05, ** represents P < 0.01, *** represents P < 0.001.

CXCL2 relating M1 Macrophages in HCC

The above results revealed that CXCL2 was positively correlated with macrophage infiltration. We then analyzed the associations between CXCL2 expression and classical macrophage phenotype markers of M0 (undifferentiated) (AIF1), M1 (anti-tumor) (IL12A, TNF, NOS2, PTGS2) and M2 (tumor-promoting) (IL10, CD163, TGFB1, CSF1R) in

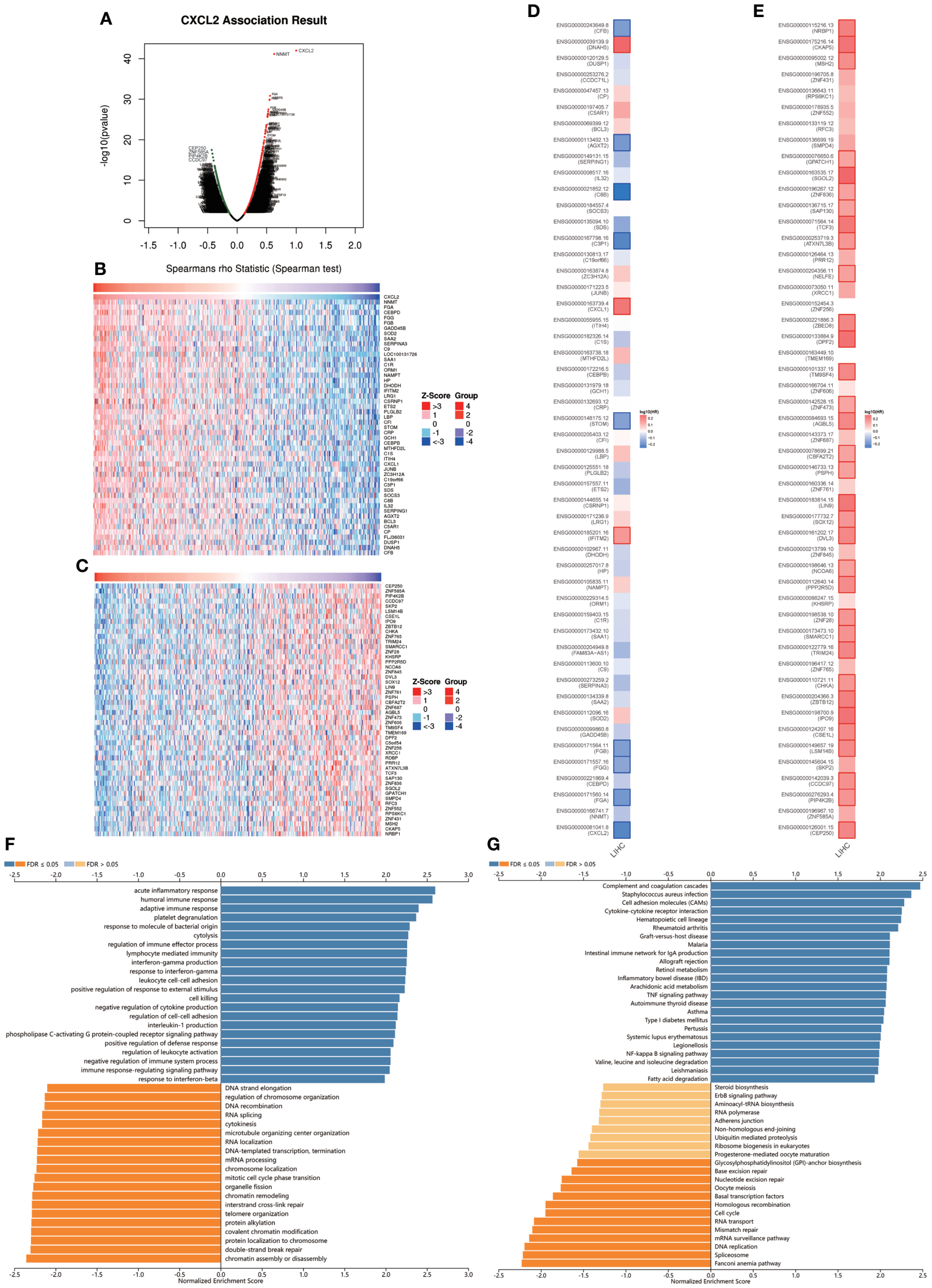

FIGURE 5
The co-expression network of CXCL2 in HCC. **(A)** Volcano plot for genes positively or negatively associated with CXCL2 in TCGA-LIHC cohort by LinkedOmics database. Red dots represent genes positively correlated with CXCL2, and green dots represent negative correlation **(B, C)** Heatmaps of the top 50 genes positively and negatively correlated with CXCL2 in HCC, respectively. **(D, E)** survival maps of the top 50 genes harboring positive and negative correlations with CXCL2 in HCC. **(F, G)** GO and KEGG pathways of CXCL2-associated network in TCGA-LIHC cohort.

TCGA-LIHC cohort with Spearman's rank correlation test. As shown in Figures 7A–C, M1 macrophage marker PTGS2 showed the highest positive correlation with CXCL2 ($r = 0.32$, $P < 0.001$). In addition, we employed the GEPIA2 database to cross-validate the association and the results were similar to our previous finding (Supplementary Figure S3). This finding indicated that CXCL2 may regulate immune response by promoting the formation of the M1 macrophage.

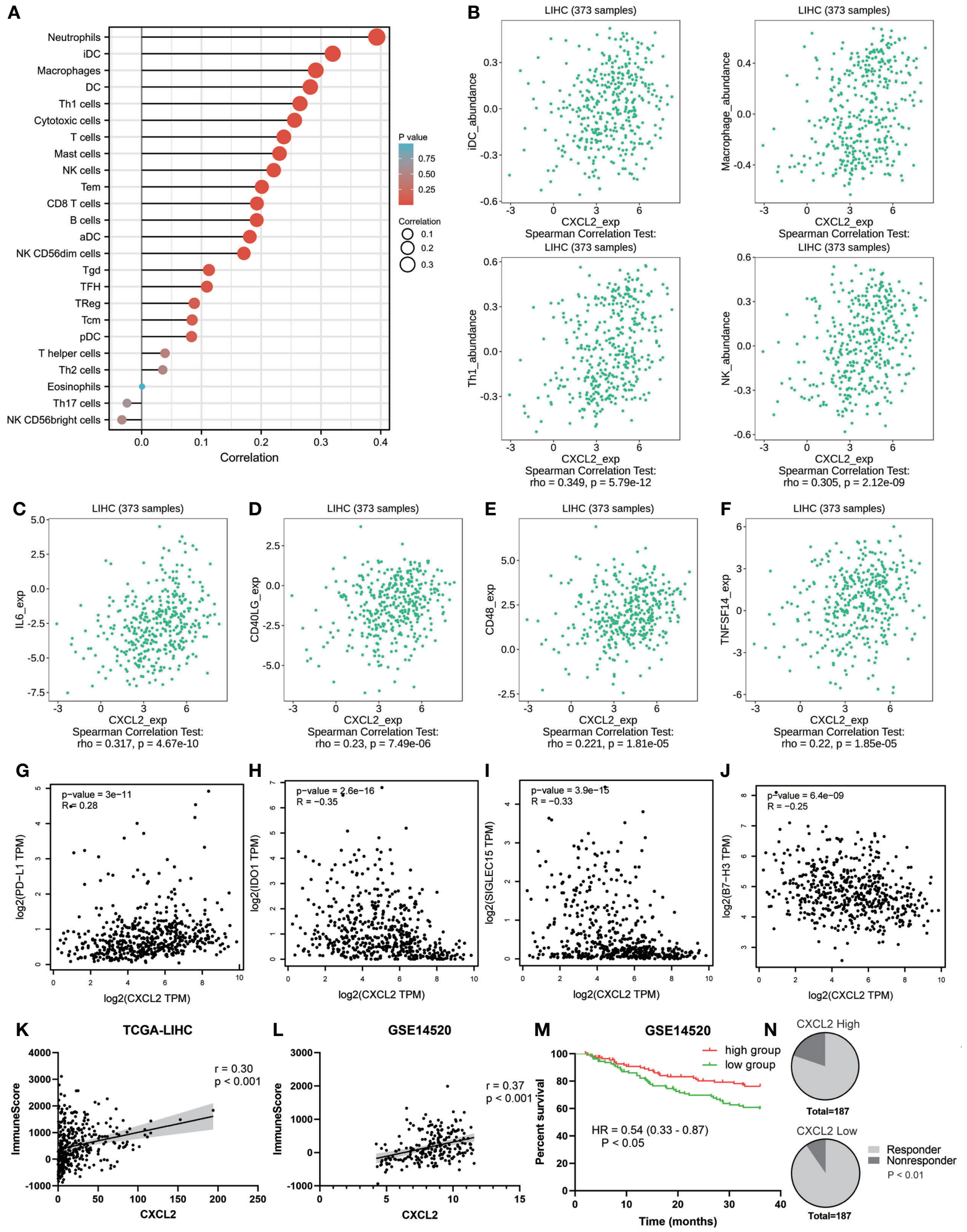

FIGURE 6

The role of CXCL2 in immune microenvironment of HCC. **(A)** Lollipop diagram exhibiting tumor-infiltrating immune cells associated with CXCL2 by Xiantao tool. **(B)** Scatter plots cross-validating the associations between CXCL2 expression and several TILs, including iDC, macrophage, Th1, and NK cells. **(C-F)** Positive correlations between CXCL2 expression and several immunostimulators, including IL-16, CD40LG, CD48, and TNFSF14. **(G-J)** Association between CXCL2 expression and immune checkpoints. **(K, L)** Association between CXCL2 expression and immune score in TCGA-LIHC cohort and GSE14520 evaluated by ESTIMATE algorithm. **(M)** Kaplan-Meier survival curves showing 3-year overall survival based on immune score in GSE14520 dataset. **(N)** The predicted response rate of the CXCL2 high expression group was lower than that of the CXCL2 low expression group.

Discussion

This study aimed to explore critical and novel ferroptosis-related biomarkers for prognosis of HCC patients. Through three GEO datasets and a ferroptosis-related gene dataset, we screened six co-DEGs, including one up-regulated gene, ACSL4, and five down-regulated genes, STEAP3, MT1G, GCH1, HAMP, and CXCL2. We also found the low-expressed CXCL2 exhibited potential prognostic significance in patients with HCC, and low expression of CXCL2 was associated with malignancy clinical features, such as AFP > 400 ng/ml, nodal metastasis, and higher grades. Furthermore, *in vitro* experiments demonstrated that CXCL2 was down-regulated in HCC samples and the overexpression of CXCL2 inhibited cell proliferation. ssGSEA analysis revealed that enrichment of genes co-expressed with CXCL2 were mainly involved in inflammation and immune-related pathways. These findings provided a new perspective on CXCL2 as a prognostic marker in HCC.

Ferroptosis is characterized as a form of non-apoptotic regulated cell death driven by iron accumulation and lipid peroxidation (40, 41). Increasing evidence suggests that ferroptosis plays pivotal roles in tumor development and is strongly correlated with therapeutic responses in various cancer types (42, 43). Sorafenib, a multi-kinase inhibitor, remains the first-line targeted therapy for advanced HCC patients (44). Previously studies indicated that sorafenib exerted antitumor effects not only by inhibiting cell proliferation and inducing apoptosis, but also by antiangiogenic activity (45, 46). However, recent studies have shown that sorafenib may exert its antitumoral activity mainly by promoting ferroptosis by inhibiting the function of system Xc- (cystine/glutamate antiporter system) (47–49). High expression of ACSL4 (Acyl-CoA synthetase long chain family member 4), a driver of ferroptosis, was positively associated with the sensitivity of sorafenib in HCC (50). Combination of sorafenib and ferroptosis inducers may be a new and effective therapeutic strategy in HCC patients.

Chemokine CXCL2 is a small secreted protein with a Glu-Leu-Arg (ELR) motif that binds to CXC chemokine receptor 2 (CXCR2) to promote tumor angiogenesis and endothelial cell survival (51). According to a recent study by Linkermann et al. (52), the expression level of CXCL2 was significantly reduced upon the application of ferroptosis inhibitor ferrostatin-1 (Fer-1) in a mouse model of oxalate nephropathy. Ferroptosis inducer RLS3 increased the expression of CXCL2 in vascular smooth muscle cells (53). In this study, bioinformatics analysis and experimental validation confirmed the down-regulation of CXCL2 in HCC, and overexpression of CXCL2 increased intracellular ROS, Fe^{2+} and MDA levels. These results might provide further insights into the potential role of CXCL2 in mediating ferroptosis. The ROC curve, based on a series of cut-off points with sensitivity and specificity, is an effective method to evaluate the performance of diagnostic tests (54, 55). In our study, we found the area under the ROC curve (AUC) for CXCL2 to diagnose HCC reached 0.903, indicating a promising clinical diagnostic significance of CXCL2 which needed further clinical validation.

An accumulating body of evidence suggests that immune microenvironment affects tumor development and response to therapy (56–58). Single-cell RNA sequencing analysis revealed the immunosuppressive landscape in HCC patients (59). Checkpoint blockade immunotherapies have redefined cancer treatment paradigm (60). The combination therapy of atezolizumab (anti-PD-L1) and bevacizumab (anti-VEGF) improved overall survival in patients with HCC compared to sorafenib, leading to FDA approval of this regimen (3, 61). Consistent with previous findings, ferroptosis-related gene CXCL2 was down-regulated in HCC samples compared with adjacent normal tissues and overexpression of CXCL2 could inhibit cell proliferation (19, 62). However, previous studies mainly focused on apoptosis pathways. In this paper, ssGSEA showed that co-expression genes of CXCL2 were mainly enriched in inflammation and immune-associated pathways, such as acute inflammatory response, humoral immune response, adaptive immune response. The interaction analysis between CXCL2 and immune system further indicated that CXCL2 expression was positively correlated with lymphocytes, including neutrophils and macrophages, especially the M1 macrophages (anti-tumor). The positive correlation was also found between CXCL2 and immunostimulators, such as IL-16, CD40LG, CD48, and TNFSF14. In addition, correlation analysis between CXCL2 and immune infiltration score in GSE14520

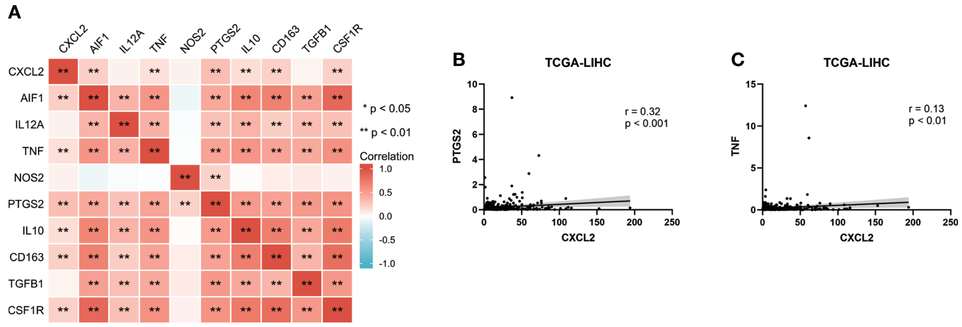

FIGURE 7
CXCL2 associated with M1 macrophage in HCC. **(A)** Heat map of correlation between CXCL2 and classical macrophage phenotype markers. **(B, C)** Scatter plots showing the association between CXCL2 and M1 macrophage markers (PTGS2 and TNF).

dataset indicated that patients with high immune infiltration score had higher CXCL2 expression and better prognosis. Together, these findings suggested that ferroptosis-related gene CXCL2 may regulate tumor immune response to influence cancer development and serve as a biomarker for diagnosis and prognosis in patients with HCC.

Conclusion

Conclusively, our study provides a novel insight into the biological role of CXCL2 and its interaction with immune microenvironment in HCC patients. CXCL2 was down-regulated in HCC tissues and cell lines, and overexpression of CXCL2 could inhibit cell proliferation. High expression of CXCL2 exhibited a favorable prognostic indicator in patients with HCC. Furthermore, CXCL2 expression was obviously correlated with the immune signatures, including tumor-infiltrating immune cells and immunostimulators. Therefore, our findings suggest ferroptosis-related gene CXCL2 plays a pivotal role in the development of HCC by regulating immune response and may be a promising diagnostic and prognostic indicator in patients with HCC.

Data availability statement

The datasets presented in this study can be found in online repositories. The names of the repository/repositories and accession number(s) can be found in the article/Supplementary Material.

Author contributions

QY and YY: Acquisition of data. QY and YY: Analysis and interpretation of data. YY: Conception and design. QL: Data curation. QL and YL: Development of methodology. QY and ZG: Writing and/or revising the manuscript. All authors contributed to the article and approved the submitted version.

Funding

This study is supported by grants from the Science and Technology Innovation Program of Hunan Province (2021RC3029), the horizontal project (2022, 143010100; 2021-021, 143010100), the China Postdoctoral Science Foundation (2021T140754, 2020M672521) and the Postdoctoral Science Foundation of Central South University (248485).

Conflict of interest

The authors declare that the research was conducted in the absence of any commercial or financial relationships that could be construed as a potential conflict of interest.

Publisher's note

Supplementary material

The Supplementary Material for this article can be found online at: https://www.frontiersin.org/articles/10.3389/fonc.2022.998736/full#supplementary-material

SUPPLEMENTARY TABLE 1
Differentially expressed genes in GSE6764, GSE14323, and GSE14520.

SUPPLEMENTARY FIGURE 1
Prognostic values of CXCL2, GCH1, and HAMP in HCC with the GEPIA2 database. **(A-F)** Kaplan-Meier curves for overall survival and disease-free survival of CXCL2, GCH1, and HAMP in patients with HCC by the GEPIA2 database.

SUPPLEMENTARY FIGURE 2
Functional enrichment analysis of CXCL2-associated network. **(A, B)** GO and KEGG enrichment analysis of CXCL2-associated network in TCGA-LIHC cohort with the Xiantao database.

SUPPLEMENTARY FIGURE 3
The association between CXCL2 expression and classical macrophage phenotype markers in TCGA-LIHC cohort. **(A)** Scatter plots showing the association between CXCL2 and M0 (undifferentiated) macrophage markers (AIF1). **(B-E)** Scatter plots showing the association between CXCL2 and M1 (anti-tumor) macrophage markers (IL12A, TNF, NOS2, PTGS2). **(F-I)** Scatter plots showing the association between CXCL2 and M2 (tumor-promoting) macrophage markers (IL10, CD163, TGFB1, CSF1R).

References

1. Anwanwan D, Singh SK, Singh S, Saikam V, Singh R. Challenges in liver cancer and possible treatment approaches. *Biochim Biophys Acta Rev Cancer* (2020) 1873(1):188314. doi: 10.1016/j.bbcan.2019.188314

2. Sung H, Ferlay J, Siegel RL, Laversanne M, Soerjomataram I, Jemal A, et al. Global cancer statistics 2020: GLOBOCAN estimates of incidence and mortality worldwide for 36 cancers in 185 countries. *CA Cancer J Clin* (2021) 71(3):209–49. doi: 10.3322/caac.21660

3. Llovet JM, Kelley RK, Villanueva A, Singal AG, Pikarsky E, Roayaie S, et al. Hepatocellular carcinoma. *Nat Rev Dis Primers* (2021) 7(1):6. doi: 10.1038/s41572-020-00240-3

4. Zelber-Sagi S, Noureddin M, Shibolet O. Lifestyle and hepatocellular carcinoma what is the evidence and prevention recommendations. *Cancers (Basel)* (2021) 14(1):103. doi: 10.3390/cancers14010103

5. Liu CY, Chen KF, Chen PJ. Treatment of liver cancer. *Cold Spring Harb Perspect Med* (2015) 5(9):a021535. doi: 10.1101/cshperspect.a021535

6. El-Khoueiry AB, Sangro B, Yau T, Crocenzi TS, Kudo M, Hsu C, et al. Nivolumab in patients with advanced hepatocellular carcinoma (CheckMate 040): an open-label, non-comparative, phase 1/2 dose escalation and expansion trial. *Lancet* (2017) 389(10088):2492–502. doi: 10.1016/S0140-6736(17)31046-2

7. Murciano-Goroff YR, Warner AB, Wolchok JD. The future of cancer immunotherapy: microenvironment-targeting combinations. *Cell Res* (2020) 30 (6):507–19. doi: 10.1038/s41422-020-0337-2

8. Wu Y, Zhang S, Gong X, Tam S, Xiao D, Liu S, et al. The epigenetic regulators and metabolic changes in ferroptosis-associated cancer progression. *Mol Cancer* (2020) 19(1):39. doi: 10.1186/s12943-020-01157-x

9. Zheng J, Conrad M. The metabolic underpinnings of ferroptosis. *Cell Metab* (2020) 32(6):920–37. doi: 10.1016/j.cmet.2020.10.011

10. Liang C, Zhang X, Yang M, Dong X. Recent progress in ferroptosis inducers for cancer therapy. *Adv Mater* (2019) 31(51):e1904197. doi: 10.1002/adma.201904197

11. Ren Z, Hu M, Wang Z, Ge J, Zhou X, Zhang G, et al. Ferroptosis-related genes in lung adenocarcinoma: Prognostic signature and immune, drug resistance, mutation analysis. *Front Genet* (2021) 12:672904. doi: 10.3389/fgene.2021.672904

12. Jiang L, Kon N, Li T, Wang SJ, Su T, Hibshoosh H, et al. Ferroptosis as a p53-mediated activity during tumour suppression. *Nature* (2015) 520(7545):57–62. doi: 10.1038/nature14344

13. Stockwell BR, Jiang X, Gu W. Emerging mechanisms and disease relevance of ferroptosis. *Trends Cell Biol* (2020) 30(6):478–90. doi: 10.1016/j.tcb.2020.02.009

14. Stockwell BR, Jiang X. A physiological function for ferroptosis in tumor suppression by the immune system. *Cell Metab* (2019) 30(1):14–5. doi: 10.1016/j.cmet.2019.06.012

15. Su Y, Zhao B, Zhou L, Zhang Z, Shen Y, Lv H, et al. Ferroptosis, a novel pharmacological mechanism of anti-cancer drugs. *Cancer Lett* (2020) 483:127–36. doi: 10.1016/j.canlet.2020.02.015

16. De Filippo K, Dudeck A, Hasenberg M, Nye E, van Rooijen N, Hartmann K, et al. Mast cell and macrophage chemokines CXCL1/CXCL2 control the early stage of neutrophil recruitment during tissue inflammation. *Blood* (2013) 121(24):4930–7. doi: 10.1182/blood-2013-02-486217

17. Girbl T, Lenn T, Perez L, Rolas L, Barkaway A, Thiriot A, et al. Distinct compartmentalization of the chemokines CXCL1 and CXCL2 and the atypical receptor ACKR1 determine discrete stages of neutrophil diapedesis. *Immunity* (2018) 49(6):1062–1076 e1066. doi: 10.1016/j.immuni.2018.09.018

18. Zhang H, Ye YL, Li MX, Ye SB, Huang WR, Cai TT, et al. CXCL2/MIF-CXCR2 signaling promotes the recruitment of myeloid-derived suppressor cells and is correlated with prognosis in bladder cancer. *Oncogene* (2017) 36(15):2095–104. doi: 10.1038/onc.2016.367

19. Ding J, Xu K, Zhang J, Lin B, Wang Y, Yin S, et al. Overexpression of CXCL2 inhibits cell proliferation and promotes apoptosis in hepatocellular carcinoma. *BMB Rep* (2018) 51(12):630–5. doi: 10.5483/BMBRep.2018.51.12.140

20. Wurmbach E, Chen YB, Khitrov G, Zhang W, Roayaie S, Schwartz M, et al. Genome-wide molecular profiles of HCV-induced dysplasia and hepatocellular carcinoma. *Hepatology* (2007) 45(4):938–47. doi: 10.1002/hep.21622

21. Wang C, Liao Y, He W, Zhang H, Zuo D, Liu W, et al. Elafin promotes tumour metastasis and attenuates the anti-metastatic effects of erlotinib *via* binding to EGFR in hepatocellular carcinoma. *J Exp Clin Cancer Res* (2021) 40(1):113. doi: 10.1186/s13046-021-01904-y

22. Mas VR, Maluf DG, Archer KJ, Yanek K, Kong X, Kulik L, et al. Genes involved in viral carcinogenesis and tumor initiation in hepatitis c virus-induced hepatocellular carcinoma. *Mol Med* (2009) 15(3-4):85–94. doi: 10.2119/molmed.2008.00110

23. Yan Y, Liang Q, Xu Z, Huang J, Chen X, Cai Y, et al. Downregulated ferroptosis-related gene STEAP3 as a novel diagnostic and prognostic target for hepatocellular carcinoma and its roles in immune regulation. *Front Cell Dev Biol* (2021) 9:743046. doi: 10.3389/fcell.2021.743046

24. Zhou N, Bao J. FerrDb: a manually curated resource for regulators and markers of ferroptosis and ferroptosis-disease associations. *Database (Oxford)* (2020), baaa021. doi: 10.1093/database/baaa021

25. Lanczky A, Gyorffy B. Web-based survival analysis tool tailored for medical research (KMplot): Development and implementation. *J Med Internet Res* (2021) 23(7):e27633. doi: 10.2196/27633

26. Tang Z, Li C, Kang B, Gao G, Li C, Zhang Z. GEPIA: A web server for cancer and normal gene expression profiling and interactive analyses. *Nucleic Acids Res* (2017) 45(W1):W98–W102. doi: 10.1093/nar/gkx247

27. Bartha A, Gyorffy B. TNMplot.com: A web tool for the comparison of gene expression in normal, tumor and metastatic tissues. *Int J Mol Sci* (2021) 22(5):2622. doi: 10.3390/ijms22052622

28. Chandrashekar DS, Bashel B, Balasubramanya SAH, Creighton CJ, Ponce-Rodriguez I, Chakravarthi B, et al. UALCAN: A portal for facilitating tumor subgroup gene expression and survival analyses. *Neoplasia* (2017) 19(8):649–58. doi: 10.1016/j.neo.2017.05.002

29. Vasaikar SV, Straub P, Wang J, Zhang B. LinkedOmics: analyzing multi-omics data within and across 32 cancer types. *Nucleic Acids Res* (2018) 46(D1): D956–63. doi: 10.1093/nar/gkx1090

30. Ru B, Wong CN, Tong Y, Zhong JY, Zhong SSW, Wu WC, et al. TISIDB: an integrated repository portal for tumor-immune system interactions. *Bioinformatics* (2019) 35(20):4200–2. doi: 10.1093/bioinformatics/btz210

31. Jiang P, Gu S, Pan D, Fu J, Sahu A, Hu X, et al. Signatures of T cell dysfunction and exclusion predict cancer immunotherapy response. *Nat Med* (2018) 24(10):1550–8. doi: 10.1038/s41591-018-0136-1

32. Fu J, Li K, Zhang W, Wan C, Zhang J, Jiang P, et al. Large-Scale public data reuse to model immunotherapy response and resistance. *Genome Med* (2020) 12 (1):21. doi: 10.1186/s13073-020-0721-z

33. Subramanian A, Tamayo P, Mootha VK, Mukherjee S, Ebert BL, Gillette MA, et al. Gene set enrichment analysis: a knowledge-based approach for interpreting genome-wide expression profiles. *Proc Natl Acad Sci U.S.A.* (2005) 102(43):15545–50. doi: 10.1073/pnas.0506580102

34. Yoshihara K, Shahmoradgoli M, Martinez E, Vegesna R, Kim H, Torres-Garcia W, et al. Inferring tumour purity and stromal and immune cell admixture from expression data. *Nat Commun* (2013) 4:2612. doi: 10.1038/ncomms3612

35. Qiu Y, Cao Y, Cao W, Jia Y, Lu N. The application of ferroptosis in diseases. *Pharmacol Res* (2020) 159:104919. doi: 10.1016/j.phrs.2020.104919

36. Yuan H, Pratte J, Giardina C. Ferroptosis and its potential as a therapeutic target. *Biochem Pharmacol* (2021) 186:114486. doi: 10.1016/j.bcp.2021.114486

37. Xu Z, Peng B, Liang Q, Chen X, Cai Y, Zeng S, et al. Construction of a ferroptosis-related nine-lncRNA signature for predicting prognosis and immune response in hepatocellular carcinoma. *Front Immunol* (2021) 12:719175. doi: 10.3389/fimmu.2021.719175

38. Deng J, Zhou M, Liao T, Kuang W, Xia H, Yin Z, et al. Targeting cancer cell ferroptosis to reverse immune checkpoint inhibitor therapy resistance. *Front Cell Dev Biol* (2022) 10:818453. doi: 10.3389/fcell.2022.818453

39. Niu X, Chen L, Li Y, Hu Z, He F. Ferroptosis, necroptosis, and pyroptosis in the tumor microenvironment: Perspectives for immunotherapy of SCLC. *Semin Cancer Biol* (2022) S1044-579X(22):00065–7. doi: 10.1016/j.semcancer.2022.03.009

40. Dixon SJ, Lemberg KM, Lamprecht MR, Skouta R, Zaitsev EM, Gleason CE, et al. Ferroptosis: an iron-dependent form of nonapoptotic cell death. *Cell* (2012) 149(5):1060–72. doi: 10.1016/j.cell.2012.03.042

41. Lei G, Zhuang L, Gan B. Targeting ferroptosis as a vulnerability in cancer. *Nat Rev Cancer* (2022) 22(7):381–396. doi: 10.1038/s41568-022-00459-0

42. Roh JL, Kim EH, Jang HJ, Park JY, Shin D. Induction of ferroptotic cell death for overcoming cisplatin resistance of head and neck cancer. *Cancer Lett* (2016) 381(1):96–103. doi: 10.1016/j.canlet.2016.07.035

43. Chen X, Kang R, Kroemer G, Tang D. Broadening horizons: the role of ferroptosis in cancer. *Nat Rev Clin Oncol* (2021) 18(5):280–96. doi: 10.1038/s41571-020-00462-0

44. Benson AB, D'Angelica MI, Abbott DE, Anaya DA, Anders R, Are C, et al. Hepatobiliary cancers, version 2.2021, NCCN clinical practice guidelines in oncology. *J Natl Compr Canc Netw* (2021) 19(5):541–65. doi: 10.6004/jnccn.2021.0022

45. Wilhelm SM, Carter C, Tang L, Wilkie D, McNabola A, Rong H, et al. BAY 43-9006 exhibits broad spectrum oral antitumor activity and targets the RAF/MEK/ERK pathway and receptor tyrosine kinases involved in tumor progression and angiogenesis. *Cancer Res* (2004) 64(19):7099–109. doi: 10.1158/0008-5472.CAN-04-1443

46. Chang YS, Adnane J, Trail PA, Levy J, Henderson A, Xue D, et al. Sorafenib (BAY 43-9006) inhibits tumor growth and vascularization and induces tumor apoptosis and hypoxia in RCC xenograft models. *Cancer Chemother Pharmacol* (2007) 59(5):561–74. doi: 10.1007/s00280-006-0393-4

47. Louandre C, Ezzoukhry Z, Godin C, Barbare JC, Maziere JC, Chauffert B, et al. Iron-dependent cell death of hepatocellular carcinoma cells exposed to sorafenib. *Int J Cancer* (2013) 133(7):1732–42. doi: 10.1002/ijc.28159

48. Dixon SJ, Patel DN, Welsch M, Skouta R, Lee ED, Hayano M, et al. Pharmacological inhibition of cystine-glutamate exchange induces endoplasmic reticulum stress and ferroptosis. *Elife* (2014) 3:e02523. doi: 10.7554/eLife.02523

49. Lachaier E, Louandre C, Godin C, Saidak Z, Baert M, Diouf M, et al. Sorafenib induces ferroptosis in human cancer cell lines originating from different solid tumors. *Anticancer Res* (2014) 34(11):6417–22. Available at: https://ar.iiarjournals.org/content/34/11/6417.long.

50. Feng J, Lu PZ, Zhu GZ, Hooi SC, Wu Y, Huang XW, et al. ACSL4 is a predictive biomarker of sorafenib sensitivity in hepatocellular carcinoma. *Acta Pharmacol Sin* (2021) 42(1):160–70. doi: 10.1038/s41401-020-0439-x

51. Vandercappellen J, Van Damme J, Struyf S. The role of CXC chemokines and their receptors in cancer. *Cancer Lett* (2008) 267(2):226–44. doi: 10.1016/j.canlet.2008.04.050

52. Linkermann A, Skouta R, Himmerkus N, Mulay SR, Dewitz C, De Zen F, et al. Synchronized renal tubular cell death involves ferroptosis. *Proc Natl Acad Sci U.S.A.* (2014) 111(47):16836–41. doi: 10.1073/pnas.1415518111

53. Jin R, Yang R, Cui C, Zhang H, Cai J, Geng B, et al. Ferroptosis due to cystathionine gamma Lyase/Hydrogen sulfide downregulation under high hydrostatic pressure exacerbates VSMC dysfunction. *Front Cell Dev Biol* (2022) 10:829316. doi: 10.3389/fcell.2022.829316

54. Park SH, Goo JM, Jo CH. Receiver operating characteristic (ROC) curve: practical review for radiologists. *Kor J Radiol* (2004) 5(1):11–8. doi: 10.3348/kjr.2004.5.1.11

55. Mandrekar JN. Receiver operating characteristic curve in diagnostic test assessment. *J Thorac Oncol* (2010) 5(9):1315–6. doi: 10.1097/JTO.0b013e3181ec173d

56. Wei SC, Duffy CR, Allison JP. Fundamental mechanisms of immune checkpoint blockade therapy. *Cancer Discovery* (2018) 8(9):1069–86. doi: 10.1158/2159-8290.CD-18-0367

57. Huang C, Zhang C, Sheng J, Wang D, Zhao Y, Qian L, et al. Identification and validation of a tumor microenvironment-related gene signature in hepatocellular carcinoma prognosis. *Front Genet* (2021) 12:717319. doi: 10.3389/fgene.2021.717319

58. Sas Z, Cendrowicz E, Weinhauser I, Rygiel TP. Tumor microenvironment of hepatocellular carcinoma: Challenges and opportunities for new treatment options. *Int J Mol Sci* (2022) 23(7):3778. doi: 10.3390/ijms23073778

59. Ho DW, Tsui YM, Chan LK, Sze KM, Zhang X, Cheu JW, et al. Single-cell RNA sequencing shows the immunosuppressive landscape and tumor heterogeneity of HBV-associated hepatocellular carcinoma. *Nat Commun* (2021) 12(1):3684. doi: 10.1038/s41467-021-24010-1

60. Merle P. The new immuno-Oncology-Based therapies and their perspectives in hepatocellular carcinoma. *Cancers (Basel)* (2021) 13(2):238. doi: 10.3390/cancers13020238

61. Galle PR, Finn RS, Qin S, Ikeda M, Zhu AX, Kim TY, et al. Patient-reported outcomes with atezolizumab plus bevacizumab versus sorafenib in patients with unresectable hepatocellular carcinoma (IMbrave150): an open-label, randomised, phase 3 trial. *Lancet Oncol* (2021) 22(7):991–1001. doi: 10.1016/S1470-2045(21)00151-0

62. Lin T, Zhang E, Mai PP, Zhang YZ, Chen X, Peng LS. CXCL2/10/12/14 are prognostic biomarkers and correlated with immune infiltration in hepatocellular carcinoma. *Biosci Rep* (2021) 41(6):BSR20204312. doi: 10.1042/BSR20204312

Frontiers | Frontiers in Oncology

TYPE Original Research
PUBLISHED 20 October 2022
DOI 10.3389/fonc.2022.1023040

Check for updates

OPEN ACCESS

EDITED BY
Yue Sheng,
Central South University, China

REVIEWED BY
Chunjie Yu,
University of Florida, United States
Lu Li,
University of Florida, United States
Peike Sheng,
University of Florida, United States

*CORRESPONDENCE
Yifen Shi
2563639640@qq.com
Songfu Jiang
2350738431@qq.com

†These authors have contributed equally to this work

SPECIALTY SECTION
This article was submitted to Surgical Oncology, a section of the journal Frontiers in Oncology

RECEIVED 19 August 2022
ACCEPTED 27 September 2022
PUBLISHED 20 October 2022

CITATION
Zhu K, Lang Z, Zhan Y, Tao Q, Yu Z, Chen L, Fan C, Jin Y, Yu K, Zhu B, Gao Y, Wang C, Jiang S and Shi Y (2022) A novel 10-gene ferroptosis-related prognostic signature in acute myeloid leukemia. *Front. Oncol.* 12:1023040.
doi: 10.3389/fonc.2022.1023040

A novel 10-gene ferroptosis-related prognostic signature in acute myeloid leukemia

Kai Zhu[1†], Zhichao Lang[1†], Yating Zhan[1†], Qiqi Tao[1], Zhijie Yu[2], Lili Chen[2], Congcong Fan[1], Yan Jin[1], Kang Yu[2], Bihan Zhu[1], Yuxiang Gao[1], Chengchi Wang[1], Songfu Jiang[2,3*] and Yifen Shi[2,3*]

[1]Key Laboratory of Diagnosis and Treatment of Severe Hepato-Pancreatic Diseases of Zhejiang Province, The First Affiliated Hospital of Wenzhou Medical University, Wenzhou, China, [2]Department of Hematology, The First Affiliated Hospital of Wenzhou Medical University, Wenzhou, China, [3]Zhejiang Provincial Clinical Research Center For Hematological disorders, Wenzhou, China

Acute myeloid leukemia (AML) is one of the most common hematopoietic malignancies and exhibits a high rate of relapse and unfavorable outcomes. Ferroptosis, a relatively recently described type of cell death, has been reported to be involved in cancer development. However, the prognostic value of ferroptosis-related genes (FRGs) in AML remains unclear. In this study, we found 54 differentially expressed ferroptosis-related genes (DEFRGs) between AML and normal marrow tissues. 18 of 54 DEFRGs were correlated with overall survival (OS) ($P<0.05$). Using the least absolute shrinkage and selection operator (LASSO) Cox regression analysis, we selected 10 DEFRGs that were associated with OS to build a prognostic signature. Data from AML patients from the International Cancer Genome Consortium (ICGC) cohort as well as the First Affiliated Hospital of Wenzhou Medical University (FAHWMU) cohort were used for validation. Notably, the prognostic survival analyses of this signature passed with a significant margin, and the riskscore was identified as an independent prognostic marker using Cox regression analyses. Then we used a machine learning method (SHAP) to judge the importance of each feature in this 10-gene signature. Riskscore was shown to have the highest correlation with this 10-gene signature compared with each gene in this signature. Further studies showed that AML was significantly associated with immune cell infiltration. In addition, drug-sensitive analysis showed that 8 drugs may be beneficial for treatment of AML. Finally, the expressions of 10 genes in this signature were verified by real-time quantitative polymerase chain reaction. In conclusion, our study establishes a novel 10-gene prognostic risk signature based on ferroptosis-related genes for AML patients and FRGs may be novel therapeutic targets for AML.

KEYWORDS

ferroptosis, TCGA database, AML, Prognosis signature, Immune infiltration, machine learning

Introduction

Acute myeloid leukemia (AML) is characterized by a heterogeneity of molecular abnormalities and the accumulation of immature myeloid progenitors in the bone marrow and peripheral blood and represents the most common type of acute leukemia in adults (1, 2). Despite novel treatment options over the last years, the 5-year survival rate of AML patient remains unsatisfactory (3). 40%~70% of AML patients relapse and become treatment-refractory, ultimately leading to treatment failure and even death. Therefore, there is an urgent need to develop novel prognostic biomarkers to monitor the prognosis of AML patients.

Ferroptosis is an iron-dependent form of regulated cell death driven by a lethal increase of lipid peroxidation (4, 5). Ferroptosis has been shown to play a key role in the suppression of tumorigenesis by removing the cells deficient in key nutrients in the environment or damaged by infection or ambient stress (6). Targeting ferroptosis is considered as a promising way for cancer patients, especially for malignancies that are resistant to traditional treatments (7, 8). Several signatures with ferroptosis-related genes have been established to predict the prognosis of patients with cancer (9). However, the role of FRGs in the prognosis of AML remains unclear.

In this study, we constructed a prognostic signature of 10 ferroptosis-related differentially expressed genes (FRDEGs) based on the transcriptomic and clinical data of AML patients from The Cancer Genome Atlas (TCGA). Then, this FRDEGs prognostic signature was validated by International Cancer Genome Consortium (ICGC) and the First Affiliated Hospital of Wenzhou Medical University (FAHWMU) cohorts. Using functional enrichment analysis and correlation analysis, we further explored the potential molecular mechanisms in our signature. Finally, we performed a drug sensitivity analysis to explore potential gene targets.

Materials and methods

Data collection

The RNA sequencing (RNA-seq) and clinical data of two AML cohorts were downloaded from public database, including 130 tumor samples (bone marrow) of AML patients from TCGA (https://portal.gdc.cancer.gov) and 92 tumor samples (bone marrow) of AML patients from ICGC (https://dcc.icgc.org/projects/LIRI-JP). Besides, RNA-seq data of 70 normal marrow samples were obtained from Genotype-Tissue Expression Project (GTEx) (https://www.genome.gov/). All the expression data from the three databases were normalized using the perl, respectively. The current research follows the TCGA and ICGC data access policies and publication guidelines. A total of 60 FRGs utilized in this study were obtained from the previous literature (Supplementary Table 1) (7).

In addition, we collected 57 tumor samples (bone marrow) of AML patients from the FAHWMU as validation data.

Construction of a prognostic 10-gene signature

The “limma” R package was used to identify the DEGs between tumor samples from TCGA and normal samples from GTEx with a false discovery rate (FDR)< 0.05 (Supplementary Table 2). Moreover, with the help of the “survival” R package, we assessed the prognostic values of 60 FRGs and calculated their FDRs using the Benjamin–Hochberg (BH) method. Protein-Protein Interaction Networks (PPI) and correlation networks of the intersecting 18 genes were generated using the STRING database (STRING: functional protein association networks (string-db.org)). Least absolute shrinkage and selection operator (LASSO) Cox regression was performed using the “glmnet” R package. The independent variable in the regression was the normalized expression matrix of candidate prognostic differentially expressed genes, and the response variables were overall survival (OS) and status of patients in the TCGA cohort. The optimum penalty parameter (λ) for the model was determined by 10-fold cross-validation following the minimum criteria (i.e. the value of λ corresponding to the lowest partial likelihood deviance). The riskscore of the patients was calculated according to the normalized expression level of each gene and its corresponding regression coefficients. The formula was established as follows:

$$\text{score} = e^{\text{sum (expression level of each gene ñ corresponding coefficient)}}$$

Patients were stratified into the high- or low-risk groups based on the median value of their risk score. Patients in the ICGC were also stratified into the high- and low-risk groups based on the values derived from this formula.

Validation of a prognostic 10-gene signature

Based on the expression levels of genes in the signature, we carried out Principal Component Analysis (PCA) using the “prcomp” package. Besides, t-distributed Stochastic Neighbor Embedding (t-SNE) was performed to explore the clustering of different groups using the “Rtsne” R package. Univariate and multivariate Cox regression analyses were used to identify independent prognostic factors. Receiver Operating Characteristic (ROC) curve analysis was used to predict OS with the R package “pROC”. All statistical analyses were carried out using the R software, with P< 0.05 being considered statistically significant.

Machine learning method analysis for 10-gene signature

SHapley Additive explanation (SHAP) was used to explore the importance of 10 genes and riskscore for the 10-gene signature. SHAP (10) is a game theory method that interprets machine-learning model and understands the decision-making process through quantifying the contribution that each feature brings to the prediction made by the model.

Functional enrichment and correlation analysis

The “clusterProfiler” R package was utilized to conduct Gene Ontology (GO) and Kyoto Encyclopedia of Genes and Genomes (KEGG) analyses based on DEGs (Supplementary Table 3, |log2FC| ≥ 1, FDR< 0.05) between the high- and low- groups from TCGA cohort. P values were adjusted using the BH method. Moreover, we estimated the infiltration score of 16 immune cell types and the activity of 13 immune-related pathways using single-sample gene set enrichment analysis (ssGSEA) in the “gsva” R package. Besides, based on the Expression data (ESTIMATE) algorithm, we estimated the proportion of infiltrating immune cells and stromal cells to get immune, stromal and ESTIMATE score for each AML patient. Using CIBERSOFT algorithm, the relative content score of 22 TICs in every AML patient was calculated. CIBERSOFT is a gene-based deconvolution algorithm that infers 22 human tumor immune infiltrating cell types and quantifies (11). The Cancer Stem Cell (CSC) correlation analysis and tumor microenvironment correlation analysis were conducted using the “limma” and “estimate” R packages.

Drug sensitivity analysis

The CellMiner website (https://discover.nci.nih.gov/cellminer/) was used to analyze the NCI-60 database (12, 13). The target gene expression status and z-score for cell sensitivity data were retrieved from the website and analyzed using Pearson correlation analysis to evaluate the relationship between target gene expression and drug sensitivity.

Quantitative real-time PCR analysis

The bone marrow samples of AML patients (n=20) as well as healthy donors (n=20) were collected from the FAHWMU. Total RNA was isolated from AML patients as well as healthy donors using the Tiangen RNA extraction reagent kit. Each sample was reversely transcribed into complementary DNA (cDNA) using a reverse-transcription (RT) reagent kit (Takara Biotechnology Co., Ltd., Dalian, China). Then, Real-time PCR was performed using SYBR Premix ExTaq (Takara). GAPDH was used as endogenous controls for mRNAs. The primer sequences for 10 genes were shown in Supplementary Table 4.

Statistical analysis

R software (version 4.0.3) and GraphPad prism 9 were used to complete all statistical work and plot drawing. The Spearman correlation method was employed to calculate the correlation between two variables. Survival plots were created using the Kaplan–Meier method. Two sets of data for qRT-PCR were analyzed using Student’s t-test. To examine the relationship between OS and riskscore as well as clinical feature, univariate or multivariate Cox regression analysis was performed. The hazard ratio (HR) and 95% confidence interval (CI) were calculated to identify genes associated with OS. P< 0.05 was considered statistically significant.

Results

Flow chart and clinical data

The flow chart of this study was shown in Figure 1. Data from a total of 130 AML tumor samples from the TCGA cohort and 92 ICGC tumor samples derived from AML patients were used. Detailed clinical characteristics of patients were summarized in Table 1.

Identification of prognostic 18 FRDEGs in the TCGA cohort

We found that the majority of FRGs were differentially expressed between TCGA tumor samples and GTEx normal samples (54/60, 90%). Eighteen of these FRDEGs (Figures 2B, C) were associated with OS in univariate Cox regression analysis (p<0.05, Figure 2A). Using PPI network construction, we identified the hub genes including SLC7A11, G6PD, GPX4, HMOX1, and FTH1 (Figure 2D). The correlation among 18 FRDEGs was shown in Figure 2E.

10 FRDEGs were selected and 10-gene signature was constructed in the TCGA cohort

10 of 18 prognostic FRDEGs, which were determined by LASSO Cox regression analysis, were selected for the next analysis (Supplementary Figures 1A, B). A riskscore was calculated using mRNA expression levels and relevant coefficients of 10 genes with the following formula:

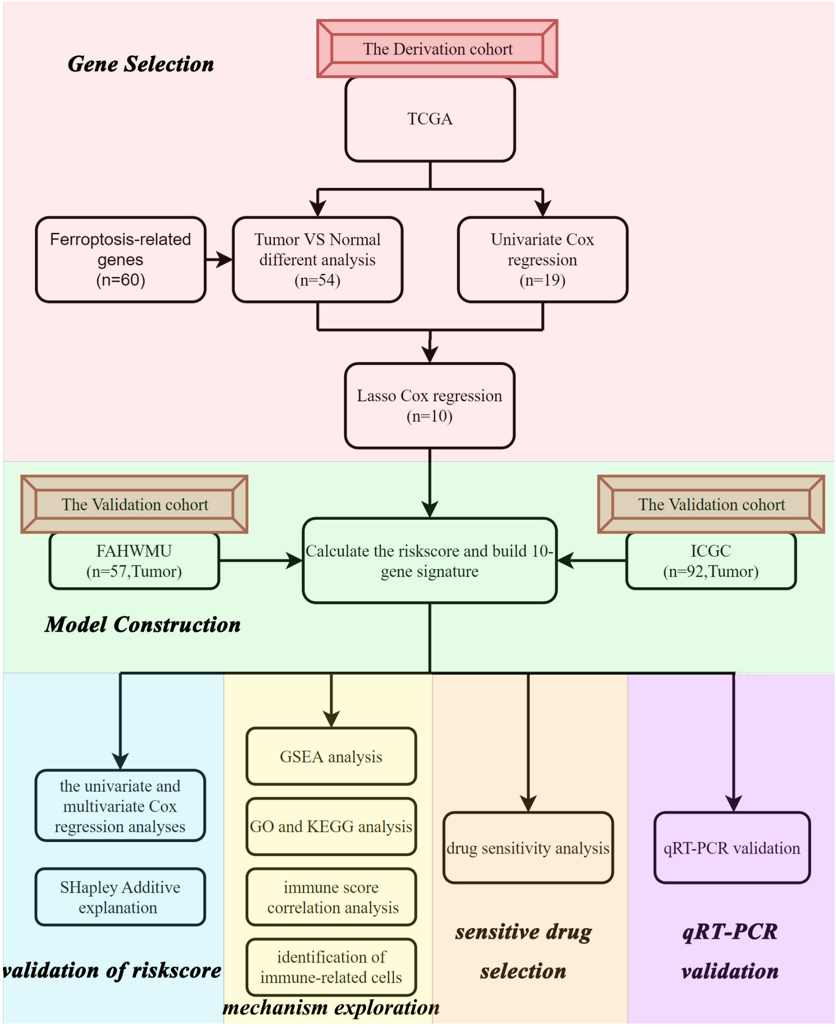

FIGURE 1
Flow chart of the data collection and analysis.

$$\begin{aligned}\text{Riskscore} = \; & (-0.548 * \text{CD44}) + (0.371 * \text{CHAC1}) + \\ & (0.629 * \text{CISD1}) + (0.399 * \text{DPP4}) + \\ & (-0.849 * \text{NCOA4}) + (0.299 * \text{SAT1}) + \\ & (0.485 * \text{SLC7A11}) + (0.280 * \text{AIFM2}) + \\ & (1.391 * \text{G6PD}) + (0.955 * \text{ACSF2})\end{aligned}$$

Survival analyses of this 10-gene signature in TCGA, ICGC and FAHWMU cohorts

Patients in the TCGA, ICGC or FAHWMU cohort were then divided into the high- or low-risk groups according to the median cut-off value. The results of Kaplan-Meier curve indicated that patients in the low-risk group exhibited a significantly better OS than those in the high-risk group in TCGA (Figure 3A, $P<0.001$), ICGC (Figure 3C, $p<0.001$) and FAHWMU cohorts (Figure 3E, $P<0.05$). The predictive performance of this riskscore for OS was evaluated by time-dependent ROC curves. In the TCGA cohort, the area under the curve (AUC) reached 0.841 for 1^{st} year, 0.811 for 2^{nd} year, and 0.849 for 3^{rd} year (Figure 3B). In the ICGC cohort, the AUC was 0.634 for 1^{st} year, 0.680 for 2^{nd} year, and 0.678 for 3^{rd} year (Figure 3D). The AUC of 10-gene signature in the FAHWMU cohort was 0.772 for 1^{st} year and 1.000 for 2^{nd} year, respectively (Figure 3F). The t-SNE and PCA plots, mapped based on the risk score of each patient, were shown in Figures 4A–F. The red point means patient in the high-risk group, while blue point means patient in the low-risk group (Figures 4A-D). It was found that the red points clustered in one part, while the blue points clustered in

TABLE 1 Clinical characteristics of AML patients used in this study.

	TCGA cohort	ICGC cohort
No.of patients	130	92
Age (median,range)	56 (21-88)	62 (18-88)
Gender (%)		
male	70	49
Female	60	43
Stage (%)		
M0	12 (9.2%)	NA
M1	30 (23%)	NA
M2	32 (24.6)	NA
M3	14 (10.8%)	NA
M4	27 (20.8)	NA
M5	12 (9.2%)	NA
M6	2	NA
M7	1	NA
Survival status (%)		
Alive	52 (40%)	0
Dead	78 (60%)	92 (100%)
Survival time (median)	364 days	303 days

NA, Not Applicable.

another part. Results of this outcome suggest that our 10-gene signature may contribute to better prognosis prediction of AML patients.

Identification of independent prognostic value

Univariate and multivariate Cox regression analyses were carried out among the available variables to determine whether the riskscore was an independent prognostic predictor for OS. In TCGA cohort, the riskscore was significantly associated with OS in both the univariate Cox regression analyses (HR = 3.563, 95% CI = 2.513-5.051, P< 0.001) (Figure 5A) and multivariate Cox regression analyses (HR = 3.517, 95% CI = 2.420-5.112, P< 0.001) (Figure 5B). Similar results including both univariate Cox regression analyses (HR = 2.136, 95% CI = 1.370-3.330, P< 0.001) (Figure 5C) and multivariate Cox regression analyses (HR = 1.969, 95% CI = 1.250-3.100, P = 0.003) (Figure 5D) were also found in the ICGC cohort. Except for the riskscore, age is another character that was identified as the independent prognostic factors (P<0.05)

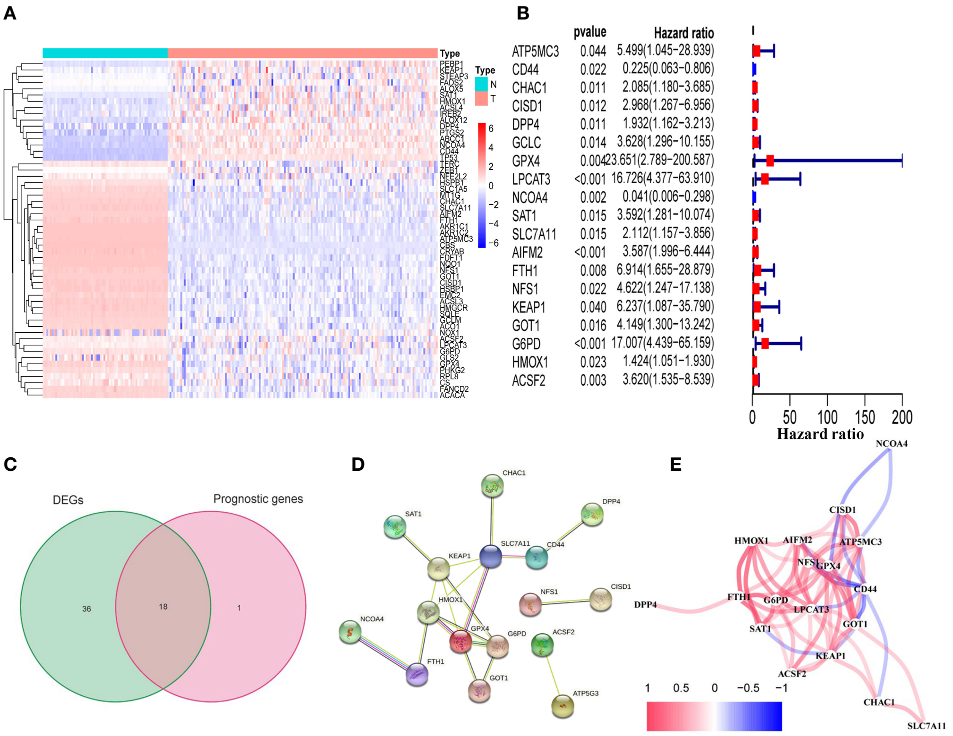

FIGURE 2
Identification of prognostic FRDEGs in the TCGA cohort. **(A)** Heat map of the 54 DEGs (T: tumor sample; N: normal sample). **(B)** Forest plots showed the results of the univariate cox regression analysis between gene expression and OS (p < 0.05). **(C)** Venn diagram identified FRDEGs. **(D)** The PPI network revealed the hub genes. **(E)** The correlation network among the 18 DEFRGs genes. Different colors represent the correlation coefficients.

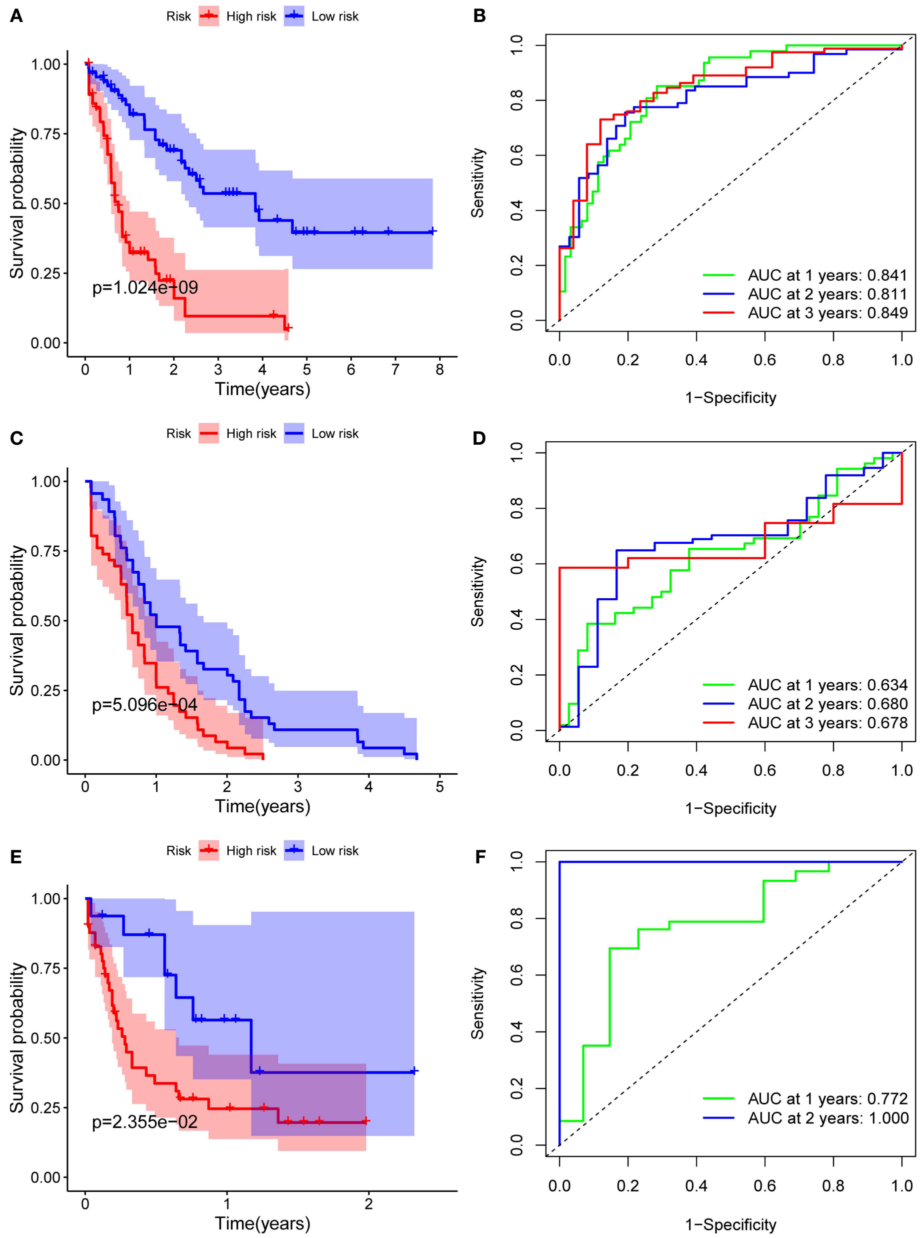

FIGURE 3
Identification of ten optimal FRGs. **(A)** Kaplan-Meier curves for the OS of patients in the high-risk and low-risk groups in the TCGA cohort. **(B)** AUC of time-dependent ROC curves verified the prognostic performance of the riskscore in the TCGA cohort **(C)** Kaplan-Meier curves in the ICGC cohort. **(D)** AUC of time-dependent ROC curves in the ICGC cohort. **(E)** Kaplan-Meier curves in the FAHWMU cohort. **(F)** AUC of time-dependent ROC curves in the FAHWMU cohort.

Machine learning method determines the importance of each feature

In order to judge the importance of each feature in our 10-gene signature, we used SHAP method. As shown in Figure 6A, riskscore had the highest correlation with this 10-gene signature compared with each gene in this signature. In addition, AIFM2 was found to have high contribution. Riskscore was positively correlated with our 10-gene signature and AIFM2 was shown to be negatively associated this signature (Figure 6B). As indicated by Figure 6C, our riskscore was shown to have a good predictive effect on the patient's survival status.

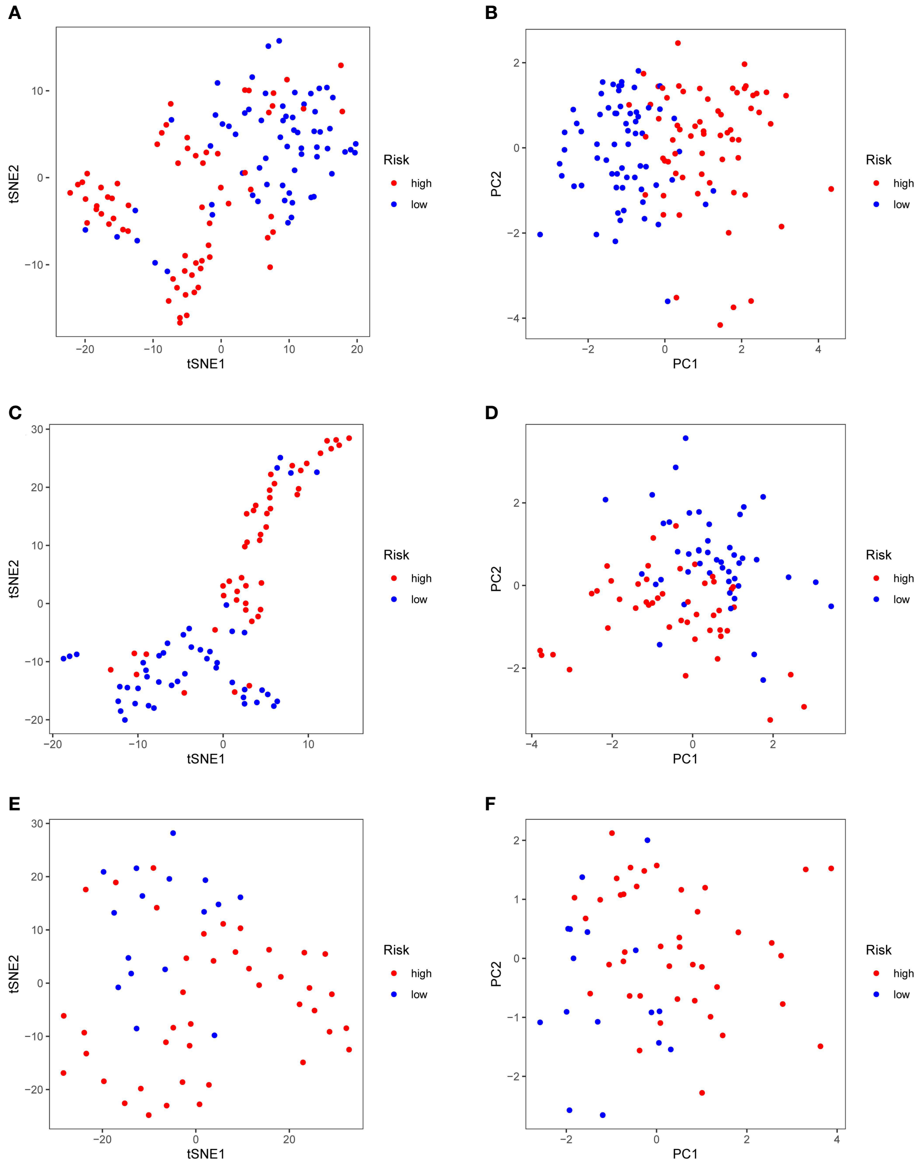

FIGURE 4
PCA and t-SNE analysis. tSNE **(A)** and PCA **(B)** dimension reduction analysis of the high- and low-risk groups based on the riskscore in TCGA cohort. tSNE **(C)** and PCA **(D)** dimension reduction analysis of the high- and low-risk groups based on the riskscore in ICGA cohort. tSNE **(E)** and PCA **(F)** dimension reduction analysis of the high- and low-risk groups based on the riskscore in FAHWMU cohort. (high: high-risk group; low: low-risk group).

GO and KEGG analysis of DEGs in the high- and low-risk groups

GO analysis (Figure 7A) showed that DEGs were significantly involved in the biological processes of extracellular structure (matrix, external side of plasma membrane collagen, cell–cell adhesion), the cellular components that occur in cytoplasmic lumen and some immune-related function (leukocyte chemotaxis, leukocyte chemotaxis, immune receptor, cytokine). The pathways of the KEGG database (Figure 7B) indicated that DEGs were significantly involved in the immune and stromal related-pathway (phagosome, chemokine, viral protein interaction with cytokine and cytokine receptor, ECM–receptor interaction). The results of GO and KEGG revealed that DEGs may play a key role in the prognosis and immune-related response in AML patients.

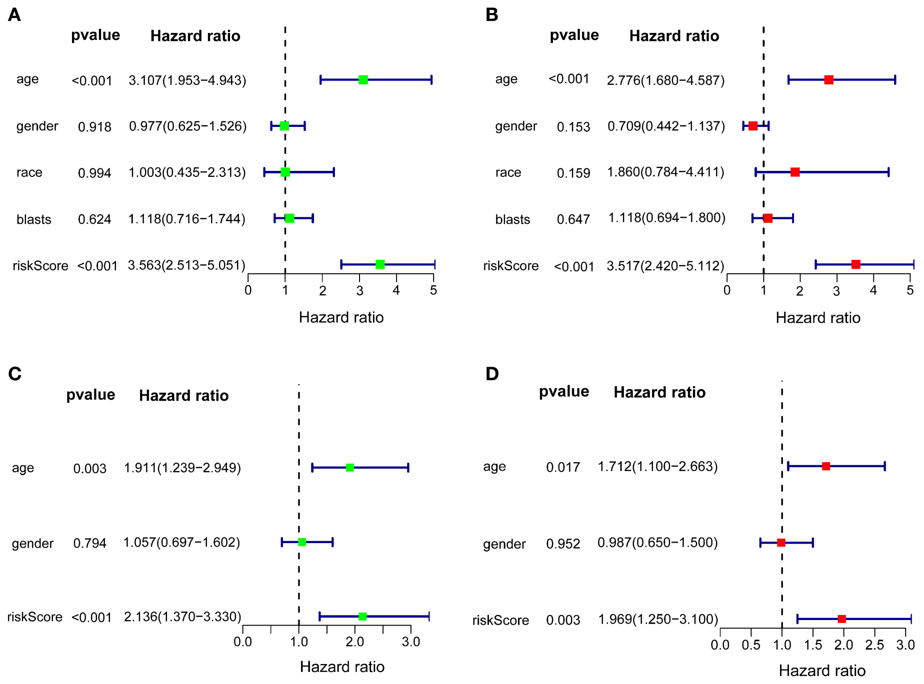

FIGURE 5
Independent prognostic value of the 10-gene signature. Forest plots of univariate cox regression analyses **(A)** and multivariate cox regression analyses **(B)** in TCGA cohort. Forest plots of univariate cox regression analyses **(C)** and multivariate cox regression analyses **(D)** in the ICGC cohort.

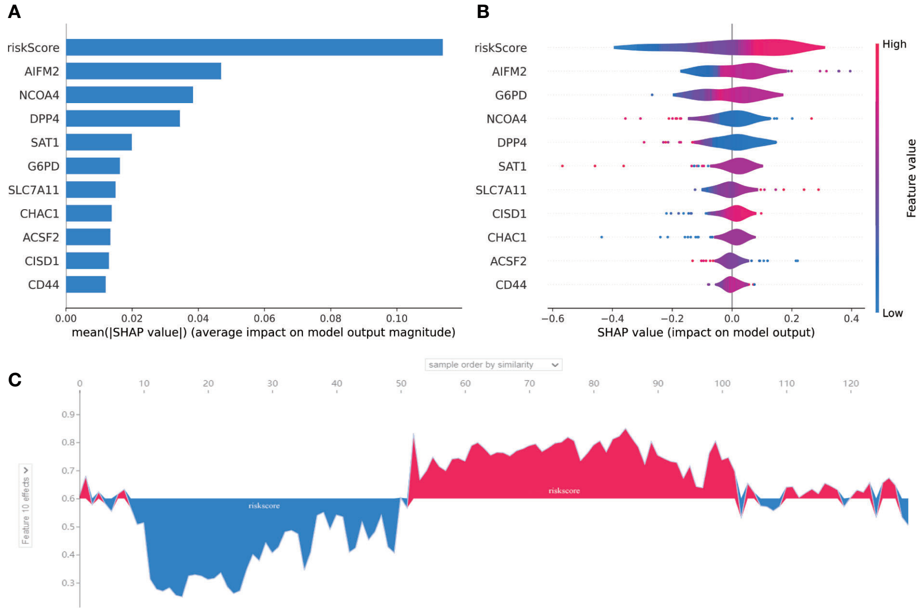

FIGURE 6
SHAP for 10-gene signature. **(A)** A score calculated by SHAP was used for each input feature. **(B)** The contribution of each input feature in the overall model. When the SHAP value is positive, if the Future value is mainly red, this feature is a positive correlation. **(C)** The performance of the riskscore in AML prognosis was assessed by SHAP. The abscissa is to sort each patient according to the riskscore from low to high, and the ordinate is the SHAP value for each patient. Blue represents patient survival and red represents patient death.

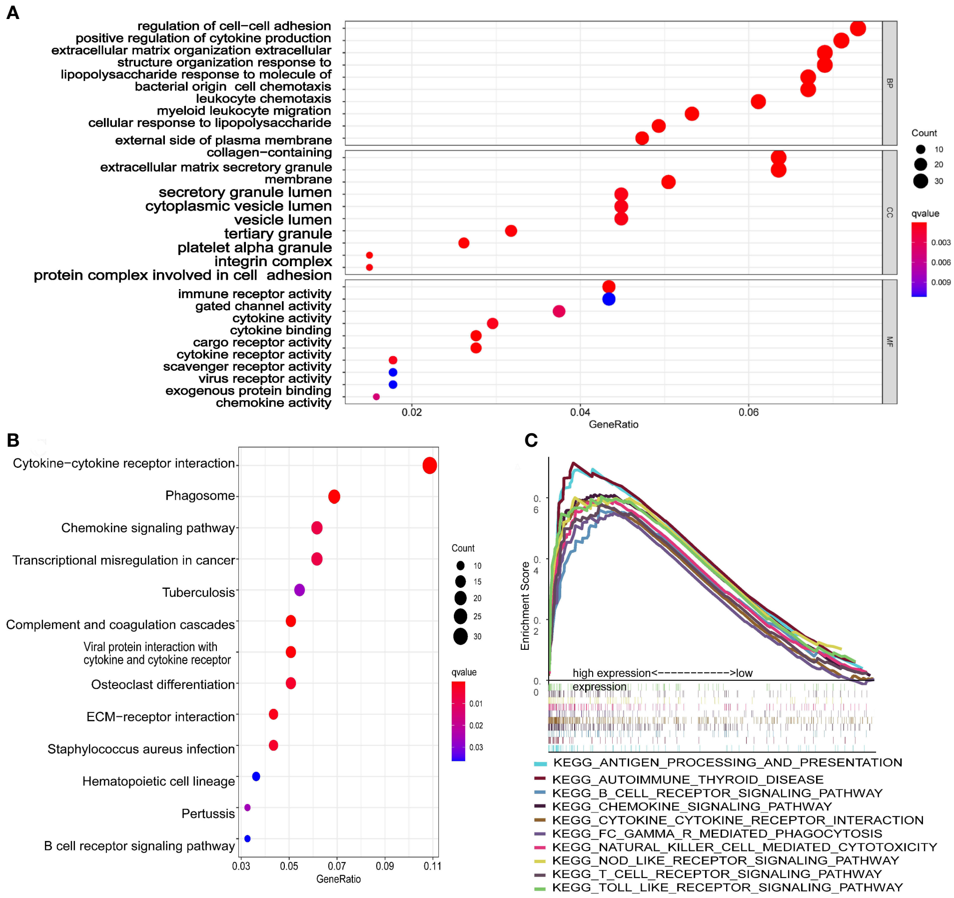

FIGURE 7
Functional analysis of the 10-gene signature. **(A)** The GSEA plot of top 10 enriched pathways. **(B)** GO enrichment analysis ($p < 0.05$, $q < 0.05$; BP, biological process; CC, cellular component; MF, molecular function). **(C)** KEGG enrichment analysis ($p < 0.05$, $q < 0.05$).

Immune infiltration was associated with the riskscore of 10-gene signature

The scatter plots were used to explore the association between the tumor microenvironment and the riskscore. As shown in Figure 8F, the immune score was positively correlated with riskscore (p<0.0001; R=0.43). GSEA analysis indicated that the top 10 pathways of DEGs between the high- and low-risk groups were involved in the biological processes of immune response (antigen processing and presentation, B cell receptor signaling pathway, chemokine signaling pathway, cytokine-cytokine receptor interaction, Fc gamma r mediated phagocytosis, natural killer cell mediated cytotoxicity, NOD-like receptor signaling pathway, T cell receptor signaling pathway, Toll like receptor signaling pathway) (Figure 7C). Therefore, we further explored the correlations between 18 immune-related cells and the riskscore *via* CIBERSOFT algorithm. 8 types of immune-related cells (naive B cells, Plasma cells, T cells CD4 memory, NK cells, Monocytes, Dendritic cells, Mast cells and Eosinophils) were correlated with immune score (Figure 8A, p<0.05). There were positive correlations between immune score and T cells CD4 memory as well as Monocytes and Mast cells. Subsequently, 4 types of cells (B cells memory, Monocytes, T cells CD4 memory, Mast cells, p<0.05) were selected for further correlation analysis between the high- and low-risk groups (Figures 8B–E). The expressions of Monocytes in the high-risk group were higher than that in the low-risk group. The expressions of T cells CD4 memory and Mast cells were lower than that in the low-risk group. However, no significant difference in the expressions of B cell memory between the high- and low-risk groups. Our data indicate that the immune infiltration is significantly related with the riskscore.

AML patients may be sensitive to 8 drugs

Drug sensitivity analysis was used to identify potential drugs that AML patients may be sensitive. Drug sensitivity analysis was

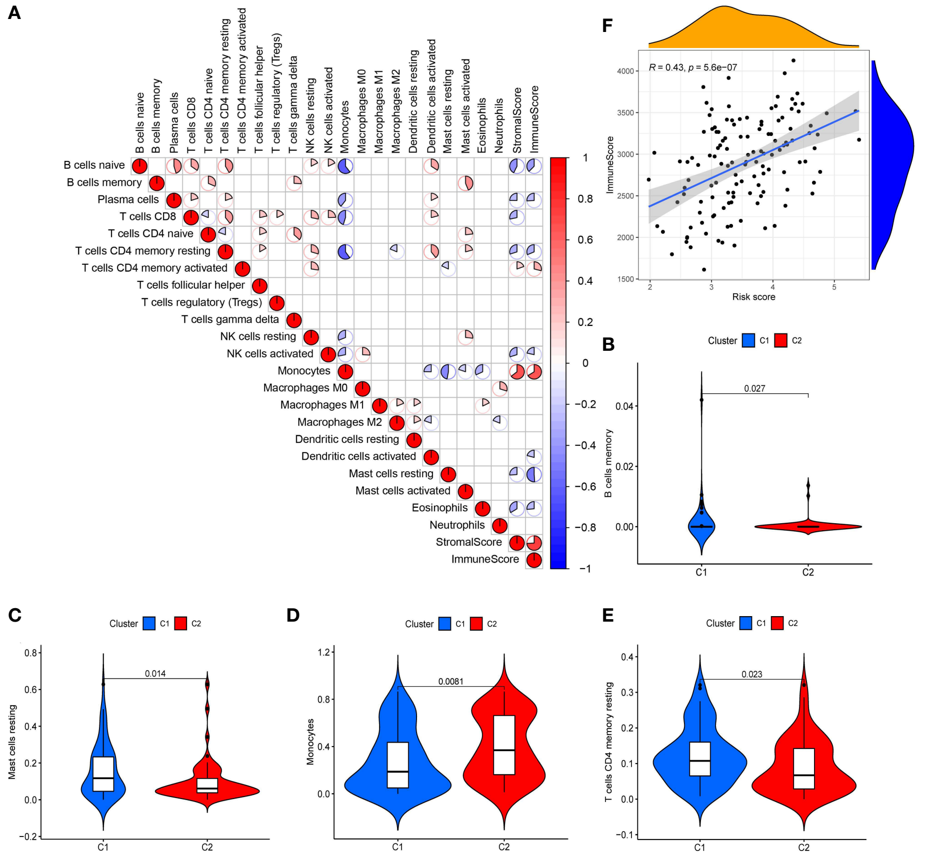

FIGURE 8
Analysis of tumor microenvironment in 10-gene signature **(A)** Correlation plots of 18 immune-related cells (derived from CIBERSOFT algorithms), stromal scores and immune score (derived from ESTIMATE algorithms) in AML (red: positive correlation; blue: negative correlation; $p < 0.05$). **(B-E)** Violin diagrams of 4 immune-related cells (B cells memory, Monocytes, T cells CD4 memory and Mast cells). **(F)** Scatter plot of the correlation between immune score and the riskscore in the 10-gene signature.

analyzed between the top 16 drugs and 10 genes. Only the results of drug sensitivity analysis with P<0.05 were shown in Figure 9. There were positive correlations between 4 drugs (ARRY-162, Cobimetinib, Mitomycin and lrofulven) and SAT1 as well as G6PD in AML patients from the TCGA cohort. In addition, there were negative correlations between 4 drugs (Tamoxifen, Oxaliplatin, Fulvestrant and lmatinib) and CD44. Combined with these, AML patients with dysregulation of SAT1, G6PD or CD44 may be sensitive to 8 drugs (ARRY-162, Cobimetinib, Mitomycin, lrofulven, Tamoxifen, Oxaliplatin, Fulvestrant and lmatinib).

Validation of expressions of 10 genes of this 10-gene signature in AML

QRT-PCR was performed to validate the mRNA expression levels of 10 genes in our signature in the FAHWMU cohort. As shown in Supplementary Figure 2, up-regulated CD44, DPP4, SAT1 and NCOA4 were found in AML patients, while CHAC1, CISD1, SLC7A11, AIFM2, G6PD, and ACSF2 were down-regulated in AML patients.

Discussion

AML patients have been reported to benefit from advances in targeted molecular and immunotherapy (14, 15), however, the 5-year survival rate of AML patients remains unsatisfactory due to high relapse rates. Stratification of patients into the high- and low-risk groups based on reliable molecular signatures may aid in selecting appropriate treatment strategies in line with precision medicine. Emerging studies have indicated the vital roles of FRGs in tumorigenesis (16–18). However, the relationship between AML prognosis and FRGs remains unclear. In this study, we established a novel ferroptosis-related prognostic gene signature

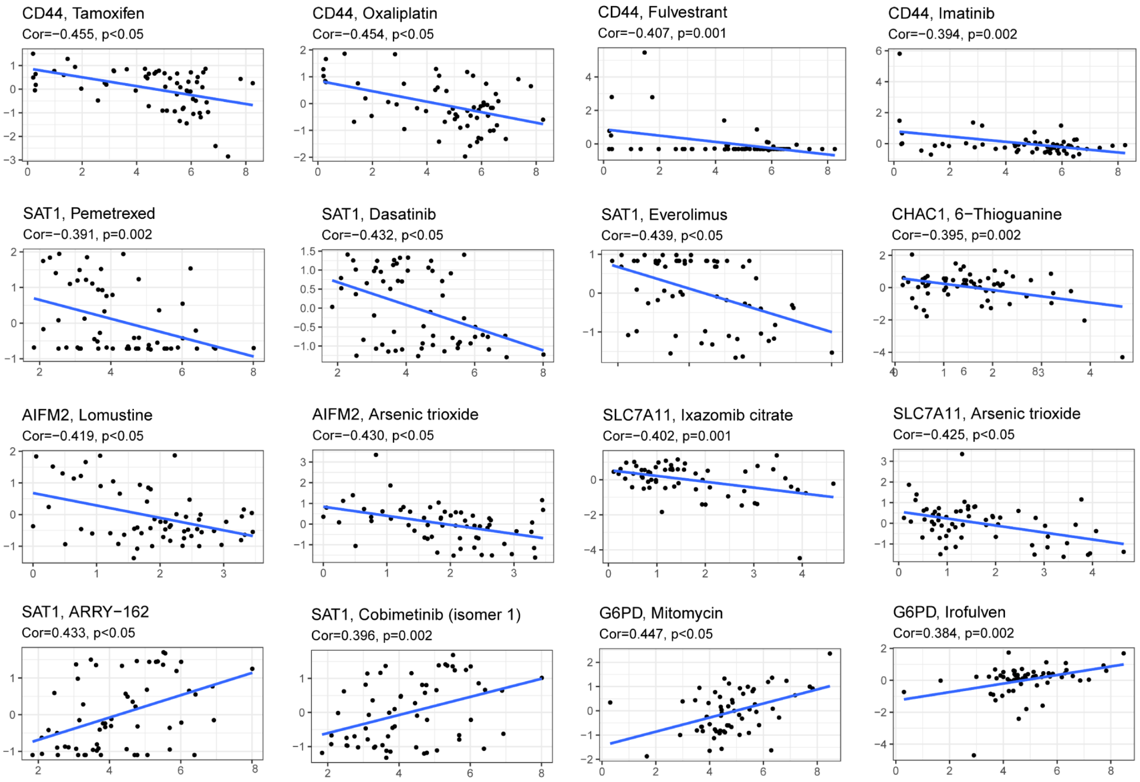

FIGURE 9
Drug sensitivity analysis of the 10-gene signature. (Cor > 0 means that patients with high expression of this gene may be sensitive to this drug; Cor< 0 means that patients with high expression of this gene may be resistant to this drug. P < 0.05).

for AML patients. We assessed the relationships between 60 FRGs and OS, and subsequently identified 18 FRDEGs. Using LASSO Cox regression, we selected 10 of 18 FRDEGs for construction of a prognostic gene signature. We also compared enrichment score of infiltration of immune cells and immune pathways between the high- and low-risk groups, investigated functional mechanisms *via* GSEA, and assessed potentially suitable drugs. This novel 10-gene signature may contribute to the improvement in the prediction of AML prognosis and patient stratification for therapeutic strategies.

The FRGs (CD44, CHAC1, CISD1, DPP4, NCOA4, SAT1, SLC7A11, AIFM2, G6PD, and ACSF2) were included in our 10-gene signature. CD44, a cell-surface glycoprotein, has been reported to be involved in cell-cell interaction, cell adhesion, and migration (19). Previously, it has been demonstrated that CD44 expression is closely related with the occurrence of tumors, including AML (20–22). Stevens et al. found that CHAC1 contributes to the inhibition of AML *via* atovaquone (23). Inhibition of CISD1 results in iron accumulation and oxidative injury in mitochondria, thus contributing to erastin-induced ferroptosis in hepatocellular carcinoma cells (24). In B-cell acute lymphoblastic leukemia, CHAC1 can overcome drug resistance and exert anti-leukemic activity (25). Loss of TP53 prevents nuclear accumulation of DPP4 and thus facilitates plasma-membrane-associated DPP4-dependent lipid peroxidation, resulting in ferroptosis (26). CARS1 has been included in a novel prognostic signature by Chen et al., which effectively predicts the prognosis of Clear Cell Renal Cell Carcinoma (27). Activation of SAT1 induces lipid peroxidation and sensitizes cells to undergo ferroptosis upon reactive oxygen species (ROS)-induced stress (28). Inactivation of SLC7A11 has a synergistic effect with APR-246 for the promotion of cell death (29). G6PD has previously been proposed as a biomarker for AML (30). A recent study has revealed a potential relationship between AIFM2 and EBF3, which acts as a tumor suppressor gene in AML (31). ACSF2 participates in the regulation of the lipid metabolism *via* peroxisome proliferator-activated receptor alpha. Recently, Wang et al. constructed a FRG signature for breast cancer patients, which included ACSF2 (32). All the 10 genes are associated with ferroptosis process and the prognosis of tumors, especially AML.

Recently, immune infiltration has been reported to be involved in the progression of AML. For example, Luca et al.

found that the bone marrow immune environment of AML patients is profoundly altered (33). A previous study demonstrated that a higher level of B and T cell activation was found in AML samples than non-tumor samples (34). NK cells can trigger the anti-leukemia responses (35) and ferroptosis has been shown to exert anti-tumor immune effects by triggering dendritic cell maturation (36). Therefore, we explored the association between immune cell infiltration and the riskscore in this study. Our data revealed that higher Monocytes levels were found in the high-risk group. In addition, Mika T et al. found that high expression of Monocytes is related to the failure of the first induction therapy in AML (37), which indicated that AML patients in the high-risk group with higher expression of Monocytes may be relate to the worse OS. Besides, it has been found that differentiated monocyte-like AML cells express diverse immunomodulatory genes and suppress T cell activity *in vitro* (38). In this study, the high-risk group with lower level of T cells CD4 memory was associated with the higher counting of differentiated monocyte-like AML cells, which may be responsible for the bad prognosis of the high-risk group. Besides, in our tumor microenvironment correlation analysis, the riskscore was positively associated with the immune score. Our findings revealed an association between the 10-gene signature and immune cell infiltration.

In the past few decades, targeted cancer therapies have developed rapidly. However, treatment of AML remains unsatisfactory (39). In this study, we performed drug sensitivity analysis to find AML drugs that may have clinical benefits. We selected 8 drugs (ARRY-162, Cobimetinib, Mitomycin, lrofulven, Tamoxifen, Oxaliplatin, Fulvestrant and lmatinib) that AML patients with dysregulation of SAT1, G6PD or CD44 may be sensitive to. Among them, ARRY-162, Cobimetinib, Mitomycin, lrofulven, Tamoxifen and Oxaliplatin have already been reported to be applied in AML patients for clinical trials or cells (40–45). Lmatinib has been authorized to treat chronic myeloid leukemia (CML) since 2001 (46). No reported have been found in the treatment of Fulvestrant in AML. Our drug sensitivity analysis provides novel promising drugs for AML patients, and more studies are still needed for further validation in the future.

Recently, several risk signatures of AML have been established based on FRGs (47–49). However, our study still has many advantages. Firstly, we firstly reported a novel prognostic risk signature of 10 FRGs for AML based on the data from TCGA and ICGC cohort. Secondly, we validated this 10-gene signature in a local cohort (FAHWMU cohort). Thirdly, this signature revealed an association between FRGs and immune cell infiltration in AML. In addition, we used a machine learning method to validate our 10-gene signature. Finally, we found 8 potential drugs for AML clinical treatment in the future. However, there are many limitations in our research. A single hallmark (ferroptosis) was used to construct a prognostic model, which may lead to the loss of many key prognostic genes of AML. In addition, the detailed roles of FRGs in AML including *in vivo* and *in vitro* should be further explored in the future.

Conclusion

Collectively, our study establishes a novel 10-FRG prognostic risk signature for AML patients. In addition, FRGs may represent novel therapeutic targets in AML.

Data availability statement

The original contributions presented in the study are included in the article/Supplementary Material. Further inquiries can be directed to the corresponding authors.

Ethics statement

The studies involving human participants were reviewed and approved by the Human Research Ethics Committee in The First Affiliated Hospital of Wenzhou Medical University. Written informed consent was obtained from the individual(s) for the publication of any potentially identifiable images or data included in this article.

Author contributions

KZ, ZL and YZ conceived the project and wrote the manuscript. LC, CF, QT, ZY, BZ, YG, CW, and KY participated in data analysis. SJ and YS participated in discussion and language editing. All authors contributed to the article and approved the submitted version.

Funding

The project was supported by the Natural Science Foundation of Zhejiang Province (No. LQ19H080002), and the Public Welfare Science and Technology Project of Wenzhou (No. Y20190119). Public Welfare Science and Technology Project of Wenzhou (No. Y20220028).

Acknowledgments

We thank the TCGA, ICGC, and GTEx databases for providing valuable datasets. This manuscript was submitted as a pre-print in the link https://www.researchsquare.com/article/rs-980809/v2 (50).

Conflict of interest

The authors declare that the research was conducted in the absence of any commercial or financial relationships that could be construed as a potential conflict of interest.

Publisher's note

Supplementary material

The Supplementary Material for this article can be found online at: https://www.frontiersin.org/articles/10.3389/fonc.2022.1023040/full#supplementary-material

SUPPLEMENTARY FIGURE 1

(A) Tenfold cross-validation for tuning parameter selection in the LASSO model. The solid vertical lines represent partial likelihood deviance ± standard error (SE) values. **(B)** LASSO coefficient profiles for the 18 DEFRGs.

SUPPLEMENTARY FIGURE 2

The mRNA expression levels of 10 genes in AML patients (n = 20) and healthy donors (n = 20).

SUPPLEMENTARY TABLE 1

60 FRGs utilized in this study that were obtained from the previous literature.

SUPPLEMENTARY TABLE 2

The DEGs between healthy donor and AML patients.

SUPPLEMENTARY TABLE 3

The DEGs between the low- and high-risk groups.

SUPPLEMENTARY TABLE 4

The primer sequence of 10 genes in our signature for RT-PCR.

References

1. Marando L, Huntly BJP. Molecular landscape of acute myeloid leukemia: Prognostic and therapeutic implications. *Curr Oncol Rep* (2020) 22(6):61. doi: 10.1007/s11912-020-00918-7

2. Thomas D, Majeti R. Biology and relevance of human acute myeloid leukemia stem cells. *Blood* (2017) 129(12):1577–85. doi: 10.1182/blood-2016-10-696054

3. Rowe JM. AML in 2017: Advances in clinical practice. *Best Pract Res Clin Haematol* (2017) 30(4):283–6. doi: 10.1016/j.beha.2017.09.010

4. Dixon SJ, Lemberg KM, Lamprecht MR, Skouta R, Zaitsev EM, Gleason CE, et al. Ferroptosis: an iron-dependent form of nonapoptotic cell death. *Cell* (2012) 149(5):1060–72. doi: 10.1016/j.cell.2012.03.042

5. Stockwell BR, Friedmann Angeli JP, Bayir H, Bush AI, Conrad M, Dixon SJ, et al. Ferroptosis: A regulated cell death nexus linking metabolism, redox biology, and disease. *Cell* (2017) 171(2):273–85. doi: 10.1016/j.cell.2017.09.021

6. Fearnhead HO, Vandenabeele P, Vanden Berghe T. How do we fit ferroptosis in the family of regulated cell death? *Cell Death Differ* (2017) 24(12):1991–8. doi: 10.1038/cdd.2017.149

7. Hassannia B, Vandenabeele P, Vanden Berghe T. Targeting ferroptosis to iron out cancer. *Cancer Cell* (2019) 35(6):830–49. doi: 10.1016/j.ccell.2019.04.002

8. Liang C, Zhang X, Yang M, Dong X. Recent progress in ferroptosis inducers for cancer therapy. *Adv Mater* (2019) 31(51):e1904197. doi: 10.1002/adma.201904197

9. Liang JY, Wang DS, Lin HC, Chen XX, Yang H, Zheng Y, et al. A novel ferroptosis-related gene signature for overall survival prediction in patients with hepatocellular carcinoma. *Int J Biol Sci* (2020) 16(13):2430–41. doi: 10.7150/ijbs.45050

10. Lundberg SM, Erion G, Chen H, DeGrave A, Prutkin JM, Nair B, et al. From local explanations to global understanding with explainable AI for trees. *Nat Mach Intell* (2020) 2(1):56–67. doi: 10.1038/s42256-019-0138-9

11. Newman AM, Liu CL, Green MR, Gentles AJ, Feng W, Xu Y, et al. Robust enumeration of cell subsets from tissue expression profiles. *Nat Methods* (2015) 12 (5):453–7. doi: 10.1038/nmeth.3337

12. Reinhold WC, Sunshine M, Liu H, Varma S, Kohn KW, Morris J, et al. CellMiner: a web-based suite of genomic and pharmacologic tools to explore transcript and drug patterns in the NCI-60 cell line set. *Cancer Res* (2012) 72 (14):3499–511. doi: 10.1158/0008-5472.CAN-12-1370

13. Reinhold WC, Sunshine M, Varma S, Doroshow JH, Pommier Y. Using CellMiner 1.6 for systems pharmacology and genomic analysis of the NCI-60. *Clin Cancer Res* (2015) 21(17):3841–52. doi: 10.1158/1078-0432.CCR-15-0335

14. Valent P, Sadovnik I, Eisenwort G, Bauer K, Herrmann H, Gleixner KV, et al. Immunotherapy-based targeting and elimination of leukemic stem cells in AML and CML. *Int J Mol Sci* (2019) 20(17):4233. doi: 10.3390/ijms20174233

15. Liu Y, Bewersdorf JP, Stahl M, Zeidan AM. Immunotherapy in acute myeloid leukemia and myelodysplastic syndromes: The dawn of a new era? *Blood Rev* (2019) 34:67–83. doi: 10.1016/j.blre.2018.12.001

16. Mou Y, Wang J, Wu J, He D, Zhang C, Duan C, et al. Ferroptosis, a new form of cell death: opportunities and challenges in cancer. *J Hematol Oncol* (2019) 12(1):34. doi: 10.1186/s13045-019-0720-y

17. Xu T, Ding W, Ji X, Ao X, Liu Y, Yu W, et al. Molecular mechanisms of ferroptosis and its role in cancer therapy. *J Cell Mol Med* (2019) 23(8):4900–12. doi: 10.1111/jcmm.14511

18. Shen Z, Song J, Yung BC, Zhou Z, Wu A, Chen X. Emerging strategies of cancer therapy based on ferroptosis. *Adv Mater* (2018) 30(12):e1704007. doi: 10.1002/adma.201704007

19. Naor D, Nedvetzki S, Golan I, Melnik L, Faitelson Y. CD44 in cancer. *Crit Rev Clin Lab Sci* (2002) 39(6):527–79. doi: 10.1080/10408360290795574

20. Chen C, Zhao S, Karnad A, Freeman JW. The biology and role of CD44 in cancer progression: therapeutic implications. *J Hematol Oncol* (2018) 11(1):64. doi: 10.1186/s13045-018-0605-5

21. Prochazka L, Tesarik R, Turanek J. Regulation of alternative splicing of CD44 in cancer. *Cell Signal* (2014) 26(10):2234–9. doi: 10.1016/j.cellsig.2014.07.011

22. Morath I, Hartmann TN, Orian-Rousseau V. CD44: More than a mere stem cell marker. *Int J Biochem Cell Biol* (2016) 81(Pt A):166–73. doi: 10.1016/j.biocel.2016.09.009

23. Stevens AM, Xiang M, Heppler LN, Tosic I, Jiang K, Munoz JO, et al. Atovaquone is active against AML by upregulating the integrated stress pathway and suppressing oxidative phosphorylation. *Blood Adv* (2019) 3(24):4215–27. doi: 10.1182/bloodadvances.2019000499

24. Yuan H, Li X, Zhang X, Kang R, Tang D. CISD1 inhibits ferroptosis by protection against mitochondrial lipid peroxidation. *Biochem Biophys Res Commun* (2016) 478(2):838–44. doi: 10.1016/j.bbrc.2016.08.034

25. Geldenhuys WJ, Nair RR, Piktel D, Martin KH, Gibson LF. The MitoNEET ligand NL-1 mediates antileukemic activity in drug-resistant b-cell acute lymphoblastic leukemia. *J Pharmacol Exp Ther* (2019) 370(1):25–34. doi: 10.1124/jpet.118.255984

26. Xie Y, Zhu S, Song X, Sun X, Fan Y, Liu J, et al. The tumor suppressor p53 limits ferroptosis by blocking DPP4 activity. *Cell Rep* (2017) 20(7):1692–704. doi: 10.1016/j.celrep.2017.07.055

27. Chen J, Zhan Y, Zhang R, Chen B, Huang J, Li C, et al. A new prognostic risk signature of eight ferroptosis-related genes in the clear cell renal cell carcinoma. *Front Oncol* (2021) 11:700084. doi: 10.3389/fonc.2021.700084

28. Ou Y, Wang SJ, Li D, Chu B, Gu W. Activation of SAT1 engages polyamine metabolism with p53-mediated ferroptotic responses. *Proc Natl Acad Sci U S A* (2016) 113(44):E6806–E12. doi: 10.1073/pnas.1607152113

29. Birsen R, Larrue C, Decroocq J, Johnson N, Guiraud N, Gotanegre M, et al. APR-246 induces early cell death by ferroptosis in acute myeloid leukemia. *Haematologica* (2021) 107(2):403. doi: 10.3324/haematol.2020.259531

30. Poulain L, Sujobert P, Zylbersztejn F, Barreau S, Stuani L, Lambert M, et al. High mTORC1 activity drives glycolysis addiction and sensitivity to G6PD inhibition in acute myeloid leukemia cells. *Leukemia* (2017) 31(11):2326–35. doi: 10.1038/leu.2017.81

31. Tao YF, Xu LX, Lu J, Hu SY, Fang F, Cao L, et al. Early b-cell factor 3 (EBF3) is a novel tumor suppressor gene with promoter hypermethylation in pediatric acute myeloid leukemia. *J Exp Clin Cancer Res* (2015) 34:4. doi: 10.1186/s13046-014-0118-1

32. Wang D, Wei G, Ma J, Cheng S, Jia L, Song X, et al. Identification of the prognostic value of ferroptosis-related gene signature in breast cancer patients. *BMC Cancer* (2021) 21(1):645. doi: 10.1186/s12885-021-08341-2

33. Vago L, Gojo I. Immune escape and immunotherapy of acute myeloid leukemia. *J Clin Invest* (2020) 130(4):1552–64. doi: 10.1172/JCI129204

34. Zhang J, Hu X, Wang J, Sahu AD, Cohen D, Song L, et al. Immune receptor repertoires in pediatric and adult acute myeloid leukemia. *Genome Med* (2019) 11 (1):73. doi: 10.1186/s13073-019-0681-3

35. Carlsten M, Jaras M. Natural killer cells in myeloid malignancies: Immune surveillance, NK cell dysfunction, and pharmacological opportunities to bolster the endogenous NK cells. *Front Immunol* (2019) 10:2357. doi: 10.3389/fimmu.2019.02357

36. Tang D, Kepp O, Kroemer G. Ferroptosis becomes immunogenic: implications for anticancer treatments. *Oncoimmunology* (2020) 10(1):1862949. doi: 10.1080/2162402X.2020.1862949

37. Mika T, Ladigan S, Schork K, Turewicz M, Eisenacher M, Schmiegel W, et al. Monocytes-neutrophils-ratio as predictive marker for failure of first induction therapy in AML. *Blood Cells Mol Dis* (2019) 77:103–8. doi: 10.1016/j.bcmd.2019.04.008

38. van Galen P, Hovestadt V, Wadsworth Ii MH, Hughes TK, Griffin GK, Battaglia S, et al. Single-cell RNA-seq reveals AML hierarchies relevant to disease progression and immunity. *Cell* (2019) 176(6):1265–81 e24. doi: 10.1016/j.cell.2019.01.031

39. Bose P, Vachhani P, Cortes JE. Treatment of Relapsed/Refractory acute myeloid leukemia. *Curr Treat Options Oncol* (2017) 18(3):17. doi: 10.1007/s11864-017-0456-2

40. Giles F, Cortes J, Garcia-Manero G, Kornblau S, Estey E, Kwari M, et al. Phase I study of irofulven (MGI 114), an acylfulvene illudin analog, in patients with acute leukemia. *Invest New Drugs* (2001) 19(1):13–20. doi: 10.1023/A:1006432012394

41. Cremin P, Flattery M, McCann SR, Daly PA. Myelodysplasia and acute myeloid leukaemia following adjuvant chemotherapy for breast cancer using mitoxantrone and methotrexate with or without mitomycin. *Ann Oncol* (1996) 7 (7):745–6. doi: 10.1093/oxfordjournals.annonc.a010725

42. Maiti A, Naqvi K, Kadia TM, Borthakur G, Takahashi K, Bose P, et al. Phase II trial of MEK inhibitor binimetinib (MEK162) in RAS-mutant acute myeloid leukemia. *Clin Lymphoma Myeloma Leuk* (2019) 19(3):142–8.e1. doi: 10.1016/j.clml.2018.12.009

43. Seipel K, Marques MAT, Sidler C, Mueller BU, Pabst T. The cellular p53 inhibitor MDM2 and the growth factor receptor FLT3 as biomarkers for treatment responses to the MDM2-inhibitor idasanutlin and the MEK1 inhibitor cobimetinib in acute myeloid leukemia. *Cancers (Basel)* (2018) 10(6):170. doi: 10.3390/cancers10060170

44. De Conti G, Gruszka AM, Valli D, Cammarata AU, Righi M, Mazza M, et al. A novel platform to test in vivo single gene dependencies in t(8,21) and t(15,17) AML confirms Zeb2 as leukemia target. *Cancers (Basel)* (2020) 12(12):3768. doi: 10.3390/cancers12123768

45. Tsimberidou AM, Keating MJ, Jabbour EJ, Ravandi-Kashani F, O'Brien S, Estey E, et al. A phase I study of fludarabine, cytarabine, and oxaliplatin therapy in patients with relapsed or refractory acute myeloid leukemia. *Clin Lymphoma Myeloma Leuk.* (2014) 14(5):395–400.e1. doi: 10.1016/j.clml.2014.01.009

46. Shimada A. Hematological malignancies and molecular targeting therapy. *Eur J Pharmacol* (2019) 862:172641. doi: 10.1016/j.ejphar.2019.172641

47. Zhou F, Chen B. Prognostic significance of ferroptosis-related genes and their methylation in AML. *Hematology* (2021) 26(1):919–30. doi: 10.1080/16078454.2021.1996055

48. Shao R, Wang H, Liu W, Wang J, Lu S, Tang H, et al. Establishment of a prognostic ferroptosis-related gene profile in acute myeloid leukaemia. *J Cell Mol Med* (2021) 25(23):10950–60. doi: 10.1111/jcmm.17013

49. Huang X, Zhou D, Ye X, Jin J. A novel ferroptosis-related gene signature can predict prognosis and influence immune microenvironment in acute myeloid leukemia. *Bosn J Basic Med Sci* (2022). doi: 10.17305/bjbms.2021.6274

50. Kai Z, Zhichao L, Yating Z. *A novel 10-genes ferroptosis-related prognostic signature in acute myeloid leukemia* (2021). Research Square. Available at: https://www.researchsquare.com/article/rs-980809/v2 (Accessed 2022 February 01).

frontiers | Frontiers in Oncology

TYPE Original Research
PUBLISHED 01 December 2022
DOI 10.3389/fonc.2022.1032336

OPEN ACCESS

EDITED BY
Giuseppe Maurizio Campo,
University of Messina, Italy

REVIEWED BY
Xin Hai,
Harbin, China
Sean Rudd,
Karolinska Institutet (KI), Sweden

*CORRESPONDENCE
José Andrés Yunes
andres@boldrini.org.br

†PRESENT ADDRESS
Rafael Renatino Canevarolo,
Department of Cancer Physiology, H. Lee Moffitt Cancer Center &Research Institute, Tampa, FL, United States

SPECIALTY SECTION
This article was submitted to Hematologic Malignancies, a section of the journal Frontiers in Oncology

RECEIVED 30 August 2022
ACCEPTED 02 November 2022
PUBLISHED 01 December 2022

CITATION
Canevarolo RR, Melo CPS, Cury NM, Artico LL, Corrêa JR, Lau YT, Mariano SS, Sudalagunta PR, Brandalise SR, Zeri ACM and Yunes JA (2022) Glutathione levels are associated with methotrexate resistance in acute lymphoblastic leukemia cell lines. *Front. Oncol.* 12:1032336. doi: 10.3389/fonc.2022.1032336

Glutathione levels are associated with methotrexate resistance in acute lymphoblastic leukemia cell lines

Rafael Renatino Canevarolo[1†],
Carolina Pereira de Souza Melo[1], Nathalia Moreno Cury[1],
Leonardo Luiz Artico[1], Juliana Ronchi Corrêa[1],
Yanca Tonhasca Lau[1], Samara Sousa Mariano[1],
Praneeth Reddy Sudalagunta[2], Silvia Regina Brandalise[1],
Ana Carolina de Mattos Zeri[3] and José Andrés Yunes[1,4*]

[1]Centro de Pesquisa Boldrini, Centro Infantil Boldrini, Campinas, SP, Brazil, [2]Department of Cancer Physiology, H. Lee Moffitt Cancer Center & Research Institute, Tampa, FL, United States, [3]Brazilian Biosciences National Laboratory (LNBio), Brazilian Center for Research in Energy and Materials (CNPEM), Campinas, SP, Brazil, [4]Medical Genetics Department, Faculty of Medical Sciences, State University of Campinas, Campinas, SP, Brazil

Introduction: Methotrexate (MTX), a folic acid antagonist and nucleotide synthesis inhibitor, is a cornerstone drug used against acute lymphoblastic leukemia (ALL), but its mechanism of action and resistance continues to be unraveled even after decades of clinical use.

Methods: To better understand the mechanisms of this drug, we accessed the intracellular metabolic content of 13 ALL cell lines treated with MTX by 1H-NMR, and correlated metabolome data with cell proliferation and gene expression. Further, we validated these findings by inhibiting the cellular antioxidant system of the cells in vitro and in vivo in the presence of MTX.

Results: MTX altered the concentration of 31 out of 70 metabolites analyzed, suggesting inhibition of the glycine cleavage system, the pentose phosphate pathway, purine and pyrimidine synthesis, phospholipid metabolism, and bile acid uptake. We found that glutathione (GSH) levels were associated with MTX resistance in both treated and untreated cells, suggesting a new constitutive metabolic-based mechanism of resistance to the drug. Gene expression analyses showed that eight genes involved in GSH metabolism were correlated to GSH concentrations, 2 of which (gamma-glutamyltransferase 1 [GGT1] and thioredoxin reductase 3 [TXNRD3]) were also correlated to MTX resistance. Gene set enrichment analysis (GSEA) confirmed the association between GSH metabolism and MTX resistance. Pharmacological inhibition or stimulation of the main antioxidant systems of the cell, GSH and thioredoxin, confirmed their importance in MTX resistance. Arsenic trioxide (ATO), a thioredoxin inhibitor used against acute promyelocytic leukemia, potentiated MTX cytotoxicity in vitro in some of the ALL cell lines tested. Likewise, the ATO+MTX combination decreased tumor burden and extended the survival of NOD scid gamma (NSG) mice transplanted with patient-derived ALL xenograft, but only in one of four ALLs tested.

Conclusion: Altogether, our results show that the cellular antioxidant defense systems contribute to leukemia resistance to MTX, and targeting these pathways, especially the thioredoxin antioxidant system, may be a promising strategy for resensitizing ALL to MTX.

KEYWORDS

acute lymphoblastic leukemia, methotrexate, glutathione, metabolomics, drug resistance, arsenic trioxide, thioredoxin reductase

Introduction

Acute lymphoblastic leukemia (ALL) is a subtype of leukemia that affects B- or T-cell precursor cells. It is the most common type of cancer in children, accounting for one quarter of all childhood cancer cases (1). Although the cure rates of childhood ALL have reached 85% in developed countries (2, 3), drug resistance is considered the major cause of treatment failure; as so, it is an issue of continuous and intense research (4–7).

Methotrexate (MTX), a folic acid competitor (antifolate) first synthesized in 1947, has been widely used as a chemotherapeutic agent and immune system suppressor. MTX is a cornerstone drug in ALL therapy. Once internalized by the cell through the folate receptor (RFC1), MTX undergoes sequential glutamylation by folyl-polyglutamate synthase (FPGS), thus becoming MTX polyglutamates (MTX-$PG_{2\text{-}6}$). The molecule with a 2-6 glutamic residues tail is the active version of the drug; although its chemical activity is similar to the original drug, MTX-$PG_{2\text{-}6}$ is preferentially kept in the intracellular environment [whereas non-glutamylated MTX is quickly exported by ABC transporters (8)], and cellular sensitivity to MTX is directly related to the intracellular pool of MTX-PGs (9). Recently, it was shown that ALL subtypes are associated with differential accumulation of MTX-PG levels: ALL harboring TCF3-PBX1 or ETV6-RUNX1 fusions presented lower MTX-PG levels, whereas hyperdiploid and BCR-ABL-like ALL had higher MTX-PG levels than other subtypes (10).

MTX primarily acts by inhibiting dihydrofolate reductase (DHFR), which catalyzes the sequential conversion of folic acid to dihydrofolate (DHF) and tetrahydrofolate (THF). Once folic acid is a precursor in *de novo* synthesis of thymidine, MTX imbalances nucleotide pools, ultimately leading to incorrect DNA synthesis and halting cell division. A high percentage of cells in S-phase is associated with a better clinical response to MTX (11) and is accompanied by increased expression of genes involved in nucleotide biosynthesis, such as *TYMS*, *CPTS*, and an MTX target enzyme, *DHFR (*11). MTX also inhibits the bifunctional purine biosynthesis protein PURH (ATIC), blocking the conversion of the aminoimidazole carboxamide ribonucleotide (AICAR) into inosine monophosphate (IMP), thus inhibiting purine synthesis and the production of adenosine. AICAR accumulation leads to decreased one-carbon metabolism gene expression, cell proliferation, and increased global bioenergetic capacity *via* AMPK activation (12). Alternatively, MTX's mechanism of resistance has been attributed to decreased MTX uptake due to deficiencies in membrane transport (13–15); increased expression of MTX efflux transporters (16–18); deficient polyglutamylation of MTX by FPGS (18–20); altered levels or structures of target enzymes (21, 22); and increased hydrolysis of MTXPGs by lysosomal gamma-glutamyl hydrolases (GGH) (23–25), although the influence of GGH on MTX efficacy remains controversial (26–28).

In parallel with MTX's most well-known targets, several NAD+-dependent enzymes were inhibited by the antifolate *in vitro*: 2-oxoglutarate, isocitrate, malate, pyruvate, succinate, 6-phosphogluconate and glucose-6-phosphate dehydrogenases, glutamate-cysteine ligase, glutathione reductase, and glutathione peroxidase (29). MTX was shown to inhibit methionine S-adenosyltransferase (MAT) gene expression, protein levels amounts and activity *in vitro* and *in vivo*, resulting in decreased levels of S-adenosylmethionine (SAM) (30), the main methyl donor of metabolism.

Despite the number and importance of such enzymes to cellular metabolism, few studies have been conducted to better understand the effects of MTX on cellular metabolic homeostasis or find metabolic fragilities that could be exploited clinically. For instance, the depletion of multiple genes belonging to the histidine catabolism pathway increases resistance to MTX (31). This is caused by histidine catabolism draining the cellular pool of THF, which is already low in MTX-treated cells. The same study showed that *in vivo* dietary supplementation of histidine increased THF consumption by the histidine degradation pathway and enhanced the sensitivity of leukemia xenografts to MTX.

The antimetabolite nature of MTX and its inhibitory effect on many important metabolic enzymes prompted us to study the consequences of MTX treatment on cellular metabolism. We aimed to discover novel metabolic vulnerabilities that could be exploited therapeutically. Using a panel of 13 ALL cell lines (6 B-cell precursors and 7 T-cell ALL precursors) and untargeted hydrogen nuclear magnetic resonance (^{1}H-NMR)-based metabolomics, we characterized MTX-triggered metabolic disturbance in detail. Though short term (48 hours) resistance to MTX seemed to be directly related to cellular proliferation, resistance in longer exposure times (96 hours) was associated with glutathione (GSH) levels. Gene expression analysis and pharmacological modulation confirmed the relevance of the cellular antioxidant system to MTX-mediated cell death susceptibility. Finally, we showed that pharmacological inhibition of the thioredoxin system by the chemotherapeutic drug arsenic trioxide (ATO) enhanced MTX cytotoxicity *in vivo* against one out of four primary human ALL cells, suggesting a novel therapeutic rationale to be further explored against ALL.

Material and Methods

Cell lines

Six B-cell precursor (Nalm6, Nalm16, Nalm30, REH, RS4;11, and 697) and 7 T-ALL (ALL-SIL, CCRF-CEM, HPB-ALL, Jurkat, Molt-4, P12-ICHIKAWA and TALL-1) cell lines were used in the study. The cell lines REH, 697, and RS4;11 were kindly provided by Dr. Sheila A. Shurtleff from St. Jude Children's Research Hospital, Memphis, TN, USA; the cell lines Nalm16 and Nalm30 were provided by Dr. Akira Harashima from Hayashibara Biochemical Lab, Fujisaki, Japan; the cell lines ALL-SIL, HPB-ALL, P12-ICHIKAWA, and TALL-1 were kindly provided by Dr. João Barata from the Instituto de Medicina Molecular, Faculdade de Medicina da Universidade de Lisboa, Lisbon, Portugal; and the cell lines Jurkat, Nalm-6, CCRF-CEM (CEM) and Molt-4 were kindly provided by Dr. Alexandre E. Nowill from the State University of Campinas, Campinas, Brazil. Cell lines were cultured in RPMI-1640 culture medium (Cultilab, Campinas, Brazil); supplemented with 10% fetal bovine serum (Cultilab), 100 IU/ml of penicillin, and 100 µg/ml of streptomycin (Sigma-Aldrich, Saint Louis, MO, USA); and maintained at 37°C with a 5% CO_2 atmosphere in all experiments.

Reagents

All compounds were purchased from Sigma-Aldrich, resuspended according to the manufacturers' instructions, and stored at –20°C. Subsequent dilutions used in the experiments were prepared at the moment of use.

Cell viability assays

Eighty microliters of cell suspension (4×10^5 cells/ml) were seeded in a 96-well cell culture plate, followed by the addition of 20 µl of drug solution in culture medium. Each dose was tested in triplicate. Negative controls received only vehicle, whereas positive (death) controls were added with 2 µl of an 18% paraformaldehyde solution immediately before viability determination. After the treatment period, the culture medium of each well was replaced by 0.2 ml of calcein AM solution (Sigma-Aldrich) at 2 µM in phosphate buffer [PBS 1X] and the culture plates were put into the incubator for 30 minutes before fluorescence reading using a Synergy H1 microplate reader (Biotek, Winooski, VT, USA; excitation/emission: 492/518 nm). To account for heterogeneous cell distribution within each well, fluorescence was measured in 25 points (a 5 × 5 matrix layout), with values then integrated (summed) at the end. Alternatively, the MTT (thiazolyl blue tetrazolium bromide; Sigma-Aldrich) reduction test was also used. In those cases, after 4 hours of incubation, 20 µl of MTT (5 mg/ml) were added to each well for cell metabolization. After overnight incubation, 0.1 ml of a dodecyl sulfate solution (10%) containing HCl (10 mM) was added to the wells. Absorbance was measured at 570 nm. Cell viability was expressed in relation to controls. Given that almost identical IC50 values for MTX were obtained by MTT and calcein AM at 48 and 96 hours, either one or the other method was used to access cell viability, depending on experimental and laboratory logistics.

Determination of the doubling time

Two hundred microliters of a 2.5×10^5 cell/ml cell suspension were seeded in a 96-well culture plate in triplicates. Fifteen microliters of the cell suspension were collected daily for cell count under the microscope (exclusion by trypan blue). The doubling time of each cell line was determined from the proliferation curves obtained.

Cell treatment and metabolites extraction for ^{1}H-NMR

Two hundred million cells in the exponential growth phase were suspended in culture medium (200 ml) and equally divided into 2 cell culture flasks. After 12 hours of acclimatization, either MTX (25 nM) or vehicle were added to the flasks. The doses were representative of the average MTX IC50 (96 hours) across all cell lines (18.4 nM). Following 24 hours of treatment, cells were washed with phosphate buffered saline (PBS 1X) and stored at −80°C. Both conditions (treatment and control) were analyzed in 3 biological triplicates for each cell line. The intracellular polar metabolic content was obtained following the methanol/chloroform extraction protocol, adapted from La Belle (32). Briefly, cells were disrupted (Sonics Vibra Cell, Sonics & Materials Inc., Newtown, CT, USA) in an ice-cold mixture of methanol (1.66 ml) and chloroform (0.83 ml) for 3 minutes. Next, ice-cold Milli Q water (1.25 ml) and chloroform (1.25 ml) were added to the sonicated mixture, followed by rapid vortexing. After centrifugation (3.4×10^3 g for 20 minutes at 4°C), 2.6 ml of the supernatant phase (containing water, methanol, and polar metabolites) were collected and freeze-dried.

Acquisition of ^{1}H-NMR spectra and metabolic profiling

The lyophilized metabolic extracts were suspended in 0.6 ml of deuterated water (Cambridge Isotope Laboratories Inc., Tewksbury, MA, USA) containing phosphate buffer (100 mM) and TSP (3-3-(trimethylsilyl)-2,2,3,3-tetradeuteropropionic acid or TMSP-d_4, Cambridge Isotope Laboratories) (0.5 mM) and inserted into a 5 mm NMR tube for immediate acquisition. Spectra were acquired on a Varian Inova NMR spectrometer (Agilent Technologies Inc., Santa Clara, CA, USA), equipped with a triple resonance probe and operating at a resonant frequency of ^{1}H at 500 MHz and a constant temperature of 25°C. Two hundred and fifty-six scans were performed with delays of 1.5 seconds, a reading window of 16 ppm, and an acquisition time of 4 seconds. Phase and baseline corrections, as well as metabolic identification and quantification, were performed in Chenomx NMR Suite 7.1 (Chenomx Inc., Edmonton, Canada). In total, 78 ^{1}H-NMR spectra were analyzed. Metabolite set enrichment analyses were performed with the platform MetaboAnalyst (33) (http://www.metaboanalyst.ca).

Gene expression analysis

Cell lines (5 to 10 × 10^6 cells) in the exponential growth phase were maintained overnight in fresh culture medium and then had their RNA extracted using the Illustra RNAspin Mini Kit (GE Healthcare Life Sciences, Pittsburgh, PA, USA). Samples were processed with the One-Cycle Target Labeling and Control Reagents Kit (Affymetrix, Santa Clara, CA, USA) and hybridized on HG-U133 Plus 2.0 Arrays (Affymetrix). Expression values were obtained with the iterPLIER+16 algorithm and expressed in a log2 scale. For additional details, please see Silveira et al. (34). Gene set enrichment analyses (GSEA) (http://www.broadinstitute.org/gsea/) were performed with 1,000 gene set permutation. Phenotypic labels (eg, GSH levels or MTX IC50) were used as continuous labels. The GSEA platform used Pearson's correlation to determine the degree of linear relationship between gene sets and phenotypes. Only probe sets/transcript clusters annotated with a Gene Symbol were used in the analyses. Gene sets were considered significantly enriched when $P \leq 0.05$ and FDR ≤ 0.05.

High-throughput *in vitro* drug and combination screening assay

A high-throughput *in vitro* drug screening assay was used to quantify the chemosensitivity of leukemia cell lines as described previously (35, 36). Briefly, leukemia cells were seeded in 384-well, black, optically clear flat-bottom PhenoPlate (PerkinElmer, Waltham, MA) with collagen I (PureCol, Advanced Biomatrix, Carlsbad, CA) to a total volume of 9 µl, containing approximately 3,000 leukemia cells in each well. After collagen polymerization (1 hour at 5% CO_2 and 37°C), each well was filled with 73 µl of culture media and left overnight in the incubator for cell acclimatization. In the next day, 9 µl of the drug dilutions (BSO, Auranofin, BSO+Auranofin) were added to the wells so that every drug/combination was tested at 5 (fixed concentration ratio, for combinations) concentrations (1:3 serial dilution) in 2 replicates. Negative controls containing vehicle (DMSO, maximum concentration of 0.5%) were included. Plates were placed in a motorized stage microscope (EVOS Auto FL 2, Thermo Fisher Scientific, Waltham, MA) equipped with an on-stage incubator and maintained at 5% CO_2 and 37°C. Each well was imaged every 30 minutes for a total duration of 96 hours. A digital image analysis algorithm (37) was implemented to determine changes in viability of each well longitudinally across the 96-hour interval. This algorithm computes differences in sequential brightfield images and identifies live cells with continuous membrane deformations resulting from their interaction with the surrounding extracellular matrix. These interactions cease upon cell death. By applying this operation to all images acquired for each well, we were able to quantify nondestructively the effect of the drugs and their combinations as a function of concentration and exposure time – ie, by area under the curve (AUC) and lethal dose for median effect (LD50). Cell line-specific doses were chosen based on the MTT reduction assay and on previous standardization experiments. Synergy was determined by using the method described by Sudalagunta et al (38), in which percent live cells across time and the serially diluted drug(s) concentrations are used to compute additive response using the Bliss Independence Model. The additive response serves as a reference to determine the extent of synergy observed in each cell line by comparing it with the percent live cells measured when treated with the combination (at a fixed ratio of the 2 constituent single agents). The metric used to quantify *in vitro* drug synergy is given by the $\log_2$ ratio of the additive LD50 (computed from the two single agent responses as described above) and the combination LD50 for each cell line. This *in vitro* drug sensitivity characterization and combination effect framework was developed and pioneered by Dr Ariosto S. Silva's group (Moffitt Cancer Center), which resulted in several significant contributions in the field of hematological malignancies over the past five years (39–42).

Calcein AM for cell viability analysis by flow cytometry

Cells were seeded in 96 well plates at 3.0e5 cells/well in 100 µl of RPMI-1640 with 10% FBS. Methotrexate was added at different concentrations in triplicates. After 48 hours of incubation, a fixed dose of Arsenic Trioxide was added and 48 hours later cell viability was measured by the MTT method. To confirm the MTT results, a replicate plate run in parallel was developed by adding 5 µl of 2.5 µM Calcein-AM (ThermoFisher Scientific) to selected wells and incubated 15 min at room temperature. The number of viable cells was measured by flow cytometry after addition of 5 µl spike in fluorescently labeled bead (CountBright^{TM} Plus Absolute Counting Beads, ThermoFisher Scientific) for normalization. The number of Calcein-positive cells per 1.0e3 beads was computed. Some of the cell lines that were more sensitive to the drug combination were assayed in 48-hour experiments instead of 96 hours. In this case, ATO was added after the first 24 hours of treatment with MTX and the number of viable cells was measured 24 hour later. In this case, cells were cultured in 24-well plates at 1.2e5 cells/well in 500 µl of RPMI-1640 with 10% FBS. At the end of the experiment (48 hours), 100 µl were transferred to a cytometer tube, 0.5 µl of 25 µM Calcein-AM were added and, after 15 min of incubation at room temperature, 5 µl of fluorescently labeled beads plus 195 µl of PBS 1X were added and cells were analyzed by flow cytometry. Flow cytometry was performed on a LSRFortessa X-20 (Becton Dickinson, Franklin Lakes, NJ) and data were analyzed using FlowJo (v7.1.6, TreeStar).

In vivo efficacy of ATO+MTX against primary ALL

Cryopreserved primary ALL cells obtained from a mouse of the IL7R$^{<CPT>}$ knock-in model (43) or from 4 pediatric ALL patients (2 BCP- and 2 T-ALL) were used in this study. Cells were thawed, washed in PBS 1X buffer, and injected into nonirradiated mice *via* the tail vein. Sick animals were killed and had their spleen macerated, and ALL cells were obtained by Ficoll gradient centrifugation. Fresh ALL cells were then transplanted into more mice for the experiments. The murine ALL was transplanted into C57BL/6 mice. Treatment started 2 days after transplantation. Mice (n = 12) were randomly distributed into 4 treatment groups: vehicle (PBS 1X with 1% NaOH), arsenic trioxide (ATO; 2.5 mg/kg), methotrexate (MTX; 1, 5, or 10 mg/kg), and ATO+MTX. Drugs were intraperitoneally administered once a day, 5× per week. When in combination, MTX was given 6 hours before ATO (based on Szymanska et al (44), who used this interval for other drug combinations). Overall survival was measured from after 2 days the date of leukemia injection to the date of animal death or when humane endpoint criteria were reached. Differences in survival were determined by Log-rank (Mantel-Cox) test using the GraphPad Prism v7.0 (GraphPad, La Jolla, CA) software. The study was approved by the Animal Experimentation Ethics Committees of University of Campinas (CEUA/UNIMCAP, protocol 4557-1(A)/2018). Experiments with the human ALLs were carried out in nonirradiated NSG (NOD.Cg-PrkdcscidIl2rgtm1Wjl/SzJ) mice (Jackson Laboratory). Leukemia progression was monitored weekly in peripheral blood post-Ficoll mononuclear cells by flow cytometry using anti-human CD45-APC (clone HI30, ImmunoTools) and anti-mouse CD45-BV605 (clone 30-F11, BD Horizon). Flow cytometry was performed on a LSRFortessa X-20 and data were analyzed using FlowJo. When hCD45$^+$ cells reached 0.1% of total CD45$^+$ peripheral blood cells in half of the mice (n = 24), animals were randomly distributed among the 4 treatment groups. T-ALL PDXs were treated with vehicle, ATO (2.5 mg/kg), MTX (5 mg/kg for BCP-ALL; 10 mg/kg for T-ALL) or ATO+MTX, as described above. Treatment lasted for 4 weeks and was administered in consecutive weeks for T-ALL xenografts or every other week for BCP-ALL (the BCP-ALL cells used were more sensitive to MTX than T-ALL). Death by acute toxicity was censored. Overall survival was measured from the date of leukemia engraftment to either the animal death, when the proportion of hCD45$^+$ cells in the peripheral blood > 25% (45), or when humane endpoint criteria were reached. The study was approved by the Animal Experimentation Ethics Committees of Centro Infantil Boldrini (CEUA/BOLDRINI, protocol 0016-2020) and Human Ethics Committees of Centro Infantil Boldrini (CAAE 34601120.7.0000.5376).

Statistical analyses

Paired nonparametric Wilcoxon signed rank tests and other analyses and graphs (dose-response curves, estimates of IC50 values, correlation plots, Kaplan-Meier curves, and log-rank tests for survival analyses) were made in Prism v7.0 (GraphPad, La Jolla, CA, USA). $P \leq 0.05$ was considered significant.

Results

MTX impact on cellular metabolism

Initially, cells were treated with increasing doses of MTX for 48 or 96 hours to determine their IC50. IC50 at 48 hours ranged from

10.8 to 85.5 nM in T-ALL and from 14.7 to 101.1 nM in BCP-ALL. IC50 at 96 hours ranged from 5.5 to 38.4 nM in T-ALL and from 9.1 to 31.7 n in BCP-ALL (Supplementary Figure 1).

To determine the impact of MTX on cell metabolism, cell lines underwent unsupervised global metabolic profiling by ^{1}H-NMR in either the presence or in the absence of the drug (a representative ^{1}H-NMR spectrum is shown in Supplementary Figure 2). All cell lines were treated with a fixed dose of MTX (25 nM) for 24 hours, as this dose was representative of MTX's average IC50 at 96 hours across all cell lines (ie, 18.4 nM). By treating the cells with the same dose of MTX, we intended to find cell line-specific metabolic differences under the same drug challenge. We reasoned that using cell-specific IC50 doses of MTX would have overthrown any metabolic differences among cell lines. This approach is in line with previous metabolomic studies that have adopted a similar rationale (46, 47). Additionally, this condition elicited the greatest metabolic variance, compared to high-dose MTX and shorter treatment time, in a pilot study on a MTX-resistant *vs.* a MTX-sensitive cell line (Supplementary Figure 3).

In total, 70 metabolites were identified and quantified. Metabolites' identifiers, concentrations, and fold changes across all samples can be found in Supplementary Tables 1–3, respectively. We found that 19 metabolites were significantly increased by MTX, whereas 12 were decreased in response to the drug treatment (Figure 1A and Supplementary Table 4). Several amino acids had their concentrations increased following MTX treatment: glycine, alanine, phenylalanine, threonine, histidine, valine, arginine, leucine, isoleucine, tyrosine, and proline. 2-oxobutyrate, a byproduct of the conversion of cystathionine into cysteine and first intermediate in threonine degradation, was also increased with drug treatment. MTX treatment produced effects consistent with alterations in the folate cycle (formate); pyrimidine (uridine and dCTP) and purine (AMP, ADP, and NAD+) nucleotide synthesis; the pentose phosphate pathway (UDP-glucuronate, UDP-glucose, and myo-inositol); phospholipid synthesis (phosphocholine, sn-glycero-3-phosphocholine, phosphoethanolamine, and trimethylamine); the citric acid cycle (2-oxoglutarate); and the uptake of bile acids (cholate and glycocholate).

A metabolite set enrichment analysis made from the 31 metabolites significantly modulated by MTX confirmed the major impact of the drug on glycine and serine metabolism, the urea cycle, alanine metabolism, and arginine and proline metabolism (Figure 1B). A scheme integrating all MTX-modulated metabolites into a single metabolic panel can be found in Supplementary Figure 4. Interestingly, a few cases of differential metabolic changes (ie, fold change of MTX treatment over basal levels) were associated with MTX resistance (at 96 hours); for example, the greatest fold changes for alanine were observed among the most sensitive cells to MTX, whereas 2-oxoglutarate (α-ketoglutarate) greatest fold changes were found among the most resistant cells to the antifolate (Figure 1C). Although a causal relationship cannot be established, this finding indicates that MTX resistance *in vitro* is associated with specific metabolic responses by the cells under drug action.

Metabolic levels associated with MTX resistance

In addition to the association between metabolic fold change and MTX resistance, we searched for correlations between metabolic concentration and resistance to MTX (expressed as IC50) at 48 and 96 hours in either the presence or absence of the drug (Table 1). Given that MTX is more effective against dividing cells because of its effect on the nucleotide synthesis, we also examined correlations between metabolites concentrations and cell proliferation rate, as this could be a confounding factor (proliferation curves for doubling time determination are in Supplemental Figure 5). In fact, MTX resistance at 48 hours and proliferation rate were tightly correlated (Pearson r = 0.829, P < 0.001) (Figure 2A); however, the association was lost for drug resistance at 96 hours (Pearson r = 0.111, P = 0.718) (Figure 2B), and MTX resistance at 48 hours was not associated with resistance at 96 hours (Pearson r = 0.268, P = 0.399) (Figure 2C), indicating that factors unrelated to cell proliferation were contributing to cellular resistance to MTX during longer exposure times.

Several metabolites were negatively associated with MTX resistance at 48 hours: acetate, carnitine, cholate, formate, hypoxanthine, malate, and succinate (Table 1). Acetate is the product of glycolysis, malate and succinate are citric acid cycle elements, carnitine is important for lipid beta-oxidation, and hypoxanthine is a purine derivative, suggesting that, at shorter exposure times (48 hours), MTX sensitivity is associated with increased cellular metabolic activity. Alternatively, MTX resistance at 96 hours was positively associated with asparagine, guanosine, and glutathione (GSH) levels (Table 1).

GSH is the main antioxidant of the cell and is important in preventing damage caused by reactive oxygen species (ROS). Interestingly, although not associated with MTX resistance at 48 hours (Pearson r = 0.287, P = 0.366) (Figure 2D), GSH was the only metabolite associated with MTX resistance in both untreated (Pearson r = 0.764, P = 0.003) (Figure 2E) and treated cells (Pearson r = 0.780, P = 0.003) (Figure 2F) at 96 hours, indicating a constitutive metabolic trait predictive of cellular resistance to the MTX insult. Its association with MTX resistance is in line with the fact that MTX is a ROS-generating drug (48, 49). Correlation coefficients between all metabolites concentrations, cell proliferation rate, and MTX resistance (at 48 and 96 hours) in treated and untreated samples are in Supplementary Table 5.

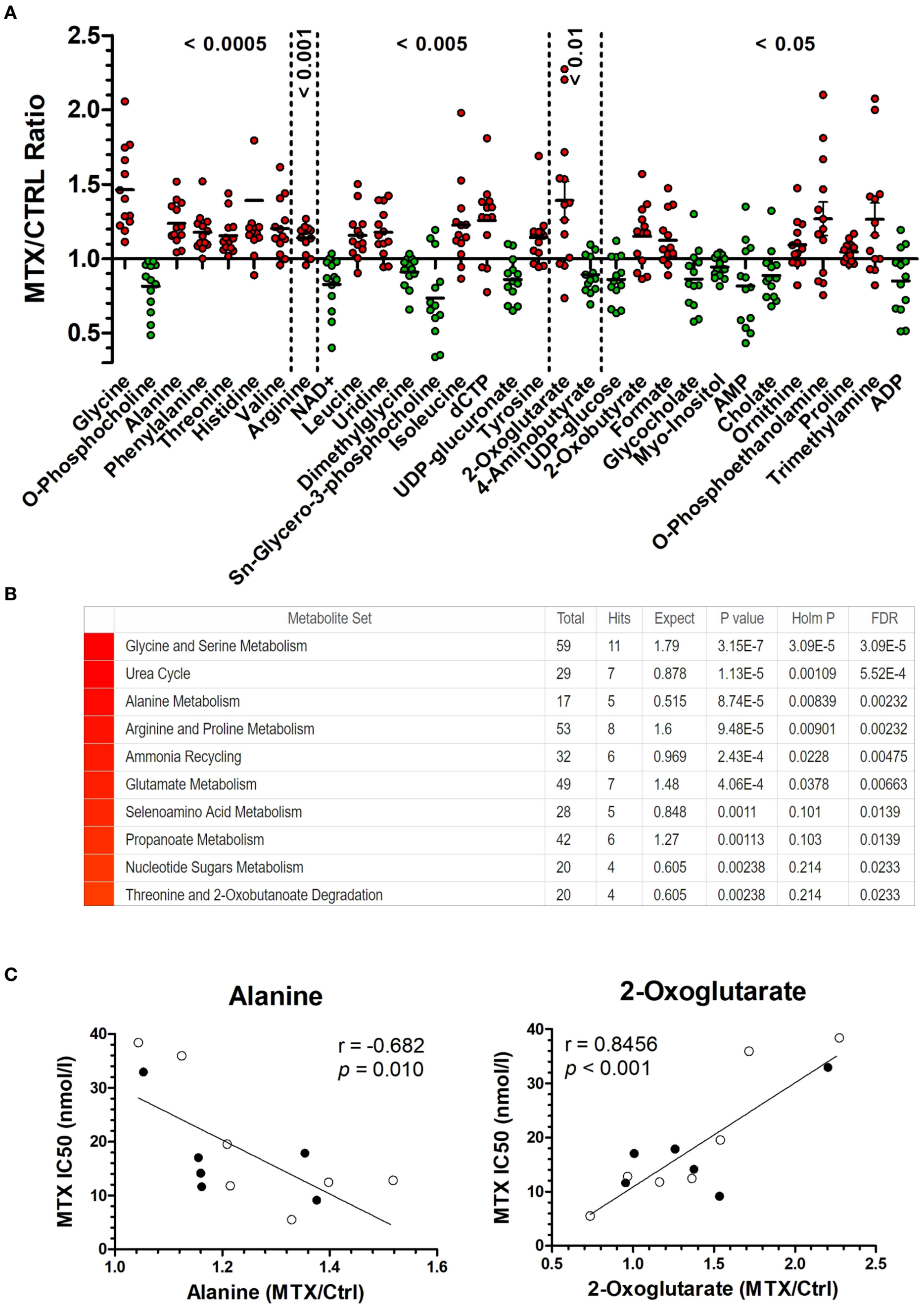

	Metabolite Set	Total	Hits	Expect	P value	Holm P	FDR
🟥	Glycine and Serine Metabolism	59	11	1.79	3.15E-7	3.09E-5	3.09E-5
🟥	Urea Cycle	29	7	0.878	1.13E-5	0.00109	5.52E-4
🟥	Alanine Metabolism	17	5	0.515	8.74E-5	0.00839	0.00232
🟥	Arginine and Proline Metabolism	53	8	1.6	9.48E-5	0.00901	0.00232
🟥	Ammonia Recycling	32	6	0.969	2.43E-4	0.0228	0.00475
🟥	Glutamate Metabolism	49	7	1.48	4.06E-4	0.0378	0.00663
🟥	Selenoamino Acid Metabolism	28	5	0.848	0.0011	0.101	0.0139
🟥	Propanoate Metabolism	42	6	1.27	0.00113	0.103	0.0139
🟥	Nucleotide Sugars Metabolism	20	4	0.605	0.00238	0.214	0.0233
🟥	Threonine and 2-Oxobutanoate Degradation	20	4	0.605	0.00238	0.214	0.0233

FIGURE 1
MTX-driven metabolic perturbations in ALL. **(A)** Metabolic disturbance caused by MTX treatment. Each dot is the mean of three biological replicates for each cell line. Metabolites' concentrations fold change (in MTX-treated/untreated cells) above 1 indicate increase caused by MTX, whereas values below 1 indicate antifolate-induced decrease (*P*-values, Wilcoxon signed ranked test, after comparison of the distributions with the hypothetical mean value of 1). **(B)** Enrichment score for metabolites in **(A)** indicate the metabolic pathways and processes most impacted by MTX. **(C)** Correlation between metabolite concentration in untreated cells and MTX resistance (IC50 at 96 hours). Black and white beads represent BCP-ALL and T-ALL cell lines, respectively. *P*-values and *r* are from Pearson correlation.

TABLE 1 Correlation between the concentration of selected metabolites and cell proliferation (expressed in terms of doubling time, in days) or MTX resistance (at 48 or 96 hours) in cells either treated or not with MTX.

Metabolite	Proliferation rate (doubling time)				MTX IC50 (48 hours)				MTX IC50 (96 hours)			
	Untreated cells		MTX-treated cells		Untreated cells		MTX-treated cells		Untreated cells		MTX-treated cells	
	Pearson r	P	Pearson r	P	Pearson r	P	Pearson r	P	Pearson r	P	Pearson r	P
2-Methylglutarate	-0.521	0.068	-0.339	0.257	-0.541	0.056	-0.512	0.074	0.248	0.415	0.064	0.836
Acetate	-0.506	0.078	-0.354	0.236	**-0.637**	**0.019**	**-0.608**	**0.028**	-0.120	0.697	-0.320	0.286
AMP	-0.228	0.454	-0.194	0.526	-0.479	0.098	-0.336	0.262	-0.436	0.136	-0.265	0.381
Asparagine	-0.141	0.647	-0.063	0.838	-0.285	0.345	-0.242	0.425	**0.602**	**0.030**	0.517	0.070
Carnitine	-0.455	0.118	-0.196	0.522	**-0.754**	**0.003**	**-0.569**	**0.043**	-0.060	0.846	0.081	0.793
Cholate	-0.548	0.053	-0.373	0.209	**-0.614**	**0.026**	-0.402	0.174	0.198	0.516	0.337	0.261
Creatine	**0.619**	**0.024**	**0.620**	**0.024**	0.325	0.279	0.356	0.233	0.291	0.335	0.290	0.337
Cytidine	**-0.609**	**0.027**	-0.434	0.139	-0.536	0.059	-0.420	0.153	-0.191	0.531	-0.212	0.487
Formate	**-0.821**	**0.001**	**-0.634**	**0.020**	**-0.814**	**0.001**	**-0.836**	**0.000**	-0.267	0.378	-0.540	0.057
Glutathione	0.217	0.477	0.258	0.395	0.161	0.600	0.186	0.543	**0.663**	**0.014**	**0.672**	**0.012**
GTP	-0.357	0.231	-0.197	0.518	-0.501	0.081	-0.253	0.404	-0.253	0.405	-0.054	0.860
Guanosine	0.436	0.136	0.488	0.090	0.368	0.216	0.527	0.064	**0.554**	**0.049**	0.449	0.123
Hypoxanthine	-0.427	0.145	-0.303	0.314	**-0.562**	**0.046**	-0.383	0.196	-0.501	0.081	-0.341	0.254
Lactate	-0.343	0.252	-0.142	0.644	-0.510	0.075	-0.304	0.312	-0.137	0.655	-0.055	0.859
Malate	-0.483	0.095	-0.264	0.384	**-0.671**	**0.012**	-0.494	0.086	-0.112	0.716	-0.078	0.801
myo-Inositol	**0.647**	**0.017**	**0.633**	**0.020**	0.357	0.231	0.332	0.268	0.169	0.581	0.188	0.539
NAD+	0.469	0.106	0.511	0.075	0.524	0.066	0.535	0.060	0.122	0.691	0.137	0.657
NADP+	0.321	0.285	0.447	0.126	0.468	0.107	0.521	0.068	0.009	0.977	0.250	0.410
Pyroglutamate	-0.316	0.293	0.015	0.961	-0.520	0.069	-0.205	0.501	-0.062	0.841	-0.036	0.908
S-Adenosylhomocysteine	-0.419	0.155	**-0.554**	**0.049**	-0.487	0.091	**-0.669**	**0.012**	-0.072	0.814	-0.227	0.457
Succinate	-0.392	0.186	-0.421	0.152	**-0.668**	**0.013**	**-0.615**	**0.025**	-0.428	0.145	-0.330	0.270
Other parameters	**Pearson r**		**P-value**		**Pearson r**		**P-value**		**Pearson r**		**P-value**	
Proliferation rate	1.000		0.000		**0.827**		**0.001**		0.113		0.714	
MTX IC50 (48 h)	**0.827**		**0.001**		1.000		0.000		0.303		0.315	
MTX IC50 (96 h)	0.113		0.714		0.303		0.315		1.000		0.000	

Dark gray and bold, significant association ($P < 0.05$); light gray, $0.05 < P < 0.10$.

GSH levels associated with the expression of GSH metabolism genes

We then searched for genetic traits that could explain the metabolite variability among the cell lines. For this purpose, the concentration of asparagine, guanosine, and GSH was correlated to the expression of genes belonging to their respective metabolic pathways. Though no associations for asparagine or guanosine-related genes were found, 8 genes that code for enzymes that participate in the GSH metabolism were positively correlated to GSH levels: *CBS*, *GCLC*, *GSTM3*, *GSTA4*, *GGT1*, *GGT1/GGT2/GGT3P*, *GGT7*, and *TXNRD3* (Figure 3A). The expression of all genes involved in asparagine, guanosine, and GSH metabolisms that did not correlate to their respective metabolite's levels are in Supplementary Figure 6. Interestingly, 2 of the GSH metabolism genes that correlated with GSH levels (*GGT1* and *TXNRD3*) were also associated with MTX resistance (Figure 3B). Moreover, a Gene Set Enrichment Analysis (GSEA) confirmed that the expression of KEGG's "Glutathione Metabolism" gene set (Supplementary Table 6) was enriched in MTX-resistant samples (Figure 3C). These findings offer a genetic basis for the differential concentration of GSH across the samples with distinct MTX sensitivity.

Promoting GSH metabolism induces proliferation and MTX resistance

Given that both metabolic and gene expression data pointed to GSH metabolism as an important factor contributing to MTX resistance in ALL cells, we evaluated the effect of either enhancing or inhibiting GSH metabolism on cellular resistance to MTX. Initially, we treated the cell lines with increasing doses of MTX in the presence of N-acetylcysteine (NAC), a precursor of the *de novo* synthesis of GSH that is converted into cysteine by glutamate-cysteine ligase (GCL). We observed that NAC not

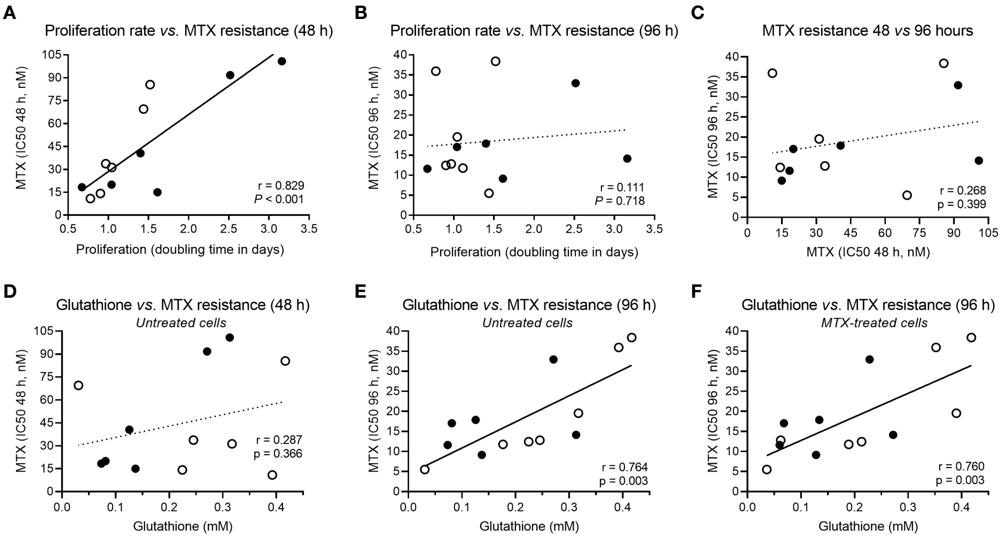

FIGURE 2

Correlation between cellular proliferation, MTX resistance and GSH levels. **(A)** Correlation between proliferation rate (cell doubling time) and MTX resistance (IC50) at 48 hours or **(B)** 96 hours, and **(C)** across MTX resistance over time (48 × 96 hours). **(D)** Correlation between constitutive GSH and MTX resistance at 48 hours or **(E)** 96 hours, and **(F)** between GSH levels in MTX-treated cells and MTX IC50 at 96 hours. Black and white beads represent BCP-ALL and T-ALL cell lines, respectively. *P*-values and *r* are from Pearson correlation.

only protected cells from MTX cytotoxicity but also promoted cell proliferation, including in RS4;11, 697, ALL-SIL and P12-ICHIKAWA (Figure 4A) — 4 cell lines with relatively low constitutive GSH levels — whereas cell lines with relatively high GSH (eg, HPB-ALL and Jurkat) tended to present less pronounced effects. The graphs for all cell lines are in Supplementary Figure 7.

Inhibiting GSH metabolism does not sensitize cells to MTX

We also treated leukemia cells with increasing doses of 4 interferents of GSH metabolism: phenethylisothiocyanate (PEITC) and piperlongumine (PL), which deplete GSH and increase ROS (50–52); hydrogen peroxide (H_2O_2), a ROS itself; and buthionine sulphoximine (BSO), a GCL inhibitor and, thus, a pharmacological inhibitor of GSH synthesis. The IC50 obtained for all these compounds across the cell lines are listed in Supplementary Table 7. Surprisingly, these ROS-promoting compounds did not enhance MTX cytotoxicity significantly (Supplementary Figure 8), even though we found a correlation between PL or H_2O_2 resistance and MTX resistance (Supplementary Figure 9). In sum, these results show that, while promoting GSH metabolism consistently increases leukemia resistance to MTX — sometimes even accompanied by simultaneous increase in proliferation — its inhibition does result in sensitization to the antifolate.

Inhibiting the thioredoxin system potentiates MTX cytotoxicity *in vitro*

The intriguing asymmetrical contribution of GSH metabolism on MTX resistance suggested that a compensatory mechanism could be counterbalancing GSH metabolism inhibition and, thus, protecting cells from MTX insult.

As showed previously, thioredoxin reductases 3 (*TXNRD3*) expression was correlated to both intracellular GSH levels and MTX resistance (Figures 3A, B). TXNRD3 is a member of the cellular antioxidant arsenal whose main role is to chemically reduce thioredoxins, antioxidant proteins that facilitate the reduction of oxidized client proteins by cysteine thiol-disulfide exchange. Oxidized thioredoxin reductases, in turn, are reduced back to their functional state by NADPH. GSH and thioredoxin, therefore, are the 2 known antioxidant systems whose co-occurrence is crucial for the maintenance of the cellular redox homeostasis. We used a high-throughput single agent and drug combination screening assay based on bright-field images to determine cell survival under treatment with auranofin (Aura), a clinically approved thioredoxin reductase inhibitor for rheumatoid arthritis, and the GSH synthesis blocker BSO (Figures 4B, C and Supplementary Figure 10). A synergistic interaction between the drugs was observed in 5 out 6 cell lines tested using the method described by Sudalagunta et al (38), in which percent live cells across time and the serially diluted drug (s) concentrations are used to compute additive response using

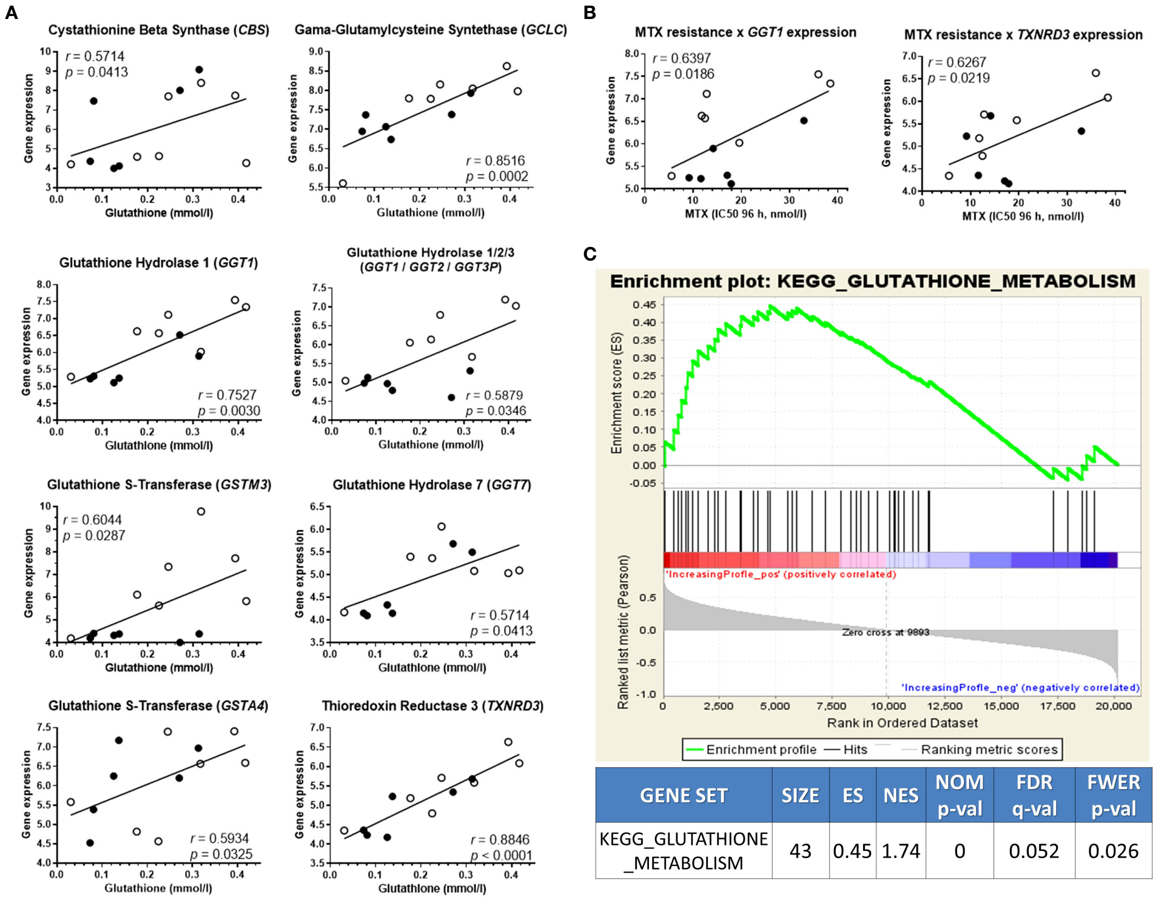

GENE SET	SIZE	ES	NES	NOM p-val	FDR q-val	FWER p-val
KEGG_GLUTATHIONE _METABOLISM	43	0.45	1.74	0	0.052	0.026

FIGURE 3
GSH-related transcriptome associates with metabolic levels and MTX resistance. **(A)** Association between glutathione (GSH) metabolism genes' expression and GSH concentration; **(B)** Gene set enrichment analysis score plot showing KEGG's Glutathione Metabolism gene set enrichment in high-GSH ALL cell lines. **(C)** Expression of two GSH-related genes also correlated to MTX resistance. Black and white beads represent BCP-ALL and T-ALL cell lines, respectively. *P*-values and *r* are from Pearson correlation.

the Bliss Independence model (Supplementary Table 8). We confirmed the co-dependence of ALL cells on these antioxidant systems in 3 cell lines by the MTT viability assay (Supplementary Figure 11).

Next, we investigated the role of the antioxidant thioredoxin system on MTX sensitivity *in vitro*. For this purpose, we tested the effect of MTX in combination with 2 thioredoxin reductase inhibitors, arsenic trioxide (53) (ATO), and auranofin. We observed a mild potentiation of the MTX effect by ATO (Figure 5A) and Auranofin (Supplementary Figure 12) but only for few of the cell lines tested.

Altogether, our results indicate that the thioredoxin system exerts a compensatory effect over the GSH pathway that is not reciprocal and suggest that the thioredoxin system might be a potential target for MTX re-sensitization in leukemia cells.

In vivo antileukemic effects of ATO and MTX in murine and patient-derived leukemia

Although mild, the antileukemic effects of the combinations between thioredoxin reductase inhibitors and MTX *in vitro* motivated us to test them *in vivo*. Here we chose the ATO+MTX combination given ATO's current use in the clinic as a chemotherapeutic agent against acute promyelocytic leukemia. Our first investigation was using an immunocompetent mouse model transplanted with a primary murine B-ALL obtained from our *Il7r* knock-in mouse model (43). We tested different doses of MTX (1, 5, and 10 mg/kg) and found a dose-response pattern, with 10 mg/kg showing best results. ATO+MTX significantly increased overall survival compared to vehicle or single agents, though the difference was modest (Supplementary Figure 13).

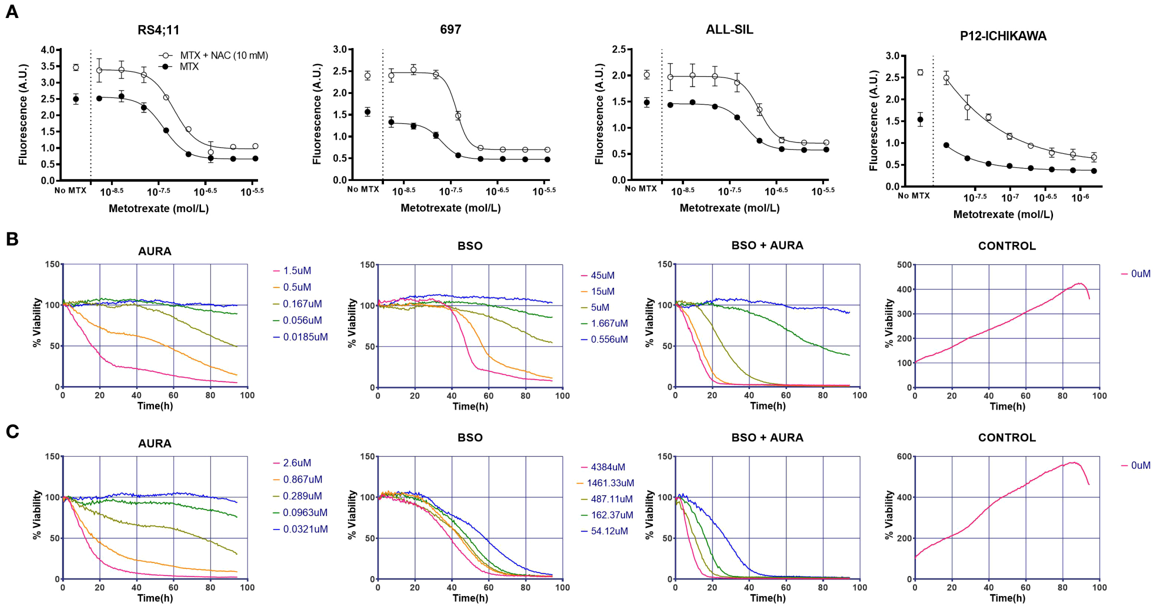

FIGURE 4
In vitro combination of GSH pathway modulators with MTX or a thioredoxin reductase inhibitor. **(A)** Survival curves to increasing doses of MTX in either the presence or absence of NAC in four representative cell lines, accessed by the calcein AM method after 96 hours of treatment. A.U. = arbitrary units. **(B)** BCP-ALL RS4;11 survival in response to auranofin (AURA), buthionine sulphoximine (BSO), BSO + AURA and vehicle (CONTROL) accessed by bright field imaging (high-throughput drug combination screening assay) over 96 hours. **(C)** Idem **(B)**, for TALL-1 cell line. In the BSO + AURA plots, curve colors indicate the corresponding doses of the single agents that were combined.

Next, we tested the efficacy of the drug combination in 4 patient-derived xenografts (PDXs; 2 BCP-ALL and 2 T-ALL) *in vivo*. The PDXs represented a diverse genetic background: T-ALL 1 carries an activating *IL7R* mutation that confers a particular aggressive phenotype (54), and BCP-ALL 1 expresses the TCF3-PBX1 fusion protein as a result of the t (1;19) chromosomal translocation. Mice transplanted with T-ALL PDXs were treated with the same dose (10 mg/kg) and schedule as mice transplanted with murine ALL cells, whereas BCP-ALL PDX-transplanted mice received MTX at a lower dose (5 mg/kg) and were treated every other week to minimize the contribution of MTX to disease control and thus maximize ATO's effect. However, this approach resulted in longer treatment periods and increased gastrointestinal toxicity with some fatalities that were censored in the analysis (Supplementary Table 9). Of the 4 PDXs tested, only one T-ALL was resistant to MTX (remission lasted for 20 days compared to ≥ 50 days in the other 3 PDXs). In this case, the ATO+MTX combination significantly decreased tumor burden in the peripheral blood (Figure 5B) and extended overall survival (Supplementary Figure 14) compared to vehicle alone or either drug used as a monotherapy. Altogether, these results suggest that MTX-resistant ALL patients could benefit from therapies that include thioredoxin reductase inhibitors in combination with MTX.

Discussion

Seventy years after MTX was first synthesized, our comprehension of its mechanism of action and impact on cellular metabolism continues to expand. In this study, we explored the metabolic-wide changes caused by MTX in a panel of T- and B-cell precursors ALL cell lines, aiming to characterize the perturbations caused by the drug on the intracellular metabolome and provide new insights about metabolic vulnerabilities for future therapeutic exploitation.

We were able to identify and quantify 70 metabolites from diverse metabolic pathways; 19 were increased with drug treatment and 12 were decreased. Enrichment analyses showed that the metabolism of several amino acids was particularly impacted, highlighting the glycine and serine metabolism as the topmost altered pathway. Tedeschi et al (55) reported a 2-fold increase in glycine concentration in breast cancer cell lines treated with MTX, which is similar to what we observed in our study. We propose that glycine accumulation is the consequence of an MTX-induced halt in the glycine cleavage system (GCS). The GCS is main mechanism for glycine degradation and requires THF and NAD+ for glycine decarboxylation. MTX leads to THF shortage by inhibiting DHFR, and NAD+ was also decreased following MTX treatment (as seen in Figure 1A). Glycine can be derived from

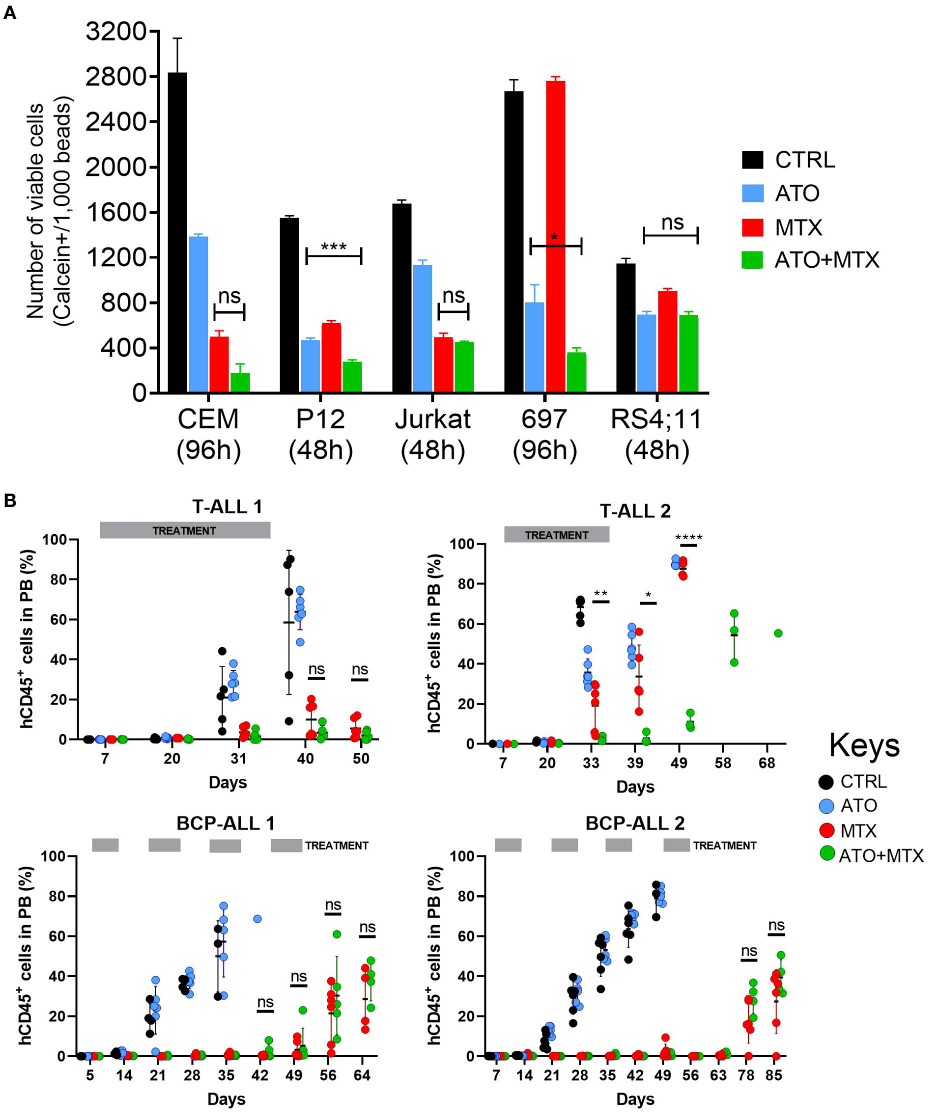

FIGURE 5
Combination of ATO and MTX *in vitro* and in PDX models of ALL. **(A)** Cell survival accessed by flow cytometry analysis of calcein-positive cells. The number of viable calcein+ cells per 1,000 fluorescent beads (spike in) was determined after 48 or 96 hours, as indicated. MTX was added at time zero while ATO was added at half-time. Results are the mean ± standard error (SE) of triplicate samples. P-values for Tukey's Test following ANOVA. *$P<0.05$; ***$P<0.001$. Doses used: CCRF-CEM: ATO = 1.5 μM, MTX = 12.5 nM; P12-ICHIKAWA: ATO = 3 μM, MTX = 13 nM; Jurkat: ATO = 1.5 μM, MTX = 36 nM; RS4;11: ATO = 1.4 μM, MTX = 18 nM; 697: ATO = 0.75 μM, MTX = 6 nM. **(B)** Human CD45-positive (hCD45+) leukemia cells in peripheral blood of PDX-transplanted NSG mice, accessed by flow cytometry. Treatment started one week after engraftment when hCD45+ cells > 0.5% in half of the mice (Day 7) and was administered for 4 consecutive weeks against T-ALL or every other week against BCP-ALL. Doses used: MTX = 10 mg/kg daily (T-ALL) or 5 mg/kg daily (BCP-ALL); ATO = 2.5 mg/kg daily; ATO was administered 6 hours after MTX in the co-treatment cohort. L.E. = leukemia engraftment period. P-value for Log-rank test. P-value for unpaired t test between MTX and ATO+MTX. *$P\leq0.05$; **$P\leq0.01$; ****$P\leq0.0001$; ns, not significant.

threonine, whose concentration was also increased in MTX-treated cells.

The pentose phosphate pathway (PPP) is an anabolic pathway diverted from glycolysis through glucose-6-phosphate dehydrogenase (G6PD), producing NADPH as well as ribose-5-phosphate, a precursor of purines biosynthesis. MTX was shown to inhibit G6PD *in vitro* (29). In our study, UDP-glucose, UDP-glucuronate, and myo-inositol, all intermediates of the PPP, were decreased after drug treatment, suggesting that G6PD inhibition in situ is also occurring and is an important feature of MTX action. Additionally, decreased levels of adenine, hypoxanthine, NAD+, AMP, ADP, and ATP also point towards ATIC inhibition — MTX's main mechanism of action as an anti-inflammatory drug (56). Decreases in NAD+, AMP, ATP, and hypoxanthine levels were also observed in the erythroblastic cell line K562 following MTX treatment (57).

Pyrimidine biosynthesis appears to be impaired by the antifolate as well. Thymidylate synthase (TS) was shown to be inhibited *in vitro* by MTX (58, 59); with TS inhibition, its substrate dUMP would be diverged from dTMP to dCMP synthesis, a precursor of uridine and dCTP — both of which were increased in our data set.

Decreases of several metabolites related to phospholipid metabolism (o-phosphocholine, sn-glycero-3-phosphocholine, phosphoethanolamine, and trimethylamine) indicated that MTX interferes with membrane synthesis. Lipid and membrane synthesis impairment has been reported in MTX-treated osteosarcoma cells (60, 61). In fact, cell cycle progression is a key determinant of phospholipid metabolism and membrane homeostasis: G1/S blockade by RNAi during cellular growth stimulation decreases phosphatidylcholine levels, the main component of cell membranes (62). Coupling lipid metabolism with cell cycle progression is thought to be an evolutionary strategy to coordinate proliferation with cell and organelle growth. The nucleotide shortage provoked by MTX, with the subsequent halt of cell division in the S phase of the cycle, seems to trigger a signal to restrain phospholipid metabolism, thus preventing decompensation of cellular components.

MTX also decreased 2 bile acids, cholate and glycocholate. Bile acids are produced in the liver from cholesterol and might have been interiorized by the cells from the fetal serum present in the culture medium. MRP3, MRP8, and SLC19A1 (folate receptor) are membrane transporters capable of interiorizing MTX, cholate, and glycocholate (63, 64). Polymorphisms and expression levels of these transporters have been associated with prognosis in childhood ALL (65–68) due to impairment on chemotherapy internalization by leukemia cells. In our gene expression data, *SLC19A1* presented a negative correlation to MTX resistance, confirming that cellular sensitivity to the drug is related to enhanced drug uptake, whereas cholate and glycocholate concentrations were marginally associated with *SLC19A1* expression ($P < 0.1$) (data not shown). Bile acids such as taurocholate and cholate have proved to be efficient competitors of MTX absorption in hepatocytes (69, 70). Further investigation is required to determine whether seric bile acids could predict MTX uptake by primary leukemia cells and offer therapeutic guidance in clinics.

We found a significant inverse correlation between formate levels in either MTX-treated or untreated cells and cell doubling time or MTX resistance at 48 hours. Formate is a one-carbon molecule that can be synthesized and metabolized in folate-dependent or -independent reactions (71). Metabolic formate elimination appears to occur *via* its oxidation to carbon dioxide. Formate, THF, and ATP are combined to form 10-formyl-THF, which is then metabolized into THF, NADPH, and CO_2. We found that formate levels increased upon MTX treatment (Figure 1A), possibly due to its accumulation by the lack of sufficient THF caused by the drug treatment, as formate production was shown to be markedly reduced in folate deficiency (72). The fact that we found formate levels in both untreated and treated cells to be negatively correlated with cell proliferation and MTX IC50 at 48 hours suggests that high formate level is a constitutive trait of MTX-sensitive cells. Further investigation will detail the mechanistic relationship between formate levels and MTX resistance, as well as show its applicability as an intracellular metabolic MTX marker.

Contrary to the conspicuous associations between formate and cell proliferation and MTX resistance, S-adenosylhomocysteine (SAH) levels were negatively correlated to these parameters only in MTX-treated cells. SAH is produced from methionine S-adenosylmethionine (SAM; the main methyl donor of the metabolism) demethylation and degraded to adenosine and L-homocysteine by the enzyme L-homocysteine hydrolase (AHCY). L-homocysteine is then converted to cystathionine (a precursor of glutathione) or is salvaged to methionine in a reaction that requires 5-methyl-THF (Supplementary Figure 15). We hypothesize that the lower levels of THF and its correlates (including 5-methyl-THF) in MTX-sensitive cells after drug treatment would contribute to SAH accumulation. Our findings showed that methionine cycle intermediates in MTX-treated cells correlate to antifolate resistance, suggesting their potential use as a metabolic biomarker of MTX response that deserves further investigation.

Asparagine regulates mTORC1 activity (73) and can act as an exchange factor, influencing serine metabolism and nucleotide synthesis by regulating serine uptake (74). We speculate that constitutive higher levels of asparagine would predispose cells to resist MTX insult by conferring an extra pool of molecules to be used as exchange factors for serine uptake, leading to 5,10-methylene-THF production and, ultimately, to pyrimidine biosynthesis even in an MTX-mediated DHFR inhibition scenario.

Guanosine is a purine nucleoside and indirect precursor of GTP; it is plausible to assume that higher constitutive levels of this intermediate would confer a natural resistance to MTX, although, to the best of our knowledge, these findings (ie, a positive correlation between basal asparagine and guanosine levels and MTX resistance) have never been described in the literature.

MTX's ability to induce the formation of ROS has already been described extensively in the literature (75–77). Our work showed that GSH levels were positively associated with MTX resistance in both untreated and treated cells, meaning that cell's constitutive antioxidant defense is predictive of MTX resistance and remains stable even after drug insult. We found the expression of 8 genes coding for enzymes involved in the GSH metabolism to be positively associated with the metabolite's level. Among these are the genes *GSTM3* and *GSTA4*, which code for GSH S-transferases capable of MTX glutathionylation (78). Intriguingly, *GSTM3* expression in ALL lymphoblasts was positively associated with favorable prognosis (79). Some GSH hydrolases (or gamma-glutamyltransferases [GGTs]) were also correlated with GSH levels. GGTs participate in the gamma-glutamyl cycle, a route of synthesis/degradation of GSH and detoxification of drugs and xenobiotics (80), which explains the positive association we observed between *GGT1* expression with both GSH content and MTX resistance. *GGT's* expression decrease during ALL treatment returns to normal levels during the chemotherapy-induced remission stage (81), though circulating enzyme levels did not show prognostic value (82).

Parallel to the GSH detox metabolism, thioredoxins are small oxidoreductase enzymes with a dithiol disulfide site that are essential for mammalian life and involved in cellular redox balance and signaling (83). When thioredoxins are oxidized, thioredoxin reductases (TrxR's) convert them back to their reduced state at the expense of NADPH, which is oxidized to NADP+. Interestingly, among the 3 thioredoxin reductase isozymes found in mammals, only thioredoxin reductase 3 (TXNRD3) contains an additional N-terminal glutaredoxin domain, which makes it a participant of both thioredoxin and glutathione systems. In this study, we found *TXNRD3* expression to be positively associated with both GSH content and MTX resistance. TrxR's enzymes are overexpressed or constitutively expressed in various cancers, contributing to tumor growth and chemoresistance (84), so its inhibition has drawn increasing attention. There are several studies demonstrating that pharmacological inhibitors of TrxR's can be effective as single agents or combined with chemo/radiotherapy in a variety of cancer types (85, 86). In a study of 14 cancer cell lines from diverse tissues treated with a panel of 19 chemotherapeutic agents, MTX resistance was directly related to the enzymatic activity of glutathione reductase and thioredoxin reductase but not to the intracellular concentration of GSH, which, in turn, was associated with ThioTEPA (an alkylating agent) and doxorubicin resistance (87). Recently, by using CRISPR-Cas9, Oshima et al (88) showed that *TXNRD3* (and *TXNRD2*) knockout in REH cells resulted in increased sensitivity to MTX, confirming the role of the thioredoxin system on MTX detoxification.

In this study, the GSH synthesis promoter N-acetylcysteine was shown to increase MTX resistance and proliferation of ALL cell lines. NAC's protective effect against diverse drugs in varied cancer types has been extensively described in the literature. However, we noticed an inverse correlation between GSH levels and NAC effect, a phenomenon that we attribute to the feedback loop that coordinates GSH synthesis, through which GSH inhibits GCL activity (89) and thus decreases metabolite synthesis when its cellular pool is already full.

If, by one hand, NAC supplementation boosts MTX resistance in ALL cell lines, co-treatment with GSH scavengers had a marginal effect on sensitizing cells to the antifolate. We hypothesized that this was due to the thioredoxin metabolism, the other antioxidant system of the cell which can compensate an impaired or blocked GSH metabolism (90, 91). We demonstrated the interplay between both antioxidant systems by treating ALL cells with auranofin, a thioredoxin reductase, and BSO, a GSH synthesis inhibitors. The remarkable combination effect observed has been previously reported in head and neck cancer (92, 93), breast cancer (94), and lymphoma and multiple myeloma (95) cells. In some cases, the thioredoxin system may be even more important than GSH to protect cells from oxidative stress. For instance, in prostate and breast cancer, the synergistic combination of 2-deoxy-glucose (2DG) with DHEA (a phosphate-pentose pathway inhibitor) was potentiated by auranofin but not BSO, whereas the cytotoxic effect was completely abrogated by the addition of NAC (96). Our metabolomic results suggest that MTX also inhibits the pentose-phosphate pathway — a theoretically similar effect to that caused by DHEA. Therefore, like the duo MTX+DHEA, the MTX+BSO+auranofin triple combination may deserve further investigation in primary ALL.

Studies in fibroblasts showing that folic acid supplementation abrogates the cytotoxic effects of arsenite have led to the suggestion that MTX could synergize with ATO (97). By causing a relative methyl insufficiency, MTX could potentiate the effects of ATO in the presence of excess folate. We investigated the effects of the thioredoxin system on MTX resistance *in vitro* by treating ALL cell lines with thioredoxin reductase inhibitors in the presence of the antifolate. Both auranofin and ATO — a rheumatologic and a chemotherapy agent, respectively — potentiated MTX cytotoxicity slightly in a few cell lines, indicating that the thioredoxin antioxidant system could be protecting the cells from the oxidative stress caused by MTX.

ATO has been used against acute promyelocytic leukemia (APL) for the last 2 decades (98), usually in combination with all-*trans* retinoic acid (ATRA) (99, 100) during both induction and consolidation phases. Prolonged maintenance with continuous low-dose chemotherapy (which includes MTX) and intermittent ATRA was beneficial for high-risk APL (101–103). Aligned with this fact and our *in vitro* data, we showed that ATO potentiated MTX cytotoxicity in an *in vivo* model of an aggressive primary murine ALL and in 1 of 4 human ALL PDXs tested, for which tumor burden in the peripheral blood was significantly decreased by the drug combination as well. Interestingly, this ATO-responsive PDX presented a particular MTX-resistant phenotype, whereas in the other 3 cases, single-agent MTX was sufficient to control leukemia progression, thus hampering any possible additive effect by ATO. Both high-dose MTX and ATO are known to cause gastrointestinal toxicity (104, 105), and although no mouse that received either MTX or ATO single-agent experienced severe gastrointestinal toxicity, this was so for 5 out of 24 animals treated with ATO+MTX, indicating that future studies are required to better evaluate the safety of the ATO+MTX combination for the treatment of ALL patients.

Although relapse/refractory ALL did not respond to single-agent ATO in a previous clinical trial (106), which is in line with our PDX results, few studies have investigated its benefits in ALL in combination with other drugs. For instance, Szymanska et al (44) tested the addition of ATO (in the same dose and regimen as ours) with vincristine, dexamethasone, and asparaginase (VXL) in 4 ALL PDXs. Although ATO, in combination with VXL, statistically improved the progression delay of 2 xenografts tested, the authors concluded that the benefit appears unlikely to be of biological significance. We believe that our study brings a new perspective by proposing the use of thioredoxin reductase inhibitors, specially ATO, in combination with MTX. Further investigation should aim to test the Auranofin+MTX combination, the benefits of a third drug inclusion (such as BSO), and the molecular features of the ALL that would most benefit from this new drug combination.

MTX's mechanisms of action and resistance are still being rewritten even after several decades of research and therapeutic use. Our study showed that the antioxidant systems of the cell are an important component of leukemia resistance to MTX, and targeting these pathways, especially the thioredoxin antioxidant system, may contribute to re-sensitize ALL to MTX. In a broad sense, this work illustrates how metabolomics can be employed as an alternative approach to unravel unexplored mechanisms of action and/or resistance of drugs, leveraging insights about new drug combinations with translational potential for life-threatening diseases such as cancer.

Data availability statement

The data presented in the study are deposited in the Gene Expression Omnibus (GEO) repository, accession number GSE218348.

Ethics statement

The studies involving human participants were reviewed and approved by Comitê de Ética em Pesquisa, Centro Infantil Boldrini, CAAE 34601120.7.0000.5376. Written informed consent to participate in this study was provided by the participants' legal guardian/next of kin. The animal study was reviewed and approved by Comissão de Ética no Uso de Animais (CEUA), Instituto de Biologia, Universidade Estadual de Campinas (UNICAMP), protocol 4557-1(A)/2018; and Comissão de Ética no Uso de Animais (CEUA), Centro Infantil Boldrini, protocol 0016-2020.

Author contributions

RRC, CPSM, SRB, ACMZ and JAY conceived the study. RRC, CPSM, NMR, LLA, JRC, YTL, SSM, and PRS performed the experiments and analyzed the data. ACMZ, SRB and JAY supervised the study. RC and JY wrote the manuscript. All authors contributed to the article and approved the submitted version.

Funding

This work was supported by São Paulo Research Foundation (FAPESP) grants (08/10034–1 to JAY and 07/00952-0 to ACMZ). RRC (2009/04167-1 and 2012/11952-0), NMC (2014/08247-8), LLA (2017/03239-5), and JRC (2017/02400-7) received FAPESP fellowships. JAY receives a productivity fellowship from the National Counsel of Technological and Scientific Development (CNPq, processes 301596.2017-4 and 308399/2021-8).

Acknowledgments

We acknowledge the Brazilian Biosciences National Laboratory (LNBio) for the use of its facilities and Dr. André B. Silveira for kindly sharing the microarray data of the cell lines.

Conflict of interest

The authors declare that the research was conducted in the absence of any commercial or financial relationships that could be construed as a potential conflict of interest.

Publisher's note

Supplementary material

The Supplementary Material for this article can be found online at: https://www.frontiersin.org/articles/10.3389/fonc.2022.1032336/full#supplementary-material

References

1. Smith OP, Hann IM. Clinical Features and Therapy of Lymphoblastic Leukemia. In: Arceci RJ, Hann IM, Smith OP, editors. *Pediatric Hematology*, *3rd ed*. (India: Blackwell Publishing) (2006). p. 450–81.

2. Pui C-H, Mullighan CG, Evans WE, Relling MV. Pediatric acute lymphoblastic leukemia: where are we going and how do we get there? *Blood* (2012) 120(6):1165–74. doi: 10.1182/blood-2012-05-378943

3. Hunger SP, Lu X, Devidas M, Camitta BM, Gaynon PS, Winick NJ, et al. Improved survival for children and adolescents with acute lymphoblastic leukemia between 1990 and 2005: a report from the children's oncology group. *J Clin Oncol Off J Am Soc Clin Oncol* (2012) 30(14):1663–9. doi: 10.1200/JCO.2011.37.8018

4. Inukai T. Mechanisms of drug resistance in acute lymphoblastic leukemia. *[Rinsho ketsueki] Japanese J Clin hematology* (2016) 57(10):2022–8. doi: 10.11406/rinketsu.57.2022

5. Zahreddine H, Borden KLB. Mechanisms and insights into drug resistance in cancer. *Front Pharmacol* (2013) 4:28. doi: 10.3389/fphar.2013.00028

6. Ross DD. Novel mechanisms of drug resistance in leukemia. *Leukemia. Mar* (2000) 14(3):467–73. doi: 10.1038/sj.leu.2401694

7. Housman G, Byler S, Heerboth S, Lapinska K, Longacre M, Snyder N, et al. Drug resistance in cancer: an overview. *Cancers* (2014) 6(3):1769–92. doi: 10.3390/cancers6031769

8. Chen ZS, Lee K, Walther S, Raftogianis RB, Kuwano M, Zeng H, et al. Analysis of methotrexate and folate transport by multidrug resistance protein 4 (ABCC4):MRP4 is a component of the methotrexate efflux system. *Cancer Res* (2002) 62(11):3144–50.

9. Masson E, Relling MV, Synold TW, Liu Q, Schuetz JD, Sandlund JT, et al. Accumulation of methotrexate polyglutamates in lymphoblasts is a determinant of antileukemic effects *in vivo*: A rationale for high-dose methotrexate. *J Clin Invest* (1996) 97(1):73–80. doi: 10.1172/JCI118409

10. Lopez-Lopez E, Autry RJ, Smith C, Yang W, Paugh SW, Panetta JC, et al. Pharmacogenomics of intracellular methotrexate polyglutamates in patients' leukemia cells in vivo. *J Clin Invest* (2020) 130(12):6600–15. doi: 10.1172/JCI140797

11. Sorich MJ, Pottier N, Pei D, Yang W, Kager L, Stocco G, et al. *In vivo* response to methotrexate forecasts outcome of acute lymphoblastic leukemia and has a distinct gene expression profile. *PloS Med* (2008) 5(4):0646–56. doi: 10.1371/journal.pmed.0050083

12. Papadopoli DJ, Ma EH, Roy D, Russo M, Bridon G, Avizonis D, et al. Methotrexate elicits pro-respiratory and anti-growth effects by promoting AMPK signaling. *Sci Rep May 12* (2020) 10(1):7838. doi: 10.1038/s41598-020-64460-z

13. Leyva-Vázquez MA, Organista-Nava J, Gómez-Gómez Y, Contreras-Quiroz A, Flores-Alfaro E, Illades-Aguiar B. Polymorphism G80A in the reduced folate carrier gene and its relationship to survival and risk of relapse in acute lymphoblastic leukemia. *J Invest Med Off Publ Am Fed Clin Res* (2012) 60 (7):1064–7. doi: 10.2310/JIM.0b013e31826803c1

14. Wojtuszkiewicz A, Peters GJ, van Woerden NL, Dubbelman B, Escherich G, Schmiegelow K, et al. Methotrexate resistance in relation to treatment outcome in childhood acute lymphoblastic leukemia. *J Hematol Oncol 2015/12//* (2015) 8 (1):61–1. doi: 10.1186/s13045-015-0158-9

15. Schuetz JD, Westin EH, Matherly LH, Pincus R, Swerdlow PS, Goldman ID. Membrane protein changes in an L1210 leukemia cell line with a translocation defect in the methotrexate-tetrahydrofolate cofactor transport carrier. *J Biol Chem* (1989) 264(27):16261–7. doi: 10.1016/S0021-9258(18)71616-5

16. Kremer JM. Toward a better understanding of methotrexate. *Arthritis rheumatism* (2004) 50(5):1370–82. doi: 10.1002/art.20278

17. Ranganathan P, McLeod HL. Methotrexate pharmacogenetics - The first step toward individualized therapy in rheumatoid arthritis. *Arthritis Rheum-Us* (2006) 54(5):1366–77. doi: 10.1002/art.21762

18. Kager L, Cheok M, Yang W, Zaza G, Cheng Q, Panetta JC, et al. Folate pathway gene expression differs in subtypes of acute lymphoblastic leukemia and influences methotrexate pharmacodynamics. *J Clin Invest* (2005) 115(1):110–7. doi: 10.1172/JCI22477

19. Fabre I, Fabre G, Goldman ID. Polyglutamylation, an important element in methotrexate cytotoxicity and selectivity in tumor versus murine granulocytic progenitor cells in vitro. *Cancer Res* (1984) 44(8):3190–5.

20. Li WW, Lin JT, Tong WP, Trippett TM, Brennan MF, Bertino JR. Mechanisms of natural resistance to antifolates in human soft tissue sarcomas. *Cancer Res* (1992) 52(6):1434–8.

21. Matherly LH, Taub JW, Ravindranath Y, Proefke SA, Wong SC, Gimotty P, et al. Elevated dihydrofolate reductase and impaired methotrexate transport as elements in methotrexate resistance in childhood acute lymphoblastic leukemia. *Blood* (1995) 85(2):500–9. doi: 10.1182/blood.V85.2.500.500

22. Srimatkandada S, Schweitzer BI, Moroson BA, Dube S, Bertino JR. Amplification of a polymorphic dihydrofolate reductase gene expressing an enzyme with decreased binding to methotrexate in a human colon carcinoma cell line, HCT-8R4, resistant to this drug. *J Biol Chem* (1989) 264(6):3524–8. doi: 10.1016/S0021-9258(18)94097-4

23. Rhee MS, Wang Y, Nair MG, Galivan J. Acquisition of resistance to antifolates caused by enhanced gamma-glutamyl hydrolase activity. *Cancer Res* (1993) 53(10 Suppl):2227–30.

24. Wang Y, Dias JA, Nimec Z, Rotundo R, O'Connor BM, Freisheim J, et al. The properties and function of gamma-glutamyl hydrolase and poly-gamma-glutamate. *Adv Enzyme Regul* (1993) 33:207–18. doi: 10.1016/0065-2571(93)90019-a

25. Organista-Nava J, Gómez-Gómez Y, Del Moral-Hernandez O, Illades-Aguiar B, Gómez-Santamaria J, Rivera-Ramírez AB, et al. Deregulation of folate pathway gene expression correlates with poor prognosis in acute leukemia. *Oncol letters* (2019) 18(3):3115–27. doi: 10.3892/ol.2019.10650

26. Rots MG, Pieters R, Peters GJ, van Zantwijk CH, Mauritz R, Noordhuis P, et al. Circumvention of methotrexate resistance in childhood leukemia subtypes by rationally designed antifolates. *Blood* (1999) 94(9):3121–8. doi: 10.1182/blood.V94.9.3121

27. Panetta JC, Yanishevski Y, Pui C-H, Sandlund JT, Rubnitz J, Rivera GK, et al. A mathematical model of *in vivo* methotrexate accumulation in acute lymphoblastic leukemia. *Cancer chemotherapy Pharmacol* (2002) 50(5):419–28. doi: 10.1007/s00280-002-0511-x

28. Waltham MC, Li WW, Gritsman H, Tong WP, Bertino JR. gamma-Glutamyl hydrolase from human sarcoma HT-1080 cells: characterization and inhibition by glutamine antagonists. *Mol Pharmacol* (1997) 51(5):825–32. doi: 10.1124/mol.51.5.825

29. Babiak RMV, Campello AP, Carnieri EGS, Oliveira MBM. Methotrexate: pentose cycle and oxidative stress. *Cell Biochem Funct* (1998) 16(4):283–93. doi: 10.1002/(SICI)1099-0844(1998120)16:4<283::AID-CBF801>3.0.CO;2-E

30. Wang YC, Chiang EP. Low-dose methotrexate inhibits methionine S-adenosyltransferase *in vitro* and in vivo. *Mol Med* (2012) 18:423–32. doi: 10.2119/molmed.2011.00048

31. Kanarek N, Keys HR, Cantor JR, Lewis CA, Chan SH, Kunchok T, et al. Histidine catabolism is a major determinant of methotrexate sensitivity (vol 5592021). *Nature* (2022) 602(7895):pg 632:E17-E18. doi: 10.1038/s41586-021-03487-2

32. Le Belle JE, Harris NG, Williams SR, Bhakoo KK. A comparison of cell and tissue extraction techniques using high-resolution 1H-NMR spectroscopy (vol 15, pg 37, 2002). *Nmr Biomed Apr* (2016) 29(4):527–7. doi: 10.1002/nbm.3503

33. Xia J, Wishart DS. Using metaboanalyst 3.0 for comprehensive metabolomics data analysis. *Curr Protoc Bioinf* (2016) 2016:14.10.11–14.10.91. doi: 10.1002/cpbi.11

34. Silveira AB, Laranjeira ABA, Rodrigues GOL, Leal R, Cardoso BA, Barata JT, et al. PI3K inhibition synergizes with glucocorticoids but antagonizes with methotrexate in T-cell acute lymphoblastic leukemia. *Oncotarget* (2015) 6 (15):13105–18. doi: 10.18632/oncotarget.3524

35. Khin ZP, Ribeiro MLC, Jacobson T, Hazlehurst L, Perez L, Baz R, et al. A Preclinical Assay for Chemosensitivity in Multiple Myeloma. *Cancer Res* (2014) 74 (1):56–67. doi: 10.1158/0008-5472.CAN-13-2397

36. Silva A, Silva MC, Sudalagunta P, Distler A, Jacobson T, Collins A, et al. An Ex Vivo Platform for the Prediction of Clinical Response in Multiple Myeloma. *Cancer Res* (2017) 77(12):3336–51. doi: 10.1158/0008-5472.CAN-17-0502

37. Silva A, Jacobson T, Meads M, Distler A, Shain K. An Organotypic High Throughput System for Characterization of Drug Sensitivity of Primary Multiple Myeloma Cells. *J Vis Exp* (2015) 101):e53070. doi: 10.3791/53070

38. Sudalagunta P, Silva MC, Canevarolo RR, Alugubelli RR, DeAvila G, Tungesvik A, et al. A pharmacodynamic model of clinical synergy in multiple myeloma. *EBioMedicine* (2020) 54:102716. doi: 10.1016/j.ebiom.2020.102716

39. Zhao X, Ren Y, Lawlor M, Shah BD, Park PMC, Lwin T, et al. BCL2 Amplicon Loss and Transcriptional Remodeling Drives ABT-199 Resistance in B Cell Lymphoma Models. *Cancer Cell* (2019) 35(5):752–766.e759. doi: 10.1016/j.ccell.2019.04.005

40. Mostofa A, Distler A, Meads MB, Sahakian E, Powers JJ, Achille A, et al. Plasma cell dependence on histone/protein deacetylase 11 reveals a therapeutic target in multiple myeloma. *JCI Insight* (2021) 6(24). doi: 10.1172/jci.insight.151713

41. Ren Y, Bi C, Zhao X, Lwin T, Wang C, Yuan J, et al. PLK1 stabilizes a MYC-dependent kinase network in aggressive B cell lymphomas. *J Clin Invest* (2018) 128 (12):5517–30. doi: 10.1172/JCI122533

42. Zhou L, Zhang Y, Meads MB, Dai Y, Ning Y, Hu X, et al. IAP and HDAC inhibitors interact synergistically in myeloma cells through noncanonical NF-κB– and caspase-8–dependent mechanisms. *Blood Advances* (2021) 5(19):3776–88. doi: 10.1182/bloodadvances.2020003597

43. Almeida ARM, Neto JL, Cachucho A, Euzebio M, Meng X, Kim R, et al. Interleukin-7 receptor alpha mutational activation can initiate precursor B-cell acute lymphoblastic leukemia. *Nat Commun* (2021) 12(1):7268. doi: 10.1038/s41467-021-27197-5

44. Szymanska B, Wilczynska-Kalak U, Kang MH, Liem NL, Carol H, Boehm I, et al. Pharmacokinetic modeling of an induction regimen for *in vivo* combined testing of novel drugs against pediatric acute lymphoblastic leukemia xenografts. *PloS One* (2012) 7(3)::e33894. doi: 10.1371/journal.pone.0033894

45. Lock RB, Liem N, Farnsworth ML, Milross CG, Xue C, Tajbakhsh M, et al. The nonobese diabetic/severe combined immunodeficient (NOD/SCID) mouse model of childhood acute lymphoblastic leukemia reveals intrinsic differences in biologic characteristics at diagnosis and relapse. *Blood. Jun 1* (2002) 99(11):4100–8. doi: 10.1182/blood.v99.11.4100

46. Tiziani S, Lodi A, Khanim FL, Viant MR, Bunce CM, Gunther UL. Metabolomic profiling of drug responses in acute myeloid leukaemia cell lines. *PloS One* (2009) 4(1):e4251. doi: 10.1371/journal.pone.0004251

47. Sharaf BM, Giddey AD, Alniss H, Al-Hroub HM, El-Awady R, Mousa M, et al. Untargeted Metabolomics of Breast Cancer Cells MCF-7 and SkBr3 Treated With Tamoxifen/Trastuzumab. *Cancer Genomics Proteomics* (2022) 19(1):79–93. doi: 10.21873/cgp.20305

48. Paul M, Hemshekhar M, Thushara RM, Sundaram MS, NaveenKumar SK, Naveen S, et al. Methotrexate Promotes Platelet Apoptosis *via* JNK-Mediated Mitochondrial Damage: Alleviation by N-Acetylcysteine and N-Acetylcysteine Amide. *PloS One* (2015) 10(6):e0127558. doi: 10.1371/journal.pone.0127558

49. Kubota M, Nakata R, Adachi S, Watanabe K, Heike T, Takeshita Y, et al. Plasma homocysteine, methionine and S-adenosylhomocysteine levels following high-dose methotrexate treatment in pediatric patients with acute lymphoblastic leukemia or Burkitt lymphoma: association with hepatotoxicity. *Leuk Lymphoma* (2014) 55(7):1591–5. doi: 10.3109/10428194.2013.850684

50. Hoffman JD, Ward WM, Loo G. Effect of antioxidants on the genotoxicity of phenethyl isothiocyanate. *Mutagenesis* (2015) 30(3):421–30. doi: 10.1093/mutage/gev003

51. Hong Y-H, Uddin MH, Jo U, Kim B, Song J, Suh DH, et al. ROS Accumulation by PEITC Selectively Kills Ovarian Cancer Cells *via* UPR-Mediated Apoptosis. *Front Oncol* (2015) 5:167. doi: 10.3389/fonc.2015.00167

52. Raj L, Ide T, Gurkar AU, Foley M, Schenone M, Li X, et al. Selective killing of cancer cells by a small molecule targeting the stress response to ROS. *Nature* (2011) 475(7355):231–4. doi: 10.1038/nature10167

53. Lu J, Chew EH, Holmgren A. Targeting thioredoxin reductase is a basis for cancer therapy by arsenic trioxide. *P Natl Acad Sci USA* (2007) 104(30):12288–93. doi: 10.1073/pnas.0701549104

54. Zenatti PP, Ribeiro D, Li W, Zuurbier L, Silva MC, Paganin M, et al. Oncogenic IL7R gain-of-function mutations in childhood T-cell acute lymphoblastic leukemia. *Nat Genet* (2011) 43(10):932–9. doi: 10.1038/ng.924

55. Tedeschi PMPM, Johnson-Farley N, Lin H, Shelton LM, Ooga T, Mackay GMG, et al. Quantification of folate metabolism using transient metabolic flux analysis. *Cancer Metab* (2015) 3(1):6–6. doi: 10.1186/s40170-015-0132-6

56. Budzik GP, Colletti LM, Faltynek CR. Effects of methotrexate on nucleotide pools in normal human T cells and the CEM T cell line. *Life Sci* (2000) 66 (23):2297–307. doi: 10.1016/S0024-3205(00)00559-2

57. Funk RS, Singh RK, Becker ML. Metabolomic Profiling to Identify Molecular Biomarkers of Cellular Response to Methotrexate In Vitro. *Clin Transl Sci* (2020) 13(1):137–46. doi: 10.1111/cts.12694

58. Hornung N, Stengaard-Pedersen K, Ehrnrooth E, Ellingsen T, Poulsen JH. The effects of low-dose methotrexate on thymidylate synthetase activity in human peripheral blood mononuclear cells. *Clin Exp Rheumatol* (2000) 18(6):691–8.

59. Chu E, Drake JC, Boarman D, Baram J, Allegra CJ. Mechanism of thymidylate synthase inhibition by methotrexate in human neoplastic cell lines and normal human myeloid progenitor cells. *J Biol Chem* (1990) 265(15):8470–8. doi: 10.1016/S0021-9258(19)38912-4

60. Lamego I, Duarte IF, Marques MPM, Gil AM. Metabolic Markers of MG-63 Osteosarcoma Cell Line Response to Doxorubicin and Methotrexate Treatment: Comparison to Cisplatin. *J Proteome Res* (2014) 13(12):6033–45. doi: 10.1021/pr500907d

61. Lamego I, Marques MP, Duarte IF, Martins AS, Oliveira H, Gil AM. Impact of the Pd2Spermine Chelate on Osteosarcoma Metabolism: An NMR Metabolomics Study. *J Proteome Res* (2017) 16(4):1773–83. doi: 10.1021/acs.jproteome.7b00035

62. Sanchez-Alvarez M, Zhang Q, Finger F, Wakelam MJO, Bakal C. Cell cycle progression is an essential regulatory component of phospholipid metabolism and membrane homeostasis. *Open Biol* (2015) 5(9):150093–3. doi: 10.1098/rsob.150093

63. Kruh GD, Zeng H, Rea PA, Liu G, Chen ZS, Lee K, et al. MRP subfamily transporters and resistance to anticancer agents. *J Bioenerg Biomembr* (2001) 33 (6):493–501. doi: 10.1023/a:1012827221844

64. Chen Z-S, Guo Y, Belinsky MG, Kotova E, Kruh GD. Transport of bile acids, sulfated steroids, estradiol 17-beta-D-glucuronide, and leukotriene C4 by human multidrug resistance protein 8 (ABCC11). *Mol Pharmacol* (2005) 67(2):545–57. doi: 10.1124/mol.104.007138

65. Ansari M, Sauty G, Labuda M, Gagné V, Rousseau J, Moghrabi A, et al. Polymorphism in multidrug resistance-associated protein gene 3 is associated with outcomes in childhood acute lymphoblastic leukemia. *pharmacogenomics J* (2012) 12(5):386–94. doi: 10.1038/tpj.2011.17

66. Steinbach D, Wittig S, Cario G, Viehmann S, Mueller A, Gruhn B, et al. The multidrug resistance-associated protein 3 (MRP3) is associated with a poor outcome in childhood ALL and may account for the worse prognosis in male patients and T-cell immunophenotype. *Blood* (2003) 102(13):4493–8. doi: 10.1182/blood-2002-11-3461

67. Laverdière C, Chiasson S, Costea I, Moghrabi A, Krajinovic M, Laverdiere C, et al. Polymorphism G80A in the reduced folate carrier gene and its relationship to methotrexate plasma levels and outcome of childhood acute lymphoblastic leukemia. *Blood* (2002) 100(10):3832–4. doi: 10.1182/blood.V100.10.3832

68. Dulucq S, Laverdière C, Sinnett D, Krajinovic M. Pharmacogenetic considerations for acute lymphoblastic leukemia therapies. *Expert Opin Drug Metab Toxicology* (2014) 10(5):699–719. doi: 10.1517/17425255.2014.893294

69. Said HM, Strum WB, Hollander D. Inhibitory effect of unconjugated bile acids on the enterohepatic circulation of methotrexate. *J Pharmacol Exp Ther Dec* (1984) 231(3):660–4.

70. Honscha W, Petzinger E. Characterization of the bile acid sensitive methotrexate carrier of rat liver cells. *Naunyn Schmiedebergs Arch Pharmacol May* (1999) 359(5):411–9. doi: 10.1007/pl00005369

71. Lamarre SG, Morrow G, Macmillan L, Brosnan ME, Brosnan JT. Formate: an essential metabolite, a biomarker, or more? *Clin Chem Lab Med* (2013) 51 (3):571–8. doi: 10.1515/cclm-2012-0552

72. Morrow GP, MacMillan L, Lamarre SG, Young SK, MacFarlane AJ, Brosnan ME, et al. *In vivo* kinetics of formate metabolism in folate-deficient and folate-replete rats. *J Biol Chem* (2015) 290(4):2244–50. doi: 10.1074/jbc.M114.600718

73. Meng D, Yang Q, Wang H, Melick CH, Navlani R, Frank AR, et al. Glutamine and asparagine activate mTORC1 independently of Rag GTPases. *J Biol Chem* (2020) 295(10):2890–9. doi: 10.1074/jbc.AC119.011578

74. Krall AS, Xu S, Graeber TG, Braas D, Christofk HR. Asparagine promotes cancer cell proliferation through use as an amino acid exchange factor. *Nat Commun* (2016) 7:11457. doi: 10.1038/ncomms11457

75. Yiang GT, Chou PL, Hung YT, Chen JN, Chang WJ, Yu YL, et al. Vitamin C enhances anticancer activity in methotrexatetreated Hep3B hepatocellular carcinoma cells. *Oncol Rep* (2014) 32(3):1057–63. doi: 10.3892/or.2014.3289

76. Baquero JM, Benitez-Buelga C, Rajagopal V, Zhenjun Z, Torres-Ruiz R, Muller S, et al. Small molecule inhibitor of OGG1 blocks oxidative DNA damage repair at telomeres and potentiates methotrexate anticancer effects. *Sci Rep* (2021) 11(1):3490. doi: 10.1038/s41598-021-82917-7

77. Phillips DC, Woollard KJ, Griffiths HR. The anti-inflammatory actions of methotrexate are critically dependent upon the production of reactive oxygen species. *Br J Pharmacol* (2003) 138(3):501–11. doi: 10.1038/sj.bjp.0705054

78. Barros S, Mencia N, Rodríguez L, Oleaga C, Santos C, Noé V, et al. The Redox State of Cytochrome C Modulates Resistance to Methotrexate in Human MCF7 Breast Cancer Cells. *PloS One* (2013) 8(5):e63276. doi: 10.1371/journal.pone.0063276

79. Kearns PR, Chrzanowska-Lightowlers ZM, Pieters R, Veerman A, Hall AG. Mu class glutathione S-transferase mRNA isoform expression in acute lymphoblastic leukaemia. *Br J Haematol* (2003) 120(1):80–8. doi: 10.1046/j.1365-2141.2003.04039.x

80. Courtay C, Oster T, Michelet F, Visvikis A, Diederich M, Wellman M, et al. γ-Glutamyltransferase: Nucleotide sequence of the human pancreatic cDNA: Evidence for a ubiquitous γ-glutamyltransferase polypeptide in human tissues. *Biochem Pharmacol* (1992) 43(12):2527–33. doi: 10.1016/0006-2952(92)90140-E

81. Russo SA, Harris MB, Greengard O. Diminished lymphocyte and granulocyte gamma-glutamyltranspeptidase activity in acute lymphocytic leukemia and response to chemotherapy. *Am J Hematol* (1987) 26(1):67–75. doi: 10.1002/ajh.2830260108

82. Roberts BE, Child JA, Cooper EH, Turner R, Stone J. Evaluation of the usefulness of serum gamma-glutamyl transpeptidase levels in the management of haematological neoplasia. *Acta Haematol* (1978) 59(2):65–72. doi: 10.1159/000207747

83. Nordberg J, Arnér ESJ. Reactive oxygen species, antioxidants, and the mammalian thioredoxin system. *Free Radical Biol Med* (2001) 31(11):1287–312. doi: 10.1016/S0891-5849(01)00724-9

84. Liu JJ, Liu Q, Wei HL, Yi J, Zhao HS, Gao LP. Inhibition of thioredoxin reductase by auranofin induces apoptosis in adriamycin-resistant human K562 chronic myeloid leukemia cells. *Pharmazie* (2011) 66(6):440–4. doi: 10.1691/ph.2011.0835

85. Wang H, Bouzakoura S, de Mey S, Jiang H, Law K, Dufait I, et al. Auranofin radiosensitizes tumor cells through targeting thioredoxin reductase and resulting overproduction of reactive oxygen species. *Oncotarget* (2017) 8(22):35728–42. doi: 10.18632/oncotarget.16113

86. Zhang J, Li X, Han X, Liu R, Fang J. Targeting the Thioredoxin System for Cancer Therapy. *Trends Pharmacol Sci Sep* (2017) 38(9):794–808. doi: 10.1016/j.tips.2017.06.001

87. Bracht K, Liebeke M, Ritter CA, Gr??nert R, Bednarski PJ. Correlations between the activities of 19 standard anticancer agents, antioxidative enzyme activities and the expression of ATP-binding cassette transporters: comparison with the National Cancer Institute data. *Anti-Cancer Drugs* (2007) 18(4):389–404. doi: 10.1097/CAD.0b013e3280140001

88. Oshima K, Zhao J, Perez-Duran P, Brown JA, Patino-Galindo JA, Chu T, et al. Mutational and functional genetics mapping of chemotherapy resistance mechanisms in relapsed acute lymphoblastic leukemia. *Nat Cancer* (2020) 1 (11):1113–27. doi: 10.1038/s43018-020-00124-1

89. Griffith OW. Biologic and pharmacologic regulation of mammalian glutathione synthesis. *Free Radic Biol Med* (1999) 27(9-10):922–35. doi: 10.1016/s0891-5849(99)00176-8

90. Benhar M, Shytaj IL, Stamler JS, Savarino A. Dual targeting of the thioredoxin and glutathione systems in cancer and HIV. *J Clin Invest* (2016) 126 (5):1630–9. doi: 10.1172/JCI85339

91. Scarbrough PM, Mapuskar KA, Mattson DM, Gius D, Watson WH, Spitz DR. Simultaneous inhibition of glutathione- and thioredoxin-dependent metabolism is necessary to potentiate 17AAG-induced cancer cell killing *via* oxidative stress. *Free Radical Biol Med* (2012) 52(2):436–43. doi: 10.1016/j.freeradbiomed.2011.10.493

92. Sobhakumari A, Love-Homan L, Fletcher EVM, Martin SM, Parsons AD, Spitz DR, et al. Susceptibility of Human Head and Neck Cancer Cells to Combined Inhibition of Glutathione and Thioredoxin Metabolism. *PloS One* (2012) 7(10): e48175. doi: 10.1371/journal.pone.0048175

93. Roh JL, Jang H, Kim EH, Shin D. Targeting of the Glutathione, Thioredoxin, and Nrf2 Antioxidant Systems in Head and Neck Cancer. *Antioxid Redox Sign* (2017) 27(2):106–14. doi: 10.1089/ars.2016.6841

94. Harris Isaac S, Treloar Aislinn E, Inoue S, Sasaki M, Gorrini C, Lee Kim C, et al. Glutathione and Thioredoxin Antioxidant Pathways Synergize to Drive Cancer Initiation and Progression. *Cancer Cell* (2015) 27(2):211–22. doi: 10.1016/j.ccell.2014.11.019

95. Kiebala M, Skalska J, Casulo C, Brookes PS, Peterson DR, Hilchey SP, et al. Dual targeting of the thioredoxin and glutathione antioxidant systems in malignant B cells: A novel synergistic therapeutic approach. *Exp Hematology* (2015) 43(2):89–99. doi: 10.1016/j.exphem.2014.10.004

96. Li L, Fath MA, Scarbrough PM, Watson WH, Spitz DR. Combined inhibition of glycolysis, the pentose cycle, and thioredoxin metabolism selectively increases cytotoxicity and oxidative stress in human breast and prostate cancer. *Redox Biol* (2015) 4:127–35. doi: 10.1016/j.redox.2014.12.001

97. Ruan Y, Peterson MH, Wauson EM, Waes JG, Finnell RH, Vorce RL. Folic acid protects SWV/Fnn embryo fibroblasts against arsenic toxicity. *Toxicol Lett* (2000) 117(3):129–37. doi: 10.1016/s0378-4274(00)00254-x

98. Lengfelder E, Hofmann WK, Nowak D. Impact of arsenic trioxide in the treatment of acute promyelocytic leukemia. *Leukemia* (2012) 26(3):433–42. doi: 10.1038/leu.2011.245

99. Platzbecker U, Avvisati G, Cicconi L, Thiede C, Paoloni F, Vignetti M, et al. Improved Outcomes With Retinoic Acid and Arsenic Trioxide Compared With Retinoic Acid and Chemotherapy in Non-High-Risk Acute Promyelocytic Leukemia: Final Results of the Randomized Italian-German APL0406 Trial. *J Clin Oncol* (2017) 35(6):605–12. doi: 10.1200/JCO.2016.67.1982

100. Lo-Coco F, Avvisati G, Vignetti M, Thiede C, Orlando SM, Iacobelli S, et al. Retinoic acid and arsenic trioxide for acute promyelocytic leukemia. *N Engl J Med* (2013) 369(2):111–21. doi: 10.1056/NEJMoa1300874

101. Ades L, Guerci A, Raffoux E, Sanz M, Chevallier P, Lapusan S, et al. Very long-term outcome of acute promyelocytic leukemia after treatment with all-trans retinoic acid and chemotherapy: the European APL Group experience. *Blood* (2010) 115(9):1690–6. doi: 10.1182/blood-2009-07-233387

102. Muchtar E, Vidal L, Ram R, Gafter-Gvili A, Shpilberg O, Raanani P. The role of maintenance therapy in acute promyelocytic leukemia in the first complete remission. *Cochrane Database Syst Rev* (2013) 3):CD009594. doi: 10.1002/14651858.CD009594.pub2

103. Huang H, Qin Y, Xu R, You X, Teng R, Yang L, et al. Combination therapy with arsenic trioxide, all-trans retinoic acid, and chemotherapy in acute promyelocytic leukemia patients with various relapse risks. *Leuk Res* (2012) 36 (7):841–5. doi: 10.1016/j.leukres.2012.03.027

104. Howard SC, McCormick J, Pui CH, Buddington RK, Harvey RD. Preventing and Managing Toxicities of High-Dose Methotrexate. *Oncologist* (2016) 21(12):1471–82. doi: 10.1634/theoncologist.2015-0164

105. Zhang P. On arsenic trioxide in the clinical treatment of acute promyelocytic leukemia. *Leuk Res Rep* (2017) 7:29–32. doi: 10.1016/j.lrr.2017.03.001

106. Litzow MR, Lee S, Bennett JM, Dewald GW, Gallagher RE, Jain V, et al. A phase II trial of arsenic trioxide for relapsed and refractory acute lymphoblastic leukemia. *Haematologica* (2006) 91(8):1105–8.

frontiers | Frontiers in Oncology

TYPE Original Research
PUBLISHED 05 January 2023
DOI 10.3389/fonc.2022.972434

Check for updates

OPEN ACCESS

EDITED BY
Guo-Dong Lu,
Guangxi Medical University, China

REVIEWED BY
Yi Hu,
Jinan University, China
Emily Werth,
Boehringer Ingelheim, United States
Jian Yin,
Jiangnan University, China

*CORRESPONDENCE
Yuhua Zhang
✉ zhangyuhua1013@126.com

†These authors have contributed equally to this work

SPECIALTY SECTION
This article was submitted to Molecular and Cellular Oncology, a section of the journal Frontiers in Oncology

RECEIVED 15 July 2022
ACCEPTED 15 December 2022
PUBLISHED 05 January 2023

CITATION
Han F, Cao D, Zhu X, Shen L, Wu J, Chen Y, Xu Y, Xu L, Cheng X and Zhang Y (2023) Construction and validation of a prognostic model for hepatocellular carcinoma: Inflammatory ferroptosis and mitochondrial metabolism indicate a poor prognosis. *Front. Oncol.* 12:972434. doi: 10.3389/fonc.2022.972434

Construction and validation of a prognostic model for hepatocellular carcinoma: Inflammatory ferroptosis and mitochondrial metabolism indicate a poor prognosis

Fang Han[1†], Dan Cao[1,2†], Xin Zhu[3], Lianqiang Shen[4], Jia Wu[1], Yizhen Chen[1,5], Youyao Xu[1,5], Linwei Xu[1], Xiangdong Cheng[1] and Yuhua Zhang[1,5*]

[1]Hepatobiliary and Pancreatic Surgery Department, The Cancer Hospital of the University of Chinese Academy of Sciences (Zhejiang Cancer Hospital), Institute of Basic Medicine and Cancer (IBMC), Chinese Academy of Sciences, Hangzhou, Zhejiang, China, [2]College of Food and Pharmacy, Zhejiang Ocean University, Zhoushan, Zhejiang, China, [3]Hepatobiliary and Pancreatic Surgery Department, Shaoxing Peoples's Hospital, Shaoxing, Zhejiang, China, [4]Department of General Surgery, The First People's Hospital of Linping District, Hangzhou, Hangzhou, Zhejiang, China, [5]Clincal Dept. Zhejiang Chinese Medical University, Hangzhou, Zhejiang, China

Background: An increasing number of innovations have been discovered for treating hepatocellular carcinoma (HCC or commonly called HCC) therapy, Ferroptosis and mitochondrial metabolism are essential mechanisms of cell death. These pathways may act as functional molecular biomarkers that could have important clinical significance for determining individual differences and the prognosis of HCC. The aim of this study was to construct a stable and reliable comprehensive model of genetic features and clinical factors associated with HCC prognosis.

Methods: In this study, we used RNA-sequencing (fragments per kilobase of exon model per million reads mapped value) data from the Cancer Genome Atlas (TCGA) database to establish a prognostic model. We enrolled 104 patients for further validation. Gene Ontology (GO) and Kyoto Encyclopedia of Genes and Genomes enrichment analyses (KEGG) analysis were used for the functional study of differentially expressed genes. Pan-cancer analysis was performed to evaluate the function of the Differentially Expressed Genes (DEGs). Thirteen genes were identified by univariate and least absolute contraction and selection operation (LASSO) Cox regression analysis. The prognostic model was visualized using a nomogram.

Results: We found that eight genes, namely EZH2, GRPEL2, PIGU, PPM1G, SF3B4, TUBG1, TXNRD1 and NDRG1, were hub genes for HCC and differentially expressed in most types of cancer. EZH2, GRPEL2 and NDRG1 may indicate a poor prognosis of HCC as verified by tissue samples. Furthermore, a gene set variation analysis algorithm was created to analyze the relationship between these eight genes and oxidative phosphorylation, mitophagy, and FeS-containing proteins, and it showed that ferroptosis might affect inflammatory-related pathways in HCC.

Conclusion: EZH2, GRPEL2, NDRG1, and the clinical factor of tumor size, were included in a nomogram for visualizing a prognostic model of HCC. This nomogram based on a functional study and verification by clinical samples, shows a reliable performance of patients with HCC.

KEYWORDS

hepatocellular carcinoma, prognostic model, inflammation, ferroptosis, mitochondrial metabolism, bioinformatics, survival analysis

Introduction

Liver hepatocellular carcinoma (HCC) is the third leading cause of cancer-related death worldwide (1). Most patients with HCC have a history of chronic hepatitis B virus (HBV) infection. Although HBV has been effectively controlled in China, morbidity and mortality are currently rising (2). Nevertheless, HCC is the sixth most common cancer worldwide (3). Several innovative methods have been developed for the treatment of HCC. However, the effectiveness of these treatments markedly varies between individuals. The main reason for this variation is a lack of therapeutic evaluation of efficacy. Therefore, more effective biomarkers and/or prognostic models are requied. Effective biomarkers should be able to predict the prognosis of HCC and participate in specific functions of tumor biology. In particular, biomarkers described for specific anti-tumor phenotypes may be the most meaningful (4, 5).

Intracellular iron is a crucial target for the induction of cell death because it mediates ferroptosis and mitochondrial metabolism (6). Ferroptosis is a non-apoptotic regulated form of cell death that has gradually attracted attention in cancer pathogenesis research (7). Ferroptosis induces abnormal mitochondrial metabolism and reactive oxygen species (ROS) accumulation, and it may promote anti-tumor mechanisms in the microenvironment (8, 9). These finding suggests that ferroptosis is an important mechanism contributing to the development of the tumor microenvironment. Some researchers have suggested that ferroptosis or metabolic-related gene signatures could provide relevant information on the prognosis of HCC (10, 11). The unique tumor microenvironment in HCC includes considerable immune infiltration because of chronic inflammation (12). Therefore, a prognostic model for HCC in the context of inflammation in mainland China is required.

In this study, a bioinformatics analysis method was used to analyze a data set from the Cancer Genome Atlas (TCGA) database to determine the differentially expressed genes (DEGs) in HCC compared with healthy individuals. A prognostic model based on the hub genes was constructed using least absolute contraction and selection operation (LASSO) regression. To determine the validity and stability of this model, we used clinical tissue samples to verify the hub genes. To verify the function of these critical genes in tumors, we performed a series of functional analyses. Using these results, we hoped to identify the most stable and reliable gene signatures and clinical factors that contribute to the progression of HCC.

Materials and methods

Data sources

Our analysis results are based on the omics data set generated by the TCGA (http://cancergenome.nih.gov/). A total of 33 types of cancer were enrolled from TCGA. All data sets include Count data, Transcripts Per Kilobase Million (TPM) data, RNA-seq, Copy number variation (CNV), Mutation and Clinical Information, were downloaded from UCSC XENA (https://xenabrowser.net/). We enrolled a total of 50 normal liver tissues and 374 HCC in the TCGA database. We used the limma package for R to analyze the differential expression between HCC and normal liver tissues.

Clustering differentially expressed genes for HCC

To identify the Fold Changes in gene expression in each cancer data set, we used the Deseq2 package for R software to identify the DEGs using TCGA count data. We consider adjusting P value < 0.05 and Log|FC| > 1 as DEGs. Meanwhile, to determine the DEGs related to the prognosis of HCC, we used univariate COX regression, which is analyzed in R using survival package to screen the genes that affect the prognosis of HCC. HCC-specific genes are considered meaningful to both differential expression and prognostic analysis.

GO and KEGG analysis

Gene Ontology (GO) and Kyoto Encyclopedia of Genes and Genomes Enrichment Analyses were functional enrichment. Go analysis is a bioinformatics tool including three functional analyses, which are cellular components (CC), molecular function (MF), and biological pathways (BP) (13). KEGG stores a multigene signature pathway to which hub genes belong (14). We conducted a functional enrichment analysis to study the underlying mechanism of DEGs-based clustering at different levels. We first converted the gene names of the differential genes into ENTREZ IDs, and further, enriched using the enrichment function in the cluterprofiler. For the P value of the results of the analysis, the BH algorithm is used to correct it. Finally, we select the corrected P value of < 0.05 as the meaningful enrichment result

LASSO Cox regression analysis and visualization

We first performed COX regression on differentially expressed genes to screen genes related to the prognosis of HCC. The LASSO regression analysis model eliminates the collinearity problem between prognostic-related genes (15). Finally, we obtained the characteristic genes that affect HCC. We used a nomogram, which constructed specific models related to HCC for clinical application to show the clinical model. Lasso returns to the Glmnet package using the R language. We used the Rms package to construct the nomogram graph.

Patients and tissue samples collection

A total of 104 HCC patients were enrolled in The Cancer Hospital of the University of Chinese Academy of Sciences (Zhejiang Cancer Hospital) from 2011 to 2020. Each patient was collected one pair of normal and cancer tissue within 30 minutes after surgical resection. *Normal tissue* was defined as greater than 1cm beyond the tumor margin. A frozen section was identified by senior pathologists, who were more than 15 years of practitioners, to exclude tumor lesions under the microscope. HCC lesions, which senior pathologists diagnosed, were acquired about 1cm inside the tumor margin. All patients were pathologically confirmed as Hepatocellular carcinoma. The clinical stage of the tumor was determined according to the Cancer Staging Manual of the American Joint Committee on Cancer(version 8, 2017), while the Edmondson Steiner classification defined the tumor pathological differentiation stage. All 104 patients were enrolled, including 19 females and 85 males. There were 58 patients older than 60 years old and another 46, respectively. The follow-up ended in March 2021 or at death. HCV infections were excluded in our study.

Immunohistochemistry stain

All 104 pairs of lesions were paraffin-fixed tissue. All slice tissue was deparaffinized, rehydrated, and then heated in citric acid buffer (0.01M) at 105°C for 10 min. After antigen recovery, the sliced tissue was blocked with 3% hydrogen peroxide solution and bovine serum albumin. Subsequently, the slides were incubated with rabbit antibodies, including anti-EZH2, anti-GRPEL2, anti-PIGU, anti-PPM1G, anti-SF3B4, anti-TCOF1, anti-TUBG1, anti-TXNRD1, anti-MYCN, anti-NDRG1, anti-SQSTM1, anti-UCK2, at 4°C overnight, then incubated with horseradish peroxidase (HRP)-conjugated secondary antibody at room temperature for 20 min. Finally, the slides were counterstained with hematoxylin, dehydrated in graded alcohol and xylene, cleared, and mounted. The antibody or catalogue and dilutions are listed in Supplementary Table 1.

IHC quantification

All slices were measured by Pannoramic DESK II DW Digital Slide Scanner(Coherent Scientific Ltd.). After the tissue section was set on the scanner, the section gradually moved under the scanner lens. While moving, all tissue information would be scanned and recorded to form a folder containing all image details. The folder was opened by using CaseViewer2.2 software. It can be magnified at any multiple of 1x-400x for observation. Use the TMA plug-in in the Quant Center2.1 analysis software to set the diameter of the chip organization point and the number of rows and columns. The software will automatically generate the number. Use the PatternQuant module in the Quant Center2.1 analysis software to distinguish the brown area (including positive) from the blue part. The two parts of the Mask Area are used as the tissue area; add HistoQunant is merged in the next layer of the brown area. Finally, the area and grayscale of the positive part are calculated based on the optical density.

Pan-cancer analysis for DEGs

To determine the role of the above 13 DEGs, we used the genes to perform pan-cancer analysis to observe the expression, mutation frequency, and copy number change frequency of these genes in pan-cancer. All TCGA pan-carcina data can be downloaded from UCSC XENA. In gene mutation analysis, we calculated the proportion of mutations in each gene in different cancer samples to compare which gene was more likely to mutate. In copy number analysis, the proportion of each gene that increases or decreases in copy number is calculated. We observed changes in gene copy number using the increase in copy number and the decrease in ratio. Finally, we used Deseq2 to calculate the differential expression of each gene. The differential expression of core genes in multiple cancers and the effect of gene expression on the prognosis of different tumors were observed.We used TCGA+GTEx and GSE101685 to validate the core genes. TCGA+GTEx contains 369 cancers and 160 normals, while GSE101685 includes 24 cancer samples and eight normal samples.

Identification of hub genes and functional enrichment analysis

The Gene Set Variation Analysis(GSVA) algorithm is an algorithm that obtains phenotypic scores based on the amount of gene expression associated with different phenotypes. We first collected genes associated with each immune cell. Further, based on the expression of these genes, each immune cell score is obtained. First, we used the Gene Set Variation Analysis(GSVA) to calculate the impact of 24 types of immune cells on HCC. The relationship between core genes and immune cell scores was analyzed. Pearson correlation analysis was further used for the relationship between hub genes and immune cells in HCC. To investigate the relationship between risk score and immune checkpoints, we extracted the expression of 30 immune checkpoints, including the B7-CD28 family (CD274, CD276, CTLA4, HHLA2, ICOS, ICOSLG, PDCD1, PDCD1LG2, TMIGD2, VTCN1), TNF superfamily (BTLA, CD27, CD40LG, CD40, CD70, TNFRSF18, TNFRSF4, TNFRSF9, TNFSF14, TNFSF4, TNFSF9), and another immune checkpoint (HAVCR2, IDO1, LAG3, FGL1, ENTPD1, NT5E, SIGLEC15, VSIR, NCR3). Furthermore, we measured the coexpression relationship between DEGs and Ferroptosis. As all we know, cell death is affected by mitochondria dysfunction generally. Therefore, we downloaded the data from MITOCARTA 3.0 to evaluate mitochondria-related pathways. The GSEA algorithm was used to analyze the effect of DEGs on OXPHOS, Mitophagy and Fe.S containing proteins.

Identification of hub genes and drug sensitivity and regulatory mechanisms

We assessed the drug sensitivity of each patient using pRRophetic (R package, University of Minnesota System), and further used correlation analysis to relate the relationship between prognostic models and tumor drug sensitivity. pOSTAR3 is a database used to predict post-transcriptional regulation of genes, and to understand the transcriptional regulatory relationships of three iron death-associated genes, we constructed a post-transcriptional regulatory network using POSTAR3. GSE106988 is a dataset of RNA-seq performed after knockdown of NDRG1. Using this database. We analyzed the potential functions of NDRG1 and used cytoscape software for the visualization of protein pathway construction.

Statistical analysis

R (version 3.6.2, www.r-project.org) and relative packages for R were used for bioinformatics and statistical analysis. SPSS (Version 25.0) was used for statistical analysis. Visualization mainly used the R package ggplot2(version 3.3.3). The chi-square test and Fisher's exact test were used to evaluate the statistical significance of the relationship between DEGs expression and clinicopathological parameters. The Student's unpaired t-test is used to express customarily distributed DEGs; otherwise, the Mann-Whitney U test is used. The Wilcoxon signed-rank test was used to analyze the difference between HCC and adjacent non-HCC lesion distribution. Survival curves were assessed by the Kaplan-Meier method and Cox proportional hazards regression model, and a log-rank test analyzed the differences. Before performing the Kaplan-Meier analysis, the Best Separation method was used to cut gene expression into high and low groups. $P < 0.05$ was considered as statistical significance. After building the model, we evaluated our model by C-index and decision curve.

Results

Identification of DEGs from the TCGA

The entire analysis flow of the manuscript results is shown in Figure 1. DESeq2 was performed for DEG analysis using RNA-sequencing fragments per kilobase of the exon model per million mapped fragment data from the HCC TCGA database. We found a total of 7009 DEGs, of which 5156 genes were up-regulated and 1853 genes were downregulated (Figure 2A).

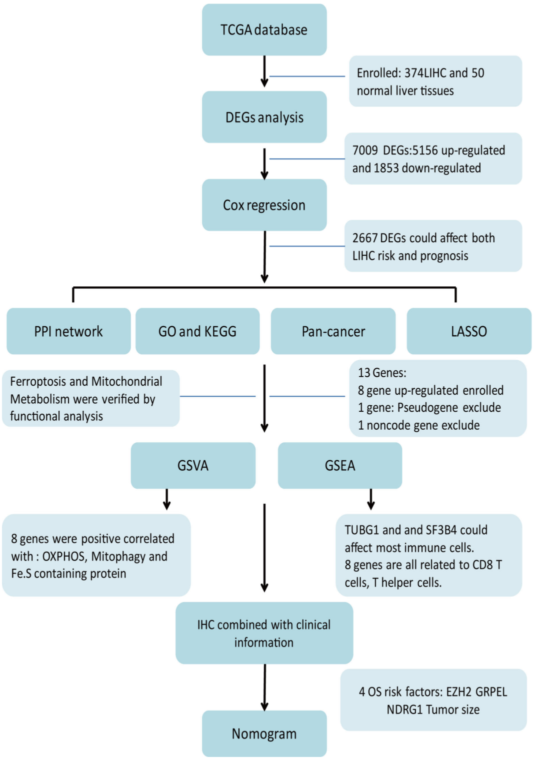

FIGURE 1
Workflow-process diagram of the present study.

Furthermore, to determine the genes that affect the risk and prognosis of HCC, we performed survival analysis by Cox regression for all 7009 genes. We found that 2667 genes might affect the risk of HCC and its prognosis.

Function analysis of DEGs by Gene Ontology and Kyoto Encyclopedia of Genes and Genomes

To better understand the function of the 2667 DEGs, we performed Gene Ontology (GO) and Kyoto Encyclopedia of Genes and Genomes (KEGG) functional enrichment analysis. The GO enrichment analyses. The GO enrichment analysis showed 387 items were related to the DEGs, such as histone −serine phosphorylation and mitotic DNA replication checkpoint. KEGG analysis showed that the DEGs were mainly involved in the nuclear lamina prespliceosome mitotic DNA replication checkpoint. Other pathways included cellular senescence, DNA replication, and oxidation (Figure 2B). Supplementary Tables 2, 3 show more details of GO and KEGG analyses.

Risk scoring model for the application of the LASSO algorithm for HCC

We used LASSO regression to eliminate 2,667 covariates of DEGs that affect the risk of HCC and its prognosis (16). We screened the LASSO regression model using $\lambda = 0.08869376$ (Figure 2C). The LASSO regression visualization results are shown in Figure 2D. Finally, 13 hub genes that might predict the prognosis of HCC were obtained. These 13 genes that were DSTNP2, EZH2, GRPEL2, MYCN, NDRG1, PIGU, PPM1G, SF3B4, SQSTM1, TCOF1, TUBG1, TXNRD1, and UCK2. The details of these hub genes are shown in Tables 1, 2. We excluded the pseudogene DSTNP2 because we were more interested in protein expression genes. In addition, we chose eight upregulated genes in HCC and compared with healthy tissues as hub genes. These genes were TXNRD1, TUBG1, SF3B4, PPM1G, PIGU, NDRG1, GRPEL2 and EZH2.

Pan-cancer analysis of DEGs

The eight hub genes upregulated in HCC mentioned above were differentially expressed as shown by pan-cancer analysis (Figure 3A) These eight genes were differentially expressed in digestive tract tumors, such as stomach adenocarcinoma and esophageal carcinoma. GRPEL2 and EZH2 were highly expressed in most cancer types, such as HCC, esophageal carcinoma, and stomach adenocarcinoma. NDRG1 was also highly expressed in HCC, lung squamous cell carcinoma, and head and neck squamous carcinoma. Uterine corpus endometrial carcinoma was associated with genetic mutations in the analyzed samples, and there were only a few mutations in the remaining types of cancer (Figure 3B). In addition, we performed a copy number alteration analysis and showed that most cancer types, inculding HCC, had minor changes in the copy number (Figure 3C). These findings indicated that these eight hub genes were characteristic genes of HCC, and their expression may not be affected by other genomic changes. We then examined the effect of these eight genes on the prognosis of all cancers. We found that these eight genes might affect the prognosis of LGG, HCC, and LUAD. Therefore, a high expression of these genes is a risk factor for these cancers (Figure 3D).

Functional analysis of genes

We conducted a functional analysis of the eight genes described above. First, we used the Gene Set Variation Analysis (GSVA) to calculate the effect of 24 types of immune cells on HCC. This was performed by comparing the correlations between the eight hub genes and immune cells. We found that TUBG1 and SF3B4 could affected most immune cells, and eight of the hub

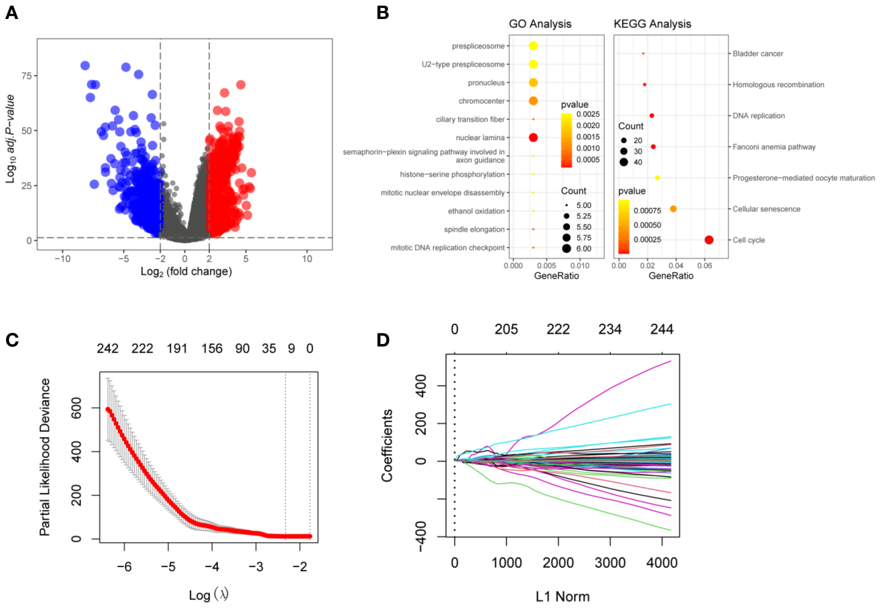

FIGURE 2
Identification of The Differentially Expressed Genes (DEGs) in HCC and normal liver tissues: **(A)** Volcano plot of the DEGs in TCGA dataset. Log|FC|>2 was considered as DEGs In the figure, red represents high-expression genes, and blue represents low-expression genes **(B)** Functional analyzing by GO and KEGG. The yellower the color indicates that the result is more meaningful, and the larger the circle, the more genes are enriched within the result. **(C)** LASSO Cox regression was performed to identify the DEGs related to the prognosis of HCC (λ = 0.08869376). **(D)** Visulization of LASSO Cox regression. These 13 genes that were DSTNP2, EZH2, GRPEL2, 227 MYCN, NDRG1, PIGU, PPM1G, SF3B4, SQSTM1, TCOF1, TUBG1, TXNRD1, and UCK2 might predict prognosis of HCC.

genes were positively related to CD8 T cells and T helper cells. These findings indicated that these eight genes might affect the prognosis of HCC by affecting T helper cells (Figure 4A). Eight of the immune checkpoint genes were related to TNFRSF9, TNFSF9, HAVCR2, and ENTPD1 (Supplementary Table 8 and Supplementary Figure 5). We also analyzed the correlations between the eight hub genes and ferroptosis-related genes. The results showed that the eight genes are positively correlated with most of the ferroptosis-related genes (Supplementary Figure 1, Supplementary Table 5). There was a strong positive correlation between FA complementation group D2(FANCD2), and three characteristic genes, namely EZH2, TUBG1, and PPM1G (Figure 4B). These results indicated that these eight hub genes may affect ferroptosis in HCC. We used a gene set enrichment analysis (GSEA) algorithm to analyze the relationship between the eight hub genes and mitochondria-related pathways. We found that oxidative phosphorylation (OXPHOS), apoptosis, mitophagy, and Fe.S-containing proteins were positively related to these genes according to the enrichment score (Figure 4C). The enrichment scores were positively related to OXPHOS, mitophagy, and Fe.S-containing proteins. On the basis of these results, we hypothesize that ferroptosis affects the prognosis of HCC *via* mitochondria-related mechanisms.

Validation of gene expression differences and the clinical significance of the prognosis

We measured the expression of the 13 identified hub genes (EZH2, GRPEL2, MYCN, NDRG1, PIGU, PPM1G, DSTNP2, SF3B4, SQSTM1, TCOF1, TUBG1, TXNRD1, and UCK2) by immunohistochemistry (IHC) in tissue samples of 104 patients. We found that eight genes, EZH2, GRPEL2, PIGU, PPM1G, SF3B4, TUBG1, TXNRD1, and NDRG1, were expressed differently between HCC and adjacent non-HCC (Supplementary Table 5, Supplementary Figures 2, 3 and Figure 5A). These results were consistent with bioinformatics analysis. Moreover, the expression levels of these genes were significantly different between HCC and adjacent non-HCC lesions (Supplementary Table 5). In conclusion, these eight genes could be used as potential risk factor indicators to determine clinical indications for prognosis. To further ensure the accuracy of core genes, we used TCGA+GTEx and GSE101685 data to further analyze the differential expression of these genes. We found that the eight hub genes identified above were all differentially expressed (Figure 6 and Supplementary Table 7).

TABLE 1 Details of the Hub genes.

Gene Symbol	Gene name	Ensembl ID	Transcript Biotype	Chromosome	Start Position	End Position	Band
DSTNP2	Destrin Pseudogene 2	ENSG00000248593	processed_transcript	12	6884682	6885786	p13.31
EZH2	Enhancer of zeste 2 polycomb repressive complex 2 subunit	ENSG00000106462	nonsense_mediated_decay	7	148807257	148884321	q36.1
GRPEL2	GrpE Like 2, Mitochondrial	ENSG00000164284	protein_coding	5	149345430	149354583	q32
MYCN	MYCN Proto-Oncogene	ENSG00000134323	protein_coding	2	15940550	15947007	p24.3
NDRG1	N-Myc Downstream Regulated 1	ENSG00000104419	protein_coding	8	133237175	133302022	q24.22
PIGU	Phosphatidylinositol Glycan Anchor Biosynthesis Class U	ENSG00000101464	protein_coding	20	34560542	34698790	q11.22
PPM1G	Protein Phosphatase, Mg2+/Mn2+ Dependent 1G	ENSG00000115241	retained_intron	2	27381195	27409591	p23.3
SF3B4	Splicing Factor 3b Subunit 4	ENSG00000143368	protein_coding	1	149923317	149927803	q21.2
SQSTM1	Sequestosome 1	ENSG00000161011	processed_transcript	5	179806398	179838078	q35.3
TCOF1	Treacle Ribosome Biogenesis Factor 1	ENSG00000070814	protein_coding	5	150357629	150400308	q32
TUBG1	Tubulin Gamma 1	ENSG00000131462	retained_intron	17	42609641	42615238	q21.2
TXNRD1	Thioredoxin Reductase 1	ENSG00000198431	protein_coding	12	104215779	104350307	q23.3
UCK2	Uridine-Cytidine Kinase 2	ENSG00000143179	protein_coding	1	165827614	165911618	q24.1

Obtained from National Center of Biotechnology Information (NCBI) database.

TABLE 2 Hazard ratio of 14 hub genes.

gene	HR	95%CI	p	p.val
EZH2	1.144	1.096 - 1.195	9.71E-10	< 0.001
UCK2	1.034	1.025 - 1.044	1.88E-12	< 0.001
PIGU	1.078	1.048 - 1.108	1.27E-07	< 0.001
SF3B4	1.014	1.01 - 1.019	2.25E-10	< 0.001
TCOF1	1.037	1.026 - 1.049	1.01E-10	< 0.001
DSTNP2	4.334	2.892 - 6.495	1.21E-12	< 0.001
TUBG1	1.02	1.013 - 1.028	1.41E-07	< 0.001
GRPEL2	1.261	1.179 - 1.347	9.94E-12	< 0.001
PPM1G	1.015	1.01 - 1.019	1.32E-10	< 0.001
MYCN	1.177	1.109 - 1.248	5.87E-08	< 0.001
TXNRD1	1.002	1.001 - 1.003	3.52E-12	< 0.001
SQSTM1	1.103	1.001-1.003	1.53E-10	< 0.001
NDRG1	1.001	1 - 1.001	5.79E-07	< 0.001

HCC prognosis-related model construction

In addition to analyzing expression of the eight hub genes, we collected basic information on all 104 patients, such as sex, age, histological differentiation, vascular cancer embolus, cirrhosis, tumor size (cm), alpha-fetoprotein concentrations (ng/mL), hepatitis B surface antigen concentrations, alanine aminotransferase, underlying diseases, and total bilirubin concentrations. We excluded hepatitis C viruse infection

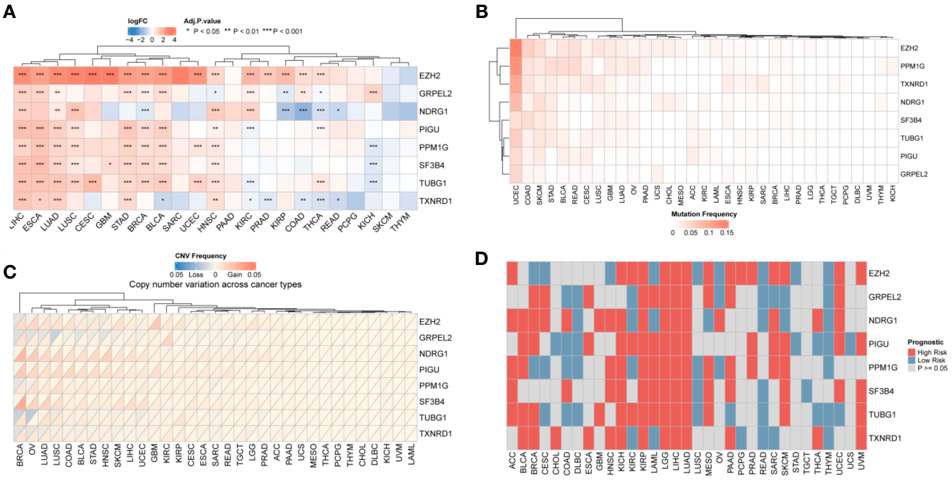

FIGURE 3
Pan-cancer results of hub genes. **(A)** Differential Expression of genes: eight genes were differentially expressed in most cancer types. The darker the color, the greater the fold change **(B)** Mutation frequency: the hub gene mutation was relative stable in all types of cancer except UCEC. **(C)** Copy number variation of hub genes. HCC had minor changes in the copy number of the 8 hub genes **(D)** Prognosis of hub genes. The red square represents a risk factor in the cancer, and the blue square represents a protective factor. Gray indicates that the prognosis of the tumor does not affect the prognosis.

patients in our study. These clinical factors are generally considered indicators of the prognosis of HCC. In our dataset, the one-factor survival analysis showed that a larger tumor size and positive vascular cancer embolus indicated a poor prognosis. Therefore, we incorporated these factors into the Cox regression model in the multivariate analysis. The high expression of EZH2, GRPEL2, TCOF1 and NDRG1 genes suggested a poor prognosis, as shown in the multivariate regression analysis (Table 3, Figure 5B). Furthermore, a nomogram was used for visualization to better use as a clinical prognostic model. The nomogram showed that a larger tumor size and higher EZH2, GRPEL2, and NDRG1expression predicted the higher likelihood of a worse prognosis (Figure 5C). The nomogram was able to predict the probability of 1- and 3-year survival (Figure 5D). These findings indicated a close relation to survival, which suggested that our nomogram may be a reliable prognostic model for HCC. Furthermore, we computed the C-index to evaluate our model. The C-index of this model was 0.811 (0.797-0.825). A decision curve showed that this model had reliable clinical practicability (Supplementary Figure 4).

HCC prognosis-related model functional analysis

To further understand the function of the HCC prognostic model, we analyzed the relationship between model scores and clinical parameters. We found that the prognostic model score was mainly related to alpha-fetoprotein, T stage. Among them, the model score is higher when the disease is more severe (Figure 7A). In addition, we analyzed the relationship between 3 genes and HBV infection. EZH2 was related to HBV infection, and the expression of EZH2 expression was high in patients with HBV infection (Supplementary Table 9). In addition, GSVA scores were calculated for tumor-related pathways, and the correlations between model scores and tumor-related pathways were determined. We found that the HCC model was mainly related to the inflammatory response and other pathways (Figure 7B).

Prognostic models and drug resistance

Our analysis using GSE106988 showed that NDRG1 was mainly associated with functions such as RNA shearing (Figure 8A), but the other two genes need to be verified in subsequent experiments. After analyzing the targets of anti-tumor drug sensitivity action in patients with HCC, we found that the prognostic model of ferroptosis was associated with multiple chemotherapy efficacy, with the strongest correlation with axitinib (Figure 8B). We also analyzed the function of the three core genes for ferroptosis and the regulatory relationships. Finally, to understand the post-transcriptional regulatory relationships of these three genes, analysis using POSTAR3 analysis showed that these three genes were affected by multiple post-transcriptional regulatory genes, among which

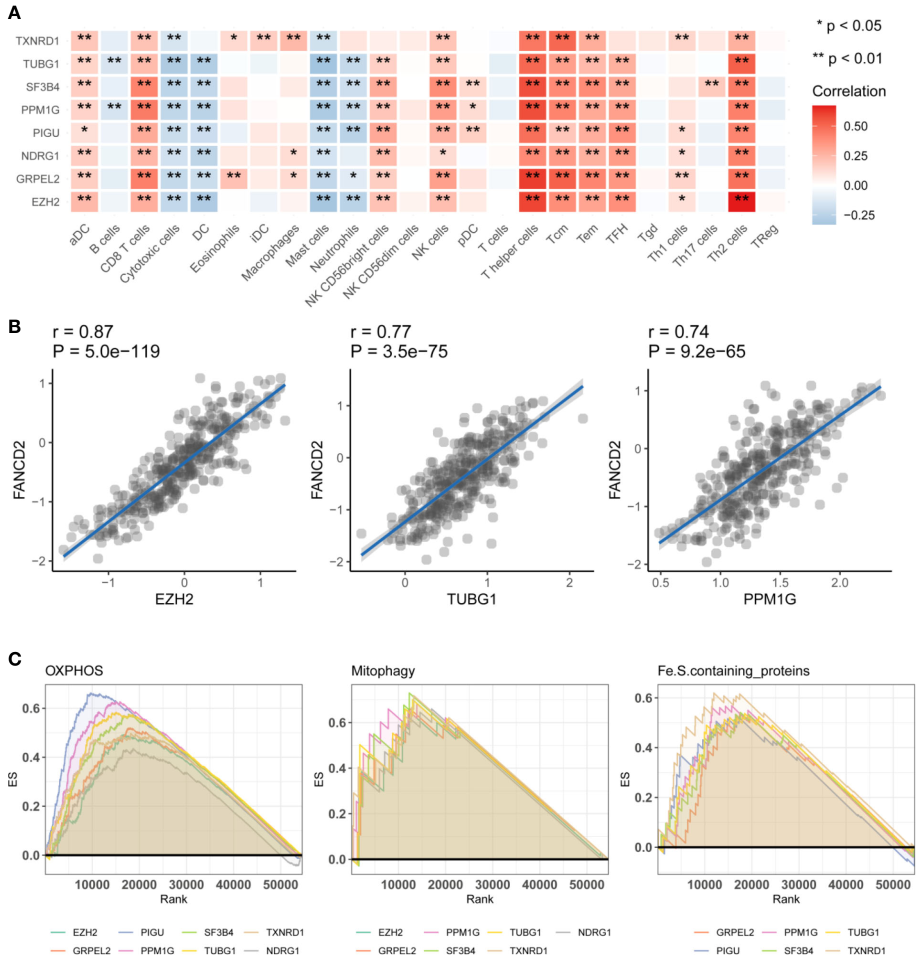

FIGURE 4

Functional analysis of the hub genes. **(A)** Immunoinfiltration analysis. Gene Set Variation Analysis were used to calculate the effect of 24 types of immune cells on HCC. Significance is presented by using *p < 0.05, **p < 0.01. The darker the red color, the higher the correlation coefficient. **(B)** The correlation analysis between hub genes and ferroptosis related genes FANCD2. EZH2, TUBG1, PPM1G were significantly positive effective with FANCD2. **(C)** The correlation analysis of three hub genes, EZH2, GRPEL2, NDRG1, and FANCD2. Gene Set Enrichment Analysis, (GSEA) the hub genes were enriched in OXPHOS, Mitophagy, Fe.S.containing proteins. It has been partially confirmed that ferroptosis and mitochondrial metabolism were related to prognosis in HCC.

IGF2BP2, FIPILI, TARDBP, ELF2, ATXN2, DDx3X, AGO2, IGF2BP1, and HNRNPC regulated these three genes simultaneously (Figure 8C).

Discussion

HCC is a common and highly malignant tumor. Patients with HCC have a poor prognosis (17). At present, surgery is the most effective treatment method for HCC (18). However, at diagnosis, most patients with HCC show intra- and extra-hepatic metastases, vascular tumor thrombi and inadequate future liver volume, which indicate that the opportunity for surgery has already passed. With the development of advanced therapies, various emerging treatments have achieved positive results (19, 20). However, because of the complexity of the genetic background of HCC, the benefits of these treatments remain unclear (20, 21). Therefore, in-depth studies of the pathogenesis of HCC, including machine learning, will have clinical significance for predicting the interaction of hub genes and investgating prognostic-related molecular markers for individuals. In this study, we constructed a prognostic model combined with clinical information, functional analysis, and pan-cancer analyses to verify our bioinformatic results (22).

In this study, we used the TCGA data sets to predict cancer the risk of HCC and its prognosis. We found that the DEGs were

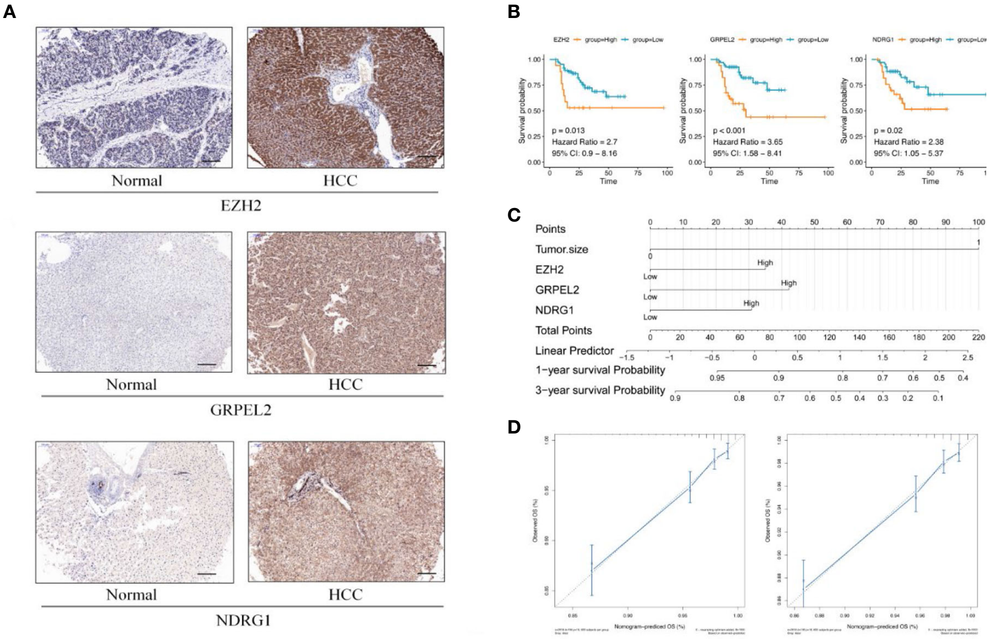

FIGURE 5
Establishment of prognostic model **(A)** Differential expression between HCC and adjacent non-HCC lesions. IHC image for EZH2, GRPEL2, NDRG1, paired with non-LIHC tissues and LIHC tissues. **(B)** KM curves of EZH2, GRPEL2, NDRG1. Higher expression of hub genes meant poor prognosis of HCC. **(C)** Nomogram was for visulizing the prognostic model. Three factors, EZH2, GRPEL2, NDRG1, and tumor size, were enrolled in the prognostic model to predict the survival rate of 1,3 years survival in HCC **(D)** The nomogram calibration curves of 1-, 3-year survival probabilities. The tool bar =100μm.

highly related to DNA replication, oxidation, and inflammatory response. According to previous studies, these mechanisms are consistent with the activity of tumor cell growth and mitochondrial metabolism (23). Therefore, we speculate that abnormal mitochondrial function is related to the occurrence and development of HCC. The LASSO regression analysis was performed to generate a prognostic signature. We found 13 hub genes that were potentially related to the prognosis of HCC. Eight upregulated genes (EZH2, GRPEL2, PIGU, PPM1G, SF3B4, TUBG1, TXNRD1, and NDRG1) were not only found to be tumorigenesis risk factors, but also factors of a poor prognosis of HCC. In addition, we analyzed 104 clinical samples to validate our predictions. These eight genes were differentially expressed between HCC and adjacent non-HCC lesions, which suggested that these genes could be used as biomarkers for risk factors. The multivariate regression analysis showed that EZH2, NDRG1 and GRPEL2, as well as the tumor size were independent factors for the prognosis of HCC. According to recent surveys, TOCF1 (11) and UCK2 (24) may also indicate the prognosis in the patients with HCC. Unfortunately, our study did not show any statistical significance for the differentiated expression of TOCF1 or UCK2. Therefore, a larger sample size and multicenter study would be useful to further validate the relationship between the expression of these two genes and the prognosis of HCC.

We also constructed a prognostic nomogram model, which included EZH2, GRPEL2, NDRG1, and the tumor size. EZH2 is a transcriptional suppressor gene (25). EZH2 combines with EED, SUZ12, and RBBP4 to generate a PRC2 subunit, which is overexpressed in multiple types of cancer (26). EZH2 has a bidirectional tumorigenic effect involving mTOR signaling, as shown in EZH2-deficient leukemia cells (27). In addition, detecting EZ gene expression by tissue puncture biopsy can be used as a molecular marker for the prognosis of patients with HCC (28). There have been several recent clinical trials of EZH2 inhibitors in various cancers being studied (29–32). Our study showed that EZH2 was involved in autophagy, which is consistent with previous studies. EZH2 may also have specific effects on mitophagy, ferroptosis, and OXPHOS. Determining the specific mechanism of EZ2H should be considered in future research. NDRG1 plays a crucial role in angiogenesis, proliferation, invasion, and prognosis of HCC (33, 34). NDRG1 may also be a molecular marker for metastasis and prognosis in HCC. NDRG1 may predict the recurrence of HCC in liver transplant patients after surgery (35). This gene plays an anti-tumor role by involving the Wnt signaling pathway and other carcinogenesis signaling pathways. We speculate that NDRG1 may be involved in metabolic processes related to ferroptosis. However, more experimental studies still need to verify the mechanism of NDRG1 in ferroptosis. Overexpression

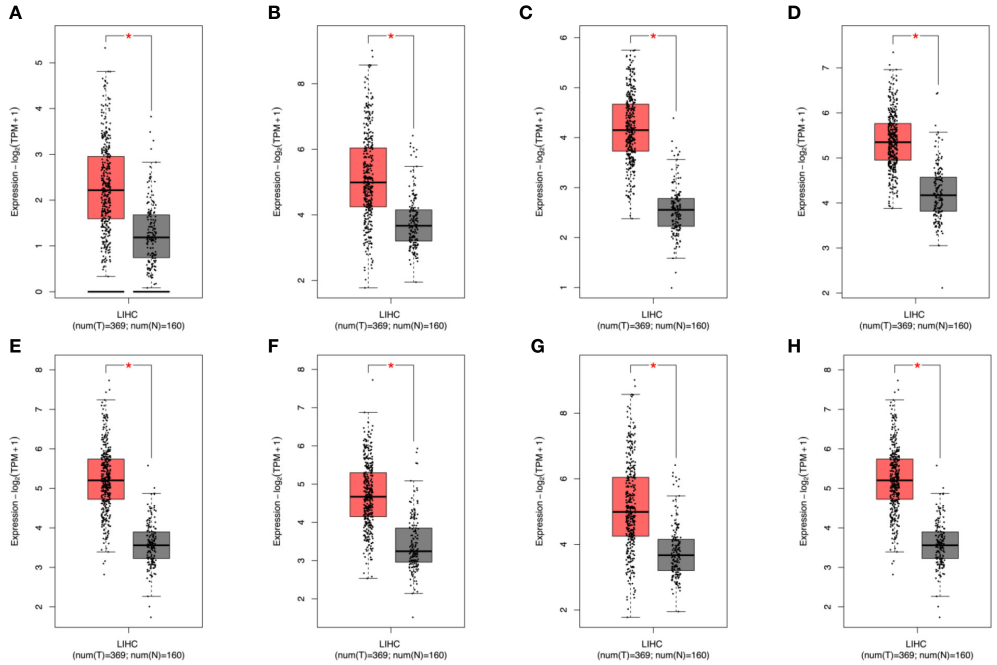

FIGURE 6
TCGA+GTEx and GSE101685 data to further analyze the differential expression of genes. After analysis, it was found that the eight genes verified above were all differentially expressed. In the figure, red represents cancer patients and gray represents normal samples **(A–H)** EZH2,GRPEL2, PIGU, PPM1G, SF3B4, TXNRD1, NDRG1, TUBG1. * stands for *P* value < 0.05.

of GRPEL2 affects the stability of mitochondrial proteins, and GRPEL2 may protect protein stability under mitochondrial oxidative stress (36). GRPEL2 is responsible for maintaining mitochondrial homeostasis through the nuclear factor-kappa B pathway, which affects the cell cycle in HCC (37). In particular, the composition of Fe.S-containing proteins is related to DEGs, may have an anti-tumor effect *via* mitochondrial-related pathways, such as complex I, OXPHOS, and mitophagy. Our finding suggested that upregulated NDRG1 could be related to poor prognosis through mitochondrial-related proteins in HCC. On the basis of the results of available datasets, we found that NDRG1 silencing was associated with various tumor biological functions such as RNA splicing, histone modification, and peptidyl-lysine modification. We concluded that the ferroptosis-related model was associated with the prognosis of HCC. These 3 genes may be essential targets and regulatory proteins in the biological progression of HCC. Using drug sensitivity analysis, we found a significant negative association of multiple anti-cancer drugs with the model. Multiple post-transcriptional regulatory mechanisms may be involved. Among them, Axitinib is an anti-tumor agent used clinically in adult patients with progressive renal cell carcinoma (RCC) who have failed prior treatment with a tyrosine kinase inhibitor or cytokine. This study provides some theoretical reference to determine whether Axitinib can be administered to patients with HCC based on ferroptosis-related prediction models. However clinical trials are still required to validate this theory. We also included a clinical factor, tumor size, in the prognosis model. Patients with more extensive tumor volumes have a worse prognosis, because the tumor has adapted to the body's growth or because the tumor is discovered late. Therefore, the current research results suggest that EZH2, GRPEL2, NDRG1, and tumor size are reliable prognostic indicators.

The pan-cancer analysis results suggest that the eight hub genes (TXNRD1, TUBG1, SF3B4, PPM1G, PIGU, NDRG1, GRPEL2, and EZH2) were differentially expressed in gastrointestinal tumors. These eight genes may have unique roles in the digestive tract and are relatively stable in genomics. Cirrhosis-related HCC characteristics of HBV infection have a particular tumor immune microenvironment. This microenvironment may be in a state of immunosuppression over a long period, may play a unique role in promoting HCC to escape host immune surveillance (38). Therefore, we speculate that prognosis-related genes could affect the prognosis through the tumor immune microenvironment in HCC. However, further studies are required to determine the mechanisms of interaction between hub genes and immune cells. We also wanted to determine the role of the tumor microenvironment and energy metabolism in HCC. One of our study aim was to detect an unknown mechanism that links programmed cell

TABLE 3 Survival analysis combined with clinical parameter by Immunosotochemistry.

Variability	n	One-factor cox regression model		Multi-factor cox regression model	
		HR(CI 95%)	*P*	HR(CI 95%)	*P*
Gender					
Female	19	2.218(0.968, 5.086)	0.060		
Male	85				
Age					
>60	58	0.917(0.428,1.965)	0.823		
<=60	46				
Histological differentiation					
Poorly	29	0.606(0.229, 1.603)	0.313		
Well	75				
Microvascular cancer embolus					
Positive	65	0.433(0.198,0.943)	0.035	1.661(0.739,3.731)	0.219
Negative	39				
Cirrhosis					
Positive	64	0.565(0.265,1.204)	0.139		
Negative	40				
Tumor size (cm)					
≤5	42	6.167(2.487,15.293)	8.60E-05	5.358(2.126,13.506)	3.73E-04
> 5	62				
AFP (ng/mL)					
> 40	41	0.882(0.403,1.931)	0.754		
≤40	63				
ALT (U/L)					
> 40	39	1.649(0.772,3.520)	0.196		
≤40	65				
Total bilirubin					
> 17.1	45	1.680(0.787,3.585)	0.180		
≤17.1	59				
Albumin					
≤40	57	1.258(0.584,2.711)	0.558		
> 40	40				
EZH2					
high	87	0.368(0.161,.843)	0.018	0.272(0.113,0.659)	0.004
low	17				
GRPEL2					
high	70	0.272(0.126,0.587)	0.001	0.321(0.148,0.697)	0.004
low	34				

(Continued)

TABLE 3 Continued

Variability	n	One-factor cox regression model		Multi-factor cox regression model	
		HR(CI 95%)	*P*	HR(CI 95%)	*P*
PIGU					
high	74	0.614(0.271,1.388)	0.241	0.663(0.286,1.537)	0.338
low	30				
PPMIG					
high	74	0.514(0.226,1.171)	0.113	0.676(0.285,1.606)	0.375
low	30				
DSTP2					
high	47	1.252(0.588,2.669)	0.560	0.743(0.336,1.647)	0.465
low	57				
SF3B4					
high	70	0.885(0.383,2.041)	0.774	0.886(0.377,2.081)	0.780
low	34				
TCOF1					
high	52	0.683(0.319,1.465)	0.328	0.503(0.230,1.104)	0.087
low	52				
TUBG1					
high	41	1.641(0.770,3.499)	0.199	1.102(0.484,2.511)	0.817
low	63				
txnRD1					
high	42	1.091(.509,2.340)	0.823	0.714(0.311,1.641)	0.428
low	62				
Mycn					
high	49	0.577(0.266,1.254)	0.165	0.590(0.268,1.300)	0.191
low	55				
NDRG1					
high	70	0.420(0.197,0.894)	0.024	0.408(0.190,0.878)	0.022
low	34				
SQSTM1					
high	49	1.031(0.483,2.200)	0.938	1.078(0.501,2.321)	0.848
low	55				
UCK2					
high	49	0.924(0.433,1.971)	0.838	0.456(0.194,1.071)	0.072
low	55				

Tumor size and Microvascular cancer embolus was considered as the clinical parameters which effect prognosis. HR, hazard ratio; CI, confidence interval. $P < 0.05$ considered as statistical significance. Survival analysis combined with clinical parameter by Immunosotochemistry. We enrolled all 104 pairs of HCC and adjacent non-HCC lesions. All patients were HBsAg positive. There are ten clinical factors were enrolled, which are Gender, Age, Histological differentiation, Microvascular cancer embolus, Cirrhosis, Tumor size (cm), Alpha-fetoprotein (AFP) (ng/mL), Alanine aminotransferase (ALT), Total bilirubin, Albumin. EZH2, GRPEL2, NDRG1, Tumor size were independent prognostic risk factors. (P < 0.05) Albumin test results were missing in 2 of 104 patients.HCV infection was excluded in the cohort.

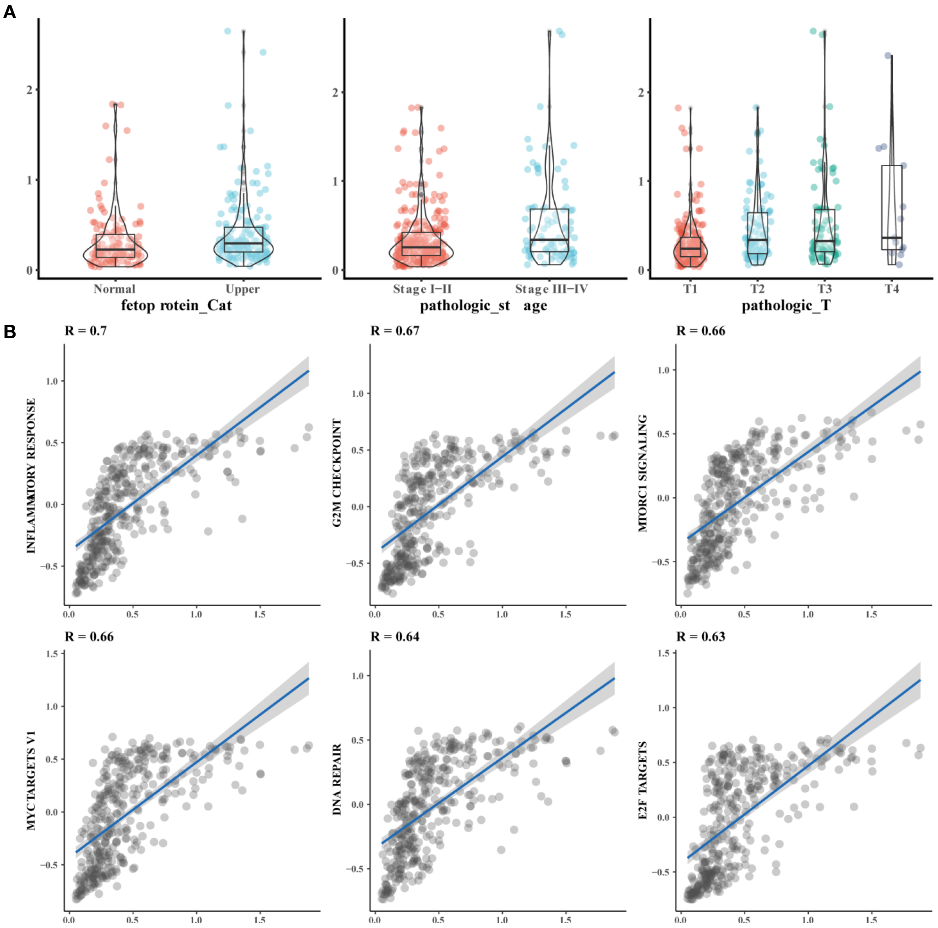

FIGURE 7
Functional of prognosis related model function. **(A)** The model score is correlated with the severe of clinical parameters Alpha-fetoprotein abnormalities, the higher the pathologic stage and the higher the T stage, the higher the prognostic model score; **(B)** The Model was mainly related to the inflammatory response and other pathways. GSVA scores were performed on tumor-related pathways, and the correlation between model scores and tumor-related pathways was observed through correlation analysis of pathway scores and model scores.

death, and mitochondrial metabolism in HCC. Therefore, we performed an immune infiltration analysis and a GSEA analysis. In the immune infiltration analysis, we found that expression of the eight hub genes (TXNRD1, TUBG1, SF3B4, PPM1G, PIGU, NDRG1, GRPEL2, EZH2) and the immune infiltration of T helper cells, Tcm cells, and Th2 cells were related to HCC. Studies have shown that the infiltration of multiple immune cells plays a role in HBV-related HCC (39). T cells may mediate cell death by various mechanisms. Previous studies have demonstrated that Th17 cells may activate and induce cell death by Fas-mediated apoptosis, which is consistent with our results (40, 41).

Ferroptosis is an iron-dependent regulatory form of cell death caused by excessive lipid peroxidation, which is associated with the occurrence and response to treatment of various types of tumors. Ferroptotic injury triggers inflammation-related immunosuppression in the tumor microenvironment, which favors tumor growth. Ferroptosis can also lead to the activation of the Renin-angiotensin system, TP53 and other signaling pathways, which then leads to poor survival of patients with HCC (42). We constructed a model in which EZH2, TUBG1, and PPM1G were strongly correlated with the FANCD2. FANCD2 is an intersection protein associated with multiple ferroptosis in clear cell renal cell carcinoma and bladder cancer (43, 44). According to our results, EZH2, TUBG1, and PPM1G may play a role in ferroptosis through the key gene FANCD2. Fe.S-containing proteins were also significantly correlated with the eight hub genes. Current research has shown that Fe.S proteins participate in vital pathways such as oxidative phosphorylation and iron metabolism. Fe.S proteins are involved in the critical steps of the pathway that involve the maturation of mitochondrial proteins. The vital predisposing

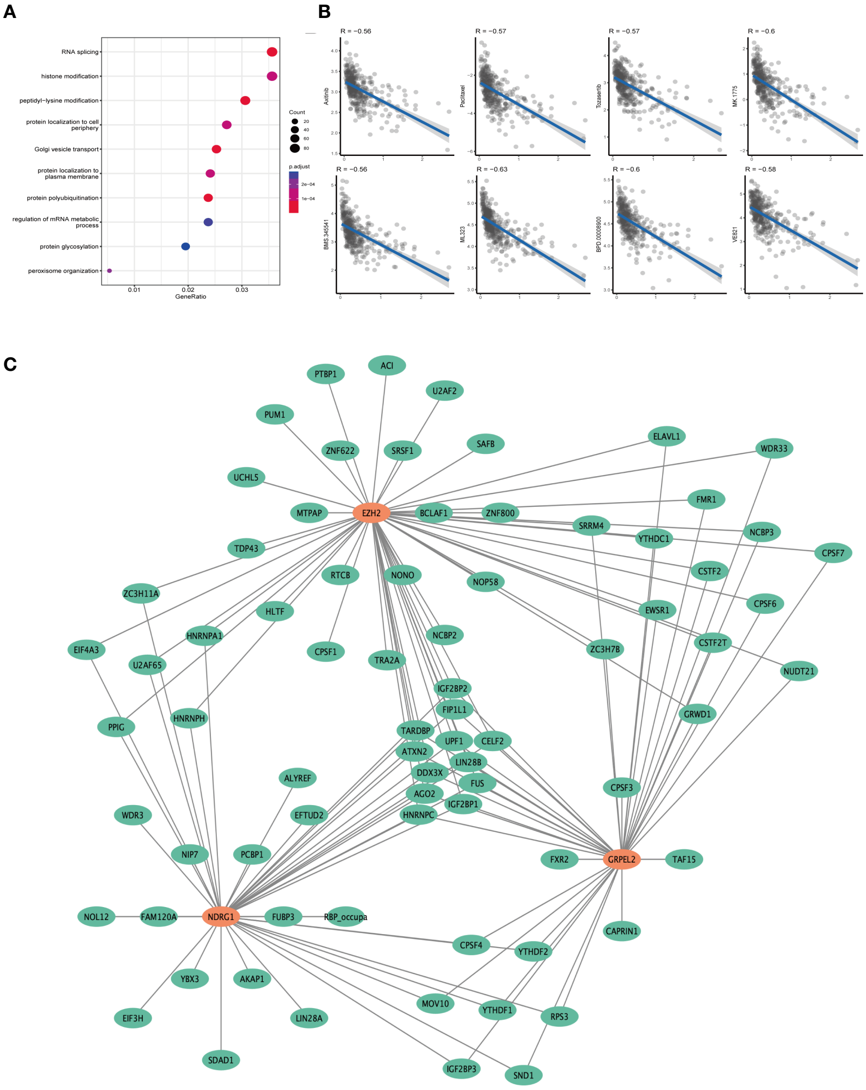

FIGURE 8
Prognostic model related related functional analysis. **(A)** Functional enrichment analysis results of NDRG1 knockout dataset. The bluer the color in the figure, the more meaningful the result. **(B)** The relationship between prognostic model and drug sensitivity. Each point in the graph represents the model score of a sample as well as the drug sensitivity score. **(C)** Post-transcriptional regulatory network of genes associated with prognostic models. The orange circle represents the gene in the model, and the green circle represents the poor post-transcriptional regulatory protein.

factors for ferroptosis are iron leakage, lipid peroxidation, and increased ROS (45, 46). The suppression of ferroptosis may contribute to tumor progression and survival (47). Some scholars believe that mitochondria play a crucial role in ferroptosis caused by erastin or cystine deprivation. However, a lack of mitochondria is affected by erastin concentrations, leading to cell death, which suggests that mitochondria may participate in ferroptosis through other currently unknown mechanisms (48). Because of that, ferroptosis mediates various tumor effects. In different damage-associated molecular patterns, ferroptosis can protect cells from drug damage (42). Such mechanisms may aggravate the damage caused by immune cells (49). Therefore, we speculate that the development of HCC may be affected by ferroptosis *via* mitochondrial metabolism and ROS. Additional mechanistic studies are still required to confirmed this possibility.

On the basis of the above-mentioned verification results of our model's function, ferroptosis, mitochondrial metabolism, ROS, and immune infiltration are closely related to the inflammatory background of HCC. The background of hepatitis B infection and chronic inflammation exhibits a unique immune microenvironment (50, 51). Inflammation is tightly associated with cell death (52). Functional studies have shown that clinical parameters and inflammation are positively correlated with the prognostic models. Programmed cell death is affected by chronic inflammation, which results in tissue DNA damage (53). This study showed that our model was positively correlated with inflammation and DNA damage repair. Therefore, this model can reflect the inflammation associated with cell death in HCC. mTOR complex I can regulate endoplasmic reticulum (ER) stress (54). Transcription factor families, such as Myc and E2F, target various tumorigenesis and mediate inflammatory progression (55). Therefore, our model can reflect the prognosis of HCC in the context of inflammation.

There are some limitations to our study. First, this study recruited 104 patients with HCC in East China. This sample size was limited to a specific race and a single center. To apply our findings in the clinic, multicenter studies with a larger sample size are required. In particular, whether our prognostic model can be used as a biomarker in a large sample size needs to be investigated. Second, we developed a prognostic model for cell death associated with ferroptosis. However, several mechanisms have not yet been fully determined, and more evidence is required. In particular, ferroptosis-related therapeutic regimens should be designed for these targets and validated in *in vivo* and *in vitro* studies. Finally, further experiments are still required to verify the mechanism of action of FANCD2 through ferroptosis affecting the inflammatory and immune microenvironment of HCC. The most appropriate treatment required for patients with a high risk of recurrence and the most suitable types of surgery or adjuvant treatment required to prolong patients' overall survival are still unknown.

In conclusion, we used bioinformatics analysis methods to predict DEGs for the occurrence and development of HCC and found eight hub genes (EZH2, GRPEL2, PIGU, PPM1G, SF3B4, TUBG1, TXNRD1, and NDRG1). We further verified the clinical tissue sample results to develop a reliable nomogram, which could be used as a prognostic model for HCC. These hub genes are involved in mitophagy, OXPHOS, and Fe.S-containing proteins. EZH2, TUBG1, and PPM1G are related to the ferroptosis gene, FANCD2, and may be involved in tumor biological behaviors mediated by ferroptosis. The background of chronic hepatitis may play an essential role in the development of HCC. According to our data set, three genes, EZH2, GRPEL2, and NDRG1, and one clinical factor, tumor size, could be used as reliable indicators for evaluating the prognosis in patients with HCC.

Data availability statement

Publicly available datasets were analyzed in this study. This data can be found here: The Cancer Genome Atlas (TCGA) database.

Ethics statement

The studies involving human participants were reviewed and approved by the Human Ethics Review Committee of The Cancer Hospital of the University of Chinese Academy of Sciences (Zhejiang Cancer Hospital). The Ethical Review Committee number of this study was IRB-2021-234. The patients/participants provided their written informed consent to participate in this study.

Author contributions

YZ, JW, FH made substantial contributions to conception and design; FH and YZ designed the study and performed the analysis; XZ and LS acquired the data, YC and FH performed the analysis and interpretation of data; FH, YX, LX, LS drew the Figures and tables; FH and DC took part in drafting the article or revising it critically for important intellectual content; FH and YZ gave final approval of the version to be published. XC gave a direction of this study and took part in the manuscript. XC, FH, YZ gave financial support through their own research funds. All authors contributed to the article and approved the submitted version.

Funding

This work was supported by the Medical and public health projects in Zhejiang Province (2022499342, FH); the Medical and public health projects in Zhejiang Province (2022505268, YZ); Diagnosis And Therapy Center of Upper Gastrointestinal Tumor (JBZX-202006, XC).

Acknowledgments

We would like to thank Dr. Hao Li (The First Hospital of China Medical University, Shenyang) for the guidance of statistics support to the present study. Thanks to Mrs. Han for her great support to the family over the years.

Conflict of interest

The authors declare that the research was conducted in the absence of any commercial or financial relationships that could be construed as a potential conflict of interest.

Publisher's note

Supplementary material

The Supplementary Material for this article can be found online at: https://www.frontiersin.org/articles/10.3389/fonc.2022.972434/full#supplementary-material

References

1. Estes C, Razavi H, Loomba R, Younossi Z, Sanyal AJ. Modeling the epidemic of nonalcoholic fatty liver disease demonstrates an exponential increase in burden of disease. *Hepatology* (2018) 67:123–33. doi: 10.1002/hep.29466

2. Michielsen PP, Francque SM, van Dongen JL. Viral hepatitis and hepatocellular carcinoma. *World J Surg Oncol* (2005) 3:27. doi: 10.1186/1477-7819-3-27

3. Bray F, Ferlay J, Soerjomataram I, Siegel RL, Torre LA, Jemal A. Global cancer statistics 2018: GLOBOCAN estimates of incidence and mortality worldwide for 36 cancers in 185 countries. *CA Cancer J Clin* (2018) 68:394–424. doi: 10.3322/caac.21492

4. Wu J, Lu WY, Cui LL. Clinical significance of STAT3 and MAPK phosphorylation, and the protein expression of cyclin D1 in skin squamous cell carcinoma tissues. *Mol Med Rep* (2015) 12:8129–34. doi: 10.3892/mmr.2015.4460

5. Wang L, Wu J, Song S, Chen H, Hu Y, Xu B, et al. Plasma exosome-derived sentrin SUMO-specific protease 1: A prognostic biomarker in patients with osteosarcoma. *Front Oncol* (2021) 11:625109. doi: 10.3389/fonc.2021.625109

6. Rizzollo F, More S, Vangheluwe P, Agostinis P. The lysosome as a master regulator of iron metabolism. *Trends Biochem Sci* (2021) 46(12):960–75. doi: 10.1016/j.tibs.2021.07.003

7. Ye Z, Liu W, Zhuo Q, Hu Q, Liu M, Sun Q, et al. Ferroptosis: Final destination for cancer? *Cell Prolif* (2020) 53:e12761. doi: 10.1111/cpr.12761

8. Liu Y, Gu W. The complexity of p53-mediated metabolic regulation in tumor suppression. *Semin Cancer Biol* (2021) 85:4–32. doi: 10.1016/j.semcancer.2021.03.010

9. Su Y, Zhao B, Zhou L, Zhang Z, Shen Y, Lv H, et al. Ferroptosis, a novel pharmacological mechanism of anti-cancer drugs. *Cancer Lett* (2020) 483:127–36. doi: 10.1016/j.canlet.2020.02.015

10. Wan S, Lei Y, Li M, Wu B. A prognostic model for hepatocellular carcinoma patients based on signature ferroptosis-related genes. *Hepatol Int* (2021) 16(1):112–24. doi: 10.21203/rs.3.rs-614871/v1

11. Wang Z, Fu Y, Xia A, Chen C, Qu J, Xu G, et al. Prognostic and predictive role of a metabolic rate-limiting enzyme signature in hepatocellular carcinoma. *Cell Prolif* (2021) 54(10):e13117. doi: 10.1111/cpr.13117

12. Li P, Zhang Y, Xu Y, Cao H, Li L, Xiao H. Characteristics of CD8+ and CD4+ tissue-resident memory lymphocytes in the gastrointestinal tract. *Advanced Gut Microbiome Res* (2022) 2022:1–12. doi: 10.1155/2022/9157455

13. Gene Ontology C. The gene ontology (GO) project in 2006. *Nucleic Acids Res 34* (2006) 34(Database issue):D322–6. doi: 10.1093/nar/gkj021

14. Kanehisa M, Goto S, Kawashima S, Okuno Y, Hattori M. The KEGG resource for deciphering the genome. *Nucleic Acids Res* (2004) 32:D277–80. doi: 10.1093/nar/gkh063

15. Tibshirani R. The lasso method for variable selection in the cox model. *Stat Med* (1997) 16:385–95. doi: 10.1002/(SICI)1097-0258(19970228)16:4<385::AID-SIM380>3.0.CO;2-3

16. Simon N, Friedman J, Hastie T, Tibshirani R. Regularization paths for cox's proportional hazards model *via* coordinate descent. *J Stat Softw* (2011) 39:1–13. doi: 10.18637/jss.v039.i05

17. Wen N, Cai Y, Li F, Ye H, Tang W, Song P, et al. The clinical management of hepatocellular carcinoma worldwide: A concise review and comparison of current guidelines: 2022 update. *Biosci Trends* (2022) 16:20–30. doi: 10.5582/bst.2022.01061

18. Midorikawa Y, Takayama T, Higaki T, Aramaki O, Teramoto K, Yoshida N, et al. Comparison of the surgical outcomes in patients with synchronous versus metachronous multiple hepatocellular carcinoma. *Biosci Trends* (2021) 14:415–21. doi: 10.5582/bst.2020.03313

19. Harada M, Aramaki O, Midorikawa Y, Higaki T, Nakayama H, Moriguchi M, et al. Impact of patient age on outcome after resection for hepatocellular carcinoma. *Biosci Trends* (2021) 15:33–40. doi: 10.5582/bst.2020.03437

20. Liu D, Song T. Changes in and challenges regarding the surgical treatment of hepatocellular carcinoma in China. *Biosci Trends* (2021) 15:142–7. doi: 10.5582/bst.2021.01083

21. Tang H, Cao Y, Jian Y, Li X, Li J, Zhang W, et al. Conversion therapy with an immune checkpoint inhibitor and an antiangiogenic drug for advanced hepatocellular carcinoma: A review. *Biosci Trends* (2022) 16:130–41. doi: 10.5582/bst.2022.01019

22. Wu J, Chen ZP, Shang AQ, Wang WW, Chen ZN, Tao YJ, et al. Systemic bioinformatics analysis of recurrent aphthous stomatitis gene expression profiles. *Oncotarget* (2017) 8:111064–72. doi: 10.18632/oncotarget.22347

23. Xiao Z, Dai Z, Locasale JW. Metabolic landscape of the tumor microenvironment at single cell resolution. *Nat Commun* (2019) 10:3763. doi: 10.1038/s41467-019-11738-0

24. Li Y, Qi D, Zhu B, Ye X. Analysis of m6A RNA methylation-related genes in liver hepatocellular carcinoma and their correlation with survival. *Int J Mol Sci* (2021) 22(3):1474. doi: 10.3390/ijms22031474

25. Guo J, Dai X, Laurent B, Zheng N, Gan W, Zhang J, et al. AKT methylation by SETDB1 promotes AKT kinase activity and oncogenic functions. *Nat Cell Biol* (2019) 21:226–37. doi: 10.1038/s41556-018-0261-6

26. Margueron R, Reinberg D. The polycomb complex PRC2 and its mark in life. *Nature* (2011) 469:343–9. doi: 10.1038/nature09784

27. Gu Z, Liu Y, Cai F, Patrick M, Zmajkovic J, Cao H, et al. Loss of EZH2 reprograms BCAA metabolism to drive leukemic transformation. *Cancer Discov* (2019) 9:1228–47. doi: 10.1158/2159-8290.CD-19-0152

28. Cai MY, Tong ZT, Zheng F, Liao YJ, Wang Y, Rao HL, et al. EZH2 protein: a promising immunomarker for the detection of hepatocellular carcinomas in liver needle biopsies. *Gut* (2011) 60:967–76. doi: 10.1136/gut.2010.231993

29. Yin H, Wang Y, Wu Y, Zhang X, Zhang X, Liu J, et al. EZH2-mediated epigenetic silencing of miR-29/miR-30 targets LOXL4 and contributes to tumorigenesis, metastasis, and immune microenvironment remodeling in breast cancer. *Theranostics* (2020) 10:8494–512. doi: 10.7150/thno.44849

30. Rizq O, Mimura N, Oshima M, Saraya A, Koide S, Kato Y, et al. Dual inhibition of EZH2 and EZH1 sensitizes PRC2-dependent tumors to proteasome inhibition. *Clin Cancer Res* (2017) 23:4817–30. doi: 10.1158/1078-0432.CCR-16-2735

31. Lang JD, Hendricks WPD, Orlando KA, Yin H, Kiefer J, Ramos P, et al. Ponatinib shows potent antitumor activity in small cell carcinoma of the ovary hypercalcemic type (SCCOHT) through multikinase inhibition. *Clin Cancer Res* (2018) 24:1932–43. doi: 10.1158/1078-0432.CCR-17-1928

32. Zhang P, Xiao Z, Wang S, Zhang M, Wei Y, Hang Q, et al. ZRANB1 is an EZH2 deubiquitinase and a potential therapeutic target in breast cancer. *Cell Rep* (2018) 23:823–37. doi: 10.1016/j.celrep.2018.03.078

33. Nishio S, Ushijima K, Tsuda N, Takemoto S, Kawano K, Yamaguchi T, et al. Cap43/NDRG1/Drg-1 is a molecular target for angiogenesis and a prognostic

indicator in cervical adenocarcinoma. *Cancer Lett* (2008) 264:36–43. doi: 10.1016/j.canlet.2008.01.020

34. Yan X, Chua MS, Sun H, So S. N-myc down-regulated gene 1 mediates proliferation, invasion, and apoptosis of hepatocellular carcinoma cells. *Cancer Lett* (2008) 262:133–42. doi: 10.1016/j.canlet.2007.12.010

35. Cheng J, Xie HY, Xu X, Wu J, Wei X, Su R, et al. NDRG1 as a biomarker for metastasis, recurrence and of poor prognosis in hepatocellular carcinoma. *Cancer Lett* (2011) 310:35–45. doi: 10.1016/j.canlet.2011.06.001

36. Konovalova S, Liu X, Manjunath P, Baral S, Neupane N, Hilander T, et al. Redox regulation of GRPEL2 nucleotide exchange factor for mitochondrial HSP70 chaperone. *Redox Biol* (2018) 19:37–45. doi: 10.1016/j.redox.2018.07.024

37. Lai MC, Zhu QQ, Xu J, Zhang WJ. Experimental and clinical evidence suggests that GRPEL2 plays an oncogenic role in HCC development. *Am J Cancer Res* (2021) 11(9):4175–98.

38. Bonnel AR, Bunchorntavakul C, Reddy KR. Immune dysfunction and infections in patients with cirrhosis. *Clin Gastroenterol Hepatol* (2011) 9:727–38. doi: 10.1016/j.cgh.2011.02.031

39. Oura K, Morishita A, Tani J, Masaki T. Tumor immune microenvironment and immunosuppressive therapy in hepatocellular carcinoma: A review. *Int J Mol Sci 22* (2021) 22(11):5801. doi: 10.3390/ijms22115801

40. Yu Y, Iclozan C, Yamazaki T, Yang X, Anasetti C, Dong C, et al. Abundant c-fas-associated death domain-like interleukin-1-converting enzyme inhibitory protein expression determines resistance of T helper 17 cells to activation-induced cell death. *Blood* (2009) 114:1026–8. doi: 10.1182/blood-2009-03-210153

41. Bortner CD, Scoltock AB, Cain DW, Cidlowski JA. T-Cell development of resistance to apoptosis is driven by a metabolic shift in carbon source and altered activation of death pathways. *Cell Death Differ* (2016) 23:889–902. doi: 10.1038/cdd.2015.156

42. Chen X, Kang R, Kroemer G, Tang D. Broadening horizons: the role of ferroptosis in cancer. *Nat Rev Clin Oncol* (2021) 18:280–96. doi: 10.1038/s41571-020-00462-0

43. Wu G, Wang Q, Xu Y, Li Q, Cheng L. A new survival model based on ferroptosis-related genes for prognostic prediction in clear cell renal cell carcinoma. *Aging (Albany NY)* (2020) 12:14933–48. doi: 10.18632/aging.103553

44. Liu J, Ma H, Meng L, Liu X, Lv Z, Zhang Y, et al. Construction and external validation of a ferroptosis-related gene signature of predictive value for the overall survival in bladder cancer. *Front Mol Biosci* (2021) 8:675651. doi: 10.3389/fmolb.2021.675651

45. Wang Y, Wei Z, Pan K, Li J, Chen Q. The function and mechanism of ferroptosis in cancer. *Apoptosis* (2020) 25:786–98. doi: 10.1007/s10495-020-01638-w

46. Dixon SJ, Lemberg KM, Lamprecht MR, Skouta R, Zaitsev EM, Gleason CE, et al. Ferroptosis: an iron-dependent form of nonapoptotic cell death. *Cell* (2012) 149:1060–72. doi: 10.1016/j.cell.2012.03.042

47. Xie Y, Hou W, Song X, Yu Y, Huang J, Sun X, et al. Ferroptosis: process and function. *Cell Death Differ* (2016) 23:369–79. doi: 10.1038/cdd.2015.158

48. Zheng J, Conrad M. The metabolic underpinnings of ferroptosis. *Cell Metab* (2020) 32:920–37. doi: 10.1016/j.cmet.2020.10.011

49. Zdralevic M, Vucetic M, Daher B, Marchiq I, Parks SK, Pouyssegur J. Disrupting the 'Warburg effect' re-routes cancer cells to OXPHOS offering a vulnerability point *via* 'ferroptosis'-induced cell death. *Adv Biol Regul* (2018) 68:55–63. doi: 10.1016/j.jbior.2017.12.002

50. Xia Y, Carpentier A, Cheng X, Block PD, Zhao Y, Zhang Z, et al. Human stem cell-derived hepatocytes as a model for hepatitis b virus infection, spreading and virus-host interactions. *J Hepatol* (2017) 66:494–503. doi: 10.1016/j.jhep.2016.10.009

51. Khanam A, Chua JV, Kottilil S. Immunopathology of chronic hepatitis b infection: Role of innate and adaptive immune response in disease progression. *Int J Mol Sci* (2021) 22(11):5497. doi: 10.3390/ijms22115497

52. Ciccarone F, Castelli S, Ciriolo MR. Oxidative stress-driven autophagy acROSs onset and therapeutic outcome in hepatocellular carcinoma. *Oxid Med Cell Longev* (2019) 2019:6050123. doi: 10.1155/2019/6050123

53. Malcov-Brog H, Alpert A, Golan T, Parikh S, Nordlinger A, Netti F, et al. UV-Protection timer controls linkage between stress and pigmentation skin protection systems. *Mol Cell* (2018) 72:444–456 e7. doi: 10.1016/j.molcel.2018.09.022

54. Appenzeller-Herzog C, Hall MN. Bidirectional crosstalk between endoplasmic reticulum stress and mTOR signaling. *Trends Cell Biol* (2012) 22:274–82. doi: 10.1016/j.tcb.2012.02.006

55. Wen Z, Jin K, Shen Y, Yang Z, Li Y, Wu B, et al. N-myristoyltransferase deficiency impairs activation of kinase AMPK and promotes synovial tissue inflammation. *Nat Immunol* (2019) 20:313–25. doi: 10.1038/s41590-018-0296-7

Glossary

HCC or LIHC	Hepatocellular carcinoma
FPKM	Fragments Per Kilobase of exon model per Million mapped fragments
TCGA	The Cancer Genome Atlas
GO	Gene Ontology
KEGG	Kyoto Encyclopedia of Genes and Genomes Enrichment Analyses
LASSO	least absolute contraction and selection operation
GSVA	the Gene Set Variation Analysis
CC	cellular components
MF	molecular function
BP	biological pathways
DEGs	The Differentially Expressed Genes
HRP	horseradish peroxidase
AFP	Alpha-fetoprotein
ALT	Alanine aminotransferase
HBsAg	Hepatitis B surface antigen
ALT	Alanine aminotransferase
OXPHOS	oxidative phosphorylation
HIAC	hepatic arterial infusion chemotherapy
FLV	inadequate future liver volume
OS	overall survival
KIRP	kidney renal papillary cell carcinoma
KICH	kidney chromophobe
LGG	brain lower-grade glioma
GBM	glioblastoma multiforme
BRCA	breast cancer
LUSC	lung squamous cell carcinoma
LUAD	lung adenocarcinoma
READ	rectum adenocarcinoma
COAD	colon adenocarcinoma
UCS	uterine carcinosarcoma
UCEC	uterine corpus endometrial carcinoma
OV	ovarian serous cystadenocarcinoma
HNSC	head and neck squamous carcinoma
THCA	thyroid carcinoma
PRAD	prostate adenocarcinoma
STAD	stomach adenocarcinoma
SKCM	skin cutaneous melanoma
BLCA	bladder urothelial carcinoma
CESC	cervical squamous cell carcinoma and endocervical adenocarcinoma
ACC	adrenocortical carcinoma
PCPG	pheochromocytoma and paraganglioma
SARC	sarcoma
LAML	acute myeloid leukaemia
PAAD	pancreatic adenocarcinoma
ESCA	oesophageal carcinoma
TGCT	testicular germ cell tumours
THYM	thymoma
MESO	mesothelioma
UVM	uveal melanoma
DLBC	lymphoid neoplasm diffuse large B-cell lymphoma
CHOL	cholangiocarcinoma

frontiers | Frontiers in Oncology

TYPE Original Research
PUBLISHED 09 February 2023
DOI 10.3389/fonc.2023.1072941

OPEN ACCESS

EDITED BY
Ali Vaziri-Gohar,
Case Western Reserve University,
United States

REVIEWED BY
Rui Wang,
Case Western Reserve University,
United States
Priyanka S. Rana,
Case Western Reserve University,
United States

*CORRESPONDENCE
Yonghui Yuan
✉ yuanyonghuiln@outlook.com
Xun Qi
✉ qixun716@hotmail.com

SPECIALTY SECTION
This article was submitted to
Cancer Metabolism,
a section of the journal
Frontiers in Oncology

RECEIVED 18 October 2022
ACCEPTED 23 January 2023
PUBLISHED 09 February 2023

CITATION
Yuan Y, Zhang Z, Ma B, Ji P, Ma S and Qi X
(2023) Effective oxygen metabolism-based
prognostic signature for colorectal cancer.
Front. Oncol. 13:1072941.
doi: 10.3389/fonc.2023.1072941

Effective oxygen metabolism-based prognostic signature for colorectal cancer

Yonghui Yuan[1]*, Zhong-guo Zhang[2], Bin Ma[3], Pengfei Ji[4], Shiyang Ma[5] and Xun Qi[6]*

[1]Liaoning Cancer Hospital & Institute, Clinical Research Center for Malignant Tumor of Liaoning Province, Cancer Hospital of China Medical University, Shenyang, Liaoning, China, [2]Large-Scale Data Analysis Center of Cancer Precision Medicine, Cancer Hospital of Chinese Medical University, Liaoning Provincial Cancer Institute and Hospital, Shenyang, China, [3]Department of Colorectal Surgery, Liaoning Cancer Hospital & Institute, Cancer Hospital of China Medical University, Shenyang, Liaoning, China, [4]Department of Medical Image of Liaoning Province, Liaoning Cancer Hospital & Institute, Cancer Hospital of China Medical University, Shenyang, Liaoning, China, [5]Department of Radiology, Key Laboratory of Diagnostic Imaging and Interventional Radiology of Liaoning Province, The First Affiliated Hospital of China Medical University, Shenyang, Liaoning, China, [6]Key Laboratory of Diagnostic Imaging and Interventional Radiology of Liaoning Province, Department of Radiology, The First Affiliated Hospital of China Medical University, Shenyang, China

Backgroud: Oxygen metabolism is an important factor affecting the development of tumors, but its roles and clinical value in Colorectal cancer are not clear. We developed an oxygen metabolism (OM) based prognostic risk model for colorectal cancer and explored the role of OM genes in cancer.

Methods: Gene expression and clinical data obtained from The Cancer Genome Atlas, Clinical Proteomic Tumor Analysis Consortium databases were consider as discovery and validation cohort, respectively. The prognostic model based on differently expressed OM genes between tumor and GTEx normal colorectal tissues were constructed in discovery cohort and validated in validation cohort. The Cox proportional hazards analysis was used to test clinical independent. Upstream and downstream regulatory relationships and interaction molecules are used to clarify the roles of prognostic OM genes in colorectal cancer.

Results: A total of 72 common differently expressed OM genes were detected in the discovery and validation set. A five-OM gene prognostic model including *LRT2*, *ATP6V0E2*, *ODC1*, *SEL1L3* and *VDR* was established and validated. Risk score determined by the model was an independent prognostic according to routine clinical factors. Besides, the role of prognostic OM genes involves transcriptional regulation of MYC and STAT3, and downstream cell stress and inflammatory response pathways.

Conclusions: We developed a five-OM gene prognostic model and study the unique roles of oxygen metabolism in of colorectal cancer

KEYWORDS

oxygen metabolism, prognosis model, transcriptional regulation, colorectal cancer, hub gene

1 Introduction

Colorectal cancer has always been the third largest malignant tumor in the world (1). Although the treatment level has been significantly improved in recent years, the morbidity rate remains high and the 5-year survival rate is still low due to the complex and elusive mechanism of cancer formation and development (2, 3). Therefore, finding suitable prognostic markers and new therapeutic targets is still an urgent problem to be solved in the treatment of colorectal cancer

Oxygen (O_2) is an important catalyst for mitochondria to produce ATP and other intracellular reactions. Hypoxia can induce adaptive responses at multiple cell and body levels to enable individuals to maintain normal metabolism and life activities in a hypoxic environment (4). When in hypoxia environment, cancer cells utilize O_2-sensing pathways like HIF transcriptional regulators, mTOR and mitochondrial ROS regulation, to overcome oxygen/nutrient deprived microenvironment stresses (5, 6). HIF stabilization and activation are highly responsive to hypoxia and redox stresses, as well as genetic alterations in oncogene or tumor suppressor signaling pathways to support tumor cell survival, growth, and proliferation (5, 7). Some regulators of HIF activity like ROS and cellular ascorbate levels are associated with weaker invasive ability in colorectal cancers (8). A common feature of tumor cells is that even under the normal oxygen condition, increased rates of glycolysis (the "Warburg effect") which is the critical step for the biosynthesis of ATP and other compounds essential for cell growth and division (6). Additionally, hypoxia has been shown to be associated with therapeutic resistance, including radiation therapy and cytotoxic drugs (9, 10). As an attractive therapeutic target in cancer (11), drugs target on HIFs often lack of specificity on inhibiting subunit (12). Thus, finding credible molecular markers and drug targets related to oxygen metabolism is still challenging.

In recent years, cancer omics research reveals several molecular markers for prognosis monitoring and target therapy of colorectal cancer (13, 14). However, as far as we know, molecular markers related to oxygen metabolism have not been studied in colorectal cancer. A previous study established an eleven gene diagnostic model, and this metadata gene signature had been developed to have an excellent ability to predict diagnosis of TCGA colon cancer patients (15). Another study (16) found that a signature based on 15 metabolites generated from energy supply, macromolecules and oxidative stress has great prognosis potential for colon cancer. The genes significantly correlated to the level of oxygen stress are GPX1, GSTP1, GSR, GSS, GGCT, ANPEP, CAT and ERCC2. Among them, the genes related to oxygen metabolism, such as GPX1, have been included in our gene set. Different from us, the author focused on metabolites, and did not study whether the expression of these genes in tumors was different from normal tissues (16). These studies suggest us that the oxygen metabolism is very likely to have high prognostic and therapeutic value in the colon cancer, but it has not been studied in colorectal cancer so far. So, our research focused on genes related to oxygen metabolism. We found more than 3000 genes related to oxygen metabolism (not just the oxygen metabolism pathway, see methods). Then we determined that the signature of five oxygen metabolism genes, such as VDR, has the highest prognostic potential through DEG analysis, modeling and evaluation of prognosis performance. In order to study the possible mechanism of these genes in colon cancer, we further conducted a detailed functional analysis of each of them to improve the reliability and reference of our research.

In this report, we investigated the expression profile of oxygen metabolism genes, developed and validated a reliable prognostic model of colorectal cancer using differentially expressed oxygen metabolism (OM, Table 1) genes. In addition, we set up a protein regulatory network of prognostic genes and explored its potential role in tumorigenesis. This study comprehensively uncovered the prognostic and therapeutic value of oxygen metabolism genes in colorectal cancer patients.

2 Materials and methods

2.1 Sample collection

The gene expression data and clinical information of Colorectal cancer patients (n=288) downloaded from TCGA database (https://portal.gdc.cancer.gov/) were used as discovery cohort. The CPTAC-2 prospective data set including gene expression and clinical data of Colorectal cancer patients (n=110) obtained from cBioPortal (https://www.cbioportal.org) were used as validation cohort. Gene expression of Colorectal tissues obtained from GTEx database (https://gtexportal.org/home/)was used as normal control in the downstream analysis (n=253).

TABLE 1 List of abbreviation used in this paper.

Abbreviation	Definition
OM	oxygen metabolism
TCGA	The Cancer Genome Atlas
GTEx	Genotype-Tissue Expression
DEG	Differential expressed oxygen metabolic gene
MSigDB	Molecular SignaturesDatabase
GSEA	gene set enrichment analysis
OS	overall survival
LASSO	Least absolute shrinkage and selection operator
RS	Risk score
ROC	Receiver operating characteristic curve
AUC	area under the ROC
PPI	protein-protein interaction
TF	transcription factors
K-M	Kaplan-Meier
KEGG	Kyoto Encyclopedia of Genes and Genomes
GO	Gene Ontology
MCODE	Molecular Complex Detection

2.2 Identification of differentially expressed metabolic genes

We first obtained pathways and biological processes from Molecular Signatures Database (MSigDB) C2 curated gene sets on gene set enrichment analysis (GSEA) website. Then, a total of 3524 genes in these gene sets that associated with oxygen metabolism were identified as oxygen metabolism related genes in our study. Differential expressed oxygen metabolic genes (DEG) between tumor and normal samples were analyzed in discovery and validation cohort using 'limma' R package, respectively. Genes with FDR< 0.05 and $|\log_2(\text{FoldChange})| > 1$ were extracted as differentially expressed genes. The "Pheatmap" and "ggplots" package was used to plot heatmaps and volcano maps for DEGs. Venn plots of up- and down-regulated DEGs between discovery and validation cohort were achieved using a Venn online tool (https://bioinformatics.psb.ugent.be/webtools/Venn/)

2.3 Construction of the prognostic model

DEGs significantly associated with overall survival (OS) in the entire discovery cohort were identified using univariate Cox proportional hazards regression analyses. A P-value ≤.05 was considered statistically significant. Then, we performed the least absolute shrinkage and selection operator (LASSO) penalty Cox regression analysis to eliminate genes that might overfit the model (Combined-24). Finally, we calculated risk score (RS) for each patient by a linear combination of Cox coefficient and expression of optimal prognostic DEGs identified by multivariate Cox analysis. The risk score calculation formula was as following:

$$\text{RS} = \sum\nolimits_{1}^{N} (Ei \times Ci)$$

Ei and *Ci* represented *i*th gene expression and corresponding coefficient value. N is the number of optimal prognostic DEGs. Patients with RS values greater than the median were defined as high-risk groups, otherwise as low-risk groups. Kaplan-Meier analysis was conducted using the "survival" and "survminer" R package. Receiver operating characteristic curve (ROC) and the "area under the ROC" (AUC) analysis were used to evaluate the performance of the prognostic model.

2.4 Validation of the prognostic model

We used validation cohort (CPTAC) to verify the prognostic risk model. RS of each patient in validation cohort was calculated using formula mentioned above based prognostic DEGs and coefficient identified in discovery cohort. Survival and ROC analysis were used to validate the performance of prognostic risk model.

2.5 Independent prognostic value of prognostic model

To assess the independent prognostic value of oxygen metabolic gene-based risk models in colorectal cancer, we performed both univariate and multivariate analyses of prognostic factors using Cox proportional hazards regression. Age, gender, pathological stage and TNM stage were treated as covariates. Factors with p value< 0.05 in both univariate and multivariate Cox analysis were defined as independent prognostic indicators.

2.6 Protein-protein interaction network based on prognostic genes

We constructed the PPI network of prognostic oxygen-metabolic genes using the PathwayCommon (https://www.pathwaycommons.org/) PPI database. Analysis of functional interactions between proteins was performed in order to elucidate the potential roles of prognostic genes in colorectal cancer tumorigenic process. The PPI networks were visualized using the Cytoscape software.

2.7 Hub prognostic genes and their upstream transcription factors

The hub genes were identified using DMNC, MNC, Degree, EPC, BottleNeck, EcCentricity, Closeness, Radiality, Betweenness, Stress and ClusteringCoefficient algorithms with Cytoscape's plug-in cytoHubba in the PPI network. Then, we obtained all possible transcription factors (TFs) of hub gene from ChiIP seq experimental data of human samples in the ENCODE project, and identified upstream TFs that play a role in colon cancer by calculating the expression correlation between these TFs and hub genes in our tumor samples. The correlationship of gene expression between hub genes and their TFs was conducted using the spearman method. The most relevant TF-hub gene relationship was shown by scatter plots.

3 Results

3.1 Identification of differentially expressed and survival-related OM genes

The workflow of this study is shown in Figure 1. Tumor samples (n=288) obtained from the TCGA database were regarded as the discovery cohort, while tumor samples (n=102) obtained from the CPTAC project were regarded as validation cohort. We compared expression levels of 3524 oxygen metabolic genes between tumor and normal samples in discovery set and validation set, respectively. The distributions of all genes including identified DEGs according to the two dimensions of $-\log_{10}(\text{FDR})$ and $\log_2(\text{FoldChange})$ were displayed by volcano maps (Figures 2A, B). It was found that there were 262 up-regulated and 188 down-regulated genes in the discovery set, 175 up-regulated and 27 down-regulated genes in the validation set (Figure 2C). To obtained the more reliable prognostic gene signature, we established the prognostic model with 72 DEGs up-regulated in both the discovery set and the validation set (Figures 1, 2D). We didn't obtaied reliable down-regulated DEGs which were identified in the discovery and validation cohorts Figure 2E)

Univariate Cox regression analysis revealed that 95 OM DEGs were significantly (*P*<.05) associated with OS in the discovery cohort. Among them, 73 DEGs were associated with good OS, while 22 DEGs were associated with bad OS.

3.2 Construction of a five-OM gene prognostic model

Based on the discovery cohort, we obtained eight candidate prognostic OM genes using Lasso Cox regression analysis. Then, we acquired five optimal genes, including *FLRT2* (Fibronectin Leucine Rich Transmembrane Protein 2), *ATP6V0E2* (ATPase H+ Transporting V0 Subunit E2), *ODC1* (Ornithine Decarboxylase 1), *SEL1L3* (SEL1L Family Member 3) and *VDR* (Vitamin D Receptor). Four of these genes were high hazard genes, and one gene (SEL1L3) was low hazard gene, and all these genes were up-regulated DE genes (Table 2). The risk score of each tumor sample was calculated as follows: risk score = $(1.0232\times FLRT2_{exp}) + (1.0046\times ATP6V0E2_{exp}) + (0.9806\times SEL1L3_{exp}) + (1.0015\times ODC1_{exp}) + (1.0493\times VDR_{exp})$.

Based on the optimized risk score threshold, all colorectal cancer patients of discovery cohort were divided into a high-risk group (n = 30) and a low-risk group (n = 252). The K-M survival analysis shown those OS times of high-risk patients were significantly longer than that of low-risk patients ($p< 0.001$) (Figure 3A). The median survival time of patients in the high-risk group was shorter than 5 years, while that of patients in the low-risk group was longer than 10 years. From the perspective of survival rate, the 1-year, 3-year and 5-year survival rates of the high-risk group were only 72%, 63% and 35% respectively, while the corresponding survival rates of the low-risk group reached 91%, 85% and 71% respectively. In addition, the AUC values of the five-OM gene prediction model were 0.753, 0.674, and 0.714 when predicting one -, three -, and five-year OS, respectively (Figure 3B). To find out whether all 5 prognosis OM genes are associated with advanced stages and therefore are associated with worse prognosis, we analyzed the OS time of patients with high- and low-RS from tumor stage I, II, III and IV. Results indicated that the OS time of patients with high RS was significantly shorter than that of patients with low RS in stage II and IV, which proved the prognostic effectiveness of our 5-OM gene signature in these two stages. But in stage I and III, there was no significant difference in the OS time of patients with high- and low-RS, suggesting the prognostic limitations of the model in these two stages (Figure S1).

3.3 Validation of the prognostic model

We validated the performance of the model using the validation cohort. Patients in validation cohort were divided into high- and low-risk groups based on RS threshold determined in discovery cohort. Results indicated that 12 patients and 90 patients were categorized as high- and low- risk groups, respectively. K-M survival curves were significant different between the two risk groups ($p < 0.001$) (Figure 3C) and the AUC values at 1- and 3-year were 0.974 and 0.958 in the validation cohort, respectively (Figure 3D). At the same time, the RSs of patients in the high-risk group were higher than those

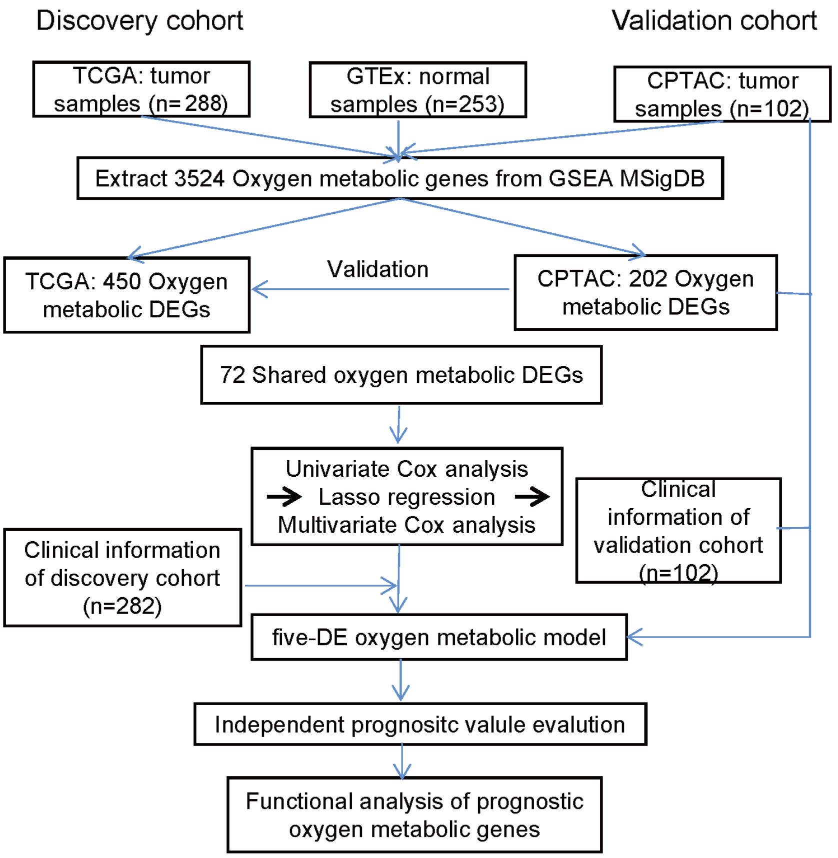

FIGURE 1
The workflow of this study. The prognostic model based on oxygen metabolism genes was established and validated in two independent CRC cohorts, and the roles of prognostic genes in CRC was further analyzed.

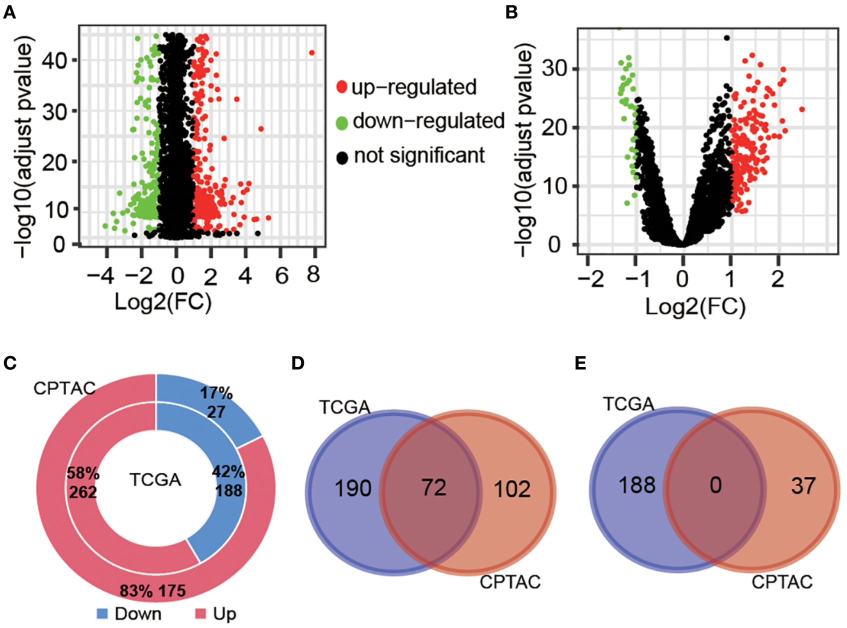

FIGURE 2
Different expressed gene analysis between tumor and normal samples. Volcanic map showing the difference of gene levels between tumor and normal samples in the TCGA cohort **(A)** and CPTAC cohort **(B)**. Genes with |Log2(FC)| >1 and adjust pvalue<0.01 were defined as different expressed genes. **(C)**, Proportion and number of significantly up-regulated and down-regulated genes obtained from two cohort samples. Venn diagrams of up-regulated genes **(D)** and down-regulated genes **(E)** in TCGA and CPTAC samples.

in the low-risk group, which proved that the model had a good performance in the prognosis evaluation and monitoring of colorectal cancer.

3.4 Independent prognostic ability of prognostic model

To assess whether the RS determined by five oxygen-metabolic prognostic model is an independent prognostic indicator for patients, we carried out a univariate Cox analysis to assess the impact of risk scores and clinicopathological parameters on prognosis, such as age, gender, histological type, longest dimension, pathological stage and so on. We found that the longest dimension, lymphatic invasion, pathological stage and risk score were associated with poor outcomes of prognosis in patients (Table 3). Therefore, these characteristics were included in a multivariate Cox regression analysis, which indicated that age, pathological stage and the risk score estimated based the prognostic model was an independent prognostic factor for colorectal cancer (Table 3). This result indicates that there is significant potential for these oxygen-metabolic genes to predict the prognosis outcome of patients with the colorectal cancer.

3.5 Transcriptional regulation of prognostic oxygen-metabolic genes

We investigated the regulatory relationships between TFs and prognostic genes. Firstly, we obtained upstream TFs of each gene from the ChIP-Seq experiment in the ENCODE project (https://www.encodeproject.org). Then, we analyzed expression correlation of between TFs and genes in TCGA tumor samples to validate the TF regulation *in vivo*. We found that 11 cancer-related TFs including CTBP2, E2F1, EP300, ETS1, FOS, JUN, MYC, RELA, STAT1, STAT3 and TCF7L2 were significantly correlated with our prognostic genes. Among them,*STAT3* and *MYC* were significantly correlated with all prognostic genes, in which positively correlated with *FLRT2*, *ODC1*, *SEL1L3* and *VDR*, and negatively correlated with *ATP6V0E2*

TABLE 2 Five prognostic oxygen-metabolic genes.

Genes	HR	CI(95%) Lower	CI(95%) Upper	pvalue
FLRT2	1.0232	1.0008	1.0461	0.0424
ATP6V0E2	1.0046	1.0015	1.0076	0.0037
ODC1	1.0015	1.0004	1.0026	0.0059
SEL1L3	0.9806	0.9690	0.9923	0.0012
VDR	1.0493	1.0262	1.0731	0.0000

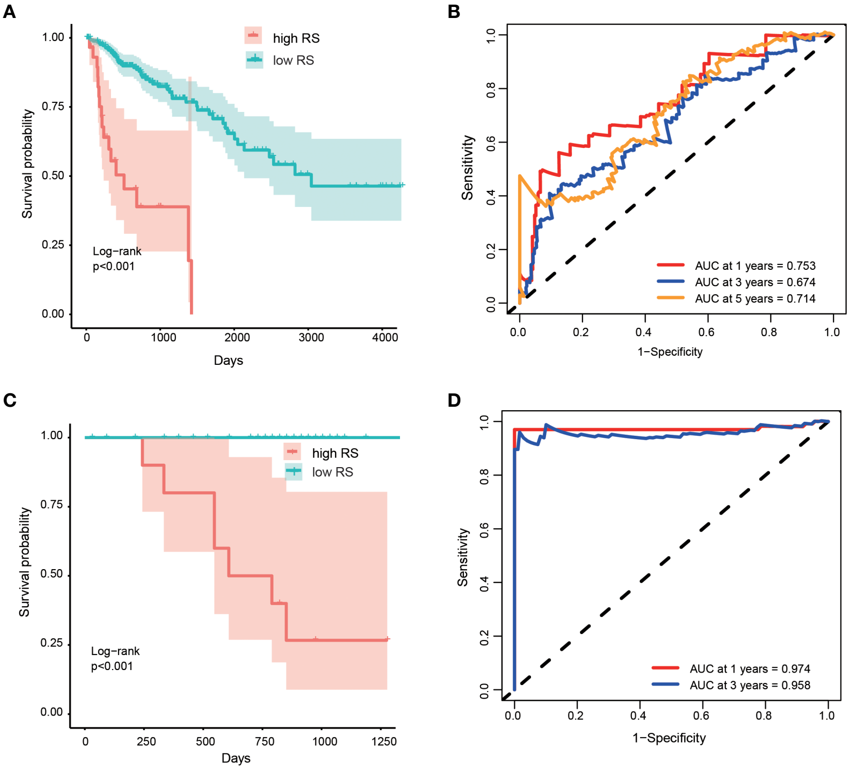

FIGURE 3
Performance of prognostic risk model in discovery and validation cohort. Kaplan-Meier curves shown the overall survive among patients classified into high- and low- RS groups in discovery **(A)** and validation **(C)** cohorts. The difference of survival time between the two groups was tested by log rank method. ROC curves and their AUC value shown the performance of the prognostic risk model in predicting the one, three and five years survive time in discovery **(B)** and validation **(D)** cohort.

(Figure 4).These results indicates that the prognostic genes we screened are important downstream molecules of classic cancer driver genes like STAT3 and MYC.

3.6 Functional analysis of prognostic oxygen-metabolic genes

In order to study the possible function and mechanism of prognostic oxygen metabolic genes in colorectal cancer, we screened KEGG cancer pathway genes that can interact with prognostic genes, and then used the metascape to analyze the gene ontology (GO) and pathway enrichment of interacting genes It was found that the interaction genes were significantly enriched in GO terms including “response to inorganic substance”, “response to xenobiotic stimulus”, “response to oxidative stress”, and the enriched pathways were “transport of small molecules”, “ion channel transport”, “mineral absorption” and so on (Figure 5A). To further capture the relationships between these enriched terms, we constructed a network diagram using Metascape analysis. Spots represented GO terms or pathways. Larger and connected points represented the presence of more similar genes between the terms or pathways. The “Transport of small molecules” pathway contained many genes participating in Ion channel transport, while the “response to oxidative stress” gene set contained many genes participating in cell stress and inflammatory response terms or pathways (Figure 5B). In addition, the PPI network showed a relationship between different genes and proteins in two sub-modules (Figure 5B). The “Fluid shear stress and atherosclerosis” sub-module seeded by the MYC included IL1B, TP53, PIP, MYC, IL2, NFKBIA. AGT, CXCL8, BLM and MMP2, which can identify the structural components of the extracellular matrix to provide tensile strength; the “extracellular matrix organization” sub-module included SPP1, IGFBP4, GAS6, MXRA8, and SPARCL1, which play a central role in vascular biology; the “Signaling by Interleukins” sub-module seeded by the F2 included KNG1, KRT6B, PARP1, TNFRSF1A. KRT2, ZBTB16. ABCB1, BCL2, KRT1. PML, C3, TXN, KRT6C, F2, PTK2, TNF, which could enable HIF-mediated inflammatory response during cancer development (Figure 5C).

4 Discussion

The colorectal cancer is the malignant tumor with the third highest incidence rate and the second highest mortality rate in the world (17). In 2020 alone, 1.9 million people were diagnosed, of which 0.9 million died (1). Several prognostic models have been established in colorectal cancer (18–20). However, there are some drawbacks in currently existing prognostic risk models of colorectal cancer. Firstly, the sample sizes are insufficient to represent the whole disease population, which makes the risk score summarized from the level of gene expression uncertain for clinical personalized prognosis.

TABLE 3 Cox regression analyses of RS and clinicopathological parameters related to prognosis in CRC patients.

Variables	OS			
	Univariate analysis		Multivariate analysis	
	HR (95% CI)	*P*	HR (95% CI)	*P*
Gender(male/female)	1.160 (0.495-2.717)	.733		
Age (>70/≤70)	1.013 (0.990-1.038)	.072	2.205 (1.200-4.052)	.011
Longest_dimension (>1 cm/≤ 1 cm)	2.275 (1.296-3.994)	.004	1.835 (1.295-3.650)	.067
Histological type Adenocarcinoma Mucinous	1.323 (0.526-3.328)	.552		
Lymphatic_invasion (Yes/No)	1.000 (1.081-3.281)	.025	1.984 (1.043-3.601)	.051
pathologic_stage (I/II/III/IV)	1.516 (1.156-1.987)	.003	1.962 (1.196-3.684)	.031
number_of_lymphnodes	1.017 (0.913-1.038)	.242		
postoperative_rx_tx	1.032 (0.826-1.328)	.552		
Risk score (high/low)	2.497 (1.380-4.516)	.002	1.896 (1.004-3.481)	.021

Because patients' risk scores often depend on other samples used for normalization data (21). Secondly, most of the existing prognostic models are based on the expression of all genes. Because there is no focus on a certain biological process, it is difficult to study the relationship between prognostic genes and explain the biological mechanism behind the prognostic model. Thirdly, those prognostic models based on non-coding genes or omic modification features have the problem of high detection cost and easy to produce bias during applications (18, 19). Several studies have reported the roles of the oxygen metabolism in tumorigenesis and development of cancer (6, 7, 22). In this study, we built and validated a prognostic model using five oxygen metabolic genes higher expressed in tumor samples. The survival time of high-risk patients predicted by the model is significantly shorter than that of low-risk patients. At the same time, the model is good in predicting the survival time of patients stratified by survival time. Additionally, Multivariate cox analysis indicates that the model can predict overcome of CRC patients independently when mixed with age, stage, pathological grade and other factors. So, we demonstrate the important but long neglected clinical prognostic value of OM genes in CRC.

Five oxygen metabolic genes named *FLRT2*, *ATP6V0E2*, *ODC1*, *SEL1L3* and *VDR* were prognostic genes determined by the prognostic model. The expression of these genes was all higher in tumor than in normal tissues, which might play important roles in CRC progression and contribute to the early diagnosis. The *FLRT2* is highly expressed in tumor neovascularization and forms abnormal endothelial adhesion to prevent oxidative stress of cells. Its expression level is positively correlated with the short-term survival in the advanced colorectal cancer (23). The expression of FLRT2 is dependent on oxidative stress but not on VEGF (24), indicates that

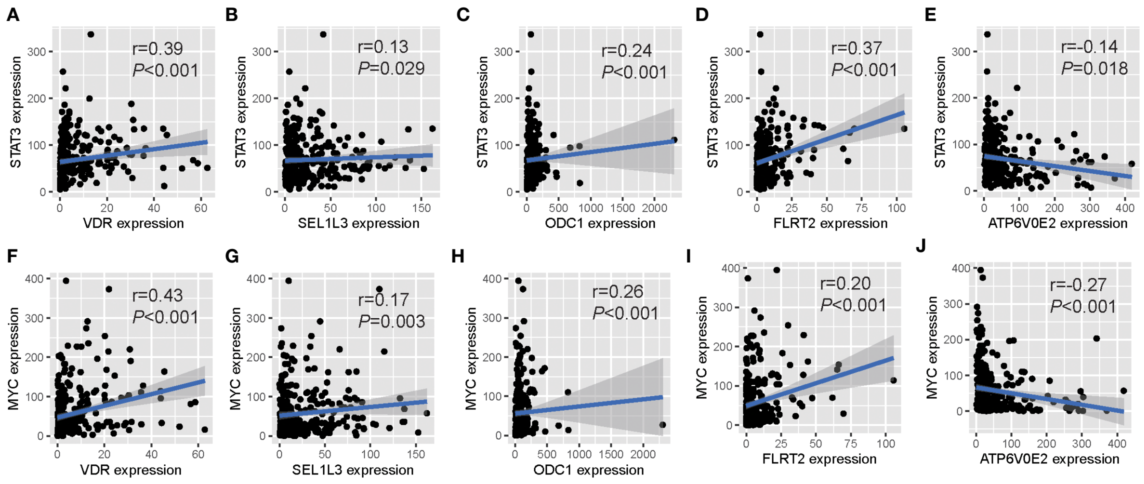

FIGURE 4
Expression relationships between prognostic OM genes and upstream TFs. Significant correlations of gene expression between five prognostic OM genes and their common upstream TFs: STAT3 **(A-E)** and MYC **(F-J)**.

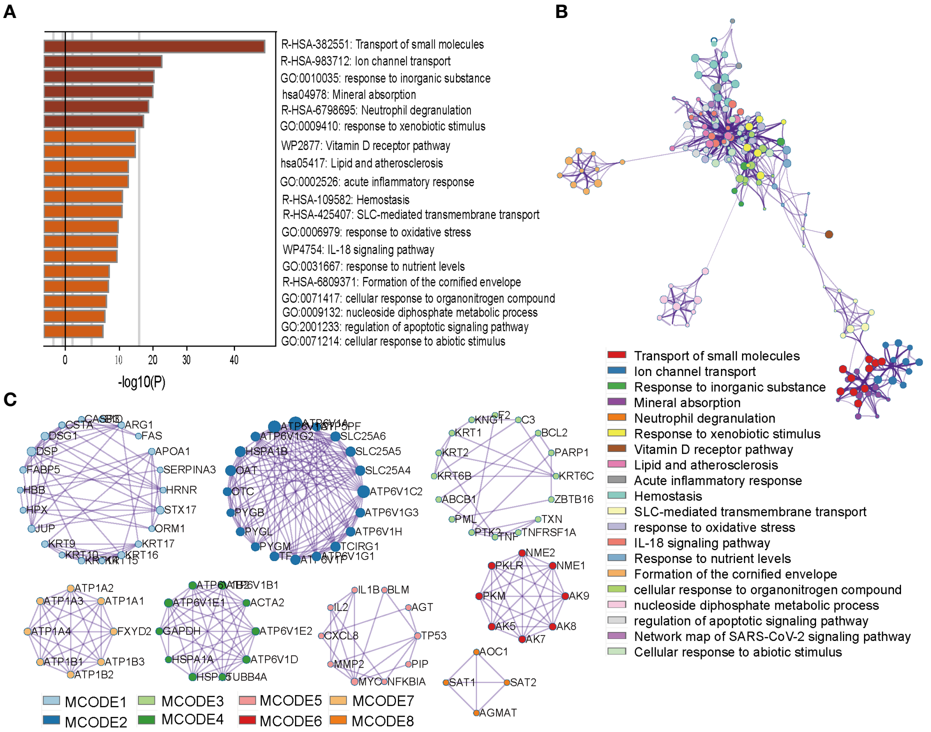

FIGURE 5

Enrichment and interact network of prognostic OM genes participating. **(A)** Bar graph of terms enriched across prognostic OM genes and their interacting genes. **(B)** Network of enriched terms colored by cluster ID, where nodes that share the same cluster ID are typically close to each other. **(C)**, Densely connected network components identified by the Molecular Complex Detection (MCODE) algorithm.

FLRT2 may play an important role in oxygen metabolism. The *ATP6V0E2* might promote cancer cell death and tumor suppression with high levels of ROS (reactive oxygen species) through inhibition of lysosomal function (25). *ODC1* activity is frequently elevated in cancer through deregulation of MYC, resulting in higher polyamine content to support rapid tumor cell proliferation (26). A study has shown that the expression of *SEL1L3* is elevated in endometrial cancer. In white patients with low mutation load, the expression level of this gene is related to the patient's recurrence free productivity and is considered as a potential driver and tumor marker of endometrial cancer (27).. SEL1L3 was also positively correlated with reactive oxygen species such as hydrogen peroxide (28). An elegant series of studies found that the VDR signaling affect tumor development by the delicate interplay with E-cadherin and the Wnt signaling pathway (29–32). All five identified prognostic genes are proved to play certain roles in tumors, which prove the reliability of our prognosis model in biological sense.

Transcriptional regulation and functional analysis gives us an in-depth understanding of the possible molecular mechanisms behind the prognostic model. An upstream regulatory factor MYC and STAT3 are constitutively activated in many cancers and plays a pivotal role in tumor growth and metastasis by regulating cell proliferation, invasion, migration, and angiogenesis (33–36). Myc promotes the transcription of STAT3 (37), then hypoxic stress markedly increased phosphorylated STAT3 level in a time-dependent fashion, and activated STAT3 was translocated into the nucleus (38). After that, the lysosomal activation was blocked by down-regulating ATP6V0E2 through the JAK2-STAT3-VEGFA singling pathway, to inhibit cell apoptosis in human colon cancer (25). SEL1L3 which is a target of transcript factor STAT3 and MYC plays important roles in oxygen metabolism related pathway " SUNG_METASTASIS_ STROMA_UP". Downstream interaction genes are mainly enriched in angiogenesis and inflammatory response in tumors. Angiogenesis is a critical step in cancer progression and is considered one of the hallmarks of cancer, and validated as an independent prognostic factor and the culprit of drug resistance in a variety of solid malignancies including colorectal cancer (39–42).

This study has several advantages. Firstly, we constructed a prognostic model based on DE OM genes in colorectal cancer for the first time. Secondly, the prognostic model was proved to be accurate and reliable using an independent cohort. Thirdly, the risk score determined by the model could be used as an independent prognostic index in predicting OS. Finally, we found that five prognostic OM genes regulate angiogenesis and inflammatory response in colorectal cancer. However, in our study, the RNA-seq data was used to obtain the gene expression levels in tumor and normal tissues, and determined the risk thresholds of patients with a prognosis model based on expression levels of the gene signature. Studies (21, 43, 44) have shown that RNA-seq data set-generated risk thresholds cannot be directly applied to independent microarray data sets because the gene expression levels are sensitive to systematic biases of microarray measurements owing to batch effects and platform differences. We also did not verify our prognostic risk model at the protein level in an independent cohort. So, we have started to collect patients and CRC samples so that we can obtain the protein levels by IHC and verify the risk model in an independent cohort in the future.

Data availability statement

The datasets presented in this study can be found in online repositories. The names of the repository/repositories and accession number(s) can be found in the article/Supplementary Material.

Author contributions

YY conceptualized the study and designed the research. YY, XQ and ZZ organized all the studies. YY, ZZ and BM completed data analysis and interpretation. YY, ZZ, XQ, PJ and SM wrote and revised the article. All authors contributed to the article and approved the submitted version.

Funding

This research was supported by the Natural Science Foundation of Liaoning Province (Grant No. 2020-MS-066) in China. We appreciate the data support provided by the Large-scale Data Analysis Center of Liaoning provincial Cancer Precision Medicine.

Conflict of interest

The authors declare that the research was conducted in the absence of any commercial or financial relationships that could be construed as a potential conflict of interest.

Publisher's note

Supplementary material

The Supplementary Material for this article can be found online at: https://www.frontiersin.org/articles/10.3389/fonc.2023.1072941/full#supplementary-material

References

1. Xi Y, Xu P. Global colorectal cancer burden in 2020 and projections to 2040. *Trans Oncol* (2021) 14:101174. doi: 10.1016/j.tranon.2021.101174

2. Center MM, Jemal A, Smith RA, Ward E. Worldwide variations in colorectal cancer. *CA Cancer J Clin* (2009) 59:366–78. doi: 10.3322/caac.20038

3. Edwards BK, Ward E, Kohler BA, Eheman C, Zauber AG, Anderson RN, et al. Annual report to the nation on the status of cancer, 1975-2006, featuring colorectal cancer trends and impact of interventions (risk factors, screening, and treatment) to reduce future rates. *Cancer* (2010) 116:544–73. doi: 10.1002/cncr.24760

4. Lee KE, Simon MC. SnapShot: Hypoxia-inducible factors. *Cell* (2015) 163:1288–1288.e1. doi: 10.1016/j.cell.2015.11.011

5. Qiu B, Simon MC. Oncogenes strike a balance between cellular growth and homeostasis. *Semin Cell Dev Biol* (2015) 43:3–10. doi: 10.1016/j.semcdb.2015.08.005

6. Pavlova NN, Thompson CB. The emerging hallmarks of cancer metabolism. *Cell Metab* (2016) 23:27–47. doi: 10.1016/j.cmet.2015.12.006

7. Ratcliffe PJ. Oxygen sensing and hypoxia signalling pathways in animals: the implications of physiology for cancer. *J Physiol* (2013) 591:2027–42. doi: 10.1113/jphysiol.2013.251470

8. Kuiper C, Dachs GU, Munn D, Currie MJ, Robinson BA, Pearson JF, et al. Increased tumor ascorbate is associated with extended disease-free survival and decreased hypoxia-inducible factor-1 activation in human colorectal cancer. *Front Oncol* (2014) 4:10. doi: 10.3389/fonc.2014.00010

9. Brizel DM, Scully SP, Harrelson JM, Layfield LJ, Bean JM, Prosnitz LR, et al. Tumor oxygenation predicts for the likelihood of distant metastases in human soft tissue sarcoma. *Cancer Res* (1996) 56:941–3.

10. Hockel M, Knoop C, Schlenger K, Vorndran B, Baussmann E, Mitze M, et al. Intratumoral pO2 predicts survival in advanced cancer of the uterine cervix. *Radiother Oncol J Eur Soc Ther Radiol Oncol* (1993) 26:45–50. doi: 10.1016/0167-8140(93)90025-4

11. Bertout JA, Patel SA, Simon MC. The impact of O2 availability on human cancer. *Nat Rev Cancer* (2008) 8:967–75. doi: 10.1038/nrc2540

12. Semenza GL. HIF-1 inhibitors for cancer therapy: from gene expression to drug discovery. *Curr Pharm Des* (2009) 15:3839–43. doi: 10.2174/138161209789649402

13. Kohne CH. Successes and limitations of targeted cancer therapy in colon cancer. *Prog Tumor Res* (2014) 41:36–50. doi: 10.1159/000356436

14. Yang C, Zhang Y, Xu X, Li W. Molecular subtypes based on DNA methylation predict prognosis in colon adenocarcinoma patients. *Aging (Albany NY)* (2019) 11:11880–92. doi: 10.18632/aging.102492

15. Zuo D, Li C, Liu T, Yue M, Zhang J, Ning G. Construction and validation of a metabolic risk model predicting prognosis of colon cancer. *Sci Rep* (2021) 11:6837. doi: 10.1038/s41598-021-86286-z

16. Qiu Y, Cai G, Zhou B, Li D, Zhao A, Xie G, et al. A distinct metabolic signature of human colorectal cancer with prognostic potential. *Clin Cancer Res an Off J Am Assoc Cancer Res* (2014) 20:2136–46. doi: 10.1158/1078-0432.CCR-13-1939

17. Keum N, Giovannucci E. Global burden of colorectal cancer: emerging trends, risk factors and prevention strategies. *Nat Rev Gastroenterol Hepatol* (2019) 16:713–32. doi: 10.1038/s41575-019-0189-8

18. Luo H, Zhao Q, Wei W, Zheng L, Yi S, Li G, et al. Circulating tumor DNA methylation profiles enable early diagnosis, prognosis prediction, and screening for colorectal cancer. *Sci Transl Med* (2020) 12. doi: 10.1126/scitranslmed.aax7533

19. Zeng H, Xu Y, Xu S, Jin L, Shen Y, Rajan KC, et al. Construction and analysis of a colorectal cancer prognostic model based on N6-Methyladenosine-Related lncRNAs. *Front Cell Dev Biol* (2021) 9:698388. doi: 10.3389/fcell.2021.698388

20. Liu C, Wang T, Yang J, Zhang J, Wei S, Guo Y, et al. Distant metastasis pattern and prognostic prediction model of colorectal cancer patients based on big data mining. *Front Oncol* (2022) 12:878805. doi: 10.3389/fonc.2022.878805

21. Qi L, Chen L, Li Y, Qin Y, Pan R, Zhao W, et al. Critical limitations of prognostic signatures based on risk scores summarized from gene expression levels: a case study for resected stage I non-small-cell lung cancer. *Brief Bioinform* (2016) 17:233–42. doi: 10.1093/bib/bbv064

22. Semenza GL. HIF-1 mediates metabolic responses to intratumoral hypoxia and oncogenic mutations. *J Clin Invest* (2013) 123:3664–71. doi: 10.1172/JCI67230

23. Ando T, Tai-Nagara I, Sugiura Y, Kusumoto D, Okabayashi K, Kido Y, et al. Tumor-specific interendothelial adhesion mediated by FLRT2 facilitates cancer aggressiveness. *J Clin Invest* (2022) 132(6). doi: 10.1172/JCI153626

24. Jauhiainen S, Laakkonen JP, Ketola K, Toivanen PI, Nieminen T, Ninchoji T, et al. Axon guidance-related factor FLRT3 regulates VEGF-signaling and endothelial cell function. *Front Physiol* (2019) 10:224. doi: 10.3389/fphys.2019.00224

25. Sun X, Shu Y, Yan P, Huang H, Gao R, Xu M, et al. Transcriptome profiling analysis reveals that ATP6V0E2 is involved in the lysosomal activation by anlotinib. *Cell Death Dis* (2020) 11:702. doi: 10.1038/s41419-020-02904-0

26. Hogarty MD, Norris MD, Davis K, Liu X, Evageliou NF, Hayes CS, et al. ODC1 is a critical determinant of MYCN oncogenesis and a therapeutic target in neuroblastoma. *Cancer Res* (2008) 68:9735–45. doi: 10.1158/0008-5472.CAN-07-6866

27. Mei Y, Chen MM, Liang H, Ma L. A four-gene signature predicts survival and anti-CTLA4 immunotherapeutic responses based on immune classification of melanoma. *Commun Biol* (2021) 4:383. doi: 10.1038/s42003-021-01911-x

28. Bekeschus S, Liebelt G, Menz J, Singer D, Wende K, Schmidt A. Cell cycle-related genes associate with sensitivity to hydrogen peroxide-induced toxicity. *Redox Biol* (2022) 50:102234. doi: 10.1016/j.redox.2022.102234

29. Ferrer-Mayorga G, Gomez-Lopez G, Barbachano A, Fernandez-Barral A, Pena C, Pisano DG, et al. Vitamin d receptor expression and associated gene signature in tumour stromal fibroblasts predict clinical outcome in colorectal cancer. *Gut* (2017) 66:1449–62. doi: 10.1136/gutjnl-2015-310977

30. Alvarez-Diaz S, Valle N, Garcia JM, Pena C, Freije JM, Quesada V, et al. Cystatin d is a candidate tumor suppressor gene induced by vitamin d in human colon cancer cells. *J Clin Invest* (2009) 119:2343–58. doi: 10.1172/JCI37205

31. Pendas-Franco N, Garcia JM, Pena C, Valle N, Palmer HG, Heinaniemi M, et al. DICKKOPF-4 is induced by TCF/beta-catenin and upregulated in human colon cancer, promotes tumour cell invasion and angiogenesis and is repressed by 1alpha,25-dihydroxyvitamin D3. *Oncogene* (2008) 27:4467–77. doi: 10.1038/onc.2008.88

32. Palmer HG, Larriba MJ, Garcia JM, Ordonez-Moran P, Pena C, Peiro S, et al. The transcription factor SNAIL represses vitamin d receptor expression and responsiveness in human colon cancer. *Nat Med* (2004) 10:917–9. doi: 10.1038/nm1095

33. Dang CV. MYC on the path to cancer. *Cell* (2012) 149:22–35. doi: 10.1016/j.cell.2012.03.003

34. Wong KE, Ngai SC, Chan KG, Lee LH, Goh BH, Chuah LH. Curcumin nanoformulations for colorectal cancer: A review. *Front Pharmacol* (2019) 10:152. doi: 10.3389/fphar.2019.00152

35. Nguyen AV, Wu YY, Lin EY. STAT3 and sphingosine-1-phosphate in inflammation-associated colorectal cancer. *World J Gastroenterol WJG* (2014) 20:10279–87. doi: 10.3748/wjg.v20.i30.10279

36. Wang SW, Sun YM. The IL-6/JAK/STAT3 pathway: potential therapeutic strategies in treating colorectal cancer (Review). *Int J Oncol* (2014) 44:1032–40. doi: 10.3892/ijo.2014.2259

37. Barre B, Vigneron A, Coqueret O. The STAT3 transcription factor is a target for the myc and riboblastoma proteins on the Cdc25A promoter. *J Biol Chem* (2005) 280:15673–81. doi: 10.1074/jbc.M413203200

38. Kang SH, Yu MO, Park KJ, Chi SG, Park DH, Chung YG. Activated STAT3 regulates hypoxia-induced angiogenesis and cell migration in human glioblastoma. *Neurosurgery* (2010) 67:1386–95. doi: 10.1227/NEU.0b013e3181f1c0cd

39. Holash J, Maisonpierre PC, Compton D, Boland P, Alexander CR, Zagzag D, et al. Vessel cooption, regression, and growth in tumors mediated by angiopoietins and VEGF. *Science* (1999) 284:1994–8. doi: 10.1126/science.284.5422.1994

40. Jacobsen J, Rasmuson T, Grankvist K, Ljungberg B. Vascular endothelial growth factor as prognostic factor in renal cell carcinoma. *J Urol* (2000) 163:343–7. doi: 10.1016/S0022-5347(05)68049-4

41. Maeda K, Chung YS, Ogawa Y, Takatsuka S, Kang SM, Ogawa M, et al. Prognostic value of vascular endothelial growth factor expression in gastric carcinoma. *Cancer* (1996) 77:858–63. doi: 10.1002/(SICI)1097-0142(19960301)77:5<858::AID-CNCR8>3.0.CO;2-A

42. Carmeliet P, Jain RK. Angiogenesis in cancer and other diseases. *Nature* (2000) 407:249–57. doi: 10.1038/35025220

43. Leek JT, Scharpf RB, Bravo HC, Simcha D, Langmead B, Johnson WE, et al. Tackling the widespread and critical impact of batch effects in high-throughput data. *Nat Rev Genet* (2010) 11:733–9. doi: 10.1038/nrg2825

44. Geman D, d'Avignon C, Naiman DQ, Winslow RL. Classifying gene expression profiles from pairwise mRNA comparisons. *Stat Appl Genet Mol Biol 3* (2004). doi: 10.2202/1544-6115.1071

frontiers | Frontiers in Oncology

TYPE Original Research
PUBLISHED 09 February 2023
DOI 10.3389/fonc.2023.990551

GPX3 expression was down-regulated but positively correlated with poor outcome in human cancers

Qingyi Hu[†], Jiaoshun Chen[†], Wen Yang[†], Ming Xu, Jun Zhou, Jie Tan* and Tao Huang*

Department of Breast and Thyroid Surgery, Union Hospital, Tongji Medical College, Huazhong University of Science and Technology, Wuhan, China

Introduction: Cancer is a crucial public health problem and one of the leading causes of death worldwide. Previous studies have suggested that GPX3 may be involved in cancer metastasis and chemotherapy resistance. However, how GPX3 affects cancer patients' outcomes and the underlying mechanism remains unclear.

Methods: Sequencing data and clinical data from TCGA, GTEx, HPA, and CPTAC were used to explore the relationship between GPX3 expression and clinical features. Immunoinfiltration scores were used to assess the relationship between GPX3 and the tumor immune microenvironment. Functional enrichment analysis was used to predict the role of GPX3 in tumors. Gene mutation frequency, methylation level, and histone modification were used to predict the GPX3 expression regulation method. Breast, ovarian, colon, and gastric cancer cells were used to investigate the relationship between GPX3 expression and cancer cell metastasis, proliferation, and chemotherapy sensitivity.

Results: GPX3 is down-regulated in various tumor tissues, and GPX3 expression level can be used as a marker for cancer diagnosis. However, GPX3 expression is associated with higher stage and lymph node metastasis, as well as poorer prognosis. GPX3 is closely related to thyroid function and antioxidant function, and its expression may be regulated by epigenetic inheritance such as methylation modification or histone modification. In vitro experiments, GPX3 expression is associated with cancer cell sensitivity to oxidant and platinum-based chemotherapy and is involved in tumor metastasis in oxidative environments.

Discussion: We explored the relationship between GPX3 and clinical features, immune infiltration characteristics, migration and metastasis, and chemotherapy sensitivities of human cancers. We further investigated the potential genetic and epigenetic regulation of GPX3 in cancer. Our results suggested that GPX3 plays a complicated role in the tumor microenvironment, simultaneously promoting metastasis and chemotherapy resistance in human cancers.

KEYWORDS

GPX3, pan-cancer, glutathione peroxidase, chemotherapy resistance, metastasis, tumor microenvironment (TME)

EDITED BY
Ira Ida Skvortsova,
Innsbruck Medical University, Austria

REVIEWED BY
Shaoyan Xi,
Sun Yat-sen University Cancer Center (SYSUCC), China
Lujun Shen,
Sun Yat-sen University Cancer Center (SYSUCC), China

*CORRESPONDENCE
Tao Huang
huangtaowh@163.com
Jie Tan
tj505_210@126.com

[†]These authors have contributed equally to this work

SPECIALTY SECTION
This article was submitted to Cancer Molecular Targets and Therapeutics, a section of the journal Frontiers in Oncology

RECEIVED 10 July 2022
ACCEPTED 13 January 2023
PUBLISHED 09 February 2023

CITATION
Hu Q, Chen J, Yang W, Xu M, Zhou J, Tan J and Huang T (2023) GPX3 expression was down-regulated but positively correlated with poor outcome in human cancers.
Front. Oncol. 13:990551.
doi: 10.3389/fonc.2023.990551

1 Introduction

According to the latest worldwide data, crude cancer incidence is still increasing, reflecting its significant socioeconomic burden (1, 2). Lung cancer (LUAD) and breast cancer (BRCA) are the leading malignancies in men and women, respectively. Morbidity and mortality rates for colorectal cancer (COAD), breast cancer, thyroid cancer (THCA), lung cancer, and prostate cancer (PRAD) continue to rise. Cancer metastasis, recurrence, and chemotherapy resistance threaten the life of cancer patients (3). Therefore, we continue to search for new adjuvant therapy and drug combination therapy regimens to enhance the antitumor effect of chemotherapy strategies.

Reactive oxygen species (ROS) and oxidative stress are thought to play several roles in carcinogenesis. For instance, when the gene expression of important molecules governing cell proliferation, apoptosis, or the cell cycle is aberrant, oxidative stress can lead to long-lasting DNA damage and may induce cancer. ROS can promote cancer development by activating multiple signaling pathways (4–9). Therefore, Antioxidants were recommended for cancer prevention and treatment (10–13). Unfortunately, the use of antioxidants in cancer treatment produced disappointing results (14, 15). Antioxidant dietary supplementation has been associated increased incidence and mortality of lung and prostate cancers and promoted breast cancer (16–20). ROS has a dual role in cancer, particularly their contradictory ability to induce cancer cell proliferation or apoptosis (13). In early precancerous and tumor stages, where antioxidant activity was decreased, ROS contribute to cancer progression by generating mutations in oncogenes and tumor suppressor genes (such as RAS and TP53) (4–9). However, as cancer develops into more advanced stages, tumor cells produce large amounts of antioxidants like NADPH and GSH to protect themselves against apoptosis and the associated intratumoral oxidative damage (21, 22). According to previous studies, antioxidants like GSH play a significant role in promoting the emergence and progression of several cancers (23, 24).

Glutathione peroxidase (GPX) is a family of enzymes that protect cells from ROS and play an important role in regulating redox balance (25–28). Glutathione peroxidase 3 (GPX3) located in 5q23 is the only exocrine member of the GPX family and plays an important role in the detoxication of hydrogen peroxide and other oxygen-free radicals (29). GPX3 is expressed in the gastrointestinal, kidney, brain, breast, liver, heart, lung, and adipose tissues (30). Studies have found that serum GPX3 content can be used as a tumor marker (31, 32). GPX3 may be involved in cancer processes by regulating ROS levels. GPX3 is an effective inhibitor of cancer development and progression (33–35). In addition, specific downregulation of GPX3 was found in many types of cancer (36–40). However, GPX3 has also been implicated in metastasis and cancer progression in ovarian, kidney, and thyroid cancers (41–44). It has been reported that the high expression of GPX3 may be associated with abdominal metastasis of serous ovarian adenocarcinoma (41). However, the expression level of GPX3 in tumors has not been extensively studied. The role that GPX3 plays in cancer is unclear. In addition, as a secretory GPX member, the relationship between GPX3 and the tumor microenvironment has not been discussed.

In this study, we explored the role of GPX3 in human tumor diagnosis, prognosis, and sensitivity to treatment and its relationship to the tumor microenvironment.

2 Materials and methods

2.1 Chemicals, reagents, and antibodies

The Cisplatin (CDDP), Carboplatin (NSC 241240) were purchased from MCE Biological Corporation (CA: HY-17394, NSC 241240). The rabbit normal IgG and antibodies against GPX3 (1:1000, ab256470) was purchased from Abcam (Shanghai, China). Antibodies against GAPDH (1:2000, 60004-1-Ig), HRP-conjugated secondary antibody (1:10000, SA00001-2) were purchased from proteintech (Shanghai, China).

2.2 Cell lines, culture conditions, and transduction

MDA-MB-231 and BT-549 are human breast cancer, Lovo and SW480 are human colorectal cancer cell lines, Ovcar-4 is human ovarian cancer, and MKN45 is human gastric cancer cell lines. They were obtained from American Type Culture Collection (ATCC). MDA-MB-231 cultured in L15 (Boster, CA) supplemented with 10% FBS in a humidified atmosphere without CO_2 at 37°C. BT-549, MKN45 were cultured in RPMI 1640 medium (Gibco, Darmstadt, Germany) supplemented with 10% FBS, Lovo and SW480 was cultured in DMEM (Gibco, Darmstadt, Germany) supplemented with 10% FBS, and they were cultured in a humidified atmosphere of CO2/air (5%/95%) at 37°C. Ovcar-4 was cultured in DMEM/F12 (Gibco, Darmstadt, Germany) supplemented with 10% FBS, and cultured in a humidified atmosphere of CO2/air (5%/95%) at 37°C. We transfected GPX3 knockout adenovirus (shGPX3, 116908-1), GPX3 overexpression adenovirus (oeGPX3, 77869-1) and corresponding control (Ctrl, CON525) into breast cancer (MDA-MB-231, BT-549), colorectal cancer (Lovo, SW480), gastric cancer (MKN45), and ovarian cancer (Ovcar-4) cell lines. All adenovirus were purchased from (Genechem, Shanghai, China).

2.3 qRT-PCR

Total RNA was extracted from the samples with TRIzol (Vazyme, Nanjin, China). In this study, we extracted untreated ovarian cancer (Ovcar-4), breast cancer (MDA-MB-231, BT-549), colorectal cancer (Lovo, SW480) and gastric cancer (MKN45) cells' RNA to examine the basal expression level of GPX3 in these cells. After transfected GPX3 knockout adenovirus (shGPX3), GPX3 overexpression adenovirus (oeGPX3) and corresponding control (Ctrl) into breast cancer (MDA-MB-231, BT-549), colorectal cancer (Lovo, SW480), gastric cancer (MKN45), and ovarian cancer (Ovcar-4) cells for 72h, their RNA was extracted. Later, we examined the efficiency of adenovirus transfection in regulating GPX3 expression. The complementary DNA was synthesized using a PrimeScript RT reagent Kit (Takara Bio, Otsu, Japan), messenger RNA expression was examined by real-time polymerase chain reaction (RT-PCR) using FastStart Universal SYBR Green Master Mix (Takara Bio, Otsu, Japan) and performed in ABI StepOne Plus Real-time PCR Detection System (Applied Biosystems, Foster City, CA). PCR recycling condition: 95 °C, 5min; 95 °C for 10s, 60 °C for 30s, 40 cycles.

The expression level of GAPDH was simultaneously quantified as an internal standard control. The sequences of all primers (Sangon, Shanghai, China) used were as follows:

GAPDH-F: 5'- TGACATCAAGAAGGTGGTGA-3'
GAPDH-R: 5'- TCCACCACCCTGTTGCTGTA-3'
GPX3-F: 5'- GAGAAGTCGAAGATGGACTGCC-3'
GPX3-R: 5'- AGACCGAATGGTGCAAGCTC-3'

2.4 Wound healing assay

The cells were seeded into 6-well-plates. When shGPX3, oeGPX3 and Ctrl cells cover the entire well, we wounded the cells with 200 µL sterile pipette tips. After washing off the floating cells with PBS, the cells were cultured in 1% FBS medium. H_2O_2 (5 µM) treated shGPX3, oeGPX3 and Ctrl cells for 4h. After washing off H_2O_2 with PBS, the cells were seeded into 6-well-plates. After cells cover the entire well, we performed wound healing procedure as above. The photos were taken under the microscope at 0, 48 hours after injury. Wound Healing size % = (width0 h – width48h)/width0h * 100%.

2.5 Transwell assay

5×10^5 cells were seeded into the upper chambers of transwell culture plates (Corning, Shanghai, China). Medium supplemented with 20% FBS (500 µl) was put into the lower chambers. H_2O_2 (5 µM) treated shGPX3, oeGPX3 and Ctrl cells for 4h. After washing off H_2O_2 with PBS, 5×10^5 cells were seeded into the upper chambers of transwell culture plates. We performed Transwell assay as above. After incubation for 24 h for migration assays, cells penetrated to the lower surface of the membrane and fixed with 4% paraformaldehyde for 60 min and then stained with crystal violet for 30 min and counted.

2.6 Clonogenicity assays

For traditional, 5000 cells/well were seeded per well in 6-well plates, and wete cultured for 14 days under normal culture conditions. For cisplatin treatment, cisplatin (dissolved in PBS) was added to cells at clonal density in serum free media for 1 h, cells were then washed twice, and complete growth media was added. In total, 10 - 14 days after seeding plates were fixed with 4% paraformaldehyde for 60 min and then stained with crystal violet for 30 min.

2.7 CCK-8 viability assay

The viability of cells seeded in 96-well plates (1000 cells/well) was tested using Cell Counting Kit 8 (CCK-8, (Beyotime, Shanghai, China)). CCK-8 reagent containing serum free media (1:100, 100 µL) was added to each well, and cells were incubated for 1 h. The absorbance was measured at 450 nm using a microplate reader (BioTek, VT).

2.8 Drug sensitivity assay

Equal number of cells were seeded into 96-well plates (3000 cells/well) and cell viability in response to different concentration of H_2O_2 and cisplatin was measured following 24h after treatment. Cell viability was assessed by using the Cell Counting Kit 8 (CCK-8, (Beyotime, Shanghai, China)) according to the manufacturer's instructions. The absorbance was measured at 450 nm using a microplate reader (BioTek, VT).

2.9 Breast cancer lung metastasis assay in nude mice

Animal experimental procedures were approved by the Ethics Committee of Tongji Medical College, Huazhong University of Science and Technology (IACUC Number: 2612). Athymic nude (nu/nu) mice (4-5 weeks old, female) were purchased from gempharmatech (Jiangsu, China) and fed in a special pathogen-free animal facility and allowed to eat and drink ad libitum. The mice were randomized into 2 groups with 10 mice per group, and then separately inoculated subcutaneously MDA-MB-231/shGPX3 and MDA-MB-231/shCtrl cell suspension. BALB/c nude mice received $2*10^6$ cells (in 100 µL serum-free 1640), directly injected into the tail vein. At the 28 days after injection, lung tissues were harvested, imaged, embedded in 10% paraffin, and subjected to H&E staining.

2.10 Bioinformatics analysis

RNA sequencing data and DNA methylation450 data were downloaded from the Cancer Genome Atlas Database (TCGA) (https://portal.gdc.cancer.gov/). Genome-wide GPX3 expression profiles patients were downloaded from TCGA (https://portal.gdc.cancer.gov/). And genetic alteration from TCGA was explored in cBioPortal (https://www.cbioportal.org/). Protein expression of GPX3 was collected from Clinical Proteomic Tumor Analysis Consortium (CPTAC, https://proteomics.cancer.gov/programs/cptac). GPX3 expression in tissue was collected from human protein atlas version 22.0 (HPA, http://www.proteinatlas.org/) (45). The URL links of normal tissues: normal breast tissue (https://www.proteinatlas.org/ENSG00000211445-GPX3/tissue/breast#img), ovarian tissue (https://www.proteinatlas.org/ENSG00000211445-GPX3/tissue/ovary#img), colon tissue (https://www.proteinatlas.org/ENSG00000211445-GPX3/tissue/colon#img), renal tissue (https://www.proteinatlas.org/ENSG00000211445-GPX3/tissue/kidney#img), lung tissue (https://www.proteinatlas.org/ENSG00000211445-GPX3/tissue/lung#img), and endometrium tissue (https://www.proteinatlas.org/ENSG00000211445-GPX3/tissue/endometrium#img). The URL links of cancer tissues: breast cancer (https://www.proteinatlas.org/ENSG00000211445-GPX3/pathology/breast+cancer#img), ovarian cancer (https://www.proteinatlas.org/ENSG00000211445-GPX3/

pathology/ovarian+cancer#img), colon cancer (https://www.proteinatlas.org/ENSG00000211445-GPX3/pathology/colorectal+cancer#img), renal cancer (https://www.proteinatlas.org/ENSG00000211445-GPX3/pathology/renal+cancer#img), lung cancer (https://www.proteinatlas.org/ENSG00000211445-GPX3/pathology/lung+cancer#img), and endometrium cancer (https://www.proteinatlas.org/ENSG00000211445-GPX3/pathology/endometrial+cancer#img).GPX3 expression profiles in cell lines were downloaded from Broad Institute Cancer Cell Line Encyclopedia (CCLE, https://portals.broadinstitute.org/ccle/) (46), and drug sensitivity of cancer cell lines were collected from Genomics of Drug Sensitivity in Cancer (GDSC. https://www.cancerrxgene.org/) (47). Median expression was used to dichotomize expression of GPX3, the cutoff to define "high value" at or above the median and below the median define "low value". Kaplan-Meier curve and receiver operating characteristic (ROC) curve analysis was performed by SPSS 22.0 (SPSS Inc., Chicago, IL, USA). Correlation between drug sensitivity and GPX3 was obtained from TCGA database, Pairwise Pearson correlation between the expression of GPX3 and IC50 of drugs were examined, only a significant correlation ($p < 0.05$) was retained. DAVID Functional Annotation Bioinformatics Microarray Analysis (https://david.ncifcrf.gov/) was used to perform Gene ontology term enrichment (GO) and Kyoto Encyclopedia of Genes and Genomes (KEGG) pathway analysis. Immune infiltration analysis was performed using CIBERSORT (48), MCPcounter (49), TIMER (50), and xCELL (51) algorithms and online websites.

2.11 Statistical analysis

All experiments were performed at least three times. Parametric data are shown as means ± standard deviations (SDs) and nonparametric data as medians and ranges. Two-way ANOVA or one-way ANOVA with Tukey' s multiple comparison test was used for multiple group analysis. Unpaired Student' s t-tests were used to compare data between two groups. Two-tailed P-values < 0.05 were considered statistically significant. Statistical analyses were performed using GraphPad prism 9 software (GraphPad software, Inc., La Jolla, CA) and SPSS.

3 Results

3.1 The expression and correlations of GPX3 in human cancers

We compared the expression of GPX3 in human cancers and normal tissues in several public databases. In the TCGA and GTEx databases, we found that GPX3 mRNA expression was downregulated in various types of cancers (Figure 1A), including BRCA, COAD, LUAD, ovarian cancer (OV), kidney renal clear cell carcinoma (KIRC), and endometrial cancer (EC). CPTAC analysis and the HPA database demonstrated that the protein expression of GPX3 was also downregulated in BRCA, OV, COAD, ccRCC, LUAD, and EC (Figure 1B). ROC curves were used to verify that GPX3 is a valuable diagnostic biomarker in several types of cancers, including BRCA, COAD, LUAD, stomach adenocarcinoma (STAD), head and neck squamous cell carcinoma (HNSC), kidney renal papillary cell carcinoma (KIRP), and THCA, as shown in Figure 1C (AUCs > 0.7).

We used the TCGA database to examine the relationship between GPX3 expression and the pathological stages of human cancer. In COAD, READ, STAD, and PAAD, GPX3 expression was positively correlated with the T stage (Figure 2A). However, in PRAD, HNSC, KIRC, BRCA, KIPA, skin cutaneous melanoma (SKCM), bladder urothelial carcinoma (BLCA), and adenoid cystic carcinoma (ACC), GPX3 expression was lower in the higher T stage (Figure 2B). In addition, we found in BRCA, COAD, and READ that high GPX3 expression was associated with a higher N stage (Figure 2C). We

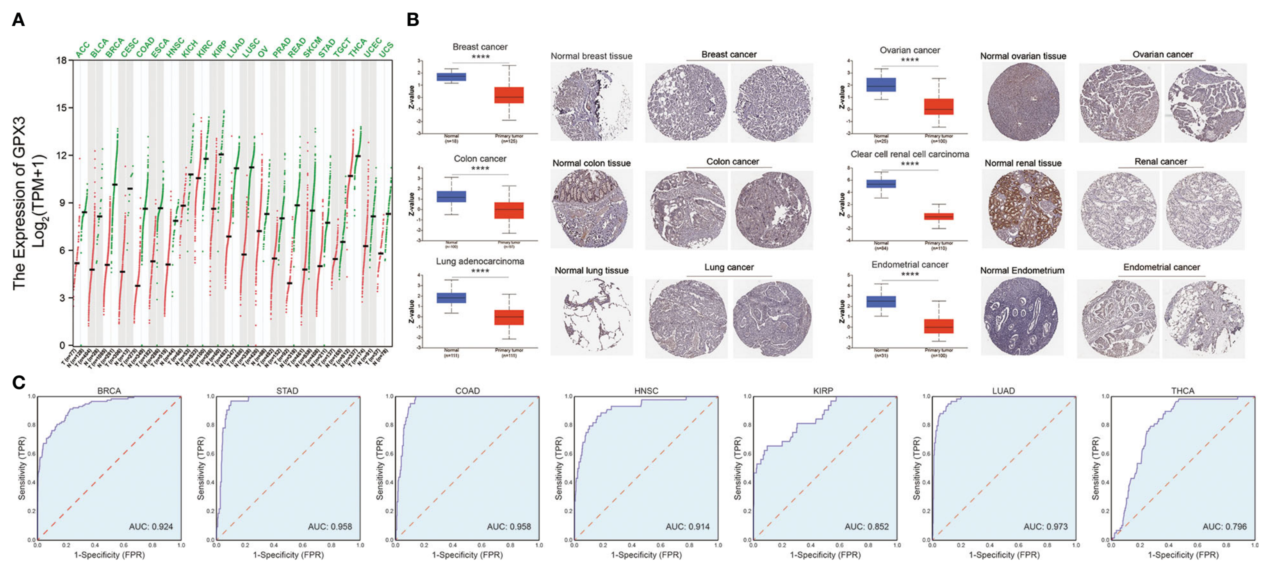

FIGURE 1
The expression of GPX3 in human cancer. **(A)** The expression of the GPX3 gene in pan-cancer was explored in TCGA and GTEx database. **(B)** Based on the CPTAC analysis and the HPA database, the expression of the GPX3 protein. **(C)** ROC analysis of GPX3 gene in TCGA database.

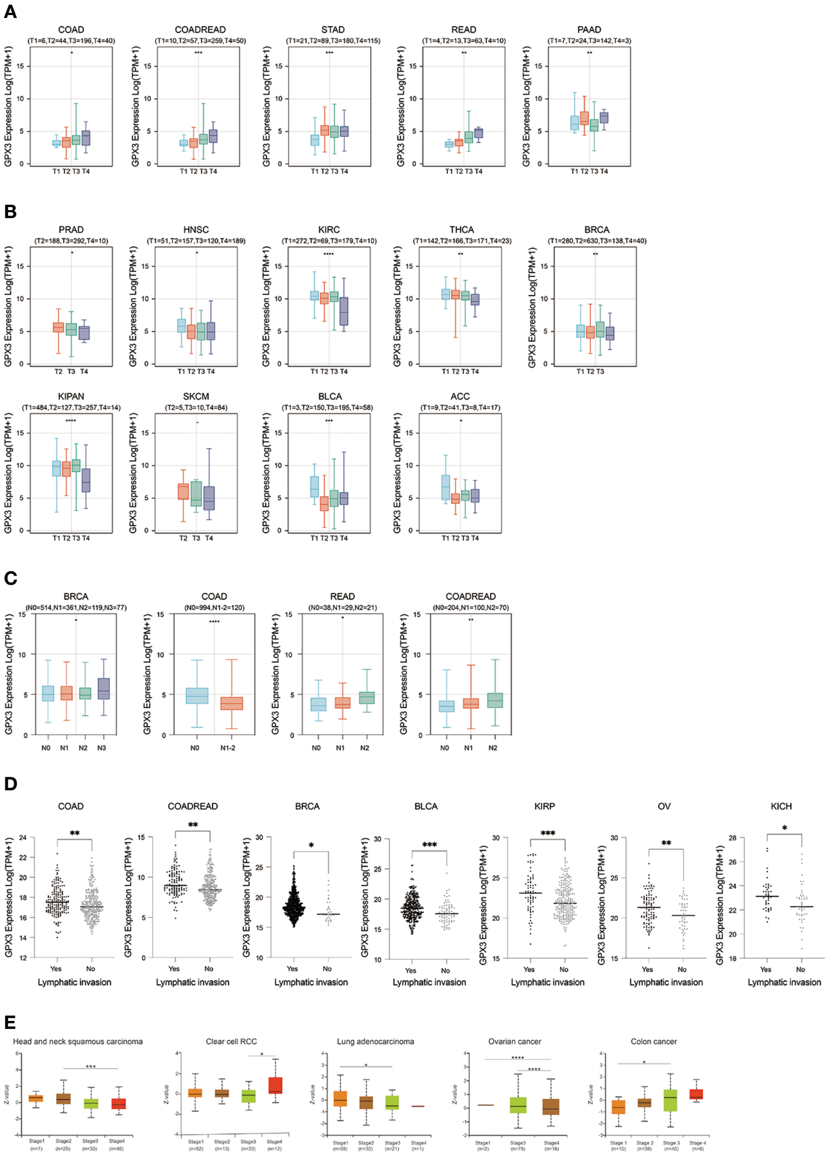

FIGURE 2
The expression of GPX3 was correlated with stage and lymph node metastases. **(A)** The GPX3 expression was positively correlated with T stage in COAD, READ, STAD, and PAAD. **(B)** The GPX3 expression was negatively correlated with T stage in PRAD, HNSC, KIRC, BRCA, KIPA, SKCM, BLCA, and ACC. **(C)** High GPX3 expression was associated with higher N stage in COAD, READ, BRCA, BLCA, KIRP, OV and KICH. **(D)** High GPX3 expression was associated with lymph node metastases in COAD, READ, BRCA, BLCA, KIRP, OV and KICH. **(E)** GPX3 protein expression was correlated with the pathological stages of HNSC, ccRcc, LUAD, OV, and COAD in CPTAC database.

compared the relationship between GPX3 expression level and the presence or absence of lymph node metastasis (Figure 2D). In COAD, READ, BRCA, BLCA, KIRP, OV, and KICH, GPX3 expression was increased in the lymph node metastatic group compared with the control group. CPTAC databases showed that GPX3 expression was correlated with the pathological stages of HNSC, ccRcc, LUAD, OV, and COAD (Figure 2E).

The correlations between GPX3 expression and the clinical characteristics of several human cancers, including COAD, prostate adenocarcinoma (PRAD), KIRC, LUAD, and STAD, are shown in Table 1. We collected Data from the TCGA database. Patients were divided into a high group and a low group based on the median level of GPX3 expression. Then we compared the differences between the two groups in clinical characteristics. In COAD, GPX3 expression is associated with T-, N-, M-stage, and lymph node metastasis. In PRAD, GPX3 expression is associated with T-, M-stage, lymph node metastasis, and recurrence. GPX3 expression is associated with the M stage in KIRC. In LUAD, GPX3 expression was associated with recurrence. In STAD, GPX3 expression is associated with the M stage and recurrence. Overall, patients with high GPX3 expression and low GPX3 expression in COAD, PRAD, KIRC, LUAD, and STAD showed differences in T-, N-, and M-stage, lymph node metastasis, and occurrence of recurrence. Survival analysis showed that GPX3 expression was associated with the survival of multiple human cancers. High GPX3 expression was associated with poor overall survival (OS) in COAD, READ, LUSC, STAD, and STES (Figure 3A) and was associated with poor disease-specific survival (DSS) in COAD, READ, ESCA, LUSC, PAAD,

TABLE 1 Relation of GPX3 expression and the clinical characteristic of patients with cancers.

Characteristic	COAD			PRAD			KIRC			LUAD			STAD		
	Low	High	p	Low	High	p	Low	High	p	Low	High	p	Low	High	p
num	209	181		252	299		255	280		307	275		213	194	
T stage			**0.009**			**0.007**			0.383			0.625			0.125
T1	9 (3.1%)	2 (0.9%)					126(49%)	149(53%)		99 (32%)	92 (33%)		15 (7%)	7 (4%)	
T2	56 (19.3%)	24(13.0%)		81 (32%)	137 (46%)		35 (14%)	35 (13%)		175 (57%)	146 (53%)		39 (18%)	52 (27%)	
T3	198(68.2%)	121(68.0%)		163(65%)	150 (50%)		86 (34%)	93 (33%)		24 (8%)	26 (9%)		97 (45.5%)	84 (43%)	
T4	24 (11%)	34 (19%)		6 (2%)	7 (2%)		8 (3%)	3 (1%)		8 (3%)	12 (4%)		62 (29%)	43 (22%)	
N stage			**0.036**			**0.002**			0.37			0.899			0.452
N0	184(63.4%)	93(54.5%)		171(67.5%)	222(74.2%)		109(43%)	131(47%)		200(65.1%)	171(61.5%)		70 (32.8%)	53 (27.3%)	
N1	62(30%)	45 (25%)		51(20.2%)	29 (9.6%)		10 (4%)	6 (2%)		54 (17.5%)	53 (19%)		52 (24.4%)	56 (28.8%)	
N2-3	42(20.0%)	43 (24.0%)								45 (14.6%)	44(15.7%)		81(39.1%)	73(37.5%)	
M stage			**0.045**						**0.009**			0.13			**0.011**
M0	214(73.3%)	129(70.2%)		/	/		188(74%)	236(84%)		197(64.1%)	197(70.8%)		197(92.4%)	161(82.9%)	
M1	33 (16%)	32 (18%)		/	/		45(18%)	33(12%)		13 (4%)	14 (5%)		7 (3.2%)	20 (10.3%)	
Lymph Node Positive	99 (47%)	86 (48%)	**0.008**	52 (21%)	29 (10%)	**0.001**	10 (4%)	7 (3%)	0.344				132 (62%)	123 (63%)	0.411
Relapse, n(%)	/	/		24 9.5%)	64(21.4%)	**0.008**		5 (1.6%)		94 (30.6%)	67 (24.1%)	**0.046**	20 (9.3%)	42 (21.6%)	**<0.001**

P<0.05, showed bold values.

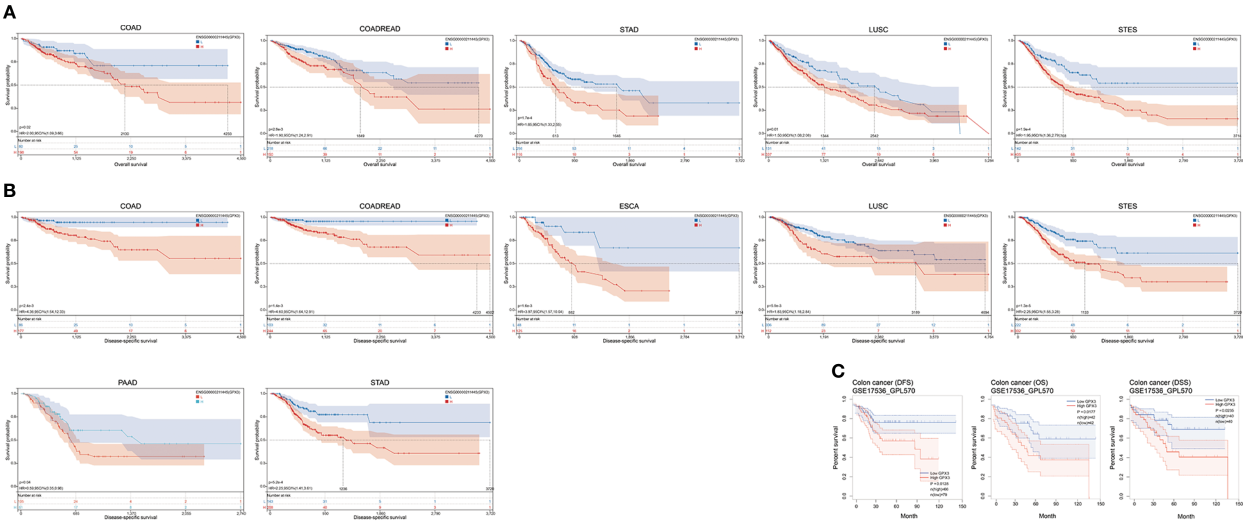

FIGURE 3
The correlations between GPX3 expression and the prognosis of human cancers. **(A)** GPX3 was negatively associated with OS of COAD, READ, LUSC, STAD, and STES. **(B)** GPX3 was negatively associated with DSS of COAD, READ, ESCA, LUSC, PAAD, STAD, and STES. **(C)** higher GPX3 expression was correlated with poor outcome of COAD patients in GEO database.

STAD, and STES (Figure 3B). The GEO database was also used to show that higher GPX3 expression was correlated with poor outcomes in patients with COAD (Figure 3C). Univariate and multivariate Cox analyses were performed to explore the association between GPX3 expression and OS in BRCA, COAD, LUAD, and STAD (Table 2). In BRCA, we used univariate analysis to find that risk factors for OS included higher GPX3 expression (p = 0.0170; HR = 1.410), M1 stage (p = 0.009; HR = 1.681), N1-3 stage

TABLE 2 Univariate and multivariate analyses of overall survival.

Cancer type (N)	Characteristics	Uni-variate COX analysis		Multivariate COX analysis	
		Hazard ratio (95%CI)	P	Hazard ratio (95%CI)	P
BRCA (1194)	GPX3 (low vs. high)	1.410 (1.063, 1.870)	**0.0170**	1.587 (1.162, 2.167)	**0.004**
	M stage (M0 vs. M1)	1.681 (1.164, 2.426)	**0.009**	0.977 (0.616, 1.547)	0.920
	N stage (N0 vs. N1-3)	2.285 (1.678, 3.110)	< **0.001**	1.788 (0.777, 4.113)	0.172
	T stage (T1-3 vs. T4)	3.220 (2.019, 5.135)	< **0.001**	(1.546, 4.594)	< **0.001**
	lymph node (no vs. yes)	2.208 (1.601, 3.046)	< **0.001**	1.162 (0.514, 2.627)	0.718
COAD	GPX3 (low vs. high)	1.180 (0.779, 1.786)	0.435	0.861 (0.543, 1.364)	0.523
	M stage (M0 vs. M1)	4.626 (2.931, 7.303)	< **0.001**	3.023 (1.756, 5.204)	< **0.001**
	N stage (N0 vs. N1-3)	2.502 (1.639, 3.818)	< **0.001**	1.413 (0.228, 8.761)	0.710
	T stage (T1-3 vs. T4)	3.377 (2.029, 5.622)	< **0.001**	2.394 (1.346, 4.258)	**0.003**
	lymph node (no vs. yes)	2.549 (1.650, 3.937)	< **0.001**	1.248 (0.207, 7.545)	0.809
LUAD	GPX3 (low vs. high)	0.754 (0.574, 0.989)	**0.041**	0.823 (0.603, 1.124)	0.221
	M stage (M0 vs. M1)	2.059 (1.244, 3.410)	**0.005**	1.665 (0.963, 2.880)	0.068
	N stage (N0 vs. N1-3)	2.641 (2.006, 3.479)	< **0.001**	2.649 (1.933, 3.630)	< **0.001**
	T stage (T1-3 vs. T4)	1.955 (1.090, 3.507)	**0.041**	1.181 (0.634, 2.201)	0.601
STAD	GPX3 (low vs. high)	1.533 (1.117, 2.106)	**0.008**	2.428 (1.000, 2.040)	**0.050**
	M stage (M0 vs. M1)	2.052 (1.159, 3.632)	**0.014**	2.033 (1.043, 3.962)	**0.037**
	N stage (N0 vs. N1-3)	1.783 (1.206, 2.635)	**0.004**	0.410 (0.048, 3.524)	0.417
	T stage (T1-3 vs. T4)	1.277 (0.897, 1.817)	0.175	1.320 (0.888, 1.962)	0.170
	lymph node (no vs. yes)	1.933 (1.268, 2.946)	**0.002**	4.437 (0.545, 36.089)	0.164

P<0.05, showed bold values.

(p < 0.001; HR = 2.285), T4 stage (p < 0.001; HR = 3.220), and lymph node metastasis (p < 0.001; HR = 2.208). By using multivariate analysis, we found that higher GPX3 expression (p = 0.004; HR = 1.410) and T4 stage (p < 0.001; HR = 2.665) were risk factors for OS. Similarly, in STAD, we used univariate analysis to find that higher GPX3 expression (p = 0.008; HR = 1.533), M1 stage (p = 0.014; HR = 2.052), N1-3 stage (p = 0.004; HR = 1.783), lymph node metastasis (p = 0.002; HR = 1.933) were risk factors for OS. We used multivariate analysis and found that higher GPX3 expression (p = 0.050; HR = 2.428) and the M1 stage (p = 0.037; HR = 2.033) were risk factors for OS. Specific data are shown in Table 2. Overall, higher GPX3 expression is a risk factor for OS of BRCA and STAD.

3.2 Intracellular function and regulation of GPX3

We used the STRING online database to create a GPX3-binding PPI network (Figure 4A) and GO and KEGG analyses (Figure 4B) to explore the potential function of GPX3. The results indicated that GPX3 and GPX3-binding proteins were mainly involved in thyroid hormone synthesis and glutathione metabolism.

Furthermore, we explored the relationship between GPX3 and immune invasion in the tumor microenvironment (TME). Through the CIBERSORT, MCPcounter, TIMER, and xCELL algorithms and online websites, we carefully analyzed the relationship between GPX3 expression levels in human cancers and immune score, stromal score, and various cell components in the TME (Figure 4C–E; Table S1). In most cancer types, the expression level of GPX3 was positively correlated with the stromal score and immune score. Notably, macrophages, especially M2 macrophages, had a consistently positive correlation with GPX3 in various cancers. In addition, immunosuppressive cells in the TME, including myeloid dendritic cells (MDCs) and CD4+ Th1 and Th2 T cells, also had a positive correlation with GPX3. These results suggested that higher GPX3 expression may be related to the immunosuppressive state in the TME.

Next, we analyzed the factors regulating GPX3 expression. The epigenetic modification and regulation of GPX3 expression were explored with the Illumina Infinium human methylation 450 and ChIP-Atlas (https://chip-atlas.org) platforms (52, 53). We confirmed that in several cancer types, including lung squamous cell carcinoma (LUSC), PRAD, KIRP, LUAD, BRCA, and COAD, the expression of GPX3 was significantly lower in tumor tissues (Figure 5A). Our further analysis showed a negative correlation between GPX3 expression and DNA methylation of the GPX3 promoter region (Figure 5B). Enrichment peaks of H3K4me3 and dH3K27ac upstream of GPX3 were also observed in the brain, breast, lung, liver, spleen, kidney, and prostate tissues in our analysis (Figure 5C). Taken together, these results indicated that lower expression of GPX3 may be associated with epigenetic factors, including DNA methylation and histone acetylation.

Genetic alteration analysis showed that the overall alteration frequency of GPX3 was > 6%. Missense mutations were found to be the primary type of genetic alteration (Figure 5D, E). R123*/G, K147I, and R180S/H were essential alteration sites. They were detected in 1 case of bladder urothelial carcinoma (BUC) and LUAD, 1 case of ccRCC and uterine corpus endometrial carcinoma (UCEC), and 1 case of ccRCC and READ.

3.3 GPX3 promotes cancer cell migration

We compared GPX3 expression levels in ovarian cancer, renal clear cell carcinoma, breast cancer, colorectal cancer, and gastric cancer cell

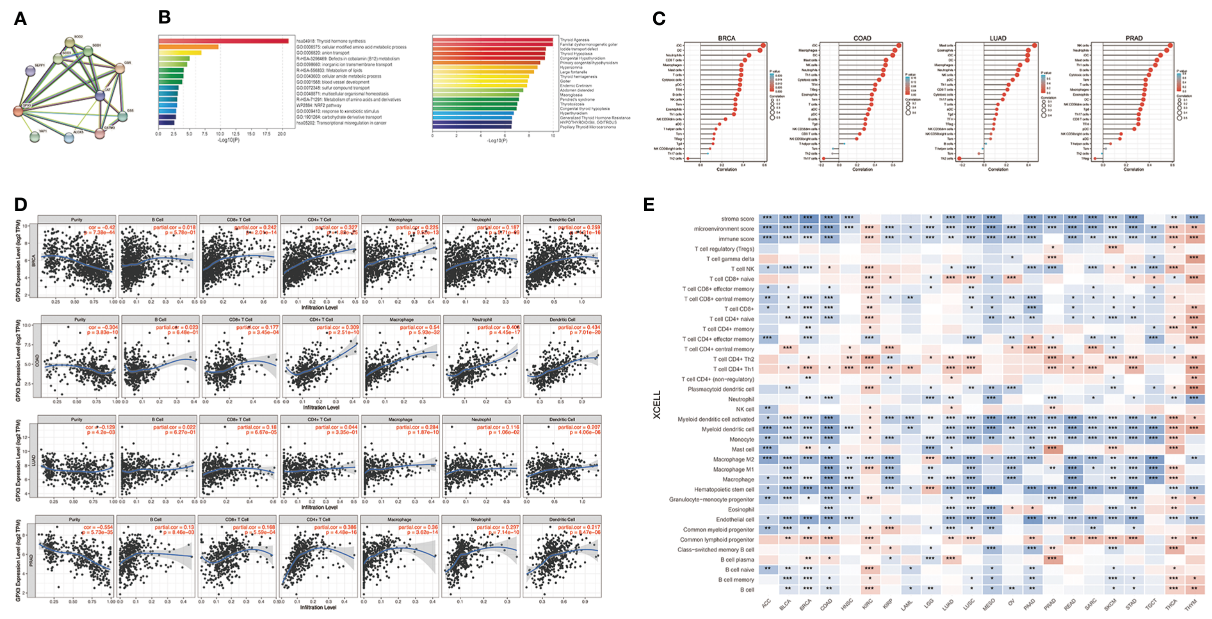

FIGURE 4
The potential function of GPX3 and effects on immune infiltration in cancers. **(A)** The GPX3-binding PPI analysis. **(B)** The GO and KEGG analysis of GPX3 and GPX3-related partners. **(C)** Correlation analysis between GPX3 expression and immune cells in scatter plots. **(D)** Correlation analysis between GPX3 expression and immune cells in stem-and-leaf display. **(E)** The immune score and cells analysis of GPX3 in pan-cancer.

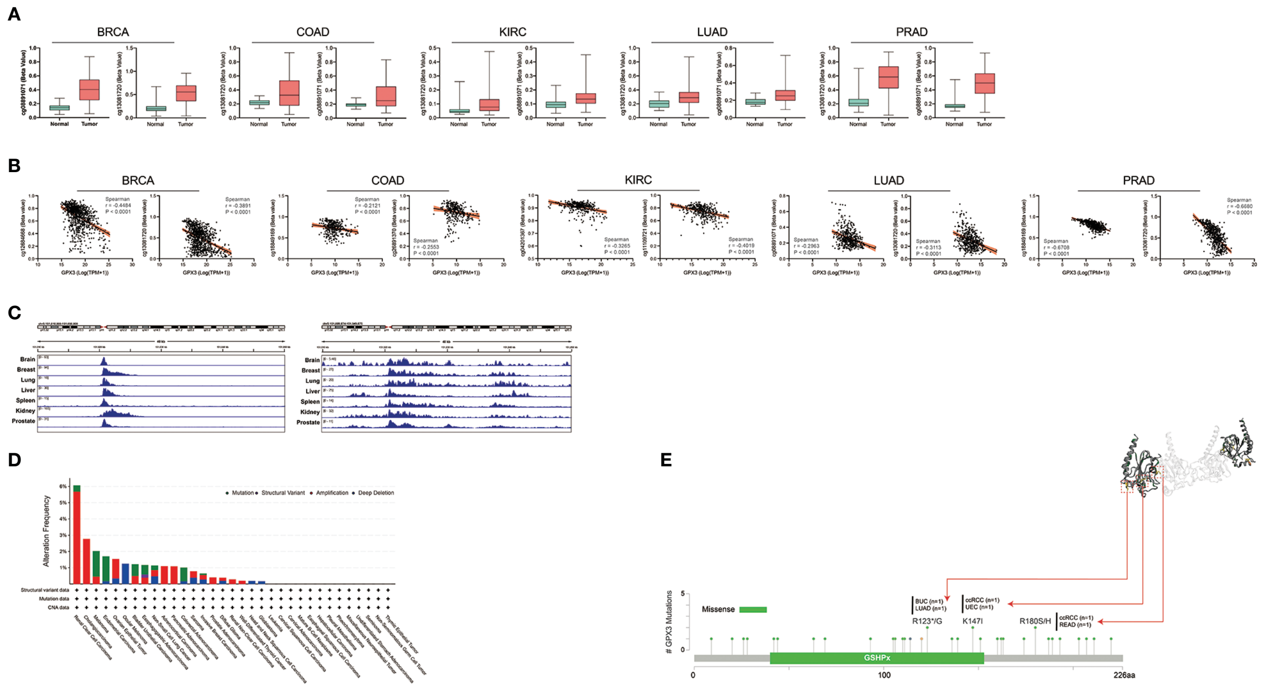

FIGURE 5
Epigenetic regulation and genetic alteration associated to the expression and structure of GPX3. **(A)** Based on the TCGA database, the DNA methylation level of GPX3 was analyzed in BRCA, COAD, KIRC, LUAD, and PRAD. **(B)** The correlation between GPX3 gene expression and DNA methylation level was analyzed in BRCA, COAD, KIRC, LUAD, and PRAD. **(C)** Enrichment of H3K4me3 and H3K27ac at the upstream of GPX3 in various organs. **(D)** The alteration frequency and mutation type of GPX3. Parts of the mutation sites were displayed within red dotted boxes in the 3D structure of GPX3.

lines using the CCLE database. We found that GPX3 expression levels were high in ovarian and renal clear cell carcinoma and moderate in breast, colorectal, and gastric cancers (Figure 6A). Then, we used RT-PCR (Figure 6B) and WB (Figure 6C) to test GPX3 expression levels in ovarian cancer (Ovcar-4), breast cancer (MDA-MB-231, BT-549), colorectal cancer (Lovo, SW480) and gastric cancer (MKN45) cell lines were examined. The results were consistent with CCLE, with the highest expression in ovarian cancer, followed by colorectal cancer and gastric cancer, and moderate expression in breast cancer. We transfected GPX3 knockout adenovirus (shGPX3), GPX3 overexpression adenovirus (oeGPX3), and corresponding control (Ctrl) into breast cancer (MDA-MB-231, BT-549), colorectal cancer (Lovo, SW480), gastric cancer (MKN45), and ovarian cancer (Ovcar-4) cell lines. We used RT-PCR (Figure 6D) and WB (Figure 6E) to demonstrate the regulatory efficiency of GPX3 expression.

We first examined the effect of GPX3 expression on metastasis. We found that knockdown GPX3 reduced wound healing ability and transmembrane migration ratio of ovarian and colorectal cancer cells (Figure S1, S2). But there was no significant effect on the wound healing percentage between shGPX3 and Ctrl of breast and gastric cancer. We used H_2O_2 with low concentration to simulate oxidative stress in anoikis during the initial stage of metastasis. After treatment with low concentrations of H_2O_2, shGPX3 significantly inhibited the metastasis of cancer cells. In the transwell experiment, compared with the Ctrl, the number of shGPX3 cells decreased significantly under the same magnification field of vision, while the number of oeGPX3 cells did not change compared with the Ctrl (Figure 7A). The wound healing experiment was used to compare the change in wound area at the same time. In MDA-MB-231 and BT549 cells, the wound area in the Ctrl group healed 74.4% and 71.0%, respectively, after 48 hours, while that in the shGPX3 group healed only 40.3% and 26.1%, respectively. Similarly, the wound healing area of the shGPX3 group was significantly less than that of the Ctrl group in other cell lines (Figure 7B).

Pulmonary metastasis of breast cancer is a manifestation of poor prognosis. We compared the effect of GPX3 on lung metastasis in breast cancer *in vivo*. The MDA-MB-231 cell line bearing shGPX3 showed fewer pulmonary nodules than the NC group *in vivo*. HE staining of lung tissues showed more and larger metastatic cancer cell nests in the Ctrl group (Figure S3).

3.4 GPX3 showed little effect on proliferation

We first used the CCK-8 assay to compare the effect of GPX3 on the proliferation rate of tumor cells (Figure S4A). In ovarian cancer, shGPX3 caused Ovcar-4 proliferation to slow down compared to Ctrl. However, no difference in proliferation rate was observed in the breast, colorectal, or gastric cancer cells. oeGPX3 had no significant effect on the proliferation of these tumor cells.

We observed a different phenomenon in the plate cloning experiment (Figure S4B). In ovarian and breast cancer, we observed that the number of clones formed in the shGPX3 group was less than that in Ctrl. However, we found no difference on the number of plate clones between shGPX3 and Ctrl in colorectal or gastric cancer.

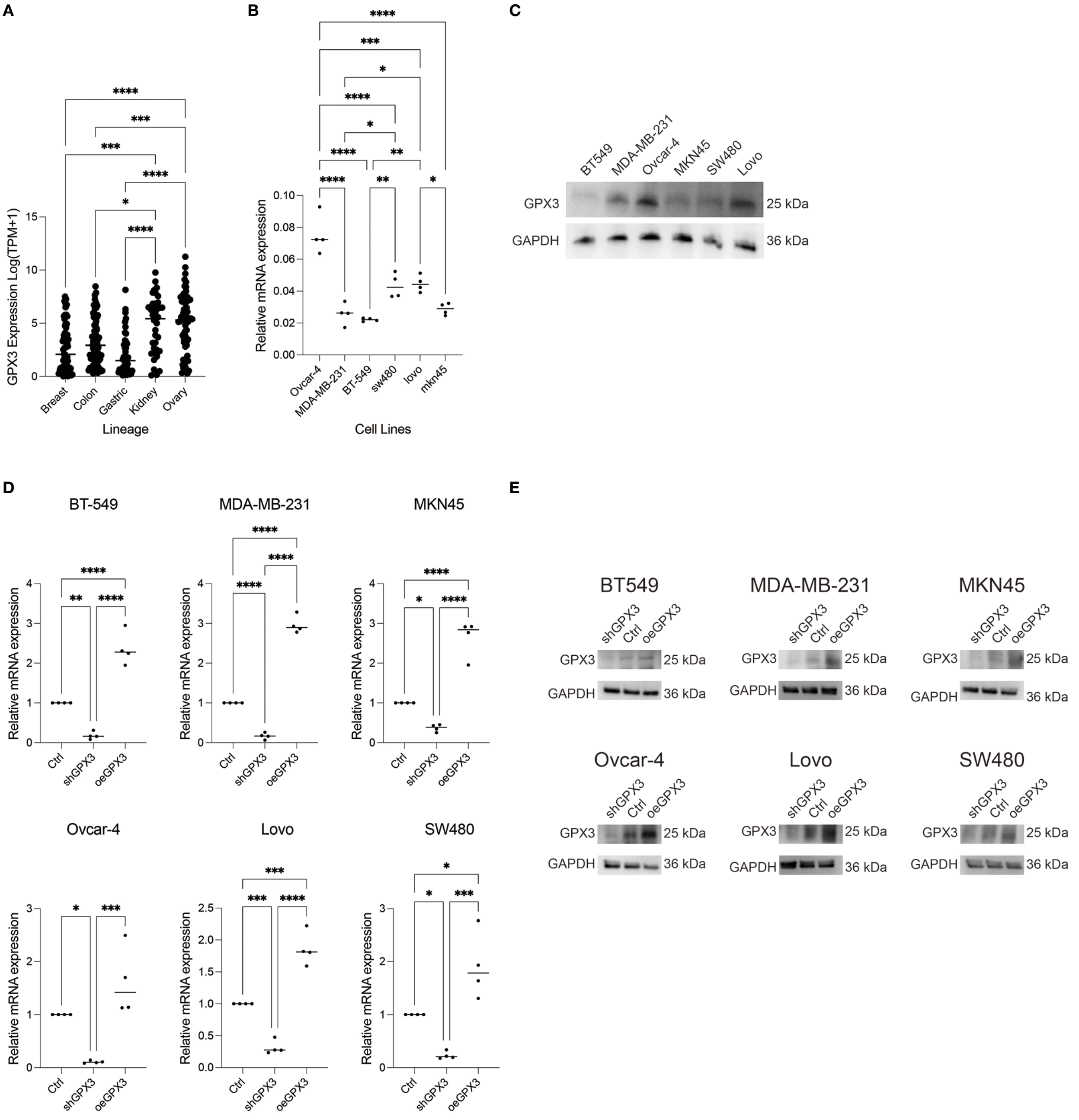

FIGURE 6
GPX3 expression in ovarian cancer (Ovcar-4), breast cancer (MDA-MB-231, BT-549), colorectal cancer (Lovo, SW480) and gastric cancer (MKN45) cell lines. **(A)** GPX3 expression levels in cancer cells analysed from CCLE database. **(B)** GPX3 expression in cancer cell lines examined by RT-PCR. **(C)** GPX3 expression in cancer cell lines examined by WB. **(D)** GPX3 expression regulation efficiency in cancer cells examined by RT-PCR. **(E)** GPX3 expression regulation efficiency in cancer cells examined by WB. *(p<0.05), **(p<0.01), ***(p<0.001), ****(p<0.0001).

oeGPX3 also showed no significant influence on the number of clones formed in these cancer cells.

3.5 shGPX3 increases oxidative stress damage to cancer cells

GPX3 is an important member of the cellular antioxidant system. We examined the effect of GPX3 on cellular oxidative stress resistance. We used a common oxidant, H_2O_2, and first compared the sensitivity of several tumor cell lines to H_2O_2. We found that downregulated GPX3 caused tumor cells to be more sensitive to oxidants (Figure 8A). When a certain concentration of H_2O_2 was used to treat tumor cells, shGPX3 resulted in more cell death than the Ctrl, while oeGPX3 partially rescued the loss of cell viability.

We explored the effect of GPX3 on ROS production in tumor cells. We found no significant increase in ROS levels in shGPX3 cells compared with Ctrl cells (Figure 8B). We then treated the cells with a lower concentration of H_2O_2 and examined intracellular ROS levels. Compared with the Ctrl, oeGPX3 partially reduced intracellular ROS levels, while shGPX3 significantly increased intracellular ROS levels (Figure 8C).

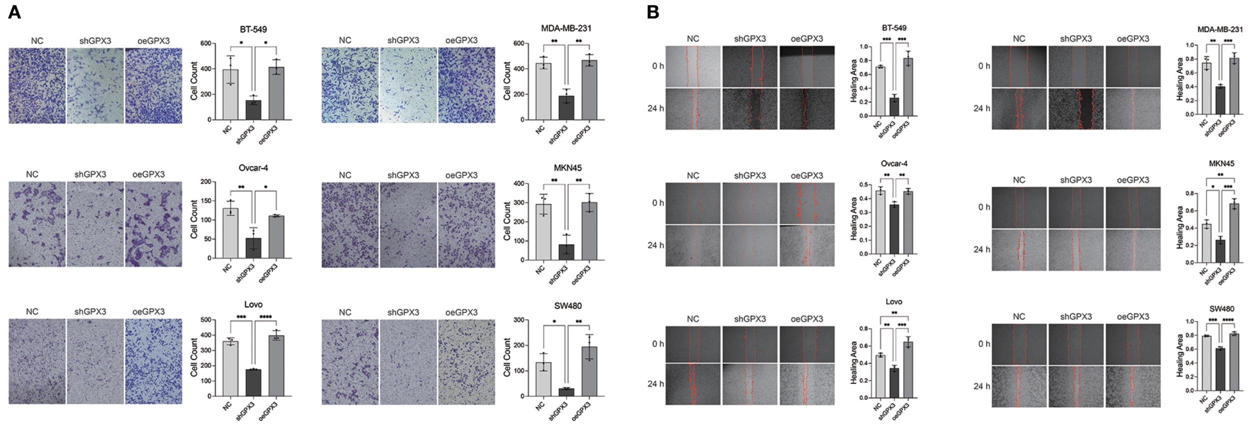

FIGURE 7
GPX3 promoted human cancer cell migration under oxidation environment. **(A)** Cell migration was assessed 4h following treatment with H_2O_2 by using transwell chamber assay. **(B)** Cell migration was assessed 4h following treatment with H_2O_2 by by using wound healing assay.

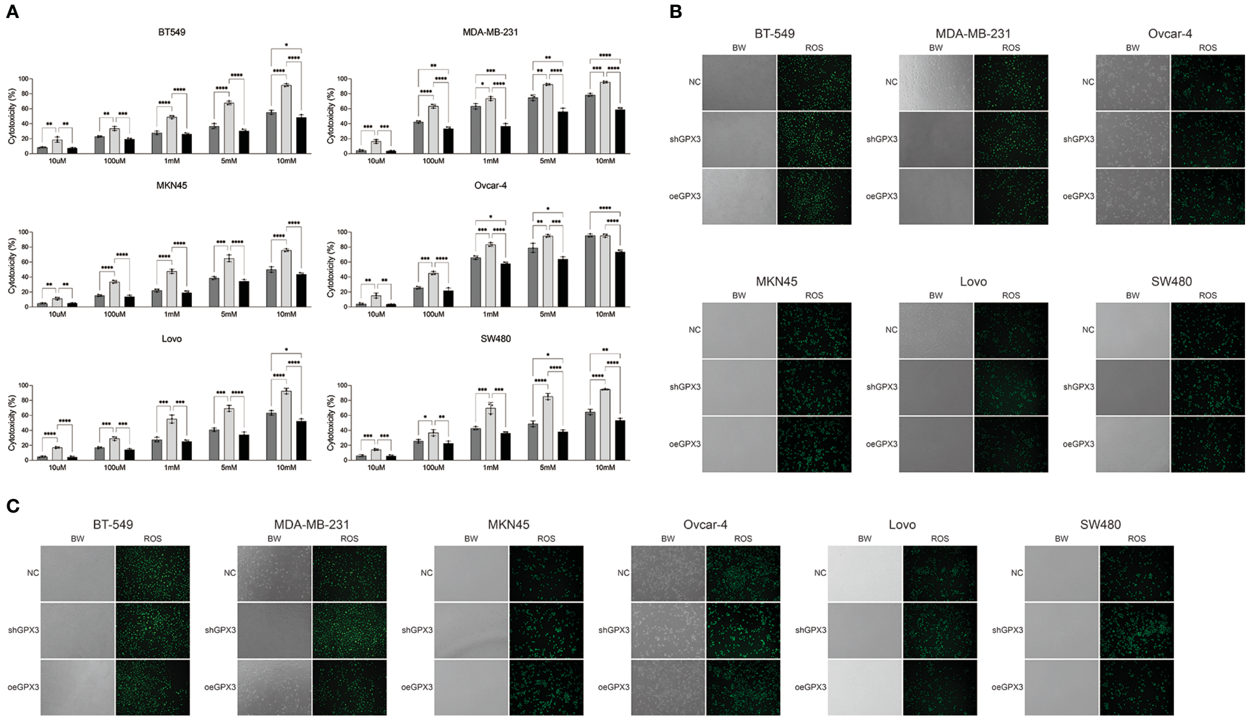

FIGURE 8
Knockdown GPX3 increased oxidative stress damage in human cancer. **(A)** Cell viability was assessed 24h following treatment with H_2O_2 by using cck-8 assay. **(B)** ROS in shGPX3, oeGPX3 and corresponding control cells was assessed by using DCFH-DA probe. **(C)** ROS in cells was assessed 4h following treatment with H_2O_2 by using DCFH-DA probe. *(p<0.05), **(p<0.01), ***(p<0.001), ****(p<0.0001).

3.6 shGPX3 increases the sensitivity of tumor cells to platinum-based chemotherapy

Many chemotherapeutic drugs played antitumor effects by increasing intracellular ROS and causing oxidative stress. Platinum-based chemotherapy, for example, increases intracellular ROS levels and causes large molecules (such as nucleic acids and proteins) damage, ultimately leading to death. We explored the correlation between GPX3 expression and chemotherapy sensitivities in cancer cell lines (54, 55). GPX3 expression data in cancer cells were collected from the cancer cell line encyclopedia (CCLE, https://portals.broadinstitute.org/ccle/) (46) The IC50 drug-sensitive data of cancer cells were collected from genomics of drug sensitivity in cancer (GDSC, https://www.cancerrxgene.org/) (47) (Figure 9A). We found that GPX3 expression level was positively correlated with the IC50 of many drugs, including paclitaxel, 5-fluorouracil, carboplatin, etoposide, cisplatin, and mitomycin. Higher GPX3 expression levels were associated with increased IC50 of drugs which means a reduced cell sensitivity to drugs. We speculated that GPX3 played a role in chemotherapy drug resistance in cancers.

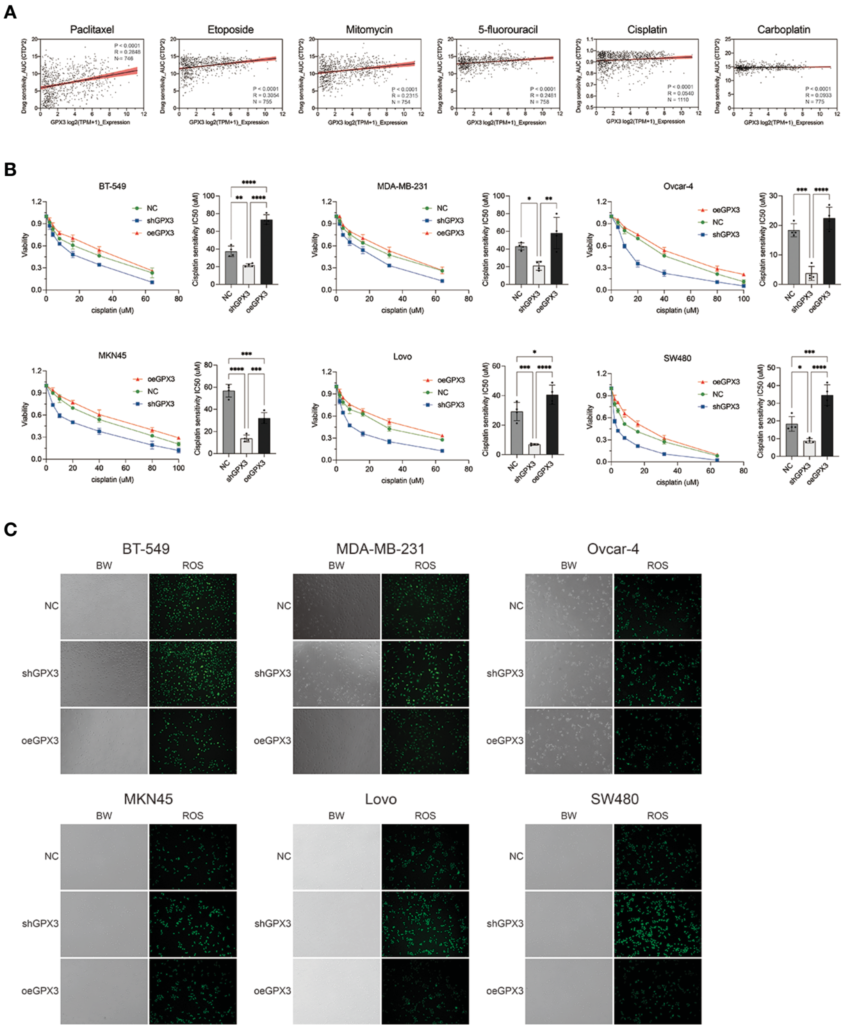

FIGURE 9
Knockdown GPX3 increased human cancer cell's sensitivity to cisplatin. **(A)** Expression of GPX3 was positively correlated to IC50 of chemotherapy drugs, including paclitaxel, etoposide, mitomycin, 5-fluorouracil, cisplatin, and carboplatin in pancancer. **(B)** Cell viability was assessed 24h following treatment with cisplatin by using cck-8 assay. **(C)** ROS in cells was assessed 4h following treatment with cisplatin by using DCFH-DA probe. *(p<0.05), **(p<0.01), ***(p<0.001), ****(p<0.0001).

We compared the effect of GPX3 on platinum-based chemotherapy sensitivity in several types of cancer cells (Figure 9B), and the results showed that shGPX3 resulted in increased sensitivity to platinum-based chemotherapy in breast cancer, ovarian cancer, colorectal cancer, and gastric cancer. We also compared the relationship between ROS level changes induced by cisplatin and GPX3. After the shGPX3 group was treated with cisplatin, the intracellular ROS level increased significantly more than that of the Ctrl and oeGPX3 groups (Figure 9C).

4 Discussion

GPX3 plays a role in cancer occurrence, progression, and treatment. Our results showed that GPX3 expression was significantly reduced in tumor tissues compared with normal tissues, including BRCA, COAD, HNSC, KIRC, KIRP, LUAD, PRAD, and STAD. The GPX3 expression level had good diagnostic accuracy (AUC>0.75, even 0.9) in BRCA, STAD, COAD, HNSC, KIRP, LUAD, and THCA. In addition, we found that the GPX3 protein expression level was related to the stage. Higher GPX3 expression is significantly associated with higher N-stage in BRCA, COAD, and READ. Compared with primary disease, the expression of GPX3 is higher in metastatic lymph node lesions. These suggested that higher GPX3 expression levels may be associated with early metastasis of human cancers, including COAD, READ, BRCA, BLCA, KIRP, OV, and KICH. For the T-stage, GPX3 played an inconsistent role in different types of cancer, possibly because of the difference in mRNA and protein data from several sources. We investigated the function of GPX3 in the prognosis of cancers. Based on the TCGA and GEO databases, we found that higher GPX3 expression was associated with poor OS in COAD, READ, LUSC, STAD, and STES patients and poor DSS in COAD, READ, ESCA, LUSC, PAAD, STAD, and STES patients. Cui et al. (56) used metabolic-related genes (MRGs) to predict the prognosis of COAD patients. They identified GPX3 as a risk factor in the COAD prognostic model ($p < 0.001$, HR: 1.006 - 1.023). Khan et al. (57) established the necroptosis-related genes prognostic index (NRGPI). They divided gastric cancer patients into high-risk and low-risk subgroups. The high-risk group showed higher GPX3 expression. Besides, GPX3 was associated with pathways relating to cancer progression and immunosuppression, such as Wnt and TGF-β. GPX3 acted as one of the eight NRGPI oncogenic driver genes and had been validated in gastric cancer cell lines and clinical samples.

Through enrichment analysis of GPX3 and GPX3-related genes, we found that these genes were mainly enriched in thyroid hormone metabolism, glutathione metabolism, and antioxidant activity. This result suggested that GPX3 played an essential role in antioxidant defense. Studies have shown that oxidative stress is a critical metabolic feature of TME inflammatory cell recruitment and may promote the function of tumor-associated fibroblasts (CAFs) (58–60). Malignant tumors can escape immune detection and immunological therapy owing to the development of an immunosuppressive microenvironment. For example, advanced tumors stimulate the formation of an inflammatory immune microenvironment, which inhibits immune-dependent cancer killing. Immune cells secrete cytokines and chemokines, promoting tumor growth, metastasis, and angiogenesis (61–64). Thus, we analyzed the relationship between GPX3 and the tumor immune microenvironment (TIME). The microenvironment of refractory tumors can be divided into immune and inflammatory. In this study, we found that the expression level of GPX3 was positively correlated with immune and stromal scores. We hope GPX3 expression can predict the types of TIME and help select immunotherapy strategies. We found that GPX3 was positively correlated with M2 macrophages, MDCs, CD4+ Th1 cells, Th2 cells, and HSCs. Tumor-associated macrophages (TAMs) in the TME are type M2, which promote angiogenesis and tumor invasion by secreting Th2 cytokines (65). Therefore, GPX3 may be used as a target to rescue immunosuppression in the TME. Notably, the composition of cells in the TME is related to hypoxia. The function of immune cells is impaired by hypoxia and the inflammatory environment. GPX3 plays a role in regulating redox equilibrium, which may be its mechanism in affecting the TIME. M2 macrophages and HSCs are involved in tumor invasion and metastasis (66–70). They are positively related to GPX3 expression. Subsequently, we hoped to explore the relationship between GPX3 expression and tumor metastasis.

In addition, we simply predicted the regulatory mechanism of GPX3 in cancers. We found that there was a significant negative correlation between GPX3 promoter methylation and GPX3 gene expression levels. This suggested that higher DNA methylation in the GPX3 promoter region leads to its lower expression levels in cancer. We also found enrichment peaks of H3K4me3 and H3K27ac in the upstream region of GPX3, suggesting that low GPX3 expression may also be related to histone modification. For genomic variation, the overall alteration frequency of GPX3 was > 6%. Genetic changes may impact the function of GPX3 and further induce malignant transformation and affect the clinical prognosis of cancer patients.

ROS may increase DNA instability, trigger oncogenic mutations and activate oncogenic signaling pathways. Thus, antioxidants may inhibit the initiation or progression of cancer (71). However, in clinical trials, the use of antioxidants did not reduce cancer incidence (72). In contrast, increasing dietary antioxidants increased lung and prostate cancer morbidity and mortality in some studies (16–18). Dietary supplementation with folic acid increases the progression of breast cancer (19, 20). I Antioxidants may promote melanoma metastasis and disease progression in another study (73). It has been reported that glutathione is necessary for the development of some cancers and that antioxidants can promote the development and progression of cancer (74, 75). Clinical studies have shown that compared with benign hyperplasia or precursor lesions, the expression or activity of antioxidant enzymes and GSH content in malignant tumors were increased in the thyroid, ovarian, breast, prostate, and pancreatic cancers (76–81). During carcinogenesis, cells undergo many adaptive changes, especially during metastasis. One such adaptation is that cancer cells enhance their antioxidant defenses to overcome the oxidative stress of anoikis (31). For example, breast and lung cancer cells undergo metabolic changes during metastasis *in vivo* and *in vitro* that reduce ROS production (75, 82–86). In this study, we used multiple human cancer cell lines to examine the effect of GPX3 on metastasis. We found that downregulation of GPX3 expression inhibited metastasis in breast cancer (MDA-MB-231, BT-549), colorectal cancer (Lovo, SW480), gastric cancer (MKN45), and ovarian cancer (Ovcar-4). In terms of proliferation, GPX3 appeared to play a smaller role. Downregulating GPX3 expression slowed the proliferation rate of ovarian cancer (Ovcar-4) and colorectal cancer (Lovo, SW480) cells but did not significantly affect the proliferation of breast cancer or gastric cancer cells. Downregulation of GPX3 significantly inhibited clone formation. shGPX3 significantly reduced the number of clones in ovarian cancer (Ovcar-4), colorectal cancer (Lovo, SW480), and breast cancer (MDA-MB-231). Studies have reported the relationship between the downregulation of GPX3 and tumor metastasis. GPX3 inhibited the migration and invasion of gastric cancer cells (36). However, some studies have found that GPX3 has no antitumor effect in AGS and MKN28 gastric cancer cell lines (87). GPX3 had also been reported to inhibit the progression of breast cancer (35). GPX3 was found to be expressed higher in clear cell type ovarian adenocarcinoma than in other types of ovarian cancer (88). Overall, more studies are needed to determine the role of GPX3 in cancer occurrence, progression, or metastasis. The seemingly contradictory results of GPX3 in cancer may be closely related to ROS. In early cancer and precancer, the expression of GPX3 is decreased and the production of ROS is increased to promote cancer occurrence. However, in advanced cancer, the up-regulation of GPX3 in cancer cells plays a role in eliminating excessive ROS production and protecting cells from anoikis.

GPX3 protected cells from ROS damage in the extracellular environment. We compared the effect of downregulated GPX3 on the antioxidant stress ability of cells. Downregulation of GPX3 expression impairs the antioxidant capacity of cancer cells. Ovarian, breast, colorectal, and gastric cancer cells showed significantly increased sensitivity to oxidants (H_2O_2) in shGPX3 compared with Ctrl. In addition, compared to Ctrl, ROS levels in shGPX3 cells were significantly increased after treatment of H_2O_2. Knockdown GPX3 significantly decreased the ability of cancer cells to clear ROS. Barrett et al. (34) used the reverse genetics method to study the effect of GPX3 on the occurrence of inflammatory colorectal tumors. GPX3-deficient mouse tumors showed increased inflammation, overactivity of Wnt signaling, and increased DNA damage. Subsequently, they silenced GPX3 in Caco2 making ROS production increase, DNA damage, increased apoptosis in response to H_2O_2, and reduced contact-independent growth. Non-contact cell growth is a hallmark of the tumorigenic type. This suggested that acute GPX3 knockdown is indeed detrimental to established cancer growth.

Chemotherapeutic drugs induced ROS accumulation and oxidative stress to produce cytotoxic effects (89). The relationship between the antioxidant capacity of cancer cells and chemotherapy resistance was also frequently reported. By investigating the CCLE and GDSC databases, we found that the expression level of GPX3 was positively correlated with the IC50 of various chemotherapeutic agents. IC50 is commonly used clinically to reflect the sensitivity of cells to drugs. The higher the IC50, the larger the dose of drugs needed to kill cancer cells, thus the lower the sensitivity of cancer cells to chemotherapy. It has been reported that GPX3 was highly expressed in ovarian cancer cells and was associated with platinum resistance (90). Similarly, Pelosof et al. (40) found that decreased GPX3 expression increased the sensitivity of colorectal cancer cell lines to oxaliplatin and cisplatin. Zhou et al. found that GPX3 was the core gene mediating both 5-FU resistance and oxaliplatin resistance in colorectal cancer. They also used tissue chip analysis to determine that patients with high GPX3 expression who received high-intensity chemotherapy regimens (oxaliplatin combination, 6 months of chemotherapy, or 8 cycles of Xeloda) had a significantly increased risk of recurrence and death (91). Platinum is a commonly used chemotherapy drug in the clinic. Pharmacological studies have shown that platinum-induced DNA damage by direct covalent binding with DNA and induced ROS production to destroy protein, DNA, and membrane. GPX3 knockdown resulted in a significant increase in cancer cell sensitivity to platinum-based drugs. In this study, we found that downregulated GPX3 significantly increased the sensitivity of cancer cells to cisplatin, while oeGPX3 promoted the resistance of cancer cells to chemotherapy. Interestingly, we also found that platinum-induced ROS accumulation was most significant in shGPX3, while oeGPX3 eliminated ROS levels.

Overall, pan-cancer analysis of GPX3 illustrated the prospect of GPX3 expression in the prognosis, chemotherapy sensitivity, and immune infiltration of several types of human cancers, providing diagnostic and prognostic biomarkers. Our study further revealed the mechanisms by which GPX3 promotes tumor metastasis, growth, and chemotherapy resistance. There are still many shortcomings in this study. We found a relationship between GPX3 and immune infiltration through bioinformatics analysis. Further experiments are needed to verify how GPX3 affects the tumor immune microenvironment. The specific mechanism by which GPX3 affects cancer susceptibility to chemotherapy also needs further study. In addition, we preliminarily found that GPX3 expression in cancer may be epigenetically regulated, which also needs further verification. In future studies, we will explore these unclear questions in depth.

Data availability statement

The original contributions presented in the study are included in the article/Supplementary Material. Further inquiries can be directed to the corresponding authors.

Ethics statement

The animal study was reviewed and approved by the Ethics Committee of Tongji Medical College, Huazhong University of Science and Technology (IACUC Number: 2612).

Author contributions

QH, JC, WY, JT, and TH contributed conception and design of the study. QH, JC, and WY performed experiments and statisitical analysis. QH, JC, MX, and JZ performed the bioinformatics data analysis. QH and WY wrote the first manuscript, QH and JC wrote the revised manuscript. JT and TH edited the language. All authors contributed to the article and approved the submitted version.

Funding

This work is supported by Key Program of Natural Science Foundation of Hubei Province (Grant No. 2021BCA142) (TH). This work was supported by National Natural Science Foundation of China Grant (82002834) and this study is supported by the Thyroid Research Program of Young and Middle-aged Physicians of China Health Promotion Foundation (JT).

Acknowledgments

The authors acknowledge Dr. Haoxiang Zhang from Department of Pancreatic Surgery, Union Hospital, Tongji Medical College, Huazhong University of Science and Technology, for their guidance in animal experiments. We thank the Medical Subcenter of HUST Analytical & Testing Center in data acquisition.

Conflict of interest

The authors declare that the research was conducted in the absence of any commercial or financial relationships that could be construed as a potential conflict of interest.

Publisher's note

Supplementary material

The Supplementary Material for this article can be found online at: https://www.frontiersin.org/articles/10.3389/fonc.2023.990551/full#supplementary-material

References

1. Sung H, Ferlay J, Siegel RL, Laversanne M, Soerjomataram I, Jemal A, et al. Global cancer statistics 2020: GLOBOCAN estimates of incidence and mortality worldwide for 36 cancers in 185 countries. *CA Cancer J Clin* (2021) 71:209–49. doi: 10.3322/caac.21660

2. Schuhmacher C, Gretschel S, Lordick F, Reichardt P, Hohenberger W, Eisenberger CF, et al. Neoadjuvant chemotherapy compared with surgery alone for locally advanced cancer of the stomach and cardia: European organisation for research and treatment of cancer randomized trial 40954. *J Clin Oncol* (2010) 28:5210–8. doi: 10.1200/jco.2009.26.6114

3. Dent R, Trudeau M, Pritchard KI, Hanna WM, Kahn HK, Sawka CA, et al. Triple-negative breast cancer: Clinical features and patterns of recurrence. *Clin Cancer Res* (2007) 13:4429–34. doi: 10.1158/1078-0432.Ccr-06-3045

4. Khandrika L, Kumar B, Koul S, Maroni P, Koul HK. Oxidative stress in prostate cancer. *Cancer Lett* (2009) 282:125–36. doi: 10.1016/j.canlet.2008.12.011

5. Sies H. Oxidative stress: a concept in redox biology and medicine. *Redox Biol* (2015) 4:180–3. doi: 10.1016/j.redox.2015.01.002

6. Ushio-Fukai M. Compartmentalization of redox signaling through NADPH oxidase-derived ROS. *Antioxid Redox Signal* (2009) 11:1289–99. doi: 10.1089/ars.2008.2333

7. Morgan MJ, Kim YS, Liu ZG. TNFalpha and reactive oxygen species in necrotic cell death. *Cell Res* (2008) 18:343–9. doi: 10.1038/cr.2008.31

8. Liu B, Chen Y, St Clair DK. ROS and p53: a versatile partnership. *Free Radic Biol Med* (2008) 44:1529–35. doi: 10.1016/j.freeradbiomed.2008.01.011

9. Acharya A, Das I, Chandhok D, Saha T. Redox regulation in cancer: a double-edged sword with therapeutic potential. *Oxid Med Cell Longev* (2010) 3:23–34. doi: 10.4161/oxim.3.1.10095

10. Chandel NS, Tuveson DA. The promise and perils of antioxidants for cancer patients. *N Engl J Med* (2014) 371:177–8. doi: 10.1056/NEJMcibr1405701

11. Yi Z, Jiang L, Zhao L, Zhou M, Ni Y, Yang Y, et al. Glutathione peroxidase 3 (GPX3) suppresses the growth of melanoma cells through reactive oxygen species (ROS)-dependent stabilization of hypoxia-inducible factor 1-α and 2-α. *J Cell Biochem* (2019) 120:19124–36. doi: 10.1002/jcb.29240

12. Li AE, Ito H, Rovira II, Kim KS, Takeda K, Yu ZY, et al. A role for reactive oxygen species in endothelial cell anoikis. *Circ Res* (1999) 85:304–10. doi: 10.1161/01.Res.85.4.304

13. Giannoni E, Buricchi F, Grimaldi G, Parri M, Cialdai F, Taddei ML, et al. Redox regulation of anoikis: reactive oxygen species as essential mediators of cell survival. *Cell Death Diff* (2008) 15:867–78. doi: 10.1038/cdd.2008.3

14. Teoh-Fitzgerald ML, Fitzgerald MP, Zhong W, Askeland RW, Domann FE. Epigenetic reprogramming governs EcSOD expression during human mammary epithelial cell differentiation. *Tumorigen Metastasis Oncogene* (2014) 33:358–68. doi: 10.1038/onc.2012.582

15. Glasauer A, Chandel NS. Targeting antioxidants for cancer therapy. *Biochem Pharmacol* (2014) 92:90–101. doi: 10.1016/j.bcp.2014.07.017

16. Alpha-Tocopherol, Beta Carotene Cancer Prevention Study Group. The effect of vitamin e and beta carotene on the incidence of lung cancer and other cancers in male smokers. *N Engl J Med* (1994) 330(15):1029–35. doi: 10.1056/nejm199404143301501

17. Klein EA, Thompson IMJr., Tangen CM, Crowley JJ, Lucia MS, Goodman PJ, et al. Vitamin e and the risk of prostate cancer: the selenium and vitamin e cancer prevention trial (SELECT). *Jama* (2011) 306:1549–56. doi: 10.1001/jama.2011.1437

18. Goodman GE, Thornquist MD, Balmes J, Cullen MR, Meyskens FLJr., Omenn GS, et al. The beta-carotene and retinol efficacy trial: incidence of lung cancer and cardiovascular disease mortality during 6-year follow-up after stopping beta-carotene and retinol supplements. *J Natl Cancer Inst* (2004) 96:1743–50. doi: 10.1093/jnci/djh320

19. Deghan Manshadi S, Ishiguro L, Sohn KJ, Medline A, Renlund R, Croxford R, et al. Folic acid supplementation promotes mammary tumor progression in a rat model. *PloS One* (2014) 9:e84635. doi: 10.1371/journal.pone.0084635

20. Ebbing M, Bønaa KH, Nygård O, Arnesen E, Ueland PM, Nordrehaug JE, et al. Cancer incidence and mortality after treatment with folic acid and vitamin B12. *Jama* (2009) 302:2119–26. doi: 10.1001/jama.2009.1622

21. Dokic I, Hartmann C, Herold-Mende C, Régnier-Vigouroux A. Glutathione peroxidase 1 activity dictates the sensitivity of glioblastoma cells to oxidative stress. *Glia* (2012) 60:1785–800. doi: 10.1002/glia.22397

22. Lee HC, Kim DW, Jung KY, Park IC, Park MJ, Kim MS, et al. Increased expression of antioxidant enzymes in radioresistant variant from U251 human glioblastoma cell line. *Int J Mol Med* (2004) 13:883–7. doi: 10.3892/ijmm.13.6.883

23. Harris IS, Treloar AE, Inoue S, Sasaki M, Gorrini C, Lee KC, et al. Glutathione and thioredoxin antioxidant pathways synergize to drive cancer initiation and progression. *Cancer Cell* (2015) 27:211–22. doi: 10.1016/j.ccell.2014.11.019

24. Sayin VI, Ibrahim MX, Larsson E, Nilsson JA, Lindahl P, Bergo MO. Antioxidants accelerate lung cancer progression in mice. *Sci Trans Med* (2014) 6(221):221ra15. doi: 10.1126/scitranslmed.3007653

25. Takahashi K, Avissar N, Whitin J, Cohen H. Purification and characterization of human plasma glutathione peroxidase: a selenoglycoprotein distinct from the known cellular enzyme. *Arch Biochem Biophysics* (1987) 256:677–86. doi: 10.1016/0003-9861(87)90624-2

26. Winther JR, Jakob U. Redox control: A black hole for oxidized glutathione. *Nat Chem Biol* (2013) 9:69–70. doi: 10.1038/nchembio.1161

27. Ufer C, Borchert A, Kuhn H. Functional characterization of cis- and trans-regulatory elements involved in expression of phospholipid hydroperoxide glutathione peroxidase. *Nucleic Acids Res* (2003) 31:4293–303. doi: 10.1093/nar/gkg650

28. Ren Z, He Y, Yang Q, Guo J, Huang H, Li B, et al. A comprehensive analysis of the glutathione peroxidase 8 (GPX8) in human cancer. *Front Oncol* (2022) 12:812811. doi: 10.3389/fonc.2022.812811

29. Qi X, Ng KT-P, Shao Y, Li CX, Geng W, Ling CC, et al. The clinical significance and potential therapeutic role of GPx3 in tumor recurrence after liver transplantation. *Theranostics* (2016) 6:1934–46. doi: 10.7150/thno.16023

30. An BC, Choi Y-D, Oh I-J, Kim JH, Park J-I, Lee S-w. GPx3-mediated redox signaling arrests the cell cycle and acts as a tumor suppressor in lung cancer cell lines. *PloS One* (2018) 13(9):e0204170. doi: 10.1371/journal.pone.0204170

31. Yu YP, Yu G, Tseng G, Cieply K, Nelson J, Defrances M, et al. Glutathione peroxidase 3, deleted or methylated in prostate cancer, suppresses prostate cancer growth and metastasis. *Cancer Res* (2007) 67:8043–50. doi: 10.1158/0008-5472.Can-07-0648

32. Yi Z, Jiang L, Zhao L, Zhou M, Ni Y, Yang Y, et al. Glutathione peroxidase 3 (GPX3) suppresses the growth of melanoma cells through reactive oxygen species (ROS)-dependent stabilization of hypoxia-inducible factor 1-alpha and 2-alpha. *J Cell Biochem* (2019) 120:19124–36. doi: 10.1002/jcb.29240

33. Chang S-N, Lee JM, Oh H, Park J-H. Glutathione peroxidase 3 inhibits prostate tumorigenesis in TRAMP mice. *Prostate* (2016) 76:1387–98. doi: 10.1002/pros.23223

34. Barrett CW, Ning W, Chen X, Smith JJ, Washington MK, Hill KE, et al. Tumor suppressor function of the plasma glutathione peroxidase Gpx3 in colitis-associated carcinoma. *Cancer Res* (2013) 73:1245–55. doi: 10.1158/0008-5472.Can-12-3150

35. Lou W, Ding B, Wang S, Fu P. Overexpression of GPX3, a potential biomarker for diagnosis and prognosis of breast cancer, inhibits progression of breast cancer cells *in vitro*. *Cancer Cell Int* (2020) 20(1):378. doi: 10.1186/s12935-020-01466-7

36. Cai M, Sikong Y, Wang Q, Zhu S, Pang F, Cui X. Gpx3 prevents migration and invasion in gastric cancer by targeting NFκB/Wnt5a/JNK signaling. *Int J Clin Exp Pathol* (2019) 12:1194–203.

37. Zhou C, Pan R, Li B, Huang T, Zhao J, Ying J, et al. GPX3 hypermethylation in gastric cancer and its prognostic value in patients aged over 60. *Future Oncol* (2019) 15:1279–89. doi: 10.2217/fon-2018-0674

38. Cao S, Yan B, Lu Y, Zhang G, Li J, Zhai W, et al. Methylation of promoter and expression silencing of GPX3 gene in hepatocellular carcinoma tissue. *Clinics Res Hepatol Gastroenterol* (2015) 39:198–204. doi: 10.1016/j.clinre.2014.09.003

39. Agnani D, Camacho-Vanegas O, Camacho C, Lele S, Odunsi K, Cohen S, et al. Decreased levels of serum glutathione peroxidase 3 are associated with papillary serous ovarian cancer and disease progression. *J Ovarian Res* (2011) 4:18. doi: 10.1186/1757-2215-4-18

40. Pelosof L, Yerram S, Armstrong T, Chu N, Danilova L, Yanagisawa B, et al. GPX3 promoter methylation predicts platinum sensitivity in colorectal cancer. *Epigenetics* (2017) 12:540–50. doi: 10.1080/15592294.2016.1265711

41. Worley BL, Kim YS, Mardini J, Zaman R, Leon KE, Vallur PG, et al. GPx3 supports ovarian cancer progression by manipulating the extracellular redox environment. *Redox Biol* (2019) 25:101051. doi: 10.1016/j.redox.2018.11.009

42. Miess H, Dankworth B, Gouw AM, Rosenfeldt M, Schmitz W, Jiang M, et al. The glutathione redox system is essential to prevent ferroptosis caused by impaired lipid metabolism in clear cell renal cell carcinoma. *Oncogene* (2018) 37:5435–50. doi: 10.1038/s41388-018-0315-z

43. Zhao H, Li J, Li X, Han C, Zhang Y, Zheng L, et al. Silencing GPX3 expression promotes tumor metastasis in human thyroid cancer. *Curr Protein Pept Sci* (2015) 16:316–21. doi: 10.2174/138920371604150429154840

44. Zhang X, Zheng Z, Shen Y, Kim H, Jin R, Li R, et al. Downregulation of glutathione peroxidase 3 is associated with lymph node metastasis and prognosis in cervical cancer. *Oncol Rep* (2014) 31:2587–92. doi: 10.3892/or.2014.3152

45. Uhlén M, Fagerberg L, Hallström BM, Lindskog C, Oksvold P, Mardinoglu A, et al. Proteomics. tissue-based map of the human proteome. *Science* (2015) 347:1260419. doi: 10.1126/science.1260419

46. Barretina J, Caponigro G, Stransky N, Venkatesan K, Margolin AA, Kim S, et al. The cancer cell line encyclopedia enables predictive modelling of anticancer drug sensitivity. *Nature* (2012) 483:603–7. doi: 10.1038/nature11003

47. Garnett MJ, Edelman EJ, Heidorn SJ, Greenman CD, Dastur A, Lau KW, et al. Systematic identification of genomic markers of drug sensitivity in cancer cells. *Nature* (2012) 483:570–5. doi: 10.1038/nature11005

48. Newman AM, Liu CL, Green MR, Gentles AJ, Feng W, Xu Y, et al. Robust enumeration of cell subsets from tissue expression profiles. *Nat Methods* (2015) 12:453–7. doi: 10.1038/nmeth.3337

49. Becht E, Giraldo NA, Lacroix L, Buttard B, Elarouci N, Petitprez F, et al. Estimating the population abundance of tissue-infiltrating immune and stromal cell populations using gene expression. *Genome Biol* (2016) 17:218. doi: 10.1186/s13059-016-1070-5

50. Li T, Fan J, Wang B, Traugh N, Chen Q, Liu JS, et al. TIMER: A web server for comprehensive analysis of tumor-infiltrating immune cells. *Cancer Res* (2017) 77:e108–10. doi: 10.1158/0008-5472.Can-17-0307

51. Aran D, Hu Z, Butte AJ. xCell: digitally portraying the tissue cellular heterogeneity landscape. *Genome Biol* (2017) 18:220. doi: 10.1186/s13059-017-1349-1

52. Zou Z, Ohta T, Miura F, Oki S. ChIP-atlas 2021 update: a data-mining suite for exploring epigenomic landscapes by fully integrating ChIP-seq, ATAC-seq and bisulfite-seq data. *Nucleic Acids Res* (2022) 50:W175–182. doi: 10.1093/nar/gkac199

53. Oki S, Ohta T, Shioi G, Hatanaka H, Ogasawara O, Okuda Y, et al. ChIP-atlas: a data-mining suite powered by full integration of public ChIP-seq data. *EMBO Rep* (2018) 19(12):e46255. doi: 10.15252/embr.201846255

54. Haibe-Kains B, El-Hachem N, Birkbak NJ, Jin AC, Beck AH, Aerts HJ, et al. Inconsistency in large pharmacogenomic studies. *Nature* (2013) 504:389–93. doi: 10.1038/nature12831

55. Cancer Cell Line Encyclopedia Consortium and Genomics of Drug Sensitivity in Cancer Consortium. Pharmacogenomic agreement between two cancer cell line data sets. *Nature* (2015) 528(7580):84–7. doi: 10.1038/nature15736

56. Cui Y, Han B, Zhang H, Liu H, Zhang F, Niu R. Identification of metabolic-associated genes for the prediction of colon and rectal adenocarcinoma. *Onco Targets Ther* (2021) 14:2259–77. doi: 10.2147/ott.S297134

57. Khan M, Lin J, Wang B, Chen C, Huang Z, Tian Y, et al. A novel necroptosis-related gene index for predicting prognosis and a cold tumor immune microenvironment in stomach adenocarcinoma. *Front Immunol* (2022) 13:968165. doi: 10.3389/fimmu.2022.968165

58. Hartwig T, Montinaro A, von Karstedt S, Sevko A, Surinova S, Chakravarthy A, et al. The TRAIL-induced cancer secretome promotes a tumor-supportive immune microenvironment *via* CCR2. *Mol Cell* (2017) 65:730–742.e735. doi: 10.1016/j.molcel.2017.01.021

59. Vu LT, Peng B, Zhang DX, Ma V, Mathey-Andrews CA, Lam CK, et al. Tumor-secreted extracellular vesicles promote the activation of cancer-associated fibroblasts via the transfer of microRNA-125b. *J Extracell Vesicles* (2019) 8:1599680. doi: 10.1080/20013078.2019.1599680

60. Motz GT, Santoro SP, Wang LP, Garrabrant T, Lastra RR, Hagemann IS, et al. Tumor endothelium FasL establishes a selective immune barrier promoting tolerance in tumors. *Nat Med* (2014) 20:607–15. doi: 10.1038/nm.3541

61. Gentles AJ, Newman AM, Liu CL, Bratman SV, Feng W, Kim D, et al. The prognostic landscape of genes and infiltrating immune cells across human cancers. *Nat Med* (2015) 21:938–45. doi: 10.1038/nm.3909

62. Karachaliou N, Cao MG, Teixidó C, Viteri S, Morales-Espinosa D, Santarpia M, et al. Understanding the function and dysfunction of the immune system in lung cancer: the role of immune checkpoints. *Cancer Biol Med* (2015) 12(2):79–86. doi: 10.7497/j.issn.2095-3941

63. Hu X, Zhang J, Wang J, Fu J, Li T, Zheng X, et al. Landscape of b cell immunity and related immune evasion in human cancers. *Nat Genet* (2019) 51:560–7. doi: 10.1038/s41588-018-0339-x

64. Ribas A. Adaptive immune resistance: How cancer protects from immune attack. *Cancer Discovery* (2015) 5:915–9. doi: 10.1158/2159-8290.Cd-15-0563

65. Shi Y, Ping YF, Zhou W, He ZC, Chen C, Bian BS, et al. Tumour-associated macrophages secrete pleiotrophin to promote PTPRZ1 signalling in glioblastoma stem cells for tumour growth. *Nat Commun* (2017) 8:15080. doi: 10.1038/ncomms15080

66. Murgai M, Ju W, Eason M, Kline J, Beury DW, Kaczanowska S, et al. KLF4-dependent perivascular cell plasticity mediates pre-metastatic niche formation and metastasis. *Nat Med* (2017) 23:1176–90. doi: 10.1038/nm.4400

67. Brian BF, Freedman TS. The src-family kinase Lyn in immunoreceptor signaling. *Endocrinology* (2021) 162(10):bqab152. doi: 10.1210/endocr/bqab152

68. Samimi A, Khodayar MJ, Alidadi H, Khodadi E. The dual role of ROS in hematological malignancies: Stem cell protection and cancer cell metastasis. *Stem Cell Rev Rep* (2020) 16:262–75. doi: 10.1007/s12015-019-09949-5

69. Chen Y, Zhang S, Wang Q, Zhang X. Tumor-recruited M2 macrophages promote gastric and breast cancer metastasis *via* M2 macrophage-secreted CHI3L1 protein. *J Hematol Oncol* (2017) 10:36. doi: 10.1186/s13045-017-0408-0

70. Zhao S, Mi Y, Guan B, Zheng B, Wei P, Gu Y, et al. Tumor-derived exosomal miR-934 induces macrophage M2 polarization to promote liver metastasis of colorectal cancer. *J Hematol Oncol* (2020) 13:156. doi: 10.1186/s13045-020-00991-2

71. Gorrini C, Harris IS, Mak TW. Modulation of oxidative stress as an anticancer strategy. *Nat Rev Drug Discov* (2013) 12:931–47. doi: 10.1038/nrd4002

72. Gao P, Zhang H, Dinavahi R, Li F, Xiang Y, Raman V, et al. HIF-dependent antitumorigenic effect of antioxidants *in vivo*. *Cancer Cell* (2007) 12:230–8. doi: 10.1016/j.ccr.2007.08.004

73. Piskounova E, Agathocleous M, Murphy MM, Hu Z, Huddlestun SE, Zhao Z, et al. Oxidative stress inhibits distant metastasis by human melanoma cells. *Nature* (2015) 527:186–91. doi: 10.1038/nature15726

74. DeNicola GM, Karreth FA, Humpton TJ, Gopinathan A, Wei C, Frese K, et al. Oncogene-induced Nrf2 transcription promotes ROS detoxification and tumorigenesis. *Nature* (2011) 475:106–9. doi: 10.1038/nature10189

75. Dey S, Sayers CM, Verginadis II, Lehman SL, Cheng Y, Cerniglia GJ, et al. ATF4-dependent induction of heme oxygenase 1 prevents anoikis and promotes metastasis. *J Clin Invest* (2015) 125:2592–608. doi: 10.1172/jci78031

76. Ros S, Santos CR, Moco S, Baenke F, Kelly G, Howell M, et al. Functional metabolic screen identifies 6-phosphofructo-2-kinase/fructose-2,6-biphosphatase 4 as an important regulator of prostate cancer cell survival. *Cancer Discovery* (2012) 2:328–43. doi: 10.1158/2159-8290.Cd-11-0234

77. Ghalia AA, Rabboh NA, el Shalakani A, Seada L, Khalifa A. Estimation of glutathione s-transferase and its pi isoenzyme in tumor tissues and sera of patients with ovarian cancer. *Anticancer Res* (2000) 20:1229–35.

78. Hu Y, Rosen DG, Zhou Y, Feng L, Yang G, Liu J, et al. Mitochondrial manganese-superoxide dismutase expression in ovarian cancer: role in cell proliferation and response to oxidative stress. *J Biol Chem* (2005) 280:39485–92. doi: 10.1074/jbc.M503296200

79. Kumaraguruparan R, Subapriya R, Viswanathan P, Nagini S. Tissue lipid peroxidation and antioxidant status in patients with adenocarcinoma of the breast. *Clin Chim Acta* (2002) 325:165–70. doi: 10.1016/s0009-8981(02)00292-9

80. Bostwick DG, Alexander EE, Singh R, Shan A, Qian J, Santella RM, et al. Antioxidant enzyme expression and reactive oxygen species damage in prostatic intraepithelial neoplasia and cancer. *Cancer* (2000) 89:123–34. doi: 10.1002/1097-0142(20000701)89:1<123::AID-CNCR17>3.0.CO;2-9

81. Schieber M, Chandel NS. ROS function in redox signaling and oxidative stress. *Curr Biol* (2014) 24:R453–462. doi: 10.1016/j.cub.2014.03.034

82. Dong C, Yuan T, Wu Y, Wang Y, Fan TWM, Miriyala S, et al. Loss of FBP1 by snail-mediated repression provides metabolic advantages in basal-like breast cancer. *Cancer Cell* (2013) 23:316–31. doi: 10.1016/j.ccr.2013.01.022

83. Kamarajugadda S, Cai Q, Chen H, Nayak S, Zhu J, He M, et al. Manganese superoxide dismutase promotes anoikis resistance and tumor metastasis. *Cell Death Dis* (2013) 4:e504. doi: 10.1038/cddis.2013.20

84. Qu Y, Wang J, Ray PS, Guo H, Huang J, Shin-Sim M, et al. Thioredoxin-like 2 regulates human cancer cell growth and metastasis via redox homeostasis and NF-κB signaling. *J Clin Invest* (2011) 121:212–25. doi: 10.1172/jci43144

85. Chen EI, Hewel J, Krueger JS, Tiraby C, Weber MR, Kralli A, et al. Adaptation of energy metabolism in breast cancer brain metastases. *Cancer Res* (2007) 67:1472–86. doi: 10.1158/0008-5472.Can-06-3137

86. Lu X, Bennet B, Mu E, Rabinowitz J, Kang Y. Metabolomic changes accompanying transformation and acquisition of metastatic potential in a syngeneic mouse mammary tumor model. *J Biol Chem* (2010) 285:9317–21. doi: 10.1074/jbc.C110.104448

87. Xie J, Fu L, Zhang J. Analysis of influencing factors on the occurrence and development of gastric cancer in high-incidence areas of digestive tract tumors based on high methylation of GPX3 gene. *J Oncol* (2022) 2022:3094881. doi: 10.1155/2022/3094881

88. Lee HJ, Do JH, Bae S, Yang S, Zhang X, Lee A, et al. Immunohistochemical evidence for the over-expression of glutathione peroxidase 3 in clear cell type ovarian adenocarcinoma. *Med Oncol* (2011) 28:S522–7. doi: 10.1007/s12032-010-9659-0

89. Dharmaraja AT. Role of reactive oxygen species (ROS) in therapeutics and drug resistance in cancer and bacteria. *J Med Chem* (2017) 60:3221–40. doi: 10.1021/acs.jmedchem.6b01243

90. Saga Y, Ohwada M, Suzuki M, Konno R, Kigawa J, Ueno S, et al. Glutathione peroxidase 3 is a candidate mechanism of anticancer drug resistance of ovarian clear cell adenocarcinoma. *Oncol Rep* (2008) 20:1299–303. doi: 10.3892/or_00000144

91. Zhou R, Wen Z, Liao Y, Wu J, Xi S, Zeng D, et al. Evaluation of stromal cell infiltration in the tumor microenvironment enable prediction of treatment sensitivity and prognosis in colon cancer. *Comput Struct Biotechnol J* (2022) 20:2153–68. doi: 10.1016/j.csbj.2022.04.037

frontiers | Frontiers in Oncology

TYPE Original Research
PUBLISHED 01 March 2023
DOI 10.3389/fonc.2023.1129352

OPEN ACCESS

EDITED BY
Elavarasan Subramani,
University of Texas MD Anderson Cancer Center, United States

REVIEWED BY
Shubhangi Agarwal,
University of California, San Francisco, United States
Flora Guerra,
University of Salento, Italy
Kanikkai Raja Aseer,
National Institute on Aging (NIH), United States

*CORRESPONDENCE
Emine C. Koc
✉ koce@marshall.edu

SPECIALTY SECTION
This article was submitted to Cancer Metabolism, a section of the journal Frontiers in Oncology

RECEIVED 21 December 2022
ACCEPTED 08 February 2023
PUBLISHED 01 March 2023

CITATION
Koc ZC, Sollars VE, Bou Zgheib N, Rankin GO and Koc EC (2023) Evaluation of mitochondrial biogenesis and ROS generation in high-grade serous ovarian cancer.
Front. Oncol. 13:1129352.
doi: 10.3389/fonc.2023.1129352

Evaluation of mitochondrial biogenesis and ROS generation in high-grade serous ovarian cancer

Zeynep C. Koc[1], Vincent E. Sollars[2], Nadim Bou Zgheib[3], Gary O. Rankin[2] and Emine C. Koc[2]*

[1]Department of Obstetrics, Gynecology and Reproductive Sciences, Temple University, Philadelphia, PA, United States, [2]Department of Biomedical Sciences, Joan C. Edwards School of Medicine, Marshall University, Huntington, WV, United States, [3]Edwards Comprehensive Cancer Center, Joan C. Edwards School of Medicine, Marshall University, Huntington, WV, United States

Introduction: Ovarian cancer is one of the leading causes of death for women with cancer worldwide. Energy requirements for tumor growth in epithelial high-grade serous ovarian cancer (HGSOC) are fulfilled by a combination of aerobic glycolysis and oxidative phosphorylation (OXPHOS). Although reduced OXPHOS activity has emerged as one of the significant contributors to tumor aggressiveness and chemoresistance, up-regulation of mitochondrial antioxidant capacity is required for matrix detachment and colonization into the peritoneal cavity to form malignant ascites in HGSOC patients. However, limited information is available about the mitochondrial biogenesis regulating OXPHOS capacity and generation of mitochondrial reactive oxygen species (mtROS) in HGSOC.

Methods: To evaluate the modulation of OXPHOS in HGSOC tumor samples and ovarian cancer cell lines, we performed proteomic analyses of proteins involved in mitochondrial energy metabolism and biogenesis and formation of mtROS by immunoblotting and flow cytometry, respectively.

Results and discussion: We determined that the increased steady-state expression levels of mitochondrial- and nuclear-encoded OXPHOS subunits were associated with increased mitochondrial biogenesis in HGSOC tumors and ovarian cancer cell lines. The more prominent increase in MT-COII expression was in agreement with significant increase in mitochondrial translation factors, TUFM and DARS2. On the other hand, the ovarian cancer cell lines with reduced OXPHOS subunit expression and mitochondrial translation generated the highest levels of mtROS and significantly reduced SOD2 expression. Evaluation of mitochondrial biogenesis suggested that therapies directed against mitochondrial targets, such as those involved in transcription and translation machineries, should be considered in addition to the conventional chemotherapies in HGSOC treatment.

KEYWORDS

mitochondrial biogenesis, mitochondrial translation and transcription, mitochondrial reactive oxygen species (mtROS), oxidative phosphorylation (OXPHOS), high-grade serous ovarian cancer (HGSOC), MT-COII, TFAM, TUFM

1 Introduction

Ovarian cancer is one of the deadliest gynecological cancers worldwide and is the fifth leading cause of death for women in the United States (1). Despite success in attaining remission in many cases, over half of the women with ovarian cancer experience resistance to chemotherapy, metastasis, and recurrence. Changes in energy and antioxidant metabolism have been highlighted as major factors in chemoresistance and peritoneal metastasis in recent epithelial high-grade serous ovarian cancer (HGSOC) studies (2–6). Determining the metabolic remodeling of energy generation for metastatic development and tumor growth has the potential to introduce pathway-specific therapies.

In recent biomarker studies, mitochondrial energy metabolism is emerging as one of the major contributors to aggressiveness and chemoresistance in HGSOC (7, 8). The mitochondrial mass and oxidative phosphorylation (OXPHOS) capacities are increased 3.3-8.4-fold in epithelial ovarian carcinoma (9). It is believed that tumors preferentially use aerobic glycolysis rather than the much more efficient OXPHOS to generate ATP, described as the Warburg effect (10–12). However, evidence suggests that tumor cells require a metabolically rich microenvironment allowing a combination of aerobic glycolysis and OXPHOS to promote growth and metastasis (13, 14). In addition to increased OXPHOS, high levels of reactive oxygen species (ROS) generated in HGSOC cause sensitivity to platinum-based chemotherapy (7, 15). However, HGSOC tumors have been shown to develop resistance to platinum-based chemotherapy over time, possibly due to remodeling of the energy metabolism and apoptotic pathways (5, 7, 16–18).

The metabolic flexibility of HGSOC tumors requires changes in the expression of both nuclear and mitochondrial genomes to encode subunits of OXPHOS complexes (complex I-V). Mitochondrial transcription supports the synthesis of 13 OXPHOS subunits encoded by the mitochondrial genome, two ribosomal RNAs (rRNAs), and 22 tRNAs (19, 20). Malignant transformation of mitochondrial function and mtDNA mutations have been observed in age-related cancer development (21, 22). A comprehensive list of mitochondrial genes and proteins causing mitochondrial dysfunction in ovarian cancer can be found in a recent review published by Shukla and Singh (23).

The significant variation in the expression of mitochondrial-specific transcription factors, such as PGC1α and TFAM, implies a highly modulated expression of mt-transcription in HGSOC (9, 24–26). Activation of PGC1α, promoted by chronic oxidative stress and aggregation of PML-nuclear bodies, results in high OXPHOS capacity and chemosensitivity in HGSOC (7). On the other hand, the knock-down of PGC1α or TFAM diminishes the generation of mitochondrial reactive oxygen species (mtROS) and cisplatin-induced apoptosis (27).

The role of mitochondrial translation in HGSOC is limited. Nuclear-encoded protein factors and mitochondrial-specific 55S ribosomes support mitochondrial translation. While the mitochondrial ribosomal proteins (MRPs) are all nuclear-encoded genes, 55S ribosomes are composed of the two mitochondrial(mt)-encoded rRNAs and 80 MRPs identified in our previous proteomics studies (28–32). For the mitochondrial translation-related genes, high transcript levels of mitochondrial ribosomal small (MRPS) and large (MRPL) subunit proteins, MRPS12, MRPS14, MRPL15, MRPL34, and MRPL49, are suggested as novel prognostic markers predicting reduced overall survival in ovarian cancer patients (33–35). Additionally, a single nucleotide polymorphism (SNP) of the mitochondrial elongation factor Tu (TUFM) gene is associated with epithelial ovarian cancer risk (36). Therefore, further evaluation of factors involved in mitochondrial biogenesis, specifically mitochondrial translation, is required to determine the mechanism(s) behind the remodeling of energy metabolism in HGSOC and resistance to chemotherapy.

Here, we provide evidence, for the first time, that changes in mitochondrial biogenesis support the metabolic flexibility in HGSOC tumor biopsies and ovarian cancer cell lines. Specifically, mitochondrial translation and transcription factors played an essential role in the modulation of OXPHOS subunit expression. Datamining analyses of mass spectrometry (MS)-based proteomics studies of HGSOC performed by the Clinical Proteomic Tumor Analysis Consortium (CPTAC) and Institute Curie cohort also supported our findings with concurrent changes in mt-encoded subunit II of the complex IV, MT-COII, and mitochondrial translation factors, TUFM and DARS2. We also observed higher mtROS generation in ovarian cancer cell lines with lower OXPHOS subunit expression and mitochondrial biogenesis. These observations suggest that the steady-state expression of mt-encoded OXPHOS subunits and components of the mitochondrial translation could be used as prognostic biomarkers to determine more targeted chemotherapy options in HGSOC.

2 Materials and methods

2.1 Ovarian tissue biopsies

Fifteen de-identified ovarian tumors and normal tissue biopsies were removed by surgical excision from patients treated at the Marshall University Edwards Comprehensive Cancer Center, Huntington, WV. Ethical review and approval were not required for the human de-identified biopsies used in this study in accordance with the local legislation and institutional requirements. Tumor characteristics of biopsies are given in Table S1. Ovarian cancer subtypes were determined by immunohistochemistry, immunofluorescence, and fluorescence *in situ* hybridization techniques by the Edwards Comprehensive Cancer Center. Tissue protein lysates were prepared by resuspension and sonication of biopsies in RIPA buffer containing 1% SDS and NP40. Protein concentration was determined by the bicinchoninic acid (BCA) assay (Pierce, Rockford, USA).

2.2 Cell culture and [^{35}S]-Met pulse labeling

The NCI-ovarian cancer cell line panel (OVCAR-4, OVCAR-5, OVCAR-8, SKOV-3, and IGROV-1) was purchased from NCI. Using gene expression compositional assignment, the OVCAR-5 cell line is also reported as being gastrointestinal in origin (37); however, NCI did not confirm this report. The OVCAR-3 cell line was obtained from Dr. Sarah Miles (Marshall University). The NCI-60 panel of ovarian cancer cell lines, OVCAR-4, OVCAR-5, OVCAR-8, SKOV-3, and IGROV-1, was cultured in RPMI media (HyClone, Thermo-Scientific, Waltham, MA) as recommended by NCI. OVCAR3 cells were maintained in RPMI media containing 20% fetal bovine serum (FBS) (Rocky Mountain Biologicals, Missoula, MT), 10 mL/mL human insulin, 0.1% penicillin/streptomycin (Corning Cellgro, Manassas, VA). The cells were grown in a humidified incubator at 37°C with 5% CO_2. All experiments with the cell lines were limited to passages 5-15 from frozen stocks and repeated with a minimum of nine biological replicates conducted in three separate experiments for all results.

Expression of the 13 mt-encoded subunits of OXPHOS complexes was determined by [^{35}S]-Met pulse labeling described previously (38, 39). Pulse labeling experiments were performed with breast cancer cell lines grown to 60-70% confluency in RPMI media. After arresting cytosolic protein synthesis by emetine, cells were incubated in 0.2 mCi/mL of [^{35}S]-EasyTag^{TM} Protein Labeling Mix (Perkin Elmer Inc., Waltham, MA) containing media for 2 h. Cells were lysed in RIPA buffer supplemented with protease and phosphatase inhibitors (Calbiochem, Darmstadt, Germany). Whole-cell lysates (30 µg) were separated on 13% SDS-PAGE. The gels were dried on 3MM chromatography paper (Whatman) after Coomassie Blue staining, and the signal intensities of the bands were quantified by UN-Scan-It (Silk Scientific Inc, Orem, UT).

2.3 Immunoblotting analyses

Tissue lysates obtained from biopsies and cell lines were either diluted further or lysed in RIPA buffer containing 50 mM Tris-HCl (pH 7.6), 150 mM NaCl, 1 mM EDTA, 1 mM EGTA, 1% NP40, 0.1% SDS, 0.5% deoxycholate, and protease and phosphatase inhibitor cocktails (Calbiochem, Darmstadt, Germany). Protein concentrations were determined using BCA assays (Pierce, Rockford, USA). Approximately 20 µg of the protein lysate was separated on 12% SDS-PAGE, transferred to nitrocellulose membranes (Amersham, GE Healthcare, UK), and stained with Ponceau S to ensure equal protein loading (Figures S1, S2). The Ponceau S staining of nitrocellulose membranes was used to normalize total protein loading to signal intensities detected by immunoblotting analyses. Antibodies were commercially obtained as follows: the human OXPHOS antibody cocktail from Abcam (Eugene, OR); mitochondrial NDUSF2, DARS2, TUFM, and TFAM from Santa Cruz (Dallas, TX); PGC1α and SSBP1 from ProteinTech (Rosemont, IL), SOD2 from Cell Signaling Technologies (Danvers, MA), and GAPDH from Fitzgerald (Acton, MA). The secondary anti-rabbit and mouse HRP-conjugate antibodies were obtained from Pierce (Rockford, USA). The protein immunoreactivity was detected using the ECL Western blotting kit (Amersham, GE Healthcare, UK) as directed by the manufacturer. Immunoblotting signal intensities were quantified by UN-Scan-It (Silk Scientific Inc, Orem, UT) and normalized to total protein loading detected by Ponceau S staining of the membranes.

2.4 Flow cytometry analyses

Mitochondrial mass and ROS generation determinations in ovarian cancer cell lines were performed using MitoTracker-Red CMXRos (Invitrogen) and MitoSOX-Red (ThermoFisher), respectively, by flow cytometry analyses using the Agilent Novocyte 3000. Data analysis was performed using NovoExpress Software vX. Optimal concentrations of Mito-SOX-Red and Mito-Tracker-Red were 5 and 0.5 µM, respectively.

2.5 Statistical analyses

Statistical and graphical analyses were performed using Excel and GraphPad Prism 9.3. Statistical significance was determined using unpaired Welch's *t*-tests. Probability values less than 0.05 were regarded as statistically significant. All the values were in triplicates wherever possible and expressed as the mean ± SD unless otherwise described.

3 Results and discussion

3.1 Heterogeneity of mitochondrial energy metabolism in ovarian cancer

Changes in mitochondrial energy metabolism have recently been suggested as possible causes for chemoresistance and tumor recurrence in HGSOC (2, 7, 23, 40, 41). To further investigate the changes in mitochondrial function, we obtained nine surgically removed normal ovarian and ovarian tumor tissue biopsies from the Tissue Procurement Center at the Marshall University Edwards Comprehensive Cancer Center, Huntington, WV. The tumor characteristics and stages of HGSOC biopsies are given in the Supplemental Table S1.

In our earlier studies, the steady-state expression of OXPHOS subunits by immunoblotting agrees with OXPHOS complex activities and is sufficient for evaluating energy metabolism in mitochondria (7, 42–44). Therefore, we determined the steady-state expression of OXPHOS subunits in HGSOC biopsies by immunoblotting using an antibody cocktail. The antibody cocktail is a mixture of five antibodies recognizing four nuclear-encoded OXPHOS subunits, including complex V (ATP5A1), III (UQCRC2), II (SDHB), and I (NDUFB8) and a mt-encoded subunit of complex IV (MT-COII). The same OXPHOS membrane was also probed with GAPDH antibody (Figure 1A). The signal intensity detected by NDUFB8 antibody would not be quantified in most of the biopsies. Instead, an additional antibody against NDUFS2 was used to confirm changes in another nuclear-encoded subunit of complex I (Figure 1A). Signal intensities obtained for each subunit were normalized to total protein loading detected by Ponceau S staining and mean signal intensities for normal and tumor biopsies rather than a direct comparison of normal and tumor biopsies from the same patient (Figure 1B). Changes in OXPHOS subunit expressions were at least

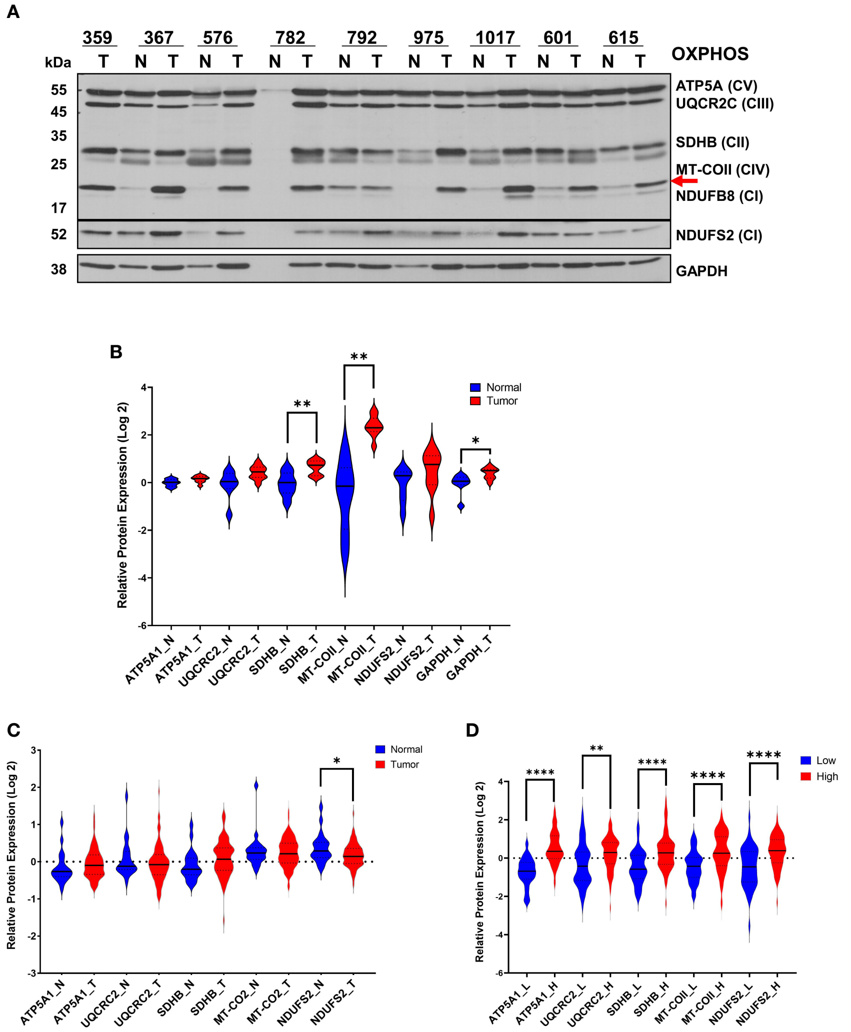

FIGURE 1
Modulation of OXPHOS subunit expression in ovarian cancer. **(A)** The expression of OXPHOS subunits, including ATP5A1 (CV; Complex V), UQCRC2 (CIII; Complex III), SDHB (CII, Complex II), MT-COII (CIV; Complex IV), NDUFB8 and NDUFS2 (CI; Complex I), and GAPDH were detected by immunoblotting in normal (N; blue) and ovarian tumor (T; red) biopsies. Only a tumor biopsy was available for patient 359. Approximately 20 µg of protein lysates obtained from normal and tumor tissues were separated by 12% SDS-PAGE, and the immunoblotting analyses were performed using antibodies shown on the left side. For patient 782, the normal tissue protein amount was extremely low, and it was not included in the quantitation. The red arrow shows the mt-encoded complex IV subunit, MT-COII. **(B)** Relative protein expression was quantified by normalizing the signal intensities of antibodies to protein loading and presented as violin graphs after conversion to log 2 values. **(C)** Log2 protein expression values of OXPHOS subunit expression determined by MS-based proteomics of 20 normal (N; blue) and 83 HGSOC ovarian biopsies (T) published by McDermott et al. [Log 2 values are taken from Supplemental Data in reference (45)] as part of the CPTAC. **(D)** Log2 OXPHOS subunit expression values for 53 low (L; blue) and 74 high (H; red) HGSOC tumors were reported by Gentric et al. [Log 2 values are taken from Supplemental Data in reference (7)] as part of the Curie cohort. For the statistical analysis, unpaired Welch's t-test was used, and the P values ≤ 0.05 were represented as (*), ≤ 0.01 (**) and ≤ 0.0001 (****).

2-3-fold higher for some of the subunits in tumor biopsies relative to the normal tissue biopsies obtained from the same patient (Figures 1A, B). Specifically, we observed an overall statistically significant increase in complex II and IV subunits, SDHB and MT-COII ($P < 0.01$), as well as GAPDH in tumors relative to the normal tissues (Figures 1A, B). Although GAPDH is usually used as a loading control, here we observed an increase in the glycolytic enzyme, GAPDH ($P < 0.05$), confirming the metabolic remodeling in HGSOC (10).

Recent proteomics data published by CPTAC has provided a more comprehensive MS-based quantitation of 20 normal and 83 ovarian tumor biopsies obtained from HGSOC patients (45). The Log2 expression values for mitochondrial proteins are reported in Supplemental Data provided by McDermott et al. (45). The majority of the OXPHOS subunit expression slightly increased in tumor biopsies relative to the normal tissues; however, NDUFS2 expression is reduced in tumor biopsies ($p < 0.05$) (Figure 1C). The HGSOC proteome analyses by CPTAC compares 83 HGSOC tumor tissues to the mean values determined from 20 normal tissues (Figure 1B). Here, the slight discrepancy in the magnitude of expression changes in our results compared to those by CPTAC is possibly due to the direct comparison of the normal and tumor tissues obtained from the same patient in our analyses rather than a comparison to a mean as performed by CPTAC. However, when

Gentric et al. compared the OXPHOS subunit expression by MS-based proteomics, HGSOC biopsies were classified as low- and high- OXPHOS subunit expressing HGSOC tumors (7). The expression of nuclear-encoded subunits ATP5A1, UCQRC2, SDHB, and NDUFS2, and the mt-encoded subunits, including MT-COII, were graphed to demonstrate a significant increase in OXHOS subunits in HGSOC tumors with high mitochondrial energy metabolism (Figure 1D). The agreement observed between our immunoblotting analyses and MS-based proteomics data by McDermott et al. and Gentric et al. suggests that the modulation of mitochondrial energy metabolism is required for tumor growth and proliferation in HGSOC (7, 45).

3.2 Mitochondrial biogenesis modulates OXPHOS in HGSOC

The up-regulation of mt-encoded MT-COII protein expression shown above (Figure 1A) indicates a role for mitochondrial biogenesis in HGSOC. Due to the presence of seven mt-encoded subunits in complex I, the nuclear-encoded complex I subunit, NDUFS2, was also concurrently affected by the changes in mitochondrial biogenesis (Figure 1A). However, the overall increase in NDUFS2 expression was not statistically significant in tissue biopsies (Figure 1B). Additionally, the transcription factors involved in nuclear- and mt-encoded OXPHOS transcripts, PGC1α and TFAM, respectively, are suggested as putative markers of chemoresistance in epithelial ovarian carcinoma (7, 25, 46). Therefore, we postulated that the mitochondrial transcription and translation proteins directly related to the biogenesis of 13 mt-encoded subunits also contribute to the modulation of OXPHOS in HGSOC.

To assess the role of mitochondrial biogenesis in HGSOC biopsies, we determined PGC1α and TFAM protein expression and the single-stranded mitochondrial DNA-binding protein (SSBP1) by immunoblotting using the same HGSOC biopsies described above (Figures 2A, S2). Although the PGC1α levels were slightly decreased and a doublet observed, TFAM and SSBP1 protein expression were elevated in some of the HGSOC tumor biopsies relative to the normal values (Figure 2A). The overall mean modulation of protein expression in normal *vs.* tumor biopsies was not significant ($P>0.05$) (Figure 2B). On the other hand, TFAM and SSBP1 levels were significantly elevated in the HGSOC tumor biopsies reported by the CPTAC proteome ($P<0.0001$) (Figure 2C) (45). These findings supported the altered mitochondrial transcription and replication in HGSOC.

The modulation of OXPHOS requires cooperation between mitochondrial transcription and translation for synthesizing 13 mt-encoded subunits. We next determined the expression of two mitochondrial translation factors, elongation factor Tu (TUFM) and aspartyl-tRNA synthetase 2 (DARS2), in HGSOC biopsies by immunoblotting. Interestingly, the TUFM and DARS2 protein

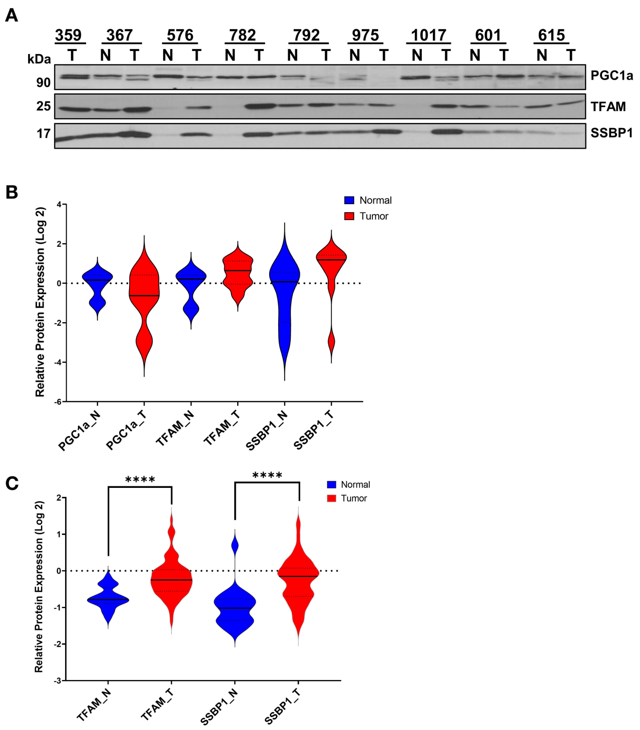

FIGURE 2
Expression of Mitochondrial Transcription- and Replication-Related Proteins in HGSOC. **(A)** Expression of PGC1α, TFAM, and SSBP1 proteins were detected in normal and HGSOC biopsies by immunoblotting analyses as described in Figure1A. **(B)** Log 2 relative protein expression values of PGC1a, TFAM, and SSBP1 shown in **(A)** were presented using violin plots. **(C)** MS-based quantitation of TFAM and SSBP1 published by McDermott et al. (45) as part of the CPTAC data set described in Figure 1C. The normal (N; blue) and HGSOC biopsies (T; red) were compared using violin plots as described in Figure 1B legend. P values ≤ 0.0001 were represented as (****).

expressions were much higher and significant, P<0.05 and P<0.005, respectively, in tumor biopsies (Figures 3A, B). The CPTAC proteomics data mining analyses for TUFM and DARS2 were also in agreement with our observation (Figure 3C). In fact, the majority of mitochondrial translation-related proteins and factors are higher in the HGSOC tumor biopsies reported by the CPTAC (data not shown (45)).

Higher expression of several MRP genes has been associated with reduced overall survival and tumor recurrence using the publicly available ovarian cancer transcriptomics databases (33, 34). We searched the CPTAC proteome data to determine the expression of these MRPs, including MRPS12, MRPS14, MRPL15, and MRPL49, published by McDermott et al. (45). Log2 protein expression values for MRPS12, MRP L15, and MRPL49 were graphed and shown to be significantly elevated in tumor biopsies (Figure 3D). Here, the synergy between the MRP expression and mitochondrial translation factors along with the MT-COII expression confirmed the remodeling of energy metabolism and mitochondrial biogenesis, particularly the protein synthesis, in HGSOC (Figures 1A, 3).

3.3 mtROS generation is increased in ovarian cancer cell lines with reduced OXPHOS subunit expression

Tumor-initiating cells undergo hypoxic conditions as they form spheroids and malignant ascites in the peritoneal cavity, causing changes in mitochondrial morphology and ROS levels during the progression of ovarian cancer (41, 47). mtROS produced as byproducts of OXPHOS when electrons leak from complexes I and III play a critical role in regulating a wide variety of cellular signaling pathways, including stabilization of hypoxia-inducible factor 1 alpha (HIF1α) in cancer (11, 27, 48–50). Therefore, it is critical to correlate OXPHOS status, mitochondrial biogenesis, and mtROS generation in ovarian cancer cell lines. For this purpose, we acquired the NCI-60 ovarian cancer cell line panel containing OVCAR-3, OVCAR-4, OVCAR-5, OVCAR-8, SKOV-3, and IGROV-1 cells derived from adenocarcinomas and peritoneal ascites (Table S2). Among these cell lines, OVCAR-3 and OVCAR-4 are the closest cell line models to HGSOC by comparing the genomic profiles (51, 52). The cells originated

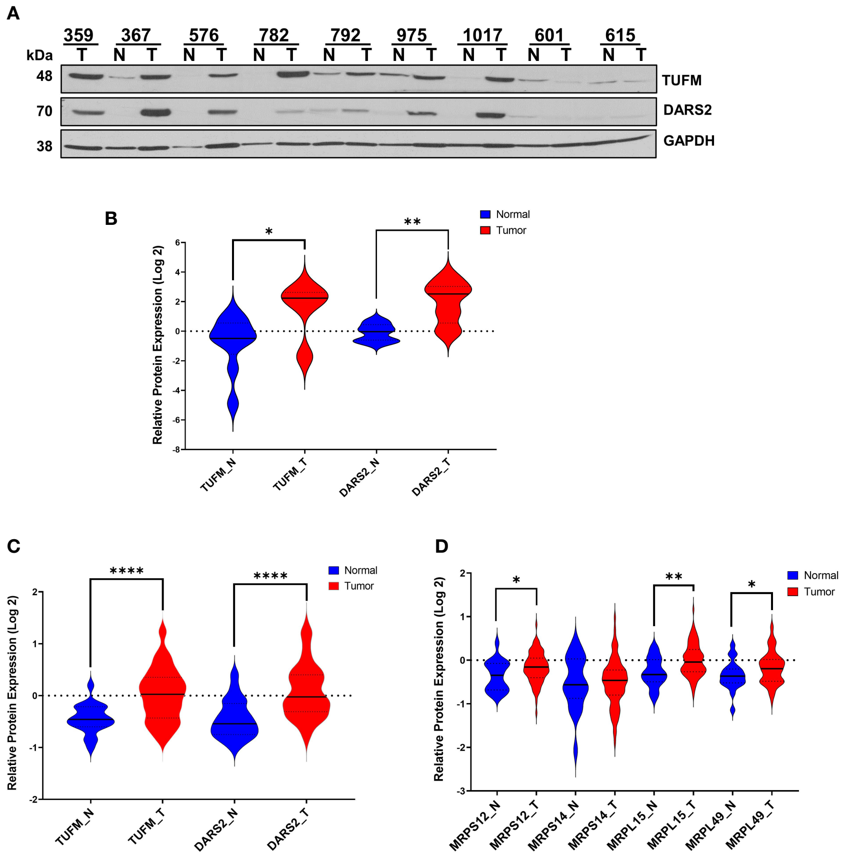

FIGURE 3
Expression of Mitochondrial Translation-Related Proteins in HGSOC. **(A)** Relative protein expression of TUFM and DARS2 were detected in normal ovarian (N) and HGSOC biopsies (T) by immunoblotting analyses. Equal protein loading was evaluated by Ponceau S staining and GAPDH probing. **(B)** Log 2 relative protein expression values of TUFM and DARS2 shown in panel A was presented using violin plots. **(C)** MS-based quantitation of TUFM and DARS2 protein expression, and **(D)** expression of mitochondrial ribosomal proteins, MRPS12, MRPS14, MRPL15, and MRPL49 in normal (N; blue) and HGSOC (T; red) in HGSOC published by McDermott et al. as part of the CPTAC data set [Log 2 values are taken from Supplemental Data in reference (45)]. P values ≤ 0.05 were represented as (*), ≤ 0.01 (**), and ≤ 0.0001 (****).

from ascites form aggressive peritoneal tumors and malignant ascites in animal models (Table S2) (53–55). In fact, the diversity of these cell lines might provide distinct mitochondrial characteristics and allow us to evaluate mitochondrial biogenesis and mtROS in these cell lines and compare it to HGSOC tumors. We first performed the immunoblotting analyses of cell lysates using the OXPHOS antibody cocktail as described in Figure 1A. The steady-state expression of OXPHOS subunits was relatively higher in OVCAR-3, OVCAR-4, and OVCAR-5 cells than that of the OVCAR-8, SKOV-3, and IGROV-1 cell lines (Figure 4A). These observations are all in agreement with high- and low-OXPHOS ovarian cancer cell line classification determined by Gentric et al. (7). Expressions of both mt-encoded, MT-COII (shown by a red arrow) and nuclear-encoded subunits, UQCRC2, NDUFB8, and COX4, were highly modulated between the two groups, confirming the high- and low-OXPHOS capacities in these cell lines (Figure 4A). Additionally, the increase in Mn-superoxide dismutase, SOD2, expression was more prominent in cells with high-OXPHOS capacity except the SKOV-3 cells (Figure 4A). The cells with higher OXPHOS subunit expression (Figure 4A) are suggested to be more sensitive to chemotherapy relative to the low OXPHOS expressing cells (7). As summarized in Table S2, some of the cell lines, specifically OVCAR-8 and SKOV-3, with reduced OXPHOS subunit expression and mitochondrial mass cause subcutaneous and intraperitoneal tumor formation in mice xenografts (54, 55).

Above, we demonstrated that the low-OXPHOS subunit expressing cell lines, OVCAR-8 and SKOV-3, are derived from

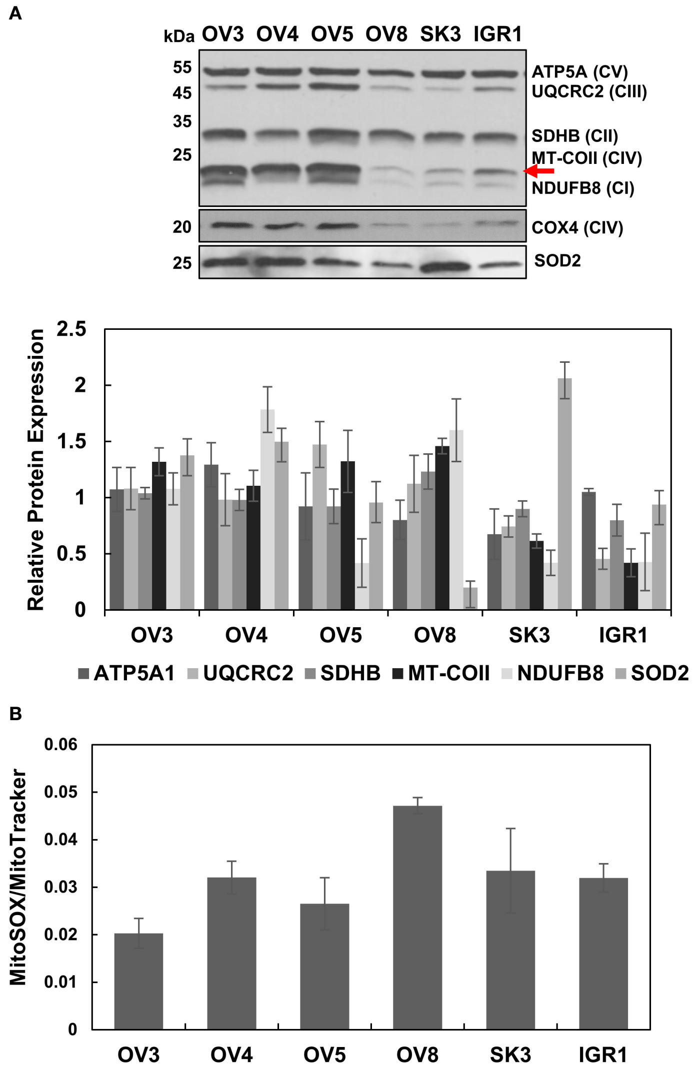

FIGURE 4
Altered OXPHOS subunit and SOD2 expressions and generation of reactive oxygen species in ovarian cancer cell lines. **(A)** The OXPHOS subunit and SOD2 expressions were detected by immunoblotting of lysates obtained from ovarian cancer cell lines, OVCAR-3 (OV3), OVCAR-4 (OV4), OVCAR-5 (OV5), OVCAR-8 (OV8), SKOV-3 (SK3), and IGROV-1 (IGR1) as described in Figure 1A. The red arrow shows the mt-encoded complex IV subunit, MT-COII. The relative quantitation of OXPHOS subunit and SOD2 expression represents the mean ± SD of at least three experiments. Signal intensity for each antibody was normalized to the mean of high (OV3, OV4, and OV5) and low (OV8, SK3, and IGR1) OXPHOS expressing cell lines and Ponceau S staining (Figures S2, S3). **(B)** mtROS and mitochondrial mass were determined by MitoSOX-Red (MitoSOX) and MitoTracker-Red (MitoTracker) stains, respectively, using flow cytometry of live ovarian cancer cell lines. MitoSOX/MitoTracker ratio reflects mtROS formation per functional mitochondrion for each cell line.

highly malignant and chemo-resistant peritoneal ascites (Figure 4A) (Table S2). Due to the varying levels of OXPHOS subunit expression, one may speculate that the different mtROS levels adapted these cell lines to hypoxic conditions and survival in the peritoneal cavity. To correlate the OXPHOS subunit expression to mtROS generation, we performed flow cytometry analyses using MitoSOX-Red as well as the MitoTracker-Red staining of live ovarian cancer cell lines. The MitoSOX-Red and MitoTracker-Red ratios allowed us to determine the generation of mtROS per functional mitochondrion in these cell lines. This ratio was higher for OVCAR-8 cells relative to the other cell lines, specifically OVCAR-3, OVCAR-4, and OVCAR-5 cells (Figure 4B). In other words, lower MitoSOX/MitoTracker ratio in these cells with higher OXPHOS subunit expression could be either due to the increased mitochondrial mass or mtROS scavenging capacity. The reduced OXPHOS subunit expression was in agreement with the increased mtROS generation, specifically for OVCAR-8 and SKOV3 cells (Figures 4A, B). Although the reduced expression of SOD2 explains the increased mtROS generation in OVCAR-8 cells, the high SOD2 protein expression was not sufficient to suppress mtROS generation in SKOV-3 cells (Figures 4A, B). These cell lines were highly proliferative and resistant to cisplatin treatments [data not shown and (7)]. Again, the OVCAR-8 and SKOV3 cell lines are known to develop subcutaneous and intraperitoneal tumors in mice (54, 55); the reduced OXPHOS subunit expression can be associated with increased mtROS generation and resistance to chemotherapy, as also suggested by Gentric et al. (6, 23). Our observations and findings from other laboratories indicate that the remodeling of OXPHOS and mtROS generation could be highly informative in explaining tumor aggressiveness, metastasis to the peritoneal cavity, and recurrence in ovarian cancer (3, 18, 34, 41, 56).

3.4 Mitochondrial biogenesis is altered in ovarian cancer cell lines

Similar to our observations with HGSOC biopsies, the substantial change in the steady-state MT-COII expression implied the modulation of mitochondrial biogenesis in some of the ovarian cancer cell lines (Figure 4A). To further investigate this phenomenon, immunoblotting analyses of ovarian cancer cell lysates were carried out using PGC1α, TFAM, SSBP1, TUFM, and DARS2 antibodies. Expression of the major mitochondrial transcription factors, PGC1α and TFAM, and SSBP1 were relatively similar in these cell lines, with some exceptions (Figure 5A). Reduced SSBP1 protein expression was noteworthy in SKOV3 cells (Figure 5A). Like TFAM expression, variation in translation elongation factor TUFM expressions was negligible in these cell lines (Figure 5B). Another translation-related protein DARS2 expression was higher in cell lines with high OXPHOS capacity (Figure 5B). The lower DARS2 expression in OVCAR-3 cell lines is noteworthy and possibly attributable to the reduced aspartate levels in HGSOC (57). In general, the lack of any significant trend in the data suggests mitochondrial biogenesis could be regulated at different stages to modulate OXPHOS subunit expression in these cell lines.

One of the best methods to explore the functionality of mitochondrial biogenesis *in situ* is to perform pulse-labeling of *de novo* synthesized mitochondrial proteins in the presence of [^{35}S]-Met. For this purpose, pulse labeling of ovarian cancer cell lines was carried out using cells grown to 70% confluency in regular media, as described previously (58). The *de novo* synthesized thirteen mt-encoded subunits were expressed by autoradiography after adding emetine in the media containing [^{35}S]-Met and normalized to the total protein loading stained with Coomassie Blue. (Figure 5C). The expression of [^{35}S]-Met-labeled subunits was clearly higher in OVCAR-4, OVCAR-5, and SKOV-3 cells relative to OVCAR-3, OVCAR-8, and IGROV-1 cells. Therefore, the reduced *de novo* protein synthesis observed in OVCAR-8 and IGROV-1 cell lines could be caused by mitochondrial translation and transcription defects (Figure 5C).

The steady-state expression of nuclear and mt-encoded OXPHOS subunits (Figure 4A) supported the results obtained with the *de novo* expression of 13 mt-encoded subunits for OVCAR-4, OVCAR-5, OVCAR-8, and IGROV-1 cells, with some exceptions (Figure 5C). The discrepancies observed between the steady-state and *de novo* expression of subunits in OVCAR-3 and SKOV-3 cell lines was conceivably caused by a difference in their proliferation rates (data not shown). For example, although the OVCAR-3 cells had higher steady-state subunit expression levels, the *de novo* subunit expression of OXPHOS subunits was lower than that of OVCAR-4 and OVCAR-5 cells. On the contrary, the SKOV-3 cell line had shown relatively high *de novo* OXPHOS subunit expression, possibly due to the proliferation rates of these cell lines.

Among the cells with low OXPHOS subunit expression, OVCAR-8, and SKOV-3, have higher invasion and metastatic capabilities supported by glycolytic energy metabolism rather than OXPHOS compared to the cell lines with higher OXPHOS capacity and resistance to cisplatin-induced apoptosis (Figure 4A and Table S2) (7, 27). The changes in *de novo* protein synthesis and the expression of mitochondrial translation components in these cell lines could also be correlated to alterations observed in HGSOC tumor biopsies.

4 Conclusions and future directions

HGSOC is one of the most common ovarian cancer subtypes and remains one of the deadliest cancers due to its high metastatic capacity and development of resistance to chemotherapy. With the metabolic heterogeneity of tumors in mind, one of the controversies that need to be resolved is the contribution of OXPHOS to aggressiveness and the development of chemoresistance and recurrence in ovarian cancer. One proposed mechanism for the high metastatic capacity and chemoresistance in ovarian cancer is the formation of spheroids from primary tumors with metabolic flexibility adapted to hypoxia in an ascitic environment. The increased metabolic flexibility of spheroids caused by modulation of mitochondrial function and morphology allows them to disseminate or reattach in the peritoneal cavity (4, 41, 47, 53, 59).

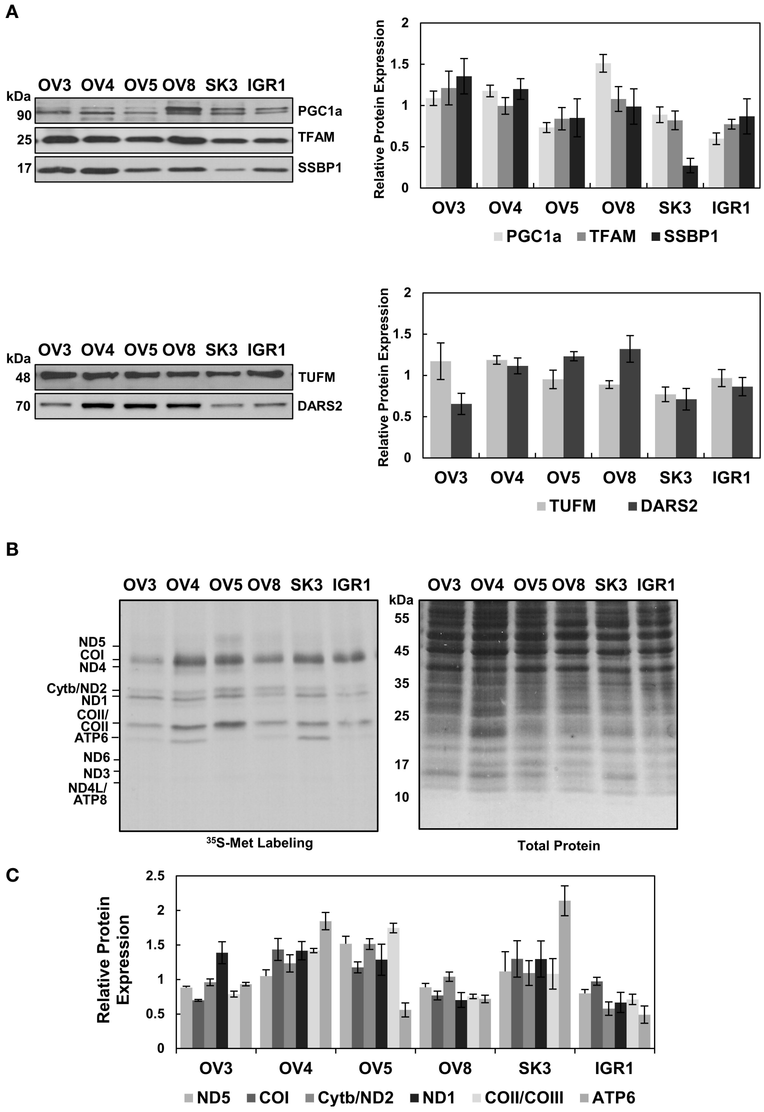

FIGURE 5
Evaluation of Mitochondrial Biogenesis in Ovarian Cancer Cell Lines. **(A)** Mitochondrial transcription and replication-related proteins, PGC1a, TFAM, and SSBP1, and **(B)** mitochondrial translation-related proteins, TUFM and DARS2, were detected by immunoblotting analyses of ovarian cancer cell lines described in Figure 4A. Ponceau S staining ensured equal protein loading Results represent the mean ± SD of at least three experiments. **(C)** Mitochondrial translation is determined by ^{35}S-Met pulse labeling of 13 mt-encoded OXPHOS subunits in ovarian cancer cell lines. The pulse-labeled protein lysates (30 µg) were separated on 13% SDS-PAGE and 13 mt-encoded subunits, ND1-ND6 (complex I), Cyt b (complex III), COI-COIII (complex IV), and ATP6 and ATP8 (complex V), were labeled on the autoradiography of the gel. Total protein loading was visualized by Coomassie Blue. The relative quantitation of *de novo* synthesized subunits, ND5, COI, Cyt b/ND2, ND1, COII/COIII, and ATP6, was determined from at least three experiments, with the mean ± SD displayed. The signal intensity of each protein band was normalized to the mean of high (OV3, OV4, and OV5) or low (OV8, SK3, and IGR1) OXPHOS expressing cell lines.

In this study, we investigated the role of mitochondrial biogenesis in the modulation of mitochondrial energy metabolism in HGSOC biopsies and ovarian cancer cell lines derived from adenocarcinomas and peritoneal ascites. The mitochondrial energy metabolism is evaluated by OXPHOS subunit expression belonging to the electron transport chain complexes (complexes I-IV) and ATP synthase (complex V). The primary and significant changes were observed in complex II and IV subunits, SDHB and MT-COII, respectively, in HGSOC biopsies (Figures 1A, B). In MS-based proteomics studies performed by McDermott et al., the overall change was insignificant except for a reduction in NDUFS2 expression (Figure 1C) (45). On the other hand, the difference and increase between the low- and high-OXPHOS expressing HGSOC biopsies was significant for all the subunits (Figure 1D) (7). The heterogeneity and the increased OXPHOS subunit expression in most of the HGSOC biopsies reported by Gentric et al. (7) strongly agree with the bimodal distribution observed in our analyses, specifically for MT-COII expression (Figure 1). Interestingly, the high-OXPHOS tumors have shown an increased response to conventional chemotherapy and are associated with better prognosis in HGSOC patients (7).

Expression of the mt-encoded OXPHOS subunit quantified in our analysis, MT-COII, depends on mitochondrial biogenesis; thus, the modulation of transcription and translation machineries in mitochondria is essential. Probing normal and HGSOC biopsies for the expression of PGC1α, TFAM, SSBP1, TUFM, and DARS2 allowed us to demonstrate the correlation between the changes in OXPHOS subunit expression and mitochondrial biogenesis for the first time (Figures 1–3). The strong agreement between our findings on mitochondrial biogenesis and the data mining analyses of MS-based proteomics studies allowed us to suggest that the remodeling of energy metabolism or metabolic flexibility in HGSOC is regulated by mitochondrial biogenesis (Figures 1–3) (7, 45). Since metabolic flexibility is one of the determinants of the survival of tumor cells in the peritoneal cavity, deciphering mitochondrial biogenesis and its role in the remodeling of energy metabolism is crucial for better prognosis in HGSOC patients.

The mechanism behind the chemotherapy resistance and recurrence is still an unresolved issue in HGSOC (60, 61). The role of mitochondrial function and oxidative stress in chemoresistance and metastatic capacity is under investigation by many groups using ovarian cancer cell line models (5, 7, 27, 41, 47, 53). Here, we aimed to correlate mitochondrial biogenesis and mtROS generation to OXPHOS status in commonly used NCI-60 ovarian cancer cell line panel, including highly metastatic and chemoresistant cell lines listed in Table S2. Two of the cell lines with lower OXPHOS subunit expression, OVCAR-8, and SKOV-3 (Figure 4A), are the more aggressive cell lines forming subcutaneous and intraperitoneal tumors in mice xenografts (Table S2) (54, 55). Gentric et al. have suggested that ovarian cancer cell lines, including OVCAR-8 and SKOV-3, and HGSOC tumors with low-OXPHOS subunit expression have decreased chemosensitivity to platinum-based treatments due to reduced oxidative stress and ferroptosis (7). Modulating oxidative stress and ROS generation is proposed as one of the mechanisms behind the cis-platin induced cell death (3, 5, 27, 56, 62); however, it might not be possible to modulate mtROS generation in cells or tumors with low-OXPHOS. Although the overall cellular ROS generation is lower in low-OXPHOS cells (7), we found that the mtROS per functional mitochondrion was higher in OVCAR-8 cells, which is known for its resistance to cis-platin cell death relative to the high-OXPHOS cell lines (Figure 4B). It is conceivable that the low-OXPHOS cells or HGSOC tumors already have leaky electron transport chain generating high mtROS levels due to reduced mitochondrial biogenesis and SOD2 levels (Figure 4A). The decreased SOD2 levels or antioxidant capacity of ovarian cancer cells with low-OXPHOS, such as OVCAR-8, is not sufficient to scavenge mtROS generated in these cells (Figure 4). One possible mechanism for resistance to platinum-based treatments in OVCAR-8 cells could be due to the low SOD2 levels and increased mtROS generation. Dual role of SOD2 expression has been suggested in ovarian cancer as tumor suppressor and protumoregenic factor (53, 63–65); therefore, antioxidant capacity of HGSOC need to be critically evaluated in future studies.

As discussed above, the association between the OXPHOS subunit expression and mitochondrial biogenesis is clearly shown in HGSOC tumor biopsies (Figures 1–3). This correlation was not clear with the ovarian cancer cell lines with low-OXPHOS subunit expression; specifically, the OVCAR-8 cells had normal levels and, in some cases, higher levels of PGC1α, TFAM, TUFM, and DARS2 protein expression (Figures 5A, B). On the other hand, the *de novo* synthesis of mt-encoded proteins determined by the ^{35}[S]-Met pulse labeling experiments was consistent with the MT-COII expression detected by immunoblotting analyses in some of the cell lines (Figures 4A, 5C). The *de novo* protein synthesis data obtained with the ovarian cancer cells suggests mitochondrial biogenesis, at both transcription and translation levels, remodels the mitochondrial energy metabolism and possibly mtROS generation in ovarian cancer.

Changes in mitochondrial mRNA and biogenesis related transcript levels are previously utilized in predicting overall survival and tumor progression and suggested as possible prognostic biomarkers in HGSOC (33–35). In this study, we validated these predictions at the protein expression levels and have shown the role of mitochondrial biogenesis in metabolic remodeling of HGSOC tumors and ovarian cancer cell lines derived from ascites. One of the major limitations of our study is the absence of normal ovarian and true HGSOC cell lines for a better comparison of changes in OXPHOS and mitochondrial biogenesis. The role of mitochondria in metabolic remodeling of HGSOC is now better-understood (2, 5, 7, 18, 66, 67); however, the role of mitochondrial biogenesis in formation of peritoneal spheroids and ascites as well as mtROS generation need to be investigated further to improve efficacy of current chemotherapy options in HGSOC treatment.

Data availability statement

The original contributions presented in the study are included in the article/Supplementary materials, further inquiries can be directed to the corresponding author/s.

Ethics statement

Ethical review and approval were not required for the human de-identified biopsies used in this study in accordance with the local legislation and institutional requirements.

Author contributions

ZK and EK designed the study. ZK and EK performed immunoblotting analyses of biopsies and ovarian cancer cell lines. EK performed ^{35}S-Met pulse labeling assays. ZK and EK performed the data mining analysis of the CPTAC proteome and prepared the figures. EK and VS performed flow cytometry analyses of ovarian cancer cell lines. ZK, VS, NB, GR, and EK involved in manuscript writing and revision. All authors contributed to the article and approved the submitted version.

Funding

The tissue procurement center at the Marshall University Edwards Comprehensive Cancer Center was supported by a grant (2U54GM104942) from the National Institute for General Medical Sciences (NIGMS) awarded to the West Virginia Clinical and Translational Science Institute (WV-CTSI). This work was supported in part by NIH grant P20GM103434 to the West Virginia IDeA Network of Biomedical Research Excellence.

Acknowledgments

The authors thank the Tissue Procurement Center at the Edwards Comprehensive Cancer Center at Marshall University for providing normal ovarian and tumor biopsies. We also gratefully acknowledge the Department of Biomedical Sciences at the Joan C. Edwards School of Medicine, Marshall University, for its support.

Conflict of interest

The authors declare that the research was conducted in the absence of any commercial or financial relationships that could be construed as a potential conflict of interest.

Publisher's note

Supplementary material

The Supplementary Material for this article can be found online at: https://www.frontiersin.org/articles/10.3389/fonc.2023.1129352/full#supplementary-material

References

1. *Cancer facts & figures 2022.* American Cancer Society (2022).
2. Emmings E, Mullany S, Chang Z, Landen CNJr., Linder S, Bazzaro M. Targeting mitochondria for treatment of chemoresistant ovarian cancer. *Int J Mol Sci* (2019) 20 (1):229. doi: 10.3390/ijms20010229
3. Pakula M, Mikula-Pietrasik J, Stryczynski L, Uruski P, Szubert S, Moszynski R, et al. Mitochondria-related oxidative stress contributes to ovarian cancer-promoting activity of mesothelial cells subjected to malignant ascites. *Int J Biochem Cell Biol* (2018) 98:82–8. doi: 10.1016/j.biocel.2018.03.011
4. Dar S, Chhina J, Mert I, Chitale D, Buekers T, Kaur H, et al. Bioenergetic adaptations in chemoresistant ovarian cancer cells. *Sci Rep* (2017) 7(1):8760. doi: 10.1038/s41598-017-09206-0
5. Matassa DS, Amoroso MR, Lu H, Avolio R, Arzeni D, Procaccini C, et al. Oxidative metabolism drives inflammation-induced platinum resistance in human ovarian cancer. *Cell Death Differ* (2016) 23(9):1542–54. doi: 10.1038/cdd.2016.39
6. Amoroso MR, Matassa DS, Agliarulo I, Avolio R, Lu H, Sisinni L, et al. Trap1 downregulation in human ovarian cancer enhances invasion and epithelial-mesenchymal transition. *Cell Death Dis* (2016) 7(12):e2522. doi: 10.1038/cddis.2016.400
7. Gentric G, Kieffer Y, Mieulet V, Goundiam O, Bonneau C, Nemati F, et al. Pml-regulated mitochondrial metabolism enhances chemosensitivity in human ovarian cancers. *Cell Metab* (2019) 29(1):156–73 e10. doi: 10.1016/j.cmet.2018.09.002
8. Li N, Li H, Cao L, Zhan X. Quantitative analysis of the mitochondrial proteome in human ovarian carcinomas. *Endocr Relat Cancer* (2018) 25(10):909–31. doi: 10.1530/ERC-18-0243
9. Bindra S, McGill MA, Triplett MK, Tyagi A, Thaker PH, Dahmoush L, et al. Mitochondria in epithelial ovarian carcinoma exhibit abnormal phenotypes and blunted associations with biobehavioral factors. *Sci Rep* (2021) 11(1):11595. doi: 10.1038/s41598-021-89934-6
10. Warburg O. On the origin of cancer cells. *Science* (1956) 123(3191):309–14. doi: 10.1126/science.123.3191.309
11. Wallace DC. Mitochondria and cancer: Warburg addressed. *Cold Spring Harb Symp Quant Biol* (2005) 70:363–74. doi: 10.1101/sqb.2005.70.035
12. Hanahan D, Weinberg RA. Hallmarks of cancer: The next generation. *Cell* (2011) 144(5):646–74. doi: 10.1016/j.cell.2011.02.013
13. Chiavarina B, Martinez-Outschoorn UE, Whitaker-Menezes D, Howell A, Tanowitz HB, Pestell RG, et al. Metabolic reprogramming and two-compartment tumor metabolism: Opposing Role(S) of Hif1alpha and Hif2alpha in tumor-associated fibroblasts and human breast cancer cells. *Cell Cycle* (2012) 11(17):3280–9. doi: 10.4161/cc.21643
14. Curry JM, Tuluc M, Whitaker-Menezes D, Ames JA, Anantharaman A, Butera A, et al. Cancer metabolism, stemness and tumor recurrence: Mct1 and Mct4 are functional biomarkers of metabolic symbiosis in head and neck cancer. *Cell Cycle* (2013) 12(9):1371–84. doi: 10.4161/cc.24092
15. Berndtsson M, Hagg M, Panaretakis T, Havelka AM, Shoshan MC, Linder S. Acute apoptosis by cisplatin requires induction of reactive oxygen species but is not associated with damage to nuclear DNA. *Int J Cancer* (2007) 120(1):175–80. doi: 10.1002/ijc.22132
16. Housman G, Byler S, Heerboth S, Lapinska K, Longacre M, Snyder N, et al. Drug resistance in cancer: An overview. *Cancers (Basel)* (2014) 6(3):1769–92. doi: 10.3390/cancers6031769
17. de Jongh FE, van Veen RN, Veltman SJ, de Wit R, van der Burg ME, van den Bent MJ, et al. Weekly high-dose cisplatin is a feasible treatment option: Analysis on prognostic factors for toxicity in 400 patients. *Br J Cancer* (2003) 88(8):1199–206. doi: 10.1038/sj.bjc.6600884
18. Zampieri LX, Grasso D, Bouzin C, Brusa D, Rossignol R, Sonveaux P. Mitochondria participate in chemoresistance to cisplatin in human ovarian cancer cells. *Mol Cancer Res* (2020) 18(9):1379–91. doi: 10.1158/1541-7786.MCR-19-1145
19. Shadel GS. Coupling the mitochondrial transcription machinery to human disease. *Trends Genet* (2004) 20(10):513–9. doi: 10.1016/j.tig.2004.08.005
20. D'Souza AR, Minczuk M. Mitochondrial transcription and translation: Overview. *Essays Biochem* (2018) 62(3):309–20. doi: 10.1042/EBC20170102
21. Smith ALM, Whitehall JC, Greaves LC. Mitochondrial <Scp>DNA</Scp> mutations in ageing and cancer. *Mol Oncol* (2022) 16(18):3276–94. doi: 10.1002/1878-0261.13291
22. Wallace DC. Mitochondria and cancer. *Nat Rev Cancer* (2012) 12(10):685–98. doi: 10.1038/nrc3365
23. Shukla P, Singh KK. The mitochondrial landscape of ovarian cancer: Emerging insights. *Carcinogenesis* (2021) 42(5):663–71. doi: 10.1093/carcin/bgab033
24. Kim YS, Hwan JD, Bae S, Bae DH, Shick WA. Identification of differentially expressed genes using an annealing control primer system in stage iii serous ovarian carcinoma. *BMC Cancer* (2010) 10:576. doi: 10.1186/1471-2407-10-576
25. Gabrielson M, Bjorklund M, Carlson J, Shoshan M. Expression of mitochondrial regulators Pgc1alpha and tfam as putative markers of subtype and chemoresistance in epithelial ovarian carcinoma. *PloS One* (2014) 9(9):e107109. doi: 10.1371/journal.pone.0107109
26. Signorile A, De Rasmo D, Cormio A, Musicco C, Rossi R, Fortarezza F, et al. Human ovarian cancer tissue exhibits increase of mitochondrial biogenesis and cristae remodeling. *Cancers (Basel)* (2019) 11(9):1350. doi: 10.3390/cancers11091350
27. Kleih M, Bopple K, Dong M, Gaissler A, Heine S, Olayioye MA, et al. Direct impact of cisplatin on mitochondria induces ros production that dictates cell fate of ovarian cancer cells. *Cell Death Dis* (2019) 10(11):851. doi: 10.1038/s41419-019-2081-4
28. Koc EC, Burkhart W, Blackburn K, Moseley A, Spremulli LL. The small subunit of the mammalian mitochondrial ribosome: Identification of the full complement of ribosomal proteins present. *J Biol Chem* (2001) 276:19363–74. doi: 10.1074/jbc.M100727200
29. Koc EC, Burkhart W, Blackburn K, Moyer MB, Schlatzer DM, Moseley A, et al. The Large subunit of the mammalian mitochondrial ribosome. analysis of the complement of ribosomal proteins present. *J Biol Chem* (2001) 276(47):43958–69. doi: 10.1074/jbc.M106510200
30. Koc EC, Cimen H, Kumcuoglu B, Abu N, Akpinar G, Haque ME, et al. Identification and characterization of Chchd1, Aurkaip1, and Crif1 as new members of the mammalian mitochondrial ribosome. *Front Physiol* (2013) 4:183. doi: 10.3389/fphys.2013.00183
31. O'Brien TW, Denslow ND, Anders JC, Courtney BC. The translation system of mammalian mitochondria. *Biochim Biophys Acta* (1990) 1050(1-3):174–8. doi: 10.1016/0167-4781(90)90162-U
32. Suzuki T, Terasaki M, Takemoto-Hori C, Hanada T, Ueda T, Wada A, et al. Proteomic analysis of the mammalian mitochondrial ribosome. identification of protein components in the 28 s small subunit. *J Biol Chem* (2001) 276(35):33181–95. doi: 10.1074/jbc.M103236200

33. Xu H, Zou R, Li F, Liu J, Luan N, Wang S, et al. Mrpl15 is a novel prognostic biomarker and therapeutic target for epithelial ovarian cancer. *Cancer Med* (2021) 10 (11):3655–73. doi: 10.1002/cam4.3907

34. Sotgia F, Lisanti MP. Mitochondrial mrna transcripts predict overall survival, tumor recurrence and progression in serous ovarian cancer: Companion diagnostics for cancer therapy. *Oncotarget* (2017) 8(40):66925–39. doi: 10.18632/oncotarget.19963

35. Qiu X, Guo D, Du J, Bai Y, Wang F. A novel biomarker, Mrps12 functions as a potential oncogene in ovarian cancer and is a promising prognostic candidate. *Med (Baltimore)* (2021) 100(8):e24898. doi: 10.1097/MD.0000000000024898

36. Permuth-Wey J, Chen YA, Tsai Y-Y, Chen Z, Qu X, Lancaster JM, et al. Inherited variants in mitochondrial biogenesis genes may influence epithelial ovarian cancer risk. *Cancer Epidemiol Biomarkers Prev* (2011) 20(6):1131–45. doi: 10.1158/1055-9965.epi-10-1224

37. Blayney JK, Davison T, McCabe N, Walker S, Keating K, Delaney T, et al. Prior knowledge transfer across transcriptional data sets and technologies using compositional statistics yields new mislabelled ovarian cell line. *Nucleic Acids Res* (2016) 44(17):e137. doi: 10.1093/nar/gkw578

38. Chomyn A. *In vivo* labeling and analysis of human mitochondrial translation products. *Methods Enzymol* (1996) 264:197–211. doi: 10.1016/s0076-6879(96)64020-8

39. Sasarman F, Shoubridge EA. Radioactive labeling of mitochondrial translation products in cultured cells. *Methods Mol Biol* (2012) 837:207–17. doi: 10.1007/978-1-61779-504-6_14

40. Shen L, Zhan X. Mitochondrial dysfunction pathway alterations offer potential biomarkers and therapeutic targets for ovarian cancer. *Oxid Med Cell Longev* (2022) 2022:5634724. doi: 10.1155/2022/5634724

41. Grieco JP, Allen ME, Perry JB, Wang Y, Song Y, Rohani A, et al. Progression-mediated changes in mitochondrial morphology promotes adaptation to hypoxic peritoneal conditions in serous ovarian cancer. *Front Oncol* (2020) 10:600113. doi: 10.3389/fonc.2020.600113

42. Koc EC, Haciosmanoglu E, Claudio PP, Wolf A, Califano L, Friscia M, et al. Impaired mitochondrial protein synthesis in head and neck squamous cell carcinoma. *Mitochondrion* (2015) 24:113–21. doi: 10.1016/j.mito.2015.07.123

43. Hunter CA, Kartal F, Koc ZC, Murphy T, Kim JH, Denvir J, et al. Mitochondrial oxidative phosphorylation is impaired in tallyho mice, a new obesity and type 2 diabetes animal model. *Int J Biochem Cell Biol* (2019) 116:105616. doi: 10.1016/j.biocel.2019.105616

44. Hunter CA, Koc H, Koc EC. C-src kinase impairs the expression of mitochondrial oxphos complexes in liver cancer. *Cell Signal* (2020) 72:109651. doi: 10.1016/j.cellsig.2020.109651

45. McDermott JE, Arshad OA, Petyuk VA, Fu Y, Gritsenko MA, Clauss TR, et al. Proteogenomic characterization of ovarian hgsc implicates mitotic kinases, replication stress in observed chromosomal instability. *Cell Rep Med* (2020) 1(1):100004. doi: 10.1016/j.xcrm.2020.100004

46. Zhang Y, Ba Y, Liu C, Sun G, Ding L, Gao S, et al. Pgc-1alpha induces apoptosis in human epithelial ovarian cancer cells through a ppargamma-dependent pathway. *Cell Res* (2007) 17(4):363–73. doi: 10.1038/cr.2007.11

47. Compton SLE, Grieco JP, Gollamudi B, Bae E, Van Mullekom JH, Schmelz EM. Metabolic reprogramming of ovarian cancer spheroids during adhesion. *Cancers (Basel)* (2022) 14(6):1399. doi: 10.3390/cancers14061399

48. Hoffman DL, Brookes PS. Oxygen sensitivity of mitochondrial reactive oxygen species generation depends on metabolic conditions. *J Biol Chem* (2009) 284 (24):16236–45. doi: 10.1074/jbc.M809512200

49. Diebold L, Chandel NS. Mitochondrial ros regulation of proliferating cells. *Free Radic Biol Med* (2016) 100:86–93. doi: 10.1016/j.freeradbiomed.2016.04.198

50. Bell EL, Klimova TA, Eisenbart J, Schumacker PT, Chandel NS. Mitochondrial reactive oxygen species trigger hypoxia-inducible factor-dependent extension of the replicative life span during hypoxia. *Mol Cell Biol* (2007) 27(16):5737–45. doi: 10.1128/MCB.02265-06

51. Domcke S, Sinha R, Levine DA, Sander C, Schultz N. Evaluating cell lines as tumour models by comparison of genomic profiles. *Nat Commun* (2013) 4:2126. doi: 10.1038/ncomms3126

52. Beaufort CM, Helmijr JC, Piskorz AM, Hoogstraat M, Ruigrok-Ritstier K, Besselink N, et al. Ovarian cancer cell line panel (Occp): Clinical importance of in vitro morphological subtypes. *PloS One* (2014) 9(9):e103988. doi: 10.1371/journal.pone.0103988

53. Kim YS, Gupta Vallur P, Jones VM, Worley BL, Shimko S, Shin DH, et al. Context-dependent activation of Sirt3 is necessary for anchorage-independent survival and metastasis of ovarian cancer cells. *Oncogene* (2019) 39(8):1619–33. doi: 10.1038/s41388-019-1097-7

54. Mitra AK, Davis DA, Tomar S, Roy L, Gurler H, Xie J, et al. *In vivo* tumor growth of high-grade serous ovarian cancer cell lines. *Gynecol Oncol* (2015) 138 (2):372–7. doi: 10.1016/j.ygyno.2015.05.040

55. Hernandez L, Kim MK, Lyle LT, Bunch KP, House CD, Ning F, et al. Characterization of ovarian cancer cell lines as in vivo models for preclinical studies. *Gynecol Oncol* (2016) 142(2):332–40. doi: 10.1016/j.ygyno.2016.05.028

56. Pons DG, Sastre-Serra J, Nadal-Serrano M, Oliver A, Garcia-Bonafe M, Bover I, et al. Initial activation status of the antioxidant response determines sensitivity to Carboplatin/Paclitaxel treatment of ovarian cancer. *Anticancer Res* (2012) 32 (11):4723–8.

57. Zand B, Previs RA, Zacharias NM, Rupaimoole R, Mitamura T, Nagaraja AS, et al. Role of increased n-acetylaspartate levels in cancer. *J Natl Cancer Inst* (2016) 108 (6):djv426. doi: 10.1093/jnci/djv426

58. Sasarman F, Karpati G, Shoubridge EA. Nuclear genetic control of mitochondrial translation in skeletal muscle revealed in patients with mitochondrial myopathy. *HumMolGenet* (2002) 11(14):1669–81. doi: 10.1093/hmg/11.14.1669

59. Ricci F, Corbelli A, Affatato R, Chila R, Chiappa M, Brunelli L, et al. Mitochondrial structural alterations in ovarian cancer patient-derived xenografts resistant to cisplatin. *Am J Cancer Res* (2021) 11(5):2303–11.

60. Christie EL, Bowtell DDL. Acquired chemotherapy resistance in ovarian cancer. *Ann Oncol* (2017) 28(suppl_8):viii13–viii5. doi: 10.1093/annonc/mdx446

61. Slaughter K, Holman LL, Thomas EL, Gunderson CC, Lauer JK, Ding K, et al. Primary and acquired platinum-resistance among women with high grade serous ovarian cancer. *Gynecol Oncol* (2016) 142(2):225–30. doi: 10.1016/j.ygyno.2016.05.020

62. Jiang Z, Fletcher NM, Ali-Fehmi R, Diamond MP, Abu-Soud HM, Munkarah AR, et al. Modulation of redox signaling promotes apoptosis in epithelial ovarian cancer cells. *Gynecol Oncol* (2011) 122(2):418–23. doi: 10.1016/j.ygyno.2011.04.051

63. Cui Y, She K, Tian D, Zhang P, Xin X. Mir-146a inhibits proliferation and enhances chemosensitivity in epithelial ovarian cancer *Via* reduction of Sod2. *Oncol Res* (2016) 23(6):275–82. doi: 10.3727/096504016X14562725373798

64. Hemachandra LP, Shin DH, Dier U, Iuliano JN, Engelberth SA, Uusitalo LM, et al. Mitochondrial superoxide dismutase has a protumorigenic role in ovarian clear cell carcinoma. *Cancer Res* (2015) 75(22):4973–84. doi: 10.1158/0008-5472.CAN-14-3799

65. Hempel N, Carrico PM, Melendez JA. Manganese superoxide dismutase (Sod2) and redox-control of signaling events that drive metastasis. *Anticancer Agents Med Chem* (2011) 11(2):191–201. doi: 10.2174/187152011795255911

66. Gentric G, Mieulet V, Mechta-Grigoriou F. Heterogeneity in cancer metabolism: New concepts in an old field. *Antioxid Redox Signal* (2017) 26(9):462–85. doi: 10.1089/ars.2016.6750

67. Saed GM, Diamond MP, Fletcher NM. Updates of the role of oxidative stress in the pathogenesis of ovarian cancer. *Gynecol Oncol* (2017) 145(3):595–602. doi: 10.1016/j.ygyno.2017.02.033

frontiers | Frontiers in Oncology

TYPE Review
PUBLISHED 23 March 2023
DOI 10.3389/fonc.2023.1123420

Regulatory roles of copper metabolism and cuproptosis in human cancers

Zhe Wang[1†], Dekui Jin[2†], Shuaishuai Zhou[1], Niujing Dong[3], Yuting Ji[1], Peng An[1], Jiaping Wang[3*], Yongting Luo[1*] and Junjie Luo[1*]

[1]Department of Nutrition and Health, China Agricultural University, Beijing, China, [2]Department of General Practice, The Third Medical Center of Chinese PLA General Hospital, Beijing, China, [3]China Astronaut Research and Training Center, Beijing, China

OPEN ACCESS

EDITED BY
Alessandra di Masi,
Roma Tre University, Italy

REVIEWED BY
Wukun Liu,
Nanjing University of Chinese Medicine,
China
Mariana Paranhos Stelling,
Instituto Federal de Educação, Ciência e
Tecnologia do Rio de Janeiro, Brazil

*CORRESPONDENCE
Jiaping Wang
✉ wangjiaping_1113@163.com
Yongting Luo
✉ luo.yongting@cau.edu.cn
Junjie Luo
✉ luojj@cau.edu.cn

[†]These authors have contributed equally to this work

SPECIALTY SECTION
This article was submitted to
Cancer Metabolism,
a section of the journal
Frontiers in Oncology

RECEIVED 16 December 2022
ACCEPTED 08 March 2023
PUBLISHED 23 March 2023

CITATION
Wang Z, Jin D, Zhou S, Dong N, Ji Y, An P, Wang J, Luo Y and Luo J (2023) Regulatory roles of copper metabolism and cuproptosis in human cancers.
Front. Oncol. 13:1123420.
doi: 10.3389/fonc.2023.1123420

Copper is an essential micronutrient for human body and plays a vital role in various biological processes including cellular respiration and free radical detoxification. Generally, copper metabolism in the body is in a stable state, and there are specific mechanisms to regulate copper metabolism and maintain copper homeostasis. Dysregulation of copper metabolism may have a great connection with various types of diseases, such as Wilson disease causing copper overload and Menkes disease causing copper deficiency. Cancer presents high mortality rates in the world due to the unlimited proliferation potential, apoptosis escape and immune escape properties to induce organ failure. Copper is thought to have a great connection with cancer, such as elevated levels in cancer tissue and serum. Copper also affects tumor progression by affecting angiogenesis, metastasis and other processes. Notably, cuproptosis is a novel form of cell death that may provide novel targeting strategies for developing cancer therapy. Copper chelators and copper ionophores are two copper coordinating compounds for the treatment of cancer. This review will explore the relationship between copper metabolism and cancers, and clarify copper metabolism and cuproptosis for cancer targeted therapy.

KEYWORDS

copper, cancer, copper metabolism, cuproptosis, copper complexes, cancer therapeutics

1 Introduction

Copper (Cu) is an essential micronutrient for the human body. Copper has four oxidation states: metallic copper, Cu^+, Cu^{2+} and Cu^{3+}. As a transition metal, copper plays a key role in many biological processes, such as cellular respiration (1), free radical detoxification (2–5), cellular iron metabolism (6), angiogenesis (7), and neurotransmitter synthesis (8). However, excess intracellular copper ions can be toxic to cells (9). The transfer of electrons will occur in the transfer of copper ions with different valence states, resulting in the formation of reactive oxygen species (ROS).ROS can injury biological organic molecules such as proteins, nucleic acids and lipids, and also interfere with the synthesis of iron sulfur clusters to injury countless essential enzymes in cells. In addition, copper overload is seen in Wilson disease (WD), which is a manifestation of dysregulation of organismal copper homeostasis (10). Deficiency of copper ions results in the reduction of multiple enzyme activities, which is also thought to underlie the pathologies of Menkes disease (MD) (11). Therefore, no matter whether copper ions are excessive or deficient, it may be harmful to human body. Copper homeostasis is essential in organisms and dysregulation of copper metabolism leads to the occurrence of some diseases.

Copper is closely related to cancer. It is well known that copper is also involved in tumor formation and progression. Copper levels are elevated in a variety of malignancies, and high levels of copper ions affect tumor proliferation, angiogenesis, as well as metastasis (12–14). In recent years, a novel form of cell death induced by intracellular copper, discovered by Tsvetkov and co-workers (15), which is distinct from oxidative stress-related cell death, is a type of copper-dependent cell death, termed cuproptosis. This review will explore the relationship between copper metabolism, cuproptosis and cancers, providing references for cancer targeted therapy.

2 Copper metabolism and cancer

2.1 Copper metabolism

In mammals, copper is required for cellular metabolism, but its excess is toxic to cells. Therefore, copper concentration in cells is tightly regulated (16). There are many components involved in cellular copper homeostasis maintenance, including (1) transporters mediating copper absorption, such as copper transporter receptor 1 (Ctr1) (also called SCL1A1), copper transporter receptor 2 (Ctr2), divalent metal transporter 1 (DMT1); (2) enzymes guiding copper ion efflux, such as copper-transporting ATPase 1 (ATP7A) and copper-transporting ATPase 2 (ATP7B); (3) biomolecules that sequester and store copper, such as metallothionein (MT), glutathione (GSH); (4) copper chaperones, such as copper chaperone for superoxide dismutase (CCS), antioxidant protein 1 (Atox1), cytochrome c oxidase copper chaperone 17 (Cox17), which direct copper to copper dependent enzymes and transport copper to organelles that requiring copper (16).

A major contributor involved in copper uptake in mammals is Ctr1 (17). It is now generally accepted that Ctr1 transports Cu^+ in a high affinity manner (18, 19), however in mammalian enterocytes the copper ion is in the form of divalent copper (Cu^{2+}), which can be directly transported by divalent metal transporter 1 (DMT1) but cannot be directly utilized by cells (20). Thus enterocytes produced intracellular reductases such as steap2/3/4 to reduce cell surface Cu^{2+} to Cu^+ and then Cu^+ can be transported by Ctr1 (21) (Figure 1).

Copper ions are transported to specific locations after entering the cell *via* utilization or detoxification pathways, and excess copper will be sequestered by copper storage proteins such as MT and GSH (22). The intracellular trafficking of copper is mediated by copper chaperones, such as CCS, Atox1, Cox17. These copper chaperones assist copper in reaching vital destinations without inflicting damage or becoming trapped in adventitious binding sites (23) In the cytoplasm, CCS mediates Cu^+ loading and activation of superoxide dismutase 1 (SOD1) (24). The chaperone Cox17 mainly functions to transfer copper to Sco1, Sco2, Cox11 (25), and Sco1/2 plays an important role for cytochrome c oxidase (Cox) formation (26). The role of Atox1 is to bind Cu^+ and deliver it to P1B type ATPases (27), which includes ATP7A and ATP7B with important roles in the systemic distribution of copper ions.

Excessive copper ion accumulation in cells may generate ROS, causing oxidative damage to cells. Thus, the excess Cu^+ will be bound by MT or GSH, maintaining the concentration of intracellular Cu ions within a suitable range (16). The copper ion export in mammals is dependent on large multi transmembrane proteins ATP7A and ATP7B (16). There are multiple routes for copper ions transport out of the cell. For example, copper ions in intestinal epithelial cells enter the blood directly *via* ATP7A, and ATP7B in hepatocytes pumps copper ions into the bile (16) (Figure 1).

2.2 Copper deficiency and copper overload

Copper metabolism is meticulously controlled in living organisms to maintain the level of copper in a reasonable range. Defects in molecules involved in copper metabolism will resultin disturbed copper homeostasis and related diseases. WD and MD are two typical copper disorders resulting from dysregulation of copper metabolism (28).

MD is a copper deficiency disease caused by mutations in *ATP7A* (28). The main function of ATP7A is to transport copper from enterocytes to the blood, where it plays a vital role in intestinal absorption of copper and renal copper reabsorption (29). Defective ATP7A impedes intestinal copper absorption, ultimately leading to severe systemic copper deficiency, as well as deficiency of cuproenzymes in tissues, such as brain. The symptoms exhibited by MD patients include neuropathy, hypopigmentation, seizures, and hypothermia (30, 31). In addition, copper deficiency can lead to impaired energy levels, increased oxidative damage, and changes in immune cell structure and function in living organisms (32).Studies have suggested that copper deficiency may result in a higher frequency of infections as well as a higher risk of cardiovascular disease (33, 34).

WD is a copper overload disease caused by mutations in *ATP7B* (28). The main functions of ATP7B is to transport copper to the trans Golgi to facilitate assembly and secretion of cuproenzymes (29). In addition to hepatocytes, ATP7B also acts as a copper ion exporter, excreting it into bile. Because of gene mutations, ATP7B dysfunction leads to copper ion accumulation in the liver. When the capacity of the liver for storage is exceeded, copper spills into the circulation and subsequently enters and deposits into other tissues (*e.g.* eye and brain), causing oxidative stress that damages the tissues (28). The typical pathological features of WD are neurological abnormalities and acute liver failure (35, 36).

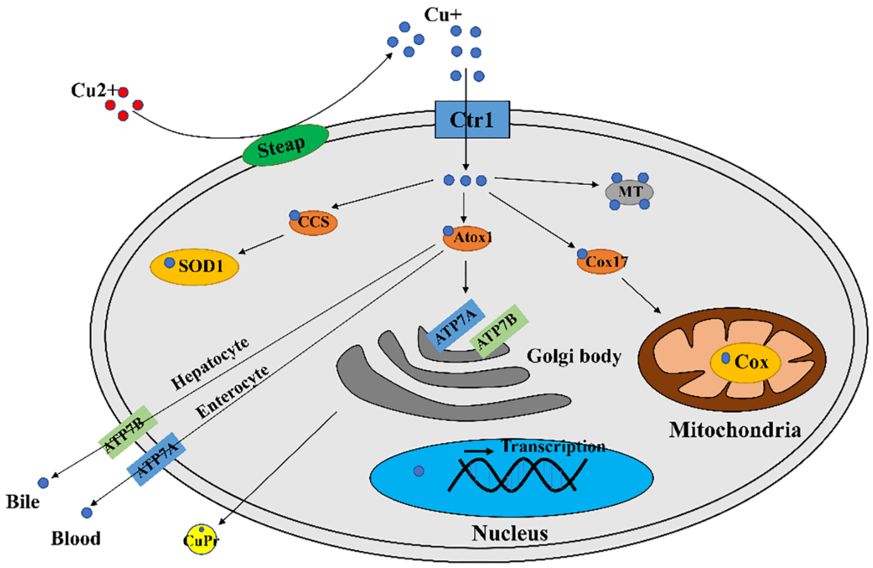

FIGURE 1
A diagram of cellular copper transport and metabolism. Extracellularly, copper exists as Cu^{2+}. The cellular reductases protein family Steap proteins (mainly Steap 2/3/4) reduce Cu^{2+} to Cu^{+}, which is transported into the cell *via* Ctr1, and a fraction of Cu^{+} is targeted to cytosolic SOD1 by the copper chaperone CCS to scavenge free radicals. A fraction of Cu^{+} is delivered by the copper chaperone Cox17 to the mitochondrial Cox to generate ATP. A portion of Cu^{+} is delivered to ATP7A/B of the trans Golgi network by the copper chaperone Atox1, which promotes cuproproteins (CuPrs) assembly and secretion. The remaining excess Cu^{+} is sequestered by metallothionein (MT). There are copper sensors in the nucleus that respond to changes in copper concentration through regulating *MT1* and *MT2* gene transcriptions. In enterocytes, ATP7A migrates to the plasma membrane to pump Cu^{+} into the blood. In hepatocytes, ATP7B pumps Cu^{+} into the bile.

2.3 Cancer and copper metabolism

Cancer has long been a research hotspot in the life sciences as well as in medicine. The incidence and mortality rates of cancer have been rising rapidly over the past few decades. It has now become the disease responsible for the largest number of deaths in the population worldwide (37). Among these, lung cancer is the most common and associated with the highest mortality in the population. The second highest incidence was for female breast cancer, followed by prostate and colorectal cancer. The top four cancers in order of mortality were lung, colorectal, stomach and liver cancer (37). Copper ion metabolism is also involved in the progression of these cancers (38).

In fact, copper in the human body has a great association with cancer, and there are a large number of medical studies showing that the serum copper levels in cancer patients, as well as in tumor tissues, can be higher or lower (mostly high) compared with normal individuals (Tables 1, 2). When tumor is removed, serum copper return to comparable levels with healthy individuals (13). In several serum medical detections of breast cancer patients, it was found that copper levels were significantly elevated in the serum of breast cancer patients compared with the healthy population (51). Similarly, elevated levels of copper have been reported in the serum of patients with oral cancer (47), gallbladder cancer (46), liver cancer (49), pancreatic cancer (57), and prostate cancer (61). Serum copper levels were found to be decreased in the serum of patients with certain cancers, such as colorectal cancer (56) and endometrial cancer (68). In colorectal and breast cancer, increased serum copper levels correlated with cancer staging and progression (69). And serum elevated copper levels are also associated with hematological malignancies either in relapse or in disease progression (70). Because of the variation of serum copper levels in cancer, it may be used as an indicator to diagnose certain tumors. The Cu/Zn ratio has been widely recognized as an indicator for the auxiliary diagnosis of tumors, and we summarized most up-to-date evidence of Cu/Zn ratio in the diagnosis of cancers (71, 72).

An increasing number of existing studies have demonstrated that copper is critical for the development of cancer not only as a component to maintain cell function, but also as a central hub in cell signaling pathways involving cell proliferation, angiogenesis, and metastasis (73). Cu^{+} is redox active and is able to promote the production of ROS and thereby activate tumor signaling, leading to tumor proliferation (69). In part, studies of the relationship between co-binding proteins (or chaperones) and cell proliferation identified that Atox1, a copper dependent transcription factor, promoted the expression of genes encoding cell replication (74). In recent studies, copper has also been found to have a specific role in the mitotic signaling pathway of tumorigenesis. Studies using drosophila and mouse models found that copper uptake *via* Ctr1 activates the mitogen activated protease kinase (MAPK) (75). Among molecules of this pathway, MEK1 is a copper binding protein that, when bound to copper ions, is able to push the MEK1-ERK interaction to promote the phosphorylation of ERK1 and ERK2, ultimately leading to carcinogenesis and promoting tumor growth (76, 77).

Copper is able to induce a number of proangiogenic responses (78), and increases proangiogenic gene expression by stabilizing nuclear hypoxia inducible factor-1 (HIF-1) (79). Copper also activates some angiogenic factors such as basic fibroblast growth

TABLE 1 Copper level variation in cancer tissues among different cancers.

Cancer types	Copper levels	Mechanism	References
Breast cancer	Elevated	Cu as an effective factor of angiogenesis	(39, 40)
Colorectal cancer	Elevated	Excess Cu damages DNA directly or through ROS.	(41)
Esophageal cancer	Elevated	Not mentioned	(42)
Ovarian cancer	Elevated	Alteration of the relationship between trace elements and decreased catabolism; Increased tumor synthesis of neurofibromin	(43)
Gastric cancer	Elevated	Alteration of the relationship between trace elements and decreased catabolism; Increased tumor synthesis of neurofibromin;High concentrations of Cu damage DNA through toxic hydroxyl radicals	(44, 45)
Gallbladder cancer	Elevated	Copper may be involved in the initial biological insult	(46)

factor (bFGF), tumor necrosis factor alpha (TNF-α), IL-1, IL-6 and IL-8 (80). In addition, copper stimulates the proliferation and metastasis of vascular endothelial cells (81). It directly binds to the angiogenic growth factor angiopoietin, enhancing its affinity for endothelial cells (82).

Copper is implicated in epithelial to mesenchymal transition (EMT), which is necessary for cancer metastasis (83). Increasing studies have shown that copper enhances the invasive and metastatic abilities of cancer cells through the activation of metabolic and proliferative enzymes (84, 85). For example, copper

TABLE 2 Copper level variation in the serum of different cancers.

Cancer types	Copper levels	Mechanism	References
Oral cancer	Elevated	Increase of oxidation process; Changes of ceruloplasmin activity	(47, 48)
Gallbladder cancer	Elevated	Malignant cell necrosis leads to copper release into the serum	(46)
Liver cancer	Elevated	Inflammatory processes activate Ceruloplasmin; Hepatocytes are damaged to release copper	(49, 50)
Breast cancer	Elevated	Cu is a cell growth promoting factor for rapid tumor cell growth; Necrosis that arises in tumor tissue occurs through the release of copper into the circulation; Copper causes mutations by damaging DNA through the generation of reactive oxygen species	(51–54)
Esophageal cancer	Elevated	Not mentioned	(55)
Colorectal cancer	Decreased	Unclear	(56)
Pancreatic cancer	Elevated	Not mentioned	(57)
Bladder cancer	Elevated	Copper accumulation has potential toxic effects; Copper is required for angiogenesis and tumor growth factor	(58, 59)
Renal cancer	Elevated	Not mentioned	(60)
Prostatic cancer	Elevated	Copper binds metallothionein with higher affinity, substituting zinc for metallothionein binding	(61)
Thyroid cancer	Elevated	High concentrations of Cu can damage DNA through toxic hydroxyl radicals; Copper as a cofactor in angiogenesis	(45, 62, 63)
Cervical carcinoma	Elevated	Copper damages DNA by generating reactive oxygen species; Copper as a tumor angiogenesis factor	(64, 65)
Lung cancer	Elevated	Ceruloplasmin may be re-catalyzed on the surface of tumor cells or in the peripheral blood in patients with cancer, thereby inhibiting its catabolism	(66, 67)
Endometrial cancer	Decreased	Not mentioned	(68)

is indispensable for the activity of lysine oxidase (LOX) and lysine oxidase like (LOXL) proteins, which catalyze the cross-linking of collagen and elastin in the extracellular matrix (ECM), and create preconditions for tumor development and metastasis (86). It was found that a copper dependent redox protein named memo affected metastasis of breast cancer cells by increasing intracellular ROS levels (87). Recently, the copper chaperone Atox1 has also been shown to be essential in breast cancer cell migration (88, 89).

Copper is redox active and easily interconverts between Cu^+ and Cu^{2+}. Many important enzymes utilize this property of copper to exert their functions in redox reactions in living organisms (69). Because copper is capable of generating excess ROS, copper transporters and chaperones have evolved to regulate copper uptake, efflux, and distribution within cells (33). Dysregulation of copper metabolism may lead to oxidative stress, such as decreased SOD1 activity and increased superoxide anion in different animal models (90, 91). Copper deficiency may also increase oxidative stress in mitochondria by inhibiting cytochrome c oxidase activity (92). And the dysregulation of copper metabolism may cause cancer, as copper deficiency may have effects on the oxidative system (33). Copper is a cofactor of SOD1, and the main function of SOD is to scavenge free radicals to prevent cells from oxidative stress injury, especially playing a crucial role in scavenging ROS generated from mitochondria (93, 94). SOD protein has three isoenzymes in humans. In particular, Cu/Zn SOD (SOD1) is a SOD with a bimetallic enzymatic function, which requires copper to catalyze the reaction and zinc to increase catalytic efficiency and enzyme stability (95–98). Copper deficiency leads to reduced SOD1 activity, and reduced SOD1 activity contributes to carcinogenesis (99). Copper deficiency also alters the activity of other enzymes involved in oxidative stress as well as ROS scavengers (*e.g.* catalase, metallothionein) (33). Alterations in these proteins may cause deregulation of oxidative stress, overproduction of ROS as well as deregulation of oxidative stress in the body may impair DNA repair machinery which is also an important mechanism in cancer development (100).

Ceruloplasmin is involved in copper metabolism, which is the main carrier of copper in the human body, and about 90% of copper in plasma is found in ceruloplasmin. In addition, ceruloplasmin is a multi-copper oxidase that plays an important role in iron homeostasis (101). When Fe^{2+} exported from ferroportin, the sole iron exporter, ceruloplasmin promotes cellular iron export by oxidizing iron ion from Fe^{2+} to Fe^{3+} (102). Although ceruloplasmin synthesis and secretion are not affected by copper levels, copper deficiency may result in decreased ceruloplasmin stability and activity (103). Ceruloplasmin is also closely linked to cancer, and studies have indicated that significant ceruloplasmin gene expression occurs in many tumors and that the overall incidence of cancer is positively correlated with serum ceruloplasmin levels and may be able to serve as a prognostic marker in some cancers (104–107).

3 Copper and targeted therapy in cancer

Among current treatments for cancer, targeted therapy is considered to be highly promising because its intervention can be selectively performed on molecules and pathways involved in the growth and developmental progression of tumors (108). Considering copper as a nutrient for cancer growth, angiogenesis, and metastasis, it may be an attractive target in cancer therapy (109). Copper metal binding compounds have great potential in cancer therapy. When copper binding compounds are mentioned, copper chelators and copper ionophores come to mind.Currently, copper chelators and copper ionophores have great potential value in cancer targeted therapy.

Copper chelators are able to bind to copper and reduce its bioavailability, thereby inhibiting angiogenesis and hindering cancer growth and metastasis (110). So far, some copper chelation methods have been used in clinical trials and provided some new strategies for the treatment of cancer (111, 112). Copper chelators with anticancer activity are tetrathiomolybdate (TTM), D-penicillamine (D-Pen) and others. There are studies demonstrating TTM exerts significant efficacy in the treatment of squamous cell carcinoma (113), lung (114), breast (115) and prostate cancer (116). It is important to note, however, that copper chelators are simply anticancer and are not sufficient by themselves to kill malignant cells, therefore, it needs to be combined with other drugs to achieve a therapeutic effect that is promising for cancer (117).

Copper ionophore in contrast to copper chelators,is able to increase intracellular copper bioavailability. There are various modes of action of copper ionophores, such as DNA interaction, proteasome inhibition as well as ROS generation (69). Typical copper ionophores are chloroquinol and disulfiram (DSF), and they can release coordinately available copper in the intracellular reducing environment, increasing the bioavailability of copper inside cells (118). Chloroquinol and DSF are able to cause intracellular production of ROS and inhibit the activity of proteasomes in cancer cells, which enables apoptosis (119). Chloroquinol and disulfiram have also been shown to reduce tumor growth in models of prostate and breast cancer (120–122). Copper chelators are able to inhibit cuproptosis, whereas copper ionophores induce cuproptosis. Cuproptosis, already introduced in a previous text, is a copper dependent cytotoxicity with a unique mechanism leading to cell death (123). However, the field of copper metal binding compounds to treat cancer is still in an early stage of development, and although clinical trials have been conducted and are able to give some strategies to treat cancer, they still need to be explored further to overcome their disadvantages. The lack of selectivity for targeting cancer cells is one of the challenges in this field.

In addition, inhibiting the expression of copper transporters may provide some reference for cancer therapy. We searched through the gepia database and analyzed for survival curves between the expression levels of the copper ion transporter SLC31A1 and cancer patient survival. We found that the expression level of copper importer in cancer tissue may have a close relationship with patient survival. Analysis of the survival curves between the expression levels of SLC31A1 and cancer patient survival showed that lower SLC31A1 expression significantly increased overall survival compared with individuals with higher SLC31A1 expression in Adrenocortical carcinoma (ACC), Breast invasive carcinoma (BRCA), Brain Lower Grade Glioma (LGG), Mesothelioma (MESO), Skin Cutaneous Melanoma (SKCM) (Figure 2). The inverse association between SLC31A1 expression and patient survival suggests that excessive copper ion uptake may promote cancer progression and increase patient mortality. This correlation may provide a potential mechanism for developing novel cancer therapies through inhibition SLC31A1 expression or removal of large amounts of copper ions in tumor tissues.

4 Cuproptosis

Recently, a novel mode of cell death was discovered by Tsvetkov et al. (15). It is a copper-dependent, regulated, distinct from other known cell death regulatory mechanisms, and this copper-dependent manner of death has been termed "cuproptosis". Heavy metal overload such as iron will cause deleterious effect on cells. An example is ferroptosis, an iron-dependent form of cell death caused by unrestricted lipid peroxidation (124). Cuproptosis results from mitochondrial stress. Copper can directly bind to ester acylated components of the tricarboxylic acid cycle, with subsequent aggregation of copper bound lipidated mitochondrial enzymes and loss of iron sulfur protein clusters, finally leading to the occurrence of cuproptosis (15).

The exact regulatory mechanism of copper induced cell death still needs further elucidation, although various pathways have been proposed, including induction of apoptosis, induction of reactive oxygen species, inhibition of the ubiquitin proteasome system. Currently in the study of Tsvetkov et al. (15), it was demonstrated that the mechanism of cuproptosis involves a copper ionophore named "elesclomol", which can bind Cu^{2+} in the extracellular environment and transport Cu^{2+} into the cells. Intracellularly, several critical genes are involved in this process. *FDX1* gene encodes a reductase ferredoxin 1 reducing Cu^{2+} to Cu^{+}. *DLAT* gene encodes an enzyme called dihydrolipoyl transacetylase that is a part of pyruvate dehydrogenase involved in the tricarboxylic acid cycle and is a protein target for lipidation. FDX1 is a key regulator of cuproptosis and an upstream regulator of protein lipoylation. On the one hand, FDX1 promotes lipoylation of pyruvate dehydrogenase, and Cu^{2+} directly binds to lipoylated proteins (mainly DLAT), followed by aberrant oligomerization of DLAT, resulting in tricarboxylic acid cycle (TCA) inhibition, and on the other hand, FDX1 reduces Cu^{2+} to Cu^{+}, leading to inhibition

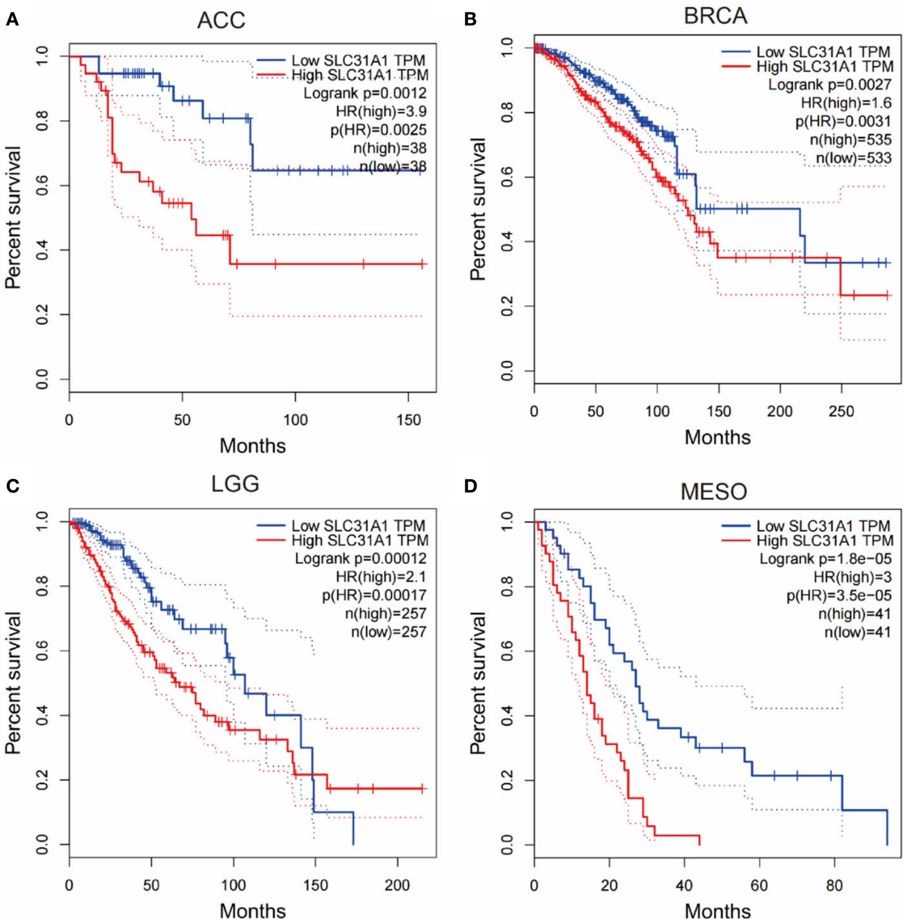

FIGURE 2
Survival curves for overall survival of high versus low expressing SLC31A1. **(A)** ACC, adrenocortical carcinoma; **(B)** BRCA, breast invasive carcinoma; **(C)** LGG, brain lower grade glioma; **(D)** MESO, mesothelioma. The overall survival rate of low expression of SLC31A1was significantly higher than that of high expression of SLC31A1. SLC31A1, solute carrier family 31 member 1 (copper ion transporter); HR, hazard rate. (http://gepia.cancer-pku.cn/index.html; Accessed 10 October 2022).

of iron sulfur protein clusters synthesis, disruption of iron sulfur protein clusters stability, and ultimately leads to proteotoxic stress and cell death (Figure 3).

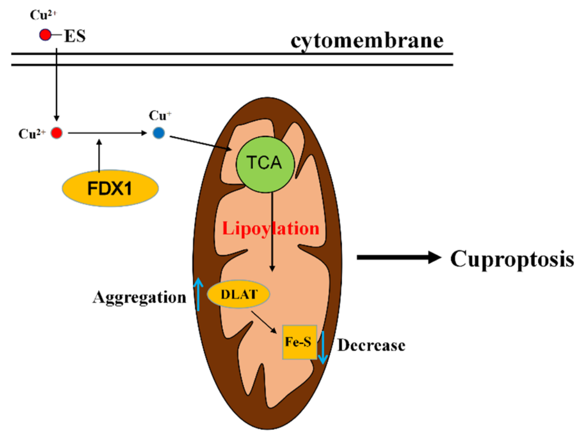

FIGURE 3
A diagram of the simple mechanism of cuproptosis. Elesclomol imports Cu^{2+} into the cell, and then reduced to Cu^{+} by FDX1. Cu^{+} binds to lipoylated components of the mitochondrial TCA cycle, promoting lipoylated protein aggregation followed by a decrease in iron-sulfur cluster proteins, thereby inducing proteotoxic stress, leading to cell death. ES, elesclomol; FDX1, ferredoxin 1; DLAT, dihydrolipoyl transacetylase; TCA, tricarboxylic acid cycle.

Cancer cells can evade the regulated cell death pathway, which is also one of the important hallmarks of cancer. Currently, one of the major challenges in cancer therapies is the escape of cancer cells from cell death pathways. The discovery of cuproptosis will provide a novel target to overcome the resistance of cancer cells for cell death. Existing evidence indicates that the Cu^{2+} carrier, elesclomol, can kill specific drug-resistant cancer cells (125). In recent studies on lower grade gliomas (LGG), arguing that copper death may serve as a potential therapeutic target for LGG (126). Researches have shown that cuproptosis related genes may play a great role in the diagnosis and prognosis of some types of cancer. In the research of pancreatic adenocarcinoma (PAAD) by Huang et al., the cuproptosis-related gene index (CRGI) was developed through machine algorithm, and its immunological characteristics were studied by exploring its impact on the expression of immune checkpoints, prospective immunotherapeutic response, etc. A new CRGI was identified and verified, and the cuproptosis-related gene was found to be a reliable diagnostic biomarker in PAAD (127). Sha et al., in a study of triple-negative breast cancer (TNBC), identified two clusters of cuproptosis related genes (CRG) with features of immune cell infiltration and demonstrated that the CRG signature may be used to assess tumor immune cell infiltration, clinical features, and prognostic status. Their study has shown the potential effect of CRG on the tumor microenvironment (TME), clinicopathological characteristics, and prognosis of TNBC which are potential tools for predicting patient outcomes (128). In the study of clear cell renal cell carcinoma (ccRCC), Wang et al. found that ccRCC samples had significantly lower FDX1 expression levels than normal tissue samples and lower FDX1 gene expression levels were strongly associated with higher cancer grades and more advanced tumor-node-metastasis stages. The results of multivariate and univariate analyses indicated that ccRCC patients with low FDX1 expression had shorter overall survival (OS) than those with high FDX1 expression. The study illustrates that in ccRCC, reduced FDX1 expression is associated with disease progression, poor prognosis and dysregulated immune cell infiltration which illustrates that the cuproptosis related gene may serve as a potential prognostic predictor for ccRCC patients and may provide new insights into cancer treatment (129, 130). Zhu et al. performed a comprehensive analysis of cuproptosis related molecular patterns in 1274 colorectal cancer specimens based on 16 cuproptosis regulators and revealed a novel cuproptosis related molecular pattern associated with TME phenotypes, and the formation of a cuproptosis score will further enhance the understanding of TME characteristics and instruct a more personalized immunotherapy schedule in colorectal cancer (131). Lv et al. explored the association of cuproptosis related genes with skin cutaneous melanoma (SKCM) prognosis by accessing and analyzing a public database, and found that 11 out 12 genes were upregulated in melanoma tissues and three genes (*LIPT1, PDHA1, and SLC31A1*) were of predictive value for melanoma prognosis. Further exploration found that *LIPT1* expression was increased in melanoma biopsies and was an independent favorable prognostic indicator for melanoma patients (132). Zhang et al. integrated a set of bioinformatics tools to analyze the expression and prognostic significance of FDX1, a key regulator of cuproptosis. The cuproptosis related risk score (CRRS) was derived by correlation analysis. The metabolic features, mutation signatures, and immune profile of CRRS-classified hepatocellular carcinoma (HCC) patients were investigated, and the role of CRRS in treatment guidance was analyzed. FDX1 was found to be significantly downregulated in HCC and its high expression was associated with longer survival time. HCC patients in the high CRRS group had significantly worse OS and enriched in tumor related pathways. Mutational analysis revealed that several tumor suppressors such as tumor protein P53 (TP53) and Breast cancer susceptibility gene 1 (BRCA1) -associated protein 1 (BAP1) were mutated at a higher frequency in high CRRS HCC patients, illustrating that cuproptosis related signatures are helpful in predicting prognosis and guiding the treatment of HCC patients (133). There are also scientists building a liver cancer prognosis model based on cuproptosis related mRNAs and lncRNAs, which can effectively predict the potential survival of liver cancer patients as well as evaluate the infiltration of immune cells, tumor mutation burden, and sensitivity to antitumor drugs in liver cancer (134). Li et al. systematically evaluated cuproptosis patterns in bladder cancer (BLCA) patients based on 46 cuproptosis related genes and correlated these cuproptosis patterns with TME phenotypes and immunotherapy effects. For the evaluation of individual patients, a cuproptosis risk score (CRS) for prognosis and a cuproptosis signature for precise TME phenotypes and immunotherapy efficacy prediction were constructed. Finally, it was demonstrated that CRS and cuproptosis signature have potential roles in predicting prognosis and immunotherapy efficacy in BLCA (135). A pan-cancer analysis revealed that transcription and protein expression of FDX1 was significantly reduced in most cancer types, and furthermore, FDX1 expression levels were closely correlated with immune cell infiltration, immune checkpoint genes, and immune regulatory genes to some extent. Due to its important role in tumorigenesis and tumor immunity, FDX1 can serve as a potential therapeutic target and prognostic marker in various malignancies (136–138). Altogether, putting the discovery of cuproptosis may provide a new strategy for cancer prognosis as well as treatment.

5 Conclusion and perspective

Copper plays an irreplaceable role as a micronutrient in the human body, and both deficiency or overload of copper in the body can negatively affect the human body, therefore, the mechanism of copper metabolism in cells keeps copper at a stable level to achieve copper homeostasis. Copper metabolism is also closely associated with cancer development, and copper is able to affect cancer cell proliferation and metastasis. Intracellular copper has a great connection with cancer, therefore, targeting copper in cancer therapy may play a great role. Currently, using copper complexes for cancer treatment, copper chelators with copper ionophores are two good choices, but the efficacy of copper chelators alone is not significant, and copper ionophores are still in the development stage, which also lack selectivity for targeting cancer cells. Therefore, improving selectivity against cancer cells is a worthy goal of investigation in the future. In a recent study on cell death, a novel concept cuproptosis, which is a copper dependent cell death induced by copper, was proposed, and the exact regulatory mechanism of this novel regulated cell death still needs to be continued to be explored. The proposal of cuproptosis presents a new avenue for the treatment of cancer.

It has a link between copper metabolism and cuproptosis. The dysregulation of copper metabolism in the body, such as copper overload may lead to cuproptosis. In addition, cuproptosis also offer a novel strategy for targeted cancer therapy. Copper metabolism and cuproptosis is worthy of further exploration and application to conquer cancer in clinic.

Author contributions

Conceptualization, JL, YL and JW; investigation, ZW, DJ and SZ; writing—original draft preparation, ZW, DJ and YJ; writing—review and editing, PA, JL, YL and JW; Visualization, ZW, ND and JL; supervision, JL, YL and JW; project administration, YL and JW; funding acquisition, YL and JL. All authors have read and agreed to the published version of the manuscript.

Funding

This work was supported by the Beijing Advanced Innovation Center for Food Nutrition and Human Health, the National Natural Science Foundation of China (31970717, 82170429), the Chinese Universities Scientific Fund (2020TC015), and the Beijing Municipal Natural Science Foundation (7222111).

Conflict of interest

The authors declare that the research was conducted in the absence of any commercial or financial relationships that could be construed as a potential conflict of interest.

Publisher's note

References

1. Tsukihara T, Aoyama H, Yamashita E, Tomizaki T, Yamaguchi H, Shinzawa-Itoh K, et al. Structures of metal sites of oxidized bovine heart cytochrome c oxidase at 2.8 a. *Science* (1995) 269(5227):1069–74. doi: 10.1126/science.7652554

2. Clement AM, Nguyen MD, Roberts EA, Garcia ML, Boillée S, Rule M, et al. Wild-type nonneuronal cells extend survival of SOD1 mutant motor neurons in ALS mice. *Science* (2003) 302(5642):113–7. doi: 10.1126/science.1086071

3. De Freitas JM, Liba A, Meneghini R, Valentine JS, Gralla EB. Yeast lacking Cu-zn superoxide dismutase show altered iron homeostasis. role of oxidative stress in iron metabolism. *J Biol Chem* (2000) 275(16):11645–9. doi: 10.1074/jbc.275.16.11645

4. Paynter DI, Moir RJ, Underwood EJ. Changes in activity of the Cu-zn superoxide dismutase enzyme in tissues of the rat with changes in dietary copper. *J Nutr* (1979) 109 (9):1570–6. doi: 10.1093/jn/109.9.1570

5. Staveley BE, Phillips JP, Hilliker AJ. Phenotypic consequences of copper-zinc superoxide dismutase overexpression in drosophila melanogaster. *Genome* (1990) 33 (6):867–72. doi: 10.1139/g90-130

6. Chan WY, Rennert OM. The role of copper in iron metabolism. *Ann Clin Lab Sci* (1980) 10(4):338–44.

7. Siegel RC. Lysyl oxidase. *Int Rev Connect Tissue Res* (1979) 8:73–118. doi: 10.1016/B978-0-12-363708-6.50009-6

8. Gerbasi V, Lutsenko S, Lewis EJ. A mutation in the ATP7B copper transporter causes reduced dopamine beta-hydroxylase and norepinephrine in mouse adrenal. *Neurochem Res* (2003) 28(6):867–73. doi: 10.1023/A:1023219308890

9. De Freitas J, Wintz H, Kim JH, Poynton H, Fox T, Vulpe C. Yeast, a model organism for iron and copper metabolism studies. *Biometals* (2003) 16(1):185–97. doi: 10.1023/A:1020771000746

10. Aggarwal A, Bhatt M. Wilson Disease. *Curr Opin Neurol* (2020) 33(4):534–42. doi: 10.1097/WCO.0000000000000837

11. Bertini I, Rosato A. Menkes disease. *Cell Mol Life Sci* (2008) 65(1):89–91. doi: 10.1007/s00018-007-7439-6

12. Finney L, Mandava S, Ursos L, Zhang W, Rodi D, Vogt S, et al. X-Ray fluorescence microscopy reveals large-scale relocalization and extracellular translocation of cellular copper during angiogenesis. *Proc Natl Acad Sci USA* (2007) 104(7):2247–52. doi: 10.1073/pnas.0607238104

13. Gupte A, Mumper RJ. Elevated copper and oxidative stress in cancer cells as a target for cancer treatment. *Cancer Treat Rev* (2009) 35(1):32–46. doi: 10.1016/j.ctrv.2008.07.004

14. Ishida S, Andreux P, Poitry-Yamate C, Auwerx J, Hanahan D. Bioavailable copper modulates oxidative phosphorylation and growth of tumors. *Proc Natl Acad Sci USA* (2013) 110(48):19507–12. doi: 10.1073/pnas.1318431110

15. Tsvetkov P, Coy S, Petrova B, Dreishpoon M, Verma A, Abdusamad M, et al. Copper induces cell death by targeting lipoylated TCA cycle proteins. *Science* (2022) 375(6586):1254–61. doi: 10.1126/science.abf0529

16. Chen J, Jiang Y, Shi H, Peng Y, Fan X, Li C. The molecular mechanisms of copper metabolism and its roles in human diseases. *Pflugers Arch* (2020) 472(10):1415–29. doi: 10.1007/s00424-020-02412-2

17. Kim BE, Nevitt T, Thiele DJ. Mechanisms for copper acquisition, distribution and regulation. *Nat Chem Biol* (2008) 4(3):176–85. doi: 10.1038/nchembio.72

18. Eisses JF, Chi Y, Kaplan JH. Stable plasma membrane levels of hCTR1 mediate cellular copper uptake. *J Biol Chem* (2005) 280(10):9635–9. doi: 10.1074/jbc.M500116200

19. Lee J, Peña MM, Nose Y, Thiele DJ. Biochemical characterization of the human copper transporter Ctr1. *J Biol Chem* (2002) 277(6):4380–7. doi: 10.1074/jbc.M104728200

20. Shawki A, Anthony SR, Nose Y, Engevik MA, EJ. Intestinal DMT1 is critical for iron absorption in the mouse but is not required for the absorption of copper or manganese. *Am J Physiol Gastrointest Liver Physiol* (2015) 309(8):G635–47. doi: 10.1152/ajpgi.00160.2015

21. Ohgami RS, Campagna DR, McDonald A, Fleming MD. The steap proteins are metalloreductases. *Blood* (2006) 108(4):1388–94. doi: 10.1182/blood-2006-02-003681

22. Lalioti V, Muruais G, Tsuchiya Y, Pulido D, Sandoval IV. Molecular mechanisms of copper homeostasis. *Front Biosci (Landmark Ed)* (2009) 14 (13):4878–903. doi: 10.2741/3575

23. Robinson NJ, Winge DR. Copper metallochaperones. *Annu Rev Biochem* (2010) 79:537–62. doi: 10.1146/annurev-biochem-030409-143539

24. Wong PC, Waggoner D, Subramaniam JR, Tessarollo L, Bartnikas TB, Culotta VC, et al. Copper chaperone for superoxide dismutase is essential to activate mammalian Cu/Zn superoxide dismutase. *Proc Natl Acad Sci USA* (2000) 97 (6):2886–91. doi: 10.1073/pnas.040461197

25. Maxfield AB, Heaton DN, Winge DR. Cox17 is functional when tethered to the mitochondrial inner membrane. *J Biol Chem* (2004) 279(7):5072–80. doi: 10.1074/jbc.M311772200

26. Leary SC, Cobine PA, Kaufman BA, Guercin GH, Mattman A, Palaty J, et al. The human cytochrome c oxidase assembly factors SCO1 and SCO2 have regulatory roles in the maintenance of cellular copper homeostasis. *Cell Metab* (2007) 5(1):9–20. doi: 10.1016/j.cmet.2006.12.001

27. Hamza I, Faisst A, Prohaska J, Chen J, Gruss P, Gitlin JD, et al. The metallochaperone Atox1 plays a critical role in perinatal copper homeostasis. *Proc Natl Acad Sci USA* (2001) 98(12):6848–52. doi: 10.1073/pnas.111058498

28. Wang X, Garrick MD, Collins JF. Animal models of normal and disturbed iron and copper metabolism. *J Nutr* (2019) 149(12):2085–100. doi: 10.1093/jn/nxz172

29. Lutsenko S, Barnes NL, Bartee MY, Dmitriev OY. Function and regulation of human copper-transporting ATPases. *Physiol Rev* (2007) 87(3):1011–46. doi: 10.1152/physrev.00004.2006

30. Kaler SG. ATP7A-related copper transport diseases-emerging concepts and future trends. *Nat Rev Neurol* (2011) 7(1):15–29. doi: 10.1038/nrneurol.2010.180

31. Menkes JH. Kinky hair disease. *Pediatrics* (1972) 50(2):181–3. doi: 10.1542/peds.50.2.181

32. Keen CL, Hanna LA, Lanoue L, Uriu-Adams JY, Rucker RB, Clegg MS. Developmental consequences of trace mineral deficiencies in rodents: Acute and long-term effects. *J Nutr* (2003) 133(5 Suppl 1):1477s–80s. doi: 10.1093/jn/133.5.1477S

33. Uriu-Adams JY, Keen CL. Copper, oxidative stress, and human health. *Mol Aspects Med* (2005) 26(4-5):268–98. doi: 10.1016/j.mam.2005.07.015

34. Bonham M, O'Connor JM, Hannigan BM, Strain JJ. The immune system as a physiological indicator of marginal copper status? *Br J Nutr* (2002) 87(5):393–403. doi: 10.1079/BJN2002558

35. Członkowska A, Litwin T, Dusek P, Ferenci P, Lutsenko S, Medici V, et al. Wilson Disease. *Nat Rev Dis Primers* (2018) 4(1):21. doi: 10.1038/s41572-018-0018-3

36. Compston A. Progressive lenticular degeneration: A familial nervous disease associated with cirrhosis of the liver, by s. a. kinnier Wilson, (From the national hospital, and the laboratory of the national hospital, queen square, London) brain 1912: 34; 295-509. *Brain* (2009) 132(Pt 8):1997–2001. doi: 10.1093/brain/awp193

37. Bray F, Ferlay J, Soerjomataram I, Siegel RL, Torre LA, Jemal A, et al. Global cancer statistics 2018: GLOBOCAN estimates of incidence and mortality worldwide for 36 cancers in 185 countries. *CA Cancer J Clin* (2018) 68(6):394–424. doi: 10.3322/caac.21492

38. Shanbhag VC, Gudekar N, Jasmer K, Papageorgiou C, Singh K, Petris MJ, et al. Copper metabolism as a unique vulnerability in cancer. *Biochim Biophys Acta Mol Cell Res* (2021) 1868(2):118893. doi: 10.1016/j.bbamcr.2020.118893

39. Mansouri B, Ramezani Z, Yousefinejad V, Nakhaee S, Azadi N, Khaledi P, et al. Association between trace elements in cancerous and non-cancerous tissues with the risk of breast cancers in western Iran. *Environ Sci pollut Res Int* (2022) 29(8):11675–84. doi: 10.1007/s11356-021-16549-9

40. Farquharson MJ, Al-Ebraheem A, Falkenberg G, Leek R, Harris AL, Bradley DA, et al. The distribution of trace elements Ca, fe, Cu and zn and the determination of copper oxidation state in breast tumour tissue using muSRXRF and muXANES. *Phys Med Biol* (2008) 53(11):3023–37. doi: 10.1088/0031-9155/53/11/018

41. Sohrabi M, Gholami A, Azar MH, Yaghoobi M, Shahi MM, Shirmardi S, et al. Trace element and heavy metal levels in colorectal cancer: Comparison between cancerous and non-cancerous tissues. *Biol Trace Elem Res* (2018) 183(1):1–8. doi: 10.1007/s12011-017-1099-7

42. Xie B, Lin J, Sui K, Huang Z, Chen Z, Hang W, et al. Differential diagnosis of multielements in cancerous and non-cancerous esophageal tissues. *Talanta* (2019) 196:585–91. doi: 10.1016/j.talanta.2018.12.061

43. Yaman M, Kaya G, Simsek M. Comparison of trace element concentrations in cancerous and noncancerous human endometrial and ovary tissues. *Int J Gynecol Cancer* (2007) 17(1):220–8. doi: 10.1111/j.1525-1438.2006.00742.x

44. Yaman M, Kaya G, Yekeler H. Distribution of trace metal concentrations in paired cancerous and non-cancerous human stomach tissues. *World J Gastroenterol* (2007) 13(4):612–8. doi: 10.3748/wjg.v13.i4.612

45. Theophanides T, Anastassopoulou J. Copper and carcinogenesis. *Crit Rev Oncol Hematol* (2002) 42(1):57–64. doi: 10.1016/S1040-8428(02)00007-0

46. Basu S, Singh MK, Singh TB, Bhartiya SK, Singh SP, Shukla VK, et al. Heavy and trace metals in carcinoma of the gallbladder. *World J Surg* (2013) 37(11):2641–6. doi: 10.1007/s00268-013-2164-9

47. Baharvand M, Manifar S, Akkafan R, Mortazavi H, Sabour S. Serum levels of ferritin, copper, and zinc in patients with oral cancer. *BioMed J* (2014) 37(5):331–6. doi: 10.4103/2319-4170.132888

48. Jayadeep A, Pillai Raveendran K, Kannan S, Nalinakumari KR, Mathew B, Nair Krishnan M, et al. Serum levels of copper, zinc, iron and ceruplasmin in oral leukoplakia and squamous cell carcinoma. *J Exp Clin Cancer Res* (1997) 16(3):295–300.

49. Fang AP, Chen PY, Wang XY, Liu ZY, Zhang DM, Luo Y, et al. Serum copper and zinc levels at diagnosis and hepatocellular carcinoma survival in the guangdong liver cancer cohort. *Int J Cancer* (2019) 144(11):2823–32. doi: 10.1002/ijc.31991

50. Deshmukh VK, Raman PH, Dhuley JN, Naik SR. Role of ceruloplasmin in inflammation: Increased serum ceruloplasmin levels during inflammatory conditions and its possible relationship with anti-inflammatory agents. *Pharmacol Res Commun* (1985) 17(7):633–42. doi: 10.1016/0031-6989(85)90070-0

51. Pavithra V, Sathisha TG, Kasturi K, Mallika DS, Amos SJ, Ragunatha S, et al. Serum levels of metal ions in female patients with breast cancer. *J Clin Diagn Res* (2015) 9(1):BC25–c27. doi: 10.7860/JCDR/2015/11627.5476

52. Feng Y, Zeng JW, Ma Q, Zhang S, Tang J, Feng JF. Serum copper and zinc levels in breast cancer: A meta-analysis. *J Trace Elem Med Biol* (2020) 62:126629. doi: 10.1016/j.jtemb.2020.126629

53. Kuo HW, Chen SF, Wu CC, Chen DR, Lee JH. Serum and tissue trace elements in patients with breast cancer in Taiwan. *Biol Trace Elem Res* (2002) 89(1):1–11. doi: 10.1385/BTER:89:1:1

54. Saleh F, Behbehani A, Asfar S, Khan I, Ibrahim G. Abnormal blood levels of trace elements and metals, DNA damage, and breast cancer in the state of Kuwait. *Biol Trace Elem Res* (2011) 141(1-3):96–109. doi: 10.1007/s12011-010-8724-z

55. Goyal MM, Kalwar AK, Vyas RK, Bhati A. A study of serum zinc, selenium and copper levels in carcinoma of esophagus patients. *Indian J Clin Biochem* (2006) 21 (1):208–10. doi: 10.1007/BF02913100

56. Khoshdel Z, Naghibalhossaini F, Abdollahi K, Shojaei S, Moradi M, Malekzadeh M. Serum copper and zinc levels among Iranian colorectal cancer patients. *Biol Trace Elem Res* (2016) 170(2):294–9. doi: 10.1007/s12011-015-0483-4

57. Lener MR, Scott RJ, Wiechowska-Kozłowska A, Serrano-Fernández P, Baszuk P, Jaworska-Bieniek K, et al. Serum concentrations of selenium and copper in patients diagnosed with pancreatic cancer. *Cancer Res Treat* (2016) 48(3):1056–64. doi: 10.4143/crt.2015.282

58. Mao S, Huang S. Zinc and copper levels in bladder cancer: A systematic review and meta-analysis. *Biol Trace Elem Res* (2013) 153(1-3):5–10. doi: 10.1007/s12011-013-9682-z

59. Linder MC, Hazegh-Azam M. Copper biochemistry and molecular biology. *Am J Clin Nutr* (1996) 63(5):797s–811s. doi: 10.1093/ajcn/63.5.797

60. Panaiyadiyan S, Quadri JA, Nayak B, Pandit S, Singh P, Seth A, et al. Association of heavy metals and trace elements in renal cell carcinoma: A case-controlled study. *Urol Oncol* (2022) 40(3):111.e11–111.e18. doi: 10.1016/j.urolonc.2021.11.017

61. Saleh SAK, Adly HM, Abdelkhaliq AA, Nassir AM. Serum levels of selenium, zinc, copper, manganese, and iron in prostate cancer patients. *Curr Urol* (2020) 14 (1):44–9. doi: 10.1159/000499261

62. Shen F, Cai WS, Li JL, Feng Z, Cao J, Xu B. The association between serum levels of selenium, copper, and magnesium with thyroid cancer: a meta-analysis. *Biol Trace Elem Res* (2015) 167(2):225–35. doi: 10.1007/s12011-015-0304-9

63. Brem S. Angiogenesis and cancer control: From concept to therapeutic trial. *Cancer Control* (1999) 6(5):436–58. doi: 10.1177/107327489900600502

64. Zhang M, Shi M, Zhao Y. Association between serum copper levels and cervical cancer risk: A meta-analysis. *Biosci Rep* (2018) 38(4):BSR20180161. doi: 10.1042/BSR20180161

65. Bobrowska B, Skrajnowska D, Tokarz A. Effect of Cu supplementation on genomic instability in chemically-induced mammary carcinogenesis in the rat. *J BioMed Sci* (2011) 18(1):95. doi: 10.1186/1423-0127-18-95

66. Zhang X, Yang Q. Association between serum copper levels and lung cancer risk: A meta-analysis. *J Int Med Res* (2018) 46(12):4863–73. doi: 10.1177/0300060518798507

67. Fisher GL, Shifrine M. Hypothesis for the mechanism of elevated serum copper in cancer patients. *Oncology* (1978) 35(1):22–5. doi: 10.1159/000225249

68. Atakul T, Altinkaya SO, Abas BI, Yenisey C. Serum copper and zinc levels in patients with endometrial cancer. *Biol Trace Elem Res* (2020) 195(1):46–54. doi: 10.1007/s12011-019-01844-x

69. Denoyer D, Masaldan S, Fontaine La S, Cater MA. Targeting copper in cancer therapy: 'Copper that cancer'. *Metallomics* (2015) 7(11):1459–76. doi: 10.1039/C5MT00149H

70. Kaiafa GD, Saouli Z, Diamantidis MD, Kontoninas Z, Voulgaridou V, Raptaki M, et al. Copper levels in patients with hematological malignancies. *Eur J Intern Med* (2012) 23(8):738–41. doi: 10.1016/j.ejim.2012.07.009

71. Kazi Tani LS, Gourlan AT, Dennouni-Medjati N, Telouk P, Dali-Sahi M, Harek Y, et al. Copper isotopes and copper to zinc ratio as possible biomarkers for thyroid cancer. *Front Med (Lausanne)* (2021) 8:698167. doi: 10.3389/fmed.2021.698167

72. Dragutinović VV, Tatic SB, Nikolic-Mandic S, Savin S, Cvejic D, Dunđerovic D, et al. Matrix metalloproteinase-9 and the Cu/Zn ratio as ancillary diagnostic tools in distinguishing between the classical and follicular variants of papillary thyroid carcinoma. *Biol Trace Elem Res* (2012) 149(1):29–33. doi: 10.1007/s12011-012-9404-y

73. Grubman A, White AR. Copper as a key regulator of cell signalling pathways. *Expert Rev Mol Med* (2014) 16:e11. doi: 10.1017/erm.2014.11

74. Itoh S, Kim HW, Nakagawa O, Ozumi K, Lessner SM, Aoki H, et al. Novel role of antioxidant-1 (Atox1) as a copper-dependent transcription factor involved in cell proliferation. *J Biol Chem* (2008) 283(14):9157–67. doi: 10.1074/jbc.M709463200

75. Turski ML, Brady DC, Kim HJ, Kim BE, Nose Y, Counter CM, et al. A novel role for copper in ras/mitogen-activated protein kinase signaling. *Mol Cell Biol* (2012) 32 (7):1284–95. doi: 10.1128/MCB.05722-11

76. Brady DC, Crowe MS, Turski ML, Hobbs GA, Yao X, Chaikuad A, et al. Copper is required for oncogenic BRAF signalling and tumorigenesis. *Nature* (2014) 509 (7501):492–6. doi: 10.1038/nature13180

77. Dankner M, Rose AAN, Rajkumar S, Siegel PM, Watson IR. Classifying BRAF alterations in cancer: new rational therapeutic strategies for actionable mutations. *Oncogene* (2018) 37(24):3183–99. doi: 10.1038/s41388-018-0171-x

78. Tisato F, Marzano C, Porchia M, Pellei M, Santini C, et al. Copper in diseases and treatments, and copper-based anticancer strategies. *Med Res Rev* (2010) 30(4):708–49. doi: 10.1002/med.20174

79. Xie H, Kang YJ. Role of copper in angiogenesis and its medicinal implications. *Curr Med Chem* (2009) 16(10):1304–14. doi: 10.2174/092986709787846622

80. Suska F, Esposito M, Gretzer C, Källtorp M, Tengvall P, Thomsen P. IL-1alpha, IL-1beta and TNF-alpha secretion during in vivo/ex vivo cellular interactions with titanium and copper. *Biomaterials* (2003) 24(3):461–8. doi: 10.1016/S0142-9612(02)00359-9

81. De Luca A, Barile A, Arciello M, Rossi L. Copper homeostasis as target of both consolidated and innovative strategies of anti-tumor therapy. *J Trace Elem Med Biol* (2019) 55:204–13. doi: 10.1016/j.jtemb.2019.06.008

82. Soncin F, Guitton JD, Cartwright T, Badet J. Interaction of human angiogenin with copper modulates angiogenin binding to endothelial cells. *Biochem Biophys Res Commun* (1997) 236(3):604–10. doi: 10.1006/bbrc.1997.7018

83. Dongre A, Weinberg RA. New insights into the mechanisms of epithelial-mesenchymal transition and implications for cancer. *Nat Rev Mol Cell Biol* (2019) 20 (2):69–84. doi: 10.1038/s41580-018-0080-4

84. Blockhuys S, Wittung-Stafshede P. Roles of copper-binding proteins in breast cancer. *Int J Mol Sci* (2017) 18(4):871. doi: 10.3390/ijms18040871

85. Shanbhag V, Jasmer-McDonald K, Zhu S, Martin AL, Gudekar N, Khan A, et al. ATP7A delivers copper to the lysyl oxidase family of enzymes and promotes tumorigenesis and metastasis. *Proc Natl Acad Sci USA* (2019) 116(14):6836–41. doi: 10.1073/pnas.1817473116

86. Farhat A, Ferns GA, Ashrafi K, Arjmand MH. Lysyl oxidase mechanisms to mediate gastrointestinal cancer progression. *Gastrointest Tumors* (2021) 8(1):33–40. doi: 10.1159/000511244

87. MacDonald G, Nalvarte I, Smirnova T, Vecchi M, Aceto N, Dolemeyer A, et al. Memo is a copper-dependent redox protein with an essential role in migration and metastasis. *Sci Signal* (2014) 7(329):ra56. doi: 10.1126/scisignal.2004870

88. Blockhuys S, Zhang X, Wittung-Stafshede P. Single-cell tracking demonstrates copper chaperone Atox1 to be required for breast cancer cell migration. *Proc Natl Acad Sci USA* (2020) 117(4):2014–9. doi: 10.1073/pnas.1910722117

89. Blockhuys S, Brady DC, Wittung-Stafshede P. Evaluation of copper chaperone ATOX1 as prognostic biomarker in breast cancer. *Breast Cancer* (2020) 27(3):505–9. doi: 10.1007/s12282-019-01044-4

90. Hawk SN, Lanoue L, Keen CL, Kwik-Uribe CL, Rucker RB, Uriu-Adams JY. Copper-deficient rat embryos are characterized by low superoxide dismutase activity and elevated superoxide anions. *Biol Reprod* (2003) 68(3):896–903. doi: 10.1095/biolreprod.102.009167

91. Lynch SM, Frei B, Morrow JD, Roberts LJ 2nd, Xu A, Jackson T, et al. Vascular superoxide dismutase deficiency impairs endothelial vasodilator function through direct inactivation of nitric oxide and increased lipid peroxidation. *Arterioscler Thromb Vasc Biol* (1997) 17(11):2975–81. doi: 10.1161/01.ATV.17.11.2975

92. Johnson WT, Thomas AC. Copper deprivation potentiates oxidative stress in HL-60 cell mitochondria. *Proc Soc Exp Biol Med* (1999) 221(2):147–52. doi: 10.3181/00379727-221-44397

93. Fridovich I. Superoxide radical: An endogenous toxicant. *Annu Rev Pharmacol Toxicol* (1983) 23:239–57. doi: 10.1146/annurev.pa.23.040183.001323

94. Cadenas E, Davies KJ. Mitochondrial free radical generation, oxidative stress, and aging. *Free Radic Biol Med* (2000) 29(3-4):222–30. doi: 10.1016/S0891-5849(00)00317-8

95. Banci L, Bertini I, Cabelli DE, Hallewell RA, Tung JW, Viezzoli MS, et al. A characterization of copper/zinc superoxide dismutase mutants at position 124. zinc-deficient proteins. *Eur J Biochem* (1991) 196(1):123–8. doi: 10.1111/j.1432-1033.1991.tb15794.x

96. Roberts BR, Tainer JA, Getzoff ED, Malencik DA, Anderson SR, Bomben VC, et al. Structural characterization of zinc-deficient human superoxide dismutase and implications for ALS. *J Mol Biol* (2007) 373(4):877–90. doi: 10.1016/j.jmb.2007.07.043

97. Potter SZ, Zhu H, Shaw BF, Rodriguez JA, Doucette PA, Sohn SH, et al. Binding of a single zinc ion to one subunit of copper-zinc superoxide dismutase apoprotein substantially influences the structure and stability of the entire homodimeric protein. *J Am Chem Soc* (2007) 129(15):4575–83. doi: 10.1021/ja066690+

98. Boyd SD, Ullrich MS, Skopp A, Winkler DD. Copper sources for Sod1 activation. *Antioxidants (Basel)* (2020) 9(6):500. doi: 10.3390/antiox9060500

99. Liaw KY, Lee PH, Wu FC, Tsai JS, Lin-Shiau SY. Zinc, copper, and superoxide dismutase in hepatocellular carcinoma. *Am J Gastroenterol* (1997) 92(12):2260–3.

100. Tang JY, Ou-Yang F, Hou MF, Huang HW, Wang HR, Li KT, et al. Oxidative stress-modulating drugs have preferential anticancer effects - involving the regulation of apoptosis, DNA damage, endoplasmic reticulum stress, autophagy, metabolism, and migration. *Semin Cancer Biol* (2019) 58:109–17. doi: 10.1016/j.semcancer.2018.08.010

101. Arredondo M, González M, Olivares M, Pizarro F, Araya M. Ceruloplasmin, an indicator of copper status. *Biol Trace Elem Res* (2008) 123(1-3):261–9. doi: 10.1007/s12011-008-8110-2

102. Drakesmith H, Nemeth E, Ganz T. Ironing out ferroportin. *Cell Metab* (2015) 22(5):777–87. doi: 10.1016/j.cmet.2015.09.006

103. Hellman NE, Gitlin JD. Ceruloplasmin metabolism and function. *Annu Rev Nutr* (2002) 22:439–58. doi: 10.1146/annurev.nutr.22.012502.114457

104. Arner E, Forrest AR, Ehrlund A, Mejhert N, Itoh M, Kawaji H, et al. Ceruloplasmin is a novel adipokine which is overexpressed in adipose tissue of obese subjects and in obesity-associated cancer cells. *PloS One* (2014) 9(3):e80274. doi: 10.1371/journal.pone.0080274

105. Knekt P, Aromaa A, Maatela J, Rissanen A, Hakama M, Aaran RK, et al. Serum ceruloplasmin and the risk of cancer in Finland. *Br J Cancer* (1992) 65(2):292–6. doi: 10.1038/bjc.1992.58

106. Zhang Y, Chen Z, Chen JG, Chen XF, Gu DH, Liu ZM, et al. Ceruloplasmin overexpression is associated with oncogenic pathways and poorer survival rates in clear-cell renal cell carcinoma. *FEBS Open Bio* (2021) 11(11):2988–3004. doi: 10.1002/2211-5463.13283

107. Han IW, Jang JY, Kwon W, Park T, Kim Y, Lee KB, et al. Ceruloplasmin as a prognostic marker in patients with bile duct cancer. *Oncotarget* (2017) 8(17):29028–37. doi: 10.18632/oncotarget.15995

108. Ciavarella S, Milano A, Dammacco F, Silvestris F. Targeted therapies in cancer. *BioDrugs* (2010) 24(2):77–88. doi: 10.2165/11530830-000000000-00000

109. Michniewicz F, Saletta F, Rouaen JRC, Hewavisenti RV, Mercatelli D, Cirillo G, et al. Copper: An intracellular achilles' heel allowing the targeting of epigenetics, kinase pathways, and cell metabolism in cancer therapeutics. *ChemMedChem* (2021) 16 (15):2315–29. doi: 10.1002/cmdc.202100172

110. Wadhwa S, Mumper RJ. D-penicillamine and other low molecular weight thiols: Review of anticancer effects and related mechanisms. *Cancer Lett* (2013) 337 (1):8–21. doi: 10.1016/j.canlet.2013.05.027

111. Lopez J, Ramchandani D, Vahdat L. Copper depletion as a therapeutic strategy in cancer. *Met Ions Life Sci* (2019) 19:19:/books/9783110527872/9783110527872-018/9783110527872-018.xml. doi: 10.1515/9783110527872-012

112. Baldari S, Di Rocco G, Toietta G. Current biomedical use of copper chelation therapy. *Int J Mol Sci* (2020) 21(3):1069. doi: 10.3390/ijms21031069

113. Cox C, Merajver SD, Yoo S, Dick RD, Brewer GJ, Lee JS, et al. Inhibition of the growth of squamous cell carcinoma by tetrathiomolybdate-induced copper suppression in a murine model. *Arch Otolaryngol Head Neck Surg* (2003) 129(7):781–5. doi: 10.1001/archotol.129.7.781

114. Khan MK, Miller MW, Taylor J, Gill NK, Dick RD, Golen Van K, et al. Radiotherapy and antiangiogenic TM in lung cancer. *Neoplasia* (2002) 4(2):164–70. doi: 10.1038/sj.neo.7900218

115. Pan Q, Bao LW, Kleer CG, Brewer GJ, Merajver SD. Antiangiogenic tetrathiomolybdate enhances the efficacy of doxorubicin against breast carcinoma. *Mol Cancer Ther* (2003) 2(7):617–22.

116. van Golen KL, Bao L, Brewer GJ, Pienta KJ, Kamradt JM, Livant DL, et al. Suppression of tumor recurrence and metastasis by a combination of the PHSCN sequence and the antiangiogenic compound tetrathiomolybdate in prostate carcinoma. *Neoplasia* (2002) 4(5):373–9. doi: 10.1038/sj.neo.7900258

117. Khan MK, Mamou F, Schipper MJ, May KS, Kwitny A, Warnat A, et al. Combination tetrathiomolybdate and radiation therapy in a mouse model of head and neck squamous cell carcinoma. *Arch Otolaryngol Head Neck Surg* (2006) 132(3):333–8. doi: 10.1001/archotol.132.3.333

118. Park KC, Fouani L, Jansson PJ, Wooi D, Sahni S, Lane DJ, et al. Copper and conquer: copper complexes of di-2-pyridylketone thiosemicarbazones as novel anti-cancer therapeutics. *Metallomics* (2016) 8(9):874–86. doi: 10.1039/C6MT00105J

119. Denoyer D, Clatworthy SAS, Cater MA. Copper complexes in cancer therapy. *Met Ions Life Sci* (2018) 18:/books/9783110470734/9783110470734-022/9783110470734-022.xml. doi: 10.1515/9783110470734-022

120. Cater MA, Haupt Y. Clioquinol induces cytoplasmic clearance of the X-linked inhibitor of apoptosis protein (XIAP): therapeutic indication for prostate cancer. *Biochem J* (2011) 436(2):481–91. doi: 10.1042/BJ20110123

121. Chen D, Cui QC, Yang H, Barrea RA, Sarkar FH, Sheng S, et al. Clioquinol, a therapeutic agent for alzheimer's disease, has proteasome-inhibitory, androgen receptor-suppressing, apoptosis-inducing, and antitumor activities in human prostate cancer cells and xenografts. *Cancer Res* (2007) 67(4):1636–44. doi: 10.1158/0008-5472.CAN-06-3546

122. Chen D, Cui QC, Yang H, Dou QP. Disulfiram, a clinically used anti-alcoholism drug and copper-binding agent, induces apoptotic cell death in breast cancer cultures and xenografts via inhibition of the proteasome activity. *Cancer Res* (2006) 66(21):10425–33. doi: 10.1158/0008-5472.CAN-06-2126

123. Duan WJ, He RR. Cuproptosis: Copper-induced regulated cell death. *Sci China Life Sci* (2022) 65(8):1680–2. doi: 10.1007/s11427-022-2106-6

124. Kazan K, Kalaipandian S. Ferroptosis: Yet another way to die. *Trends Plant Sci* (2019) 24(6):479–81. doi: 10.1016/j.tplants.2019.03.005

125. Tsvetkov P, Detappe A, Cai K, Keys HR, Brune Z, Ying W, et al. Mitochondrial metabolism promotes adaptation to proteotoxic stress. *Nat Chem Biol* (2019) 15 (7):681–9. doi: 10.1038/s41589-019-0291-9

126. Bao JH, Lu WC, Duan H, Ye YQ, Li JB, Liao WT, et al. Identification of a novel cuproptosis-related gene signature and integrative analyses in patients with lower-grade gliomas. *Front Immunol* (2022) 13:933973. doi: 10.3389/fimmu.2022.933973

127. Huang X, Zhou S, Tóth J, Hajdu A. Cuproptosis-related gene index: A predictor for pancreatic cancer prognosis, immunotherapy efficacy, and chemosensitivity. *Front Immunol* (2022) 13:978865. doi: 10.3389/fimmu.2022.978865

128. Sha S, Si L, Wu X, Chen Y, Xiong H, Xu Y, et al. Prognostic analysis of cuproptosis-related gene in triple-negative breast cancer. *Front Immunol* (2022) 13:922780. doi: 10.3389/fimmu.2022.922780

129. Wang T, Liu Y, Li Q, Luo Y, Liu D, Li B, et al. Cuproptosis-related gene FDX1 expression correlates with the prognosis and tumor immune microenvironment in clear cell renal cell carcinoma. *Front Immunol* (2022) 13:999823. doi: 10.3389/fimmu.2022.999823

130. Bian Z, Fan R, Xie L. A novel cuproptosis-related prognostic gene signature and validation of differential expression in clear cell renal cell carcinoma. *Genes (Basel)* (2022) 13(5):851. doi: 10.3390/genes13050851

131. Zhu Z, Zhao Q, Song W, Weng J, Li S, Guo T, et al. A novel cuproptosis-related molecular pattern and its tumor microenvironment characterization in colorectal cancer. *Front Immunol* (2022) 13:940774. doi: 10.3389/fimmu.2022.940774

132. Lv H, Liu X, Zeng X, Liu Y, Zhang C, Zhang Q, et al. Comprehensive analysis of cuproptosis-related genes in immune infiltration and prognosis in melanoma. *Front Pharmacol* (2022) 13:930041. doi: 10.3389/fphar.2022.930041

133. Zhang Z, Zeng X, Wu Y, Liu Y, Zhang X, Song Z. Cuproptosis-related risk score predicts prognosis and characterizes the tumor microenvironment in hepatocellular carcinoma. *Front Immunol* (2022) 13:925618. doi: 10.3389/fimmu.2022.925618

134. Liu Y, Liu Y, Ye S, Feng H, Ma L. Development and validation of cuproptosis-related gene signature in the prognostic prediction of liver cancer. *Front Oncol* (2022) 12:985484. doi: 10.3389/fonc.2022.985484

135. Li H, Zu X, Hu J, Xiao Z, Cai Z, Gao N, et al. Cuproptosis depicts tumor microenvironment phenotypes and predicts precision immunotherapy and prognosis in bladder carcinoma. *Front Immunol* (2022) 13:964393. doi: 10.3389/fimmu.2022.964393

136. Yang L, Zhang Y, Wang Y, Jiang P, Liu F, Feng N, et al. Ferredoxin 1 is a cuproptosis-key gene responsible for tumor immunity and drug sensitivity: A pan-cancer analysis. *Front Pharmacol* (2022) 13:938134. doi: 10.3389/fphar.2022.938134

137. Xiao C, Yang L, Jin L, Lin W, Zhang F, Huang S, et al. Prognostic and immunological role of cuproptosis-related protein FDX1 in pan-cancer. *Front Genet* (2022) 13:962028. doi: 10.3389/fgene.2022.962028

138. Zhang C, Zeng Y, Guo X, Shen H, Zhang J, Wang K, et al. Pan-cancer analyses confirmed the cuproptosis-related gene FDX1 as an immunotherapy predictor and prognostic biomarker. *Front Genet* (2022) 13:923737. doi: 10.3389/fgene.2022.923737

Glossary

ROS	reactive oxygen species
WD	Wilson disease
MD	Menkes disease
Ctr1	copper transporter receptor 1
Ctr2	copper transporter receptor 2
DMT1	divalent metal transporter 1
ATP7A	copper-transporting ATPase 1
ATP7B	copper-transporting ATPase 2
MT	metallothionein
GSH	glutathione
CCS	copper chaperone for superoxide dismutase
Atox1	antioxidant protein 1
Cox	cytochrome c oxidase
Cox17	cytochrome c oxidase copper chaperone 17
SOD1	superoxide dismutase 1
CuPrs	cuproproteins
MAPK	mitogen activated protease kinase
HIF-1	hypoxia inducible factor-1
bFGF	basic fibroblast growth factor
TNF-α	tumor necrosis factor alpha
EMT	epithelial to mesenchymal transition
LOX	lysine oxidase
ECM	extracellular matrix
TTM	tetrathiomolybdate
D-Pen	D-penicillamine
DSF	disulfiram
ACC	adrenocortical carcinoma
BRCA	breast invasive carcinoma
LGG	lower grade glioma
MESO	mesothelioma
SKCM	skin cutaneous melanoma
ES	elesclomol
FDX1	ferredoxin 1
DLAT	dihydrolipoyl transacetylase
TCA	tricarboxylic acid cycle
PAAD	pancreatic adenocarcinoma
TNBC	triple-negative breast cancer
HCC	hepatocellular carcinoma
ccRCC	clear cell renal cell carcinoma
BLCA	bladder cancer
TME	tumor microenvironment
TP53	tumor protein P53
BRCA1	breast cancer susceptibility gene 1
OS	overall survival
CRG	cuproptosis related genes
CRS	cuproptosis risk score
CRRS	cuproptosis related risk score
CRGI	cuproptosis-related gene index.

frontiers | Frontiers in Oncology

TYPE Original Research
PUBLISHED 23 March 2023
DOI 10.3389/fonc.2023.1145379

OPEN ACCESS

EDITED BY
Xianwei Wang,
Xinxiang Medical University, China

REVIEWED BY
Yaguang Zhang,
Sichuan University, China
Lei Qiu,
Sichuan University, China

*CORRESPONDENCE
Song Zhang
✉ qingchengguose@163.com

SPECIALTY SECTION
This article was submitted to
Breast Cancer,
a section of the journal
Frontiers in Oncology

RECEIVED 16 January 2023
ACCEPTED 27 February 2023
PUBLISHED 23 March 2023

CITATION
Gong W and Zhang S (2023) YB1 participated in regulating mitochondrial activity through RNA replacement. *Front. Oncol.* 13:1145379. doi: 10.3389/fonc.2023.1145379

YB1 participated in regulating mitochondrial activity through RNA replacement

Weipeng Gong[1] and Song Zhang[2]*

[1]Department of Gastrointestinal Surgery, Shandong Cancer Hospital and Institute, Shandong First Medical University and Shandong Academy of Medical Sciences, Jinan, Shandong, China, [2]Shandong Provincial Key Laboratory of Radiation Oncology, Shandong Cancer Hospital and Institute, Shandong First Medical University, Jinan, Shandong, China

As a relic of ancient bacterial endosymbionts, mitochondria play a central role in cell metabolism, apoptosis, autophagy, and other processes. However, the function of mitochondria-derived nucleic acids in cellular signal transduction has not been fully elucidated. Here, our work has found that Y-box binding protein 1 (YB1) maintained cellular autophagy at a moderate level to inhibit mitochondrial oxidative phosphorylation. In addition, mitochondrial RNA was leaked into cytosol under starvation, accompanied by YB1 mitochondrial relocation, resulting in YB1-bound RNA replacement. The mRNAs encoded by oxidative phosphorylation (OXPHOS)-associated genes and oncogene HMGA1 (high-mobility group AT-hook 1) were competitively replaced by mitochondria-derived tRNAs. The increase of free OXPHOS mRNAs released from the YB1 complex enhanced mitochondrial activity through facilitating translation, but the stability of HMGA1 mRNA was impaired without the protection of YB1, both contributing to breast cancer cell apoptosis and reactive oxygen species production. Our finding not only provided a new potential target for breast cancer therapy but also shed new light on understanding the global landscape of cellular interactions between RNA-binding proteins and different RNA species.

KEYWORDS

YB1, mitochondria, apoptosis, HMGA1, autophagy

Introduction

Mitochondria own a circular 16.6-kb DNA genome encoding two ribosomal RNAs, 22 transfer RNAs, and 13 open reading frames for electron transport chain complex subunits (1). During energy production, mitochondria participate in numerous metabolic reactions, such as tricarboxylic acid cycle and oxidative phosphorylation, and some intermediate metabolites are indispensable for cell proliferation and survival (2), but some by-products, such as reactive oxygen species, are harmful for most cells (3, 4). In recent years, more and more evidence indicated that there is a close relationship between cancer occurrence and mitochondria. Various studies have shown that mitochondria play a vital role in maintaining cancer cell stemness and drug resistance because of the ability of this organelle to modify cell metabolism, allowing survival and avoiding apoptosis clearance of cancer cells (5). Additionally, cancer cells can hijack the mitochondria from immune cells *via* building physical nanotubes to evade immune surveillance (6). Therefore, diving into studying the mechanisms underlying mitochondria-mediated signal flux is of great significance for understanding cellular homeostasis and cancer pathogenesis.

Y box binding protein 1 (YB1) is a member of the highly conserved cold-shock domain protein family with multifunctional properties and located in the cytoplasm and nucleus (7). Because cold-shock domains always endow proteins with the RNA/DNA binding ability (8), YB1 was implicated in various cellular processes, including transcription regulation, RNA splicing, translation, and RNA stability (9). In recent years, it was found that YB1 was upregulated in many kinds of cancers and usually indicated dismal clinical outcomes for cancer patients (10). In breast cancer cells, YB1 was aberrantly upregulated in ER-positive stem-like cancer cells. Through directly interacting with ERα, YB1 promoted ERα degradation, resulting in cancer stem cell differentiation (11). Upon DNA damaging agent exposure, YB1 was phosphorylated at the serine 102 residue by ribosomal S6 kinase and transported into the nucleus from cytosol to initiate the transcription of a set of drug-resistant and DNA repair genes (12, 13). During cancer metastasis, YB1 enhances HIF1a protein expression by directly binding to and activating translation of HIF1a message RNA (14). In addition, the transcriptions of some cell adhesion and extracellular matrix interaction proteins were also directly targeted by YB1 (15). Benefiting from the development of the RNA-seq technique, it has become accessible for us to read RNA modifications at a single-nucleotide resolution. At the same time, the novel function of YB1, as an RNA modification "reader," was also uncovered in a lot of cancer cells (16). Through interacting with other partners, m^5C and m^6A modifications on tRNAs or mRNAs can be recognized by YB1 (17, 18). It is believed that new YB1-targeted drugs for cancer therapy will get more attention on this research background.

According to endosymbiosis theory, mitochondria originated from procaryotic organisms, indicating that mitochondrial nucleic acid elements and gene expression mechanisms are different from those that worked in the eukaryotic nucleus (19). It has been reported that mitochondrial DNA release *via* the permeability transition pore can trigger cellular inflammation through activating the cGAS/STING signaling pathway (20), but the downstream effects of mitochondrial RNA accumulation in cytosol are still elusive. In our study, we have found that upregulated YB1 in breast cancer cells increased cell tolerance to environmental stress through promoting autophagy and evading apoptosis-mediated cell clearance. Serum starvation induced mitochondrial RNA leakage and initiated the transport of YB1 into mitochondria. These mitochondria-derived RNAs competitively replaced YB1 original bound transcripts and reduced their half-life time, resulting in cancer cell inhibition and mitochondrial dysfunction.

Materials and methods

Cell culture

MDA-MB-231 breast cancer cells and HEK293T cells were purchased from Shanghai Cell Collection, Chinese Academy of Sciences. The cells were cultured in Dulbecco's modified Eagle's medium (Gibco, USA) supplemented with 10% fetal bovine serum (Gibco, USA) at 37°C in a humidified atmosphere with 5% CO_2.

Quantitative real-time PCR

Briefly, total RNAs were extracted from cells or tissues using an RNA isolation kit (Yeasen Biotech Corporation, Shanghai, China), and the complementary DNA was synthesized with a Reverse Transcription kit (Yeasen, Shanghai, China) according to the manufacturer's instructions. Each gene RNA expression level was detected in SYBR Master Mixture with specific primers (listed in Supplemental Table 1). The relative expression levels of genes were calculated using the △△Ct method, and GAPDH (glyceraldehyde-3-phosphate dehydrogenase) was used as an internal normalization.

Western blot

Cells were harvested in Western blot/IP lysis buffer (Beyotime, Beijing, China) and subjected to sonication. Then, the protein lysate was separated in 12% SDS-PAGE and electrotransferred to a polyvinylidene fluoride (PVDF) membrane (Millipore, USA). After incubation in blocking solution (5% skim milk) for 2 h, the membrane was incubated with a primary antibody at 4°C overnight. Subsequently, the membrane was incubated with secondary antibodies conjugated with horseradish peroxidase (Yeasen, China) for 1 h at room temperature and the signal of protein bond was detected using ECL chromogenic solution (Yeasen, China).

Cell proliferation assay

Around 3,000 cells were seeded in each well of a 96-well plate and subjected to different treatments. At different times after seeding, each well was added with 10 μl MTS substrate (Promega, USA), followed by incubation at 37°C for 2 h. Then, the light absorbance of the plate at 480 nm was recorded by a microplate reader.

For cell colony formation assays, 1,000 cells were seeded into each well of a six-well plate and cells allowed to proliferate for 1 week. After fixation with 4% paraformaldehyde, the cells were stained with crystal violet solution for 20 min and the cell number was counted under a microscope.

Lentiviral transfection

The plasmids of psPAX, pMD2G, and shRNA-containing constructs (Vigene Biosciences, USA) were co-transfected into HEK293T cells simultaneously. At 48 h after transfection, the cell culture supernatants containing virus particles were collected and filtered with a 0.22-µm membrane. Then, the virus liquid was added to cancer cell culture medium, allowing virus infection for 24 h. The puromycin-resistant cancer cells were isolated through treating cells with 5 µg/ml of puromycin (MCE, USA) for 1 week. The shRNA-mediated target gene knockdown efficiency was demonstrated by Western blot and quantitative real-time PCR.

Cell cycle

Cells were fixed with 70% ethanol and stored at −20°C overnight. After being rinsed with PBS, the cells were treated with RNase A (20 µg/ml) for 40 min at 37°C, followed by incubation with propidium iodide (Sangon, Shanghai, China) at 37°C for 20 min. Then, the fluorescence intensity for each sample was analyzed by flow cytometry (BD, USA).

Cell apoptosis detection

After centrifugation, cells were collected and stained with FITC Annexin V and propidium iodide using cell apoptosis detection kit (Beyotime, China) according to the manufacturer's instructions. After rinsing, the signals of cells were analyzed by flow cytometry (BD Biosciences, USA) immediately.

Transwell assays

Around 4 × 10^4 cells cultured in serum-free medium were seeded into the upper chamber (8-µm pore size, Corning, USA), and the bottom well was added with 1 ml complete culture medium. At 48 h after incubation, the cells were fixed with 4% paraformaldehyde and stained with crystal violet solution. ImageJ, an image analysis software, was used to count the cell numbers for each experiment.

Wound-healing assays

For this assay, around 2 × 10^5 cells/well were seeded into a 12-well plate, allowing cells to proliferate up to around 90% confluence. The cell monolayer was scratched using a tip and washed with serum-free medium to remove detached cells. Then, the cells were cultured in complete medium and photographed at indicated times.

Mitochondrial activity detection and ROS investigation

Mitochondrial activity was detected using MitoTracker dye (Beyotime, Beijing, China) according to the manufacturer's instructions. Briefly, cells were seeded into a six-well plate 1 day before detection, and 1 µl MitoTracker dye was added into 5 ml DMEM cell culture medium to prepare cell staining solution. After mixing well, the mixture was added into each well and incubated with cells at 37°C for 90 min. Then, the cells were subjected to flow cytometry detection and fluorescence photographing. The procedure for ROS investigation was similar to the abovementioned steps, and a cellular ROS level detection kit was purchased from Beyotime Biotechnology.

Mitochondrial isolation

Mitochondria were isolated from cancer cells using a cellular mitochondria isolation kit (Beyotime, China) according to the manufacturer's instructions with some modifications. After trypsin treatment, around 1 × 10^7 cells were collected and rinsed with PBS for twice. Then, the cells were resuspended with 4 ml prechilled solution I (containing 1mM PMSF) and stored on ice for 10 min. Then, the cells were homogenized in a prechilled Dounce homogenizer and centrifuged at 800g for 10 min at 4°C to remove cell debris. Mitochondria were sedimented at 13,000g for 10 min at 4°C, and the mitochondria-removed supernatant was collected. Subsequently, the rough mitochondrial fraction was washed with prechilled solution I and centrifugated at 13,000g for 10 min again. Purified mitochondria were incubated with digitonin on ice for 30 min at the indicated concentration. After resuspension in 1 ml solution I, mitoplasts were collected through centrifugation at 18,000g for 10min at 4°C.

Fluorescence *in situ* hybridization and immunofluorescence

RNA fluorescence *in situ* hybridization (FISH) was performed with an RNA FISH kit (RiboBio, Guangzhou, China) according to the manufacturer's instructions with minor modifications. After MitoTracker staining, cells were fixed with 4% formaldehyde for 10 min at room temperature. Then, the cells were permeabilized with 70% ethanol at 4°C overnight and dehydrated through 80, 90, and 100% ethanol. After pre-hybridization at room temperature for 30 min, the cells were incubated with hybridization buffer containing a 40-nM RNA probe (Generay, Shanghai, China) at 75°C for 5 min to allow RNA denaturation. Then, the cells were subjected to hybridization overnight at room temperature. Finally, the slides were washed with 4× SSC, 2× SSC, and 1× SSC buffer successively at room temperature.

After the finishing RNA FISH process, the slides were blocked with blocking solution (PBS + 0.5% bovine serum albumin) at room temperature for 1 h and incubated with the indicated primary antibodies for 2 h. After washing with PBS, the secondary antibodies with fluorescence modifications (Thermo Fisher, USA) were added and incubated for another 2 h. Finally, the nucleus was stained with DAPI (RiboBio, China) at room temperature for 10 min for microscopic observation.

RNA-associated immunoprecipitation

After centrifugation, around 1 × 10^7 cells were collected and resuspended in 1 ml RNase-free RIPA lysis buffer (Beyotime, China) containing 1 U/μl RNase inhibitor (Promega, USA). After cell lysis, whole-cell lysate was subjected to centrifugation at 12,000g for 10 min and the supernatant was divided into two aliquots. One aliquot was incubated with YB1 antibodies (Abmart, Shanghai, China) overnight at 4°C, and another aliquot was added with equivalent IgG isoforms as control. After incubation, the anti-YB1–RNA complex was precipitated with Protein G Agarose beads (Beyotime, China). After washing with RIPA lysis buffer for five times, the RNA bound to YB1 proteins was purified from the sedimented Agarose beads using the TRIzol RNA isolation kit (Yeasen Biotech Co., Shanghai, China), followed by quantitative real-time PCR.

Protein stability

To measure protein stability, cells were treated with cycloheximide (CHX, final concentration 100 μg/ml, MCE, USA) to block the translation process. Cell samples were collected at indicated time points. In addition, to exclude the influence of protease-mediated protein degradation, MG132 (final concentration 50 μg/ml, MCE, USA) was added into the cell culture medium to inhibit protease activity for 8 h. The inhibitory efficiency was detected by Western blot.

Animal models

Around 5 × 10^6 cancer cells suspended in 800 μl PBS were mixed with Matrigel (Yeasen, China) at a volume ratio of 3:1. Then, 200 μl cell mixture was administered into each 4-week-old female BALB/c nude mouse by subcutaneous injection ($n = 5$). The width and length of tumor burdens were monitored weekly. When the tumor length was larger than 1 cm, all of the mice were sacrificed and the solid tumors were collected for the next investigation.

Online data mining

The evaluation of YB1 expression in breast clinical specimens and associated patient survival rate was achieved through referring to the GEPIA database (21) (http://gepia.cancer-pku.cn/), KM plotter (22) (http://kmplot.com/analysis/), TNM plotter database (23) (https://www.tnmplot.com/), GENT2 (24) (http://gent2.appex.kr/gent2/), and TIMER (http://timer.cistrome.org/) (25). A protein–RNA interaction model was established by SWISS-MODEL (https://swissmodel.expasy.org/) (26).

Statistical analysis

Software GraphPad Prism 8 was used for data processing and analysis. Samples with two groups were analyzed with Student's t test, and samples of more than two groups were calculated with one-way ANOVA. When $p < 0.05$, the results were regarded as statistically significant.

Results

The upregulation of YB1 in breast cancerous tissues was associated with poor clinical outcomes

Previously, we have revealed the important role of YB1 in maintaining the stemness of melanoma stem cells, but the specific molecular mechanism whereby YB1 functions in breast cancer is still needed to be elucidated. Before exploring the function of YB1 in breast cancer, the relationship between YB1 and clinical outcomes was analyzed through referring to online databases. Compared with normal tissues, breast cancerous tissues showed higher YB1 expression, and the highest expression level of YB1 was presented in metastatic breast cancerous tissues (Figure 1A). In addition, the level of YB1 increased significantly with the aggravation of clinical staging (Figure 1B) and malignancy (Figure 1C). These data helped us build a close connection between YB1 expression and the progression of breast cancer. Benefiting from the availability of online databases, Kaplan–Meier survival rates for patients with low or high YB1 expression levels were plotted. No matter at the mRNA level or protein level, patients with lower YB1 expression usually have prolonged survival time compared with those with higher YB1 levels (Figures 1D, E), and this trend becomes more obvious especially for patients diagnosed with basal or triple-negative breast cancer (Figure 1F). Furthermore, immunohistochemical analysis showed that solid tumors have a higher YB1 expression level compared with pericancerous tissue (Figure 1G), which is consistent with the results from database. All the above mentioned data revealed YB1's tumor-promoting nature and raised the potential of YB1 used as an indicator for breast cancer diagnosis.

YB1 depletion inhibited breast cancer cell proliferation and migration

In order to characterize the function of YB1 in breast cancer, breast cancer cell lines (MDA-MB-231) with stably decreased YB1 were established using lentivirus-mediated shRNA transfection. Quantitative real-time PCR and Western blot results demonstrated the good inhibitory efficiency of shRNAs on YB1 expression at the mRNA level and protein level (Figures 2A, B), respectively. Colony formation assays showed that the clonogenicity of breast cancer cells was significantly attenuated by YB1-silenced expression (Figure 2C). In addition, the role of YB1 in regulating cancer cell migration and invasion was also investigated using wound-healing and Transwell

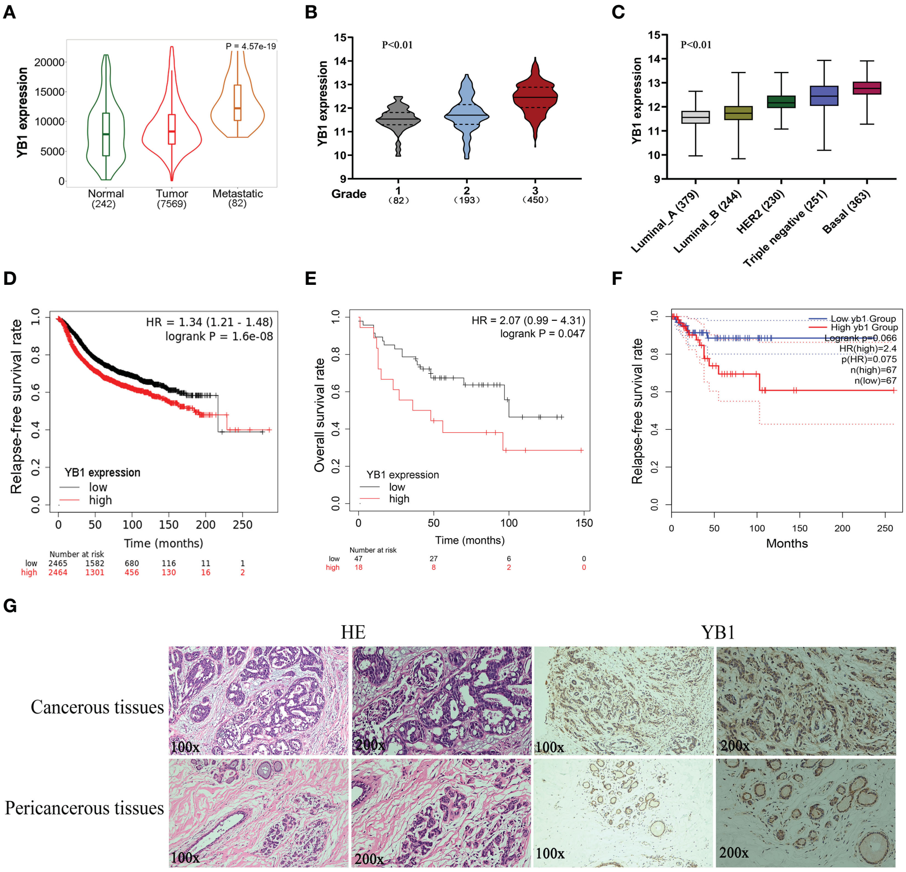

FIGURE 1

The upregulation of YB1 in breast cancerous tissues was associated with poor clinical outcomes. **(A)** Relative expression of YB1 in normal or cancerous tissues of patients with breast cancer. The expression level of YB1 in metastatic cancerous tissues was specifically elevated compared with normal or non-metastatic tissues (https://tnmplot.com). **(B)** Expression level of YB1 in breast cancer patients under different clinical stages (http://gent2.appex.kr/gent2/). **(C)** The relationship between YB1 expression and breast cancer types (http://gent2.appex.kr/gent2/). **(D-F)** Kaplan–Meier survival rates for patients with breast cancer stratified by YB1 expression. The survival rates for patients were plotted separately according to YB1 expression at the mRNA **(D)** or protein level **(E)** (http://kmplot.com/analysis/). The most remarkable difference emerged in patients with basal-like/triple-negative breast cancer **(F)**. **(G)** Immunohistochemical analysis of YB1 in solid tumors. Paired paracarcinoma and carcinoma tissues were excised from the same patient with breast cancer.

assays. The results showed that YB1 inhibition significantly impaired the invasion and migration ability of breast cancer cells (Figures 2D, E), further indicating the onco-promoting role of YB1. To further elucidate the mechanism of YB1-regulated cancer cell proliferation, cell-cycle and apoptosis levels were investigated. Flow cytometry analysis showed obvious S-stage cell-cycle arrest and increased apoptosis in cancer cells with decreased YB1 expression compared with the control groups (Figures 2F, G). All the above mentioned data indicated that YB1 functions as an oncogene in promoting breast cancer progression through regulating cell proliferation and migration.

The role of YB1 in regulating cell apoptosis and autophagy

To further explore the function of YB1 in breast cancer cells, the cellular distribution pattern of YB1 should be clarified. Here, we found that the majority of YB1 proteins was localized in cytoplasm. An obvious co-localization of YB1 with mitochondrial outer membrane marker TOM20 was also observed (Figure 3A). To figure out whether YB1 was imported into the mitochondrial matrix, the purified mitochondria were isolated from breast cancer cells using differential ultracentrifugation. Western blot results showed that YB1 existed in purified mitochondrial fraction even when the outer membrane was removed through digitonin treatment (Figure 3B), indicating that YB1 may localized to the mitochondrial matrix. The abovementioned data shed light on the potential interaction between YB1 and mitochondria; therefore, the influence of YB1 on mitochondrial activity was investigated. Quantitative real-time PCR data showed no difference in mitochondrial gene expressions in cancer cells with or without YB1 silence (Figure 3C). The status of mitochondria was investigated through loading the MitoTracker-specific probe into active cancer cells. It is surprising to find that YB1 depletion induced significantly enhanced mitochondrial membrane potential indicated by the evident fluorescence intensity shift (Figure 3D). In addition, the distribution of mitochondria was

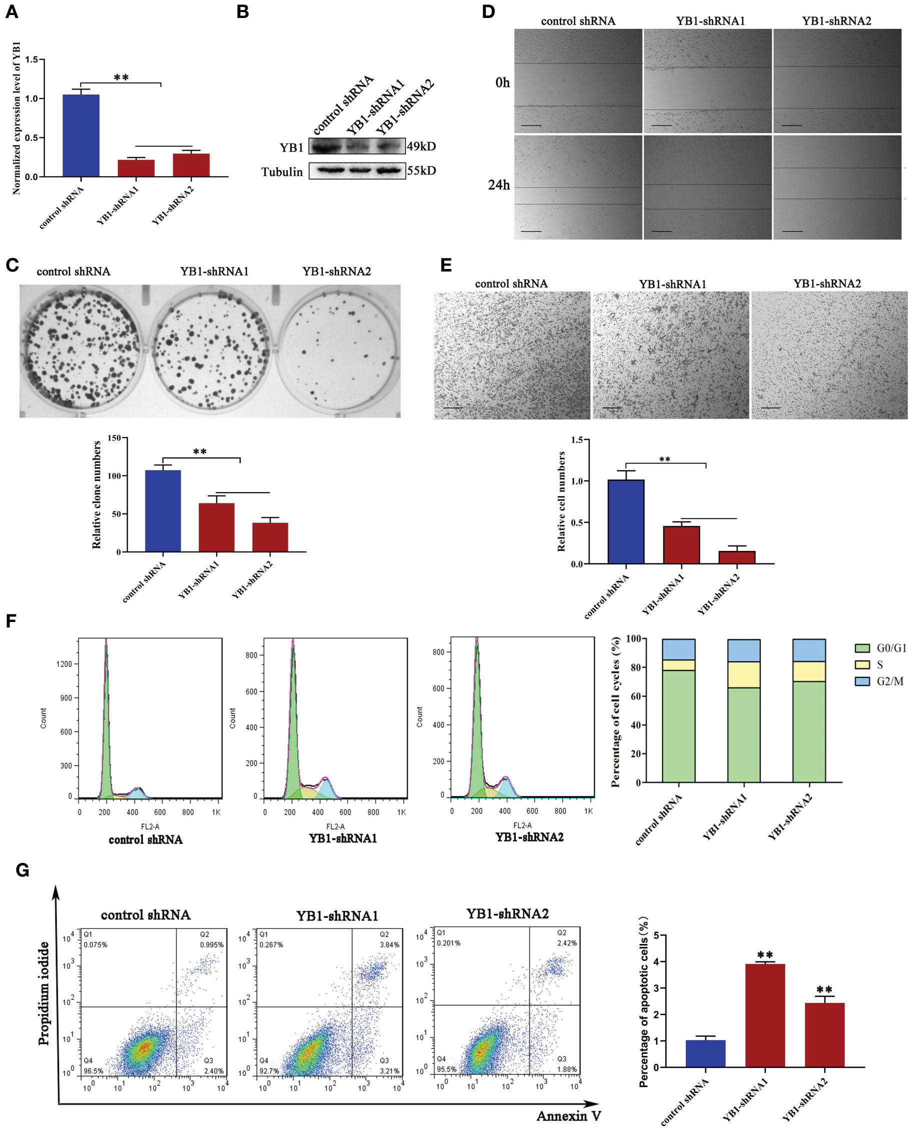

FIGURE 2

YB1 depletion inhibited breast cancer cell proliferation and migration. **(A, B)** Knockdown efficiency of YB1-targeted shRNAs in breast cancer cells (MDA-MB-231) at the mRNA level and protein level. β-Tubulin was used as a loading control. The experiment was repeated three times, $^{**}P < 0.01$. **(C)** Colony formation assay was performed to investigate the influence of YB1 depletion on cancer cell proliferation. The experiment was repeated three times, $^{**}P < 0.01$. **(D, E)** The function of YB1 on cell migration ability was investigated using wound-healing and Transwell assays. Scale bar, 100 μm. **(F)** YB1 expression silence induced obvious S-stage cell-cycle arrest in breast cancer cells. The cell cycle was investigated through flow cytometry. **(G)** The influence of YB1 knockdown on cell apoptosis detected by flow cytometry. Experiments were repeated three times.

also disrupted by YB1 silence and more mitochondria were accumulated in the perinuclear region; fewer mitochondria localized to the cellular outer region compared with control cancer cells that showed randomly distributed mitochondria in cytoplasm (Figure 3D). In agreement with increased mitochondrial membrane potential, the levels of reactive oxygen species in YB1-silenced cells were also increased compared with the control group (Figure 3E). All of these data indicated the indispensable role of YB1 in regulating mitochondrial network formation in breast cancer cells.

Mitochondria are a cellular powerhouse that plays a fundamental role in energy production and cell survival, including cell apoptosis and autophagy. Here, Western blot results demonstrated that YB1 depletion significantly reduced the expression of LC3 (Figure 3F), a well-known protein marker for autophagy. By analyzing the innate signaling pathway participating in autophagy regulation, we found that the phosphorylation of mTOR was increased triggered by YB1 knockdown (Figure 3G), suggesting that YB1 might target mTOR for autophagy initiation. One of the well-established roles of mTOR is to promote anabolic cellular metabolism by suppressing autophagy. Considering that starvation can induce cell autophagy, we starved the cells through withdrawing serum from the cell culture medium for 24 h to determine if YB1 influences the homeostasis of mitochondria. Western blot results implied that starvation induced obvious autophagy in control cells, but not in cells with decreased YB1. In

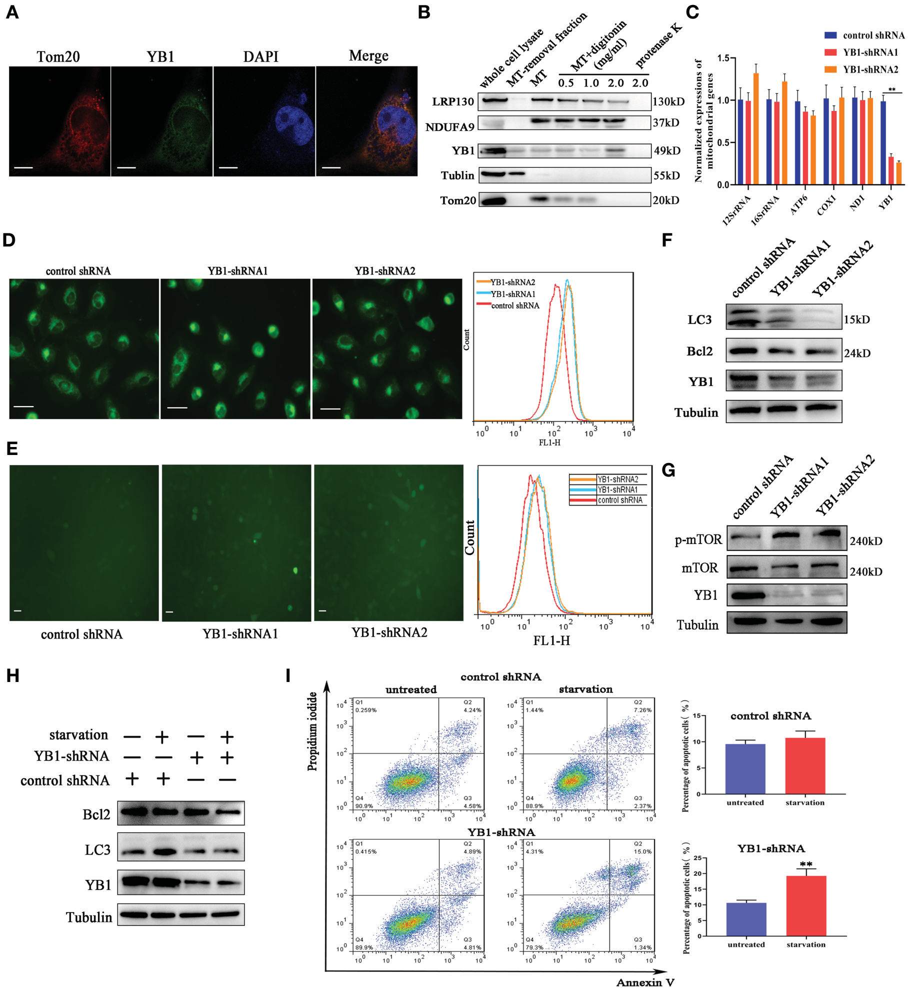

FIGURE 3

YB1 participated in balancing autophagy and cell apoptosis. **(A)** The co-localization of YB1 (green) with mitochondria (red) in breast cancer cells. Mitochondria were marked with TOM20 (red), and nuclei were stained with DAPI. Scale bars, 5 μm. **(B)** The protein level of YB1 in different mitochondrial fractions. Digitonin dose-dependently dissolved the mitochondrial outer membrane. The residual proteins were digested with protease K NDUFA9, inner membrane protein marker; LRPPRC, mitochondrial matrix localized protein. **(C)** Relative expressions of mitochondrial genome-encoded genes. The experiment was repeated three times. $^{**}p < 0.01$. **(D)** The activity of mitochondria was investigated using flow cytometry. Mitochondria were labeled with MitoTracker dye; the fluorescence signal intensity was analyzed. Scale bar, 10 μm. **(E)** The influence of YB1 knockdown on cellular reactive oxygen species. Scale bar, 10 μm. **(F)** YB1 knockdown reduced the cellular basic autophagy level in breast cancer cells. **(G)** The mTOR signaling pathway was activated in cells with deleted YB1. **(H, I)** YB1-silenced expression failed to induce autophagy under starvation but significantly increased cell apoptosis.

addition, YB1 knockdown impaired the expression of cell apoptosis inhibitors under starvation conditions (Figure 3H). Consistent with Western blot results, flow cytometry analysis demonstrated that starvation treatment induced cell apoptosis more easily in YB1-silenced cells than in control cells (Figure 3I), highlighting the important role of YB1 in balancing cell apoptosis and autophagy.

YB1 directly interacted with mitochondrial RNA

The function of YB-1 is underlain by its ability to interact with nucleic acids and proteins to form a heterocomplex. The co-localization of YB1 with mitochondria reminds us whether the RNA binding ability of YB1 was involved in regulating the activity of mitochondria. To elucidate this possibility, RNA-associated immunoprecipitation assays were performed to reveal the YB1-bound RNA library. Coomassie brilliant blue staining and Western blot results showed benign specificity of antibodies to sediment the YB1–RNA complex (Figures 4A, B). Quantitative real-time PCR revealed a strong interaction between YB1 and mitochondrial RNA, including 12S/16S rRNA, a fraction of mRNA, and transfer RNA (MT-TF) (Figure 4C). According to the data of quantitative real-time PCR, mitochondrial transfer RNA, MT-TF(phe) with the highest confidence, was picked up and focused in the next studies.

Subsequently, in order to investigate whether starvation treatment can influence the interaction between YB1 and mitochondrial RNA, mitochondria were isolated from cancer cells cultured under normal or starvation conditions. Western blot results showed an increased amount of YB1 in the purified

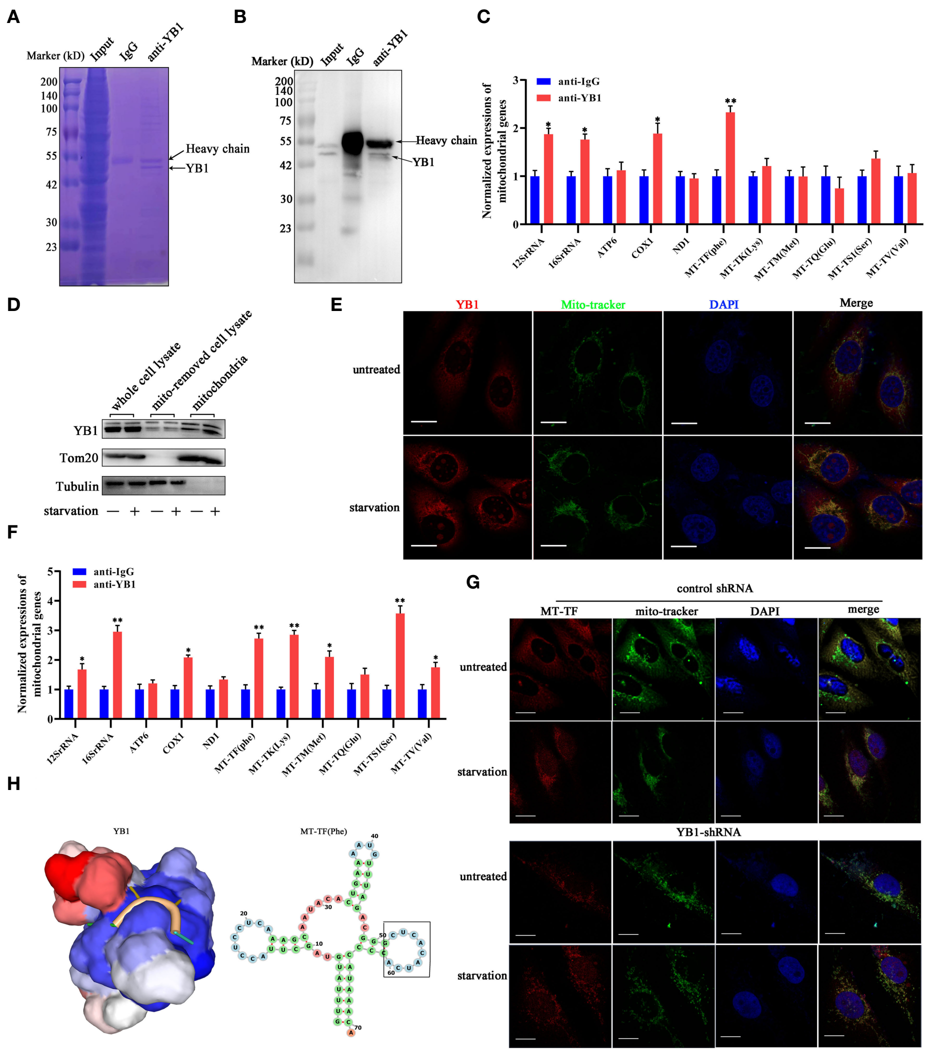

FIGURE 4
YB1 interacted with mitochondrial tRNA. **(A, B)** RNA-associated immunoprecipitation (RIP) assays. RIP was conducted in MDA-MB-231 cells to sediment the YB1–RNA complex; rabbit IgG was used as a negative control. The contents of immunoprecipitate were analyzed by SDS-PAGE with Coomassie staining **(A)** or Western blot **(B)**. **(C)** Detection of mitochondrial RNA in the YB1-immunoprecipitated complex. The RNAs co-immunoprecipitated with YB1 proteins were isolated and detected using quantitative real-time PCR. YB1 distribution was detected using the mitochondrial fraction **(D)** and immunofluorescence **(E)**; scale bar, 10 µm. **(F)** Serum-free starvation treatment increased the direct interaction between mitochondrial RNA and YB1 protein. n = 3, $^{**}p < 0.01$, $^{*}p < 0.05$. **(G)** MT-TF distribution detection using FISH. After starvation treatment, more MT-TF (red) were localized in the outside of mitochondria. Scale bar, 10 µm. **(H)** A YB1–RNA interaction model was built using the online SWISS-MODEL.

mitochondrial fraction that underwent starvation (Figure 4D), consistent with the results of immunofluorescence staining (Figure 4E), indicating the transfer of YB1 into mitochondria. In addition, it is interesting to find that the amount of mitochondrial RNA was significantly increased in YB1 immunoprecipitates after starvation induction (Figure 4F). Additionally, microscope analysis observed leakage of mitochondrial RNA (MT-TF) into the cytoplasm in response to starvation treatment, which was further augmented in cancer cells with decreased YB1 expression (Figure 4G). Next, the protein–RNA interaction model was predicted using an online tool (https://swissmodel.expasy.org/). According to the secondary structure of MT-TF(Phe), a YB1 recognition motif (UCACAU) was positioned to a loop, which greatly increased the RNA accessibility for YB1 binding (Figure 4H). Collectively, these data indicated that starvation triggered the release of mitochondrial RNA into cytosol and mitochondrial import of YB1, which facilitated the interaction between YB1 protein and mitochondrial RNA.

YB1 maintained the stability of HMGA1 mRNA

Previously, a model has been proposed in which stress-induced transfer RNA fragments would be actively competing with endogenous transcripts for YB1 binding, resulting in RNA displacement and posttranscriptional regulation (27). In order to demonstrate the feasibility of this model in this cellular background, we need to clarify the species of YB1-bound endogenous transcripts. Through referring to others' YB1-CLIP results (GSE63605), some onco-promoting gene mRNAs were found in the YB1-bound RNA library (27) and the expression levels of HMGA1 and CD151 were investigated in breast cancer cells. We have found that YB1 knockdown significantly reduced the expression of HMGA1 at the mRNA level and protein level (Figures 5B, C) but have no influence on CD151 expression, even though CD151 mRNA showed higher binding ability with YB1 protein (Figure 5A). In addition, serum-starvation treatment significantly impaired the interaction between YB1 and HMGA1 mRNA in breast cancer cells (Figure 5D). Compared with the control group, the half-life time of HMGA1 mRNA was significantly reduced in cancer cells with depleted YB1 expression (Figure 5E), indicating the important role of YB1 in regulating HMGA1 mRNA stability. To clarify whether HMGA1 was implicated in YB1-mediated cancer cell apoptosis, breast cancer cells were transfected with HMGA1-targeted siRNA and the knockdown efficiency was verified (Figure 5F). Flow cytometry analysis showed that HMGA1 silence induced significant cell apoptosis in breast cancer cells compared with the control group (Figure 5G). Correlational analysis through an interrogating online database (http://timer.comp-genomics.org/) showed a strong positive correlation between YB1 expression and HMGA1 expression in breast cancer tissues (Figure 5H). An elevated expression level of HMGA1 in cancer tissues and shorter patient survival time indicated the onco-promoting role of HMGA1 in breast cancer (Figures 5I–K). In summary, the cytosol accumulation of mitochondrial RNA and increased YB1 mitochondrial relocation induced by starvation changed YB1-bound original RNA species. Lacking YB1 protection enhanced

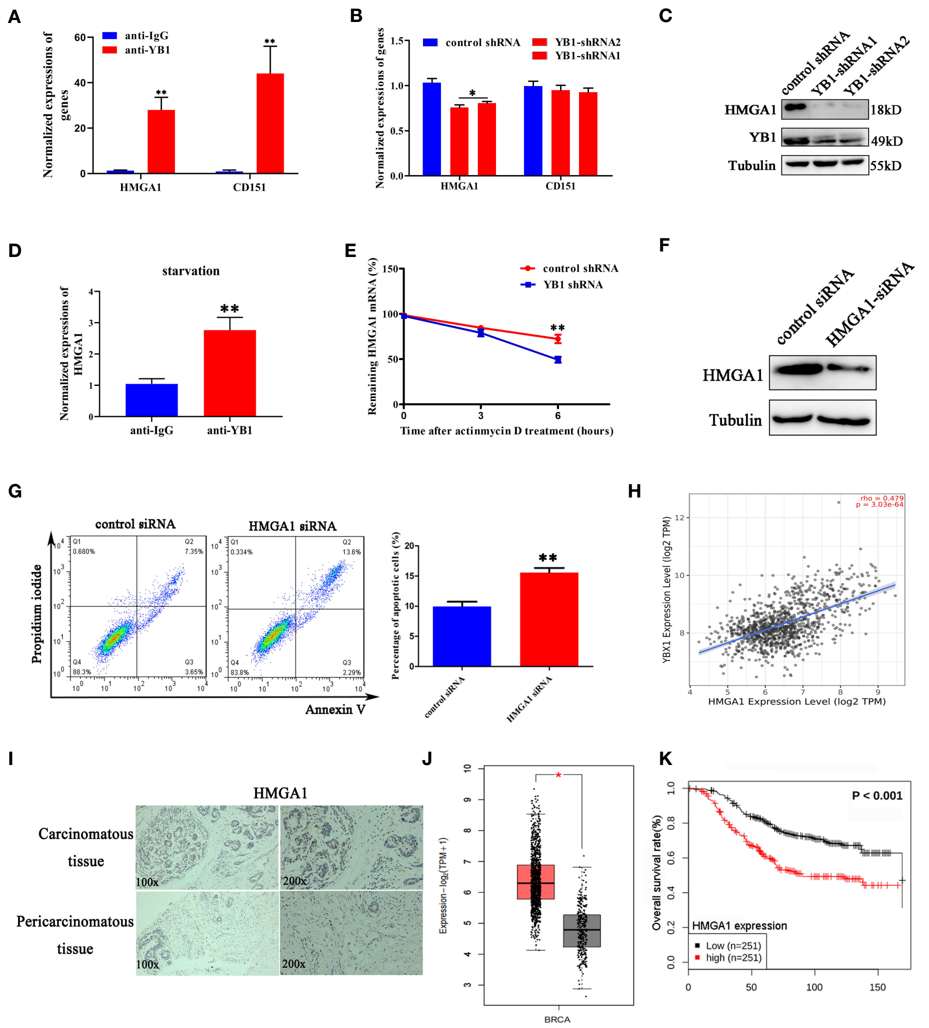

FIGURE 5
YB1 maintained the stability of HMGA1 mRNA. **(A)** Detection of oncogenes in the YB1-bound RNA library through RIP assays. **(B, C)** YB1 knockdown significantly downregulated HMGA1 expression at both mRNA level and protein level. **(D)** Serum-free starvation impaired YB1 binding ability with HMGA1 mRNA. n = 3,**p < 0.01. **(E)** Influence of YB1 knockdown on HMGA1 mRNA degradation. **(F)** The expression of HMGA1 was silenced using siRNA. **(G)** Influence of HMGA1 knockdown on cell apoptosis. n = 3, **p < 0.01. **(H)** Correlation analysis of YB1 expression with HMGA1 expression in breast cancer tissues. Data were downloaded from website http://timer.comp-genomics.org. **(I)** Immunohistochemical analysis of HMGA1 in paired breast carcinoma and paracarcinoma tissues. **(J)** Analysis of HMGA1 expression in breast cancer tissues and normal tissues through referring to an online database (http://gepia.cancer-pku.cn/). *p < 0.05. **(K)** High expression of HMGA1 in breast cancer tissues predicts adverse clinical survival outcomes (http://kmplot.com/analysis/).

HMGA1 mRNA degradation, which potentially induced cancer cell apoptosis and proliferation inhibition.

YB1 inhibited OXPHOS gene translation

Except oncogene mRNAs, YB1 was reported to preferentially bind with oxidative phosphorylation (OXPHOS) mRNAs and suppressed their recruitment from inactive messenger ribonucleoprotein particles to active polysomes, leading to OXPHOS protein translation inhibition (28). Here, NDUFA9 and SDHB, as critical genes for oxidative phosphorylation, were selected for further analysis. Quantitative real-time RCR results showed that YB1 knockdown had no influence on NDUFA9 and SDHB mRNA expressions (Figure 6A) but significantly upregulated their protein levels (Figure 6B), which offered an explanation for our previous finding that YB1 knockdown increased mitochondrial membrane potential and the cellular ROS level (Figures 3D, E). Simultaneously, starvation treatment enhanced NDUFA9 and SDHB expression in cancer cells, but the total amount of YB1 showed no difference (Figure 6C). RIP assays demonstrated the direct interaction between YB1 and NDUFA9 and SDHB mRNAs, and this interaction was impaired after starvation treatment (Figures 6D, E), indicating the functional transformation of YB1. To exclude the influence of proteasome on YB1-mediated OXPHOS protein expression, breast cancer cells were treated with MG132, an inhibitor of 26S proteasome, to block protein degradation. Western blot results showed that MG132 treatment failed to block YB1-mediated NDUFA9 and SDHB upregulation (Figure 6F). In addition, protein stability assays demonstrated that YB1 silence had no

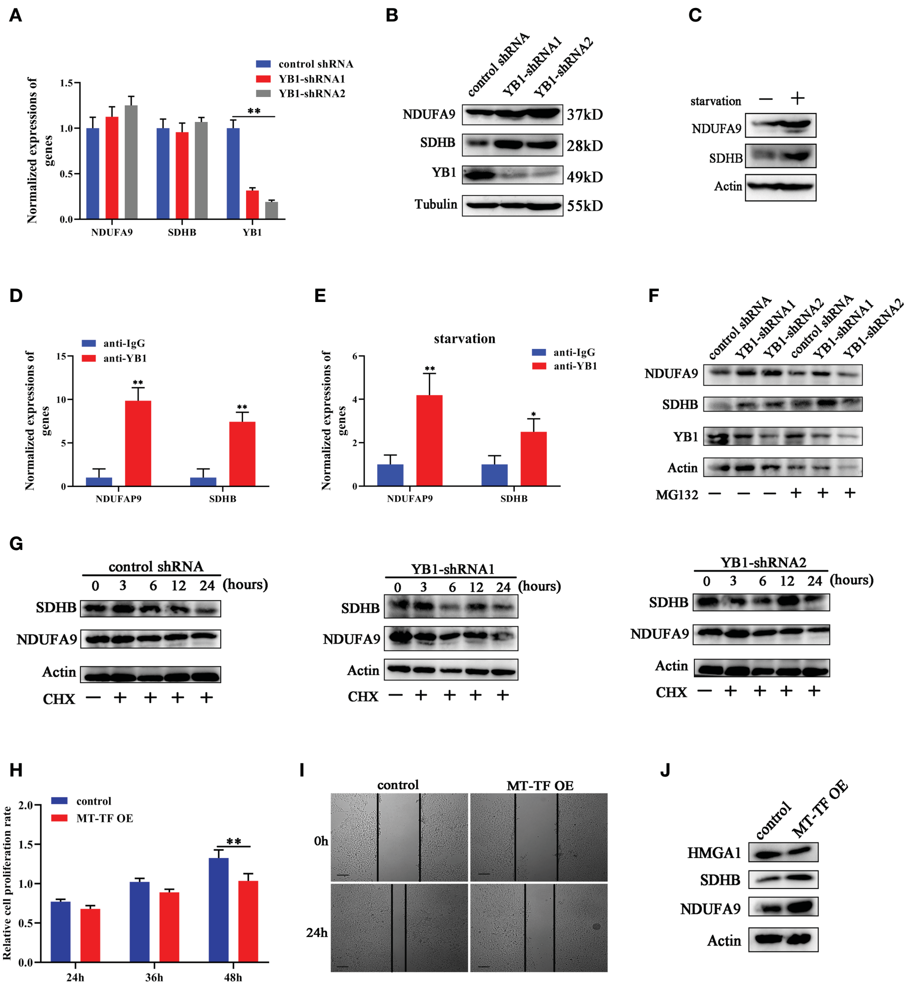

FIGURE 6

YB1 inhibited OXPHOS gene translation. **(A)** The influence of YB1 knockdown on mitochondrial oxidative phosphorylation gene (NDUFA9 and SDHB) expressions at the mRNA level. n = 3, $^{**}p < 0.01$. **(B)** YB1 expression silence enhanced NDUFA9 and SDHB protein expressions through posttranscriptional regulation. **(C)** The influence of starvation on DNUFA9 and SDHB expressions was investigated through Western blot. **(D)** YB1 directly interacted with OXPHOS mRNA. The interaction between YB1 protein and OXPHOS mRNA (NDUFA9 and SDHB) was demonstrated using RIP assay. n = 3, $^{**}p < 0.01$. **(E)** Serum-free starvation impaired YB1 binding ability with OXPHOS mRNAs. n = 3, $^{*}p < 0.05$. **(F)** The protein levels of NDUFA9 and SDHB were investigated in breast cancer cells with or without YB1 depletion. MG132 was used to block the proteasome-mediated protein degradation pathway. **(G)** The protein degradation rates of NDUFA9 and SDHB were investigated. CHX was used to block the elongation phase of eukaryotic translation. **(H)** The influence of MT-TF overexpression (MT-TF OE) on breast cancer proliferation was detected using MTT assay. **(I)** The migration ability of breast cancer was inhibited after MT-TF overexpression. Scale bar, 100 μm. **(J)** The expressions of NDUFA9, SDHB, and HMGA1 were investigated in breast cancer cells transfected with MT-TF.

influence on the degradation ratio of NDUFA9 and SDHB (Figure 6G). All of these data indicated that YB1 regulated OXPHOS-associated protein expression at the posttranscription level in a protease-independent manner, which is in accordance with others' findings that YB1 functions as an inhibitor during OXPHOS gene translation (28).

To explore whether the RNA displacement model is suitable for OXPHOS expression, MT-TF was overexpressed in breast cancer cells through RNA transfection. Compared with the control group, MT-TF overexpression significantly inhibited breast cancer cell proliferation and migration (Figures 6H, I), which is consistent with the results induced by YB1 knockdown. Moreover, Western blot results demonstrated that MT-TF overexpression modestly increased the expression of NDUFA9 and SDHB but downregulated HMGA1 expression (Figure 6J), which indicated the universality of this model. This insignificant difference may be due to the inadequacy of transfected exogenous RNAs or the lack of an RNA secondary structure or modifications.

YB1 promoted tumorigenesis of breast cancer cells

In order to explore the role of YB1 in cancer progression, breast cancer cells with stably silenced YB1 were subcutaneously injected into nude mice, followed by monitoring tumor growth every week for 7 weeks. Our results showed that YB1 knockdown significantly suppressed tumor growth *in vivo* compared with the control group (Figure 7A). After mouse sacrifice, the xenografts were collected and analyzed. Solid xenografted tumors with YB1 depletion showed smaller sizes and lower weights compared with the control group (Figures 7B, C), which revealed the positive role of YB1 in breast cancer progression.

In order to evaluate whether the RNA displacement model participated in regulating YB1-mediated cancer cell inhibition *in vivo*, the xenografts were subjected to immunohistochemical analysis. Compared with the control group, OXPHOS-associated factors (NDUFA9 and SDHB) showed an obvious expression increase in YB1-silenced tumors, but the expression of HMGA1 was decreased significantly (Figure 7D), suggesting the existence of an RNA displacement model in YB1-mediated breast cancer progression. In addition, according to Western blot investigation, LC3 and BCL2 were significantly downregulated in tumors with decreased YB1 (Figure 7E), but not in the control group, consistent with the finding *in vitro*.

Taken the abovementioned results together, we concluded that YB1 maintained cellular autophagy at a moderate level through binding with a lot of mitochondrial oxidative phosphorylation (OXPHOS) gene mRNAs to inhibit mitochondrial activity. Serum removal-mediated starvation increased the leakage of mitochondrial RNA into cytoplasm and YB1 mitochondrial relocation, resulting in YB1-bound RNA displacement. More OXPHOS and oncogene mRNAs were competitively replaced by MT-tRNA and then released from the YB1 complex. The increase of free OXPHOS mRNAs enhanced mitochondrial activity through strengthening protein translation, but the half-life time of free oncogene HMGA1 mRNA was impaired without the protection of YB1. All of these effects contributed to the downstream transformation from autophagy toward apoptosis in breast cancer cells (Figure 7F).

Discussion

Our findings revealed that upregulated YB1 protein maintained cellular native autophagy at a high level through regulating the mTOR signaling pathway to enhance cancer cell tolerance for environmental stress. Loss-of-function experiments showed that YB1 deficiency alleviated cellular autophagy, enhanced mitochondrial oxidative phosphorylation complex protein translation, and thus augmented mitochondrial activity. The mechanism underlying YB1-mediated autophagy may be a result from the binding ability of YB1 with the p110β promoter to regulate its transcription (29). Additionally, it was found that loss of YB1 decreased the mRNA stability of Pink1 and Prkn in brown adipose tissue, two key regulators of mitophagy, leading to reduced protein expression, thereby alleviating autophagy (30). Owing to the uniqueness of different cells or tissues, more effects should be paid attention to elucidate the important role of YB1 in regulating autophagy.

Evidence has demonstrated that RNA-binding proteins could capture mRNA in the nucleus and form mRNPs to suppress transcript translation during nucleus–cytosol transport (31). Here, we found that a set of mitochondrial oxidative phosphorylation complex RNA transcripts, including NDUFA9 and SDHB, were present in the YB1–RNA heterocomplex and depletion of YB1 obviously increased oxidative phosphorylation complex protein translation, concomitant with others' previous work. Through inhibiting mitochondrial functional protein production, YB1 may coordinate with mitochondrial homeostasis between autophagy and self-renewal. On whether YB1 directly interacts with these RNAs and whether other partners are indispensable during this process, some detailed issues have yet to be delineated, which defined a new direction for our next work.

An association between YB1 and transfer RNA fragments has been reported. Under serum starvation or hypoxic conditions, cells usually yield an amount of transfer RNA fragments in a short term and then suppress the stability of multiple oncogenic transcripts in breast cancer cells by displacing their 3′ untranslated regions from the RNA-binding protein YB1 (27). This kind of posttranscription regulation function mainly relied on the recognition of YB1 for the CU box motif enriched in targeted transcripts. Studies related to tRNA-mediated cellular translation suppression had also been reported in other cells and attributed to the disengagement of translational initiation factor EIF4G1 in a YB1-dependent manner (32). Here, our findings revealed that a class of distinct RNAs, mitochondria-derived RNAs, including MT-tRNA and ribosomal RNA, participated in the process of YB1-dependent transcript translation inhibition or RNA degradation regulation. Upon exposure to serum starvation, mitochondria-derived RNAs were accumulated in cytosol and this effect was reinforced especially in

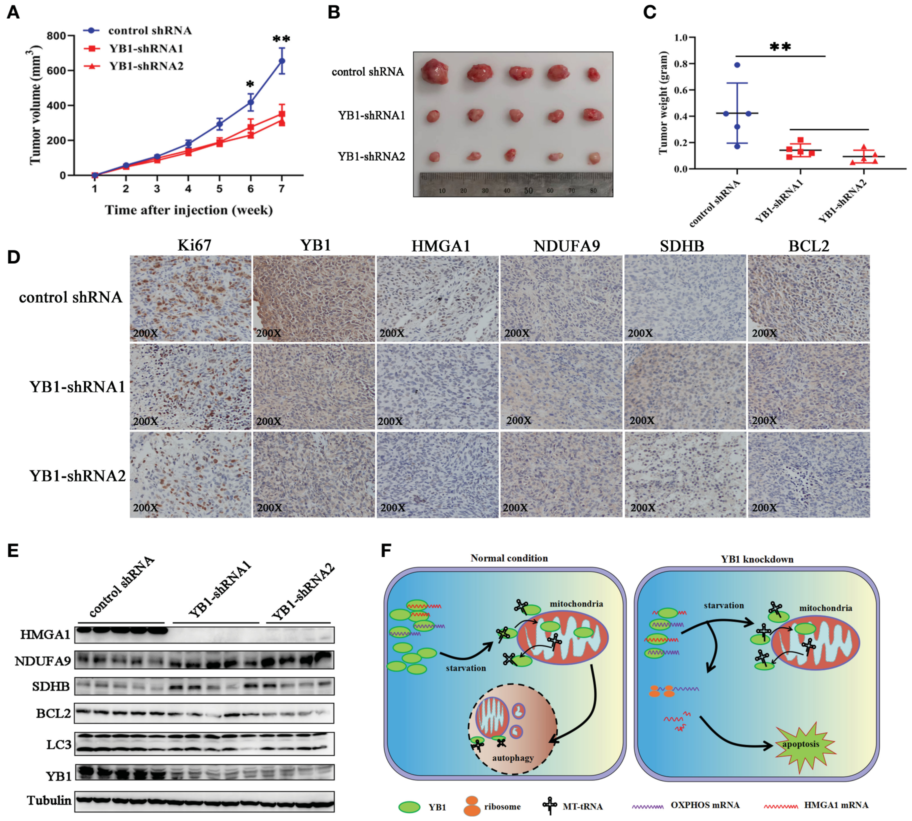

FIGURE 7
YB1 promoted tumorigenesis of breast cancer cells. **(A)** The statistics of xenograft volume in nude mice at different times. Breast cancer cells with different YB1 expression levels were subcutaneously injected into nude mice, and the volumes of tumors were monitored at different times. n = 5, $*p < 0.05$, $**p < 0.01$. **(B)** The representative pictures of solid tumors collected from nude mice. **(C)** Solid tumor weight analysis. n = 5, $**p < 0.01$. **(D)** Immunohistochemical analysis of YB-1-regulated proteins in breast cancer xenografts. Specific antibodies were used to detect each protein (brown), and nuclei were stained with hematoxylin (blue). **(E)** The levels of YB1-regulated proteins in xenografts were investigated through Western blot. **(F)** Proposed working model for the role of starvation-induced YB1-bound RNA replacement by mitochondrial RNA in regulating cell autophagy and apoptosis in breast cancer cells.

YB1-depleted cells. The transport of mitochondrial RNA into cytosol induced by starvation whether depending on specific mechanisms that are in charge of regulating permeabilization of mitochondrial membrane or just from fragmented mitochondrial debris is still unknown. During mitochondrial RNA release, some oncogenic transcripts were dissociated from the YB1 complex and their RNA decay rate was accelerated. However, according to our data regarding mitochondrial oxidative phosphorylation transcripts, YB1 inhibited these mRNA translations, which is contrary to the result of oncogenic transcripts, highlighting the complex and precise regulatory role of YB1 in balancing RNA translation and degradation. Given the extensive base modifications in tRNAs and the “reader” role of YB1 (17), further studies should be performed to decipher the interaction between YB1 and RNA at the single-nucleotide resolution level.

Taken together, we proposed an RNA displacement model in which YB1-bound RNAs were replaced by mitochondria-derived RNA under stress, resulting in targeted transcript release and induced different downstream effects. From a broader perspective, we speculated that a large regulatory network consisting of small ncRNAs and various RNA-binding proteins, not limited to YB1, orchestrated cellular homeostasis in a manner that is completely distinct from the traditional miRNA-mediated broad posttranscription regulation.

Data availability statement

The original contributions presented in the study are included in the article/Supplementary Material. Further inquiries can be directed to the corresponding authors.

Ethics statement

The studies involving human participants were reviewed and approved by The ethics committee of Shandong Cancer Hospital. The patients/participants provided their written informed consent to participate in this study. The animal study was reviewed and approved by The ethics committee of Shandong Cancer Hospital.

Author contributions

All authors contributed to the article and approved the submitted version.

Funding

This work was supported by the Natural Science Foundation of Shandong Province (ZR2021QH336).

Conflict of interest

The authors declare that the research was conducted in the absence of any commercial or financial relationships that could be construed as a potential conflict of interest.

Publisher's note

Supplementary material

The Supplementary Material for this article can be found online at: https://www.frontiersin.org/articles/10.3389/fonc.2023.1145379/full#supplementary-material

References

1. Silva J, Aivio S, Knobel PA, Bailey LJ, Casali A, Vinaixa M, et al. EXD2 governs germ stem cell homeostasis and lifespan by promoting mitoribosome integrity and translation. *Nat Cell Biol* (2018) 20(2):162–74. doi: 10.1038/s41556-017-0016-9

2. Kauppila T, Kauppila J, Larsson NG. Mammalian mitochondria and aging: An update. *Cell Metab* (2017) 25(1):57–71. doi: 10.1016/j.cmet.2016.09.017

3. Zhao Q, Liu J, Deng H, Ma R, Liao JY, Liang H, et al. Targeting mitochondria-located circRNA SCAR alleviates NASH *via* reducing mROS output. *Cell* (2020) 183 (1):76–93.e22. doi: 10.1016/j.cell.2020.08.009

4. Rambold AS, Pearce EL. Mitochondrial dynamics at the interface of immune cell metabolism and function. *Trends Immunol* (2018) 39(1):6–18. doi: 10.1016/j.it.2017.08.006

5. Garcia-Heredia JM, Carnero A. Role of mitochondria in cancer stem cell resistance. *Cells* (2020) 9(7):1693. doi: 10.3390/cells9071693

6. Saha T, Dash C, Jayabalan R, Khiste S, Kulkarni A, Kurmi K, et al. Intercellular nanotubes mediate mitochondrial trafficking between cancer and immune cells. *Nat Nanotechnol* (2022) 17(1):98–106. doi: 10.1038/s41565-021-01000-4

7. Lyabin DN, Eliseeva IA, Ovchinnikov LP. YB-1 protein: functions and regulation. *Wiley Interdiscip Rev RNA* (2014) 5:95–110. doi: 10.1002/wrna.1200

8. Zhang J, Fan JS, Li S, Yang Y, Sun P, Zhu Q, et al. Structural basis of DNA binding to human YB-1 cold shock domain regulated by phosphorylation. *Nucleic Acids Res* (2020) 48(16):9361–71. doi: 10.1093/nar/gkaa619

9. Alkrekshi A, Wang W, Rana PS, Markovic V, Sossey-Alaoui K. A comprehensive review of the functions of YB-1 in cancer stemness, metastasis and drug resistance. *Cell Signal* (2021) 85:110073. doi: 10.1016/j.cellsig.2021.110073

10. Zong WX, Rabinowitz JD, White E. Mitochondria and cancer. *Mol Cell* (2016) 61(5):667–76. doi: 10.1016/j.molcel.2016.02.011

11. Yang F, Chen S, He S, Huo Q, Hu Y, Xie N. YB-1 interplays with ERalpha to regulate the stemness and differentiation of ER-positive breast cancer stem cells. *Theranostics* (2020) 10(8):3816–32. doi: 10.7150/thno.41014

12. Marchesini M, Ogoti Y, Fiorini E, Aktas SA, Nezi L, D'Anca M, et al. ILF2 is a regulator of RNA splicing and DNA damage response in 1q21-amplified multiple myeloma. *Cancer Cell* (2017) 32(1):88–100. doi: 10.1016/j.ccell.2017.05.011

13. Stratford AL, Fry CJ, Desilets C, Davies AH, Cho YY, Li Y, et al. Y-box binding protein-1 serine 102 is a downstream target of p90 ribosomal S6 kinase in basal-like breast cancer cells. *Breast Cancer Res* (2008) 10(6):R99. doi: 10.1186/bcr2202

14. El-Naggar AM, Veinotte CJ, Cheng H, Grunewald TG, Negri GL, Somasekharan SP, et al. Translational activation of HIF1alpha by YB-1 promotes sarcoma metastasis. *Cancer Cell* (2015) 27(5):682–97. doi: 10.1016/j.ccell.2015.04.003

15. Lim JP, Nair S, Shyamasundar S, Chua PJ, Muniasamy U, Matsumoto K, et al. Silencing y-box binding protein-1 inhibits triple-negative breast cancer cell invasiveness *via* regulation of MMP1 and beta-catenin expression. *Cancer Lett* (2019) 452:119–31. doi: 10.1016/j.canlet.2019.03.014

16. Feng M, Xie X, Han G, Zhang T, Li Y, Li Y, et al. YBX1 is required for maintaining myeloid leukemia cell survival by regulating BCL2 stability in an m6A-dependent manner. *Blood* (2021) 138(1):71–85. doi: 10.1182/blood.2020009676

17. Chen X, Li A, Sun BF, Yang Y, Han YN, Yuan X, et al. 5-methylcytosine promotes pathogenesis of bladder cancer through stabilizing mRNAs. *Nat Cell Biol* (2019) 21(8):978–90. doi: 10.1038/s41556-019-0361-y

18. Zou F, Tu R, Duan B, Yang Z, Ping Z, Song X, et al. Drosophila YBX1 homolog YPS promotes ovarian germ line stem cell development by preferentially recognizing 5-methylcytosine RNAs. *Proc Natl Acad Sci U.S.A.* (2020) 117(7):3603–9. doi: 10.1073/pnas.1910862117

19. Gabaldon T. Relative timing of mitochondrial endosymbiosis and the "pre-mitochondrial symbioses" hypothesis. *IUBMB Life* (2018) 70(12):1188–96. doi: 10.1002/iub.1950

20. Yu CH, Davidson S, Harapas CR, Hilton JB, Mlodzianoski MJ, Laohamonthonkul P, et al. TDP-43 triggers mitochondrial DNA release *via* mPTP to activate cGAS/STING in ALS. *Cell* (2020) 183(3):636–649.e18. doi: 10.1016/j.cell.2020.09.020

21. Tang Z, Li C, Kang B, Gao G, Li C, Zhang Z. GEPIA: a web server for cancer and normal gene expression profiling and interactive analyses. *Nucleic Acids Res* (2017) 45 (W1):W98–W102. doi: 10.1093/nar/gkx247

22. Lanczky A, Gyorffy B. Web-based survival analysis tool tailored for medical research (KMplot): Development and implementation. *J Med Internet Res* (2021) 23(7): e27633. doi: 10.2196/27633

23. Bartha A, Gyorffy B. TNMplot.com: A web tool for the comparison of gene expression in normal, tumor and metastatic tissues. *Int J Mol Sci* (2021) 22(5):2622. doi: 10.3390/ijms22052622

24. Park SJ, Yoon BH, Kim SK, Kim SY. GENT2: an updated gene expression database for normal and tumor tissues. *BMC Med Genomics* (2019) 12(Suppl 5):101. doi: 10.1186/s12920-019-0514-7

25. Li T, Fu J, Zeng Z, Cohen D, Li J, Chen Q, et al. TIMER2.0 for analysis of tumor-infiltrating immune cells. *Nucleic Acids Res* (2020) 48(W1):W509–14. doi: 10.1093/nar/gkaa407

26. Waterhouse A, Bertoni M, Bienert S, Studer G, Tauriello G, Gumienny R, et al. SWISS-MODEL: homology modelling of protein structures and complexes. *Nucleic Acids Res* (2018) 46(W1):W296–303. doi: 10.1093/nar/gky427

27. Goodarzi H, Liu X, Nguyen HC, Zhang S, Fish L, Tavazoie SF. Endogenous tRNA-derived fragments suppress breast cancer progression *via* YBX1 displacement. *Cell* (2015) 161(4):790–802. doi: 10.1016/j.cell.2015.02.053

28. Matsumoto S, Uchiumi T, Tanamachi H, Saito T, Yagi M, Takazaki S, et al. Ribonucleoprotein y-box-binding protein-1 regulates mitochondrial oxidative phosphorylation (OXPHOS) protein expression after serum stimulation through binding to OXPHOS mRNA. *Biochem J* (2012) 443(2):573–84. doi: 10.1042/BJ20111728

29. Cui Y, Li F, Xie Q, Zhao S, Guo T, Guo P, et al. YBX1 mediates autophagy by targeting p110beta and decreasing the sensitivity to cisplatin in NSCLC. *Cell Death Dis* (2020) 11(6):476.

30. Wu R, Cao S, Li F, Feng S, Shu G, Wang L, et al. RNA-Binding protein YBX1 promotes brown adipogenesis and thermogenesis *via* PINK1/PRKN-mediated mitophagy. *FASEB J* (2022) 36(3):e22219. doi: 10.1096/fj.202101810RR

31. Qin H, Ni H, Liu Y, Yuan Y, Xi T, Li X, et al. RNA-Binding proteins in tumor progression. *J Hematol Oncol* (2020) 13(1):90. doi: 10.1186/s13045-020-00927-w

32. Ivanov P, Emara MM, Villen J, Gygi SP, Anderson P.. Angiogenin-induced tRNA fragments inhibit translation initiation. *Mol Cell* (2011) 43(4):613–23. doi: 10.1016/j.molcel.2011.06.022

frontiers | Frontiers in Oncology

TYPE Original Research
PUBLISHED 31 March 2023
DOI 10.3389/fonc.2023.1032364

Upregulation of the ferroptosis-related *STEAP3* gene is a specific predictor of poor triple-negative breast cancer patient outcomes

Lifang Yuan[1,2], Jiannan Liu[3], Lei Bao[4], Huajun Qu[3], Jinyu Xiang[3] and Ping Sun[1*]

[1]Department of Oncology, Yantai Yuhuangding Hospital, Shandong University, Yantai, China, [2]Department of Breast Oncology, Huanxing Cancer Hospital, Beijing, China, [3]Department of Oncology, The Affiliated Yantai Yuhuangding Hospital of Qingdao University, Yantai, China, [4]Department of Pathology, The Affiliated Yantai Yuhuangding Hospital of Qingdao University, Yantai, China

Check for updates

OPEN ACCESS

EDITED BY
Cristian Scatena,
University of Pisa, Italy

REVIEWED BY
Hira Lal Goel,
UMass Chan Medical School, United States
Benoit Paquette,
University of Sherbrooke, Canada

*CORRESPONDENCE
Ping Sun
✉ sunping20039@hotmail.com

SPECIALTY SECTION
This article was submitted to Breast Cancer, a section of the journal Frontiers in Oncology

RECEIVED 30 August 2022
ACCEPTED 17 March 2023
PUBLISHED 31 March 2023

CITATION
Yuan L, Liu J, Bao L, Qu H, Xiang J and Sun P (2023) Upregulation of the ferroptosis-related *STEAP3* gene is a specific predictor of poor triple-negative breast cancer patient outcomes. *Front. Oncol.* 13:1032364. doi: 10.3389/fonc.2023.1032364

Objective: This study was designed to assess ferroptosis regulator gene (FRG) expression patterns in patients with TNBC based on data derived from The Cancer Genome Atlas (TCGA). Further, it was utilized to establish a TNBC FRG signature, after which the association between this signature and the tumor immune microenvironment (TIME) composition was assessed, and relevant prognostic factors were explored.

Methods: The TCGA database was used to obtain RNA expression datasets and clinical information about 190 TNBC patients, after which a prognostic TNBC-related FRG signature was established using a least absolute shrinkage and selection operator (LASSO) Cox regression approach. These results were validated with separate data from the Gene Expression Omnibus (GEO). The TNBC-specific prognostic gene was identified *via* this method. The STEAP3 was then validated through Western immunoblotting, immunohistochemical staining, and quantitative real-time polymerase chain reaction (RT-qPCR) analyses of clinical tissue samples and TNBC cell lines. Chemotherapy interactions and predicted drug sensitivity studies were investigated to learn more about the potential clinical relevance of these observations.

Results: These data revealed that 87 FRGs were differentially expressed when comparing TNBC tumors and healthy tissue samples (87/259, 33.59%). Seven of these genes (*CA9, CISD1, STEAP3, HMOX1, DUSP1, TAZ, HBA1*) are significantly related to the overall survival of TNBC patients. Kaplan-Meier analyses and established FRG signatures and nomograms identified *CISD1* and *STEAP3* genes of prognostic relevance. Prognostic Risk Score values were positively correlated with the infiltration of CD4+ T cells ($p = 0.001$) and myeloid dendritic cells ($p = 0.004$). Further evidence showed that *STEAP3* was strongly and specifically associated with TNBC patient OS ($P<0.05$). The results above were confirmed by additional examinations of *STEAP3* expression changes in TNBC patient samples and cell lines. High *STEAP3* levels were negatively correlated with half-maximal inhibitory concentration (IC50) values for GSK1904529A (IGF1R inhibitor), AS601245 (JNK inhibitor), XMD8–85 (Erk5 inhibitor), Gefitinib, Sorafenib, and 5-Fluorouracil ($P < 0.05$) in patients with TNBC based on information derived from the TCGA-TNBC dataset.

Conclusion: In the present study, a novel FRG model was developed and used to forecast the prognosis of TNBC patients accurately. Furthermore, it was discovered that *STEAP3* was highly overexpressed in people with TNBC and associated with overall survival rates, laying the groundwork for the eventually targeted therapy of individuals with this form of cancer.

KEYWORDS

triple-negative breast cancer (TNBC), ferroptosis, prognostic signature, overall survival, *STEAP3*

Introduction

With an anticipated 290,560 new diagnoses and 43,780 related deaths in the United States in 2022 alone, breast cancer is one of the most common cancers in women. Indeed, breast cancer remains the second deadliest malignancy in women (1), and the current estimated annual incidence and mortality rates for this cancer type in China are 45.29 per 100,000 and 10.50 per 100,000, respectively (2, 3). The prognosis for patients with metastatic breast cancer remains poor (4). Thus, emphasizing the disease's continued threat to the health of women around the world despite numerous significant improvements in patient detection and treatment.

Different breast cancer subtypes have been identified based on clinical and morphological characteristics, including inflammatory breast cancer, lobular carcinoma, and ductal carcinoma. TNBC is characterized by the absence of HER-2 (Human epidermal growth factor receptor-2), progesterone receptor (PR), or estrogen receptor (ER) expression on tumor cells (5–7). TNBC tumors do not react to endocrine therapy or anti-HER2 antibody therapy because they lack these receptors, and there are no effective treatments for this breast cancer subtype. The poor prognosis of affected individuals is a result of the lack of efficient treatment choices, the highly invasive aspect of this malignancy, its high rates of recurrence, and a high potential for metastasis (8, 9). Of the different molecular subtypes of breast cancer, TNBC accounts for approximately 12% of cases on average (10), yet it accounts for 40% of breast cancer-related mortality (11, 12). The overall prognosis of TNBC is still unsatisfactory despite the use of treatments such as PARP inhibitors, immune checkpoint inhibitors (ICI), and novel antibody-drug conjugates (ADC) in clinical treatment by targeting specific mutations, proteins, and immune cell types (13–15). Clinically, approximately 70% of TNBC patients respond well to the current treatments and their prognosis is as good as that of the Luminal Breast Cancer subtype. Consequently, our efforts must be oriented to understand why the other 30% of TNBC cases do not respond well to current treatments. Therefore, new, efficient treatments for TNBC patients must be developed.

The iron-dependent cell death process known as ferroptosis is unique from necrosis, apoptosis, and autophagy on a molecular, genetic, and morphological level and is accompanied by substantial lipid peroxidation. Ferroptosis is closely related to many human malignancies (5, 16–18), and a growing understanding of the regulation of ferroptosis within tumor cells suggests that ferroptosis induction may represent an effective treatment strategy (19–22). According to a recent study, the traditional GSH/GPX4, FSP1/DHODH/CoQ10, and GCH1/BH4 pathways are not the only ones that affect ferroptosis activity. The metabolite indole-3-pyruvic acid (in3py), which is produced by the amino acid oxidase interleukin-4-induced-1 (IL4i1), was initially identified as a gene induced in B cells in response to IL-4, suppresses ferroptosis through a radical scavenging mechanism and by orchestrating a gene expression profile that attenuates ferroptosis (23). The therapeutic use of knowledge about ferroptosis may depend on the selective activation or inhibition of these genes in certain tissues, cells, and disease situations (24). Jingjing Du et al. also found that Shuganning (SGNI), a Chinese patent medicine, can selectively inhibit the proliferation of TNBC cells *in vitro* and *in vivo* by inducing ferroptosis (9). In addition, some studies have found that certain genes in TNBC cells regulate ferroptosis activity (25, 26). Moreover, the regulation of ferroptosis and the association between ferroptosis genes and prognostic effects in TNBC remains unknown.

The current work was designed to fill this knowledge gap by analyzing the patterns of ferroptosis regulator gene (FRG) expression in TNBC utilizing information from TCGA database. The LASSO Cox regression model was then used with identified DE-FRGs to establish a TNBC-related FRG signature. Furthermore, the association between this signature and the TIME was defined, and the significance of this signature was confirmed in an independent patient cohort from the GEO. The expression of core FRGs in TNBC patient clinical samples and cell lines was subsequently analyzed to validate and expand upon these results. The workflow of the study is shown in Figure 1.

Materials and methods

Data sources

RNA-sequencing (RNA-seq) data and clinical information of 190 TNBC tissue samples (“ER- AND PE- AND HER2-”) and 572 normal

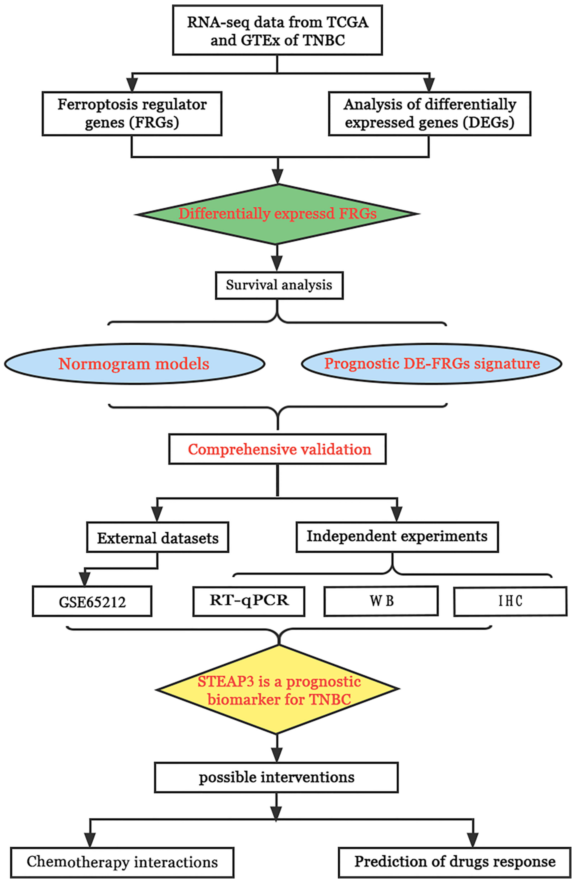

FIGURE 1
The schematic representation of the study workflow.

tissue samples (113 in TCGA, 459 in GTEx) were retrieved from the TCGA (https://portal.gdc.com) and GTEx (https://commonfund.nih.gov/gtex) databases. Moreover, transcriptomic expression data from the external GSE65212 dataset (n_{TNBC}=41, $n_{control}$=11) were downloaded from the GEO database. Table 1 compiles baseline data for TNBC patients included in the present investigation.

A total of 259 genes were defined as FRGs as per the FerrDb Version 2 (http://www.zhounan.org/ferrdb/). These FRGs were divided into drivers, suppressors, and markers. After excluding duplicate FRGs from these categories, 259 FRGs were used for the subsequent analyses.

False discovery rate (FDR)< 0.05 and |Log$_2$ (Fold Change)| > 2 were used as a criterion for differential expression, and DE-FRGs were found using the R limma program. These analyses were carried out using R (v 4.0.3, 2020).

Survival analyses

Using the R “survival” and “survminer” packages the overall survival (OS) of TNBC patients expressing low or high levels of particular DE-FRGs of interest was evaluated using a Kaplan-Meier procedure. Univariate and multivariate Cox regression analyses were used to examine the utility of DE-FRGs as predictors of patient OS, with data being compared with hazard ratios (HRs) and 95% confidence intervals (CIs) and log-rank tests, with $P< 0.05$ as the significance threshold.

Nomogram development and validation

A prognostic Nomogram capable of predicting the 1-, 3-, and 5-year OS of patients in the TCGA-TNBC cohort was developed by initially identifying prognostic factors through Cox analyses. Age, pTstage, pNstage, pMstage were included into the Cox regression analyses. The other clinical variables were excluded due to their missing values. Concordance index (C-index) values ranging from 0.5 (poor) to 1.0 (perfect) were used to evaluate the performance of the resulting Nomogram. A calibration plot was further used to validate the accuracy of the Nomogram using the “rms” and “cmprsk” R packages, with $P< 0.05$ as the significance threshold.

Establishment of a prognostic DE-FRG signature for TNBC

The effectiveness of DE-FRGs as potential prognostic biomarkers in TNBC patients was evaluated using a LASSO Cox

TABLE 1 The baseline clinical characteristics of the TNBC patients from TCGA used in this study.

Variables		N(%)
Survival tatus	Alive	165(86.84)
	Dead	25(13.16)
Age (Mean ± SD)		55.6±12.5
Gender	FEMALE	190(100.00)
Race	AMERICAN INDIAN	1(0.53)
	ASIAN	16(8.42)
	BLACK	57(30.00)
	WHITE	108(56.84)
	Unknown	8(4.17)
T	T1-T2	166(87.37)
	T3-T4	23(12.11)
	Unknown	1(0.53)
N	N0	115(60.53)
	N1	47(24.74)
	N2	16(8.42)
	N3	10(5.26)
	Unknown	2(1.05)
M	M0	166(87.37)
	M1	1(0.53)
	Unknown	23(12.10)
Stge	I	31(16.32)
	II	121(63.68)
	III	33(17.37)
	Unknown	5(2.63)
Chemotherapy	Chemotherapy	114(60.00)
	Other	76(40.00)

analysis, and an ideal predictive risk signature model was created. The penalty parameter (λ) was determined using a minimum of 10-fold cross-validation. Analyses were conducted using the R survival package. Risk Score values were calculated based on the expression of all prognostic DE-FRGs included in this signature and the corresponding coefficient values using the following formula:

$$Risk \ \ score = \sum_{i=1}^{N} (Exp_i \times Coe_i)$$

Where 'Expi' corresponds to relative DE-FRG expression in this signature for patient 'i' and 'Coefi' is the Cox coefficient for DE-FRG$_i$.

Optimal risk score cut-off values for the established DE-FRG signature were established with the "maxstat" package, with the minimum number of sample groups being > 25% and the maximum number being< 75%. Patients were divided into low- and high-risk groups based on these criteria. Log-rank tests and the "survfit" package were used to assess differences in prognostic outcomes between these groups.

The relationship between the established DE-FRG signature and levels of immune cell infiltration (B cells, CD4+ T cells, CD8+ T cells, neutrophils, macrophages, and dendritic cells) was examined with the Tumor Immune Estimation Resource database (TIMER, https://cistrome.shinyapps.io/timer/)

Identification of prognostic FRGs in TNBC

The primary prognostic FRG predictive of TNBC patient OS was discovered using the DE-FRG signature and Nomogram models used in this study as *STEAP3*. Because of this, *STEAP3* was the main focus of later functional and validation analyses.

Prediction of chemotherapeutic drug responses

A publicly available pharmacogenomics database (GDSC, https://www.cancerrxgene.org/) was used to predict the responses of individual TNBC samples to 7 different chemotherapeutic drugs (5-Fluorouracil, Cisplatin, GSK1904529A, AS601245, XMD8-85, Gefitinib, and Sorafenib). The R "pRRophetic" package was used for all studies, and the half-maximal inhibitory concentration (IC50) values were determined using a ridge regression method. Using the GDSC training set, 10-fold cross-validation was used to evaluate the predictive accuracy. Mean values were supplied for any duplicate gene names in the used datasets. In the datasets used, mean values were presented for any occurrences of duplication gene names. The "combat" and "allSolidTumours" packages were used to remove batch effects. All analyses were carried out in R 4.0.3 and a website tool.

Cell culture and sample collection

The control MCF-10A human breast cell line, the MDA-MB-231, BT-549, and MDA-MB-468 TNBC cell lines, and the MCF-7, T-47D, BT-474 non-TNBC cell lines (Procell Life Science&Technology Co.,Ltd.Wuhan,China) were cultured in DMEM (Sparkjade, Shandong, China) containing 10% fetal bovine serum (FBS, PAN, Germany) and 1% penicillin-streptomycin in a humidified 37°C 5% CO_2 incubator. Furthermore, 6 TNBC patient tissue samples were acquired from patients treated at The Department of Oncology of The Affiliated Yantai Yuhuangding Hospital of Qingdao University, China. All experiments were performed three times. Yantai Yuhuangding Hospital's Institutional Review Board approved the trial, and all patients provided informed consent.

RT-qPCR

Following the manufacturer's instructions, RNA was extracted from cells using Trizol (Sparkjade, Shandong, China), and 0.5 μg of

RNA per sample was then used to create cDNA using the SPARK script II RT Plus Kit (Sparkjade, Shandong, China). SYBR Green qPCR Mix kit with ROX (Sparkjade, Shandong, China) was subsequently used for qPCR analyses, and relative gene expression was assessed *via* the $2^{-\Delta\Delta CT}$ method (27). GAPDH served as a normalization control. All samples were analyzed in triplicate, and experiments were independently repeated three times. Utilized primers were as follows: *STEAP3* (Forward: 5'- CTGGCAGTCAAGCAGGTCTTG -3'; Reverse: 5'- TTGAGCGAGTTTGCAATGGA -3'); *GAPDH* (Forward: 5'CAT GTTCGTCATGGGTGTGAA-3'; Reverse: 5'-GGCATGGACTGTGG TCATGAG-3').

Western immunoblotting

After lysing tissue and cell samples using RIPA Lysis buffer supplemented with phosphatase inhibitors, the protein concentrations were determined using a BCA assay kit. Equal protein amounts were then separated *via* 12.5% SDS-PAGE, transferred onto PVDF blots, and incubated with rabbit anti-*STEAP3* (#55240,1:1000, Bioss, Beijing, China) or mouse anti-GAPDH (1:3000, Affinity, Shanghai, China) overnight at 4°C. Blots were then probed for 1 h with an HRP-linked secondary antibody (1:10,000, Affinity, Shanghai, China) at room temperature, after which enhanced chemiluminescence detection of protein bands was performed. ImageJ was used for densitometric analyses. GAPDH served as a loading control.

Immunohistochemical staining

From patients who had given informed consent, a total of 35 breast tissue samples, including 23 control and TNBC, 12 control and non-TNBC ($n_{\text{Luminal A}}=3$, $n_{\text{Luminal B}}=5$, $n_{\text{Her2-enriched}}=4$) were taken for IHC staining. The 4 mm tissue sections were mounted on glass slides, deparaffinized with xylene, rehydrated with an ethanol gradient, and then heated to a high temperature for antigen retrieval. After cooling and washing, samples were treated with 3% H_2O_2 to quench endogenous peroxidase activity. Following three rinses with PBS, samples were blocked for 10 min in calf serum, followed by overnight incubation with polyclonal rabbit anti-STEAP3 (#55240, 1:200, Bioss, Beijing, China) at 4°C. A suitable primary antibody was used to probe samples for 30 to 40 minutes at room temperature. Sections were then dried and photographed under a light microscope. Two pathologists blinded to sample sources analyzed all IHC staining results, and staining intensity was assessed semi-quantitatively.

Statistical analyses

Data are reported as means ± standard errors of the means ($\bar{x} \pm SEM$), and were compared using SPSS 25.0 *via* two-tailed Student's t-tests or non-parametric tests when normally and non-normally distributed, respectively. The significance threshold for these analyses was $\alpha = 0.05$.

Results

TNBC-related FRG identification

The current analysis comprised 259 previously constituted FRGs in total. When comparing TNBC tumors and healthy tissue samples (87/259, 33.59%), 87 of them were discovered to be differentially expressed (FDR< 0.05, FC > 2) (Figure 2).

Identification and assessment of prognostic TNBC-associated FRGs

Of the 87 identified DE-FRGs related to TNBC, 7 were significantly correlated with patient OS in Kaplan-Meier analyses (*CA9, CISD1, STEAP3, HMOX1, DUSP1, TAZ, HBA1*). Forest plots indicated that *CISD1* and *STEAP3* were associated with the highest level of risk for TNBC patients, as they exhibited HRs > 1 in univariate and multivariate Cox regression analyses (P< 0.05) (Figures 3A, B). These results were then used to establish a nomogram incorporating four factors associated with TNBC patient prognosis (*CISD1*, *STEAP3*, pTstage, pNstage). In this model, points were assigned for each risk factor and then summed to produce an overall value, with higher total points corresponding to worse patient OS. The C-index for this model was 0.87 (95% CI: 0.82-0.93; $P = 5.46\times10^{-42}$), and a calibration plot confirmed that this Nomogram exhibited satisfactory utility for use in clinical practice (Figures 3C, D). The R 'maxstat' package was next employed to calculate optimal Risk Score cut-off values as detailed in the Materials and Methods section, ultimately defining an ideal Risk Score threshold of 0.9395. The prognosis of the patients in these groups was compared using log-rank tests using OS values, which were used to stratify TNBC patients into two groups based on whether they were above or below this cut-off value. These analyses indicated that patients in the high-Risk Score cohort exhibited a shorter OS than patients in the low-Risk Score cohort ($P = 4.2\times10^{-6}$, Figure 3E).

Establishment of a TNBC ferroptosis-related prognostic gene signature

The expression of the 87 DE-FRGs discovered above was then used to create a prediction model using a LASSO Cox regression technique. Based on the expression of particular genes (identified by gene name), the Risk Score for this model was calculated as follows: Risk score=(-0.0863) × *HELLS* + (-0.0361) × *CA9* + (0.4763) × *CISD1* + (0.3359) × *MTDH* + (-0.0291) × *PSAT1* + (-0.1691) × *ATG5* + (-0.0738) × *CEBPG* + (-0.0423) × *SLC2A6* + (-0.0698) × *GCH1* + (0.3107) × *STEAP3* + (0.0688) × *HMOX1* + (-0.1375) × *TFAP2C* + (0.0344) × *PROM2* + (-0.318) × *SLC1A4* + (-0.0162) × *GABARAPL1* + (0.4724) × *HIC1* ($\lambda_{\min}=0.0296$) (Figures 4A, B). Patients from the TCGA-TNBC cohort were stratified into low-risk and high-risk cohorts (n=95 each) based on median Risk Score

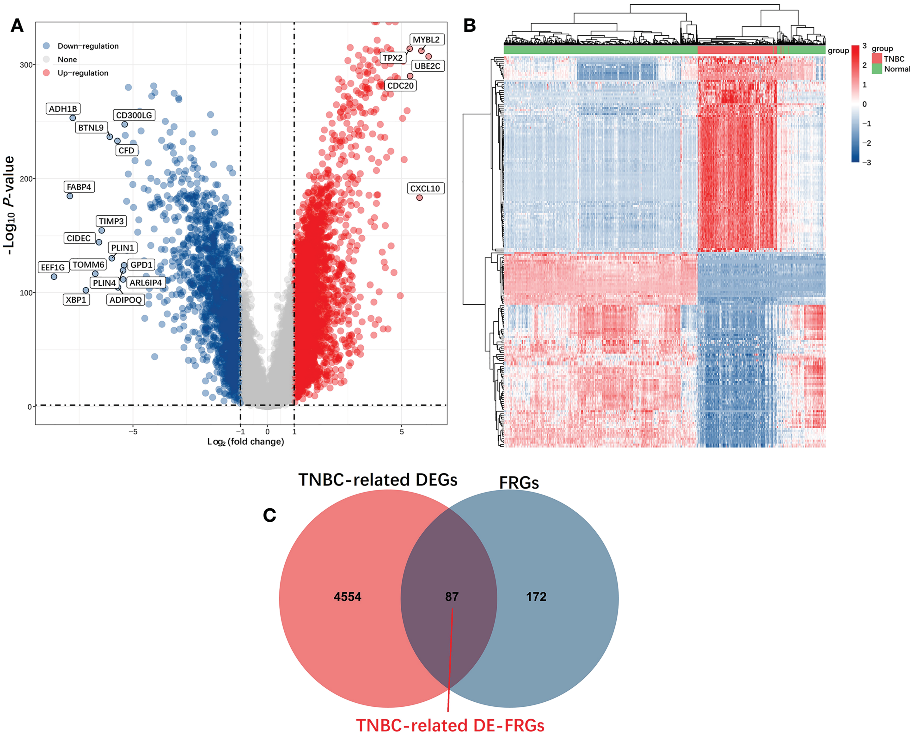

FIGURE 2
Identification of TNBC-related DE-FRGs in the TCGA database. DE-FRGs that were differentially expressed FRGs between TNBC tumors and healthy tissues (FDR < 0.05, |Log2 (Fold Change)| > 2) were presented in the form of Volcano plots **(A)**, in which blue and red dots respectively correspond to up-regulated and downregulated DE-FRGs; Heat maps **(B)**, in which each dot and its color (Red is high-expression, blue is low-expression) indicate the expression value of each DE-FRGs in different samples, the greater the expression level, the darker the color. **(C)** Venn diagrams were used to identify TNBC-associated FRGs.

values computed with this model (Figures 4C–F). Kaplan-Meier analyses indicated that the OS of high-risk patients was significantly worse than that of low-risk patients ($P = 0.00157$) (Figure 4D). AUC values of 0.945, 0.900, and 0.851 at 1, 3, and 5 years, respectively, from time-dependent ROC curve assessments of the predictive utility of this model, further confirm its good utility as a predictor of TNBC patient OS (Figure 4G).

Additionally, the TIMER database used correlation studies of risk scores and immune cell infiltration levels to investigate the clinical significance of this signature in TNBC patients (Figure 5). The results of this analysis indicated that these prognostic Risk Score values were positively correlated with the infiltration of CD4+ T cells (P = 0.001, Figure 5B) and myeloid dendritic cells (P = 0.004, Figure 5F).

Overall survival analyses

The nomogram and risk signature models established the above-identified *CISD1* and *STEAP3* predictors of TNBC patient outcomes. Accordingly, Kaplan-Meier analyses were performed for these two genes in breast cancer (BRCA) and TNBC patients. While *CISD1* expression was significantly associated with the OS of both BRCA and TNBC patients ($P<0.05$), *STEAP3* expression was specifically associated with TNBC patient OS ($P<0.05$) (Figure 6).

Validation of *STEAP3* expression in an independent TNBC patient cohort

For external validation, the GSE65212 dataset was retrieved from the GEO database to verify the differential expression of *STEAP3* in TNBC in a different patient cohort. Compared to healthy control samples, this dataset's analyses revealed that *STEAP3* was significantly up-regulated in TNBC patients (P< 0.05, Figure 7).

Analyses of *STEAP3* expression in clinical samples and cell lines

Subsequently, *STEAP3* mRNA levels were determined using RT-qPCR in the control MCF-10A human breast cell line and in the MDA-MB-231, MDA-MB-468, and BT-549 TNBC cell lines to validate the findings mentioned above (Figure 8A). These analyses revealed significantly increased *STEAP3* expression in all three TNBC cell lines relative to MCF-10A cell lines, consistent with the above bioinformatics analyses. In contrast, no significant *STEAP3* expression was observed in the non-TNBC MCF-7, T-47D, and BT-474 cell lines relative to MCF-10A cells (Figure S1). *STEAP3* protein levels were also significantly increased in MDA-MB-468 and MDA-MB-231 cells relative to MCF-10A cells, with comparable findings in 6 pairs of matched TNBC patient

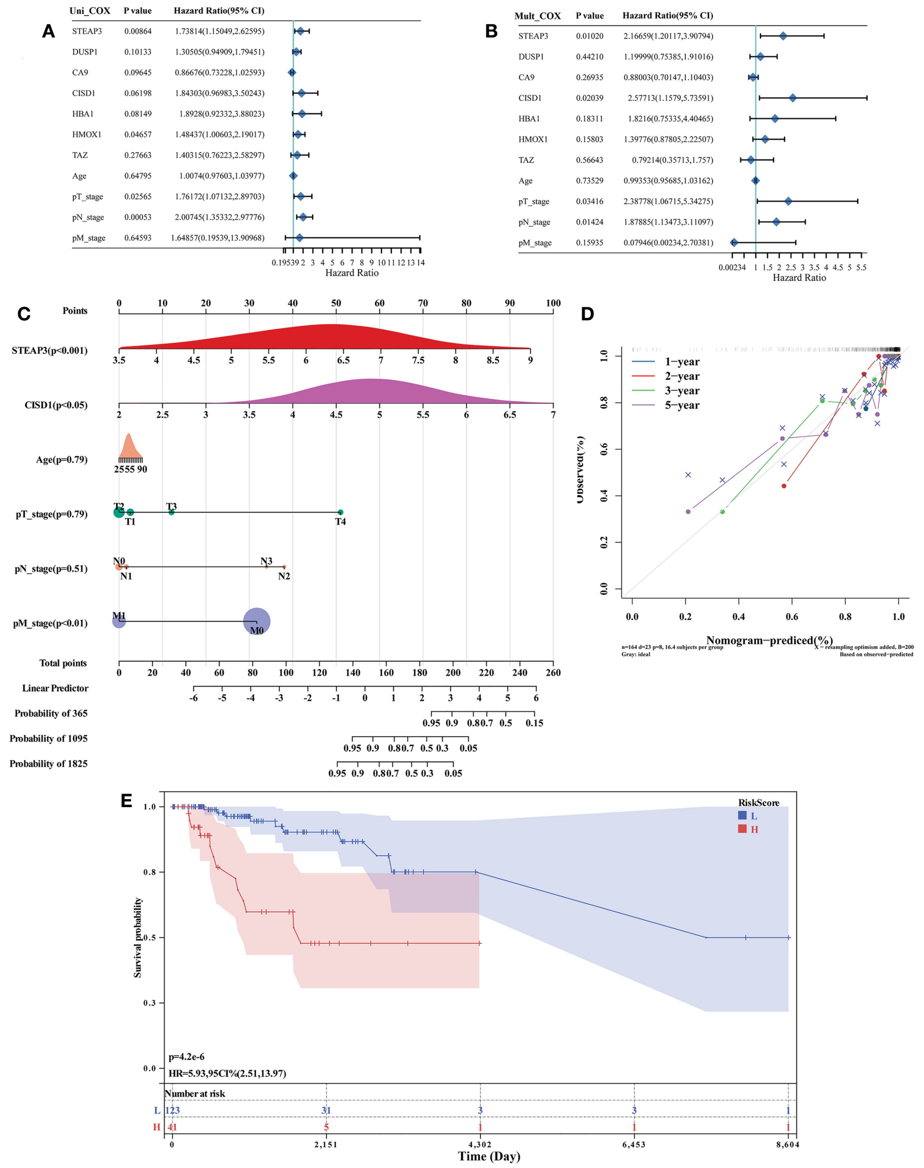

FIGURE 3
Identification and assessment of prognostic TNBC-associated FRGs. **(A, B)** Forest plot-based identification of TNBC patient risk factors identified through univariate **(A)** and multivariate **(B)** Cox regression analyses. **(C)** A nomogram was established based on multivariate Cox regression analysis results. **(D)** Calibration plot for the established Nomogram. **(E)** Evaluation of the developed Nomogram based on Kaplan-Meier OS curves.

tissue samples (Figures 8B, C). And no significant *STEAP3* expression was observed in the non-TNBC MCF-7 and BT-474 cell lines relative to MCF-10A cells (Figure S2). IHC staining was additionally used to assess *STEAP3* protein levels in Normal vs TNBC, Normal vs non-TNBC and TNBC vs non-TNBC, revealing significantly increased *STEAP3* expression in 23 TNBC tumor tissue samples relative to matched paracancerous samples but no increase *STEAP3* expression was observed in the non-TNBC and its control group. And *STEAP3* expression in TNBC was significantly higher than non-TNBC (Figures 8D, E).These findings show that, compared to relevant control samples, TNBC tumor cells and tissue exhibit a considerable up-regulation of *STEAP3* at the mRNA and protein levels.

Correlations between TNBC patient OS, *STEAP3* expression, and other clinical parameters

A multivariate logistic regression approach was next used to examine the relationship between *STEAP3* and TNBC patient OS using a multivariate logistic regression approach. These analyses revealed increased *STEAP3* levels as an independent risk factor associated with the OS of patients with TNBC (OR=5.410, 95%CI: 2.040-14.348). Chemotherapy and *STEAP3* interacted with TNBC patient prognosis (OR=0.482, 95%CI: 0.339-0.686). These findings demonstrated that high levels of *STEAP3* expression had a detrimental effect on TNBC patient OS, but chemotherapeutic therapy was sufficient to reverse this effect (Table 2).

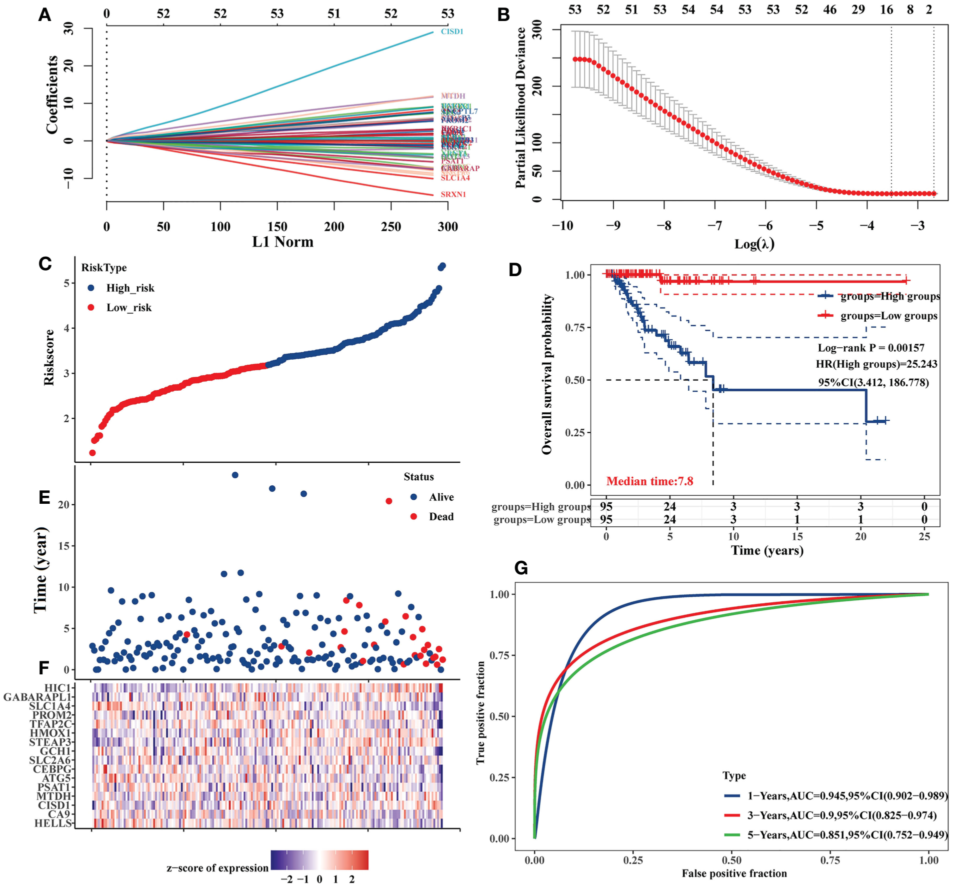

FIGURE 4
Development of an 87 DE-FRG-based prognostic risk signature in the TCGA-TNBC cohort. **(A)** LASSO coefficient profiles for 87 DE-FRGs. **(B)** LASSO regression analyses with 10-fold cross-validation yielded 16 prognostic DE-FRGs based on a minimum λ value. **(C, E)** OS distributions, OS status, and risk scores for patients in the TCGA-TNBC cohort. **(D)** Kaplan-Meier curves corresponding to the OS of TCGA-TNBC patients stratified into low- and high-risk groups. **(F)** Z-scores corresponding to the expression of the 16 prognostic DE-FRGs included in the established risk signature. **(G)** AUC values for time-dependent ROC curves were employed to assess the predictive utility of prognostic signature-derived risk scores.

STEAP3 expression levels predict TNBC patient responses to chemotherapeutic treatment

While *STEAP3* expression levels were not related to cisplatin sensitivity (P=0.33), they were significantly negatively correlated with the sensitivity of patients in the TCGA-TNBC cohort to 5-Fluorouracil, GSK1904529A (IGF1R inhibitor), AS601245 (JNK inhibitor), XMD8–85 (Erk5 inhibitor), Gefitinib, and Sorafenib ($P < 0.01$, Figures 9A–G). The expression levels of *STEAP3* and the sensitivity of Sorafenib in patient groups with low and high expression and healthy controls were also evaluated. The IC50 values between the high and low expression groups differed significantly. However, there was no discernible difference in these values between the low expression and healthy control sample groups (Figure 9H). These findings imply that *STEAP3* expression in TNBC patients may be useful as a predictor of patient responses to a variety of small molecule medications and pathway inhibitors.

Discussion

TNBC cases are account for 15-20% of all breast cancer patients yet are associated with higher recurrence and metastasis rates than other subtypes positive for these receptors, with the poorest corresponding patient prognosis in clinical settings (28, 29). However, the genetic variables that cause TNBC recurrence remain unknown. Efforts to explain the molecular aetiology of TNBC formation, progression, chemoresistance, and recurrence can potentially aid drug development efforts.

Ferroptosis is iron-dependent cell death independent of apoptosis, necroptosis, and autophagy-related cell death (16, 30). Mechanistically, ferroptosis death occurs due to severe ROS-induced lipid peroxidation within cells and iron overload

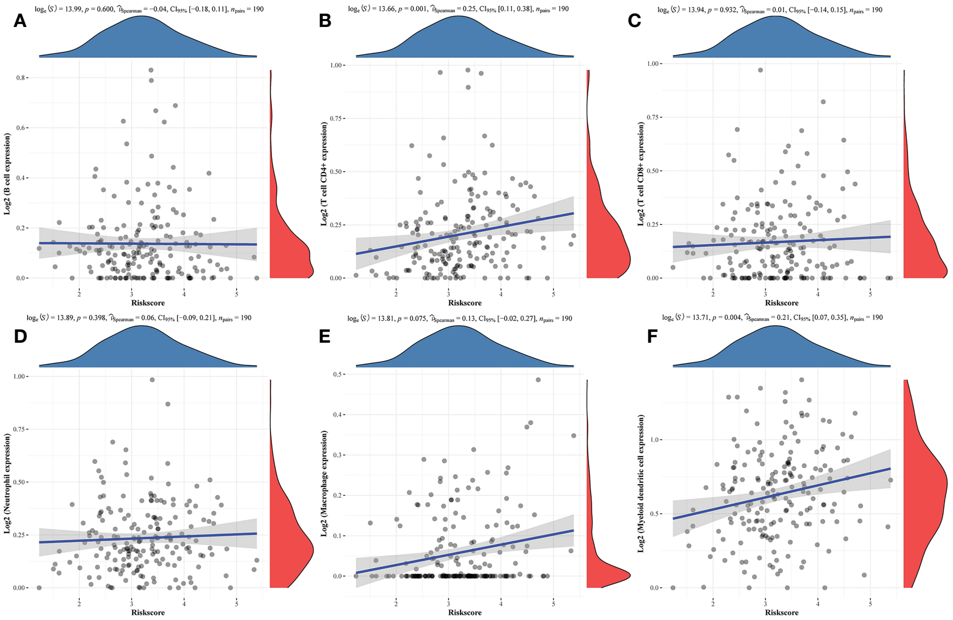

FIGURE 5
Correlations between prognostic risk score values and immune cell infiltration. **(A-F)** Correlations between predictive risk scores and the six indicated immune cell types.

(30), which is increasingly well-studied in many human diseases in recent years, including in TNBC (31, 32). However, this ferroptosis process remains extremely complex and is regulated by a diverse of biomolecular intermediaries and metabolites such that the precise mechanisms driving ferroptosis remain incompletely understood.

STEAP3 encodes a multi-pass membrane metalloreductase that serves as an iron transporter capable of reducing Fe^{3+} and Cu^{2+} cations. Mechanistically, STEAP3 may regulate downstream p53 responses and apoptotic cell death. Deficient *STEAP3* expression can contribute to anaemia. Several alternative splice variants of *STEAP3* exist. The findings of this study reveal that *STEAP3* overexpression is associated with worse OS outcomes in TNBC patients, possibly due to reduced $Fe3^{+}$ transport in these patients. *STEAP3* has previously been shown to play a role in a range of malignant solid tumor types (33–36), yet its role in TNBC has yet to

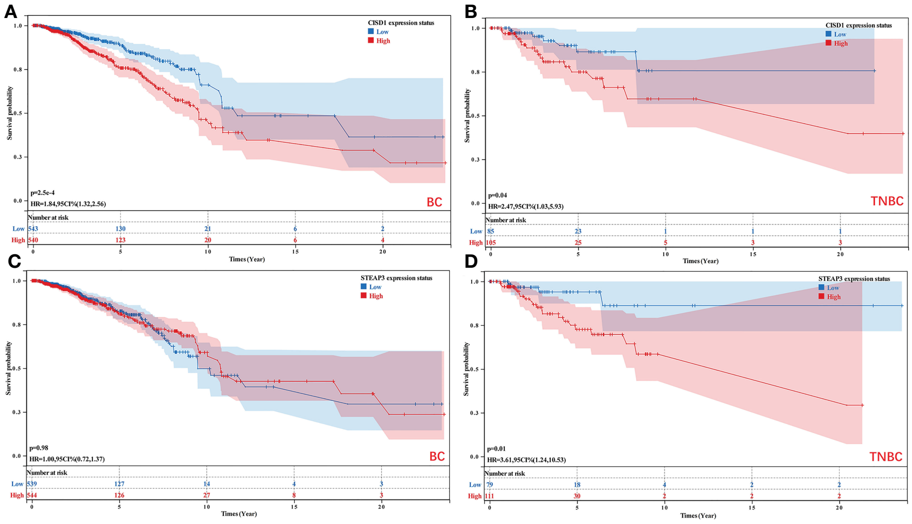

FIGURE 6
Analyses of the relationship between *CISD1* and *STEAP3* expression and the survival of BRCA and TNBC patients. **(A, B)** The relationship between the expression of *CISD1* and the OS of BC (P<0.05) and TNBC patients (P<0.05). **(C, D)** The relationship between the expression of *STEAP3* and the OS of BC (P>0.05) and TNBC patients (P<0.05).

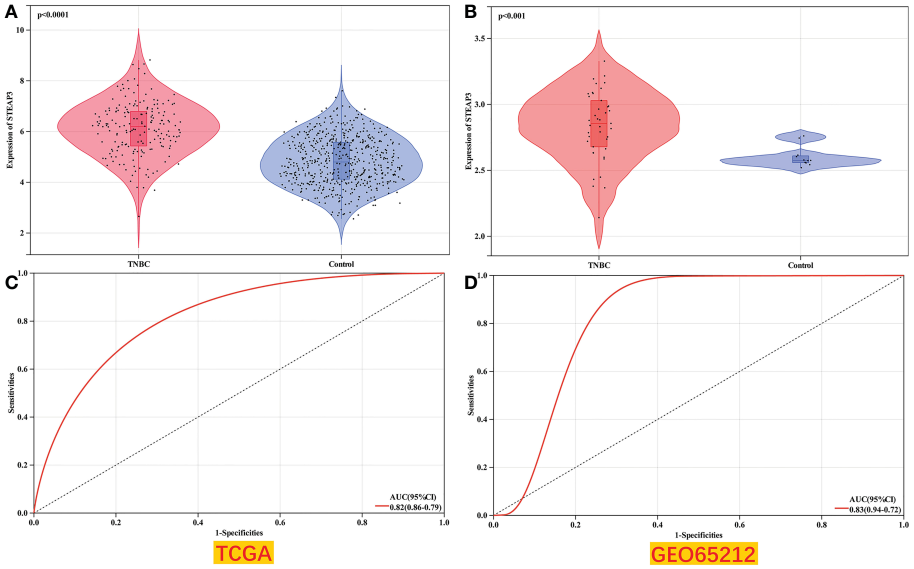

FIGURE 7
Validation of TNBC patient *STEAP3* expression levels in GEO datasets. **(A, B)** *STEAP3* expression levels were compared between TNBC and normal tissue samples in the selected TCGA (*P*<0.0001) and GEO (*P*<0.001) datasets. **(C, D)** AUC analyses for the TCGA and GEO datasets.

be established. While *STEAP3* was unrelated to any improvement in overall breast cancer patient OS, other studies have found a relationship between downregulation of the related *STEAP1*, *STEAP2*, and *STEAP4* proteins and improved outcomes (37). It was first discovered that TNBC had significantly higher levels of *STEAP3* expression, which was associated with a bad prognosis for the patient. Importantly, independent of the examined TCGA and GEO datasets, these changes in expression were verified at the mRNA and protein levels using TNBC cell lines and clinical samples. However, *STEAP3* expression in non-TNBC cell lines, non-TNBC tissue and overall breast cancer patient cohorts indicated that this gene is not up-regulated or linked to the OS of these patients (Figures S1–S3, 8D, E). As a result, *STEAP3* overexpression may represent a TNBC cell-specific biomarker. These studies confirmed the proposed predictive risk signature model for TNBC while indicating that *STEAP3* overexpression is related to a lower TNBC patient survival rate.

Further analyses were performed to conduct a cursory exploration of the mechanisms whereby *STEAP3* may influence TNBC patient OS based on TIME composition, chemotherapy interactions, and drug sensitivity profiles. Breast cancer is generally considered a "cold tumor" with low immunogenicity compared to melanoma, renal cancer and lung cancer. Although the results of the IMpassion130 and KEYNOTE-522 studies show that immunotherapy can significantly affect TNBC patients, the overall improvement in their prognosis remains suboptimal following treatment (38, 39). Studies have shown that dentritic cell and CD4+T cell are involved in tumor progression (40, 41). In this analysis, prognostic Risk Scores were also positively correlated with CD4+ T cells and myeloid dendritic cell infiltration, suggesting that these prognostic risks are may related to tumor immune regulation.

Understanding the mechanisms that cause ferroptosis better may open up new treatment options for TNBC and other disorders without effective therapy options. A possible involvement for ferroptosis cell death in the beginning and progression of this cancer type is suggested by the differential expression of 87 FRGs in TNBC. These included 29 (33.33%) TNBC suppressors, 25 (28.74%) TNBC drivers, and 42 (48.28%) TNBC markers, suggesting that ferroptosis plays diverse roles in the regulation of TNBC and underscoring the importance of further work clarifying the particular mechanisms underlying the interplay between this form of cell death and this deadly disease. At present, reliable inducers of ferroptosis remain an active area of research and drug development interest owing to the complexity of this process. These drugs may target the transporters and enzymes necessary for iron, amino acid, and lipid metabolism, as well as redox balance (1, 32). As a result, ferroptosis holds considerable potential in treating cancer cells resistant to apoptosis in future.

STEAP3 expression and chemotherapeutic treatment affect TNBC patient outcomes, suggesting that chemotherapy can reverse the adverse impacts of high levels of *STEAP3* expression on TNBC patient OS. Therefore, these TNBC patients may constitute significant high-priority candidates for chemotherapy treatment. As an alternative to standard cytotoxic chemotherapeutic treatments, there is an urgent need to develop effective drugs to treat TNBC. In this study, it was predicted that TNBC patients expressing higher levels of *STEAP3* would be more sensitive to a variety of small molecule pathway inhibitor drugs targeting the IGF1R, JNK, ERK5, EGF, and EGFR pathways, with Sorafenib sensitivity being particularly pronounced as a function of *STEAP3* expression. Prior *in vitro* work has shown that Gefitinib-based EGFR blockade may be therapeutically beneficial in TNBC patients. Combining Gefitinib

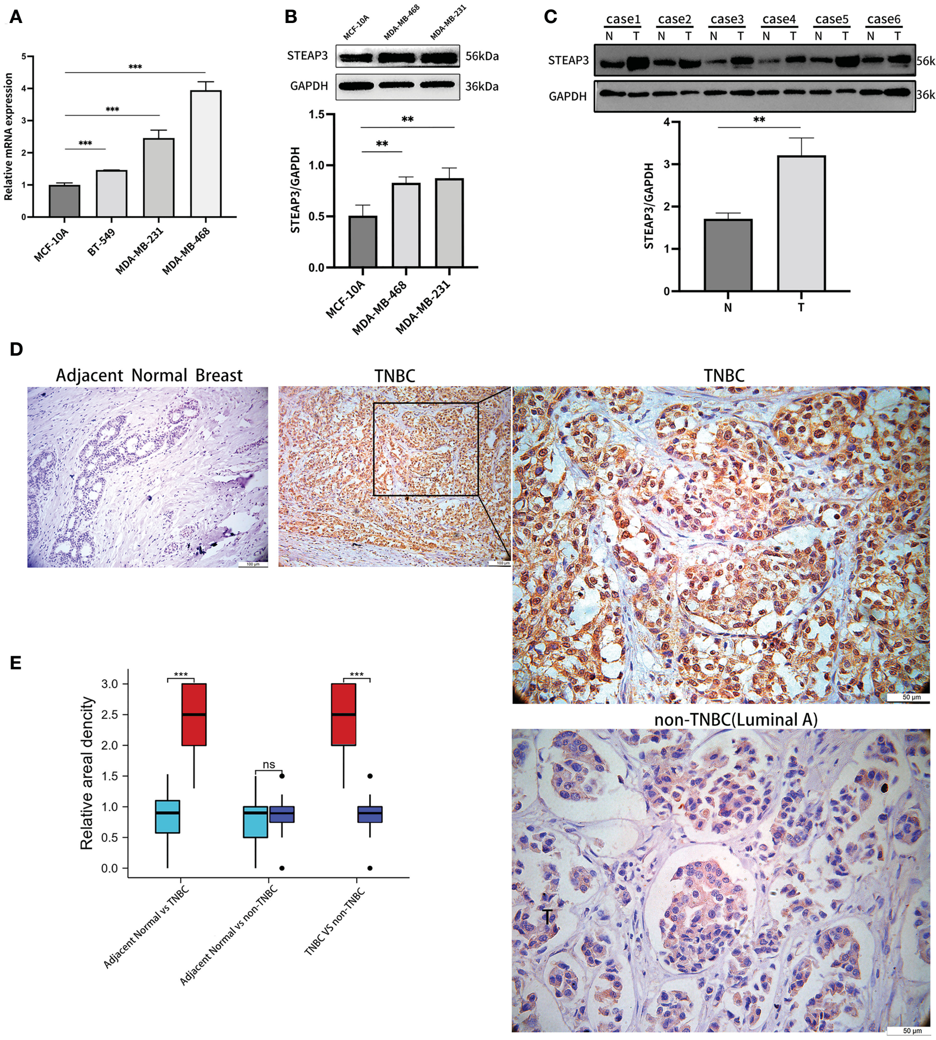

FIGURE 8
Validation of *STEAP3* expression in breast cancer cell lines and tissue samples. **(A)** *STEAP3* mRNA levels were assessed in the control MCF-10A cell line and the MDA-MB-231, BT-549, and BT-468 TNBC cell lines. **(B, C)** STEAP3 levels were detected *via* Western immunoblotting in the MCF-10A, MDA-MB-468, and MDA-MB-231 cell lines and in six pairs of TNBC (T) and adjacent normal (N) tissue samples from patients. **(D)** Representative IHC staining results for STEAP3 in adjacent normal tissues (Scale bar: 100 μm) and TNBC samples (Scale bars:100μm and 50 μm), and non-TNBC(Luminal A) samples (Scale bar: 50μm). **(E)** Quantitative data from IHC staining results for *STEAP3* expression in 23 TNBC vs adjacent normal breast,12 non-TNBC vs adjacent normal breast and 23 TNBC vs 12 non-TNBC are shown. (**P<0.01, ***P< 0.001, ^{ns} P>0.05).

TABLE 2 Interactions between *STEAP3* with chemotherapy on OS of TNBC.

Variables	*β*	*S.E.*	*Wald*	*P*	*OR*	*95% C.I. for OR*
STEAP3	1.688	0.498	11.509	0.001	5.41	2.040-14.348
STEAP3 by chemotherapy	-0.729	0.180	16.418	<0.001	0.482	0.339-0.686

with ERK pathway inhibitors is linked to reduced TNBC cell proliferation (42, 43). Here, we found numerous small-molecule pathway inhibitor drugs were anticipated to be more successful in patients with higher levels of *STEAP3* expression, these findings may be useful for researchers and physicians contemplating the usage or selection of cytotoxic therapies to treat TNBC.

There are two key limitations to the present study. These analyses were primarily based on retrospectively analyzed data from public databases. As such, additional prospective multicenter verification will be essential. Accordingly, our centre's cell-based validation studies of sorafenib sensitivity, ferroptosis sensitivity and the functional experiments of *STEAP3* are currently being performed. Secondly, this

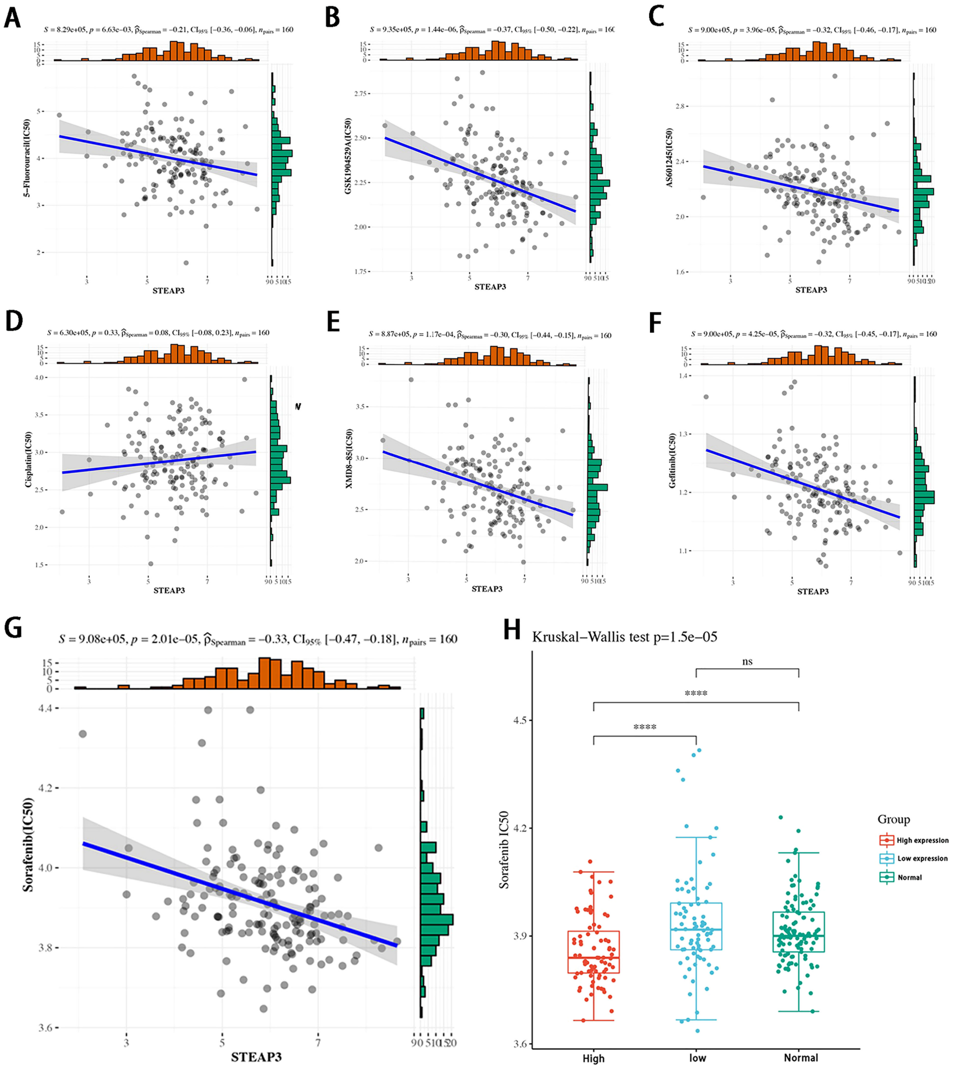

FIGURE 9
Correlations between STEAP3 expression and drug sensitivity in patients with TNBC. **(A-F)** The expression of STEAP3 and IC50 values correspond to 5–Fluorouracil, GSK1904529A, AS601245, XMD8–85, and Gefitinib in TNBC patients included in the TCGA-TNBC cohort (P < 0.05). **(G, H)** Correlations between *STEAP3* expression and Sorafenib IC50 values with further details regarding expression in the low, high, and normal groups (P<0.01). (****P< 0.0001, ns P>0.05).

study only focused on FRGs, and the relationships between these genes and other potentially relevant biomarkers were not assessed.

In conclusion, the unique FRG model developed here can be used to forecast the prognosis of TNBC patients. Future efforts to more reliably and successfully treat this lethal breast cancer subtype will be built on the realization that the altered expression of STEAP3 in these individuals may have ramifications for overall survival and therapeutic strategies.

Data availability statement

The datasets presented in this study can be found in online repositories. The names of the repository/repositories and accession number(s) can be found in the article/Supplementary Material.

Ethics statement

The studies involving human participants were reviewed and approved by Yuhuangding Hospital's Institutional Research Ethics Committee. The patients/participants provided their written informed consent to participate in this study.

Author contributions

LY, JL, LB, HQ and PS conceived, LY designed, analyzed the data and wrote the manuscript. JL and HQ revised the manuscript. LB participated in reviewing pathology. All authors read and approved the final manuscript. All authors contributed to the article and approved the submitted version.

Funding

This work was supported by Shandong Provincial Natural Science Foundation (ZR2021MH323) and Wu Jieping Medical Foundation (320.6750.2021-16-9).

Acknowledgments

We gratefully thank all members of the Central Laboratory of the Affiliated Yantai Yuhuangding Hospital of Qingdao University.

Conflict of interest

The authors declare that the research was conducted in the absence of any commercial or financial relationships that could be construed as a potential conflict of interest.

Publisher's note

Supplementary material

The Supplementary Material for this article can be found online at: https://www.frontiersin.org/articles/10.3389/fonc.2023.1032364/full#supplementary-material

References

1. Siegel RL, Miller KD, Fuchs HE, Jemal A. Cancer statistics 2022. *CA Cancer J Clin* (2022) 72:7–33. doi: 10.3322/caac.21708

2. Halbony H, Salman K, Alqassieh A, Albrezat M, Hamdan A, Abualhaija'a A, et al. Breast cancer epidemiology among surgically treated patients in Jordan: A retrospective study. *Med J Islam. Repub. Iran* (2020) 34:73. doi: 10.34171/mjiri.34.73

3. Daily K, Douglas E, Romitti PA, Thomas A. Epidemiology of *De novo* metastatic breast cancer. *Clin Breast Cancer* (2021) 21:302–8. doi: 10.1016/j.clbc.2021.01.017

4. Ezeome ER, Yawe KT, Ayandipo O, Badejo O, Adebamowo SN, Achusi B, et al. The African female breast cancer epidemiology study protocol. *Front Oncol* (2022) 12:856182. doi: 10.3389/fonc.2022.856182

5. Zhou Y, Yang J, Chen C, Li Z, Chen Y, Zhang X, et al. Polyphyllin-induced ferroptosis in MDA-MB-231 triple-negative breast cancer cells can be protected against by KLF4-mediated upregulation of xCT. *Front Pharmacol* (2021) 12:670224. doi: 10.3389/fphar.2021.670224

6. Wei Y, Zhu Z, Hu H, Guan J, Yang B, Zhao H. Eupaformosanin induces apoptosis and ferroptosis through ubiquitination of mutant p53 in triple-negative breast cancer. *Eur J Pharmacol* (2022) 924:174970. doi: 10.1016/j.ejphar.2022.174970

7. Yao X, Xie R, Cao Y, Tang J, Men Y, Peng H, et al. Simvastatin induced ferroptosis for triple-negative breast cancer therapy. *J Nanobiotechnolog* (2021) 19 (1):311. doi: 10.1186/s12951-021-01058-1

8. Ding Y, Chen X, Liu C, Ge W, Wang Q, Hao X, et al. Identification of a small molecule as inducer of ferroptosis and apoptosis through ubiquitination of GPX4 in triple negative breast cancer cells. *J Hematol Oncol* (2021) 14:19. doi: 10.1186/s13045-020-01016-8

9. Du J, Wang L, Huang X, Zhang N, Long Z, Yang Y, et al. Shuganning injection, a traditional Chinese patent medicine, induces ferroptosis and suppresses tumor growth in triple-negative breast cancer cells. *Phytomedicine* (2021) 85:153551. doi: 10.1016/j.phymed.2021.153551

10. Haffty BG, Yang Q, Reiss M, Kearney T, Higgins SA, Weidhaas J, et al. Locoregional relapse and distant metastasis in conservatively managed triple negative early-stage breast cancer. *J Clin Oncol* (2006) 24:5652–7. doi: 10.1200/JCO.2006.06.5664

11. Kassam F, Enright K, Dent R, Dranitsaris G, Myers J, Flynn C, et al. Survival outcomes for patients with metastatic triple-negative breast cancer: Implications for clinical practice and trial design. *Clin Breast Cancer* (2009) 9:29–33. doi: 10.3816/CBC.2009.n.005

12. Doval DC, Sharma A, Sinha R, Kumar K, Dewan AK, Chaturvedi H, et al. Immunohistochemical profile of breast cancer patients at a tertiary care hospital in new Delhi, India. *Asian Pac. J Cancer Prev* (2015) 16:4959–64. doi: 10.7314/APJCP.2015.16.12.4959

13. Galluzzi L, Humeau J, Buque A, Zitvogel L, Kroemer G. Immunostimulation with chemotherapy in the era of immune checkpoint inhibitors. *Nat Rev Clin Oncol* (2020) 17:725–41. doi: 10.1038/s41571-020-0413-z

14. Drago JZ, Modi S, Chandarlapaty S. Unlocking the potential of antibody-drug conjugates for cancer therapy. *Nat Rev Clin Oncol* (2021) 18:327–44. doi: 10.1038/s41571-021-00470-8

15. Singh DD, Parveen A, Yadav DK. Role of PARP in TNBC: Mechanism of inhibition, clinical applications, and resistance. *Biomedicines* (2021) 9:1512. doi: 10.3390/biomedicines9111512

16. Wu ZH, Tang Y, Yu H, Li HD. The role of ferroptosis in breast cancer patients: A comprehensive analysis. *Cell Death Discovery* (2021) 7:93. doi: 10.1038/s41420-021-00473-5

17. Cao X, Li Y, Wang Y, Yu T, Zhu C, Zhang X, et al. Curcumin suppresses tumorigenesis by ferroptosis in breast cancer. *PloS One* (2022) 17:e0261370. doi: 10.1371/journal.pone.0261370

18. Zhang J, Gao RF, Li J, Yu K, Bi K. Alloimperatorin activates apoptosis, ferroptosis and oxeiptosis to inhibit the growth and invasion of breast cancer cells in vitro. *Biochem Cell Biol* (2022) 100(3):213–22. doi: 10.1139/bcb-2021-0399

19. Tang W, Xu F, Zhao M, Zhang S. Ferroptosis regulators, especially SQLE, play an important role in prognosis, progression and immune environment of breast cancer. *BMC Cancer* (2021) 21:1160. doi: 10.1186/s12885-021-08892-4

20. Li H, Li L, Xue C, Huang R, Hu A, An X, et al. A novel ferroptosis-related gene signature predicts overall survival of breast cancer patients. *Biology (Basel)* (2021) 10 (2):151. doi: 10.3390/biology10020151

21. Jin LY, Gu YL, Zhu Q, Li XH, Jiang GQ. The role of ferroptosis-related genes for overall survival prediction in breast cancer. *J Clin Lab Anal* (2021) 35:e24094. doi: 10.1002/jcla.24094

22. Lee N, Carlisle AE, Peppers A, Pack SJ, Doshi MB, Spears ME, et al. xCT-driven expression of GPX4 determines sensitivity of breast cancer cells to ferroptosis inducers. *Antioxidants (Basel)* (2021) 10:317. doi: 10.3390/antiox10020317

23. Zeitler L, Fiore A, Meyer C, Russier M, Zanella G, Suppmann S, et al. Anti-ferroptotic mechanism of IL4i1-mediated amino acid metabolism. *Elife* (2021) 10: e64806. doi: 10.7554/eLife.64806

24. Stockwell BR. Ferroptosis turns 10: Emerging mechanisms, physiological functions, and therapeutic applications. *Cell* (2022) 185:2401–21. doi: 10.1038/nature10933

25. Brown CW, Amante JJ, Chhoy P, Elaimy AL, Liu H, Zhu LJ, et al. Prominin2 drives ferroptosis resistance by stimulating iron export. *Dev Cell* (2019) 51:575–586.e4. doi: 10.1016/j.devcel.2019.10.007

26. Yu M, Gai C, Li Z, Ding D, Zheng J, Zhang W, et al. Targeted exosome-encapsulated erastin induced ferroptosis in triple negative breast cancer cells. *Cancer Sci* (2019) 110:3173–82. doi: 10.1111/cas.14181

27. Livak KJ, Schmittgen TD. Analysis of relative gene expression data using real-time quantitative. PCR and the 2− ΔΔCT method. *Methods* (2001) 25(4):402–8. doi: 10.1006/meth.2001.1262

28. Shah SP, Roth A, Goya R, Oloumi A, Ha G, Zhao Y, et al. The clonal and mutational evolution spectrum of primary triple-negative breast cancers. *Nature* (2012) 486:395–9. doi: 10.1038/nature10933

29. The Cancer Genome Atlas Network. Comprehensive molecular portraits of human breast tumours. *Nature* (2012) 490:61–70. doi: 10.1038/nature11412

30. Li Z, Chen L, Chen C, Zhou Y, Hu D, Yang J, et al. Targeting ferroptosis in breast cancer. *biomark Res* (2020) 8:58. doi: 10.1186/s40364-020-00230-3

31. Wang LL, Luo J, He ZH, Liu YQ, Li HG, Xie D, et al. STEAP3 promotes cancer cell proliferation by facilitating. nuclear trafficking of EGFR to enhance RAC1-ERK-STAT3 signaling in hepatocellular carcinoma. *Cell Death Dis* (2021) 12:1–12. doi: 10.1038/s41419-021-04329-9

32. Lin HY, Ho HW, Chang YH, Wei CJ, Chu PY. The evolving role of ferroptosis in breast cancer: Translational implications present and future. *Cancers (Basel)* (2021) 13:4576. doi: 10.3390/cancers13184576

33. Han M, Xu R, Wang S, Yang N, Ni S, Zhang Q, et al. Six-transmembrane epithelial antigen of prostate 3. predicts poor prognosis and promotes glioblastoma growth and invasion. *Neoplasia* (2018) 20:543–54. doi: 10.1016/j.neo.2018.04.002

34. Machlenkin A, Paz A, Bar Haim E, Goldberger O, Finkel E, Tirosh B, et al. Human CTL epitopes prostatic acid. phosphatase-3 and six-transmembrane epithelial antigen of prostate-3 as candidates for prostate cancer immunotherapy. *Cancer Res* (2005) 65:6435–42. doi: 10.1158/0008-5472.CAN-05-0133

35. Wang D, Wei G, Ma J, Cheng S, Jia L, Song X, et al. Identification of the prognostic value of ferroptosis-related gene signature in breast cancer patients. *BMC Cancer* (2021) 21:645. doi: 10.1186/s12885-021-08341-2

36. Ye CL, Du Y, Yu X, Chen ZY, Wang L, Zheng YF, et al. STEAP3 affects ferroptosis and progression of renal cell. carcinoma through the p53/xCT pathway. *Technol Cancer Res Treat* (2022) 21:15330338221078728. doi: 10.1177/15330338221078728

37. Wu HT, Chen WJ, Xu Y, Shen JX, Chen WT, Liu J, et al. The tumor suppressive roles and prognostic values of STEAP. family members in breast cancer. *BioMed Res Int* (2020) 2020:9578484. doi: 10.1155/2020/9578484

38. Schmid P, Cortes J, Pusztai L, McArthur H, Kümmel S, Bergh J, et al. Pembrolizumab for early triple-negative breast cancer. *N Engl J Med* (2020) 382:810–21. doi: 10.1056/NEJMoa1910549

39. Schmid P, Rugo HS, Adams S, Schneeweiss A, Barrios CH, Iwata H, et al. Atezolizumab plus nab-paclitaxel as first-line treatment for unresectable, locally advanced or metastatic triple-negative breast cancer (IMpassion130): Updated efficacy results from a randomised, double-blind, placebo-controlled, phase 3 trial. *Lancet Oncol* (2020) 21:44–59. doi: 10.1016/S1470-2045(19)30689-8

40. Mito I, Takahashi H, Kawabata-Iwakawa R, Ida S, Tada H, Chikamatsu K. Comprehensive analysis of immune cell enrichment in the tumor microenvironment of head and neck squamous cell carcinoma. *Sci Rep* (2021) 11:1–9. doi: 10.1038/s41598-021-95718-9

41. Shi ZZ, Tao H, Fan ZW, Song SJ, Bai J. Prognostic and immunological role of key genes of ferroptosis in pan-cancer. *Front Cell Dev Biol* (2021) 9:748925. doi: 10.3389/fcell.2021.748925

42. Song X, Wang X, Liu Z, Yu Z. Role of GPX4-mediated ferroptosis in the sensitivity of triple. negative breast cancer cells to gefitinib. *Front Oncol* (2020) 10:597434. doi: 10.3389/fonc.2020.597434

43. You KS, Yi YW, Cho J, Seong YS. Dual inhibition of AKT and MEK pathways potentiates the. anti-cancer effect of gefitinib in triple-negative breast cancer cells. *Cancers* (2021) 13:1205. doi: 10.3390/cancers13061205

Frontiers in
Oncology

Advances knowledge of carcinogenesis and tumor progression for better treatment and management

The third most-cited oncology journal, which highlights research in carcinogenesis and tumor progression, bridging the gap between basic research and applications to imrpove diagnosis, therapeutics and management strategies.

Discover the latest Research Topics

See more →

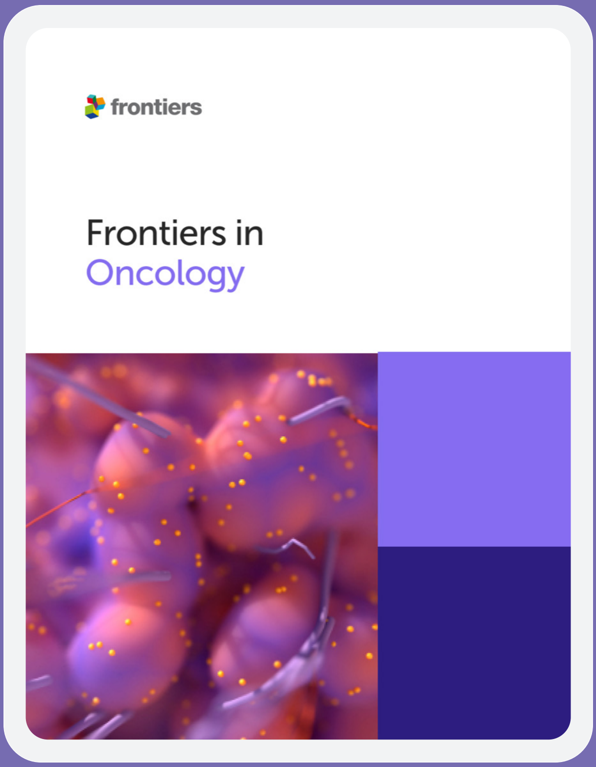

frontiers

Frontiers in
Oncology

Frontiers
Avenue du Tribunal-Fédéral 34
1005 Lausanne, Switzerland
frontiersin.org

Contact us
+41 (0)21 510 17 00
frontiersin.org/about/contact